Advancing the Understanding of Pathogenic Necroptotic Cell Death: Biomarker validation and Pathway Regulation Discovery in Immunity and Inflammatory Diseases

Doctoral thesis

for the award of the

doctoral degree

of the Faculty of Mathematics and Natural Sciences

of the **University of Cologne**

Konstantinos Kelepouras

from Athens, Greece

accepted in the year 2025

Abstract

Necroptosis is a regulated, lytic form of cell death that plays a pivotal role in inflammation and tissue damage, particularly in the context of impaired apoptotic signalling. While the molecular execution of necroptosis, mediated through RIPK3-dependent phosphorylation of MLKL, has been well defined *in vitro*, its *in vivo* relevance, regulation, and pathological outcomes have remained incompletely understood.

This thesis addresses a major technical gap by establishing and validating immunohistochemistry and immunofluorescence-based method to detect phosphorylated MLKL at serine 345 (pMLKL-S345) in murine tissues, enabling high-resolution spatial mapping of necroptotic activity *in vivo*. Applying this method across various inflammatory models, including SARS-CoV infection, Sharpin-deficient dermatitis and TNF-induced systemic inflammatory response syndrome (SIRS), this work demonstrates distinct patterns of tissue-specific necroptosis. This approach not only differentiates necroptosis from apoptosis at a cellular level but also provides a foundation for dissecting its mechanistic drivers in pathophysiological settings, without the necessity of complex genetic knockout models traditionally required to assess the involvement of necroptosis *in vivo*.

Building on this platform, this thesis investigates the upstream signalling mechanisms that trigger necroptosis in caspase-8 deficient epidermal keratinocytes (*Casp8$^{E\text{-}KO}$* mice). Loss of caspase-8 leads to the accumulation of cytosolic DNA, which activates the cGAS-STING pathway and induces a type I interferon transcriptional response. This STING-driven cascade upregulates key necroptotic effectors, notably ZBP1 and MLKL, while the combined effects of caspase-8 deficiency and aberrant STING activation promote the accumulation of Z-nucleic acids. Together, these events converge to induce ZBP1-MLKL-mediated necroptosis via formation of a ZBP1-RIPK1-RIPK3 signalling complex. Notably, this pathway functions independently of the canonical FADD-RIPK1-RIPK3 complex, enabling TNF/TNFR1-independent execution of necroptosis. Collectively, these findings position STING as a central inducer and amplifier of necroptosis, coordinating both ZBP1- and TNFR1-mediated checkpoints and acting as a critical upstream regulator of inflammatory necroptotic cell death.

Strikingly, this mechanism mirrors the pathogenesis observed in STING-associated vasculopathy with onset in infancy (SAVI), a severe human type I interferonopathy caused by gain-of-function mutations in the *STING1* gene. Comparative transcriptomic analysis between *Casp8$^{E\text{-}KO}$* mice and SAVI patients reveals a nearly identical necroptotic signature, implicating STING-induced necroptosis as a central pathological driver. This is further validated in a SAVI mouse model, where co-deletion of RIPK3 markedly rescues immune-driven tissue pathology. These findings establish STING-mediated necroptosis as a novel aetiological mechanism in both caspase-8-deficient inflammatory skin disease and SAVI, and identify this pathway as a potential therapeutic target in interferonopathies characterized by excessive necroptosis.

In summary, this thesis bridges fundamental mechanistic insights with translational relevance by delineating how aberrant STING activation orchestrates a necroptotic program that underlies severe inflammatory pathology. It also provides a validated framework for detecting and studying necroptosis *in vivo*, enabling future investigations into its role across diverse disease contexts.

Contents

Abbreviations i

I. Introduction 1

1. Tissue Homeostasis, Inflammation, and Cell Death 1

1.1. Tissue Homeostasis 1

1.2. Inflammation and Its Triggers 1

1.3. Cell Death in Homeostasis 2

1.4. Interplay between Cell Death and Inflammation 2

2. TNFR1 Signalling and Regulated Cell Death Pathways 3

2.1. The TNFR1 Signalling Hub 3

2.1.1. Overview of TNF and Its Receptors 3

2.1.2. TNFR1 Signal Transduction 3

2.1.2.1. TNFR1 Activation and Complex I Assembly 3

2.1.2.2. Recruitment of Kinase Complexes and NF-κB Activation 4

2.1.2.3. TBK1/IKKε Recruitment and Temporal Regulation 5

2.1.2.4. Regulation by Deubiquitinases 5

2.1.2.5. Complex I Destabilisation and Shift to Cell Death 5

2.2. Transition to Cell Death Signalling 7

2.2.1. Complex II formation 7

2.2.2. TNFR1-Mediated Apoptosis 8

2.2.3. Necroptosis: Molecular Machinery 9

2.2.3.1. Structure, Function and Regulation of MLKL 10

2.2.3.2. TNF/TNFR1-induced Necroptosis in Antiviral Immunity 12

2.2.3.3. TNF/TNFR1-induced Necroptosis in Sterile Inflammation 13

2.3. ZBP1-Mediated Necroptosis 16

2.3.1. Structure and Function of ZBP1 16

2.3.2. ZBP1 in Antiviral Immunity 17

2.3.3. ZBP1 in Autoimmunity and Sterile Inflammation 18

2.4. Non-Apoptotic Roles of caspase-8 in Genome Integrity 21

3. Nucleic Acid Sensing in Innate Immunity - The cGAS-STING Pathway 23

3.1. Cytosolic DNA Sensing in Innate Immunity 23

3.2. cGAS-STING Pathway: Activation and Signal Transduction 23

3.2.1. DNA Recognition via cGAS and cGAMP Production 24

3.2.1.1. Molecular Structure of cGAS and Mechanism of DNA Recognition 24

3.2.1.2. cGAMP Production 24

3.2.1.3. Self-Tolerance and Safeguards of cGAS ... 25
3.2.2. STING Activation and Trafficking ... 25
3.2.3. Downstream Signalling via TBK1, IRF3, and NF-κB ... 29
3.2.3.1. STING Palmitoylation and TBK1-IRF3 Axis Activation ... 29
3.2.3.2. IRF3 Transcriptional Activity and pLxIS Motif Conservation ... 30
3.2.3.3. STING-Mediated NF-κB and MAPK Pathway Activation ... 30
3.2.4. Ligands of the cGAS-STING Pathway ... 32
3.2.4.1. Pathogen-Derived DNA ... 32
i. Viruses ... 32
ii. Intracellular Bacteria ... 33
3.2.4.2. Self-DNA ... 34
i. Extracellular Self-DNA ... 34
ii. Mitochondrial DNA (mtDNA) ... 35
iii. Nuclear Genomic DNA and Micronuclei ... 36
iv. Endogenous Retroelements ... 37
4. Deregulation of STING in Disease ... 38
4.1. STING Hyperactivation and Interferonopathies ... 38
4.2. STING-Associated Vasculopathy with Onset in Infancy (SAVI) ... 41
5. STING and Cell Death ... 44
5.1. Emerging Links between STING and Cell Death ... 44
II. Publications ... 47
1. Publication 1 ... 47
2.Publication 2 ... 75
3.Publication 3 ... 124
III.Discussion ... 161
IV.References ... 173

Abbreviations

A20 Tumour necrosis factor alpha-induced protein 20
AGS Aicardi-Goutières syndrome
ADAR1 Deaminase acting on RNA 1
AIM2 Absent in melanoma 2
AKT AKT serine/threonine kinase
AP-1 Adaptor protein 1
ATM Ataxia telangiectasia mutated
ATR Ataxia telangiectasia and Rad3-related
ATP Adenosine triphosphate
AZI2 5-azacytidine-induced protein 2
BAF Barrier-to-autointegration factor
BAK Bcl-2 homologous antagonist/killer
BAX Bcl-2-like protein 4
BCL2 B-cell lymphoma 2
BCL-xL B-cell lymphoma-extra large
BID/tBID BH3-interacting domain death agonist / truncated BID
BLM Bloom syndrome helicase
BRCA Breast cancer
CCFs Cytoplasmic chromatin fragments
CDK Cyclin-dependent kinase
CDNs Cyclic dinucleotides
CHX Cycloheximide
CLPP Caseinolytic mitochondrial matrix peptidase proteolytic subunit
CTT C-terminal tail
cFLIP Cellular FLICE-like inhibitory protein
cGAMP Cyclic GMP-AMP
cGAS Cyclic GMP-AMP synthase
COPA Coatomer protein complex subunit alpha
Cre Causes recombination
CXCL C-X-C motif chemokine ligand
CYLD Cylindromatosis
DAI DNA-dependent activator of IFN-regulatory factors
DAMP Damage-associated molecular pattern
DDR DNA damage response
DD Death domain
DED Death effector domain
DMBA 7,12-Dimethylbenz[a]anthracene
DMEM Dulbecco's Modified Eagle Medium
DMSO Dimethyl sulfoxide
DNA Deoxyribonucleic acid
DNase Deoxyribonuclease
DR Death receptor
DSS Dextran sodium sulfate
dsDNA/dsRNA Double-stranded DNA/RNA
ER Endoplasmic reticulum
ERGIC ER-Golgi intermediate compartment
ERIS ER IFN stimulator
ERVK Endogenous retrovirus K
ESCRT Endosomal sorting complex required for transport
EV-A71 Enterovirus A71
EXO1 Exonuclease 1

FADD Fas-associated protein with death domain
FAS Fas receptor
FASL Fas ligand
FH Fumarate hydratase
FMDV Foot-and-mouth disease virus
G3BP1 GTPase-activating protein SH3 domain-binding protein 1
GSDMD Gasdermin D
GSDME Gasdermin E
GTP Guanosine triphosphate
HBV Hepatitis B virus
HIV Human immunodeficiency virus
HMGB1 High-mobility group box 1
HOIL-1 Heme-oxidized IRP2 ubiquitin ligase 1 homolog
HOIP HOIL-1 interacting protein
HSPCs Hematopoietic stem and progenitor cells
HSV Herpes simplex virus
ICP Infected cell protein
IAV Influenza A virus
IBD Inflammatory bowel disease
ICI Immune checkpoint inhibition
IF Immunofluorescence
IHC Immunohistochemistry
IEC-KO Intestinal epithelial cell-specific knock out
IFN Interferon
IFNAR Interferon alpha receptor
IFNGR Interferon gamma receptor
IKK Inhibitor of κB kinase
IL Interleukin
IR-Alus Inverted-repeat Alus
IRF Interferon regulatory factor
ISG Interferon-stimulated gene
ISREs Interferon-stimulated response elements
JAK Janus kinase
JNK c-Jun N-terminal kinase
LCD Lysosomal cell death
LDCP Lysosome-dependent pyroptosis
LINE Long interspersed nuclear element
LPS Lipopolysaccharide
LTR Long terminal repeat
LUBAC Linear ubiquitin chain assembly complex
M1 Methionine-1-linked ubiquitin chains
MAPK/MAP3K Mitogen-activated protein kinase / MAP kinase kinase kinase
MAVS Mitochondrial antiviral-signalling protein
MCMV Murine cytomegalovirus
MDA5 Melanoma differentiation-associated protein 5
MEF Mouse embryonic fibroblast
MERV Murine endogenous retrovirus
MIMP Mitochondrial inner membrane permeabilisation
MLKL Mixed lineage kinase domain-like protein
MK2 MAPK-activated protein kinase 2
MMTV Mouse mammary tumour virus
MOMP Mitochondrial outer membrane permeabilisation
mPTP Mitochondrial permeability transition pore
mtDNA Mitochondrial DNA
NAP1 Nuclear factor-associated protein 1

NAFLD Non-alcoholic fatty liver disease
NEMO NF-κB essential modulator
NET Neutrophil extracellular trap
NF-κB Nuclear factor kappa-light-chain-enhancer of activated B cells
NLR NOD-like receptor
NLRP3 NLR family pyrin domain containing 3
NONO Non-POU domain-containing octamer-binding protein
NPC1 Niemann-Pick type C1
NTase Nucleotidyltransferase
OTULIN OTU deubiquitinase with linear specificity
PAMP Pathogen-associated molecular pattern
PARP Poly(ADP-ribose) polymerase
PCD Programmed cell death
PCR Polymerase chain reaction
PKR Protein kinase R
Poly I:C Polyinosinic:polycytidylic acid
PQBP1 Polyglutamine-binding protein 1
PRR Pattern recognition receptor
PTMs Post-translational modifications
PUMA p53 upregulated modulator of apoptosis
RA Rheumatoid arthritis
RCD Regulated cell death
RHIM RIP homotypic interaction motif
RIG-I Retinoic acid-inducible gene I
RIPK Receptor-interacting serine/threonine kinase
RNA Ribonucleic acid
RNase Ribonuclease
ROS Reactive oxygen species
RPMI Roswell Park Memorial Institute medium
SARS-CoV Severe acute respiratory syndrome coronavirus
SAVI STING-associated vasculopathy with onset in infancy
SETDB1 SET domain bifurcated histone lysine methyltransferase 1
SHARPIN SHANK-associated RH domain interactor
SINE Short interspersed nuclear element
SIRS Systemic inflammatory response syndrome
SMOCs Supramolecular organizing centres
SNX9 Sorting nexin 9
SLE Systemic lupus erythematosus
SPATA2 Spermatogenesis-associated protein 2
ssRNA/ssDNA single-stranded RNA / DNA
STAT Signal transducer and activator of transcription
STEEP STING ER exit protein 1
STIM1 Stromal interaction molecule 1
STING Stimulator of interferon genes
TAB TAK1-binding protein
TAK1 TGF-β-activated kinase 1
TBK1 TANK-binding kinase 1
TFAM Mitochondrial transcription factor A
TLR Toll-like receptor
TNF Tumour necrosis factor
TNFR Tumour necrosis factor receptor
TP53 Tumour protein 53
TRADD TNFR1-associated via death domain
TRAF Tumour necrosis factor receptor-associated factor
TRIF TIR-domain-containing adapter-inducing interferon β

TRAIL TNF-related apoptosis-inducing ligand
TREX1 Three-prime repair exonuclease 1
TMD Transmembrane domain
TRX /TrxR Thioredoxin / Thioredoxin reductase
UBA1 Ubiquitin-activating enzyme 1
USP Ubiquitin-specific protease
VDAC Voltage-dependent anion channel
VSV Vesicular stomatitis virus
WNV West Nile virus
WT Wild type
YIPF5 Yip1 Domain Family Member 5
ZBP1 Z-DNA binding protein 1
Z-NAs Z-form nucleic acids

I. Introduction

1. Tissue Homeostasis, Inflammation, and Cell Death

1.1. Tissue Homeostasis

Tissue homeostasis is a dynamic and tightly regulated process that ensures the maintenance of cellular and functional equilibrium in multicellular organisms. It governs the balance between cell proliferation, differentiation and death, allowing tissues to preserve their structural integrity and adapt to physiological demands over time. This balance is essential not only during development and organogenesis but also throughout adult life, where tissues are continually exposed to diverse challenges, including mechanical, metabolic, and molecular perturbations, as well as environmental or pathogenic insults. The ability to respond appropriately to these challenges is central to organismal survival. Under steady-state conditions, homeostatic mechanisms maintain a constant turnover of cells, replacing aged or damaged ones without compromising tissue architecture[1]. Disruption of tissue homeostasis can arise from genetic mutation, infection, sterile injury, or from aberrant activation of stress and inflammatory signalling pathways, even in the absence of overt damage[2,3]. Both acute and chronic perturbations can destabilize this equilibrium, resulting in pathological outcomes such as hyperplasia, tissue atrophy, fibrosis, or cancer[2,3]. Thus, the preservation of functional tissue organisation relies on a finely tuned equilibrium between pro-survival and pro-death signals, enabling the prompt restoration of homeostasis following perturbation.

1.2. Inflammation and Its Triggers

Inflammation is a fundamental host response that can be triggered by tissue injury, infection, cellular stress, or by aberrant activation of gene activatory signalling even in the absence of overt damage[4]. It serves as a critical bridge between the disruption of homeostasis and the initiation of repair processes. Characterized by the infiltration of immune cells, the production of soluble mediators, and the activation of tissue-resident cells, inflammation plays multiple roles beyond eliminating harmful stimuli, including regulating tissue remodelling and coordinating repair. Initiation of inflammation can be triggered by a wide range of signals. These include pathogen-associated molecular patterns (PAMPs), derived from microbial invaders, and damage-associated molecular patterns (DAMPs), which are released from stressed or dying host cells. Both types of signals are detected by pattern recognition receptors (PRRs) expressed on or within immune, epithelial and stromal cells[5,6]. Once activated, these receptors initiate downstream signalling cascades that lead to the production of cytokines, chemokines, and antimicrobial peptides[4,7]. In barrier tissues such as the skin, gut, and lung, inflammation plays a particularly critical role in defending against environmental insults. Here, epithelial and stromal cells not only act as physical barriers but also contribute actively to immune surveillance and response. These cells secrete cytokines, chemokines and alarmins to recruit immune cells, promote tissue repair, and limit microbial invasion. Although inflammation is essential for the restoration of tissue integrity, it must be tightly regulated. Dysregulated inflammatory responses, whether transient or persistent, can compromise tissue homeostasis and lead to pathological outcomes such as tissue damage, fibrosis, or autoimmunity [8-10].

1.3. Cell Death in Homeostasis

Cell death is an integral component of tissue homeostasis, organismal defence, and development, ensuring the controlled elimination of damaged, infected, or superfluous cells. It allows tissues to maintain integrity, adapt to stress, and shape physiological processes during embryogenesis and beyond[11]. Cell death can be broadly categorized into non-regulated cell death (non-RCD) and regulated cell death (RCD)[12]. Non-RCD occurs in response to overwhelming physical or chemical stress and proceeds in an uncontrolled manner, whereas RCD is mediated by genetically encoded signalling pathways and responds to specific cellular and environmental cues.

RCD encompasses multiple modalities, each defined by distinct molecular mechanisms and distinct biological outcomes, collectively serving to eliminate compromised cells in a context-dependent manner (previously reviewed[13,14]). Briefly, extrinsic apoptosis is initiated by ligand-induced activation of death receptors such as FAS and TNFR, leading to activation of initiator caspase-8 and downstream effector caspases-3 and -7, resulting in orderly dismantling of the cell. Intrinsic apoptosis is induced by mitochondrial outer membrane permeabilisation (MOMP) and cytochrome c release, leading to apoptosome formation, activation of caspase-9 and downstream executioner caspases, with BCL-2 family proteins regulating the balance between pro-survival and pro-apoptotic signals. Necroptosis is executed by the activation of receptor-interacting protein kinases RIPK1 and RIPK3, with the latter phosphorylating and activating mixed lineage kinase domain-like protein (MLKL), causing plasma membrane permeabilisation. Pyroptosis is dependent on inflammasome activation and subsequent caspase-1 or caspase-11-mediated cleavage of gasdermins, which form membrane pores that lead to cell swelling and lysis. Ferroptosis is characterized by iron-dependent accumulation of lipid peroxides, typically triggered by inactivation of glutathione peroxidase 4 (GPX4) or depletion of glutathione, leading to oxidative damage of cellular membranes. Additional context-specific forms of RCD include parthanatos, induced by poly(ADP-ribose) polymerase 1 (PARP1) hyperactivation that promotes apoptosis-inducing factor (AIF) translocation and extensive DNA fragmentation; autophagy-dependent cell death, where excessive autophagic activity culminates in cellular demise; entosis, involving live cell engulfment and elimination by neighbouring cells; and NETosis, characterized by the release of neutrophil extracellular traps.

While the execution of these pathways varies, they all contribute to maintaining organismal integrity by eliminating compromised cells in a context-dependent manner. Understanding the regulation and consequences of different cell death modalities is crucial for deciphering how tissues respond to stress and how dysregulation contributes to inflammation, immune activation, and disease. In the context of this thesis, the focus is on extrinsic apoptosis and necroptosis, as these pathways are most relevant to the findings presented and provide a mechanistic framework for understanding how dysregulated cell death contributes to tissue pathology, inflammatory signalling, and disease progression.

1.4. Interplay between Cell Death and Inflammation

Cell death does not occur in isolation; it profoundly shapes the immune response and, in turn, is shaped by the surrounding inflammatory environment[15,16]. While traditionally seen as a resolution mechanism, cell death can act as a potent driver of inflammation, especially when cellular contents are released into the tissue microenvironment, as occurs during lytic forms of cell death such as necroptosis, pyroptosis, and NETosis[13,14,17-19]. Whether immune activation follows cell death or precedes it, depends on multiple factors, including the molecular context, tissue type, and efficiency of cell clearance[20]. Inadequate clearance or ongoing inflammatory cues can shift cell death from a silent process to one that amplifies immune activation. This bidirectional relationship between cell death and inflammation plays a decisive role in determining whether tissue integrity is restored or progressively compromised. A deeper understanding of this interplay is essential for uncovering how cell death and inflammation are coordinated, and will provide critical insight into the mechanisms driving chronic inflammation and autoimmunity[18,21].

A key mediator that integrates signals from both inflammatory cues and cell death pathways is tumour necrosis factor (TNF). Through its receptors, particularly TNFR1, TNF orchestrates a complex network of pro-survival, pro-inflammatory, and pro-death signalling events, making it a central hub in the regulation of tissue responses to stress and injury. Understanding TNFR1 signalling is therefore critical for elucidating how inflammatory stimuli and cell death pathways converge to influence tissue homeostasis and pathology.

2. TNFR1 Signalling and Regulated Cell Death Pathways

2.1. The TNFR1 Signalling Hub

2.1.1. Overview of TNF and Its Receptors

Tumour necrosis factor (TNF) is a pleiotropic cytokine that plays a central role in immune regulation, inflammation, and cell death[22-24]. It is rapidly induced upon infection, injury, or immune stimulation, and exerts its biological functions by engaging two receptors: TNF receptor 1 (TNFR1, also known as p55) and TNF receptor 2 (TNFR2, or p75). TNFR1 is ubiquitously expressed, while TNFR2 is largely restricted to immune and endothelial cells and signals with high efficacy primarily through membrane-bound TNF[25]. TNFR1, in contrast, responds to both membrane-bound and soluble TNF and is unique in its ability to mediate both pro-survival and pro-death signalling[25]. This dual capacity places TNFR1 at the centre of numerous physiological and pathological processes, including infection control, tissue repair, chronic inflammation, and cell death-driven disease.

2.1.2. TNFR1 Signal Transduction

2.1.2.1. TNFR1 Activation and Complex I Assembly

Engagement of tumour necrosis factor receptor 1 (TNFR1) by its ligand TNF triggers receptor trimerisation and a conformational change within its intracellular death domain (DD)[26]. This allows the sequential recruitment of adaptor and effector proteins that assemble into a membrane-bound signalling platform known as Complex I. This complex serves as the hub for the activation of transcriptional programs that support cell survival and inflammation.

The structural rearrangement in the DD domain of TNFR1, following its trimerisation, allows the recruitment of the adaptor protein TRADD (TNF receptor-associated death domain protein) and RIPK1 (receptor-interacting protein kinase 1) via homotypic DD interactions, as well as TNF receptor-associated factor 2 and 5 (TRAF2/5) and the E3 ubiquitin ligases cIAP1 and cIAP2 (cellular inhibitors of apoptosis proteins 1 and 2)[27-30]. At this stage, RIPK1 undergoes extensive post-translational modification. Specifically, cIAP1/2 mediate the conjugation of K63-linked polyubiquitin chains on RIPK1, while the linear ubiquitin chain assembly complex (LUBAC), comprising HOIL-1L, HOIP, and SHARPIN, adds linear methionine 1 (M1)-linked ubiquitin chains[27,31-33]. These ubiquitin scaffolds play a pivotal role in anchoring downstream signalling components that eventually lead to the assembly of Complex I.

2.1.2.2. Recruitment of Kinase Complexes and NF-κB Activation

The ubiquitinated scaffold recruits two major kinase modules. The first is the TAK1 (TGF-β-activated kinase 1) complex, composed of TAK1 and its regulatory adaptors TAB1 and TAB2/3[34]. This complex activates multiple downstream pathways, including MAP kinases such as JNK, p38, and ERK, which contribute to pro-inflammatory and stress responses. The second is the IκB kinase (IKK) complex, consisting of the catalytic subunits IKKα and IKKβ and the regulatory subunit NEMO (also known as IKKγ), which binds directly to M1-linked chains[35]. Upon activation by TAK1-mediated phosphorylation, the IKK complex phosphorylates the inhibitory proteins IκBα and IκBβ, which normally retain NF-κB dimers in the cytoplasm. Phosphorylated IκBα/β are ubiquitinated and degraded by the proteasome, thereby allowing NF-κB dimers (such as p65/RelA and p50) to translocate into the nucleus and initiate transcriptional activation of genes involved in inflammation (e.g., TNF, IL-6), cell survival (e.g., cFLIP, Bcl-xL), and immune modulation[36].

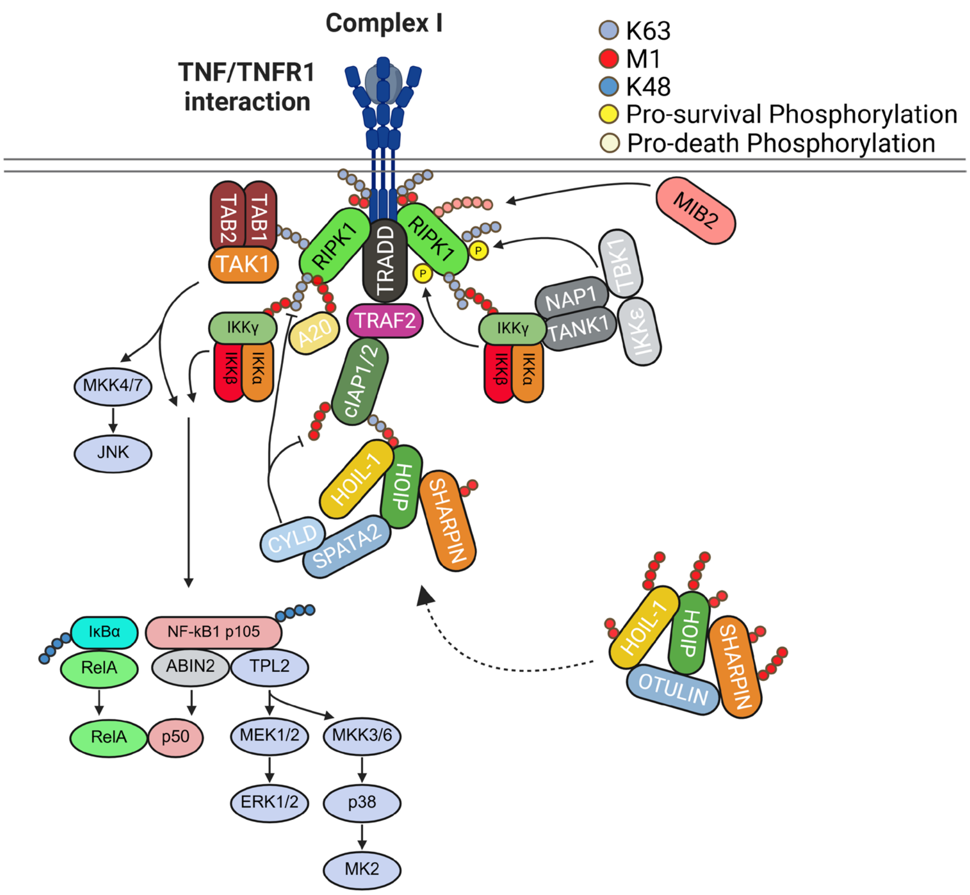

Figure 1. TNFR1 Activation and Complex I Assembly. *Engagement of TNF with TNFR1 induces receptor trimerisation and a conformational change in the intracellular death domain (DD), enabling sequential recruitment of adaptor and effector proteins to form membrane-bound Complex I. TRADD and RIPK1 are recruited via DD interactions, while TRAF2/5 and E3 ubiquitin ligases cIAP1/2 catalyse K63-linked polyubiquitination of TNFR1 intracellular part and RIPK1. The linear ubiquitin chain assembly complex (LUBAC; HOIL-1L, HOIP,*

SHARPIN) adds M1-linked ubiquitin chains, creating a scaffold for downstream signalling. Ubiquitin scaffolds recruit the TAK1 kinase complex (TAK1-TAB1-TAB2/3) to activate MAPKs (JNK, p38, ERK) and the IKK complex (IKKα/β-NEMO), which phosphorylates IκBs, leading to their degradation and nuclear translocation of NF-κB dimers (p65/RelA-p50) to drive transcription of inflammatory and pro-survival genes. Temporal recruitment of TBK1 and IKKε via TANK and NAP1/AZI2 fine-tunes transcriptional outputs. Deubiquitinases (CYLD, OTULIN, and A20) regulate ubiquitin scaffolds, ensuring controlled activation of NF-κB and modulating JNK/MAPK signalling, thereby maintaining the balance between cell survival and death. Created in BioRender, https://biorender.com/gfpc1mz.

2.1.2.3. TBK1/IKKε Recruitment and Temporal Regulation

An additional layer of complexity is introduced by TANK-binding kinase 1 (TBK1) and IKKε, which are recruited to Complex I through distinct mechanisms involving different adaptor proteins[37]. TANK1 binds directly to NEMO, leading to early-phase recruitment of TBK1 and IKKε to the TNFR1 signalosome. In contrast, AZI2 (also known as NAP1) is recruited in a delayed manner, typically dependent on the recruitment of the deubiquitinase A20 to M1-linked chains, which facilitates AZI2-dependent TBK1 and IKKε engagement[38]. This temporal regulation results in differential activation dynamics and contributes to the fine-tuning of downstream transcriptional programs, including those mediated by IRF3 and IRF7 in antiviral and interferon responses.

2.1.2.4. Regulation by Deubiquitinases

The integrity and duration of Complex I signalling are tightly regulated by the opposing actions of deubiquitinases. Cylindromatosis (CYLD), a deubiquitinase with specificity for K63- and M1-linked chains, is recruited to HOIP by spermatogenesis-associated protein 2 (SPATA2)[39-42]. This interaction allows CYLD to modulate the strength and duration of LUBAC-mediated signalling. Conversely, A20 is recruited to and protects M1-linked chains from CYLD-mediated degradation[43]. Additionally, OTULIN, which selectively cleaves linear ubiquitin chains, acts in a constitutive, LUBAC-associated manner to restrain excessive NF-κB activation by repressing LUBAC autoubiquitination[44,45]. These deubiquitination events function as molecular brakes that constrain excessive activatory signalling and inflammation and preserve the equilibrium between pro-survival and cell death signalling pathways.

2.1.2.5. Complex I Destabilisation and Shift to Cell Death

Collectively, the coordinated post-translational modifications and scaffold assemblies associated with TNFR1 facilitate the formation of a stable Complex I, which transduces context-dependent signals that promote cell survival and inflammatory responses under homeostatic conditions. Perturbations in Complex I stability can lead to disassembly of this complex and the subsequent formation of a cytotoxic, pro-death signalling platform, termed Complex II. The transition from Complex I to Complex II constitutes a critical cell-fate decision point that is tightly regulated by an array of molecular checkpoints embedded within Complex I. These checkpoints function to restrain aberrant activation of apoptotic and necroptotic pathways, ensuring that programmed cell death is initiated only under conditions that warrant it.

A central target of these checkpoints is RIPK1, which, in addition to its pro-survival scaffolding functions, can adopt a cytotoxic role as a “killer kinase” that promotes Complex II assembly following its enzymatic activation within Complex I[46]. The inhibition of RIPK1 kinase activity is primarily mediated by IKK kinases, including IKKα/β[47] but also TBK1/IKKε[48] which phosphorylate RIPK1 at Ser25[49]. These phosphorylation events inactivate RIPK1 kinase activity in a non-redundant manner, as ablation of any one of these kinases is sufficient to unleash RIPK1, promoting its incorporation into Complex II and predominantly triggering apoptosis[48,50,51]. Interestingly, although Ser25 phosphorylation prevents RIPK1 kinase activation, mutation of this site (S25A) alone is insufficient to induce RIPK1-mediated cytotoxicity following TNF stimulation[49]. This observation suggests that the inhibitory roles of IKKα/β and TBK1/IKKε on RIPK1 extend beyond Ser25 phosphorylation, potentially involving additional phosphorylation sites and/or complementary regulatory mechanisms.

Importantly, RIPK1 kinase inhibition is also controlled by the recruitment and activation of these kinases within Complex I which is critically dependent on ubiquitin chains and ubiquitin-binding adaptors. Disruption of these upstream regulators, such as deficiency of cIAP1/2 or LUBAC[27,32], mutation of the RIPK1 ubiquitin acceptor site Lys377 (Lys376 in mice)[52-56], or loss of NEMO[53,57], A20[43], or OTULIN[43-45], impairs kinase recruitment or activation, thereby indirectly compromising the IKK-dependent checkpoints. Similarly, inhibition of TAK1, which acts upstream of IKK activation, can destabilize the checkpoint machinery within Complex I[58]. Such perturbations shift the TNF response from a pro-survival program to RIPK1 kinase-dependent apoptosis and necroptosis, highlighting the tight integration of ubiquitin-dependent scaffolding, kinase activity, and checkpoint control in determining cell fate[13].

An additional layer of regulation is provided by the E3 ligase Mind Bomb-2 (MIB2), which selectively ubiquitylates RIPK1[59]. Unlike cIAPs or LUBAC, MIB2 does not influence NF-κB activation but specifically inhibits RIPK1's pro-apoptotic activity[59]. By conjugating inhibitory ubiquitin chains to residues such as K377, K604, and K634, MIB2 interferes with RIPK1 oligomerisation and its association with FADD, thereby limiting the transition from Complex I to Complex II[59]. Absence of MIB2 selectively converts TNF signalling from a predominant pro-survival signal into a death signal, highlighting its unique role in restraining RIPK1-mediated cytotoxicity without affecting upstream kinase activation[59].

Downstream of TAK1, MK2 provides an additional layer of regulation. MK2 phosphorylates RIPK1 at Ser320 and Ser335 (Ser321 and Ser336 in mice), which reduces RIPK1 activation in Complex I and therefore limits Complex II assembly[60-63]. Importantly, MK2 deficiency in mouse embryonic fibroblasts (MEFs) and bone marrow-derived macrophages (BMDMs) does not by itself switch TNF signalling toward cell death but rather, increases cytotoxicity only when one of the primary checkpoints is already compromised[60,62]. Thus, MK2 acts as a secondary protective mechanism, fine-tuning RIPK1 activity and reinforcing the overall checkpoint network.

Taken together, the integrated checkpoints within Complex I predominantly serve to restrain RIPK1 kinase activity and maintain pro-survival signalling. When these checkpoints are compromised, RIPK1 becomes enzymatically active and dissociates from the receptor-associated Complex I, triggering the nucleation of the cytotoxic platform, Complex II. This transition represents the molecular switch from TNFR1-mediated pro-survival and inflammatory signalling to regulated cell death.

2.2. Transition to Cell Death Signalling

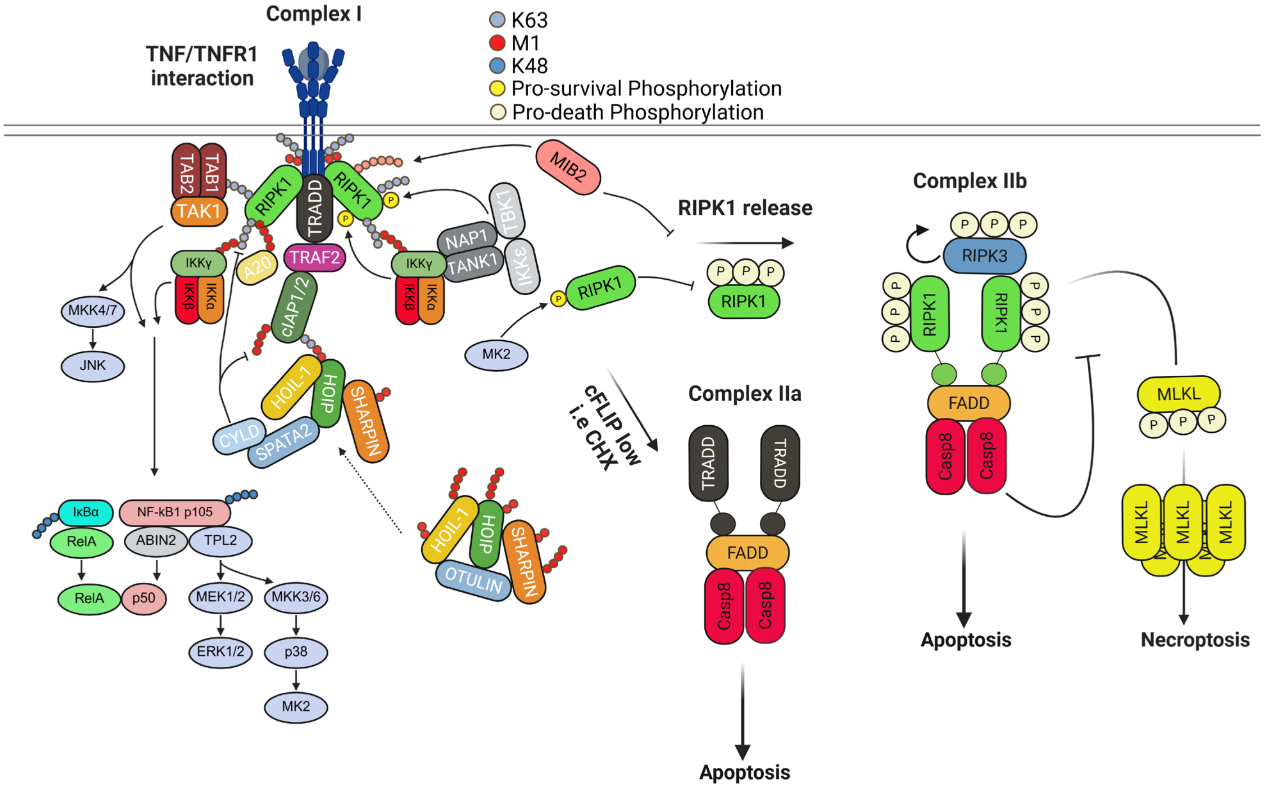

Figure 2. TNFR1 Complex I Destabilisation and Transition to Cell Death. *Under homeostatic conditions, TNFR1 signalling via Complex I promotes cell survival and inflammation. Perturbations in kinase checkpoints or ubiquitin scaffolds destabilize Complex I, allowing RIPK1 to adopt a cytotoxic role and nucleate cytosolic Complex II. Complex IIa forms in a RIPK1-independent manner, typically upon translation inhibition, initiated by TRADD recruitment, whereas Complex IIb forms in a RIPK1-dependent manner following its kinase activation. Both complexes recruit FADD and caspase-8 to drive apoptosis, with cFLIP isoforms modulating caspase-8 activity to fine-tune cell death. When caspase-8 is inhibited or absent, RIPK1 engages RIPK3 to form the necrosome, activating MLKL and triggering necroptosis. RIPK1 activity is restrained by phosphorylation (IKKα/β, TBK1/IKKε, MK2) and inhibitory ubiquitination (MIB2), collectively maintaining the balance between pro-survival, apoptotic, and necroptotic outcomes. Created in Biorender, https://BioRender.com/scpoow4.*

2.2.1. Complex II formation

In addition to their capacity to activate inflammatory gene programs through MAPK and NF-κB pathways, a subset of tumour necrosis factor receptor superfamily (TNFR-SF) members possess the unique ability to initiate regulated cell death. These so-called death receptors (DRs) include TNFR1, CD95 (also known as Fas/APO-1), death receptor 3 (DR3), and the two TNF-related apoptosis-inducing ligand (TRAIL) receptors: TRAIL-R1 (DR4) and TRAIL-R2 (DR5)[22,64]. A defining feature of these receptors is the presence of a cytoplasmic death domain (DD), which enables them to engage intracellular signalling cascades that culminate in apoptosis or, under specific conditions, necroptosis.

For TNFR1, the default signalling output is pro-survival and pro-inflammatory, mediated through the formation of membrane-bound Complex I. However, upon destabilisation of this complex, RIPK1 dissociates from the receptor-associated scaffold and nucleates the formation of a secondary cytotoxic platform, termed Complex II. This transition requires RIPK1 kinase activity, which promotes its autophosphorylation (e.g., at S166) following DD-mediated dimerisation[65-67]. Complex II assembly is further facilitated by CYLD-mediated degradation of M1- and K63-linked polyubiquitin chains[65-67] and by loss of inhibitory ubiquitylation mediated by MIB2[59], underscoring the critical integration of kinase activation and ubiquitin-dependent regulation in determining cell fate.

RIPK1 kinase-independent formation of Complex II typically occurs upon protein translation inhibition by cycloheximide (CHX) following TNF stimulation and is initiated by TRADD nucleation (typically referred to as Complex IIa)[68,69]. Regardless of whether Complex II is nucleated via RIPK1 (Complex IIb) or TRADD, the process culminates in the recruitment of the adaptor protein FAS-associated via death domain (FADD) through homotypic death domain interactions. FADD then recruits caspase-8 via death effector domain (DED) interactions, forming a cytosolic death-inducing complex capable of initiating apoptosis through caspase activation[70]. However, when caspase-8 activity is absent or inhibited, Complex IIb shifts from an apoptotic to a necroptotic output, engaging RIPK3 through RIPK1-RIPK3 RIP homotypic interaction motif (RHIM)-RHIM interactions, and ultimately leading to MLKL activation and necroptosis execution[71].

2.2.2. TNFR1-Mediated Apoptosis

Once Complex II is formed downstream of TNFR1, the cell's apoptotic machinery is engaged primarily through the activation of caspase-8. Within the cytosolic Complex II, caspase-8 is recruited via death effector domain (DED) interactions with FADD and undergoes dimerisation, which is a prerequisite for its proteolytic activation. This dimerisation can occur between caspase-8 monomers (homodimers) or between caspase-8 and its catalytically inactive paralog cellular FLICE-like inhibitory protein long isoform ($cFLIP_L$, heterodimers). The specific composition of the dimer critically determines the strength and duration of apoptotic signalling[72,73].

In the case of caspase-8 homodimers, dimerisation through the DEDs enables autocatalytic cleavage, generating the fully active subunits (p18 and p10) that assemble into the enzymatically active heterotetramer[74-76]. This active complex initiates the apoptotic cascade by cleaving downstream effector caspases such as caspase-3 and caspase-7. These effector caspases then target a wide array of substrates, including poly(ADP-ribose) polymerase (PARP), cytoskeletal proteins, and DNA repair enzymes, ultimately leading to chromatin condensation, membrane blebbing, and DNA fragmentation, hallmark features of apoptosis[77].

By contrast, when heterodimers form between caspase-8 and cFLIP isoforms, the outcome of dimerisation shifts toward regulation rather than full execution of apoptosis. The long isoform, $cFLIP_L$, closely resembles full-length pro-caspase-8 but lacks the active-site cysteine, rendering it catalytically inactive. Heterodimerisation with caspase-8 produces a complex with limited proteolytic activity, however, sufficient to inhibit apoptosis[72,74-76]. While caspase-8 homodimer is responsible for full-blown caspase-8 activation, caspase-8/$cFLIP_L$ heterodimers only transiently promote caspase-8 activity[72,74-76]. Nevertheless, this residual activity is sufficient to cleave RIPK1 and suppress its transition to necrosome and the subsequent activation of necroptosis. In contrast, the short isoforms, $cFLIP_S$ and $cFLIP_R$, consist solely of the two N-terminal DEDs and lack any catalytic or pseudo-catalytic domain, making them purely inhibitory. These short isoforms limit caspase-8 activation within cytosolic Complex II by incorporating into DED filaments and forming inactive heterodimers, thereby preventing full apoptotic signalling[78-80]. This mechanism ensures that caspase-8 activity is tightly controlled, restricting the initiation and propagation of the apoptotic cascade in response to TNFR1 stimulation.

cFLIP levels are regulated at the transcriptional and translational levels, adding another layer of control over caspase-8 activity. NF-κB-dependent transcription upregulates cFLIP as part of a cell death checkpoint. Owing to its short half-life, inhibition of protein translation with cycloheximide (CHX) reduces cFLIP abundance, lowering the threshold for caspase-8 activation within TNFR1 Complex IIa and facilitating apoptosis[68-70,81]. Conversely, maintenance or upregulation of cFLIP expression via NF-κB-dependent transcription protects cells from TNF family ligand-induced apoptosis, emphasizing the critical role of dynamic cFLIP levels in controlling cell fate.

While TNFR1-induced apoptosis is classified within the extrinsic apoptosis pathway, initiated through receptor-mediated activation of caspase-8, it frequently exhibits crosstalk with the intrinsic (mitochondrial) pathway under specific cellular contexts. For instance, caspase-8 cleaves the BH3-only protein BID, generating truncated BID (tBID), which translocates to the mitochondria to promote mitochondrial outer membrane permeabilisation (MOMP) and cytochrome c release[82]. This amplification loop engages the intrinsic caspase cascade, including caspase-9 activation, thereby intensifying the apoptotic signal. A key regulator of caspase-9 and the executioner caspases-3 and -7 is X-linked inhibitor of apoptosis protein (XIAP), which directly binds and inhibits these caspases[83]. However, XIAP does not inhibit caspase-8, and although executioner caspases are shared between intrinsic and extrinsic pathways, the relevance of XIAP in TNFR1-mediated apoptosis remains suggestive, largely restricted to Fas[84] or TRAIL[85] -driven apoptosis.

Thus, TNFR1-mediated apoptosis is a highly regulated, context-dependent process that integrates multiple checkpoints to determine cell fate. The outcome of Complex II engagement depends on the interplay between caspase-8 activation, cFLIP isoform expression, and the availability of downstream apoptotic effectors. This multilayered regulation ensures that cells respond appropriately to TNFR1 stimulation, balancing the need for controlled cell clearance with the preservation of tissue integrity and the modulation of inflammatory signalling.

2.2.3. Necroptosis: Molecular Machinery

In contrast to apoptosis, necroptosis is a lytic form of regulated cell death that becomes activated when caspase-8 function is compromised. Inhibition of caspase-8 catalytic activity[86,87] or its complete deletion[88,89], as well as genetic ablation of cFLIP or its adaptor protein FADD[81,87,89,90], prevents the proteolytic cleavage of RIPK1 at D325[91,92]. As a result, RIPK1 is no longer inactivated and instead engages receptor-interacting protein kinase 3 (RIPK3) through RIP homotypic interaction motif (RHIM)-RHIM interactions, triggering the assembly of a secondary, hetero-amyloid complex known as the necrosome. In contrast, caspase-8-mediated cleavage of RIPK3 at D333, CYLD at D215, or cFLIP at D371/D377 or loss of caspase-8 self-cleavage (D212A/D218A/D225A/D387A) is dispensable for necroptosis prevention[91-94], highlighting the non-redundant and central role of RIPK1 cleavage in suppressing this form of cell death. Interestingly, heterozygous missense mutations D324N, D324H and D324Y that prevent RIPK1 cleavage in humans, causes cleavage-resistant RIPK1-induced autoinflammatory (CRIA) syndrome driven by both RIPK1-kinase dependent aberrant apoptosis and necroptosis[92].

This multimeric complex serves as the platform for RIPK3 activation, a process that involves trans-autophosphorylation of its kinase domain (e.g., Thr231/Ser232 in mouse[95], Ser227 in human[96]), resulting in conformational stabilisation and full kinase activation. Activated RIPK3 subsequently phosphorylates the pseudokinase mixed lineage kinase domain-like protein (MLKL) at conserved serine/threonine residues (e.g., Ser345 in mouse[97], Thr357/Ser358 in human[96]). These post-translational modifications promote MLKL oligomerisation and its translocation to the plasma membrane via its N-terminal four-helix bundle (4HB) domain, a structural motif that binds to specific phospholipids in the inner leaflet of the membrane[98].

Once at the membrane, oligomerised MLKL disrupts membrane integrity, either by forming pores or by interfering with membrane homeostasis, leading to ionic imbalance, osmotic swelling, and eventual plasma membrane rupture[98]. However, this step is not necessarily immediate. The endosomal sorting complexes required for transport (ESCRT) machinery can be recruited to sites of MLKL-induced damage, where it facilitates membrane repair by shedding damaged membrane regions in the form of extracellular vesicles[99-101]. This transient repair mechanism can delay cell lysis and buffer against premature necroptotic death, but it cannot fully prevent necroptosis once the death program is engaged. Accordingly, silencing ESCRT components sensitizes cells to necroptosis, indicating that the ultimate cellular outcome depends on the dynamic balance between ongoing membrane damage and the efficacy of repair[100,101].

Necroptosis culminates in a distinct set of morphological features that clearly differentiate it from apoptosis. Instead of nuclear condensation or apoptotic body formation, necroptotic cells display organelle swelling, cytoplasmic granularity, and the uncontrolled leakage of intracellular contents. Among these contents are danger-associated molecular patterns (DAMPs) such as HMGB1, ATP, and extracellular DNA, which act as potent activators of innate immunity and drive inflammation and immune cell recruitment[102]. By releasing these inflammatory mediators, necroptosis serves as a backup form of regulated cell death when apoptosis is impaired, amplifying inflammation in host defence and sterile inflammation.

2.2.3.1. Structure, Function and Regulation of MLKL

MLKL is composed of two functional domains: an N-terminal four-helix bundle domain (4HBD) and a pseudokinase domain (PSKD), connected by a brace domain of two α-helices[103,104]. The 4HBD is essential for necroptosis execution, as the forced expression of a dimerisable 4HBD induces cell death independently of necroptotic stimuli[105,106], suggesting that post-translational modifications expose the 4HBD to form oligomeric structures that execute membrane permeabilisation[97,106-109]. The PSKD, although catalytically inactive, mediates binding to RIPK3 and allows RIPK3-dependent phosphorylation, which functions as a molecular switch releasing the 4HBD for oligomerisation and membrane translocation[103,107,110].

Species-specific differences exist between human and mouse MLKL. In mouse, phosphorylation of S345 disrupts a K219-Q343 hydrogen bond, which is sufficient to activate MLKL, whereas in human, T357/S358 phosphorylation, coupled with RIPK3 binding, is required to reach a closed-active-like conformation[111]. MLKL then oligomerises in the cytoplasm via the 4HBD before translocating to the membrane, where it binds specific phospholipids (PIPs or cardiolipin) to destabilize the membrane and induce necroptotic cell death[107,112-114].

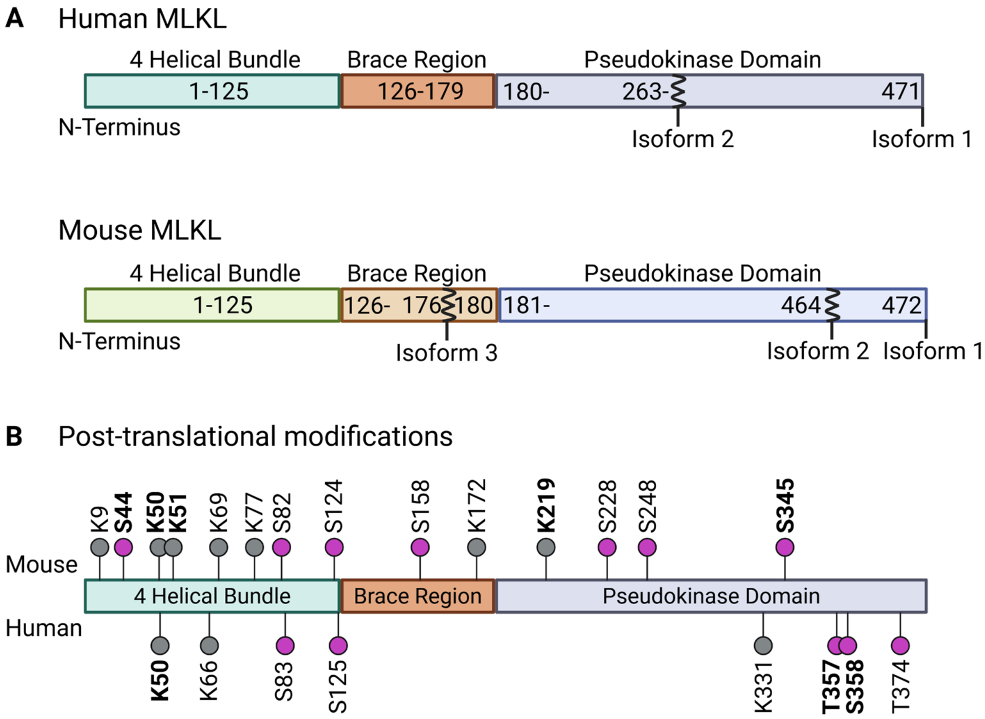

Figure 3. Domain organisation and post-translational modifications of MLKL. *(**A**) MLKL contains a four-helix bundle (4HB, aa 1-125), a brace region, and a pseudokinase domain (aa 180-471 in human, 181-472 in mouse). (**B**) Reported phosphorylation sites are shown as purple circles, including RIPK3-mediated phosphorylation at T357/S358 in human and S345 in mouse. Grey circles mark ubiquitination sites on lysine residues. Sites with defined functions are highlighted in bold. Created in BioRender, https://BioRender.com/kjuj9vl.*

MLKL is extensively regulated by post-translational modifications, notably phosphorylation and ubiquitination. While RIPK3-mediated phosphorylation on T357/S358 or S345 of human or mouse MLKL respectively is essential for necroptosis execution, additional residues, including S124, S158, S228, S248, S82 in mouse, or S125, T374, Y376 and S83 in human, fine-tune its activity[105,115-117]. MLKL undergoes ubiquitination at multiple sites (e.g., K219, K50, K77, K172), which can either promote oligomerisation and killing, target MLKL for degradation, or facilitate endosomal trafficking for cell-death independent antibacterial functions[111]. These observations suggest that different pools of MLKL, localized to distinct cellular compartments, are regulated by context-dependent ubiquitination to control the extent, timing, and localisation of necroptotic signalling.

Overall, MLKL activity is tightly controlled by a combination of structural features, post-translational modifications, and species-specific regulatory mechanisms, ensuring precise execution of necroptosis. However, despite extensive advances in understanding MLKL structure, regulation, and post-translational modifications, a critical limitation persists, the inability to detect necroptosis-associated phosphorylated MLKL *in situ* in tissues. Such capability would provide unprecedented mechanistic insight into the execution of necroptosis across different organs and pathological contexts, surpassing the current reliance on complex genetic models, such as RIPK3- or MLKL-deficient mice, which are labour-intensive and limited in physiological relevance. Reliable *in situ* detection of activated MLKL would not only refine understanding of necroptotic mechanisms but could also reveal previously unrecognized roles of MLKL in tissue homeostasis, inflammation, and disease.

2.2.3.2. TNF/TNFR1-induced Necroptosis in Antiviral Immunity

Necroptosis is widely considered to have evolved as an innate immune mechanism to counteract pathogens capable of inhibiting apoptosis[118,119]. The capacity of host cells to initiate necroptotic cell death and limit viral replication has, in turn, imposed evolutionary pressure on viruses, promoting the emergence of pathogen-specific strategies to evade necroptosis[120]. Many viruses can temporally modulate necroptosis, either inhibiting it to optimize replication or exploiting MLKL-induced cell lysis to facilitate viral egress. Some viruses that inhibit necroptosis in human cells may conversely induce it in mouse cells, underscoring the strong evolutionary co-adaptation of host MLKL and RIPK3[118,119].

MLKL involvement in viral infection can be divided into two categories: RIPK3-mediated activation (e.g., Vaccinia virus, Cytomegalovirus, Influenza virus) and direct viral targeting of MLKL (e.g., BeAn 58058 poxvirus (BAV), Cotia Poxvirus (COTV), human CMV UL36)[121,122]. The majority of studies on necroptosis in viral infection have focused on RIPK3, largely due to the prior absence of MLKL-deficient models or the later recognition of MLKL as the executioner of necroptosis. Notably, *Mlkl* mRNA is strongly upregulated during inflammation, particularly via type I and II interferon signalling, whereas *Ripk3* mRNA can be induced in certain infections independently of interferon, via promoter demethylation[123-126]. This differential regulation suggests that MLKL and RIPK3 may have partially independent roles in antiviral responses and inflammation.

A prototypical example is Vaccinia virus (VV), which induces TNF production and, by inhibiting caspases through the viral caspase inhibitor B13R, activates RIPK3- and MLKL-dependent necroptosis[86,118]. This necroptosis-driven inflammatory response is protective for the host, as both RIPK3-deficient mice and mice expressing the kinase-inactive RIPK1 D138N mutant succumb to VV infection, whereas wild-type mice mount effective antiviral immunity[118,127].

Several other viruses have evolved mechanisms to directly target MLKL. Poxviruses such as BAV and COTV express truncated MLKL homologues containing only the pseudokinase domain (PSKD), which act as decoy substrates for RIPK3 phosphorylation, preventing host MLKL activation and necroptosis execution[121]. Human CMV, in contrast, expresses the early-regulated IE1 element, which inhibits cell death downstream of MLKL phosphorylation, though the precise mechanism remains unclear[128]. Additionally, the UL36 protein targets MLKL for degradation in human cells, further emphasizing that MLKL itself represents a critical evolutionary target during infection[122].

These findings underscore the complex evolutionary interplay between viruses and host necroptotic machinery. While MLKL can be regulated directly or indirectly via RIP3 kinase, most viruses trigger necroptosis predominantly through ZBP1-mediated sensing rather than TNF/TNFR1 signalling, as discussed in the next section. This pattern suggests that evolutionary pressure has rendered many viruses resistant to TNF-induced necroptosis, prompting the host to develop ZBP1 as a backup sensor to detect and counteract viral evasion. Consequently, TNF/TNFR1-induced necroptosis appears to play a relatively limited role in antiviral immunity, whereas ZBP1-driven pathways serve as a critical alternative. In certain contexts, viruses may even exploit ZBP1-mediated pathways to enhance viral dissemination, highlighting that MLKL's contributions to host defence are highly context-dependent and determined by the upstream sensing mechanisms engaged during infection.

2.2.3.3. TNF/TNFR1-induced Necroptosis in Sterile Inflammation

While the contribution of TNF/TNFR1-induced necroptosis to antiviral immunity appears limited, its inflammatory potential becomes evident in experimental models of sterile inflammation. Unlike infection settings, where ZBP1 sensing predominates, TNF-driven necroptosis is typically engaged when the apoptotic machinery is genetically ablated or functionally inhibited. Under physiological conditions, apoptosis represents the default form of TNF-induced cell death, while necroptosis is actively suppressed. Central to this suppression is the FADD-caspase-8-FLIP axis, which prevents RIPK1-RIPK3-dependent necroptosis from being triggered downstream of TNFR1[13].

The non-apoptotic role of caspase-8 was revealed by genetic studies showing that germline deletion of *Casp8*[129], *Fadd*[130], or *Cflip*[131] resulted in embryonic lethality at E10.5 accompanied by excessive cell death. The phenotype in *Casp8*$^{-/-}$ and *Fadd*$^{-/-}$ mice was attributed to defects in vascularisation of the yolk sac and was fully rescued by concurrent deletion of *Ripk3*[81,87,88] or *Mlkl*[89], demonstrating that lethality arises from unrestrained necroptosis. Conditional deletion of *Casp8*[132] or *Fadd*[133] in endothelial cells, reproduced the embryonically lethal phenotype, implicating endothelial necroptosis as the proximate cause. Similarly, tissue-specific ablation of *Casp8* or *Fadd* in the skin or intestinal epithelium likewise provokes RIPK3-MLKL-dependent necroptosis and inflammation[134-141]. In the intestinal epithelium specifically, caspase-8 deficiency causes RIPK3-MLKL-dependent colitis and ileitis, whereas in *FADD*$^{IEC\text{-}KO}$ mice, colitis was necroptosis-driven and ileitis depended partially on necroptosis and, to a lesser extent, gasdermin D-mediated cell death[141], highlighting an additional layer of crosstalk between caspase-8 and distinct regulated cell death pathways beyond apoptosis. On the other hand, genetic ablation of necroptosis alone via RIPK3 or MLKL deletion does not impair viability, although MLKL loss has recently been implicated in protecting from age-related chronic sterile inflammation in female mice[142]. Embryonic lethality occurs only when RIPK3 kinase activity is inactivated, which unleashes caspase-8-mediated apoptosis partly dependent on RIPK1, underscoring a mechanistic distinction between RIPK3's kinase activity and its RHIM-dependent scaffolding function[143]. However, the precise role of kinase-independent RIPK3 functions remains largely unresolved, as other mutations that abolish ATP-binding site residues, such as K51A, D161G, and D143N, do not induce apoptosis, and mice harbouring these mutations remain viable and fertile[144,145].

Interestingly, even though necroptosis inhibition prevents caspase-8- or *Fadd*-deficiency-driven lethality, mice lacking both apoptotic and necroptotic arms (*Casp8*$^{-/-}$ or *Fadd*$^{-/-}$ with *Ripk3*$^{-/-}$ or *Mlkl*$^{-/-}$ or *Cflip*$^{-/-}$ *Casp8*$^{-/-}$ *Ripk3*$^{-/-}$ mice), develop splenomegaly and an autoimmune lymphoproliferative-like syndrome (ALPS)[81,87-89]. These phenotypes are characterized by expansion of autoreactive lymphocytes, including $CD3^+$ $B220^+$ T cells, reflecting caspase-8-dependent defects in Fas (CD95) death receptor signalling that impair lymphoid lineage homeostasis due to the failure to undergo cell death[146-148]. Interestingly, RIPK3 loss provides a greater survival benefit to *Casp8*$^{-/-}$ or *Fadd*$^{-/-}$ mice than MLKL loss, suggesting additional necroptosis-independent functions of RIPK3 that contribute to lymphadenopathy, autoimmunity, and cytokine dysregulation[89].

Structure-function studies further highlight non-apoptotic functions of caspase-8. Mice expressing oligomerisation-deficient (F122G and L123G) or non-cleavable caspase-8 (D387 or D212A/D218A/D225A/D387A) survive to adulthood despite apoptotic resistance, indicating that uncleaved caspase-8, particularly in heterodimers with cFLIP, is sufficient to suppress RIPK3-dependent necroptosis without initiating apoptosis[91,92,149,150]. By contrast, embryonic lethality of *Cflip*$^{-/-}$ mice is rescued only by combined deletion of *Ripk3* and *Fadd*, reflecting cFLIP's role in constraining both apoptotic and necroptotic signalling[81]. Additionally, catalytically inactive caspase-8 (C362S) causes embryonic lethality by inducing both MLKL-driven necroptosis and ASC-Casp1-mediated pyroptosis[151], indicating another intricate crosstalk of non-apoptotic caspase-8 functions in regulating pyroptotic cell death.

Subsequent studies identified RIPK1 as a central checkpoint restraining both apoptosis and necroptosis[13,33]. Although RIPK1 deficiency alone appears to rescue the embryonic lethality of *Casp8*$^{-/-}$ or *Fadd*$^{-/-}$ mice, still the double-deficient mice (*Casp8*$^{-/-}$ or *Fadd*$^{-/-}$ *Ripk1*$^{-/-}$) succumb at the survival endpoint of RIPK1-deficient mice[90,152-154]. Thus, *vice versa*, deficiency of *Casp8*, *Fadd*, or even *Ripk3* alone does not rescue the perinatal lethality of *Ripk1*$^{-/-}$ mice, but only combined ablation of both caspase-8 (or FADD) and RIPK3 fully prevents it[143-145]. Mechanistically, RIPK1 protects intestinal epithelial cells predominantly from caspase-8-mediated apoptosis and keratinocytes from RIPK3-dependent necroptosis[155,156]. This function is independent of its kinase activity, as RIPK1 catalytically inactive mice (D138N or K45A) develop normally[127,157]. By contrast, *Tnfr1* deficiency only partially prolongs survival of *Casp8*$^{-/-}$ or *Fadd*$^{-/-}$ embryos (E17.5)[152,154] and tissue-specific caspase-8 or FADD deletion is only incompletely rescued by TNF or TNFR1 deficiency[135,138,139]. These findings suggest the involvement of TNFR1-independent but RIPK3-dependent necroptotic pathways. Interestingly, while *Tnfr1* or *Tnf* loss alone does not or only incompletely rescue *Ripk1*$^{-/-}$ lethality, triple deficiency (*Ripk1*$^{-/-}$ *Tnfr1*$^{-/-}$ *Ripk3*$^{-/-}$) improves survival, though not to the extent observed in *Ripk1*$^{-/-}$ *Casp8*$^{-/-}$ *Ripk3*$^{-/-}$ mice, suggesting that caspase-8 activation contributes to the perinatal lethality of *Ripk1*$^{-/-}$ *Ripk3*$^{-/-}$ mice predominantly downstream of TNFR1, potentially involving additional regulation by other death receptors, members of the TNFRSF[152-154,158]. In line with this, TRADD partially contributes to this effect, as *Tradd* deletion in *Ripk1*$^{-/-}$ *Ripk3*$^{-/-}$ mice reduces systemic cell death and inflammation, ameliorates intestinal and thymic pathology, and delays early lethality, though not to the same extent as *Ripk1*$^{-/-}$ *Tnfr1*$^{-/-}$ *Ripk3*$^{-/-}$ (or *Ripk1*$^{-/-}$ *Casp8*$^{-/-}$ *Ripk3*$^{-/-}$) mice[159], suggesting that caspase-8 activation occurs also beyond TRADD regulation.

At the time, the mechanism by which RIPK3 could be activated in the absence of RIPK1 remained unclear, with evidence implicating TLR3/TRIF-, TLR4/MyD88-, and type I/II interferon-mediated pathways[152,154]. Similarly, loss of caspase-8, and to a lesser extent FADD, was associated with type I interferon responses and inflammatory signalling independently of necroptosis[134,160-162]. This suggested that TNFR1-independent activation of RIPK3 could be mediated by other immune receptors, potentially linking interferon responses to the RIPK3-MLKL necroptotic axis. More recent work has helped resolve this paradox by identifying an interferon-stimulated gene, ZBP1, as a sensor capable of activating RIPK3 and MLKL-dependent necroptosis independently of RIPK1[163,164], an aspect that will be discussed in detail in the following section. However, despite this discovery, it remains unclear how the loss of caspase-8, FADD, or RIPK1 leads to the type I interferon responses required to induce ZBP1 expression, leaving the connection between these cell death-regulatory proteins and interferon signalling unresolved.

<table>
<tr><th rowspan="2">Genotype</th><th rowspan="2">Phenotype</th><th colspan="2">Restored phenotype</th></tr>
<tr><th>Partial</th><th>Complete</th></tr>
<tr><td>Casp8$^{-/-}$
or
Fadd$^{-/-}$</td><td>Embryonic lethality at E10.5; yolk sac vascularisation defects; excessive cell death.</td><td>Tnfr1$^{-/-}$ (~E17.5).</td><td>Ripk3$^{-/-}$, Mlkl$^{-/-}$ (develop splenomegaly and ALPS in adulthood).</td></tr>
<tr><td>Cflip$^{-/-}$</td><td>Embryonic lethality at E10.5; yolk sac vascularisation defects; excessive cell death.</td><td>-</td><td>Ripk3$^{-/-}$Fadd$^{-/-}$(develop splenomegaly and ALPS in adulthood).</td></tr>
<tr><td>Cflip$^{D371/D377}$</td><td>Viable</td><td>-</td><td>-</td></tr>
<tr><td>Mlkl$^{-/-}$</td><td>Viable</td><td>-</td><td>-</td></tr>
<tr><td>Ripk3$^{-/-}$</td><td>Viable</td><td>-</td><td>-</td></tr>
<tr><td>Ripk3$^{D333A/D333A}$</td><td>Viable</td><td>-</td><td>-</td></tr>
<tr><td>Ripk3$^{D161N/\ D161N}$</td><td>Embryonic lethal (E11.5).</td><td>Casp8$^{+/-}$ (E15.5), Ripk1$^{+/-}$ (E18.5), Ripk1$^{-/-}$ (perinatal lethality).</td><td>Casp8$^{-/-}$ (develop splenomegaly and ALPS in adulthood).</td></tr>
<tr><td>Ripk3$^{K51A/K51A}$
or
Ripk3$^{D161G/D161G}$
or
Ripk3$^{D143N/\ D143N}$</td><td>Viable.</td><td>-</td><td>-</td></tr>
<tr><td>Casp8$^{F122GL123G/F122GL123G}$
or
Casp8$^{D387A/D387A}$</td><td>Viable.</td><td>-</td><td>-</td></tr>
<tr><td>Casp8$^{C362S/\ C362S}$

(or Casp8$^{C362A/C362A}$)</td><td>Embryonic lethality at E11.5; yolk sac vascularisation defects; excessive cell death.</td><td>Mlkl$^{-/-}$ (perinatal lethality).</td><td>Ripk3$^{-/-}$, Mlkl$^{-/-}$Casp1$^{-/-}$, Mlkl$^{-/-}$Asc$^{-/-}$ (develop splenomegaly and ALPS in adulthood).</td></tr>
<tr><td>Casp8$^{D387A/\ D387}$
or
Casp8$^{D212A/D218A/D225A/D387A}$</td><td>Viable.</td><td>-</td><td>-</td></tr>
<tr><td>Ripk1$^{-/-}$</td><td>Perinatal lethality; systemic cell death.</td><td>Tnfr1$^{-/-}$, Tnf$^{-/-}$Fasl$^{-/-}$, Fadd$^{-/-}$, Casp8$^{-/-}$, Tradd$^{-/-}$, Triff$^{-/-}$, Ifnar$^{-/-}$ (perinatal lethality), Ripk3$^{-/-}$, Mlkl$^{-/-}$, Myd88$^{-/-}$ (P4), Tnfr1$^{-/-}$ Trif$^{-/-}$ (~P15), Tnfr1$^{-/-}$ Ifnar$^{-/-}$ (~P20), Tradd$^{-/-}$ Ripk3$^{-/-}$ (~P35), Tnfr1$^{-/-}$ Ripk3$^{-/-}$ (~P75).</td><td>Casp8$^{-/-}$ Ripk3$^{-/-}$, Fadd$^{-/-}$ Ripk3$^{-/-}$ (develop splenomegaly and ALPS in adulthood).</td></tr>
<tr><td>Ripk1$^{D325A/D325A}$</td><td>Embryonic lethality between E10.5-11.5.</td><td>Mlkl$^{-/-}$, Ripk3$^{-/-}$, Ripk1$^{D138N\ /D138N}$ (~P14).</td><td>Casp8$^{-/-}$Ripk3$^{-/-}$, Fadd$^{-/-}$ Ripk3$^{-/-}$, Ripk1$^{D138N\ /D138N}$ Ripk3$^{-/-}$ (develop splenomegaly and ALPS in adulthood).</td></tr>
<tr><td>Ripk1$^{D138N/D138N}$
or
Ripk1$^{K45A/K45A}$</td><td>Viable.</td><td>-</td><td>-</td></tr>
</table>

Table 1: Genetic perturbations of caspase-8, FADD, cFLIP, RIPK1, RIPK3, and MLKL phenotypes and genetic rescues. *Genetic deletion or mutation of key regulators of apoptosis and necroptosis, reveals distinct developmental and immunological outcomes, as well as specific rescue strategies. The genotype column lists the genes deleted or mutated, while phenotype describes the major defects observed. Restored phenotype distinguishes between partial rescue (delayed embryonic lethality or perinatal survival) and complete rescue (survival to adulthood). Complete experimental details and mechanistic explanations are provided in the main text.*

2.3. ZBP1-Mediated Necroptosis

While canonical necroptosis is typically initiated through RIPK1-RIPK3-MLKL signalling downstream of TNFR1, alternative upstream sensors can trigger this pathway independently of Complex II formation. Among these, Z-DNA binding protein 1 (ZBP1, also known as DNA-dependent activator of IFN-regulatory factors, DAI) has emerged as a critical innate immune sensor and effector of necroptosis. As an interferon-stimulated gene (ISG), ZBP1 expression is tightly regulated by inflammatory cytokine signalling, linking its activation to both antiviral immunity and interferon-driven tissue pathology[165]. Once expressed, upon sensing Z-form nucleic acids, ZBP1 can activate RIPK3-dependent necroptosis, contributing to viral clearance as well as sterile inflammation and tissue damage when dysregulated.

2.3.1. Structure and Function of ZBP1

ZBP1 is a cytosolic nucleic acid sensor and one of only two mammalian proteins, alongside ADAR1, that contain two N-terminal Zα domains (Zα1 and Zα2)[166-168]. These domains specifically recognize and bind left-handed Z-form nucleic acids (Z-DNA and Z-RNA) [166-169]. Z-DNA is an unusual, left-handed DNA structure with a zig-zag backbone, distinct base conformations, a more extended (longer) and thinner helical shape, and altered groove geometry[170]. It typically forms under high-salt conditions, in GC-rich sequences, or is induced by negative supercoiling[170-174]. Similarly, Z-RNA adopts a zig-zag backbone and features a left-handed twist, a stark contrast to the more common A-form RNA, which is a right-handed helix[170]. In addition to its Zα domains, ZBP1 contains three RHIM (RIP homotypic interaction motif) domains, which mediate interactions with other RHIM-containing proteins such as RIPK1, RIPK3, and TRIF, enabling downstream inflammatory and cell death signalling. This includes NF-κB activation, leading to the expression of pro-inflammatory cytokines and chemokines, a process dependent on the recruitment and ubiquitination of RIPK1 and RIPK3[175-178]. RPK1 can also cooperate with ZBP1 to support caspase-8-mediated apoptosis independently of RIPK3[136,179,180], while RIPK3 following activation by ZBP1 phosphorylates MLKL to induce necroptosis[181,182]. Interestingly, interaction between ZBP1 and TRIF is essential for mounting effective antiviral and antibacterial responses downstream of TLR3 and TLR4, by amplifying NF-κB, MAPK, and type I IFN signalling[183,184].

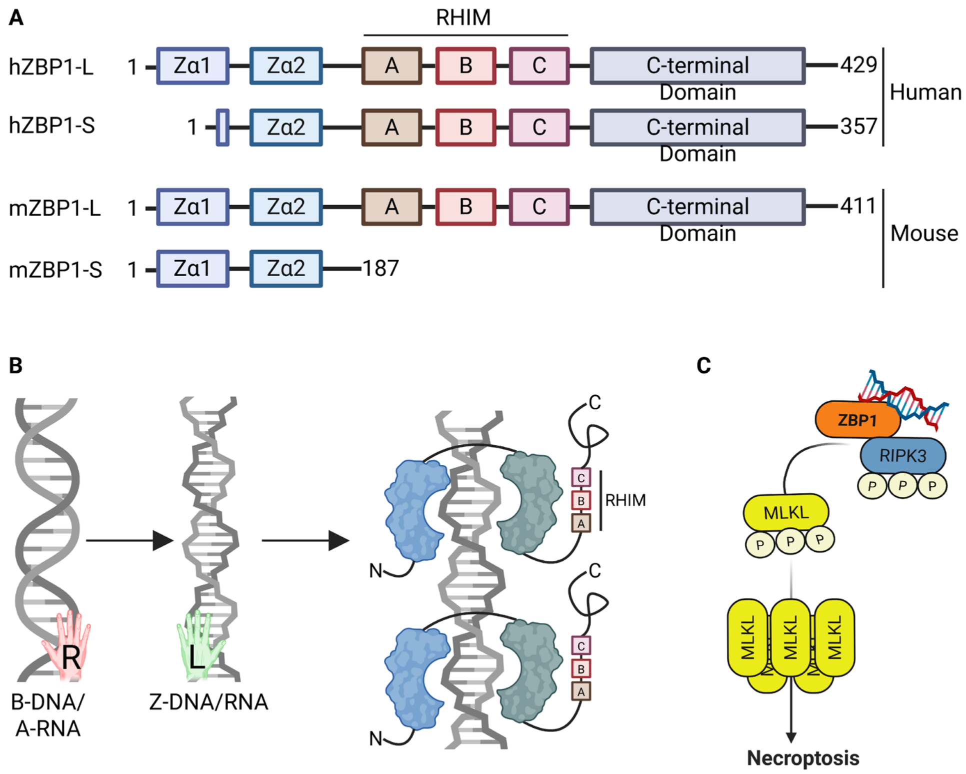

Figure 4. ZBP1 domain organisation, nucleic acid recognition and necroptosis. *(**A**) Schematic representation of the domain architectures of the two major human and mouse ZBP1 isoforms detectable by Western blot. In humans, the shorter isoform (ZBP1-S) lacks exon 2, which encodes the first Zα domain, whereas in mice the second isoform comprises only the two Zα domains. (**B**) ZBP1 can engage Z-DNA/RNA through two mechanisms: (i) conformational selection, where the Zα domains trap right-handed dsDNA/RNA transiently adopting the Z-conformation, or (ii) induced fit, where Zα domains actively drive nucleic acids into the Z-conformation. (**C**) Upon binding, activated ZBP1 activates RIPK3 via RHIM-RHIM interactions to induce MLKL-driven necroptotic cell death. Created in BioRender, https://BioRender.com/0r6sdyt.*

2.3.2. ZBP1 in Antiviral Immunity

Historically, the first biological function ascribed to ZBP1 was in antiviral immunity. Early studies proposed ZBP1 as a cytosolic DNA sensor that contributes to innate immune activation, particularly during viral infections[185]. Its role in antiviral defence was first established in murine cytomegalovirus (MCMV) infection, where ZBP1 restricts viral replication by inducing necroptosis via RIPK3, independently of RIPK1[182]. This pathway is normally suppressed by M45, an MCMV-encoded RHIM-containing protein that blocks ZBP1-RIPK3 complex formation[186,187]. Similar strategies are employed by other large DNA viruses, including herpes simplex virus-1 (HSV-1), HSV-2, varicella zoster virus (VZV), and the vaccinia poxvirus which encode either RHIM-containing homologs such as ICP6, ICP10, and ORF20, or the Zα domain protein E3 respectively, to antagonize ZBP1 signalling and evade ZBP1-RIPK3-induced necroptosis[188-193]. In influenza A virus (IAV) infection (negative-strand single-stranded RNA, ssRNA- virus), ZBP1 triggers both RIPK3-MLKL-dependent necroptosis and RIPK1-caspase-8-mediated apoptosis[179,180,194], which appear to be mutually exclusive at the single-cell level[189]. Notably, unlike many DNA viruses, IAV does not encode specific inhibitors of ZBP1-mediated cell death[188].

Upon viral infection, ZBP1 activation relies predominantly on viral-induced production of Z-RNAs. Upon IAV infection, Z-RNA species accumulate in the nucleus leading to ZBP1-RIPK3-MLKL-induced nuclear necroptosis, a highly inflammatory process which is accompanied by the release of alarmins such as IL-33 and HMGB1, contributing to lung inflammation[181,195]. In contrast, VV and SARS-CoV-2 trigger cytosolic Z-RNA accumulation, reflecting their cytoplasmic replication cycles[188,196]. Intriguingly, vaccinia Zα domain protein E3 promotes Z-RNA formation via its C-terminal A-form dsRNA-binding domain while blocking ZBP1 activation through its Zα domain[188]. Even in DNA virus infections, such as MCMV and HSV-1, ZBP1 activation depends on newly transcribed RNAs and therefore Z-RNA synthesis, rather than Z-DNA[190,197,198].

In addition to inducing cell death, ZBP1 also contributes to transcriptional activation during viral infection. It promotes NF-κB and type I IFN responses in infection with diverse DNA and RNA viruses including HSV-1, HCMV, IAV, Zika virus, and SARS-CoV-2[176,180,185,196,199-203]. ZBP1 overexpression alone can activate NF-κB independently of cell death, demonstrating that its transcriptional function is separable from its role in inducing apoptosis or necroptosis[176]. However, in natural infections, dissecting ZBP1's role in transcriptional responses is complex due to redundancy with other innate immune sensors.

2.3.3. ZBP1 in Autoimmunity and Sterile Inflammation

Beyond its role in antiviral immunity, ZBP1 has been implicated in autoimmunity and sterile inflammation. In addition to viral genomes or viral-induced nucleic acid species, endogenous retroelements, specifically B2 and Alu short interspersed nuclear elements (SINEs), have also been identified as key endogenous triggers of ZBP1 activation in autoinflammatory conditions. This was first demonstrated in mouse models expressing RHIM-mutant RIPK1 either throughout the whole body or specifically in the skin, as well as in mice with keratinocyte-specific deletion of RIPK1, which die perinatally due to unrestrained necroptosis driven by spontaneous ZBP1 activation[163,164,204,205]. Notably, ZBP1 plays a dominant role in this model, contrasting with full-body RIPK1 knockout mice where both caspase-8-driven apoptosis and ZBP1- and TRIF-mediated necroptosis via RIPK3 contribute to lethality (*Casp8*$^{-/-}$ *Ripk1*$^{-/-}$ *Trif*$^{-/-}$ *Zbp1*$^{-/-}$ mice)[163,194]. Intriguingly, in this context, RIPK1 drives necroptosis not only downstream of TNFR1 but also other death receptors, as indicated by the lower survival advantage observed in *Casp8*$^{-/-}$ *Tnfr1*$^{-/-}$ *Zbp1*$^{-/-}$ compared to *Casp8*$^{-/-}$ *Ripk1*$^{-/-}$ *Zbp1*$^{-/-}$ mice, and in *Casp8*$^{-/-}$ *Tnfr1*$^{-/-}$ *Trif*$^{-/-}$ *Zbp1*$^{-/-}$ compared to *Casp8*$^{-/-}$ *Ripk1*$^{-/-}$ *Trif*$^{-/-}$ *Zbp1*$^{-/-}$ mice[163,194,206].

The precise mechanism by which the RHIM domain of RIPK1 suppresses ZBP1-mediated necroptotic signalling remains incompletely understood, but appears to depend on caspase-8 and FADD, and partly on TNFR1. The physiological relevance of this inhibitory axis is highlighted by studies in intestinal epithelial cell-specific and keratinocyte-specific *Fadd* or *caspase-8* knockout mice, which develop both TNFR1- and ZBP1-driven, necroptosis-dependent colitis and ileitis or dermatitis, respectively[136,141,204]. Additionally, the embryonic lethality of *Casp8*$^{-/-}$ *Tnfr1*$^{-/-}$ is further prolonged by co-deletion of *Zbp1*[206]. Recent work, demonstrated that RIPK1 recruitment to Complex II regulates the mode of ZBP1-mediated RIPK3 activation, by generating a DD disruptive mutation not allowing DD-dependent oligomerisation of RIPK1 (R588E) and therefore recruitment to Complex I and II[207]. Interestingly, *RIPK1*$^{R588E/R588E}$ mice predominantly succumb to ZBP1- and TRIF- mediated necroptosis via RIPK3 (and secondarily to TNFR1-TRADD-FADD-caspase-8 apoptosis)[207].

However, in all these cases, the upstream signals responsible for ZBP1 upregulation prior to its activation, and how this contributes to necroptotic responses, remain unclear. Interestingly, previous studies have shown that loss of caspase-8 or FADD lead to ZBP1 upregulation in mouse embryonic fibroblasts (MEFs), independently of cell death[208], indicating that ZBP1 induction is not merely a secondary consequence of necroptosis-induced inflammation. Similarly, *Casp8*$^{-/-}$ *Tnfr1*$^{-/-}$ embryos presented with elevated expression of ZBP1[206]. Nevertheless, the signalling pathways and molecular mechanisms underlying ZBP1 transcriptional upregulation in this context remains unresolved, representing a critical gap in our understanding of how necroptotic responses are primed independently of canonical death receptor activation. Clarifying these mechanisms could provide important insights into the regulation of autoimmune and autoinflammatory diseases and may uncover novel therapeutic opportunities targeting ZBP1-dependent necroptotic pathways.

Equally important is understanding how ZBP1 is activated in the absence of infection and under conditions of sterile inflammation, as transcriptional upregulation alone is insufficient to trigger necroptotic signalling. The accumulation of the natural ligands for ZBP1 can endogenously arise from perturbations in cellular nucleic acid regulation. Loss of the histone methyltransferase and endogenous retroviruses (ERVs) suppressor, SETDB1[209] in intestinal epithelial cells reactivates ERVs, producing double-stranded RNAs capable of forming Z-RNA structures that activate ZBP1 and drive intestinal inflammation[210]. Similarly, the RNA-editing enzyme ADAR1 prevents ZBP1 activation by converting adenosine-to-inosine (A-to-I) within double-stranded RNA, particularly inverted repeat Alu elements (IR-Alus), thereby avoiding recognition by innate immune sensors including the MDA5-MAVS signalling pathway[211-213]. Hemizygous expression of Zα domain mutant ADAR1 leads to defective editing of IR-Alus, which are abundant in the 3′ UTRs of many mRNAs[214,215]. These IR-Alus can form double-stranded structures that adopt Z-RNA conformations and activate ZBP1, as further demonstrated by the transfection of *in vitro*-transcribed IR-Alus[214].

Beyond its editing activity, the Zα domain of ADAR1 may also exert editing-independent functions by directly binding and sequestering Z-RNA or by competing with ZBP1 for access to these structures. Additionally, ADAR1 does not only prevents ZBP1 activation and the downstream induction of caspase-8- and RIPK3-mediated cell death but also suppresses MAVS-independent but RIPK3-dependent ZBP1-induced IFN responses in *Adar*$^{-/-}$ mice and interestingly, ZBP1 Zα domain-dependent but RIPK3-independent Zbp1-driven pathology in *Adar1*$^{mZ\alpha/-}$ and *Adar*$^{P195A/p150null}$ mice[214-216]. Conversely, ZBP1 ablation completely rescued severe pathology in *Adar*$^{P195A/p150null}$ mice, a model that most closely recapitulates the human condition of Aicardi-Goutières syndrome (AGS)[216]. Notably, the anti-inflammatory function of ADAR1 extends beyond suppressing ZBP1-RIPK3-MLKL-mediated necroptosis and ZBP1-caspase-8-dependent apoptosis, the latter being partly reliant on RIPK3[215,216]. Specifically, these studies suggest that caspase-8 limits the interaction between ZBP1 and RIP kinases, thereby restraining excessive transcriptional inflammatory signalling independently of cell death[215,216].

In contrast, deletion of TREX1, a DNA exonuclease mutated in autoinflammatory diseases such as AGS, familial chilblain lupus, and SLE[217], also upregulates ZBP1 via enhanced type I IFN signalling[215], but ZBP1 loss in TREX1-deficient mice does not alleviate inflammation, ISG expression, or tissue pathology[215]. This highlights the context-dependent contribution of

ZBP1, and possibly its reliance on Z-RNA rather than Z-DNA for driving pathology via de-repressed endogenous retroelements (including LTR/ERVK, LINE/L1, SINE/Alu and SIN)[215].

ZBP1 regulation is further fine-tuned by protein isoforms and domain architecture. C-terminal truncation in mice retaining only the two Zα domains and the first RHIM renders ZBP1 constitutively active, inducing autoinflammation through both RIPK1-FADD-caspase-8-mediated apoptosis and RIPK3-MLKL-dependent necroptosis[136]. A short isoform, ZBP1-S, can antagonize full-length ZBP1-L by competing for Z-nucleic acid binding, acting as an endogenous inhibitor [218].

Genotype	Phenotype	Restored phenotype	
		Partial	Complete
Ripk1$^{-/-}$	Perinatal lethality; both caspase-8-driven apoptosis and ZBP1-/TRIF-mediated RIPK3 necroptosis.	In Table 1.	***Casp8***$^{-/-}$***Trif***$^{-/-}$***Zbp1***$^{-/-}$ (develop splenomegaly and ALPS in adulthood).
Ripk1$^{RHIM/RHIM}$	Perinatal lethality due to unrestrained ZBP1-driven necroptosis	-	***Ripk3***$^{-/-}$, ***Mlkl***$^{-/-}$, ***Zbp1***$^{-/-}$.
Ripk1$^{R588E/R588E}$	Perinatal lethality.	***Mlkl***$^{-/-}$ (~P7), ***Zbp1***$^{-/-}$ (~P7), ***Ripk3***$^{-/-}$ (~P70), ***Trif***$^{-/-}$***Zbp1***$^{-/-}$ (~P210).	***Ripk3***$^{-/-}$***Fadd***$^{-/-}$, (develop splenomegaly and ALPS in adulthood), ***Ripk3***$^{-/-}$***Tnfr1***$^{-/-}$, ***Ripk3***$^{-/-}$***Tradd***$^{-/-}$, ***Mlkl***$^{-/-}$ ***Tradd***$^{+/-}$.
Ripk1$^{-/-}$ ***Casp8***$^{-/-}$	Perinatal lethality.	***Zbp1***$^{-/-}$ (~P25).	***Trif***$^{-/-}$***Zbp1***$^{-/-}$ (develop splenomegaly and ALPS in adulthood).
Ripk1$^{-/-}$ ***Tnfr1***$^{-/-}$	Perinatal lethality.	***Triff***$^{-/-}$ (P15), ***Ifnar***$^{-/-}$ (~P20), ***Stat1***$^{-/-}$ (≤P25), ***Zbp1***$^{-/-}$ (~P35), ***Ifnar1***$^{-/-}$ ***Ifngr1***$^{-/-}$ (≤P86), ***Ripk3***$^{-/-}$ (~P75).	-
Casp8$^{-/-}$ **Tnfr1**$^{-/-}$	Embryonic lethality at ~E17.5.	***Trif***$^{-/-}$ (~E18.5), ***Zbp1***$^{-/-}$ (≤P7).	***Trif***$^{-/-}$***Zbp1***$^{-/-}$ (develop splenomegaly and ALPS in adulthood).
Adar$^{-/-}$	Embryonic lethality between E11.5 and E12.5.	***Mavs***$^{-/-}$, ***Ifih1***$^{-/-}$ (Perinatal lethality), ***Mavs***$^{-/-}$***Zbp1***$^{-/-}$ (≤P105), ***Mavs***$^{-/-}$***Ripk3***$^{-/-}$ (≤P105), ***Mavs***$^{-/-}$***Zbp1***$^{Z\alpha1\alpha2/Z\alpha1\alpha2}$ (≤P140).	**-**
Adar1$^{mZ\alpha/mZ\alpha}$	Viable	-	-
Adar1$^{mZ\alpha/-}$	Perinatal lethality (~P2).	***Mlkl***$^{-/-}$ (P5), ***Ripk3***$^{-/-}$ (~P8), ***Zbp1***$^{-/-}$, ***Zbp1***$^{mZ\alpha/mZ\alpha}$ (~P105), ***Zbp1***$^{Z\alpha1\alpha2/Z\alpha1\alpha2}$ (~P126).	***Mavs***$^{-/-}$, ***Zbp1***$^{-/-}$***Mavs***$^{+/-}$, ***Zbp1***$^{-/-}$ ***Mavs***$^{-/-}$
Adar$^{P195A/p150null}$	Postnatal lethality at P25.	***Mlkl***$^{-/-}$, ***Ripk1***$^{K45A/K45A}$ (~P25), ***Ripk3***$^{-/-}$ (~P130), ***Eif2ak2***$^{-/-}$ (~P112), ***Zbp1***$^{+/-}$ (~P175).	***Ifih1***$^{-/-}$, ***Dhx58***$^{-/-}$, ***Zbp1***$^{-/-}$
Adar$^{p150null/p150null}$	Embryonic lethality.	***Ifih1***$^{-/-}$ (P5), ***Ifih1***$^{-/-}$ ***Zbp1***$^{-/-}$ (~P10).	-

Table 2: Genetic perturbations highlighting the role of ZBP1 in sterile inflammation and necroptosis. *Genetic deletions or mutations in key regulators reveal the central role of ZBP1 in driving necroptosis and sterile inflammatory phenotypes. The genotype column lists the genes deleted or mutated, while phenotype describes the resulting developmental defects. Restored phenotype distinguishes between partial rescue (delayed embryonic lethality or perinatal survival) and complete rescue (survival to adulthood). Complete experimental details and mechanistic explanations are provided in the main text.*

In summary, ZBP1-mediated necroptosis defines a RIPK3-dependent cell death pathway responsive to both endogenous and viral Z-nucleic acids. Beyond antiviral defence, ZBP1 acts as a central driver of inflammation when regulatory checkpoints such as RIPK1, ADAR1, or the FADD/caspase-8 axis, are impaired. Understanding these mechanisms will be critical for uncovering how ZBP1 contribute to infectious, autoimmune and autoinflammatory diseases and may reveal novel opportunities for therapeutic intervention targeting ZBP1-dependent necroptosis and inflammation.

2.4. Non-Apoptotic Roles of caspase-8 in Genome Integrity

While ZBP1-mediated necroptosis is primarily engaged in antiviral defence and can also contribute to sterile inflammation, TNFR1-mediated necroptosis plays a context-dependent role in amplifying inflammatory signalling, particularly when apoptosis is inhibited. Central to these pathways is caspase-8, traditionally recognized as the initiator caspase that orchestrates apoptosis downstream of TNFR1 while restraining uncontrolled necroptosis. Beyond its canonical role in cell death, caspase-8 is increasingly appreciated for non-cell death functions that safeguard cellular and genomic integrity, highlighting its involvement in processes that extend beyond the execution of cell death. Through this dual functionality, caspase-8 acts as a molecular checkpoint, integrating signals from cell death pathways and cellular stress responses to maintain cellular homeostasis.

The role of caspase-8 in maintaining genome integrity independently of its cell death role is supported by multiple studies. In hepatocytes, caspase-8 has a non-apoptotic function in H2AX phosphorylation, an essential step in the DNA damage response to replication stress[219]. Experiments in mice lacking caspase-8 in hepatocytes demonstrated that its absence is genotoxic, impairing the DNA damage response and creating an environment conducive to genomic instability[219]. Consistent with these observations, caspase-8 deficiency has been reported to promote cellular transformation *in vitro* independently of its apoptotic function[220]. Loss of caspase-8 expression, either through mutation or epigenetic silencing, has also been reported in murine and human hepatocellular carcinoma and advanced gastric cancer[221-223]. Collectively, these observations indicate that caspase-8 deficiency may not only confer apoptosis resistance but also promote replication errors, thereby increasing genomic instability and predisposition to malignant transformation.

Caspase-8 has also been shown to play a direct role in maintaining chromosomal stability independently of cell death. Mitotic abnormalities were observed in *Casp8$^{-/-}$* embryos at E10.5 and in *Casp8$^{-/-}$ Ripk3$^{-/-}$* and *Casp8$^{-/-}$ Mlkl$^{-/-}$* embryos at E13.5, a stage at which embryonic lethality is fully rescued by loss of necroptosis activation[224]. Qualitative and quantitative analysis of these embryos revealed a clear accumulation of aberrant mitoses. Mechanistically, molecular and biochemical analyses reveal that caspase-8 regulates chromosomal segregation through cleavage of PLK1 following its recruitment to RIPK1 during mitosis, and both excessive or absent caspase-8 activity drive the accumulation of genomic instability.

Chronic liver inflammation models further illustrate the interplay between caspase-8 activity, necroptosis, and genome integrity. In mice with liver parenchymal cells (LPC)-specific deletion of *Tak1*, RIP3-dependent necroptosis limits caspase-8-dependent compensatory hepatocyte proliferation, immune cell activation, hepatic fibrogenesis, and chromosomal aberrations, thereby mitigating hepatocarcinogenesis[225]. Enhanced caspase-8 activation as a consequence of RIPK3 loss has been associated with chromosomal aberrations affecting chromosomes 4, 8, and 13, linking dysregulated caspase-8 activity to genomic instability. Caspase-8 also plays a critical role in hematopoietic cells. Loss of caspase-8 in B lymphocytes leads to impaired cytokinesis and markedly elevated levels of chromosomal aberrations, culminating in B-cell lymphomagenesis in 60-week-old mice, demonstrating an important role of caspase-8 in maintenance of genomic integrity and tumour-suppressive function[226].

However, although loss of caspase-8 has been associated with cellular transformation *in vivo*, it is important to note that persistent DNA damage and the consequent accumulation of cytosolic DNA do not inevitably lead to tumorigenesis. Accordingly, genomic instability arising from caspase-8 deficiency may not universally drive tumour formation across all tissues. In particular, the restricted survival of *Casp8$^{-/-}$ Ripk3$^{-/-}$* and *Casp8$^{-/-}$ Mlkl$^{-/-}$* mice due to the development of ALPS synrome[81,87-89], could obscure the development of tumours that might otherwise become detectable at later stages. Furthermore, evidence from multiple independent genetic models demonstrates that chronic DNA damage or cytosolic DNA accumulation does not inherently result in tumour formation. BubR1-insufficient mice[227], *Rnaseh2b*[228], and *Samhd1* knockout mice[229] all exhibit persistent genomic instability and/or cytosolic DNA accumulation without spontaneous tumour development, highlighting that DNA damage and chromosomal abnormalities can promote inflammation independently of cancer.

Taken together, these studies establish that caspase-8 has a fundamental non-cell death role in preserving genomic integrity. It orchestrates precise mitotic progression and constrains chromosomal aberrations independently of its apoptotic function and its role in preventing necroptosis activation. Notably, it remains largely unexplored whether the genomic instability resulting from caspase-8 deficiency could directly facilitate the leakage of nuclear DNA into the cytosol. Such cytosolic DNA (self-DNA) represents a potent trigger for innate immune surveillance, with nucleic acid sensors, most prominently the cGAS-STING axis, as discussed in the next section, playing a central role in its detection and downstream signalling. While the causal relationships remain primarily correlative, these observations suggest a mechanistic framework whereby caspase-8-mediated maintenance of genomic stability may indirectly influence cytosolic DNA availability, thereby modulating cGAS-STING-dependent inflammatory responses. This conceptual link provides the rationale for the current thesis, establishing a foundation for subsequent investigations into how perturbations in caspase-8 function intersect with innate immune signalling, a topic explored in detail in the following section.

3. Nucleic Acid Sensing in Innate Immunity - The cGAS-STING Pathway

3.1. Cytosolic DNA Sensing in Innate Immunity

Innate immunity serves as the first line of defence against invading pathogens and endogenous danger signals. It functions not only as an autonomous barrier to infection but also as a tightly integrated partner of the adaptive immune system, essential for establishing and maintaining tissue homeostasis. This early immune response is orchestrated by germline-encoded pattern recognition receptors (PRRs), which detect conserved molecular patterns, either pathogen-associated molecular patterns (PAMPs) derived from infectious agents, or damage-associated molecular patterns (DAMPs) released during sterile injury or cellular stress. Upon engagement, PRRs initiate a cascade of signalling events that promote cellular defence mechanisms and the secretion of soluble mediators, including type I interferons (IFNs), tumour necrosis factor (TNF), interleukins (ILs), and other pro-inflammatory cytokines[230]. These mediators amplify innate immune responses in an autocrine and paracrine manner, activating neighbouring cells and shaping the recruitment and activation of adaptive immune components if the threat persists.

Although DNA was initially regarded as an "immuno-inert macromolecule", research over the past twenty-five years has revealed its potent immunostimulatory properties when mislocalised. Under physiological conditions, DNA is compartmentalized within the nucleus and mitochondria. Its presence in the cytosol is therefore interpreted as a danger signal that activates distinct PRRs, triggering robust innate immune responses depending on its structural characteristics and intracellular context. Among the DNA-sensing PRRs identified to date are: Toll-like receptor 9 (TLR9), an endosomal sensor that recognizes unmethylated CpG-rich DNA sequences typically found in bacteria[231]; absent in melanoma 2 (AIM2), which detects cytosolic double-stranded DNA (dsDNA) and activates the inflammasome, leading to IL-1β and IL-18 maturation and pyroptosis[232]; ZBP1, which plays a critical role in sensing Z-form nucleic acid structures and regulating inflammatory cell death as previously described[185]; interferon-inducible protein 16 (IFI16), a member of the PYHIN family that localizes to both the nucleus and cytosol and signals via the STING pathway[233]; and cyclic GMP-AMP synthase (cGAS), a cytosolic DNA sensor that catalyses the production of cyclic GMP-AMP (cGAMP) to activate STING[234,235]. This multi-layered network of DNA sensors ensures robust immune surveillance against infections and endogenous threats while incorporating multiple layers of regulation to prevent excessive or autoreactive responses. Mechanisms such as nucleic acid compartmentalisation, nuclease activity (e.g., TREX1, DNase II[236-238]), and post-translational modification of signalling intermediates[239] play essential roles in maintaining this delicate balance.

3.2. cGAS-STING Pathway: Activation and Signal Transduction

Among the previously mentioned DNA sensors, the cyclic GMP-AMP synthase-stimulator of interferon genes (cGAS-STING) axis has emerged as a central and evolutionarily conserved pathway in cytosolic DNA sensing. Unlike endosomal receptors such as TLR9 or inflammasome activators like AIM2, the cGAS-STING pathway operates as a cytosolic surveillance system that couples DNA recognition directly to the induction of type I interferon responses and broader inflammatory signalling. This pathway plays a pivotal role not only in antiviral immunity but also in immune response against other pathogens including intracellular bacteria and parasites, antitumor responses, autoimmunity, and tissue homeostasis[240-243].

Due to its wide-ranging immunological roles and its sensitivity to both self and non-self DNA, the cGAS-STING pathway has garnered considerable attention as both a critical mediator of immune surveillance and a potential driver of inflammatory disease. Its activation is tightly controlled at multiple levels to prevent unwanted immune activation. The following sections explore in more detail the molecular underpinnings of cGAS-STING signalling, its regulation, and its functional impact on immune homeostasis.

3.2.1. DNA Recognition via cGAS and cGAMP Production

3.2.1.1. Molecular Structure of cGAS and Mechanism of DNA Recognition

Structurally, cGAS is a bilobular enzyme composed of a non-conserved N-terminal domain with unstructured, positively charged regions and a highly conserved C-terminal lobe containing the nucleotidyltransferase (NTase) catalytic core domain and male abnormal 21 (Mab21) domain which processes the DNA-binding sites[244-249]. The N-terminal region (residues 1-160 in human cGAS) is intrinsically disordered and enriched in basic residues, facilitating electrostatic interactions with nucleic acids, phase separation, and chromatin tethering, but is dispensable for DNA-dependent cGAMP synthesis[235,250,251]. DNA recognition is primarily mediated through the C-terminal lobe, which presents a positively charged surface groove that accommodates the DNA phosphate backbone in a sequence-independent manner[244-249]. The DNA interface comprises three main contact sites: Site A, the primary DNA interaction surface, induces conformational changes that open the catalytic pocket for ATP and GTP; Site B cooperates with Site A to form the minimal catalytically active 2:2 “ladder-like” cGAS-DNA complex[252]; and Site C stabilizes binding to long or bent DNA, favouring GC-rich or repetitive sequences[245,253]. These features promote higher-order cGAS-DNA oligomers and liquid-phase condensates[245,253], which enhance enzyme concentration and catalytic turnover while protecting DNA from TREX1 degradation, thereby amplifying downstream signalling[254,255].

The DNA-binding affinity of cGAS is largely governed by the length and structural rigidity of the DNA substrate. Human cGAS typically requires DNA fragments >40-50 bp[252], whereas murine cGAS, despite ~65% sequence identity, responds to fragments as short as ~20 bp[256]. This heightened sensitivity in mouse cGAS is attributed to subtle but functionally relevant differences in its DNA-binding interface, particularly within the α5 helix and L2 loop, which confer increased DNA-binding affinity and more efficient activation in response to structurally diverse DNA ligands[256,257].

3.2.1.2. cGAMP Production

Upon dsDNA binding, cGAS undergoes conformational rearrangement that activates its catalytic pocket, enabling synthesis of the unique second messenger 2′3′-cGAMP, which binds STING with high affinity[244-249,258-260]. The catalytic core (residues 161-522 in human cGAS) contains a conserved H-Y-E motif (His390, Tyr394, Glu397) that mediates this reaction. cGAS first generates a linear intermediate, pppG(2′-5′)pA, by transferring ATP to the 2′-OH of GTP. The intermediate then rebinds in an inverted orientation, allowing a second transfer and cyclisation, producing 2′3′-cGAMP with both 2′-5′ and 3′-5′ linkages[247,258-260].

3.2.1.3. Self-Tolerance and Safeguards of cGAS

Despite its potent activity, cGAS must be tightly regulated to prevent autoimmune activation. At the biophysical level, cGAS undergoes liquid-phase separation with dsDNA, forming condensates that amplify enzymatic activity and downstream signalling[250,251]. These assemblies are further regulated by modulatory factors, including RNA species that form cGAS-RNA granules, protein interactors (i.e. G3BP1, PKR) and the structural conformation of DNA (e.g., B- vs. Z-DNA), and viral proteins including human herpesvirus ORF52, VP22, and the SARS-CoV-2 nucleocapsid [261].

A second safeguard is subcellular compartmentalisation. Although predominantly cytosolic, a substantial fraction of cGAS resides in the nucleus, especially following nuclear envelope breakdown prior to mitosis[262-266] Here, it is tethered to the acidic patch of nucleosomes[267-273] via conserved arginine residues (R222/R241 in mouse; R236/R255 in human), which occlude DNA-binding surfaces and hold the enzyme in an autoinhibited conformation[267-272]. Additionally, barrier-to-autointegration factor 1 (BAF) provides an additional checkpoint, competing with cGAS for exposed DNA particularly during nuclear envelope rupture[274].

Further safeguards prevent inappropriate activation of cGAS. At the plasma membrane, cGAS is restrained by interactions with $PI(4,5)P_2$ via its N-terminal phosphoinositide-binding domain, serving as another spatial safeguard against self-DNA recognition and autoimmunity[275]. The exonuclease TREX1 digests cytosolic DNA[276,277], while SAMHD1, DNase I and DNase II degrade nuclear, circulating and lysosomal DNA fragments, respectively[278-281]. Deficiencies in these regulatory systems are linked to severe autoimmune disorders, such as Aicardi-Goutières syndrome, characterized by chronic interferon responses mediated through unchecked cGAS-STING activation[237].

3.2.2. STING Activation and Trafficking

Upon recognition of cytosolic DNA by cGAS and subsequent synthesis of 2′3′-cyclic GMP-AMP (cGAMP), the cyclic dinucleotide acts as a second messenger that binds directly to stimulator of interferon genes (STING), also known as methionine-proline-tyrosine-serine (MPYS), transmembrane protein 173 (TMEM173) and ER IFN stimulator (ERIS), an endoplasmic reticulum (ER)-resident transmembrane protein encoded by the *TMEM173* (*STING1*) gene. STING functions as a central adaptor in cytosolic DNA sensing, mediating signal transduction that culminates in the activation of transcriptional programs for type I interferons and inflammatory cytokines.

Structurally, STING consists of an N-terminal transmembrane domain (TMD) formed by four transmembrane α-helices (TM1-TM4; residues 1-138 in human STING) that anchor the protein in the endoplasmic reticulum (ER), followed by a large cytosolic C-terminal domain (CTD). Within the CTD, residues 139-336 fold into a bilobed ligand-binding domain (LBD), sometimes referred to as the cyclic dinucleotide-binding domain (CBD), that clamps around its agonist, while the extreme C-terminal tail (CTT; residues 337-379) remains intrinsically disordered and serves as a docking platform for downstream signalling partners[282-284]. STING structure has been thoroughly reviewed[285-288]. Briefly, the ligand-binding domain (LBD) of apo-STING (unbound state) adopts a butterfly-shaped dimer configuration, characterized by a deep V-shaped cleft formed at the interface between the two protomers, referred to as the open conformation. Upon binding of the endogenous ligand 2′3′-cGAMP, the cleft closes as a four-stranded antiparallel β-sheet covers the ligand within the deep pocket, locking the LBD into a closed conformation. This ligand-induced conformational change is a prerequisite for downstream signalling. Full-length STING forms a domain-swapped dimer, in which the last helix of the TMD and LBD are connected via a linker composed of a short amphipathic helix and a flexible hinge region. This hinge adopts a right-handed crossover configuration in the apo state and reorients into a parallel conformation upon cGAMP binding. This is induced by a remarkable 180° clockwise rotation of the LBD relative to the TMD[282], relieving the right-handed crossover of the connector helices and allowing the closure of a lid structure around cGAMP. This process in fundamental in coordinating ER exit and initiating signal transduction. In its active state, ligand-bound STING dimers can further assemble into linear oligomeric arrays through side-by-side packing, creating a high-avidity signalling platform that facilitates the robust recruitment and activation of downstream effectors such as TBK1 and IRF3[282,289]. STING oligomerisation is further stabilized by intermolecular disulfide bonds formed between adjacent dimers, as well as by palmitoylation at conserved cysteine residues C88 and C91[289-291].

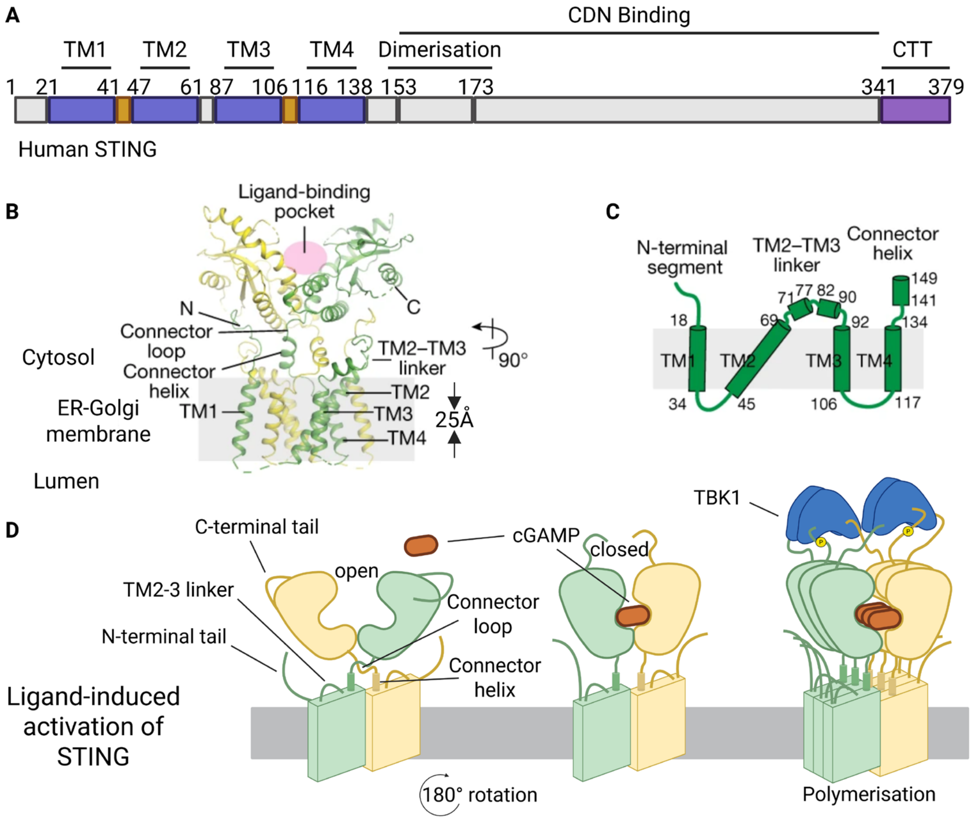

Figure 5. Structural Basis and Activation Mechanism of STING in Cytosolic DNA Sensing. *(**A**) Schematic representation of the functional domains of human STING, including the N-terminal transmembrane domain (TM1-TM4; residues 1-138) that anchors the protein in the ER/ Golgi, and the cytosolic C-terminal domain (CTD; residues 139-379). The CTD contains a bilobed ligand-binding domain (LBD; residues 139-336), while the intrinsically disordered C-terminal tail (CTT; residues 337-379) serves as a docking platform for downstream effectors. (**B**) Representation of the full-length STING structure in two orthogonal side views[282]. (**C**) Topological diagram of the transmembrane domain[282]. (**D**) Mechanism of STING activation: upon cytosolic DNA recognition, cGAS synthesizes 2'3'-cGAMP, which binds directly to STING. The LBD undergoes a conformational switch from an open butterfly-*

shaped dimer to a closed state, locking cGAMP in a deep V-shaped cleft. This transition is coupled to a 180° clockwise rotation of the LBD relative to the TMD via a hinge region, facilitating ER exit and signal initiation. Activated STING dimers assemble into higher-order oligomeric arrays stabilized by intermolecular disulfide bonds, providing a platform for TBK1 and IRF3 recruitment and activation, ultimately driving type I interferon and pro-inflammatory cytokine responses. Created in BioRender, https://BioRender.com/tv8b4ep.

However, STING can exist as an oligomer in overexpression studies even before cGAMP stimulation and concomitant activation[292]. At the ER membrane, apo-STING has been shown to organize into a bilayer structure through head-to-head and side-by-side arrangements of dimers, effectively zipping two ER membranes together[292]. This bilayer formation represents the autoinhibited resting state of STING. Disruption of ER membrane lipid composition, due to factors such as cholesterol depletion, RNA virus infection, ER stress, or gain-of-function mutations in STING (as seen in STING-associated vasculopathy with onset in infancy, SAVI), can destabilize this planar bilayer into a curved monolayer conformation, promoting ligand-independent STING activation[292].

Following its activation, STING exits the ER and traffics through the ER-Golgi intermediate compartment (ERGIC) to the Golgi apparatus[293]. According to the current model, this requires the release of STING from the ER stromal interaction molecule 1 (STIM1) which has been reported to interact with STING and retain it in the ER[294]. Upon cGAMP binding and conformational activation, STING dissociates from STIM1, allowing its packaging into coat protein complex II (COPII) vesicles. COPII vesicle formation begins with the activation of the small GTPase SAR1A, which promotes the recruitment of the SEC23/SEC24 heterodimer to form the inner coat, followed by the assembly of the tetrameric SEC13/SEC31 complex that constitutes the outer coat. STING has been shown to interact with Sec24 responsible for the recognition of cargo proteins by binding to their ER export signal[295,296]. Several accessory proteins have been implicated in facilitating the handover of STING to the SEC24C complex, including STING1 ER Exit Protein 1 (STEEP), YIP family 5 (YIPF5) and transmembrane emp24 protein transport domain containing 2 (TMED2)[296-298].

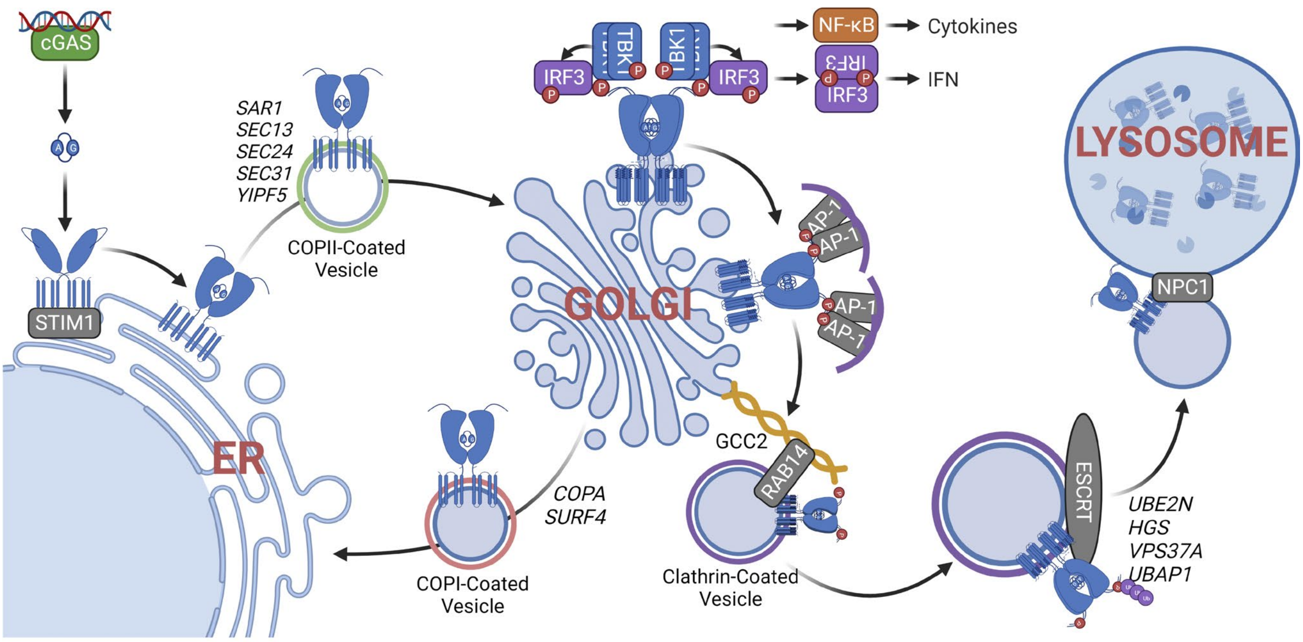

Figure 6. STING trafficking mechanism*[299]*. *In its inactive state, STING is retained in the ER through the retention factor STIM1 and COPI-mediated vesicular transport. Upon binding cyclic dinucleotides (CDNs), STING exits the ER and traffics to the Golgi, where it forms signalling complexes at the trans-Golgi network (TGN) to activate immune responses. Its subsequent exit from the Golgi is coordinated by the clathrin adaptor AP-1, along with the Golgin GCC2 and RAB14. Finally, STING-containing vesicles are directed to lysosomes for degradation via the ESCRT machinery and the lysosomal adaptor protein NPC1. P, phosphorylation*[299]*.*

Studies have suggested two models for STING signalling activation within the Golgi: one in which the STING signalling complex is assembled at the cis-Golgi and maintained as it progresses through the Golgi stack, and another in which activation is initiated later at the trans-Golgi network (TGN), the currently prevailing model[290,300]. COPI vesicles have been identified as mediators of retrograde trafficking from the Golgi to the endoplasmic reticulum (ER), a process thought to be dependent on ARF1-mediated COPI coat formation and the cargo receptor SURF4, which facilitates the loading of STING into these vesicles[301-305]. Support for this model comes from human genetic studies showing that mutations in COPI component, *COPA* (α-COP), cause COPA syndrome, a rare autoinflammatory disease marked by constitutive STING activation[301-305]. These mutations further disrupt the interaction between STING and SURF4, thereby impairing retrograde transport[303-305]. Together, these findings suggest that retrograde trafficking of STING from the Golgi to the ER is essential to suppress spontaneous STING signalling and maintain immune homeostasis.

In the later stages of activation, STING undergoes lysosomal degradation as a critical negative feedback mechanism to terminate signalling and prevent sustained immune activation. This process depends on proper lysosomal trafficking, primarily mediated by the lysosomal membrane protein Niemann-Pick type C1 (NPC1), which acts as an adaptor recognizing activated STING and facilitating its delivery for proteolysis[306]. Supporting this, NPC1-deficient cells, including those from Niemann-Pick disease type C patients, show impaired STING degradation and heightened inflammatory signalling. Additionally, the clathrin adaptor complex AP-1 contributes to this pathway by interacting with residues L364 and I365 of STING to promote its sorting into clathrin-coated vesicles for lysosomal targeting[307]. STING Golgi exit requires the trans-Golgi protein GCC2 (GCC185), a Golgin that mediates vesicle transfer to RAB GTPases via adaptor proteins[299]. Despite other Golgin redundancy, only GCC2 is essential for STING Golgi exit, with RAB GTPases such as RAB14 mediating its subsequent transport. Furthermore, STING degradation is also supported by a non-canonical autophagic response[308,309] and has recently been shown to involve the ESCRT machinery (composed of HGS, VPS37A, UBAP1, Tsg101, and Vps4), which mediates the internalisation of STING-containing vesicles into multivesicular bodies (MVBs) before they fuse with lysosomes[310-312].

3.2.3. Downstream Signalling via TBK1, IRF3, and NF-κB

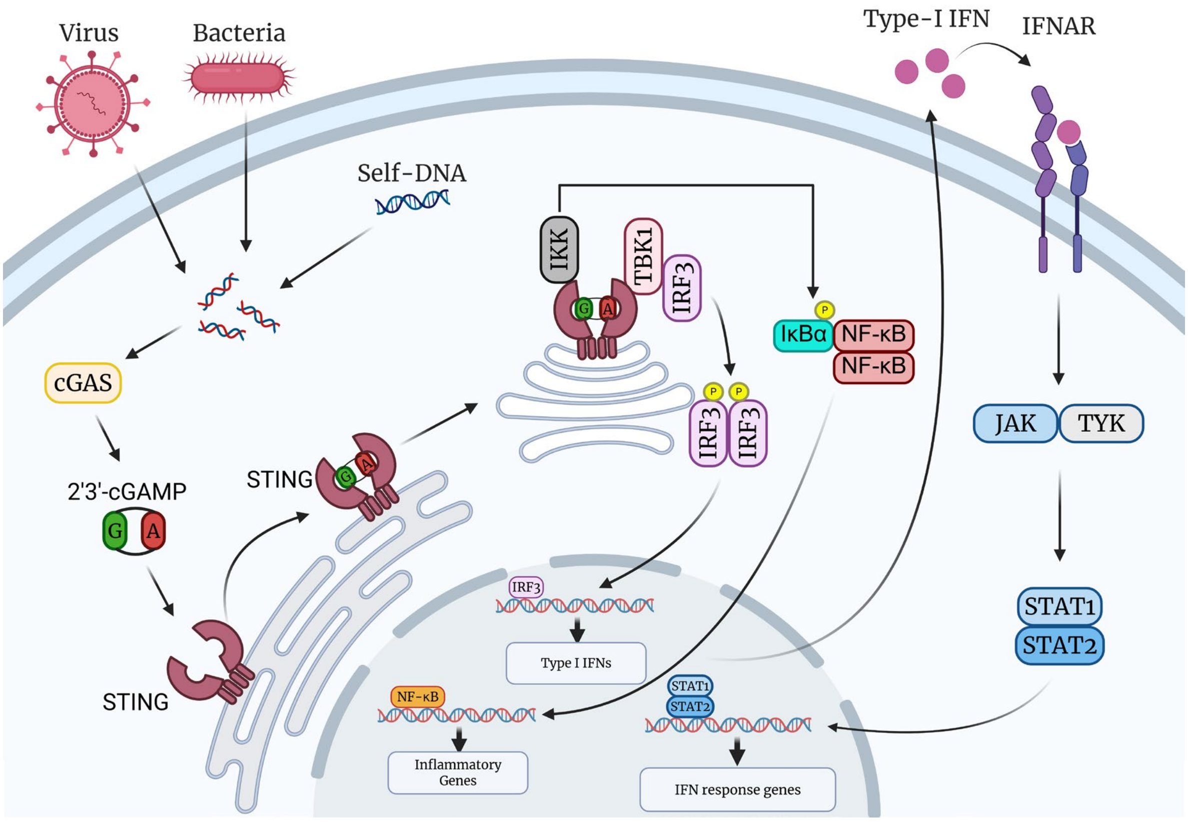

Figure 7. Activation of the cGAS-STING pathway by cytosolic double-stranded DNA. *Cytosolic double-stranded DNA (dsDNA), arising during infection or cellular stress, activates the DNA sensor cyclic GMP-AMP synthase (cGAS). Upon binding dsDNA, cGAS dimers assemble on the DNA and catalyse the synthesis of 2'3' cyclic GMP-AMP (cGAMP). cGAMP binds to stimulator of interferon genes (STING) dimers at the endoplasmic reticulum (ER) membrane, inducing conformational changes that trigger STING oligomerisation and its trafficking to the Golgi. At the Golgi, STING recruits and activates TBK1 and IKKε, which promotes STING phosphorylation and the recruitment and phosphorylation of interferon regulatory factor 3 (IRF3). Phosphorylated IRF3 dimerises and translocates to the nucleus to induce the expression of type I interferons, ISGs, and other inflammatory mediators, including cytokines and chemokines. In parallel, STING activation also stimulates NF-κB signalling, further amplifying inflammatory gene expression. Generated in https://BioRender.com/kb4d3ys.*

3.2.3.1. STING Palmitoylation and TBK1-IRF3 Axis Activation

At the Golgi, STING undergoes palmitoylation at conserved cysteine residues close to TMD3 (C88 and C91 in humans), a modification critical for recruiting downstream kinases[290]. The palmitoylation is catalysed by DHHC-family palmitoyltransferases, most notably DHHC3, DHHC7 and DHHC15, and is required for the formation of STING signalosomes, higher-order oligomers that cluster in lipid drafts at the trans-Golgi network (TGN)[290]. These oligomers act as platforms for the recruitment and activation of TANK-binding kinase 1 (TBK1).

TBK1 binds to the PLPLRT/SD motif of the STING C-terminal tail (CTT)[313,314]. This motif inserts into a groove formed between the kinase domain of one TBK1 subunit and the scaffold and dimerisation domain (SDD) of the other subunit within the TBK1 dimer. This bipartite binding surface allows for the precise docking of STING onto TBK1, with the leucine residue at position 374 (Leu374) playing a significant role in stabilizing the complex and ensuring effective signal transduction downstream of STING activation. Furthermore, STING oligomerisation brings ‘cis’ TBK1 molecules, those bound directly to the same STING dimer, into close proximity with ‘trans’ TBK1 molecules bound to adjacent STING dimers. This spatial arrangement positions the activation loop of the ‘trans’ TBK1 molecules within reach of the catalytic centre of the ‘cis’ TBK1 kinase domain, enabling TBK1 to phosphorylate neighbouring TBK1 molecules in ‘trans’ at Ser172. This trans-autophosphorylation mechanism is critical for full TBK1 activation and amplification of the downstream signalling cascade. Once catalytically active, TBK1 phosphorylates the Ser366 (Ser365 in mouse) residue within the pLxIS motif (where “p” is a hydrophilic residue, “x” is any amino acid, and “S” is the phosphorylation site), which is located upstream of the PLPLRT/SD motif in the STING CTT[315]. Importantly, TBK1 phosphorylates the pLxIS motif of STING dimers adjacent to the one it is directly bound to, rather than the STING dimer it engages via the PLPLRT/SD motif. Phosphorylation of Ser366 creates a docking site for the transcription factor IRF3, which is subsequently recruited into close proximity with catalytically active TBK1 molecules[282,314]. Specifically, IRF3 binds to phosphorylated Ser366 via its N-terminal domain, which features a positively charged surface. IRF3 also contains a conserved C-terminal cLxIS motif (“c” representing a charged residue) that resembles the STING pLxIS motif and can similarly be phosphorylated by TBK1. Once IRF3 is phosphorylated at its cLxIS motif, this site serves as a binding platform for a second IRF3 molecule, which interacts through its own positively charged N-terminal domain. This reciprocal interaction enables IRF3 homodimer formation. Subsequently, the cLxIS motif of the second IRF3 molecule is also phosphorylated by TBK1, completing the activation process. Interestingly, in the absence of TBK1, IKKε can function redundantly to activate IRF3. Studies in murine embryonic fibroblasts (MEFs) and human monocytes have shown that only the combined deletion of both TBK1 and IKKε fully abrogates type I IFN signalling[316,317]. Mechanistically, IKKε is recruited to STING via the same PLPLRT/SD motif that mediates TBK1 docking, suggesting a conserved mode of STING-kinase interaction[318].

3.2.3.2. IRF3 Transcriptional Activity and pLxIS Motif Conservation

The formation of this IRF3 dimer is essential for its nuclear translocation and transcriptional activity. In the nucleus, the IRF3 dimer binds to interferon-stimulated response elements (ISREs) in the promoters of target genes, initiating the transcription of type I interferons and interferon-stimulated genes (ISGs). This mechanism of sequential phosphorylation and dimerisation illustrates a finely tuned licensing process that ensures IRF3 activation only occurs in the appropriate signalling context. Notably, this pLxIS/cLxIS-mediated recruitment and activation mechanism is conserved across other interferon-inducing adaptors, including TRIF, MAVS, and TLR adaptor interacting with endo-lysosomal SLC15A4 (TASL), highlighting its central role in innate immune signalling[315,319].

3.2.3.3. STING-Mediated NF-κB and MAPK Pathway Activation

In parallel, STING also activates the NF-κB and MAPK pathways, although the precise molecular mechanisms remain less well understood than for IRF3 activation. Specifically, the exact way in which STING interacts with components of the NF-κB pathway at a molecular level is still unclear. Two models have been proposed to explain this. One model suggests that NF-κB activation downstream of STING does not require the C-terminal tail (CTT) region that contains the docking site for TBK1[320,321]. This theory is further supported by the observation that, despite the high homology of STING across different phyla, the CTT is found only in vertebrates. In organisms like *Drosophila melanogaster* and *Nematostella vectensis*, which lack the STING CTT, pathways homologous to NF-κB are still activated[320,322]. This has also been observed in human T cells stimulated with 2′3′-cGAMP and in HEK293T cells in reconstitution experiments using various CTT mutants[323,324]. However, it has been reported that an extension of the CTT in zebrafish STING significantly increases NF-κB activation, even when transfected into human cells[321]. These data suggest that the different CTT motifs play a functional role in regulating both the NF-κB and IFN responses, rather than being redundant for NF-κB activation while CTT region likely evolved in vertebrates to specifically modulate the IFN response.

In contrast, the second model argues that NF-κB activation does require the STING CTT and its TBK1 interaction motif. Supporting this, bone marrow-derived dendritic cells (BMDCs) from mice expressing STING mutants, either lacking the CTT (ΔCTT) or bearing the L373A substitution that disrupts TBK1 binding, fail to induce NF-κB activation upon stimulation with the murine STING agonist DMXAA[325]. This suggests that, at least in certain cellular contexts, the CTT is essential for coupling STING to the NF-κB signalling machinery.

Further supporting this, the role of TBK1 in regulating NF-κB signalling becomes especially prominent in bone marrow-derived macrophages (BMDMs), MEFs, and HeLa cells[316,326,327]. In these cell types, TBK1 functions redundantly with IKKε to drive NF-κB activation[316,327], whereas IKKα[327] and IKKβ[326,327], establish a positive feedback loop that amplifies and sustains the signal. It is proposed that intermediates such as TAK1 and NEMO[326] may bridge the STING-TBK1/IKKε axis with the classical IKK complex (IKKα/β), integrating upstream STING signals into full-fledged NF-κB activation.

Because NEMO, IKKβ, and TRIM32- and TRIM56-mediated ubiquitination of NEMO are required for TBK1 activation and full NF-κB and interferon responses downstream of STING, as previously described[326], it has been postulated that STING may activate NF-κB within the architectural framework of supramolecular organizing centres (SMOCs)[328]. Within such a STING SMOC, TBK1 and IKKβ are proposed to function cooperatively in a high-dimensional signalosome complex, coordinated by STING itself.[316]. However, the precise mechanisms by which these kinases are recruited to STING remain under debate. One potential mechanism involves TRAF6. In certain vertebrate species such as zebrafish and other ray-finned fish, the STING C-terminal tail (CTT) has evolved additional motifs capable of recruiting TRAF6, thereby enhancing NF-κB activation[321]. Supporting this, knockdown of TRAF6 in MEFs significantly reduces NF-κB activation in response to cytosolic DNA or DMXAA[327]. Similarly, non-canonical activation of STING via IFI16, recruits TRAF6 to activate NF-κB, following Etoposide-induced DNA damage[329]. In this context, the recruitment of adaptor proteins and kinases to STING may also be facilitated by ubiquitin scaffolds. Recent studies have shown that STING can be modified with LUBAC-induced M1-linked chains and consequent K63-linked chains[330] (potentially via TRAF6[329] and/or TRIM32- and TRIM56[326]). These modifications may serve as docking platforms for signalling proteins like NEMO and TRAF6, promoting the formation of a multivalent, higher-order SMOC signalosome that enables full NF-κB activation downstream of STING.

Activation of the cGAS-STING pathway also induces non-canonical NF-κB signalling by promoting the nuclear translocation of p52-RELB[331,332]. This mechanism has been particularly observed in malignant settings, where STING-driven non-canonical NF-κB activity supports tumour progression by modulating dendritic cell and T cell responses[331].

At similarly unresolved mechanistic levels, STING activation has also been shown to induce MAPK pathway activation in T cells, BMDMs, and MEFs[318,333]. In MEFs and BMDMs, this response appears to depend on TBK1 and IKKε, which function redundantly and signal through the MAP3K TAK1[318].

3.2.4. Ligands of the cGAS-STING Pathway

The cGAS-STING pathway has its evolutionary origin in bacterial defence systems, where it served to protect against bacteriophage infection[334,335]. In mammalian cells, this system has evolved into a complex surveillance mechanism capable of detecting DNA when it is mislocalised, outside its physiological compartments, the nucleus and mitochondria. The presence of DNA in the cytosol, regardless of whether it is derived from pathogens (non-self) or endogenous sources (self), can trigger potent immunostimulatory responses via the cGAS-STING axis. Sources of non-self DNA include DNA viruses, intracellular bacteria, and retroviruses, while self-DNA may arise from mitochondrial or genomic DNA released during cellular stress, nuclear envelope rupture, or apoptosis, as well as from engulfment of dying cells by monocytes.

However, even in the presence of cytosolic DNA, the cell employs multiple safeguard mechanisms to prevent premature activation of the immunostimulatory cGAS-STING pathway. These include: (1) degradation of aberrant DNA by exonucleases such as TREX1; (2) spatial compartmentalisation of cGAS; (3) biophysical properties of the DNA itself that influence the activation threshold, such as fragment length, oxidation state, and sequence context (e.g., bacterial CpG motifs); and (4) as previously discussed, regulation of cGAS by long and concentrated DNA fragments that promote liquid-phase separation, which determines its activation[251,252,336,337]. These controls collectively ensure that cGAS distinguishes between self and non-self, maintaining immune tolerance while remaining responsive to danger.

3.2.4.1. Pathogen-Derived DNA

i. Viruses

Viruses, particularly DNA viruses and retroviruses, are among the most potent non-self-triggers of the cGAS-STING pathway. Upon infection, many DNA viruses deposit their genomes into the cytosol or inadvertently expose DNA during replication or uncoating, making those prime substrates for cGAS recognition. Double-stranded DNA (dsDNA) viruses including Herpes Simplex Virus 1 (HSV-1) and vaccinia virus[338], Cytomegalovirus (CMV)[339,340] and adenoviruses[341], release their genomes into the cytoplasm either during entry or viral replication, directly engaging cGAS and triggering a type I interferon (IFN-I) response. The essential role of this pathway in antiviral defense is further supported by the fact that STING KO mice are more susceptible to DNA virus infection[342]. Interestingly, in the context of Hepatitis B virus (HBV), the susceptibility of hepatocytes to infection is linked to their intrinsic lack of STING expression[343].

Retroviruses such as Human Immunodeficiency Virus 1 (HIV-1), although classified as RNA viruses, also engage the cGAS-STING pathway indirectly. During reverse transcription, cytosolic complementary DNA (cDNA) intermediates are generated and accumulate in infected cells. These reverse-transcribed DNA molecules, if not rapidly degraded, are recognized by cGAS. Indeed, cGAS activation has been observed in retroviral infections, including those caused by HIV-1, murine leukemia virus, and simian immunodeficiency virus[344]. Interestingly, in the case of HIV-2, viral DNA recognition by cGAS has been reported to occur in the nucleus, challenging the prevailing view that cGAS-mediated detection of viral DNA is restricted to the cytoplasm[345].

In the case of HIV-2 infection, cGAS-mediated recognition occurs in the nucleus with the assistance of a host factor known as non-POU domain-containing octamer-binding protein (NONO)[345]. NONO binds and captures HIV-2 DNA along with associated capsid proteins, thereby guiding cGAS to the viral DNA. Beyond NONO, several other host factors-including Polyglutamine Binding Protein 1 (PQBP1)[346], CCHC-type zinc finger protein 3 (ZCCHC3)[347], and GTPase-activating protein SH3 domain-binding protein 1 (G3BP1)[348], also recognize viral DNA and facilitate its engagement by cGAS, ultimately promoting downstream STING activation.

Things become more intriguing in the context of RNA virus infection. Although cGAS cannot synthesize cGAMP upon direct binding to RNA, several RNA viruses have been shown to activate the cGAS-STING pathway indirectly through the release of host mitochondrial DNA (mtDNA) into the cytosol. This mislocalised mtDNA acts as an endogenous ligand for cGAS, triggering downstream immune signalling. Such activation has been reported in infections with severe acute respiratory syndrome coronavirus 2 (SARS-CoV-2)[349], Flaviviruses like Dengue virus[350] and West Nile virus (WNV),[351] and Picornaviruses including enterovirus 71 (EV-A71), Seneca Valley virus (SVV), and foot-and-mouth disease virus (FMDV)[352].

ii. Intracellular Bacteria

The cGAS-STING pathway also contributes to antibacterial immunity. In macrophages infected with *Mycobacterium tuberculosis*, cGAS detects cytosolic bacterial DNA, triggering robust type I IFN production and initiating ubiquitin-mediated selective autophagy to eliminate the pathogen[353]. Similarly, during *Francisella novicida* infection, cGAS cooperates with IFI16 to sense cytosolic bacterial DNA, driving potent STING-dependent type I IFN responses[354]. During *Burkholderia* infection, cGAS initially senses micronuclei-derived chromatin in multinucleated giant cells, triggering a STING-dependent type I IFN response, which later transitions toward autophagy and apoptosis as part of the host defense[355-357].

The role of cGAS-STING in antibacterial immunity gets more complicated, considering that STING can also be activated directly by bacterial-derived cyclic dinucleotides (CDNs)[353,358]. For instance, while cGAS-deficient mice show increased susceptibility to *Mycobacterium tuberculosis* (*Mtb*), STING-deficient mice do not, indicating STING-independent functions of cGAS during *Mtb* infection[359]. The impact of STING also varies with the pathogen: its deletion impairs control of *Listeria monocytogenes*, *Chlamydia trachomatis*, and *Salmonella enterica*[342,358,360], but is protective in models of sepsis and *Helicobacter pylori* infection[361], highlighting the pathogen- and context-specific roles of STING in bacterial immunity.

3.2.4.2. Self-DNA

i. Extracellular Self-DNA

Extracellular self-DNA can arise from aberrant accumulation of DNA in the cytosol, usually due to exacerbated non-apoptotic cell death, defects in phagocytosis and digestion, or impaired clearance when extracellular and lysosomal DNases are defective. For example, during radiotherapy of solid tumours, large amounts of tumour-derived DNA are released from irradiated cells into the extracellular space in exosomes, which are taken up by dendritic cells (DCs) via direct endocytosis, leading to activation of the cGAS-STING pathway and enhancement of antitumor immunity[362-364]. Similarly, in murine models of hepatocellular carcinoma, induction of immunogenic cell death (ICD)-through inhibition of thioredoxin reductase (TrxR) activity, thereby inducing endoplasmic reticulum stress (ERS)-in combination with liver- and mitochondria-targeting gold(I) complexes, activates cGAS-STING signalling and contributes to anti-tumour immune responses[365]. Acute ischemic events, such as coronary artery occlusion, cause extensive cell death and the release of nuclear DNA, which is subsequently phagocytosed by infiltrating monocytes, triggering STING-dependent inflammatory activation[366]. Adjuvant-mediated cell death has also been shown to induce host cell DNA release that promotes immune activation via STING[367]. Additionally, neutrophil extracellular trap (NET) formation, bearing oxidised mitochondrial DNA (mtDNA), leads to neutrophil death and extrusion of DNA-protein complexes into the extracellular space, which in turn activates STING signalling[368].

Clearance of cytosolic DNA, is tightly regulated by a series of nucleases. One key enzyme is deoxyribonuclease II (DNase II), a lysosomal endonuclease that plays a critical role in degrading DNA derived from phagocytosed apoptotic cells[369,370]. DNase II is particularly important for processing exogenous DNA from dead cells, DNA from developing erythroblasts, and expelled nuclei that are engulfed by macrophages during erythropoiesis[369-372]. The essential role of DNase II is underscored by studies in DNase II-deficient mice, which exhibit embryonic lethality due to defective erythropoiesis, severe anemia, and hyperinterferonemia[373]. Co-deletion of *Ifnar1* rescued from embryonic lethality, but the mice develop polyarthritis and autoimmune phenotypes[237,369]. Notably, co-deletion of *Cgas* or *Sting1* rescues the mice from embryonic lethality[236,369,374]; however, these animals develop polyarthritis in adulthood (10-month old) driven by TLR7/9-induced anti-DNA autoantibodies, highlighting a compensatory shift toward endosomal DNA sensing in the absence of cytosolic DNA clearance[375]. Biallelic *DNASE2*, mutation, which encodes DNase II, have also been identified in humans and are associated with anemia and type I interferon-driven autoinflammation[376].

Three prime repair exonuclease 1 (TREX1), also known as DNase III, is a 3′ to 5′ exonuclease that digests cytosolic DNA[377]. It is localized to the cytosolic face of the endoplasmic reticulum (ER), where it anchors to the outer ER membrane. TREX1 degrades both unmodified and oxidized DNA, albeit at different rates[336,377]. In mice, *Trex1* deficiency leads to perinatal lethality due to systemic multi-organ inflammation and severe autoimmune manifestations, particularly affecting the heart[378,379]. Only 39% of *Trex1* knockout (KO) mice survive beyond 7 months of age[237]. Remarkably, co-deletion of cGAS or STING fully rescues the survival of *Trex1*-deficient mice by 7 months and prevents the accumulation of cGAMP in *Cgas*-deficient *Trex1* KO animals[237,380,381]. Similarly, co-deletion of *Ifnar1* protects against pathology induced by *Trex1* deficiency, although elevated IFN-β levels persist, in contrast to the more complete protection observed with *Irf3* co-deletion by 14 months of age[382]. The complete rescue observed upon *Cgas*-, *Sting1*-, or *Irf3*-co-deletion, compared to partial protection from *Ifnar1* co-deletion, highlights the central role of the cGAS-STING pathway in directly regulating type I interferon responses and driving autoimmunity in *Trex1* KO mice, even in the absence of the IFNAR/JAK/STAT amplification loop. In humans, mutations in the TREX1 gene are associated with a spectrum of autoimmune diseases, including Aicardi-Goutières syndrome (AGS), systemic lupus erythematosus (SLE), familial chilblain lupus, and retinal vasculopathy with cerebral leukodystrophy[383,384].

Apart from the cytosol, DNA can also be found extracellularly, including in peripheral compartments such as serum, urine, and other bodily secretions. This extracellular DNA exists either as soluble or deposited autoantigenic nucleoprotein complexes. It may also be contained in circulating microparticles derived from apoptotic debris, due to their inefficient clearance or their excessive accumulation[385-388]. DNase I is the principal enzyme responsible for degrading extracellular DNA in tissues with high cellular turnover. Mutations in *DNASE1* have been reported in patients with systemic lupus erythematosus (SLE), and DNaseI-deficient mice develop a lupus-like autoimmune phenotype[385,386]. Similarly, DNase1L3, a DNase I-related endonuclease, plays a critical role in degrading DNA-rich microparticles from apoptotic cells. Loss-of-function mutations in *DNASE1L3* are also associated with SLE in both humans and mice[387,388]. However, the role of cGAS in sensing DNA substrates normally cleared by DNase I or DNase1L3 remains unclear. These diseases might be more complicated as the accumulated extracellular DNA may also engage additional DNA sensors within the phagolysosomal compartment, such as Toll-like receptor 9 (TLR9), as observed in DNase II-deficient mice[375].

ii. Mitochondrial DNA (mtDNA)

Release of mitochondrial DNA (mtDNA) into the cytosol serves as a potent trigger for activation of the cGAS-STING pathway. During the execution phase of the intrinsic (mitochondrial) apoptotic pathway, both the outer and inner mitochondrial membranes undergo permeabilisation (termed as MOMP and MIMP respectively) to facilitate the release of cytochrome c, which subsequently activates executioner caspases. This membrane permeabilisation is mediated by BAX/BAK pore formation, which not only disrupts mitochondrial integrity but also results in the extrusion of the inner mitochondrial membrane into the cytosol, enabling the release of mtDNA. However, executioner caspases prevent activation of cGAS and other cytosolic nucleic acid sensors through their proteolytic cleavage, a process that also targets numerous cellular proteins and facilitates the immunologically silent clearance of apoptotic cells via apoptotic body formation[389,390]. In certain contexts, sublethal BAX/BAK-dependent MOMP, termed minority MOMP (miMOMP), as observed in senescent cells, can lead to mtDNA release and subsequent cGAS-STING-mediated regulation of the senescence-associated secretory phenotype (SASP)[391]. Interestingly, under non-apoptotic cellular stress conditions, such as mitochondrial oxidative damage, mtDNA release can occur independently of BAX/BAK through voltage-dependent anion channels 1 and 3 (VDAC1/3)-dependent pores[392,393]. This alternative route has been associated with mitochondrial permeability transition pore (mPTP) formation[394] and implicated in disease models such as ALS, where mutant TDP-43 enhances mPTP activity[392], and lupus-like disease in endonuclease G (Endog)-deficient mice[393], both leading to mtDNA leakage and subsequent activation of the cGAS-STING pathway. Moreover, mitochondrial defects in replication, repair, or metabolism can also provoke mtDNA release and subsequent cGAS-STING activation. For instance, depletion of the transcription factor A, mitochondrial (TFAM) or Caseinolytic mitochondrial matrix peptidase proteolytic subunit (CLPP), leads to improper nucleoid packaging and leakage of mtDNA into the cytosol[395,396]. Similarly, loss of mitochondrial Endog or exposure to certain chemotherapeutic agents induces cGAS activation[393,397]. Oxidized mtDNA is more resistant to TREX1 degradation and is therefore more immunostimulatory[397]. Loss of fumarate hydratase (FH) promotes mtDNA export via SNX9-dependent mitochondrial-derived vesicles (MDVs)[398]. Additionally, pro-inflammatory cytokines such as IL-1β and IFN-α have been shown to disrupt mitochondrial homeostasis, further promoting mtDNA release and cGAS-STING pathway activation, thereby amplifying the immune response[399].

iii. Nuclear Genomic DNA and Micronuclei

DNA damage and replication stress are potent triggers of cGAS-STING activation through the release of genomic DNA fragments into the cytosol. Replication stress can result from oncogene activation, DNA-damaging agents (e.g., ionizing radiation, mitomycin C, or cisplatin), nucleotide pool imbalances, R-loop accumulation, and defects in DNA repair machinery or replication fork. Such stress can lead to fork collapse and DNA fragmentation, driving leakage of chromatin into the cytoplasm triggering the activation of the cGAS-STING pathway[400-407]. For instance, in prostate cancer cells, oncogenes like c-Myc and HRAS promote MUS81- and PARP-dependent DNA damage and subsequent cytosolic DNA accumulation[400]. Similarly, in breast cancer cell lines, Bloom syndrome (BLM) helicase and exonuclease 1 (EXO1) are implicated in the generation of ssDNA fragments in response to genotoxic stress[404].

R-loop-induced DNA fragments, and genetic deficiencies in DNA damage response (DDR) components, including ATM or ATR, contribute to cytosolic DNA accumulation in various disease contexts[405]. In non-alcoholic steatotic liver disease (NAFLD), replication stress caused by nucleotide imbalance leads to ATR-dependent DNA leakage and cGAS-STING activation[401]. In Eμ-Myc B cell lymphoma cell lines, treatment with genotoxic agents increased cytosolic content of genome-derived ssDNA and dsDNA induced by R-loop formation[403]. Cytoplasmic chromatin fragments (CCFs) is a hallmark of cellular senescence and their presence have been linked to regulating chronic inflammation to promote tumorigenesis and SASP phenotypes to promote paracrine senescence[408,409]. Loss of members of DNA damage response machinery, such as ATM drives release of ssDNA in the cytosol that activates cGAS-STING supporting AT pathology[405]. Oxidative DNA damage, marked by 8-hydroxyguanine (8-OHG) formation upon ROS or UV exposure, also increases the immunogenicity of self-DNA and enhances STING-dependent IFN responses[336,410]. Notably, the carcinogen DMBA and chemotherapeutics like cisplatin and etoposide induce nucleosome release and STING activation, linking DNA-adducts formation with innate immune signalling[411].

Release of chromatin fragments into the cytosol and the subsequent activation of the cGAS-STING pathway is a common feature of micronuclei. This is largely due to the fragile and rupture-prone membrane structure of micronuclei compared to the main nucleus. Micronuclei typically form at the end of mitosis in response to irreversible mitotic DNA damage, chromosome mis-segregation, or DNA replication errors, and they encapsulate either chromosomal fragments or entire mis-segregated chromosomes[266,409,412,413]. These micronuclei are enriched in heterochromatin marks, such as trimethylated histone H3 at lysine 9 (H3K9me3) and lysine 27 (H3K27me3), and the DNA damage marker γ-H2AX, indicating that they originate from transcriptionally silent genomic regions[409,412]. This epigenetic state may contribute to their high immunostimulatory potential through efficient cGAS recognition. Notably, inactivation of key factors involved in DNA replication, repair, or recombination, including the RecQ-like helicase BLM[413], RNase H2[228], BRCA2[414], topoisomerase II[415], Rad51[407], or poly(ADP-ribose) polymerase 1 (PARP1)[416], has been shown to increase micronucleus formation and consequently activate the cGAS-STING signalling pathway. Recent evidence indicates that cGAS is not recruited to micronuclei, contrasting the previously accepted belief[417,418]. Therefore, micronuclei-mediated activation of the cGAS-STING pathway is more likely to occur through the release of micronuclei-derived chromosomal or DNA fragments into the cytosol, rather than within the micronuclei themselves.

Genomic DNA fragment release from the nucleus can occur under physiological conditions during processes such as DNA replication, telomere maintenance, and transcription, and these fragments may enter the cytosol to activate the cGAS-STING pathway. One well-characterized source of genomic instability arises from the misincorporation of ribonucleotides by DNA polymerases, a frequent event occurring once every ~7,000 to 10,000 bases. Failure to efficiently remove these ribonucleotides or to resolve persistent RNA-DNA hybrids (R-loops) leads to replication stress, DNA strand breaks, and cytosolic DNA leakage. The RNase H2 complex, comprising RNaseH2A, RNaseH2B, and RNaseH2C, is essential for ribonucleotide excision repair and R-loop resolution[419,420]. Deficiency in any RNase H2 subunit leads to spontaneous DNA damage, accumulation of nuclear-derived cytosolic DNA, type I interferon responses, and Aicardi-Goutières syndrome-like inflammatory phenotypes[228,419-422]. In mice, *RNaseH2B* knockout results in perinatal lethality and systemic inflammation, both of which are rescued by genetic deletion of cGAS or STING, confirming the cGAS-STING axis as the effector of the aberrant immune activation[228,421]. Moreover, loss of *RNaseH2b* function promotes micronuclei formation, further contributing to cGAS activation[266,423]. Another nuclear enzyme, SAMHD1, hydrolyzes deoxynucleoside triphosphates (dNTPs), thereby maintaining nucleotide pool homeostasis and genome stability. Mutations in SAMHD1 increase replication stress and DNA damage, leading to cGAS-STING-mediated type I IFN production and contributing to autoimmune pathogenesis[229,278,424,425].

iv. Endogenous Retroelements

Sensing of retroelements may, in fact, also be mediated by cGAS-STING. Retrotransposon sequences occupy a considerable fraction of the human genome, but most are severely truncated and thus considered non-functional. Among them, LINE-1 (L1) elements retain the capacity for retrotransposition, although several mechanisms actively restrict their propagation under homeostatic conditions. However, imbalances in the surveillance of endogenous retroelements can trigger cGAS activation due to improper accumulation of cDNA intermediates. The best-studied example of cGAS sensing retrotransposon activity is the loss of the 3′ repair exonuclease TREX1, which normally counteracts this process by degrading DNA intermediates. TREX1 deficiency leads to the accumulation of L1-derived DNA in mouse tissues and human neural stem cells[382,426]. Further upstream, de-repression of retroelements through epigenetic alterations occurs naturally during ageing, resulting in cytoplasmic L1 accumulation and cGAS-STING-dependent inflammation[427]. Although L1 retrotranscription primarily occurs in the nucleus, cDNA synthesis can also take place in the cytoplasm via the activity of the L1-encoded reverse transcriptase, ORF2p[427]. This extranuclear activity may contribute to cGAS-STING activation; however, the precise molecular mechanisms by which ORF2p functions in the cytosol to initiate cGAS signalling remain to be fully elucidated. The involvement of endogenous retroelements in cGAS-STING activation has also been established in models of sterile inflammation. For example, in a murine model of inflammatory bowel disease (IBD) induced by dextran sulfate sodium (DSS), retroelements such as MMTV, MERVK-10C, IAP, ETn, MERVL, and LINE-1 contribute to disease pathogenesis through cGAS-STING activation[428]. Notably, treatment with reverse transcriptase inhibitors ameliorates disease symptoms in this model[428]. Similarly, in the skin, sensing of endogenous retroelements, specifically LINE-1, intra*cis*ternal A-particle (IAP) elements, and the Xmv45 locus, via the cGAS-STING pathway plays a critical role in regulating both homeostatic and inflammatory responses to the microbiota[429].

4. Deregulation of STING in Disease

4.1. STING Hyperactivation and Interferonopathies

The detection of foreign nucleic acids is a fundamental function of the innate immune system, essential for mounting effective responses against pathogens, as previously reviewed. However, cellular failure to discriminate between self-versus non-self-nucleic acids has been increasingly implicated in the pathogenesis of chronic inflammatory disorders collectively termed type I interferonopathies and other autoimmune disease[217,430-434]. Aberrant accumulation of self-derived cytosolic and extracellular nucleic acids can result from a variety of intrinsic cellular defects, including impaired clearance of apoptotic cells, immunogenic non-apoptotic cell death, defective phagocytosis and lysosomal digestion, mitochondrial stress, chromosomal instability (CIN), aberrant mitosis, errors in DNA replication and repair, and the formation of micronuclei[435-437]. In parallel, erroneous recognition of cytosolic nucleic acids by pattern recognition receptors (PRRs) may arise as response to mutations in genes encoding for nucleic acid sensing, signalling or processing of nucleic acids or mutations in genes that compromise nuclear or mitochondrial integrity. Upon persistent activation of these receptors in response to self-DNA, a sustained production of type I interferons (IFNs), pro-inflammatory cytokines, chemokines, and interferon-stimulated genes (ISGs) ensues, driving pathological immune activation and contributing to the onset and progression of autoimmunity, chronic inflammatory disorders, and type I interferonopathies.

Aberrant activation of the cytosolic DNA sensor cGAS and its adaptor STING underlies a distinct group of interferon-driven disorders, encompassing both monogenic type I interferonopathies and a broader range of chronic inflammatory and autoimmune diseases. Among the best-characterized and earliest described disorders in this group is Aicardi-Goutières syndrome (AGS), which is caused by mutations in genes such as TREX1, RNASEH2A/B/C and SAMHD1[384,422,438,439]. These genetic defects impair nucleic acid metabolism or sensing, leading to the accumulation of endogenous nucleic acids, which come from either endogenous retroelements or DNA damage, and chronic activation of type I interferon signalling[381,440,441]. Clinically, AGS presents with early-onset neuroinflammation, intracranial calcifications, leukodystrophy, hepatosplenomegaly, and chilblain-like skin lesions, closely resembling a congenital viral infection. STING-associated vasculopathy with onset in infancy (SAVI) is another monogenic interferonopathy caused by gain-of-function mutations in TMEM173, encoding STING[442-444]. This leads to constitutive STING pathway activation and results in systemic vasculopathy, interstitial lung disease, and ulcerative skin lesions from early infancy. Familial chilblain lupus (FCL), caused by mutations in *TREX1*, *SAMHD1*, or *TMEM173*, is a cutaneous lupus variant that presents with painful, inflammatory lesions on acral surfaces[445-449]. Like AGS, it involves inappropriate sensing of self-DNA. COPA syndrome, caused by mutations in COPA, a gene involved in retrograde vesicular transport, results in mislocalisation of immune signalling molecules[301,450]. Patients typically develop interstitial lung disease, arthritis, autoantibodies, and kidney disease, accompanied by heightened IFN-I responses. DNASE2 deficiency, a recessive disorder, leads to defective degradation of DNA in lysosomes, resulting in IFN-driven anemia and systemic inflammation, via both the cGAS-STING and TLR9 pathways[376]. USP18 deficiency, a defect in a critical negative regulator of the IFN-I response, results in uncontrolled JAK-STAT signalling and leads to neonatal-onset systemic inflammation and encephalopathy[451,452].

In addition to these Mendelian disorders, systemic lupus erythematosus (SLE) represents a paradigmatic multifactorial autoimmune disease with strong involvement of type I IFN signalling. Although most SLE cases are polygenic, rare monogenic forms have been associated with mutations in genes involved in nucleic acid metabolism, such as TREX1, DNASE1, and DNASE1L3[453-457]. These defects lead to impaired clearance of self-DNA and the formation of immune complexes that can activate innate immune sensors, including cGAS-STING and TLR9, promoting chronic type I interferon (IFN-I) production[454,458-464]. More than 80% of SLE patients exhibit an IFN-I signature, and cGAS-STING has been shown to contribute to this response through sensing of mitochondrial or extracellular DNA[463,464]. However, its role is complex, as cGAS or STING deficiency does not uniformly protect against disease in lupus models, indicating both pathogenic and regulatory functions[465,466]. Beyond SLE, a growing number of inflammatory diseases not classically defined as interferonopathies are now recognized to involve aberrant activation of the cGAS-STING pathway and chronic type I IFN responses. For example, psoriasis features sustained STING activation in keratinocytes, promoting IFN-dependent inflammation in the skin[467,468]. Similarly, rheumatoid arthritis (RA) exhibits a type I IFN signature in synovial tissue, and STING-mediated responses have been implicated in disease pathogenesis and joint damage[469-471]. Other conditions with emerging links to interferon dysregulation include dermatomyositis, systemic sclerosis, and type 1 diabetes mellitus, all of which show evidence of chronic IFN-I activity even in the absence of clear monogenic causes[472-474].

Disease	Clinical Manifestations	Mutations / Genetic Defects
Aicardi-Goutières syndrome (AGS)	Early-onset neuroinflammation, intracranial calcifications, leukodystrophy, hepatosplenomegaly, chilblain-like skin lesions (resembles congenital viral infection)	*TREX1, RNASEH2A, RNASEH2B, RNASEH2C, SAMHD1*
STING-associated vasculopathy with onset in infancy (SAVI)	Systemic vasculopathy, interstitial lung disease, ulcerative skin lesions (from early infancy)	*TMEM173* (gain-of-function, encodes STING)
Familial chilblain lupus (FCL)	Painful, inflammatory lesions on acral surfaces (cutaneous lupus variant)	*TREX1, SAMHD1, TMEM173*
COPA syndrome	Interstitial lung disease, arthritis, autoantibodies, kidney disease; systemic inflammation with IFN-I signature	*COPA* (retrograde vesicular transport defects)
DNASE2 deficiency	IFN-driven anaemia, systemic inflammation	*DNASE2* (defective lysosomal DNA degradation; activates cGAS-STING & TLR9 pathways)
USP18 deficiency	Neonatal-onset systemic inflammation, encephalopathy	*USP18* (negative regulator of IFN-I/JAK-STAT signalling)
Systemic lupus erythematosus (SLE)	Autoantibodies, systemic inflammation, multi-organ involvement (skin, joints, kidneys, CNS); >80% show IFN-I signature	Mostly polygenic; rare monogenic forms in *TREX1, DNASE1, DNASE1L3*
Psoriasis	Chronic inflammatory skin disease; sustained STING activation in keratinocytes drives IFN-dependent inflammation	Multifactorial (STING pathway activation, no single gene)
Rheumatoid arthritis (RA)	Synovial inflammation, joint damage, type I IFN signature	Multifactorial (STING-mediated IFN responses, no single gene)
Dermatomyositis, systemic sclerosis, type 1 diabetes mellitus	Chronic IFN-I activity contributing to inflammation and autoimmunity	Multifactorial (no single monogenic cause; aberrant IFN regulation)

Table 3: Interferon-driven diseases associated with cGAS-STING dysregulation. *Overview of monogenic and multifactorial disorders linked to aberrant activation of the cytosolic DNA sensor cGAS and its adaptor STING. The table lists each disease, its main clinical manifestations, and the associated genetic mutations or defects. Monogenic interferonopathies such as AGS, SAVI, and COPA syndrome result from defined mutations that impair nucleic acid metabolism, sensing, or downstream signalling, while multifactorial autoimmune and inflammatory diseases (e.g., SLE, psoriasis, RA) involve chronic type I interferon activity with more complex or polygenic contributions.*

Thus, the spectrum of interferon-driven disease extends beyond rare Mendelian disorders and includes a broader group of multifactorial autoimmune and inflammatory diseases in which aberrant nucleic acid sensing and type I IFN signalling play a pivotal role. This underscores the importance of maintaining strict regulation over nucleic acid metabolism, sensing, and downstream interferon responses to prevent self-directed immunity and tissue pathology.

4.2. STING-Associated Vasculopathy with Onset in Infancy (SAVI)

Human STING exhibits considerable genetic variability. The STING R232 allele is the most common variant, present in approximately 45% of the population[475,476]. The R71H-G230A-R293Q haplotype (HAQ) is the second most common allele, with a prevalence of 16.07% in East Asians, 7.78% in South Americans, and 6.75% in South Asians[475]. Gain-of-function mutations in human *STING1* have been reported to induce overactive STING as a driver of STING-associated vasculopathy with onset in infancy (SAVI)[477]. These include mutation in both the dimeric interface of STING that stabilizes cyclic dinucleotide (CDN) binding domain, and in the cytosolic domain, which stabilizes STING in an active state[478-481]. Notably, mutations in the spiral ring of the connector domain, including N154S, V155M, and G158A, induce a 180° rotation of the ligand binding domain (LBD), leading to cGAMP independent STING oligomerisation and activation[482]. Mutations at the polymerisation interface, including C206, C207, R281, and R284, promote activation by relieving the auto-inhibition of STING oligomerisation independently of the LBD rotation[482,483]. Similarly, mutations such as H72N, F153V, V147L, and V147M relieve the constraint on the polymer interface and auto-activate STING without requiring rotation[282,482]. H72 and V147 stabilize the ligand-binding head and C-terminal tail interaction, while F153 constrains the polymer interface as substitution to smaller residues (e.g., p.F153V) increases flexibility and relieves autoinhibition. Additionally, p.G166E in the ligand-binding pocket causes weak autoactivation and loss of cGAMP responsiveness, though its pathogenic role in SAVI remains unclear[282,482].

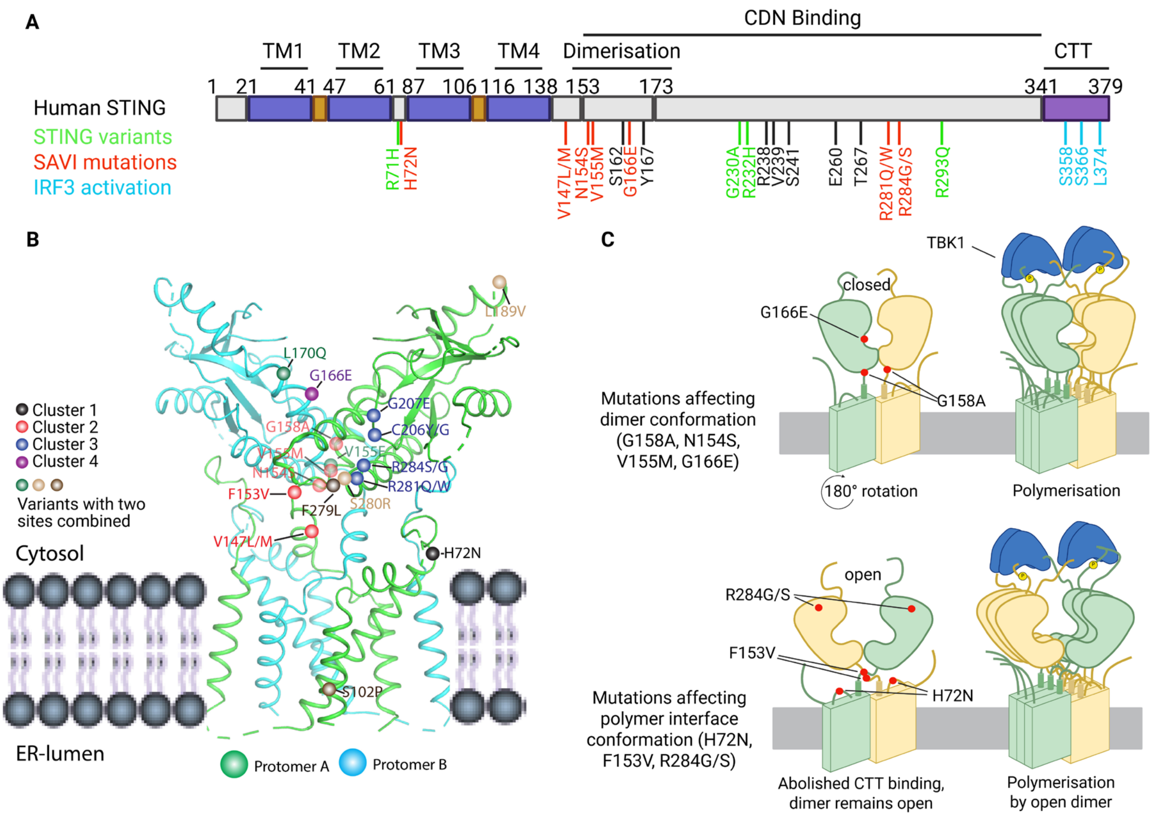

Figure 8. Structural and Functional Mapping of Human STING and SAVI Mutations. *(**A**) Domain organisation of the human STING protein. TM, transmembrane region; CDN, cyclic dinucleotide. Key residues for CDN binding are shown in black, common human STING variants in green, residues critical for IRF3 activation in blue, and SAVI-associated mutations in red. (**B**) Structural mapping of SAVI mutations on the human STING protein. Mutations are grouped into four clusters: Cluster 1 (black sphere) at the N-terminal domain (H72N); Cluster 2 (red sphere) at the dimer interface (V147L/M, F153V, N154S, V155M, G158A); Cluster 3 (blue sphere) at the LBDα2-α3 helical bundle and extended LBDβ1-β2 loop (C206Y/G, G207E, R281Q/W, R284G/S); and Cluster 4 (purple sphere) at the ligand-binding pocket (G166E). Additional compound mutations are represented by coloured spheres: brown (S102P/F279L), green (V155E/L170Q), and light brown (L189V/S280R)[286]. (**C**) Proposed model of STING auto-activation. Mutations in clusters 1, 3 and members of cluster 2 (V147L/M, F153V,) disrupt the polymer interface and release C-terminal tail binding, leaving the dimer in an open state but permitting polymerisation and activation. Mutations in members of cluster 2 (N154S, V155M, G158A) and cluster 4 promote closed-dimer formation, mimicking ligand binding and driving constitutive activation. Created in BioRender. https://BioRender.com/x4qgvut.*

From a clinical aspect, SAVI is an autosomal-dominant genetic disorder characterized by early-onset systemic inflammation, interstitial lung disease (ILD), severe skin vascular disease of the acellular region, chronic anaemia, polyarthritis-like symptoms and growth failure[442,484]. SAVI patients with *de novo TMEM173* mutations have an early-onset of disease (from birth) and present with more severe phenotype [442,485] compared to patients with familial *TMEM173* mutations that had a later-onset (teenager or adulthood) and milder clinical manifestations[448,484]. However, in both cases, the therapeutic management of the disease is challenging. Steroids are partially effective while disease-modifying therapies, such as methotrexate, mycophenolate mofetil (MMF), anti-malarials, infliximab (anti-TNF) and rituximab (antri-CD20) showed poor patient response [442,486,487]. Recent studies utilizing JAK1/2 inhibitors have shown encouraging data especially in patients with variants in the dimerisation over the cytosolic domain of STING [488-491]. However, it only temporarily manages the disease while it failed to decrease the IFN signature in the bloodstream, a hallmark of SAVI pathology, it is not curative but instead disease frequently relapses and patients present with life-threatening secondary viral infections [491]. At the same time, prognosis is poor especially in patients with a severe lung involvement, with a high mortality rate in the first two decades of life [442]. Currently, there is no curative therapy for SAVI. The limited effectiveness of available treatments, including TNF inhibition and JAK/STAT pathway blockade, indicates that the molecular mechanisms driving the disease remain incompletely understood. This therapeutic gap highlights the urgent need for further mechanistic studies to identify the signalling pathways and cellular processes that sustain chronic inflammation, which could inform the development of targeted interventions capable of controlling inflammation and preventing severe organ damage and early mortality.

In SAVI patients, a constitutive and chronic STING-mediated inflammatory response, particularly within hematopoietic populations and endothelial cells, has been implicated as the main driver of disease pathology. Bone marrow transplantation from *Sting1*^{V154M} mice into irradiated wild type hosts was sufficient to transfer myeloid abnormalities, confirming that hematopoietic immune cells are capable of driving the disease phenotype[492]. Recipient mice displayed an increase in inflammatory macrophages and neutrophils, along with a depletion of mature B cells in both spleen and bone marrow. In contrast, transplantation of hematopoietic stem and progenitor cells (HSPCs) isolated from *Sting1^{N153S}* mice into irradiated wild-type recipients did not reproduce interstitial lung disease or lethality[492]. Instead, it led only to an increased interferon stimulated gene (ISG) signature in the lung and reduced body weight. In both models, a severe T cell deficiency was observed, caused by cell intrinsic defects in T cell development. The N153S mutation predominantly impaired mature T cells in the periphery, whereas the V154M mutation restricted early T cell development in the thymus, a defect that could be partially compensated by irradiation resistant host T cells. These findings suggest that T cells play an important role in SAVI pathogenesis in mice. The differing outcomes between models reflect the experimental design and specific mutations rather than excluding mutation-specific contributions to T cell mediated disease. This role for T cells is further supported by genetic evidence in murine models. *Rag1$^{-/-}$ Sting1^{N153S}* mice, which lack both T and mature B cells, show no histological signs of lung disease[493,494]. Similarly, *Tcrβ$^{-/-}$ Sting1^{N153S}* mice, lacking mature T cells, develop only mild pulmonary involvement[493,494]. In contrast, *μMT$^{-/-}$ Sting1^{N153S}* mice, which lack mature B cells developed severe perivascular inflammation in the lung, indicating that mature B cells and antibodies are not required for STING N153S-driven lung pathology[493]. Interestingly, this T-cell dependency is further supported by the observation αβ T cell but not γδ T cell cytopenia is observed in these models, together with expansion of inflammatory macrophages and monocyte[493,494]. Consistently, SAVI patients show spontaneous T cell death[323,442].

The pathogenesis of SAVI has been linked to lung inflammation, scarring, and fibrosis, as well as increased vascular permeability, vascular occlusion and rupture leading to tissue ischemia, necrotic skin ulcers, and systemic immune dysregulation. Although the inflammatory nature of the disease is well recognized, the exact cell death mechanisms responsible for tissue damage remain poorly defined. Mechanistically, T cell cytopenia in SAVI has been associated with impaired T cell development and activation that predominantly depends on IFN-γ but is independent of type I and III interferons in mice[494,495]. Other studies have implicated STING driven endoplasmic reticulum stress as a cause of T cell exhaustion and death[496]. In line with these observations, spontaneous death of T cells, monocytes, and endothelial cells has been reported in SAVI patients[323,442]. Furthermore, *in vitro* exposure to STING agonists induces apoptosis in isolated T cells, as demonstrated by Annexin V staining and flow cytometry[497]. Notably, this effect is absent in other primary cell types such as MEFs, BMDMs, suggesting that the T cell phenotype may reflect context specific vulnerability rather than a universal mechanism across all cell types[497].

Overactive STING is the primary driver of SAVI, and clinical data from patients suggest that type I interferons downstream of STING and IFNAR contribute to STING associated autoinflammation, consistent with the classification of SAVI as a type I interferonopathy[159,442,490]. In contrast, findings from mouse models indicate that type I interferon responses are largely redundant. Previous studies have shown that disease in *Sting1^{N153S}* mice proceeds independently of type I interferons, IRF3, and IRF7[492,493,498]. T cell depletion, inflammatory monocyte and neutrophil expansion occurred independently of *Irf3/7*, and *Ifnar1*, suggesting that type I IFNs are not required for the effects of N153S or V154M mutations in haematopoietic cell populations. Although *Irf3* or *Ifnar1* deficiency does not provide a survival advantage, *Irf3* deletion leads to a substantial reduction in interferon-stimulated gene (ISG) expression[492,493,498], indicating that IRF3 remains functionally important for regulating interferon responses, even if it is not strictly essential for disease progression. However, expression of NFκB-induced genes like *TNFα*, *Nfkb2* and *Cxcl10* was even enhanced when type I interferon signalling was abrogated by IFNAR or IRF3 knock-out. Interestingly, deletion of TNFR1 and TNFR2 partially ameliorates T cell loss in the spleen and thymus and improves lung pathology at 10 weeks of age, while it does not prevent lymph node loss[499]. Based on these findings, the authors of that study proposed that available TNFR antagonists might benefit SAVI patients. However, clinical administration of the TNF blocker etanercept in SAVI patients failed to provide any disease amelioration[491].

Taken together, while species-specific differences in SAVI pathogenesis between mice and humans cannot be fully excluded, these studies suggest that disease is driven by a complex mechanistic network downstream of STING rather than a single isolated pathway. This network likely involves both type I interferon and TNF signalling, which contribute distinct yet interconnected aspects of the inflammatory and immunopathological phenotype. The limited efficacy of monotherapies targeting only a single axis, as well as JAK inhibitors that suppress only the amplification loop of IFN responses without addressing STING's direct role in inducing type I IFN responses via IRF3, underscores the need for a more comprehensive understanding of these pathways. Elucidating the precise contributions, interactions, and potential points of convergence within this network will be essential to guide the development of more effective and durable therapeutic strategies. Importantly, such insights may extend beyond SAVI, offering broader therapeutic potential for other STING-driven autoimmune and autoinflammatory diseases.

5. STING and Cell Death

5.1. Emerging Links between STING and Cell Death

The cGAS-STING pathway has been previously implicated in the regulation of different cell death programs. Agonist-induced activation of STING has been reported to drive pro-apoptotic functions in T and B lymphocytes, including malignant B cells[323,497,500], through a process dependent on endoplasmic reticulum (ER) stress and TBK1-IRF3-dependent induction of Bax, leading to cytochrome c release[501]. Interestingly, Bax-mediated mitochondrial permeabilisation can trigger mtDNA release, generating a positive feedback loop that further activates cGAS-STING[502,503]. This ER stress-associated, STING-mediated apoptotic cell death has been observed in multiple contexts, including macrophages during mycobacterial infection[504], hepatocytes in a murine model of early alcoholic liver disease[505], murine chronic lymphocytic leukaemia, and normal non-malignant B cells[500]. Additionally, STING-induced apoptosis via the p53-BH3-only protein axis has been demonstrated in primary and lymphoblastic leukaemia murine T cells[497], and specifically via PUMA, NOXA, and BIM in TRP53/TP53-mutant mouse B lymphoma, human NK/T lymphoma, and acute myeloid leukaemia cells[506]. However, no STING agonist-induced cell death has been observed in MEFs, B16 melanoma, Hepa 1-6, or LL/2 Lewis lung cancer cell lines[500]. Interestingly, while some studies indicate that primary T cells undergo apoptosis upon STING agonism[497], others report the opposite[500]. In these studies, primary MEFs, BMDCs, and BMDMs were not sensitized to STING-induced apoptosis, suggesting that T cell susceptibility may reflect context-specific effects rather than a generalizable mechanism. Contrasting the pro-apoptotic role of STING, several studies have shown that executioner caspases, caspase-3/7, can inhibit cGAS-STING activation by directly cleaving cGAS and IRF3, thereby suppressing STING-dependent type I IFN responses[507].

Beyond apoptosis, cGAS-STING signalling has also been implicated in necroptosis, particularly under conditions of caspase inhibition. However, most data either do not directly address the role of STING in inducing necroptosis or fail to address the exact mechanism by which STING could modulate necroptotic cell death. For instance, in BMDMs, type I IFNs are considered essential for necroptosis induction, as evidenced by *Salmonella Typhimurium* infection of IFNAR-deficient mice, which prevented necroptosis[508]. Similarly, TLR stimulation with polyinosinic-polycytidylic acid (poly I:C), LPS, TNFα, or IFN-β following caspase inhibition failed to induce necroptosis in IFNAR-deficient BMDMs[123]. These findings suggest that type I IFNs could drive necroptosis when caspases are inhibited, but they do not directly implicate STING as the initiator of this IFN response. The role of STING becomes more apparent in studies showing that STING-mediated type I IFNs sustain MLKL or RIPK3 transcriptional levels, which could potentially prime BMDMs to undergo necroptosis[124]. However, overexpression of MLKL in IFNAR-deficient BMDMs failed to induce necroptotic cell death[124,509]. Similarly, treatment with IFNs alone or cGAS-STING-dependent cytosolic DNA sensing failed to induce necroptotic death in BMDMs but triggered necroptosis only when combined with TNF under conditions of caspase inhibition[510]. Additionally, PUMA-induced mtDNA release combined with caspase inhibition triggered necroptosis in HT29 colon cancer cells and MEFs[511].

Taken together, these findings suggest that while cGAS-STING signalling and its downstream type I IFN responses may help create a permissive environment for necroptosis, the existing evidence remains largely correlative, often relying on indirect readouts, transcriptional changes, overexpression systems, or genetic models (e.g., IFNAR knockout) that do not directly address the specific contribution of the cGAS-STING pathway. Mechanistic evidence supporting a role for STING as an essential mediator of necroptotic execution is lacking, and the precise molecular links between STING activation and the necroptotic machinery remain unresolved.

cGAS-STING has also been implicated in lysosomal cell death (LCD) or lysosome-dependent pyroptosis (LDCP). In human myeloid cells, STING can induce lysosomal trafficking, leading to lysosomal membrane permeabilisation, potassium efflux, and activation of NLR (NOD-like receptors) family pyrin domain containing 3 (NLRP3), resulting in pyroptosis[512]. STING can further amplify AIM2-mediated inflammatory signalling by priming, in an IFN-dependent manner, the upregulation of inflammasome components such as AIM2 during murine cytomegalovirus infection in BMMs[513]. Similarly, during *Chlamydia trachomatis* infection, cGAS-driven IFN responses increase caspase-1 and caspase-11 expression, promoting IL-1β release and pyroptotic cell death[514].

It remains unclear what determines the selective activation of cGAS, AIM2, or NLRP3 upon cytosolic DNA sensing. Current evidence suggests that cGAS may exhibit higher sensitivity to diverse DNA species, even at lower cytosolic concentrations, due to its complex DNA-binding architecture. This enhanced sensitivity could allow cGAS to respond earlier and to a broader range of DNA stimuli. Depending on the cellular context and the specific trigger, cGAS-STING downstream responses appear to modulate AIM2 and NLRP3 expression and activation, although additional, yet unidentified factors may also dictate which sensor predominates in initiating the inflammatory or cell death program.

Despite extensive investigation into the relationship between STING signalling and regulated cell death, it remains unresolved whether STING serves merely as a modulator of the cytokine milieu or whether it can act as a direct upstream activator of necroptosis. This question becomes particularly relevant in the context of caspase-8 deficiency, which, as discussed earlier, leads to genomic instability and potentially accumulation of cytosolic self-DNA. Such DNA represents a potent ligand for the cGAS-STING pathway, suggesting a potential link whereby loss of caspase-8 function may couple endogenous DNA sensing to RIPK3-MLKL-dependent necroptosis. In addition, caspase-8 deficiency leads to spontaneous upregulation of ZBP1[208], further suggesting that STING could influence the necroptotic axis via the ZBP1-RIPK3-MLKL pathway. This possibility raises the intriguing scenario that caspase-8 is not only a suppressor of necroptosis through direct regulation of RIPK1, but also an indirect guardian against aberrant STING-driven necroptosis by limiting the release of self-DNA and consequently activation of cGAS, modulating ZBP1 expression and potentially activation. Importantly, determining whether STING-driven necroptosis can also occur independently of caspase-8 loss is critical for understanding the broader physiological and pathological relevance of STING as a direct necroptotic trigger. Establishing such a mechanistic link would have broad biological implications and could open new avenues for therapeutic intervention in interferonopathies characterised by excessive necroptosis.

In this context, the present work addresses two complementary aspects. First, the development of *in situ* phosphorylated MLKL (pMLKL) detection as a robust and reliable approach to qualitatively identify necroptosis *in vivo*, which is essential for assessing its contribution to disease pathogenesis and progression. Second, the investigation of the potential mechanistic involvement of STING in necroptosis and its impact on tissue pathology and disease pathogenesis in STING-driven interferonopathies, thereby providing a rationale for therapeutic intervention. Together, these aims seek to close critical gaps by enabling rigorous detection of necroptosis *in vivo*, elucidating how perturbations in caspase-8 function intersect with innate immune signalling to orchestrate necroptosis, and providing a conceptual framework for therapeutic strategies targeting the STING-necroptosis axis in STING-driven autoinflammatory and autoimmune diseases characterized by excessive necroptosis.

II. Publications

1. Publication 1
Declaration and Rationale

The importance of murine phospho-MLKL-S345 *in situ* detection for Necroptosis assessment *in vivo*

https://doi.org/10.1038/s41418-024-01313-6

Declaration: This study was undertaken to address the critical need for a reliable and specific marker to detect necroptosis *in vivo*, particularly in murine models. Although phosphorylation of murine MLKL at serine 345 (pMLKL-S345) is widely recognized as a hallmark of necroptotic activation, a robust and validated method for its *in situ* detection has been lacking. Prior studies have largely relied on RIPK3- or MLKL-deficient models, or on total MLKL expression as indirect proxy for necroptosis, approaches that often lack spatiotemporal resolution and functional specificity. This work aimed to systematically evaluate and optimize conditions for immunohistochemical detection of pMLKL-S345, thereby providing a valuable tool for the spatial and contextual analysis of necroptosis in tissue sections, and for distinguishing it temporally and functionally from other forms of cell death, such as apoptosis. Importantly, the study reinforces the specificity of pMLKL-S345 as a surrogate marker of necroptosis across a range of physiological and pathological contexts, laying a foundation for future research into the regulation and immunological consequences of necroptotic cell death *in vivo*.

Contribution:

- Designed and optimized the immunohistochemical and immunofluorescent protocols *for in situ* detection of murine pMLKL-S345.
- Generated and analysed *Casp8*$^{E\text{-}KO}$ mice used in the study.
- Performed, analysed and quantified all stainings across all examined tissues and experimental conditions.
- Interpreted the experimental results, prepared all figures, and drafted and edited the manuscript.

CDDpress

www.nature.com/cdd

ARTICLE OPEN

Check for updates

The importance of murine phospho-MLKL-S345 in situ detection for necroptosis assessment in vivo

Konstantinos Kelepouras [1,2], Julia Saggau [1,2,3,4,10], Ana Beatriz Varanda [3,4,10], Matea Zrilic [2,10], Christine Kiefer [1,2], Hassan Rakhsh-Khorshid [1,2], Ina Lisewski [2], Iratxe Uranga-Murillo [5,6], Maykel Arias [5,6], Julian Pardo [5,6], Wulf Tonnus [7], Andreas Linkermann [7,8], Alessandro Annibaldi [2], Henning Walczak [3,4,9] and Gianmaria Liccardi [1,2]✉

Necroptosis is a caspase-independent modality of cell death implicated in many inflammatory pathologies. The execution of this pathway requires the formation of a cytosolic platform that comprises RIPK1 and RIPK3 which, in turn, mediates the phosphorylation of the pseudokinase MLKL (S345 in mouse). The activation of this executioner is followed by its oligomerisation and accumulation at the plasma-membrane where it leads to cell death via plasma-membrane destabilisation and consequent permeabilisation. While the biochemical and cellular characterisation of these events have been amply investigated, the study of necroptosis involvement in vivo in animal models is currently limited to the use of *Mlkl*$^{-/-}$ or *Ripk3*$^{-/-}$ mice. Yet, even in many of the models in which the involvement of necroptosis in disease aetiology has been genetically demonstrated, the fundamental in vivo characterisation regarding the question as to which tissue(s) and specific cell type(s) therein is/are affected by the pathogenic necroptotic death are missing. Here, we describe and validate an immunohistochemistry and immunofluorescence-based method to reliably detect the phosphorylation of mouse MLKL at serine 345 (pMLKL-S345). We first validate the method using tissues derived from mice in which Caspase-8 (Casp8) or FADD are specifically deleted from keratinocytes, or intestinal epithelial cells, respectively. We next demonstrate the presence of necroptotic activation in the lungs of SARS-CoV-infected mice and in the skin and spleen of mice bearing a Sharpin inactivating mutation. Finally, we exclude necroptosis occurrence in the intestines of mice subjected to TNF-induced septic shock. Importantly, by directly comparing the staining of pMLKL-345 with that of cleaved Caspase-3 staining in some of these models, we identify spatio-temporal and functional differences between necroptosis and apoptosis supporting a role of RIPK3 in inflammation independently of MLKL versus the role of RIPK3 in activation of necroptosis.

Cell Death & Differentiation (2024) 31:897–909; https://doi.org/10.1038/s41418-024-01313-6

INTRODUCTION

Necroptosis is a caspase-independent form of regulated cell death whose untoward activation drives loss of tissue homoeostasis during development as well as the pathogenesis of many inflammatory and infectious diseases [1]. Necroptosis can be induced in response to the activation of death receptors (DRs) [1, 2], (i.e., the tumour necrosis factor (TNF) receptor superfamily (TNFR-SF) members TNFR1 [3–5], FAS/CD95 [6–8], TRAIL-R1/DR4 and TRAIL-R2/DR5 [9–11]), as well as pattern recognition receptors (PRRs) including toll-like receptor 3 (TLR3) and TLR4 [12–14]. The downstream events elicited by the activation of DRs or PRRs lead to assembly of the necrosome, a cytosolic complex canonically formed by the association of Receptor-Interacting Protein Kinase 1 (RIPK1) and 3 (RIPK3) via their RIP homotypic interaction motif (RHIM) domains [15]. This complex has also been shown to form via the association of the cytosolic DNA and RNA sensor, ZBP1, with RIPK3, however, only in absence of RIPK1 expression or of its RHIM domain (*RIPK1*$^{\Delta RHIM}$) [16]. The activation of this complex culminates in the phosphorylation, ubiquitination and oligomerisation of the pseudokinase Mixed Lineage Kinase Domain-Like (MLKL), responsible for membrane destabilisation and consequent pore formation necessary for the execution of necroptosis and release of the inner cellular content [1, 15, 17–21]. The activation of MLKL relies on RIPK3-mediated phosphorylation of threonine 357/serine 358 (T357/S358) in human and of serine 345 (S345) in murine MLKL [1, 22–24]. Whilst other phosphorylation events have been described for both human and mouse MLKL by other kinases, the above-mentioned are recognised to be the sole, so far

[1]Genome Instability, Inflammation and Cell Death Laboratory, Institute of Biochemistry I, Centre for Biochemistry, Faculty of Medicine, University of Cologne, 50931 Cologne, Germany. [2]Center for Molecular Medicine Cologne (CMMC), University of Cologne, 50931 Cologne, Germany. [3]Cell Death, Inflammation and Immunity Laboratory, CECAD Cluster of Excellence, University of Cologne, 50931 Cologne, Germany. [4]Cell Death, Inflammation and Immunity Laboratory, Institute of Biochemistry I, Centre for Biochemistry, Faculty of Medicine, University of Cologne, 50931 Cologne, Germany. [5]Department of Microbiology, Radiology, Paediatry and Public Heath, Faculty of Medicine, University of Zaragoza/IIS, Aragon, Spain. [6]Centro de Investigacion Biomedica en Red de Enfermedades infecciosas (CIBERINFEC), Instituto de Salud Carlos III, Madrid, Spain. [7]Division of Nephrology, Department of Internal Medicine 3, University Hospital Carl Gustav Carus at the Technische Universität Dresden, Dresden, Germany. [8]Division of Nephrology, Department of Medicine, Albert Einstein College of Medicine, Bronx, NY, USA. [9]Centre for Cell Death, Cancer and Inflammation, UCL Cancer Institute, University College London, WC1E 6BT London, UK. [10]These authors contributed equally: Julia Saggau, Ana Beatriz Varanda, Matea Zrilic. ✉email: Gianmaria.liccardi@uk-koeln.de

Received: 20 December 2023 Revised: 2 May 2024 Accepted: 7 May 2024
Published online: 23 May 2024

discovered, mediated by RIPK3 and to be responsible for the execution of necroptosis [23–25]. Currently, these are widely utilised as conclusive markers to detect this specific cell death modality, however, their utilisation has been limited to western blotting and/or immunofluorescence in adherent cells [26]. To date, there is no reliable and reproducible way of addressing necroptosis in situ in tissues derived from different animal models. The assessment of cell death in vivo relies on detection of cleaved Caspase-3 (c-Casp3) [27] or so called TUNEL (terminal deoxynucleotidyl transferase dUTP nick end labelling) staining (a hallmark of intrinsic and extrinsic apoptosis but also necrosis, necroptosis, pyroptosis and parthanatos [28–33]). Yet, neither are they specific to necroptosis execution nor can they discriminate between different modalities of cell death and MLKL-driven necroptosis. Being able to differentiate between distinct modalities of cell death impacts profoundly on the molecular understanding of the biochemical process responsible for a given pathological condition and importantly, allows (a) the possibility to test pharmacologically targeting of a specific cell death mechanism in an informed way, (b) the discovery and prediction of necroptotic cell death involvement in the aetiology of any disease in a tissue-specific manner prior the utilisation of a genetic knock out model and (c) the ability to investigate and distinguish the role of RIPK3 in inflammation independently of MLKL (mostly pro-apoptotic) from its role in MLKL-driven necroptosis.

In this study, we show how necroptosis can be molecularly detected in vivo. Following a thorough optimisation strategy, we provide a detailed methodology for the immunohistochemical and immunofluorescent in situ detection of S345-phosphorylated murine MLKL (pMLKL-S345) in different tissues (skin, intestine, lung, spleen and liver). We, first, optimise our detection method in genetic mouse models of necroptosis induction via conditional deletion of Caspase-8 (Casp8) or FADD from basal epidermal keratinocytes [34] or intestinal epithelial cells [35], respectively. Additionally, once demonstrated the validity and specificity of our protocol, we provide evidence of the applicability and advantages of detecting pMLKL-S345 in situ by utilising three additional models that uncover, clarify and support (1) the role of necroptosis in SARS-CoV infection, (2) the role of RIPK3 in inflammation independently of MLKL via the analysis of the chronic proliferative dermatitis mutation (cpdm) mice (*Sharpin$^{cpdm/cpdm}$*) and *Sharpin$^{cpdm/cpdm}$*; *Ripk3$^{-/-}$* animals and (3) the role of necroptosis in systemic inflammatory response syndrome (SIRS) following TNF injection. In some of these models we directly compare the in situ detection of pMLKL-S345 with the broadly used c-Casp3 demonstrating the importance of specifically detecting pMLKL-S345 in situ to identify which cells undergo necroptosis as well as highlighting functional and temporal differences with apoptotic cell death.

MATERIALS AND METHODS

Mouse models

The *Casp8$^{fl/fl}$* mice were kindly provided by Hedrick [36], *K14-Cre* [37], *Fadd$^{fl/fl}$* [38], *Villin-Cre-ERT^2* [39] were obtained as previously described. *Shpn$^{m/m}$* mice were obtained from the Jackson laboratory [40]. *Mlkl$^{-/-}$* was generated by the Walczak lab as previously described [41], *Casp8$^{+/-}$* mice were kindly provided by Hakem [42], *Ripk3$^{-/-}$* animals by Dixit and Newton from Genentech [43]. C57Bl/6N wild-type mice were purchased from Charles River (Germany). Mice were bred to obtain *Casp8$^{fl/fl}$*; *K14cre$^{tg/wt}$* carrying the conditional deletion of *Casp8* in keratinocytes (*Casp8^{E-KO}*). Mice heterozygous for *Casp8* and homozygous for *Ripk3* (*Casp$^{+/-}$; Ripk3$^{-/-}$*) or *Mlkl* (*Casp8$^{+/-}$; Mlkl$^{-/-}$*) were bred to obtain *Casp8$^{-/-}$; Ripk3$^{-/-}$* and *Casp8$^{-/-}$; Mlkl$^{-/-}$* double-KO mice. To generate knock out mice with inducible intestinal-epithelial cell-specific FADD deletion (*Fadd$^{iIEC-KO}$*), we crossed *Fadd$^{fl/fl}$* mice with *Villin-Cre-ERT^2* mice. These were further crossed with *Mlkl$^{-/-}$* to generate *Fadd$^{iIEC-KO}$*; *Mlkl$^{-/-}$*. *Fadd* deletion was induced by tamoxifen injections of 11 weeks old *Fadd$^{fl/fl}$; Villin-Cre-ERT^2* and *Fadd$^{fl/fl}$; Mlkl$^{-/-}$; Villin-Cre-ERT^2* mice at 10 mg/mL (T5648, Sigma-Aldrich) for 3 consecutive days and then sacrificed at 14 weeks of age. As control, *Fadd$^{fl/fl}$* littermates not expressing Cre were treated with tamoxifen in the same way. All mice were kept in individually ventilated cages under a stable 12 h day/night cycle at the animal facilities of the Medical Faculty, the CECAD Research Center of the University of Cologne or the Medizinisch-Technisches Zentrum at the TU Dresden. Water and standard chow were provided ad libitum, room temperature and humidity were automatically maintained. Mice were daily monitored, scored blindly by two independent researchers and humanely sacrificed once reached endpoint criteria via cervical dislocation. Experiments were performed according to German animal protection laws and were approved by local ethics committees as well as local government authorities (*Landesamt für Natur, Umwelt und Verbraucherschutz Nordrhein* Westfalen or *Landesdirektion Dresden*, number: VSG2020.A022).

SARS-CoV infection

Lung sections from SARS-CoV MA15-infected mice were obtained from a recently published study where experimental material and methods with regards to the model and infection are fully described [44]. SARS-CoV MA15 was kindly provided by S. Zúñiga and L. Enjuanes (CNB-CSIC, Madrid, Spain). Mice were infected intranasally with 10^6 TCID50/ml in a total volume of 40 µl of PBS after isoflurane anaesthesia. A clinical score was meticulously derived, if deemed necessary, through the assessment of various components, including the appearance of the mouse, level of consciousness, activity level, responsiveness to stimuli, ocular appearance, and the frequency and quality of respiration. Mice were considered to have reached the humane endpoint when the clinical score was equal or exceeded 21, or when respiratory parameters surpassed a score of 3 [45], or when weight loss was >25% of the initial weight. Animals were kept under standard conditions of temperature, humidity and light at the Research Center on Encephalopathies and Emerging Diseases of the University of Zaragoza. Animal experimentation was approved by the Animal Experimentation Ethics Committee of the University of Zaragoza (number: PI44/20).

Systemic inflammatory response syndrome (SIRS)

Co-housed 8–12 weeks old female C57Bl/6N mice were divided in pairs of two and each pair received two different doses of ice-cold recombinant, LPS-free mouse TNF (TNF) (575208, lot: B306769, BioLegend) in a final volume of 100 µl (dissolved in PBS) intravenously via tail-vein injection (i.v.). The administered doses were adjusted to 0.75 µg/g or 1 µg/g TNF. Control mice received a corresponding volume of ice-cold LPS-free PBS. The experiment was performed in a double-blinded manner. Mice were monitored every 2 h for body temperature drop and sacrificed 6 h after injection. Animal experimentation was approved by German animal protection laws and were approved by local ethics committees as well as local government authorities (number: TVA57/2017).

Dermatitis scoring criteria

Skin lesions in *Shpn$^{m/m}$* mice were scored as previously described [40]. Briefly, two main clinical criteria were assessed to determine a total score: (1) the number of body regions presenting lesions and (2) the characteristics of each lesion. For the first criteria skin from four different body regions were assessed and appearance of lesions in each of these body regions generated a score of 1 (head = 1, neck = 1, back = 1 and flank = 1). For the second criteria, the characteristic of each lesion was defined by its severity. Punctuated small crusts received a score of 1, coalescent crusts received a score of 2 and ulceration received a score of 3. The sum of all individual scores according to these two was calculated to determine total severity. Scoring of skin lesions was performed by two independent researchers in a double-blinded fashion.

Tissue harvesting and fixation

Mice were humanely sacrificed once reached endpoint criteria. Mouse skin samples were collected by harvesting skin biopsies from the dorsomedial region of the back of the mouse into a rectangle shape so that the long side of the rectangle follows the anterior–posterior axis of the mouse. Colon and small intestine were longitudinally cut and washed with PBS to remove faeces and then rolled up from proximal to distal (Swiss-rolls). Spleens, lungs and livers were carefully extracted, and washed in PBS. It was previously reported that crosslinking fixatives can interfere with specific detection of MLKL, RIPK1 and RIPK3 and methanol fixation was pointed as a more efficacious methodology to prevent false positive staining [26]. However, it is important to note that this conclusion was specific for detecting total and phosphorylated protein signal via immunofluorescence in adherent cells. In tissues, it is still a matter of debate if coagulant fixatives (ethanol and methanol) impact less on the steric configuration of the proteins and therefore on the antigenic site recognition [46, 47]. We opted for a formalin fixation because the advantages of formalin fixation include a good preservation of tissue morphology and because it is widely used for many different established antibodies, therefore, maximising the utilisation of the same tissue block (from the same animal) for the in situ detection of different markers. Importantly, formalin fixation sterilises tissues more reliably than precipitating fixatives, in particular for viruses (which is currently the requested fixative by European authorities for the transportation and utilisation of samples outside of S3 facilities such as SARS-CoV) and, therefore, relevant to investigate necroptosis activation following viral infection. In this study, we utilised tissues from different organs: skin, spleen, lung, gut and liver. Tissues were placed in an embedding cassette and fixed with either 10% buffered formalin (skin from *Casp8*$^{E\text{-}KO}$, small intestine, colon and liver from TNF-induced shock model, HT501128-4L, Sigma-Aldrich) or 4% formaldehyde (skin and spleen from *Shpn*$^{m/m}$ mice, lungs from the SARS-CoV infection model and small intestine and colon from *Fadd*$^{iIEC\text{-}KO}$ mice, WAL60622, Walter CMP GmbH) overnight (O/N). The cassettes were stored in 70% EtOH (skin) or PBS (spleen, lung, small intestine, colon and liver) for at least 24 h before further processing.

Tissue processing (paraffin embedding and microtomy)

Fixed tissues were paraffin embedded using a vacuum tissue processor (Model: ASP200S, Leica Biosystems) through standard automatic tissue embedding protocols. The paraffin-embedded blocks were cut to obtain 3 µm thick (lung, small intestine, colon and liver) or 5 µm thick (skin and spleen) consecutive sections, then placed on labelled polysine adhesion slide and dried O/N at 40 °C.

Haematoxylin & eosin staining of paraffin-fixed tissues

Tissue sections were deparaffinised with xylene and rehydrated in reducing concentrations of EtOH (100%, 95%, 70%, 50 and 0%). The haematoxylin and eosin (H&E) staining was performed by incubating the tissue sections in haematoxylin (T865.3, Carl Roth) for 4 min, followed by thorough washing and a 15 min incubation in tap water. The slides were then incubated in eosin (X883.2, Carl Roth) for 30 s (skin) or 1 min (spleen, small intestine and colon), washed thoroughly in tap water, dehydrated (75%, 95%, 100% EtOH and xylene) and mounted (H-5700, Vector Laboratories).

Optimisation strategy of in situ detection of pMLKL-S345 via IHC

The optimisation strategy took place at six different levels that we categorised as:

Level 1 – antibody selection, Level 2 – retrieval method, Level 3 – retrieval time, Level 4 – antibody dilution, Level 5 – usage of detergents, Level 6 – amplification method and in a total of 47 different conditions (Supplementary Fig. 1).

Out of all the commercially available antibodies claiming to detect pMLKL-S345 we decided to focus specifically on those that were known to provide a clean and reliable signal by western blotting and also those that had been most recently published in the literature to avoid any batch issues: a recombinant rabbit monoclonal antibody (EPR9515) to pMLKL-S345 antibody from abcam (ab196436) and a recombinant rabbit monoclonal antibody (D6E3G) to pMLKL-S345 antibody from Cell Signalling Technologies (CST, 37333) which was previously reported to successfully stain murine pMLKL-S345 in fixed adherent murine cells [26]. Importantly, the ab196436 was previously published to detect pMLKL-S345 in tissues via IHC [48]. However, despite several attempts, we (and others) could not obtain convincing results by following the published protocols, which therefore, prompted us to optmise the staining procedure.

It is well established that potential masking of epitopes arising from formalin fixation can be successfully overcome by the correct antigen retrieval. Initially, the two antibodies were tested with heat-induced epitope retrieval (HIER) method, in sodium citrate-based retrieval buffer, pH 6. Antibodies were diluted 1:200, 1:400, 1:800, 1:1600 and 1:2000. Standardised retrieval time for TintoRetriever Pressure Cooker (10 min) and a previously verified maximum retrieval time (13 min) were compared. In addition, an avidin–biotin–HRP signal amplification system was implemented to improve signal detection (data with regular anti-rabbit HRP conjugated antibody not shown). Under these conditions, the abcam antibody failed to show signal specificity because of high background levels and consequent low signal-to-noise ratio. The CST antibody showed promising results at this initial stage and was further validated. To improve antigen retrieval, a commercially available Tris-EDTA based buffer, pH 9 (S236784-2, Agilent Technologies) was utilised, as Tris-EDTA based buffers at pH 9 are usually employed for either low affinity antibodies or when difficult epitopes require more effective retrieval. Different retrieval times were tested: 5, 7 (data not shown), 10 and 13 min. In parallel, an enzymatic/proteolytic antigen retrieval method utilising Proteinase K (20 µg/ml in TE Buffer: 50 mM Tris Base, 1 mM EDTA, 0.5% Triton X-100, pH 8.0) was tested. From this, we concluded that pressure cooker-based HIER using Tris-EDTA based buffer, pH 9 and 1:2000 antibody dilution of the pMLKL-S345 antibody from Cell Signalling Technologies (CST, 37333) were the most favourable conditions to detect in situ pMLKL-S345. To further optimise the signal/noise ratio, 0.05% v/v Tween20 was added to the retrieval buffer to obtain better permeabilisation. Serial antibody dilutions (CST37333) of 1:2000–1:10000 were further assessed to test background detection. Since further dilutions above 1:2000 incurred into decreased antibody-signal detection, despite decreasing background, we decided to carry forward with 1:2000 dilution of the CST37333 antibody. We also validated the staining method with a 'homemade' 0.05% v/v Tween20, Tris-EDTA based retrieval buffer, pH 9 and HIER using a standard, commercially available microwave oven.

Immunostaining

After standard deparaffinisation and rehydration, the paraffin sections were retrieved differently for the detection of different antibodies. For pMLKL-S345 detection (37333, Cell Signalling Technology, 1:2000) slides were retrieved in 0.05% v/v Tween20, Tris-EDTA based antigen retrieval buffer, pH 9 (S236784-2, Agilent Technologies) for 13 min at 114–121 °C using the TintoRetriever Pressure Cooker (BSB7008, BioSB). For c-Casp3 staining (9664, Cell Signalling Technology, 1:100, for skin sections and 9661, Cell Signalling Technology, 1:200, for spleen, lung, small intestine, colon and liver) slides were retrieved in sodium citrate buffer, pH 6 (C9999, Sigma-Aldrich) for 10 min at 114–121 °C using the TintoRetriever Pressure Cooker. Endogenous peroxidase activity, antibody non-specific binding sites, avidin binding sites and endogenous biotin and biotin receptors were blocked according to the manufacturer's instructions (SP-6000-100, SP-5035-100 and SP-2001, Vector Laboratories, respectively). Biotinylated goat anti-rabbit secondary antibody (1:200, BA-1000, Vector Laboratories) in combination with either the avidin–biotin–HRP amplification system (PK-6100, Vector Laboratories) with DAB substrate (SK-4105, Vector Laboratories) or Alexa Fluor 594 Streptavidin (S11227, Thermo Fisher Scientific) were used for antibody detection. All sections were counterstained with haematoxylin (H-3401, Vector Laboratories) or DAPI (D9564, Sigma-Aldrich). The sections were then mounted using commercially available mounting media (H-5700, Vector Laboratories or P36930, Thermo Fisher Scientific).

Lambda protein phosphatase (lambda PP) treatment

Slides were treated with lambda PP (40.000U/ml) diluted in Lambda PP buffer (P0753S, New England Biolabs) or with Lambda PP buffer alone according to manufacturer instructions. Slides were incubated at 37 °C for 24 h in a wet chamber and then washed three times (5 min) in TBS-T 0.1% v/v Tween20 before being incubated with the pMLKL-S345 antibody as described above.

Histopathological analysis

Histopathological evaluation was performed in H&E stained 3 µm thick intestinal Swiss-roll sections using the scoring system as described before [35]. Briefly, histopathology scores are composed of four parameters: epithelial hyperplasia, epithelial injury, tissue inflammation and epithelial cell death. Histological sub-scores for each parameter: 0, absent; 1, mild; 2, moderate; 3, severe. An 'area factor' for the fraction of affected tissue was assigned and multiplied with the respective parameter score (1 = 0–25%; 2 = 25–50%; 3 = 50–75%; 4 = 75–100%). Each area was scored individually and multiplied with the correlating area factor. Total histology score was calculated as a sum of all parameter scores multiplied with their area factors. Maximum score was 48. Evaluation was performed in a blinded fashion.

Imaging

Immunohistochemistry slides were digitalised via acquisition in a digital slide scanner (NanoZoomer S360MD Slide scanner system, Hamamatsu

Photonics K.K.) with 40× magnification lens. Additional bright field images were acquired with Leica DM750 Binocular microscope and LAS X Life Science Microscope Software, Leica, objective 10×, 20× or 63×. Immunofluorescence pictures were acquired with LSM 980 with Airyscan 2 and ZEN Microscopy Software, Zeiss, objective 20× and 63×, Zeiss.

Image analysis

The acquired bright field images were analysed in QuPath, an open-source software [49]. To quantify the positively stained cells, a pixel classifier was generated in order to exclude tissue areas that should not be accounted for during the quantification step and would otherwise interfere with the 'positive cell detector' leading to false positive results. After setting the parameters and threshold, the 'positive cell detector' was run and the quantification results were acquired. The percentages of positive cells per total number of cells for each section or image for the different biological replicates were plotted utilising GraphPad. One-way or two-way Anova statistical analysis and Tukey's multiple comparisons test or unpaired two-tailed *t*-test was calculated via graph pad/prism to determine significance among the different groups (*$P \leq 0.05$, **$P \leq 0.01$, ***$P \leq 0.001$, ****$P \leq 0.0001$, ns = not significant).

RESULTS

Reliable in situ detection of pMLKL-S345 allows to distinguish apoptotic from necroptotic cell death in different subcellular populations

To initially optimise and validate the in situ detection of pMLKL-S345 we decided to employ a published model of Casp8 deletion from epidermal keratinocytes (*Casp8$^{E\text{-}KO}$*). These mice are known to succumb to aberrant skin inflammation induced by RIPK3 and MLKL-mediated necroptosis. Accordingly, mice bearing deletion of Casp8 from epidermal keratinocytes (*Casp8$^{E\text{-}KO}$*) presented with severe skin inflammation leading to lethality by P7 [34] (Fig. 1A, B). Mice with heterozygous deletion of Casp8 from keratinocytes (*Casp8$^{E\text{-}KO/wt}$*) showed no sign of inflammation, neither at P7 nor at a later stage throughout their monitored life span and were indistinguishable from wild-type mice (Fig. 1A, B). These mice were utilised as negative controls to validate the pMLKL-S345 antibody and staining specificity in the presence of the single K14-*Cre* allele. As previously reported, the embryonic lethality induced by constitutive Casp8 deficiency is completely rescued by genetic removal of either RIPK3 or MLKL suggesting that its pathological cause is due to aberrant necroptosis [34]. Since removal of MLKL or RIPK3, the kinase responsible for phosphorylation of MLKL at S345, would impede detection of pMLKL-S345, we utilised *Casp8$^{-/-}$; Mlkl$^{-/-}$* and *Casp8$^{-/-}$; Ripk3$^{-/-}$* mice as further negative controls. Consistent with the absence of necroptosis and with the notion that necroptosis induction is responsible for the lethal dermatitis, these mice presented no sign of necroptosis-induced skin inflammation and their survival was significantly prolonged (Fig. 1B). Due to the splenomegaly and lymphadenopathy that occurs in *Casp8$^{-/-}$; Mlkl$^{-/-}$* and *Casp8$^{-/-}$; Ripk3$^{-/-}$* mice, they were sacrificed once endpoint criteria were reached (Fig. 1B) and skin samples were collected for immunohistochemical analysis.

After establishing our model of choice, we selected two pMLKL-S345 antibodies: a previously published recombinant rabbit monoclonal antibody (EPR9515) to pMLKL-S345 antibody from abcam [48, 50] and a recombinant rabbit monoclonal antibody (D6E3G) to pMLKL-S345 antibody from Cell Signalling Technologies (CST, 37333) which we tested on skin sections obtained from the *Casp8$^{E\text{-}KO}$* animals. After performing different optimisation conditions (47 steps shown in Supplementary Fig. 1), we concluded that optimal detection of pMLKL-S345 takes place using antibody 37333 (CST) with a 1:2000 dilution using 0.05% v/v Tween20, Tris-EDTA based antigen retrieval buffer, pH 9 (S236784-2, Agilent Technologies), retrieving for 13 min at 114–121 °C. Details of the optimisation steps are provided in the 'Materials and Methods' section and in Supplementary Materials and Methods (Supplementary Fig. 1). Once the optimal staining conditions were determined, consecutive skin sections from five mice of each of the above-mentioned genotypes were stained for pMLKL-S345 or c-Casp3 and counterstained with haematoxylin to visualise tissue architecture as well as to distinguish different subcellular populations (Fig. 2A). Dying keratinocytes in the epidermis of *Casp8$^{E\text{-}KO}$* mice showed clear and specific staining for pMLKL-S345 demonstrating activation of the necroptosis executioner MLKL (Fig. 2A, B). Significantly lower signal was detected in the *Casp8$^{E\text{-}KO/wt}$* mice whereas no staining was detectable in *Casp8$^{-/-}$; Mlkl$^{-/-}$* or *Casp8$^{-/-}$; Ripk3$^{-/-}$* mice (Fig. 2A, B). Similarly, c-Casp3 was also detected in *Casp8$^{E\text{-}KO}$* mice, however, in contrast to pMLKL-S345, c-Casp3-positive cells, specifically fibroblasts and

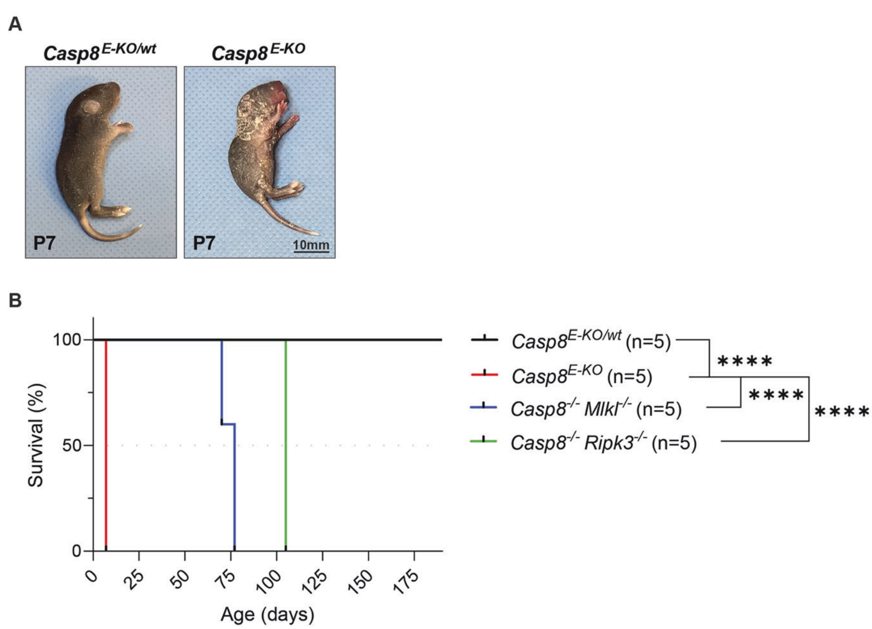

Fig. 1 ***Casp8$^{E\text{-}KO}$* is a reliable and robust model to study necroptosis. A** Representative images of *Casp8$^{E\text{-}KO}$* mice at the indicated time point (P7). Control mice included littermates with the *Casp8$^{E\text{-}KO/wt}$* genotype. **B** Kaplan–Meier survival graph of mice of the indicated genotypes ($n = 5$ in each group). *P* values were calculated by Gehan–Breslow–Wilcoxon test. ****$P \leq 0.0001$.

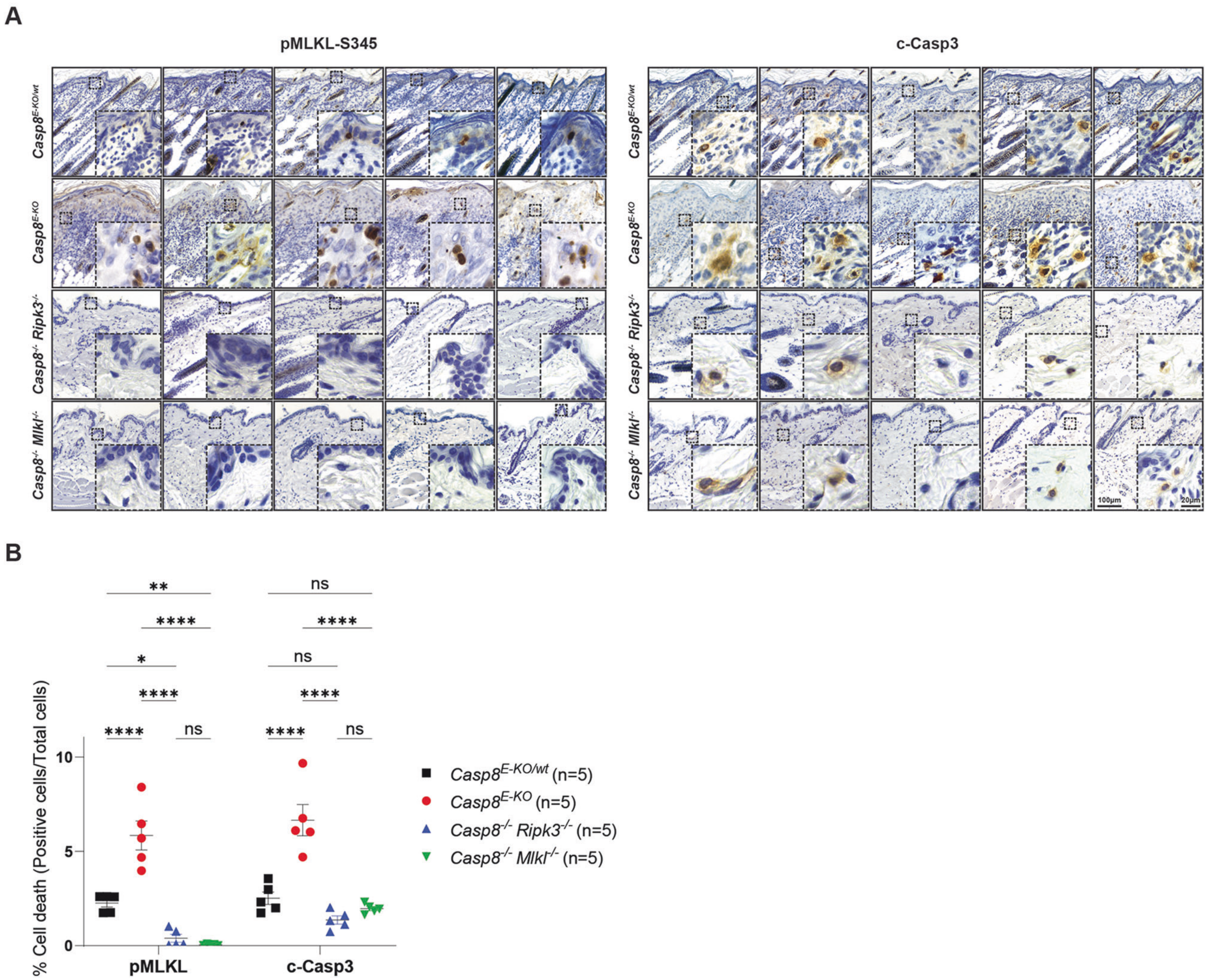

Fig. 2 Reliable detection of pMLKL-S345 in situ distinguishes necroptosis from apoptosis. A Representative bright field images of skin sections from mice with the indicated genotypes immunostained with pMLKL-S345 and c-Casp3. Consecutive skin sections from the same mice were utilised for each marker and are shown in the same order ($n = 5$ in each group). Scale bars: 100 µm (representative field) and 20 µm (magnified selected area). **B** Graph showing quantification of each immunostaining obtained via QuPath after slides were digitalised in a digital slide scanner as described in the Supplementary Methods section. For each marker, total skin section was analysed and total numbers of cells were obtained to calculate the percentage of positive cells over the total amount of cells detected. Data are presented as mean + SEM and each dot represents one mouse. *P* values were calculated via two-way Anova. $^*P \leq 0.05$, $^{**}P \leq 0.01$, $^{****}P \leq 0.0001$, ns not significant.

immune cells, were mostly located in the dermis (Fig. 2A). Although the absence of pMLKL-S345-positive cells in *Casp8*$^{-/-}$; *Ripk3*$^{-/-}$ would already exclude the possibility that the selected antibody would detect non-specifically total MLKL, we also decided to pre-treat skin samples obtained from *Casp8*$^{E\text{-}KO}$ with lambda PP to remove phosphate groups from phosphorylated residues to further validate the specificity of our protocol with the antibody of choice. Lambda PP treatment completely removed any pMLKL-S345 signal detected from consecutive skin sections obtained from *Casp8*$^{E\text{-}KO}$ animals (Supplementary Fig. 2), further confirming specificity of detection of the phosphorylated target.

These results demonstrate that the described protocol serves to specifically stain pMLKL-S345 in keratinocytes undergoing necroptotic cell death in the epidermis. Importantly, the staining pattern obtained thereby was clearly distinct from that obtained when staining for c-Casp3 in consecutive tissue sections. The latter staining identified other cells that underwent apoptotic cell death in the dermis, likely as a consequence of the necroptotic death of keratinocytes in the epidermis, as c-Casp3-positive cells were largely absent from the different control tissues (Fig. 2A, B).

In situ detection of pMLKL-S345 is applicable to immunofluorescence staining

Having established a specific and sensitive protocol for the in situ detection of pMLKL-S345 in skin sections via immunohistochemistry, we next determined whether this protocol also served to detect pMLKL-S345 by immunofluorescence via confocal microscopy in skin and intestinal sections. To this end, we applied slight modifications to the protocol due to the nature of the different fluorophore-attached secondary antibodies required for acquisition via laser excitation (details provided in 'Materials and Methods' and in Supplementary Material and Methods). Comparably to the immunohistochemical detection of the above-mentioned samples (Fig. 2B), our data showed specific staining of cells in the skin sections obtained from *Casp8*$^{E\text{-}KO}$ mice while samples from both *Casp8*$^{-/-}$; *Mlkl*$^{-/-}$ or *Casp8*$^{-/-}$; *Ripk3*$^{-/-}$ showed a clear lack of any detectable signals (Fig. 3A, B). Additionally, we employed the conditional deletion of *Fadd* in the intestinal epithelium via tamoxifen injection previously shown to lead to the disruption of the intestinal barrier via activation of necroptosis [35]. Briefly, *Fadd*$^{fl/fl}$ mice were crossed with *Villin-Cre-*

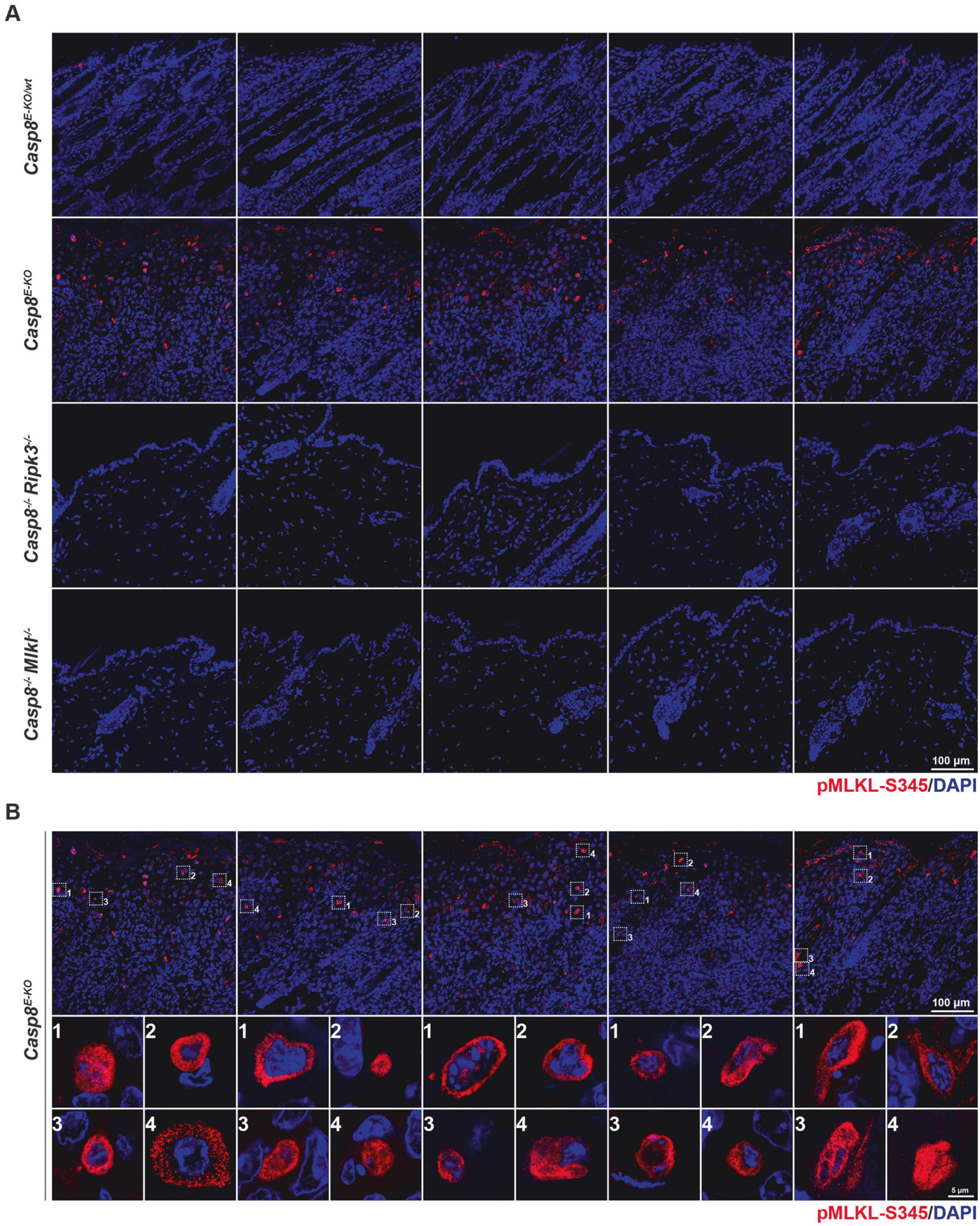

Fig. 3 In situ detection of pMLKL-S345 is applicable to immunofluorescence staining. A, B Representative images of skin sections from mice with the indicated genotypes immunostained with Alexa fluor 594 streptavidin (red) to detect pMLKL-S345 and with DAPI (blue) to detect nuclei ($n = 5$ in each group). Dashed squares indicate 4 representative pMLKL-S345-positive cells per image. Scale bars: 100 µm. **B** Representative images (single slice 0.4 µm) of pMLKL-S345 positive cells ($n = 4$ cells per mouse in a total of $n = 5$ mice). Scale bar: 5 µm.

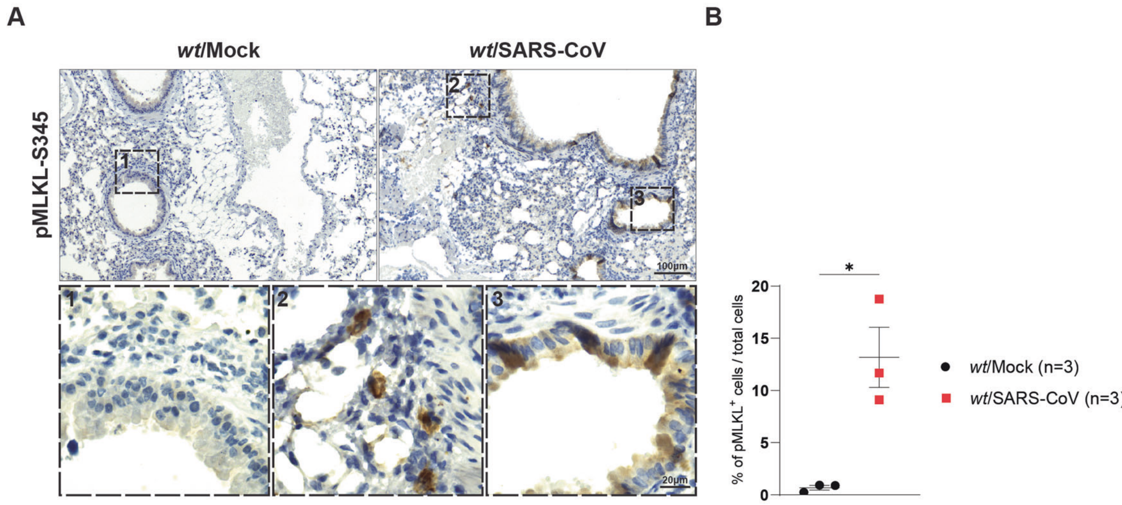

Fig. 4 SARS-CoV infection induces apoptotic and necroptotic cell death. A Representative bright field images of lung sections of wt mice infected intranasally with 10^6 TCID50/ml SARS-CoV MA15 virus at 3 days post-infection (dpi) immunostained with pMLKL-S345 ($n = 3$ for mock-infected and MA15-infected mice). Scale bars: 100 μm (representative field) and 50 μm (magnified selected area). **B** Graph showing quantification of pMLKL-S345 immunostaining obtained via QuPath after slides were digitalised in a digital slide scanner as described in the Supplementary Methods section. Total lung sections were analysed and total numbers of cells were obtained to calculate the percentage of positive cells over the total amount of cells detected. Data are presented as mean + SEM and each dot represents one mouse. *P* values were calculated via one-way Anova, Tukey's multiple comparisons test. $^*P \leq 0.05$.

ERT^2 to obtain *Fadd*$^{iIEC\text{-}KO}$. These were further crossed with the *Mlkl*$^{-/-}$ to generate the *Fadd*$^{iIEC\text{-}KO}$; *Mlkl*$^{-/-}$ which served as a negative control. At 11 weeks of age, these mice were injected with 1 mg tamoxifen (10 mg/ml) for 3 consecutive days to obtain the deletion of FADD from intestinal epithelial cells (*Fadd*$^{iIEC\text{-}KO}$ and *Fadd*$^{iIEC\text{-}KO}$; *Mlkl*$^{-/-}$). Age-matched control littermates (*Fadd*$^{fl/fl}$) were also injected with tamoxifen and served as experimental controls (*Fadd*$^{IEC\text{-}WT}$). Mice were sacrificed 3 weeks after the first tamoxifen injection (14 weeks) and intestinal samples were analysed for pMLKL-S345 detection by confocal microscopy. The ileum, duodenum and jejunum obtained from *Fadd*$^{iIEC\text{-}KO}$ animals showed intestinal epithelial cells positive for pMLKL-S345 with the ileum presenting the greatest number of positive cells and duodenum, jejunum and colon presenting progressively less to no positive cells for pMLKL-S345 (Supplementary Fig. 3). There was no detectable staining of pMLKL-S345 in any intestinal sample obtained from control *Fadd*$^{IEC\text{-}WT}$ or from *Fadd*$^{iIEC\text{-}KO}$; *Mlkl*$^{-/-}$. Conclusively, these data show the ability to specifically detect pMLKL-S345 via immunofluorescence and subsequent confocal microscopy acquisition, similarly to the detection shown via immunohistochemistry. Moreover, we highlight the usefulness of this staining in further detecting MLKL-driven necroptosis in different areas of the intestine, granting the possibility to precisely determine the exact site and extent of necroptotic cell death-induced inflammation.

SARS-CoV infection induces apoptotic and necroptotic cell death

Lagunas et al. recently showed that infection by mouse adapted SARS-CoV MA15 (SARS-CoV) leads to cell death in the bronchioles and alveoli of infected mice [44]. In this study, while apoptosis was shown to play a role (via detection of c-Casp3-positive cells) it was clear that other modalities of cell death are engaged following SARS-CoV infection as a greater number of TUNEL-positive cells, although c-Casp3-negative, were detected in sections obtained from the lungs of infected mice [44]. To test the involvement of necroptosis activation, we obtained consecutive lung sections from the published mock-infected and SARS-CoV-infected mice [44] and performed pMLKL-S345 staining in situ on these sections. Our data clearly show a significant amount of pMLKL-S345-positive staining in alveolar cells as well as in cells of different origin in the lung epithelium, demonstrating activation of necroptosis following infection (Fig. 4). Considering the previously reported data, it is plausible that both apoptosis and necroptosis contribute to the inflammatory syndrome observed in these animals following SARS-CoV infection and that the inhibition of both could be a valuable therapeutic strategy. These data show the importance of pMLKL-S345 staining to investigate and determine the occurrence of necroptosis during infection allowing to distinguish and understand how different cell death modalities affect pathological and systemic inflammation following viral infection.

pMLKL-S345 staining distinguishes between RIPK3-mediated necroptosis and RIPK3-mediated inflammation independently of necroptosis

cpdm mice bear the genetic deficiency of *Sharpin* (*Sharpin*$^{cpdm/cpdm}$, henceforth referred as *Shpn*$^{m/m}$) [51–54]. These animals are characterised by dermatitis and multi-organ inflammation including splenomegaly, liver inflammation, disrupted lymphoid architecture and loss of Peyer's patches in the gut. Overall, TNF/TNFR1-induced cell death has been demonstrated to drive these phenotypes [51, 53, 54]. Specifically, TNF-induced apoptosis is responsible for skin inflammation since *Casp8* heterozygosity can significantly ameliorate the dermatitis, while multi-organ inflammation is predominantly driven by RIPK3/MLKL-induced necroptosis [53, 54]. Interestingly, while co-deletion of Sharpin and RIPK3 delays the onset of the dermatitis, MLKL co-deletion does not affect the skin inflammation observed in the *Shpn*$^{m/m}$ [53, 54]. Previous studies that have addressed this issue have inferred that attenuated linear ubiquitination unleashes a RIPK3 function which is inflammatory in the skin, yet independent of MLKL. In other tissues (e.g., the spleen), RIPK3 exerts a purely necroptotic function [53, 54]. To further validate these conclusions via the in situ detection of pMLKL-S345, we generated the *Shpn*$^{+/m}$, *Shpn*$^{m/m}$ and *Shpn*$^{m/m}$; *Ripk3*$^{-/-}$ mice. Consistent with previously published reports, *Shpn*$^{m/m}$ mice manifested onset of dermatitis at around 11 weeks of age while *Shpn*$^{m/m}$; *Ripk3*$^{-/-}$ animals presented a modest delay in the appearance of the dermatitis [53, 54]. Nevertheless, they were all sacrificed at 14–15 weeks of age after reaching endpoint criteria (Fig. 5A, B). In accordance with previous studies [53, 54] histological analysis showed a very mild

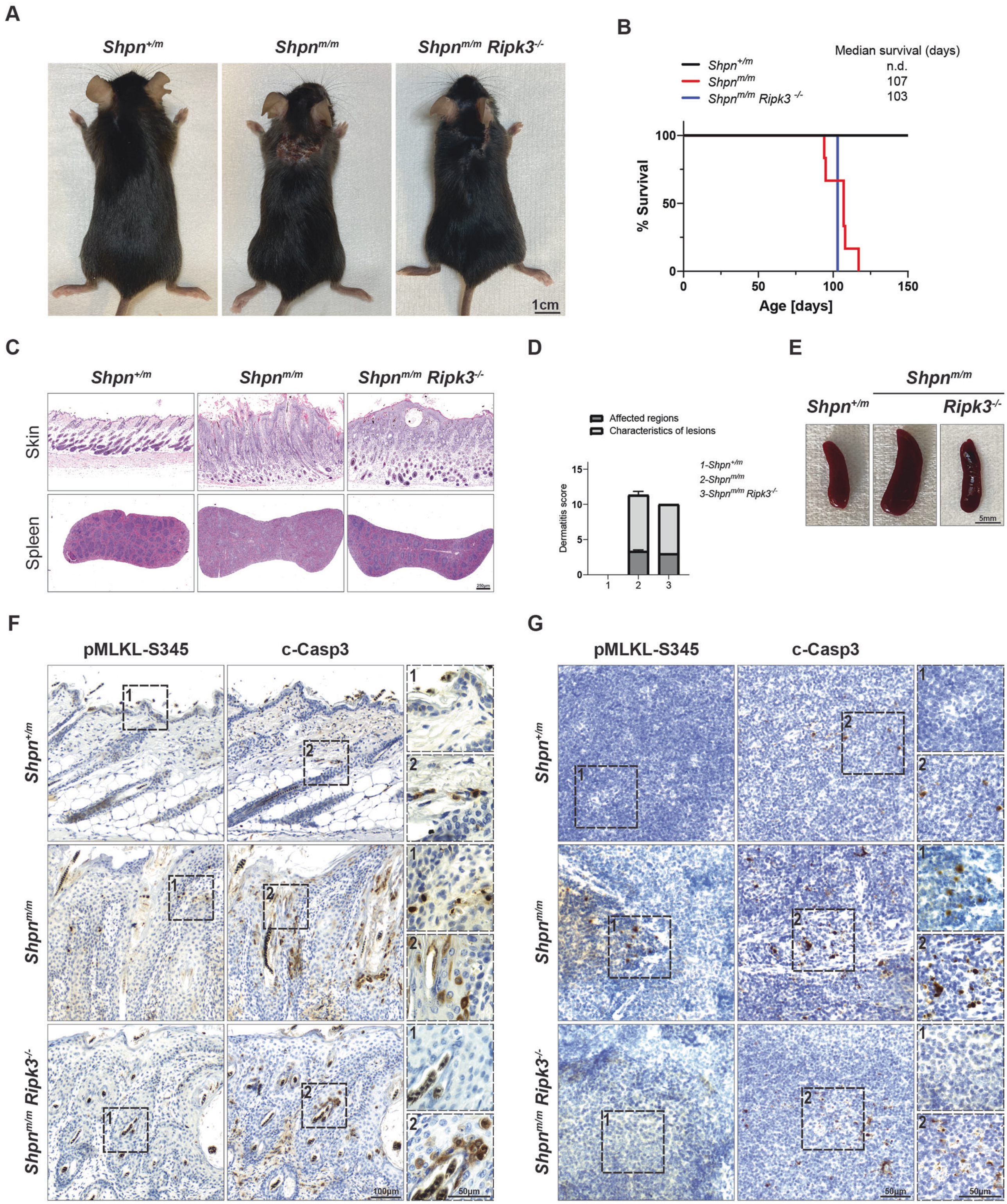

Fig. 5 pMLKL-S345 staining distinguishes between RIPK3-mediated necroptosis and RIPK3-mediated inflammation. A Representative images of mice of indicated genotypes at the endpoint (14–15 weeks). Control mice included littermates with the *Shpn*$^{+/m}$ genotype. **B** Kaplan–Meier survival graph of mice with the indicated genotypes ($n = 7$ for *Shpn*$^{+/m}$, 6 for *Shpn*$^{m/m}$, 1 for *Shpn*$^{m/m}$; *Ripk3*$^{-/-}$ mice). **C** Representative images of skin and spleen sections from mice with the indicated genotypes stained with H&E. Slides were digitalised in a digital slide scanner and images were acquired in QuPath. **D** Graph of severity score of dermatitis assessment in 14–15 weeks old mice of the indicated genotypes. *Shpn*$^{+/m}$ mice (14–21 weeks old) served as controls ($n = 5$ for *Shpn*$^{+/m}$, 6 for *Shpn*$^{m/m}$, 1 for *Shpn*$^{m/m}$; *Ripk3*$^{-/-}$ mice). **E** Representative bright field images of spleens from mice of the indicated genotypes. **F**, **G** Representative bright field images of skin (**F**) and spleen (**G**) sections from mice with the indicated genotypes immunostained with pMLKL-S345 and c-Casp3. Consecutive skin sections from the same mice were utilised for each marker and displayed according to their order ($n = 3$ for *Shpn*$^{+/m}$, 3 for *Shpn*$^{m/m}$ and 1 for *Shpn*$^{m/m}$; *Ripk3*$^{-/-}$ mice). Scale bars: skin (**F**) 100 μm (representative field) and 50 μm (magnified selected area), spleen (**G**) 50 μm for both representative field and magnified selected area.

amelioration of the epidermal thickness in $Shpn^{m/m}$; $Ripk3^{-/-}$ which was confirmed by the dermatitis score (Fig. 5C, D). As expected $Shpn^{m/m}$; $Ripk3^{-/-}$ mice presented a clear restoration of the marginal zone in the spleen which was reflected by a complete rescue of the splenomegaly observed in the $Shpn^{m/m}$ mice (Fig. 5C, E). We then obtained consecutive skin and spleen sections and compared the staining of pMLKL-S345 and c-Casp3 in situ. There was a very minor increase in the levels of pMLKL-S345 detected in localised areas of the skin of $Shpn^{m/m}$ compared to $Shpn^{+/m}$ mice, suggesting that MLKL-induced necroptosis contributes marginally to the dermatitis observed in the $Shpn^{m/m}$ animals. In contrast c-Casp3 staining was distinctly prominent in the skin of $Shpn^{m/m}$ mice as compared to $Shpn^{+/m}$ mice and only partially diminished in $Shpn^{m/m}$; $Ripk3^{-/-}$ animals, as previously published. This is suggesting that RIPK3-mediated inflammation contributes to dermatitis independently of MLKL activation and that apoptotic cell death is the main driver of dermatitis. It is tempting to speculate that apoptosis can, in turn, cause necroptosis to such a low extent that it does not contribute to the lethality of the phenotype. On the other hand, detection of pMLKL-S345 revealed a clear necroptotic phenotype in the spleen of the $Shpn^{m/m}$ which was completely absent in the spleen of $Shpn^{m/m}$; $Ripk3^{-/-}$ animals. These data suggest that, attenuation of linear ubiquitination, differently from TNF-induced apoptosis in the skin, leads to RIPK3/MLKL-mediated necroptosis and secondary apoptosis in the spleen.

Systemic inflammatory response syndrome drives apoptosis and not necroptosis in intestinal epithelial cells

It was previously shown that in the C57Bl/6 N background, $Casp8^{-/-}$; $Mlkl^{-/-}$ mice are completely unresponsive to TNF-induced SIRS [55]. While SIRS, as determined by body hypothermia, serum cytokines and chemokines levels and SIRS-induced mortality is significantly ameliorated in both RIPK3-deficient or RIPK1-catalytically inactive mice, $Mlkl^{-/-}$ animals have shown different responses to high compared to low doses of TNF [55]. Specifically, while $Mlkl^{-/-}$ mice seem to respond similarly to WT animals when treated with low doses of TNF, differences with $Ripk3^{-/-}$ are less evident following injections of high doses of TNF [55]. This puts into questions whether the unresponsiveness of the $Casp8^{-/-}$; $Mlkl^{-/-}$ mice to SIRS (C57Bl/6N) is solely due to loss of apoptosis or both, apoptosis and necroptosis and, most importantly, whether RIPK3 might play a role in inflammation independently of MLKL also in this pathological context. Considering that homozygous deletion of Casp8 leads to embryonic lethality [56], it is impossible to determine whether MLKL deletion is simply required to prevent aberrant necroptosis (as a consequence of Casp8 deletion) or whether MLKL-induced necroptosis is indeed involved in SIRS. To answer this question, we injected female C57Bl/6N mice (i.e., the same strain as in the study reported above [55]) with low or high doses of TNF (via tail-vein injection) and sacrificed them after 6 h for tissue harvesting and subsequent intestinal IHC staining with pMLKL-S345 and c-Casp3 (Fig. 6A–D). Histological analysis confirmed the intestinal damage as a result of TNF injections (Fig. 6A, B). Our data conclusively show that both doses of TNF drive predominantly apoptosis and not necroptosis, as in the area of intestinal damage we could only detect a significant increase of c-Casp3-positive cells (Fig. 6C, D and Supplementary Fig. 4). Specifically, different parts of the gastrointestinal tract, including ileum, duodenum, jejunum and colon, contained cells positive for c-Casp3 staining, with ileum and duodenum showing the highest levels. It was previously reported that necroptosis-induced liver damage contributes to TNF-mediated mortality in C57Bl/6J animals [57]. Unexpectedly, we could not detect a high number of pMLKL-S345-positive cells (although significant) nor a difference in c-Casp3 staining compared to control in our C57Bl/6N animals (Supplementary Fig. 5). Together, these results suggest that, at least in the C57Bl/6N background, the previously published amelioration observed in RIPK3-deficient mice might be due to the ability of RIPK3 to promote apoptosis and inflammation independently of necroptosis execution. This notion is further supported by the published improvement observed in $Casp8^{+/-}$ animals or in RIPK1-kinase-dead mice ($Ripk1^{K45A}$) of the same background [55]. On the other hand, the amelioration observed upon MLKL or RIPK3 deficiency following injection of high doses of TNF might be the result of secondary systemic necroptosis as a consequence of apoptosis execution which leads to the disruption of the intestinal epithelial barrier.

DISCUSSION

Currently, the detection of c-Casp3 is widely employed as a tissue marker of cell death, and whilst it has been shown to detect also Casp8-induced pyroptosis [35], it has paradoxically been utilised even in models in which the deletion of FADD or Casp8 and RIPK1 leads to necroptosis-induced lethality which has been genetically demonstrated to occur in a caspase-independent manner as completely rescued by RIPK3 co-deletion [58–60]. Hence, since necroptosis execution is not dependent on the cleavage of caspases, it follows that the cleavage of Casp3 cannot be used to specifically identify cells that undergo necroptotic cell death but rather cell death events that take place as a consequence of it. In the present study, we developed a protocol for the specific immunohistochemical and immunofluorescence staining of pMLKL-S345 in tissue specimens (skin, intestine, lung, spleen and liver) obtained from different animal models. While we acknowledge the difficulty to detect a cell death marker in every tissue, we believe that this protocol can be further extended to other tissues provided a certain degree of tissue-specific optimisation of which we provide ample example. In particular in the kidney where specifically the abcam antibody (compared in this study and excluded) has been used to successfully stain for pMLKL-S345 [50], however, deemed unspecific in another study [61].

Here, we demonstrate significant advantages of this staining over others previously employed in characterising the aetiology of different cell death-driven or involving pathologies, potentially substituting the need for genetic crosses, and at the same time, providing more informed conclusions on the role of pMLKL-S345-induced necroptosis. The comparison of the immunohistochemical staining we obtained with the in situ detection of pMLKL-S345 via the newly developed protocol to the ones obtained by staining c-Casp3 in the $Casp8^{E\text{-}KO}$ model, critically highlights important differences between these two markers of cell death. Despite the clear presence of pMLKL-S345 in the epidermis containing dying keratinocytes, the dermal layer presented a significant number of cells that stained positive for c-Casp3 which, histologically, correspond to fibroblasts and immune cells. Since the subcellular population positive for each marker was clearly different as well as located in distinct layers of the skin, we concluded that c-Casp3 staining detected a secondary cell death event in cells in which Casp8 is expressed. It is in fact known that necroptotic cell death, via the release of the content of the dying cells, which includes TNF, type I interferon, IL-6, IL-33, IL-36, HMGB1, IL-1α [62, 63], initiates a wave of systemic inflammation further augmented by other modalities of cell death including apoptosis, GSDME-mediated mitochondria pore formation and Casp8-induced pyroptosis [16, 25, 28, 35, 64, 65]. Furthermore, release of inflammatory cytokines also drives the recruitment of immune cells expressing other death ligands such as TRAIL and FasL, in addition to TNF [66], likely responsible for the cell death observed in the dermis in both fibroblasts and immune cells in the present study.

We then further extended the in situ detection of pMLKL-S345 to $Fadd^{iIEC\text{-}KO}$ allowing, for the first time the assessment of different degrees of necroptosis in different areas of the intestine.

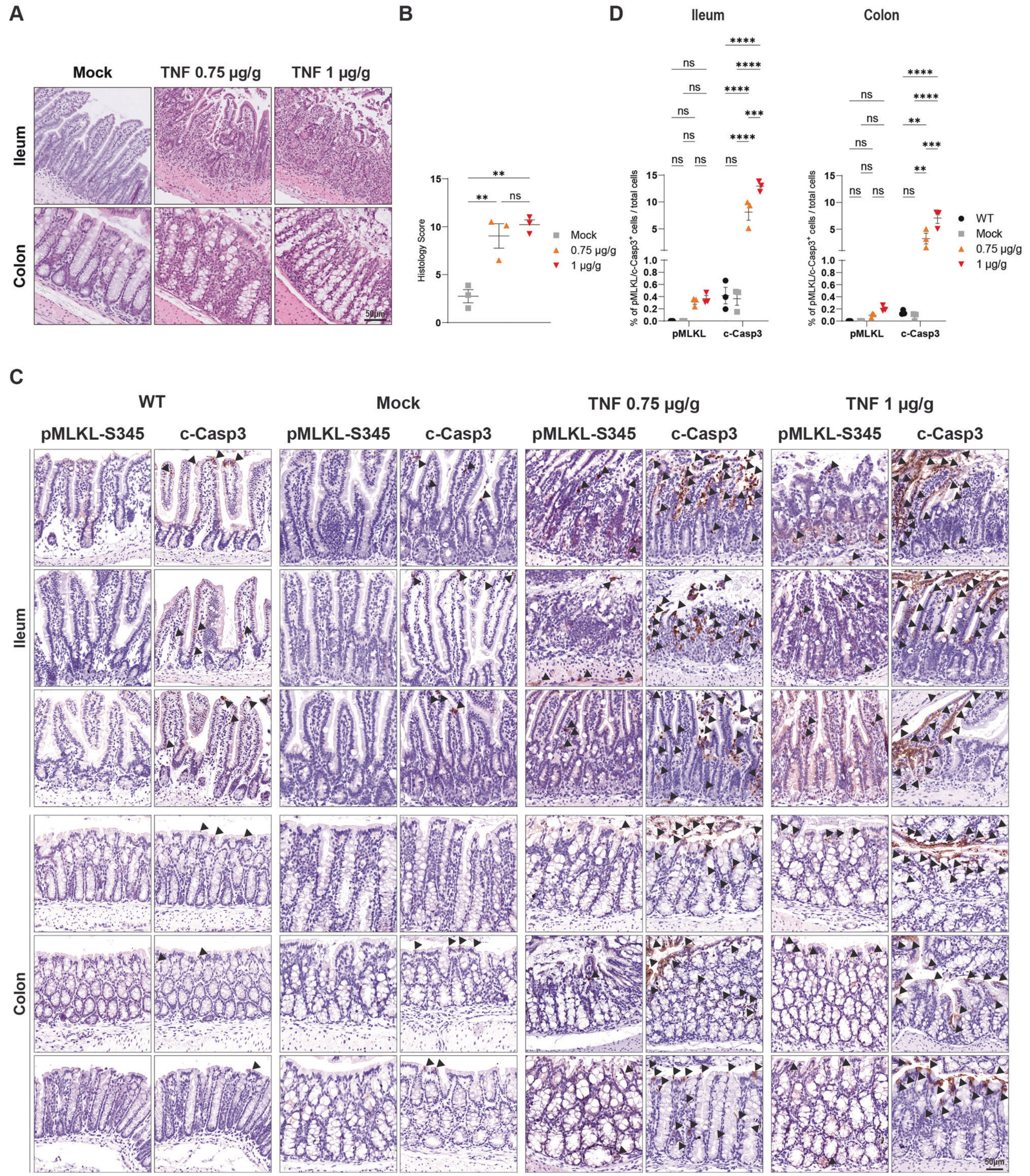

Fig. 6 Systemic inflammatory response syndrome drives apoptosis and not necroptosis in intestinal epithelial cells. Co-housed 10–12 week old female C57Bl6/N wt mice were injected with 0.75 µg/g or 1 µg/g of ice-cold recombinant, LPS-free mouse TNF intravenously. Control mice received a corresponding volume of ice-cold LPS-free PBS. Mice were sacrificed 6 h post-injection. Untreated wt mice were additionally analysed ($n = 3$ in each group). **A** Representative images of small intestine and colon sections (Swiss-rolls) of wt mice as indicated were stained with H&E. Slides were digitalised in a digital slide scanner and pictures were acquired in QuPath. Scale bars: 50 µm. **B** Graph showing histology score in whole intestine. Data are presented as mean + SEM and each dot represents one mouse. *P* values were calculated via one-way Anova, Tukey's multiple comparisons test. $^{**}P \leq 0.01$, ns not significant. **C** Representative images of ileum and colon sections (Swiss-rolls) of wt mice as indicated immunostained with pMLKL-S345 and c-Casp3. Slides were digitalised in a digital slide scanner and pictures were acquired in QuPath. Scale bars: 50 µm. Arrowheads indicate pMLKL-S345-positive cells and c-Casp3-positive areas. **D** Graph showing quantification of illustrated pictures for each immunostaining obtained via QuPath after slides were digitalised in a digital slide scanner as described in the Supplementary Methods section. Total numbers of cells were obtained to calculate the percentage of positive cells over the total amount of cells detected. Data are presented as mean + SEM and each dot represents one mouse. *P* values were calculated via two-way Anova, Tukey's multiple comparisons test. $^{**}P \leq 0.01$, $^{***}P \leq 0.001$, $^{****}P \leq 0.0001$, ns not significant.

$Fadd^{IEC\text{-}KO}$ were previously shown to suffer from severe intestinal inflammation [35]. While TNF or TNFR1 co-deletion together with co-deletion of ZBP1, significantly ameliorated colon inflammation, by preventing MLKL-induced necroptosis, this is not sufficient to prevent ileitis, where it was proposed that Casp8 also drives Gasdermin-D-mediated pyroptosis of FADD-deficient intestinal epithelial cells which contributes to the observed inflammatory phenotype [35, 67]. Importantly, MLKL co-deletion can completely prevent colitis while ileitis is only completely prevented by co-deletion of MLKL in $Fadd^{IEC\text{-}KO}$; $Casp8^{IEC\text{-}KO}$. In all published studies both colitis and ileitis were characterised by histological score, CD45 and c-Casp3 staining [35, 67, 68]. Specifically, the latter was employed only to assess residual Casp8 activity in the $Fadd^{IEC\text{-}KO}$; $Casp8^{IEC\text{-}KO}$ mice in the small intestinal epithelium and CD45 was used as the marker of choice to detect intestinal inflammation. Our pMLKL-S345 detection protocol allows, for the first time, direct detection of necroptotic cell death in situ, confirming the prominent occurrence of necroptosis in the ileum. Surprisingly, we could not detect pMLKL-S345 in the colon probably due to either the early time point at which the tamoxifen-treated mice were sacrificed or potentially highlighting substantial differences between embryonic conditional deletion of FADD versus adult conditional deletion of FADD in the intestinal epithelium.

While many viruses were shown to trigger both Casp8-mediated apoptosis and RIPK1/RIPK3- or ZBP1/RIPK3-mediated necroptosis [1], the lack of a marker for in situ detection of pMLKL-S345, has rendered it very difficult to truly determine the contribution of necroptotic cell death following viral infection. It was previously published that necroptosis plays a role in chronic obstructive pulmonary disease caused by cigarette smoke [69] and that syncytial viral infections, which induces bronchiolitis, leads to activation of necroptosis [70]. This suggests already that under certain conditions lung cells, including human airway epithelial cells, can die necroptotically. Specifically for Coronaviruses, involvement of ZBP1 or RIPK3 in SARS-CoV-2 infection has been deduced from the attenuated cytokine and chemokine production and reduced lung damage found in infected mice deficient for either ZBP1 or RIPK3 [71]. Importantly, $Mlkl^{-/-}$ animals do not present the same attenuation and appear to be more similar to control mice raising questions with regards to the exact role of necroptosis execution in SARS-CoV-2-infection-mediated systemic inflammatory syndrome [71]. While necroptosis was recently deemed dispensable from the pathogenesis of SARS-CoV-2 [72], it is not yet clear what cell death modality is truly responsible for the consequent acute respiratory disease syndrome which might engage into untoward necroptosis activation. Our data show that in lung sections obtained from SARS-CoV-infected mice, alveolar cells as well as other cells of different origin in the lung epithelium are positive for pMLKL-S345, suggesting necroptotic execution potentially in both infected and non-infected cells. This is in agreement with the data shown in Lagunas et al. [44], where c-Casp3 and TUNEL staining highlighted the involvement of cell death pathways other than apoptosis. It remains to be determined whether necroptosis activation is involved in the pathogenesis of development of severe disease following SARS-CoV infection or whether this is merely secondary cell death as a consequence of initial apoptosis without impact on disease severity. Considering the therapeutic opportunity to inhibit necroptosis pharmacologically, in the light of these results, the analysis of MLKL activation following viral infections utilising this novel detection protocol warrants further investigation.

The pro-apoptotic ability of RIPK3 was previously reported, in particular with regards to specific conformational changes that would promote Casp8 activation [55, 73]. This evidence has questioned whether the amelioration provided by $Ripk3^{-/-}$ animals in different disease models should be immediately and solely connected to inhibition of necroptosis or/and also to its role in mediating inflammatory signals that drive apoptotic cell death. The fact that, in certain models, the outcome of MLKL deficiency is different from that of RIPK3 deficiency implies that the role of RIPK3 is context-dependent whereby RIPK3 can both support apoptosis and also drive necroptosis. The data obtained by the in situ detection of pMLKL-S345 in the skin and spleen of the $Shpn^{m/m}$ and the $Shpn^{m/m}$; $Ripk3^{-/-}$ mice suggest that, in a tissue-dependent manner RIPK3 can either support apoptosis leading to secondary necroptosis (as observed in the skin) or drive necroptosis which then leads to secondary apoptosis (as observed in the spleen). Similarly, the data obtained in the SIRS model conclusively clarifies that the initial modality of cell death activated in response to TNF-induced shock is apoptosis. Our data suggest that any amelioration provided by RIPK3 or MLKL deletion is either due to prevention of RIPK3-mediated activation of Casp8 or to prevention of secondary necroptosis that might further contribute to a wave of systemic inflammation in these mice. In agreement with the study conducted by Newton et al. [55], we also find that TNF-induced mortality in C57Bl/6N is predominantly driven by apoptosis-induced intestinal damage. Differently from C57Bl/6J [57], we do not observe biologically significant levels of necroptotic cell death in the liver which was shown to be the main driver of TNF-induced mortality in this background strain. It was previously shown that C57BL/6J are exquisitely sensitive to TNF-induced shock than C57BL/6N due to presence of several passenger mutations in C57Bl/6N [74], suggesting that these different backgrounds differentially influence the organ susceptibility of the mice to TNF-induced shock.

This work provides a protocol for the specific and sensitive detection of pMLKL-S345 in situ. Thereby, we provide an important tool that, for the first time, allows to effectively and reliably distinguish necroptosis from other modalities of cell death in situ in different tissues. Moreover, this work provides evidence of substantial differences between the in situ detection of different cell death markers, demonstrating the necessity to detect different modalities of cell death utilising molecular signatures in situ. Our protocol allows to not only distinguish these pathways from one another, but also to characterise which cell types, in different tissues, succumb via different modalities of cell death respectively in a given in vivo scenario. The ability to detect pMLKL-S345 allows to specifically determine the role of necroptosis in the pathology of many inflammatory disease models, importantly, without the need to delete FADD or Casp8 which is also known to create de novo roles of necroptosis not observed in their presence. Moreover, the in situ detection of pMLKL-S345 grants the ability to distinguish the pro-apoptotic role of RIPK3 from its role in activating MLKL as well as to decipher which initial cell death pathway promotes systemic inflammation by leading to secondary cell death activation. The ability to concomitantly detect pMLKL-S345, c-Casp3 and TUNEL shall contribute to determining which cell death pathway is responsible for initiating different inflammatory processes. This, in turn, shall provide the possibility to intervene therapeutically by specifically inhibiting the cell death modality or modalities responsible for a given pathology driven by inflammatory cell death.

DATA AVAILABILITY

No datasets were generated or analysed during the current study. All raw histological images are available upon request.

REFERENCES

1. Liccardi G, Annibaldi A. MLKL post-translational modifications: road signs to infection, inflammation and unknown destinations. Cell Death Differ. 2023;30:269–78.
2. Vanden Berghe T, Linkermann A, Jouan-Lanhouet S, Walczak H, Vandenabeele P. Regulated necrosis: the expanding network of non-apoptotic cell death pathways. Nat Rev Mol Cell Biol. 2014;15:135–47.

3. Zhang DW, Shao J, Lin J, Zhang N, Lu BJ, Lin SC, et al. RIP3, an energy metabolism regulator that switches TNF-Induced cell death from apoptosis to necrosis. Science. 2009;325:332–6.
4. He SD, Wang L, Miao L, Wang T, Du FH, Zhao LP, et al. Receptor interacting protein kinase-3 determines cellular necrotic response to TNF-alpha. Cell. 2009;137:1100–11.
5. Walczak H. Death receptor-ligand systems in cancer, cell death, and inflammation. Cold Spring Harb Perspect Biol. 2013;5:a008698.
6. Holler N, Zaru R, Micheau O, Thome M, Attinger A, Valitutti S, et al. Fas triggers an alternative, caspase-8-independent cell death pathway using the kinase RIP as effector molecule. Nat Immunol. 2000;1:489–95.
7. Matsumura H, Shimizu Y, Ohsawa Y, Kawahara A, Uchiyama Y, Nagata S. Necrotic death pathway in Fas receptor signaling. J Cell Biol. 2000;151:1247–56.
8. Vercammen D, Brouckaert G, Denecker G, Van de Craen M, Declercq W, Fiers W, et al. Dual signaling of the Fas receptor: initiation of both apoptotic and necrotic cell death pathways. J Exp Med. 1998;188:919–30.
9. Jouan-Lanhouet S, Arshad MI, Piquet-Pellorce C, Martin-Chouly C, Le Moigne-Muller G, Van Herreweghe F, et al. TRAIL induces necroptosis involving RIPK1/RIPK3-dependent PARP-1 activation. Cell Death Differ. 2012;19:2003–14.
10. Lafont E, Kantari-Mimoun C, Draber P, De Miguel D, Hartwig T, Reichert M, et al. The linear ubiquitin chain assembly complex regulates TRAIL-induced gene activation and cell death. EMBO J. 2017;36:1147–66.
11. Montinaro A, Walczak H. Harnessing TRAIL-induced cell death for cancer therapy: a long walk with thrilling discoveries. Cell Death Differ. 2023;30:237–49.
12. He SD, Liang YQ, Shao F, Wang XD. Toll-like receptors activate programmed necrosis in macrophages through a receptor-interacting kinase-3-mediated pathway. Proc Natl Acad Sci USA. 2011;108:20054–9.
13. Kaiser WJ, Sridharan H, Huang CZ, Mandal P, Upton JW, Gough PJ, et al. Toll-like receptor 3-mediated necrosis via TRIF, RIP3, and MLKL. J Biol Chem. 2013;288:31268–79.
14. Lim J, Park H, Heisler J, Maculins T, Roose-Girma M, Xu M, et al. Autophagy regulates inflammatory programmed cell death via turnover of RHIM-domain proteins. Elife. 2019;8:e44452.
15. Zhang J, Yang Y, He W, Sun L. Necrosome core machinery: MLKL. Cell Mol Life Sci. 2016;73:2153–63.
16. Lin J, Kumari S, Kim C, Van TM, Wachsmuth L, Polykratis A, et al. RIPK1 counteracts ZBP1-mediated necroptosis to inhibit inflammation. Nature. 2016;540:124–8.
17. Garcia LR, Tenev T, Newman R, Haich RO, Liccardi G, John SW, et al. Ubiquitylation of MLKL at lysine 219 positively regulates necroptosis-induced tissue injury and pathogen clearance. Nat Commun. 2021;12:3364.
18. Liu Z, Dagley LF, Shield-Artin K, Young SN, Bankovacki A, Wang X, et al. Oligomerization-driven MLKL ubiquitylation antagonizes necroptosis. EMBO J. 2021;40:e103718.
19. Sun L, Wang H, Wang Z, He S, Chen S, Liao D, et al. Mixed lineage kinase domain-like protein mediates necrosis signaling downstream of RIP3 kinase. Cell. 2012;148:213–27.
20. Su L, Quade B, Wang H, Sun L, Wang X, Rizo J. A plug release mechanism for membrane permeation by MLKL. Structure. 2014;22:1489–500.
21. Wang H, Sun L, Su L, Rizo J, Liu L, Wang LF, et al. Mixed lineage kinase domain-like protein MLKL causes necrotic membrane disruption upon phosphorylation by RIP3. Mol Cell. 2014;54:133–46.
22. Petrie EJ, Sandow JJ, Jacobsen AV, Smith BJ, Griffin MDW, Lucet IS, et al. Conformational switching of the pseudokinase domain promotes human MLKL tetramerization and cell death by necroptosis. Nat Commun. 2018;9:2422.
23. Tanzer MC, Tripaydonis A, Webb AI, Young SN, Varghese LN, Hall C, et al. Necroptosis signalling is tuned by phosphorylation of MLKL residues outside the pseudokinase domain activation loop. Biochem J. 2015;471:255–65.
24. Meng Y, Sandow JJ, Czabotar PE, Murphy JM. The regulation of necroptosis by post-translational modifications. Cell Death Differ. 2021;28:861–83.
25. Zhu X, Yang N, Yang Y, Yuan F, Yu D, Zhang Y, et al. Spontaneous necroptosis and autoinflammation are blocked by an inhibitory phosphorylation on MLKL during neonatal development. Cell Res. 2022;32:407–10.
26. Samson AL, Fitzgibbon C, Patel KM, Hildebrand JM, Whitehead LW, Rimes JS, et al. A toolbox for imaging RIPK1, RIPK3, and MLKL in mouse and human cells. Cell Death Differ. 2021;28:2126–44.
27. Porter AG, Janicke RU. Emerging roles of caspase-3 in apoptosis. Cell Death Differ. 1999;6:99–104.
28. Shalini S, Dorstyn L, Dawar S, Kumar S. Old, new and emerging functions of caspases. Cell Death Differ. 2015;22:526–39.
29. Rojas J, Bermudez V, Palmar J, Martinez MS, Olivar LC, Nava M, et al. Pancreatic beta cell death: novel potential mechanisms in diabetes therapy. J Diabetes Res. 2018;2018:9601801.
30. Christofferson DE, Yuan JY. Necroptosis as an alternative form of programmed cell death. Curr Opin Cell Biol. 2010;22:263–8.
31. Fatokun AA, Dawson VL, Dawson TM. Parthanatos: mitochondrial-linked mechanisms and therapeutic opportunities. Br J Pharmacol. 2014;171:2000–16.
32. Didenko VV, Ngo H, Baskin DS. Early necrotic DNA degradation – Presence of blunt-ended DNA breaks, 3′ and 5′ overhangs in apoptosis, but only 5′ overhangs in early necrosis. Am J Pathol. 2003;162:1571–8.
33. Bergsbaken T, Fink SL, Cookson BT. Pyroptosis: host cell death and inflammation. Nat Rev Microbiol. 2009;7:99–109.
34. Kovalenko A, Kim JC, Kang TB, Rajput A, Bogdanov K, Dittrich-Breiholz O, et al. Caspase-8 deficiency in epidermal keratinocytes triggers an inflammatory skin disease. J Exp Med. 2009;206:2161–77.
35. Schwarzer R, Jiao H, Wachsmuth L, Tresch A, Pasparakis M. FADD and caspase-8 regulate gut homeostasis and inflammation by controlling MLKL- and GSDMD-mediated death of intestinal epithelial cells. Immunity. 2020;52:978–993.e6.
36. Beisner DR, Ch'en IL, Kolla RV, Hoffmann A, Hedrick SM. Cutting edge: innate immunity conferred by B cells is regulated by caspase-8. J Immunol. 2005;175:3469–73.
37. Hafner M, Wenk J, Nenci A, Pasparakis M, Scharffetter-Kochanek K, Smyth N, et al. Keratin 14 Cre transgenic mice authenticate keratin 14 as an oocyte-expressed protein. Genesis. 2004;38:176–81.
38. Mc Guire C, Volckaert T, Wolke U, Sze M, de Rycke R, Waisman A, et al. Oligodendrocyte-specific FADD deletion protects mice from autoimmune-mediated demyelination. J Immunol. 2010;185:7646–53.
39. Madison BB, Dunbar L, Qiao XT, Braunstein K, Braunstein E, Gumucio DL. Cis elements of the villin gene control expression in restricted domains of the vertical (crypt) and horizontal (duodenum, cecum) axes of the intestine. J Biol Chem. 2002;277:33275–83.
40. Taraborrelli L, Peltzer N, Montinaro A, Kupka S, Rieser E, Hartwig T, et al. LUBAC prevents lethal dermatitis by inhibiting cell death induced by TNF, TRAIL and CD95L. Nat Commun. 2018;9:3910.
41. Peltzer N, Darding M, Montinaro A, Draber P, Draberova H, Kupka S, et al. LUBAC is essential for embryogenesis by preventing cell death and enabling haematopoiesis. Nature. 2018;557:112–7.
42. Salmena L, Lemmers B, Hakem A, Matysiak-Zablocki E, Murakami K, Au PY, et al. Essential role for caspase 8 in T-cell homeostasis and T-cell-mediated immunity. Genes Dev. 2003;17:883–95.
43. Newton K, Sun X, Dixit VM. Kinase RIP3 is dispensable for normal NF-kappa Bs, signaling by the B-cell and T-cell receptors, tumor necrosis factor receptor 1, and Toll-like receptors 2 and 4. Mol Cell Biol. 2004;24:1464–9.
44. Martinez Lagunas K, Savcigil DP, Zrilic M, Carvajal Fraile C, Craxton A, Self E, et al. Cleavage of cFLIP restrains cell death during viral infection and tissue injury and favors tissue repair. Sci Adv. 2023;9:eadg2829.
45. Shrum B, Anantha RV, Xu SX, Donnelly M, Haeryfar SM, McCormick JK, et al. A robust scoring system to evaluate sepsis severity in an animal model. BMC Res Notes. 2014;7:233.
46. Taylor CR, Shi SR, Barr NJ. Techniques of immunohistochemistry: principles, pitfalls, and standardization. In: Dabbs DJ, editor. Diagnostic immunohistochemistry. 3rd ed. Philadelphia, PA: Saunders/Elsevier; 2011. p. xviii, 941 p.
47. Shi SR, Key ME, Kalra KL. Antigen retrieval in formalin-fixed, paraffin-embedded tissues: an enhancement method for immunohistochemical staining based on microwave oven heating of tissue sections. J Histochem Cytochem. 1991;39:741–8.
48. He P, Ai T, Yang ZH, Wu J, Han J. Detection of necroptosis by phospho-MLKL immunohistochemical labeling. STAR Protoc. 2021;2:100251.
49. Bankhead P, Loughrey MB, Fernandez JA, Dombrowski Y, McArt DG, Dunne PD, et al. QuPath: open source software for digital pathology image analysis. Sci Rep. 2017;7:16878.
50. Pefanis A, Bongoni AK, McRae JL, Salvaris EJ, Fisicaro N, Murphy JM, et al. Dynamics of necroptosis in kidney ischemia-reperfusion injury. Front Immunol. 2023;14:1251452.
51. Ikeda F, Deribe YL, Skanland SS, Stieglitz B, Grabbe C, Franz-Wachtel M, et al. SHARPIN forms a linear ubiquitin ligase complex regulating NF-κB activity and apoptosis. Nature. 2011;471:637–41.
52. Gerlach B, Cordier SM, Schmukle AC, Emmerich CH, Rieser E, Haas TL, et al. Linear ubiquitination prevents inflammation and regulates immune signalling. Nature .2011;471:591–6.
53. Rickard JA, Anderton H, Etemadi N, Nachbur U, Darding M, Peltzer N, et al. TNFR1-dependent cell death drives inflammation in Sharpin-deficient mice. Elife 2014;3:e03464.
54. Kumari S, Redouane Y, Lopez-Mosqueda J, Shiraishi R, Romanowska M, Lutzmayer S, et al. Sharpin prevents skin inflammation by inhibiting TNFR1-induced keratinocyte apoptosis. Elife. 2014;3:e03422.
55. Newton K, Dugger DL, Maltzman A, Greve JM, Hedehus M, Martin-McNulty B, et al. RIPK3 deficiency or catalytically inactive RIPK1 provides greater benefit than MLKL deficiency in mouse models of inflammation and tissue injury. Cell Death Differ. 2016;23:1565–76.

56. Kaiser WJ, Upton JW, Long AB, Livingston-Rosanoff D, Daley-Bauer LP, Hakem R, et al. RIP3 mediates the embryonic lethality of caspase-8-deficient mice. Nature. 2011;471:368–72.
57. Duprez L, Takahashi N, Van Hauwermeiren F, Vandendriessche B, Goossens V, Vanden Berghe T, et al. RIP kinase-dependent necrosis drives lethal systemic inflammatory response syndrome. Immunity. 2011;35:908–18.
58. Rickard JA, O'Donnell JA, Evans JM, Lalaoui N, Poh AR, Rogers T, et al. RIPK1 regulates RIPK3-MLKL-driven systemic inflammation and emergency hematopoiesis. Cell. 2014;157:1175–88.
59. Anderton H, Bandala-Sanchez E, Simpson DS, Rickard JA, Ng AP, Di Rago L, et al. RIPK1 prevents TRADD-driven, but TNFR1 independent, apoptosis during development. Cell Death Differ. 2019;26:877–89.
60. Dannappel M, Vlantis K, Kumari S, Polykratis A, Kim C, Wachsmuth L, et al. RIPK1 maintains epithelial homeostasis by inhibiting apoptosis and necroptosis. Nature. 2014;513:90–4.
61. Müller T, Dewitz C, Schmitz J, Schröder AS, Bräsen JH, Stockwell BR, et al. Necroptosis and ferroptosis are alternative cell death pathways that operate in acute kidney failure. Cell Mol Life Sci. 2017;74:3631–45.
62. Bertheloot D, Latz E, Franklin BS. Necroptosis, pyroptosis and apoptosis: an intricate game of cell death. Cell Mol Immunol. 2021;18:1106–21.
63. Kaczmarek A, Vandenabeele P, Krysko DV. Necroptosis: the release of damage-associated molecular patterns and its physiological relevance. Immunity. 2013;38:209–23.
64. Elmore S. Apoptosis: a review of programmed cell death. Toxicol Pathol. 2007;35:495–516.
65. Jiang MX, Qi L, Li LS, Li YJ. The caspase-3/GSDME signal pathway as a switch between apoptosis and pyroptosis in cancer. Cell Death Discov. 2020;6:112.
66. Falschlehner C, Schaefer U, Walczak H. Following TRAIL's path in the immune system. Immunology. 2009;127:145–54.
67. Welz PS, Wullaert A, Vlantis K, Kondylis V, Fernandez-Majada V, Ermolaeva M, et al. FADD prevents RIP3-mediated epithelial cell necrosis and chronic intestinal inflammation. Nature. 2011;477:330–4.
68. Wittkopf N, Gunther C, Martini E, He G, Amann K, He YW, et al. Cellular FLICE-like inhibitory protein secures intestinal epithelial cell survival and immune homeostasis by regulating caspase-8. Gastroenterology. 2013;145:1369–79.
69. Lu Z, Van Eeckhoutte HP, Liu G, Nair PM, Jones B, Gillis CM, et al. Necroptosis signaling promotes inflammation, airway remodeling, and emphysema in chronic obstructive pulmonary disease. Am J Respir Crit Care Med. 2021;204:667–81.
70. Simpson J, Spann KM, Phipps S. MLKL regulates rapid cell death-independent HMGB1 release in RSV infected airway epithelial cells. Front Cell Dev Biol. 2022;10:890389.
71. Li S, Zhang Y, Guan Z, Ye M, Li H, You M, et al. SARS-CoV-2 Z-RNA activates the ZBP1-RIPK3 pathway to promote virus-induced inflammatory responses. Cell Res. 2023;33:201–14.
72. Bader SM, Cooney JP, Bhandari R, Mackiewicz L, Dayton M, Sheerin D, et al. Necroptosis does not drive disease pathogenesis in a mouse infective model of SARS-CoV-2 in vivo. Cell Death Dis. 2024;15:100.
73. Mandal P, Berger SB, Pillay S, Moriwaki K, Huang CZ, Guo HY, et al. RIP3 induces apoptosis independent of pronecrotic kinase activity. Mol Cell. 2014;56:481–95.
74. Vanden Berghe T, Hulpiau P, Martens L, Vandenbroucke RE, Van Wonterghem E, Perry SW, et al. Passenger mutations confound interpretation of all genetically modified congenic mice. Immunity. 2015;43:200–9.

ACKNOWLEDGEMENTS

We would like to thank the members of the Liccardi Lab for helpful discussion. In addition, we would like to thank the Histology core facility of the SFB1403, the decentralised and CECAD animal facility staff of the University of Cologne for their support.

AUTHOR CONTRIBUTIONS

GL conceptualised and supervised the study. KK and GL designed the experiments. KK designed and optimised the staining protocol, analysed mice, conducted all the histological stainings in the manuscript. KK analysed and performed the in vivo experiments in the $Casp8^{E\text{-}KO}$ mice. ABV provided the first observation with the CST antibody and helped with quantifications and analysis optimisation. JS conducted the in vivo experiments in the $Shpn^{m/m}$ and $Shpn^{m/m}$; $Ripk3^{-/-}$, $Casp8^{-/-}$; $Ripk3^{-/-}$ and $Casp8^{-/-}$; $Mlkl^{-/-}$ models. HR and CK helped with dissections, scoring and samples preparations. AA provided the sections from SARS-CoV infected mice. AA and MZ generated the $Fadd^{iIEC\text{-}KO}$ and $Fadd^{iIEC\text{-}KO}$; $Mlkl^{-/-}$ animals and provided the sections utilised in this study. IUM, MA and JP performed the SARS-CoV infection. AL and WT provided the SIRS model, and WT, MZ and IL prepared the intestinal sections from TNF-injected mice (SIRS model). KK, JS, ABV, MZ, WT, AL, AA, HW, and GL discussed the results. KK and GL prepared the figures. KK and GL wrote the manuscript.

FUNDING

GL is funded by the Center for Biochemistry, Univeristy of Cologne – 956400, Köln Fortune, CANcer TARgeting (CANTAR) project NW21-062A, two collaborative research center grants: SFB1399-413326622 Project C06, SFB1530-455784452 Project A03 both funded by the Deutsche Forschungsgemeinschaft (DFG) and associated to the collaborative SFB1403 also funded by the DFG. AA is funded by the Center for Molecular Medicine Cologne (CMMC) Junior Research Group program, Deutsche Forschungsgemeinschaft (DFG) (project number AN1717/1-1), the Jürgen Manchot Stiftung foundation, the collaborative research center SFB1530 (Project A5, ID: 455784452), HW is funded by the Alexander von Humboldt Foundation, a Wellcome Trust Investigator Award (214342/Z/18/Z), a Medical Research Council Grant (MR/S00811X/1), a Cancer Research UK Programme Grant (A27323) and three collaborative research center grants (SFB1399, Project C06, SFB1530-455784452, Project A03 and SFB1403–414786233) funded by the Deutsche Forschungsgemeinschaft (DFG) and CANcer TARgeting (CANTAR) funded by Netzwerke 2021. AL is funded by the German Research Foundation SFB-TRR205, SFB-TRR 127, SPP2306, a Heisenberg-Professorship to AL, project number 324141047, the International Research Training Group (IRTG) 2251 and by the BMBF (FERROPath consortium), the TU Dresden/Kings College London transcampus initiative and the DFG-Sachbeihilfe LI 2107/10-1. JP is funded by FEDER (Fondo Europeo de Desarrollo Regional), Gobierno de Aragón (Group B29_23R), CIBERINFEC (CB21/13/00087), Ministerio de Ciencia, Innovación y Universidades (MCNU)/Agencia Estatal de Investigación (PID2020-113963RBI00). MA is funded by a Postdoctoral Juan de la Cierva Contract. Open Access funding enabled and organized by Projekt DEAL.

COMPETING INTERESTS

The authors declare no competing interests.

ETHICS APPROVAL

No patient data were utilised in this study. Animal ethics are listed in the 'Material and Methods' section.

ADDITIONAL INFORMATION

Supplementary information The online version contains supplementary material available at https://doi.org/10.1038/s41418-024-01313-6.

Correspondence and requests for materials should be addressed to Gianmaria Liccardi.

Supplementary Figures

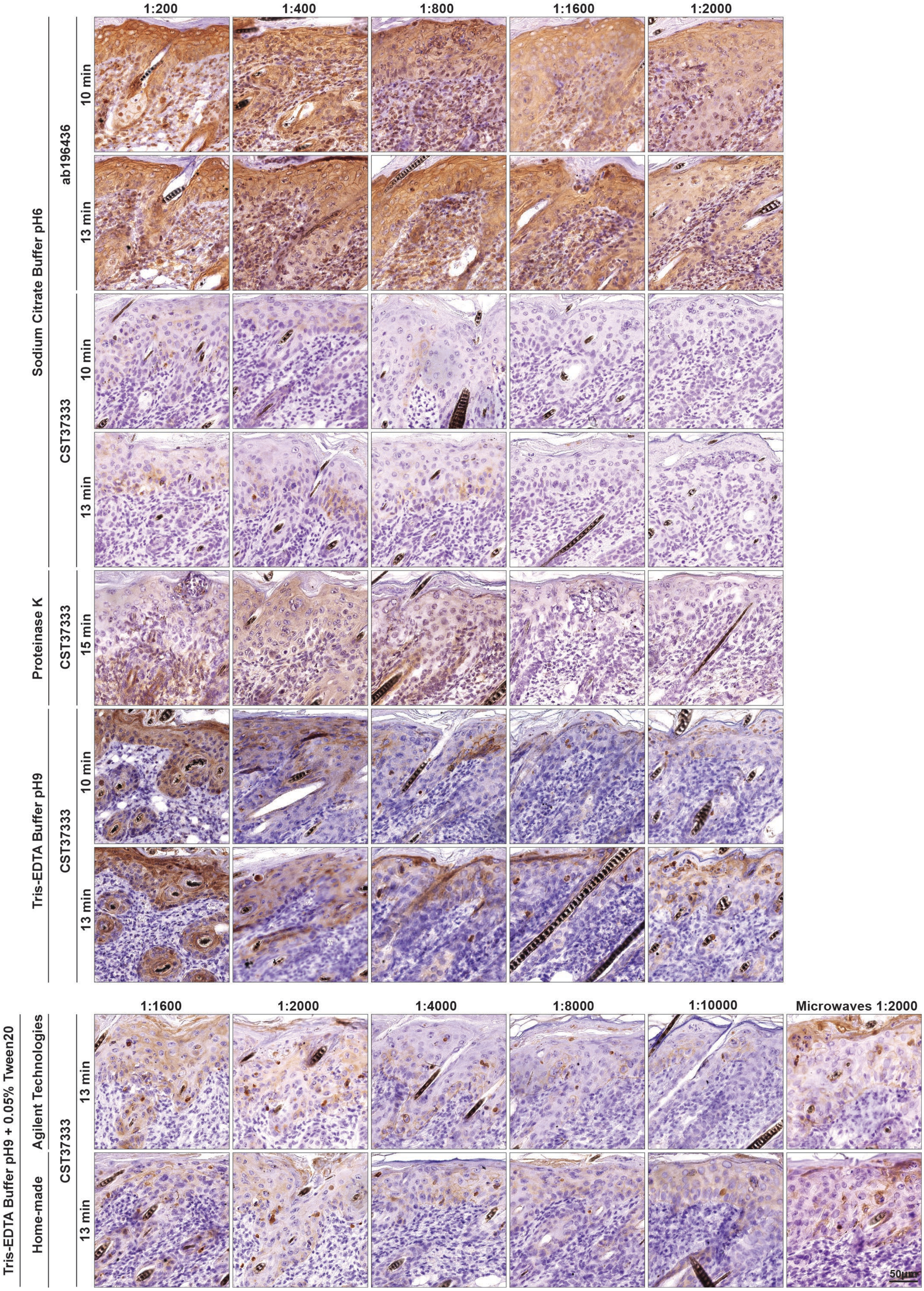

Supplementary Figure 1: Representative images of skin sections from *Casp8^{E-KO}* mice immunostained with pMLKL-S345 with the indicated α-pMLKL-S345 antibodies, antibody dilutions, retrieval method/retrieval buffer and retrieval times. Slides were digitalised in a digital slide scanner and images were acquired in QuPath. Scale bar: 50µm.

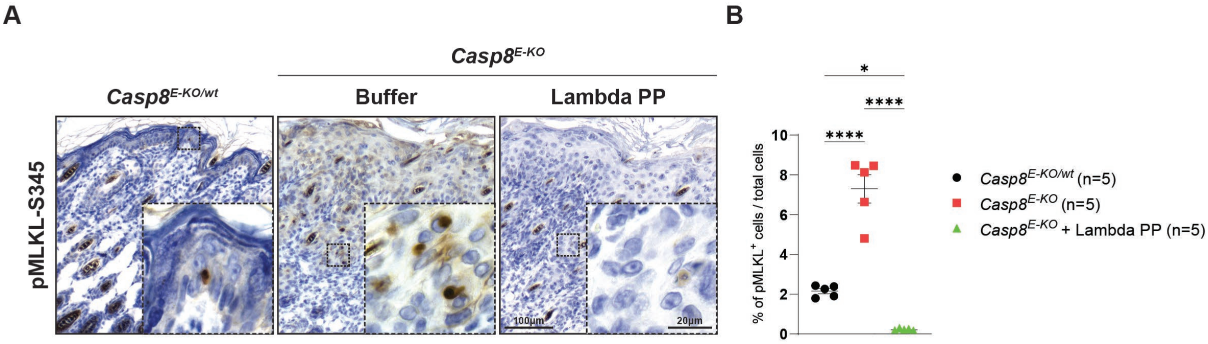

Supplementary Figure 2: (A) Representative images of skin sections from *Casp8$^{E\text{-}KO}$* mice treated with 40.000U/ml Lambda Protein Phosphatase (Lambda PP) in Lambda PP buffer and immunostained with pMLKL-S345. Control slides of skin section from *Casp8$^{E\text{-}KO}$* mice treated with Lambda PP buffer and *Casp8$^{E\text{-}KO/wt}$* mice were also immunohistochemically assessed (n=5 in each group). Scale bars: 100µm (representative field) and 20µm (magnified selcted areas). **(B)** Graph showing quantification of pMLKL-S345 immunostaining obtained via QuPath after slides were digitalized in a digital slide scanner as described in the supplementary methods section. Total skin sections were analysed and total numbers of cells were obtained to calculate the percentage of positive cells over the total amount of cells detected. Data are presented as mean + SEM and each dot represents one mouse. P values were calculated via unpaired two-tailed t-test. **P≤0.01.

A

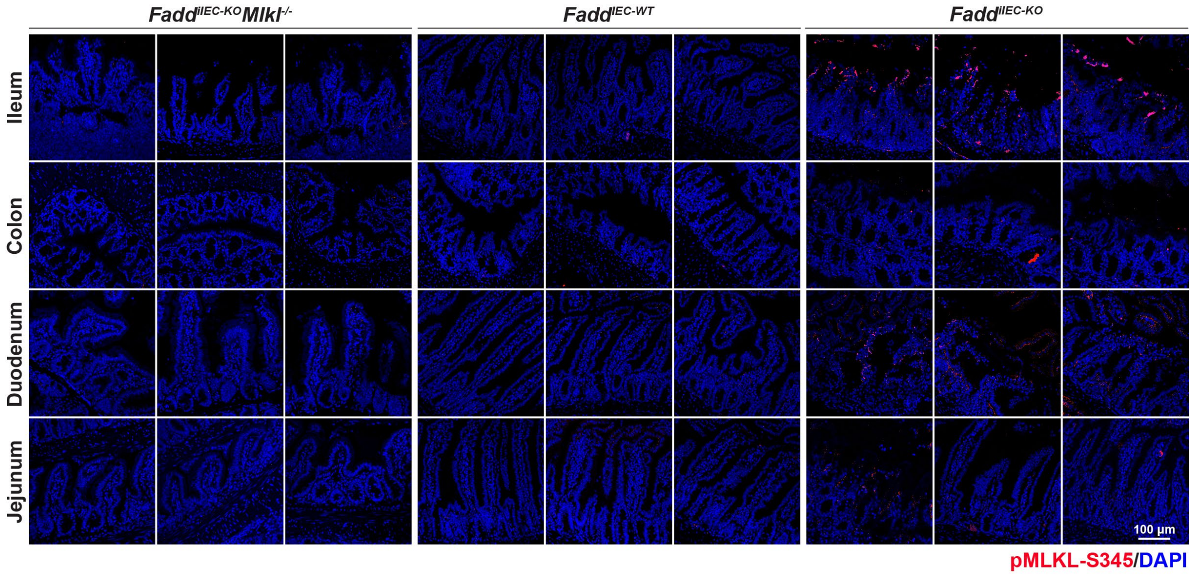

B

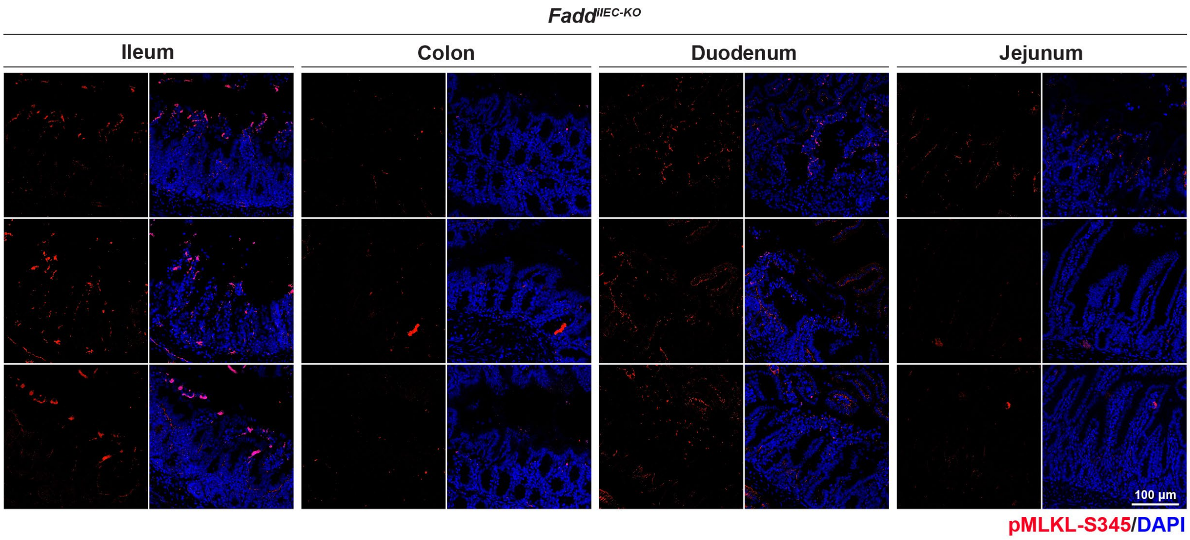

Supplementary Figure 3: Co-housed 11-weeks old *Fadd$^{fl/fl}$; Villin-Cre-ERT^2* and *Fadd$^{fl/fl}$; Mlkl$^{-/-}$; Villin-Cre-ERT^2* mice were injected with tamoxifen (10mg/mL) for 3 consecutive days to induce deletion of *Fadd* from intestinal epithelial cells (*Fadd$^{iIEC\text{-}KO}$ and Fadd$^{iIEC\text{-}KO}$; Mlkl$^{-/-}$* respectively). Age-matched *Fadd$^{fl/fl}$* mice treated with tamoxifen in the same way served as controls (*Fadd$^{iIEC\text{-}WT}$*). **(A-B)** Representative images of ileum, colon, duodenum and jejunum sections (Swiss-rolls) from mice of the indicated genotypes at the endpoint (14 weeks) immunostained with pMLKL-S345 via immunofluorescence. Red dots indicate pMLKL-S345 signal. DAPI for nuclei. Scale bar: 100µm.

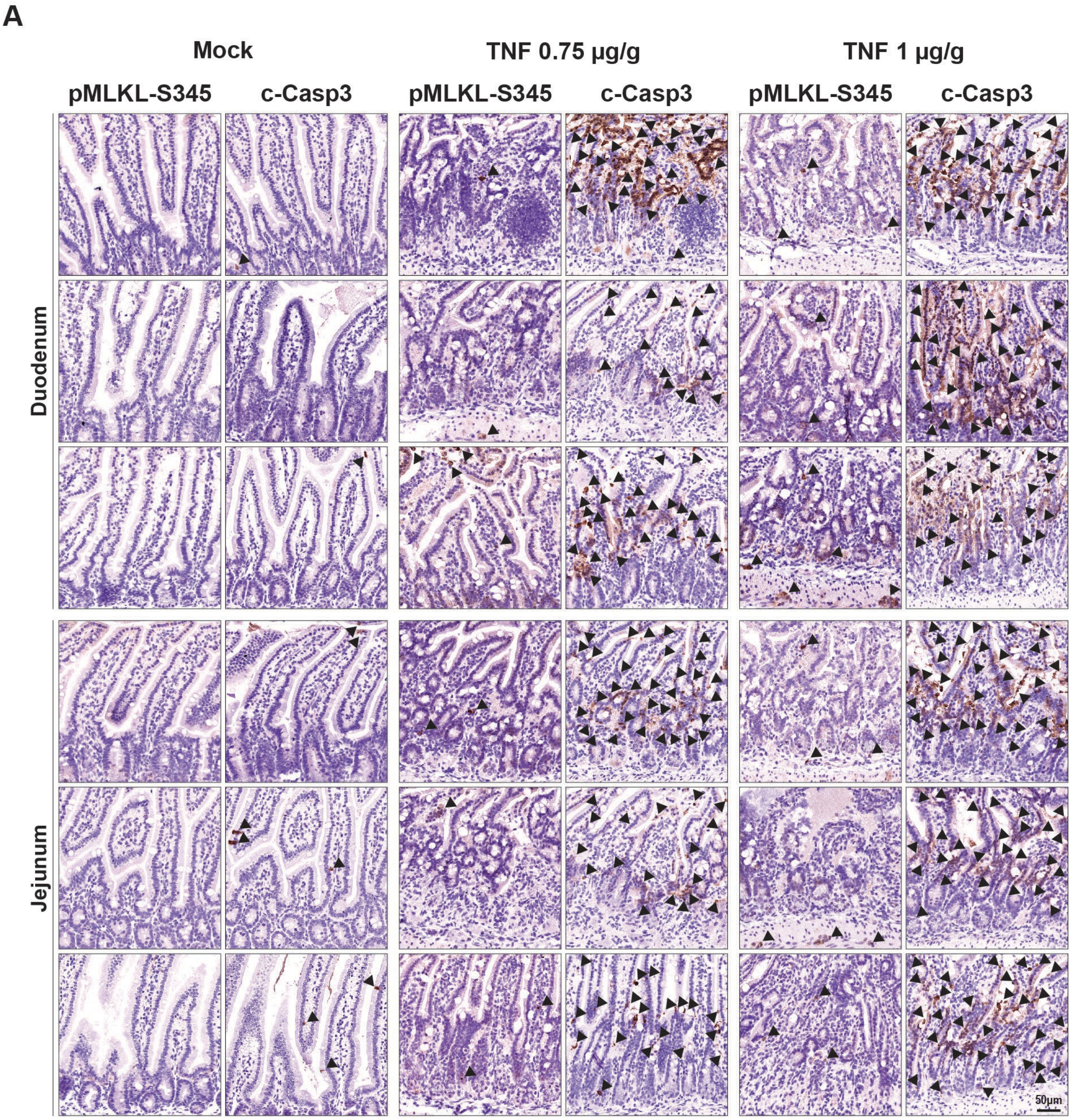
A
Mock
TNF 0.75 µg/g
TNF 1 µg/g
pMLKL-S345
c-Casp3
pMLKL-S345
c-Casp3
pMLKL-S345
c-Casp3
Duodenum
Jejunum
50µm

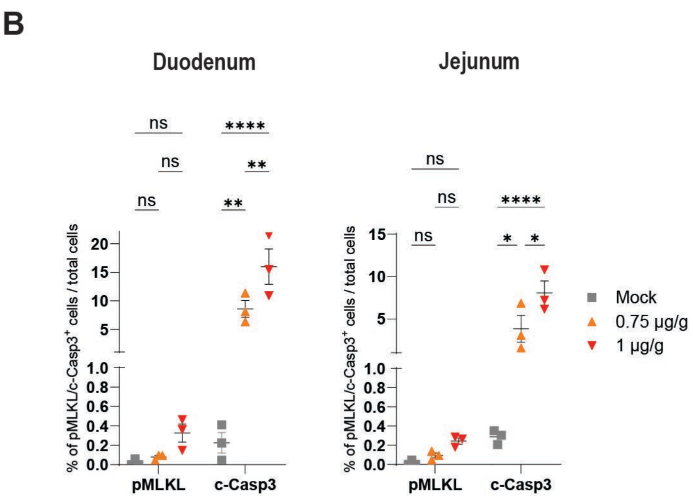
B
Duodenum
Jejunum
% of pMLKL/c-Casp3+ cells / total cells
pMLKL
c-Casp3
ns
****
**
Mock
0.75 µg/g
1 µg/g

Supplementary Figure 4: Co-housed 10–12-week-old female C57Bl6/N wt mice were injected with 0.75µg/g or 1µg/g of ice-cold recombinant, LPS-free mouse TNF intravenously. Control mice received a corresponding volume of ice-cold LPS-free PBS. Mice were sacrificed 6 hours post-injection (n=3 in each group). **(A)** Representative images of duodenum and jejunum sections (Swiss-rolls) of wt mice immunostained with pMLKL-S345 and c-Casp3 as indicated. Scale bars: 50 µm. Arrowheads indicate pMLKL-S345-positive cells and c-Casp3-positive areas. **(B)** Graph showing quantification of illustrated pictures for each immunostaining. Total numbers were obtained to calculate the percentage of positive cells over the total amount of cells detected. Data are presented as mean + SEM and each dot represents one mouse. P values were calculated via two-way Anova, Tukey's multiple comparisons test. **P≤0.01, ***P≤0.001, ****P≤0.0001, ns: not significant.

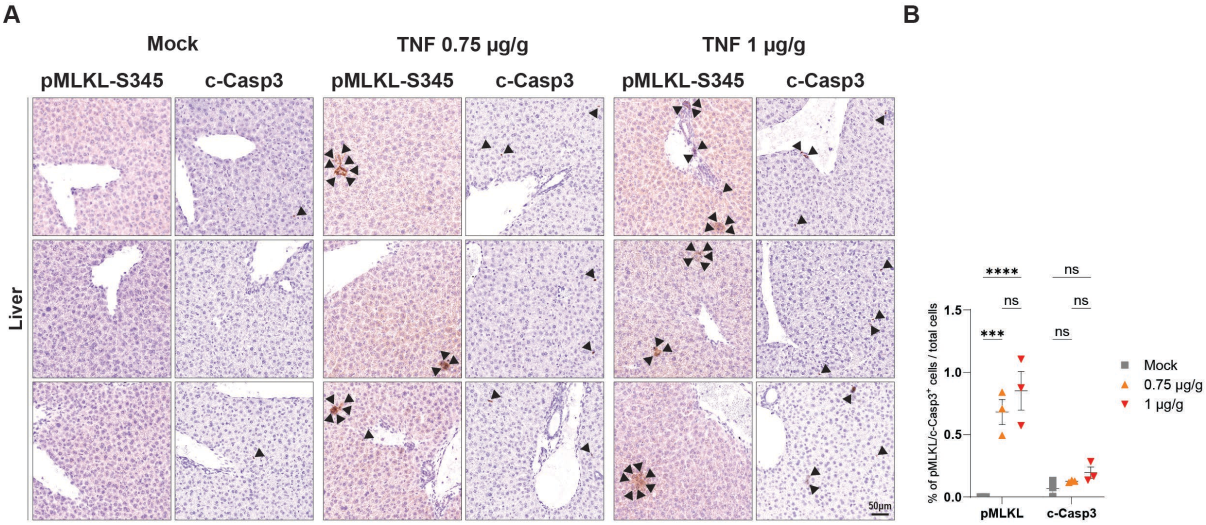

Supplementary Figure 5: Co-housed 10–12-week-old female C57Bl6/N mice were injected with 0.75µg/g or 1µg/g of ice-cold recombinant, LPS-free mouse TNF intravenously. Control mice received a corresponding volume of ice-cold LPS-free PBS. Mice were sacrificed 6 hours post-injection (n=3 in each group). **(A)** Representative images of liver sections immunostained with pMLKL-S345 and c-Casp3 as indicated. Scale bars: 50 µm. Arrowheads indicate pMLKL-S345-positive cells or c-Casp3-positive cells. **(B)** Graph showing quantification of illustrated pictures for each immunostaining obtained via QuPath. Total numbers of cells were obtained to calculate the percentage of positive cells over the total amount of cells detected. Data are presented as mean + SEM and each dot represents one mouse. P values were calculated via two-way Anova, Tukey's multiple comparisons test. **P≤0.01, ***P≤0.001, ****P≤0.0001, ns: not significant.

Supplementary Materials and Methods

Experimental Procedure

2.1 Sample preparation

Biopsy harvesting: Humanely sacrifice mice once reached endpoint criteria. Collect the mouse skin samples by harvesting skin biopsies from the dorsomedial region of the back of the mouse. Using a razor or a trimmer, remove as much hair as possible and with the scissors cut skin biopsies into a rectangle shape with the dimensions of 10 mm (L) x 5mm (W) so that the long side of the rectangle follows the Anterior-Posterior (AP) axis of the mouse (**2.1.1**). For colon and small intestine Swiss-rolls, longitudinally cut the respective tissues and wash with PBS to remove faeces. Roll up the intestinal samples from proximal to distal in a Swiss-roll shaped formation. For spleens, lungs and livers carefully extract and clean them up from any leftover adjacent tissue and wash them in PBS. Place the biopsies in an embedding cassette. Place the cassettes in 10% buffered formalin/ 4% Formaldehyde to fix the tissue overnight (O/N), *i.e.* for 8-12 hours (**2.1.2**). Store the cassettes containing the skin biopsies in 70% EtOH and the cassettes containing spleen, lung, liver and intestinal samples in PBS at 4°C at least for 24 hours before further processing (**2.1.3**).

Notes: (**2.1.1**) Make sure the rectangle-shaped biopsy is collected from the upper back of the mouse. Keep the area of harvesting consistent for all mice to obtain comparable results. (**2.1.2**) The skin specimens should be fixed O/N in formalin but it should not be kept for more than 24 hours in fixative. Over-fixation of samples may destroy the antigen site and interfere with the quality of the immunohistochemical staining. On the other hand, insufficient fixation may lead to the production of poor-quality paraffin blocks affecting the specimen cutting and its adherence to the slide during the retrieval step. (**2.1.3**) In general it is recommended to proceed with the embedding and cutting of the samples 24 hours following transfer into 70% EtOH or PBS. Please be mindful that extended storage times may harden the tissue which may negatively impact the preparation of the specimen for staining.

2.2 Tissue processing

Fixed tissues were paraffin embedded using the standard automatic tissue embedding protocols of the Vacuum tissue processor, Leica Biosystems, Model: ASP200S.

1. Transfer the cassettes containing the tissue sections to a Tissue Processor for dehydration. The skin tissues are processed in 70%, 80%, 96% EtOH for 2 hours each, 100% EtOH three times for 2 hours each and then in Xylol 2 times for 2 hours each. Spleen, lung, liver, colon and small intestine samples are processed in 30%, 50%, 70% EtOH for 2 hours each, 96% EtOH for 1 hour, 100% EtOH two times for 2 hours each and then in Xylol 2 times for 2 hours each; all steps are performed at RT. Skin tissues are then infiltrated in paraplast tissue embedding medium two times for 1 hour each and one last time for 2 hours, while the rest of the tissues two times for 1 hour each and a 2 hour incubation in between. All steps of paraffin infiltration are performed at 62°C.
2. In a Heated Paraffin Embedding Station, select the appropriate mold size. Pour the paraffin-embedding medium into the mold until one quarter of the mold is filled. Directly transfer the paraffin-infiltrated tissue inside the mold using heated tweezers. For skin sections make sure that the long side of the rectangle-shaped section is vertical to the mold's surface and in parallel to the mold's longer side. Hold the tissue in the centre and at the bottom of the mold using the tweezers to maintain its proper orientation

(2.2.1). Place the labelled lid of the sample cassette on top of the mold and slowly pour liquid paraffin into the mold until it is completely filled. Transfer the mold on a Cold Plate at -5°C for approximately 15 minutes until the paraffin is solid and hard enough to remove the block from the mold. The blocks are then placed on the Cold Plate until they are cut.

3. On a Microtome, trim the paraffin-embedded blocks by cutting thick sections of 20 μm until the complete surface of the embedded tissue is revealed. Set the cut size at 3 μm (lung, liver, colon, small intestine) or 5 μm (skin, spleen) and cut consecutive slices according to the number of sections needed.
4. Transfer the slices, grouped at a ribbon-shaped form of 6-8 slices, in a histological water bath for tissue sections set at 40°C for approximately 1-2 min. Pick every single floating section onto a correctly labelled Polysine Adhesion Slide. Transfer the slides on a Slide Dryer set at 40°C until the slides are dried and moisture-free. Continue the slide drying O/N in an incubator at 40°C **(2.2.2)**.

Notes: (**2.2.1**) Make sure all biopsies are placed in the mold in the correct orientation. This step will determine the final orientation of the biopsy in the paraffin block. This will ensure the produced cuts provide with the appropriate view of: the interfollicular epidermis, the hair follicles and hair orientation when stained for skin, white and red pulp for spleen, bronchioles, alveoli and veins for lungs, the crypts, villi and lumen for intestinal samples (**2.2.2**). The drying step is critical to ensure proper adhesion of the tissue on the slide. Insufficient drying of the sections may lead to tissue loss during the staining procedure and especially during Heat-induced Retrieval.

2.3 Staining

1. **Deparaffinisation/Rehydration:** Incubate the slides in Xylol or Xylene substitute three times for 5 minutes each, twice in 100% v/v ethanol for 5 minutes each, 95% v/v ethanol in water for 5 minutes, 70% v/v ethanol in water for 3 minutes, 50% v/v ethanol in water for 3 minutes and lastly two times in deionised (DI) water (diH_2O) for 5 minutes each (**2.3.1, 2.3.2**).

2. **Antigen Retrieval:** Prepare fresh 1x Dako Target Retrieval Solution Buffer and add 0.05% Tween20. Transfer the slides in a Slide holder and then in a Staining Dish or directly in a Coplin jar containing the retrieval buffer. Incubate the slides in the retrieval buffer for 10 minutes at room temperature. Fill the Pressure Cooker with 500-1000 ml of ddH_2O and place the Dish/Coplin jar inside the cooker. Choose the High-Pressure program (114°-121°C) and set the timer at 13 minutes (**2.3.3, 2.3.4, 2.3.5**). Directly after the end of the program release the pressure, remove the lid from the Pressure cooker and let the slides sit in the same buffer for around 1 hour to allow the buffer progressively cool down. Wash the slides in diH2O twice for 5 minutes each and air-dry them carefully. Using a Hydrophobic barrier pap pen, draw a circle around each tissue section (**2.3.6**).

3. **Blocking and Primary Antibody Incubation:**

   i. **Endogenous Peroxidase Blocking:** Block endogenous peroxidase activity by incubating the slides in BLOXALL Blocking solution for 10 minutes at RT in the dark by adding the reagent to each tissue section dropwise. Immediately rinse the slides in diH_2O and incubate them for 5 minutes in washing buffer (henceforth referred as WB, see Supplementary Table 2).

ii. **Protein Blocking:** Block the antibody non-specific binding sites by incubating the tissue sections in animal free serum RTU for 30 minutes at RT. Wash the slides in WB for 5 minutes.

iii. **Biotin/Avidin Blocking:** Block avidin binding sites by incubating the tissue sections in Avidin blocker for 5 minutes. Wash the slides in WB for 5 minutes and block endogenous biotin and biotin receptors by incubating the tissue sections in Biotin Blocker for 5 minutes. Wash slides in WB three times for 5 minutes each followed by a quick rinse in TBS.

iv. **Lambda Protein Phosphatase (Lambda PP) Treatment**
Prepare Lambda PP working solution by diluting the supplied 10x concentrated NEBuffer Pack for Protein MetalloPhosphatases (PMP) and $MnCl_2$ in diH_2O. Vortex and add Lambda PP to a final concentration of 40.000U/ml (**2.3.7**). Include internal controls by treating slides with the prepared 1x Lambda PP Buffer only. Incubate slides at 37°C in a wet chamber for 24h (**2.3.7**). Wash slides thoroughly for three times in WB for 5 minutes each followed by a quick rinse in TBS.

v. **Primary Antibody Incubation:** Apply the primary pMLKL-S345 antibody at a final dilution of 1:2000 in 0.1% v/v Triton-X, animal free blocker and incubate them overnight at 4°C in a wet chamber filled with water (**2.3.8**).

4. **Secondary Antibody Incubation:** Wash the slides in WB, three times for 10 minutes each on a shaker at 200 rpm and then quickly rinse in TBS. Incubate the tissue sections in Biotinylated Goat Anti-Rabbit IgG Antibody (H+L), by diluting it 1:200 in 0.1% v/v Triton-X, animal free blocker for 40 min.

   For the immunohistochemical assay: In the mean-time, prepare the ABC Reagent: Add 1 drop of Reagent A (Avidin, ABC Elite) in 5 ml of 1xTBS in a 15 ml falcon tube and vortex thoroughly. Add 1 drop of Reagent B (Biotinylated HRP, ABC Elite) in the same tube and mix well. Let the reagent stand at room temperature for at least 30 minutes before use. Wash the slides three times for 5 minutes in WB on the shaker and quickly rinse them in TBS. Add the ABC reagent in each tissue section dropwise and incubate them for 40 minutes. Wash the slides three times for 5 minutes in WB on the shaker and then wash the slides in diH_2O for 5 minutes.

5. **DAB staining, counterstaining and mounting:** Combine 1 drop (~30 μl) of ImmPACT DAB Reagent to 1 ml ImmPACT DAB Diluent and apply the DAB mixture to each tissue section and incubate. Stop the reaction by dipping the slide in water when the signal staining reaches the desirable intensity. Then, rinse twice with diH_2O (**2.3.9, 2.3.10**).

   For Hematoxylin counterstaining, prepare two chambers, one containing hematoxylin and the other one containing tepid tap H_2O. Transfer the slides in a slide basket/rack and dip it in hematoxylin for 2 min. Transfer the slide basket in the chamber containing tepid tap H_2O and wash the slides by moving the slide basket up and down for approximately 10 seconds. Rinse well in a container under running tap H_2O for approximately 20 sec and let the slides stand in tap water for 15 minutes, until Haematoxylin acquires a bluish tint.

   Dehydrate the tissue sections by dipping the slides in 70%, 95%, 100% ethanol and Xylene for 1 minute each.

Mount the slides by adding 1-2 drops of Mounting Medium and cover the slides with a coverslip (**2.3.11**) before letting them dry O/N at RT.

For the Immunofluorescence assay: After incubating the slides in Biotinylated Goat Anti-Rabbit IgG Antibody (H+L), wash the slides three times for 5 minutes in WB on the shaker and quickly rinse them in TBS. Incubate the tissue sections in Alexa Fluor 594 Streptavidin (1:200) and DAPI at a final concentration of 0.1-1 µg/ml in animal free blocker for 30 minutes.

Wash the slides thoroughly three times for 10 minutes each in WB in the dark on the shaker and then rinse the slides in diH_2O for 5 minutes. Mount slides in anti-fade mounting media and store at 4°C for at least 24 hours before visualization under the confocal microscope.

Notes: (**2.3.1**) Always work under a fumes' hood when using xylene to avoid its hazardous effects. (**2.3.2**) In case of incomplete deparaffinisation, incubate the slides at 60°C for 20 minutes prior to xylene incubation. (**2.3.3**) The time, temperature and pH of the retrieval buffer should be kept consistent to properly retrieve the antigenic site and avoid either inadequate retrieval or destruction of the antigenic site. This will prevent loss of signal or non-specific antibody binding and any possible background staining. (**2.3.4**) Alternatively, heat the slides in the Coplin jar in the microwave oven at half power (350 W) until the buffer starts to boil. Continue boiling at 120 W for 15 minutes. At this point, make sure to replenish retrieval buffer when you observe spillage from the Coplin jar to avoid drying the tissue. Remove the jar from the microwave oven and let the slides sit at room temperature (RT) in the same buffer for 40 minutes until the temperature reaches around 50°C. **(2.3.5)** It is often experienced that during retrieval time, tissues of different origin and age might detach from the slides. To prevent this from occurring while ensuring correct retrieval, we recommend the assembly of a "sandwich" cassette. Briefly, add retrieval buffer to a slide of interest. Place a coverslip on top of the slide and then add retrieval buffer to the coverslip. Gently place the second slide face down on top of the coverslip and secure the sandwich-like cassette with metal clips. This will apply a mechanical compression to the two tissue sections to prevent detachments and preserve tissue morphology while allowing adequate epitope retrieval. Add the sandwich into a Coplin jar and proceed with boiling into a pressure cooker for 10-13 minutes. Follow procedure as described above. (**2.3.6**) Carefully circle the tissue sections around the edges using the pap pen to prevent diffusion of the incubation buffers and reagents. Avoid drawing the circle too close to the tissue sections as this might prevent liquid diffusion over the section due to hydrophobic tension. (**2.3.7**) Concentration of Lambda PP, temperature and incubation times were optimised for skin tissue sections for this staining assay. Since this de-phosphorylation assay varies with tissue samples and temperature, we recommend you optimise these parameters for different incubation times or tissue samples. (**2.3.8**) Primary antibody dilution has been optimised for skin, spleen, lung, liver and intestinal sections. We recommend to titrate the dilution for other organs in the range of 1:1000-10000 to find optimal antibody concentration to better assess specific pathological conditions of interest or in case of high Noise/ Signal ratio. (**2.3.9**) During DAB exposure, observe the slides under the microscope until the desirable intensity is reached. Stop the reaction simply by dipping the slides in water. The reaction usually takes 15 seconds for optimal intensity (**2.3.10**) Always use a positive and a negative control to validate the performance of your staining. (**2.3.11**) To prevent any bubbles from being trapped between the coverslip and the slide, add the mounting medium on a wet slide, directly after the incubation step in xylene. Place the coverslip in a 60° angle until it touches one side of the slide and slowly release it on top of it by excreting mild pressure with an angled tweezers. To remove any bubbles that were still trapped, mildly exert pressure on top of the slide using the tweezers. Be careful as too much pressure might destroy the tissue.

2.4 Imaging Analysis

Immunohistochemistry slides were digitalised using a digital slide scanner (NanoZoomer S360MD Slide scanner system, Hamamatsu Photonics K.K.) with a 40x magnification lens. The acquired brightfield images were analysed in QuPath, an open-source software [1]. Additional 10x and 63x pictures were acquired with Leica DM750 Binocular microscope. The immunofluorescence pictures were acquired with LSM 980 with Airyscan 2, 20x and 63x lens, Zeiss at the CECAD Imaging Facility, University of Cologne.

1. Create Pixel Classifier

In QuPath, to quantify the positively stained cells, we generated, first and when necessary, a pixel classifier in order to exclude the areas of the tissue that should not be accounted for during the quantification step and would otherwise interfere with the “positive cell detector”. These areas mainly comprised of the hair follicles since the melanin from the hair can be considered falsely as positive signal by the automated detector leading to false positive results.

1. On QuPath main window, create a new project by clicking on ‘Create Project’. Select the directory you want to save your project to.
2. Click on ‘Add images’ and import the .dnpi files by drag and drop or simply by clicking on ‘Add Image’. Set image type “Brightfield (H-DAB)” and click “Import”.
3. To generate a pixel classifier, you need first to create a training image.
4. Click Classify>Training Images>Create region annotations. Set width and height at 150, Size units: µm, Classification: Region* and click on ‘Create region’ 5-10 times. Place the square training regions on representative areas that include both areas that should be classified and areas that should be excluded from the classification. Before you continue make sure to save your project (File>Save).
5. Click Classify>Training images>Create training image. Set Classification: Region*, leave the rest as default and click “OK”. A new composite image will be generated at the end of your project by combining the different numbers of region annotations you generated. If required, set image type as ‘Brightfield (H-DAB)’ and click “Apply”.
6. Select the brush tool and draw on the areas with positive cells that should be classified. On the left side of the main window click on “Annotations”. You will find listed all the annotations you generated with the brush tool. In the Annotations panel select the annotations you generated, in the class panel right next to the list with the annotations, click on ‘Positive’>Set Class. Repeat the same procedure, this time creating annotations that contain only areas that should be excluded from the classification (i.e., the hair). Set Class “Negative”. (In the “Class” Panel you can add or remove Classes by clicking at the three dots “More options”).
7. Click on Classify>Pixel classification>Train pixel classifier (Ctrl + shift + P).
8. Select Classifier: “Random Trees (RTrees)”, Resolution: “Very high (0.46 µm/px)”, leave rest as default and click on “Live prediction”.
9. The Pixel Classifier might need further optimisation. Adjust the Pixel Classifier options until best results are reached, add “Classifier name” and click on “Save”.

2. Create Regions Of Interest (ROIs) and Run Pixel Classifier

1. In the “Project” tab select the file you want to work with.

2. Click on Analyze>Deprecated>Simple Tissue Detection (deprecated). This will generate automatically annotations for the tissue sections based on a chosen threshold.
3. In the “Annotations” tab you will find the newly generated Annotations.
4. Select all the annotations in the “Annotations” tab and go to Classify>Pixel Classification>Load pixel classifier. Choose model: Select the classifier you generated, Region: “Any annotation ROI” and click on “Create objects”.
5. A new “Pixel Classifier” window will pop up. Choose parent objects: “Current selection” and click “OK”.
6. In the “Create objects” window, leave everything as default and click “OK”.
7. For every annotation two new annotations will be generated, one classified as positive and one as negative.

3. Positive cell detection and counting

1. Click on “Annotation (Positive)” in the annotation tab. Go to Analyze>Cell detection>Positive cell detection.
2. In the “Positive cell detection” window that pops up, set the parameters as desired and press “Run”. Detection annotations will be generated. By looking at them you can decide to change accordingly the “Positive cell detection” parameters and re-run the detection. In principle, we suggest you optimize your detection method by mainly trying and adjusting the “Intensity Parameters”, and “Intensity Threshold Parameters”.
3. Go to Measure>Show annotation measurements. Right click on the “Annotation results” window>Show classes>Positive. Here you will find the quantification results (including the total number of cells, the number of cells stained positive and the percentage of the positive cells).

2.5 Graph and Statistics

Plot the percentages of positive cells per total number of cells for each section or image for the different biological replicates were in a statistical software. Perform two-way Anova statistical analysis to determine significance among the different groups (P values=0.05 *; 0.01**; 0.001*** 0.0001****).

Supplementary Table 1

Reagents, materials and the equipment necessary for the execution of the protocol are given in Table 1. The recipes for the preparation of the reagents can be found in the Reagents section (Table 2).

Resources	Source	Catalogue number
Antibodies		
Phospho-MLKL (Ser345) (D6E3G)*	Cell Signalling Technology	#37333
Kits/ Assays		
Goat Anti-Rabbit IgG Antibody (H+L), Biotinylated, 1.5 mg*	Vector Laboratories	#BA-1000
VECTASTAIN Elite ABC-HRP Kit, Peroxidase (Standard)*	Vector Laboratories	# PK-6100
ImmPACT DAB Substrate Kit, Peroxidase (HRP)	Vector Laboratories	#SK-4105

Alexa Fluor 594 Streptavidin	Thermo Fisher Scientific	# S11227
Animal-Free Blocker and Diluent, R.T.U.	Vector Laboratories	#SP-5035-100
Avidin/Biotin Blocking Kit*	Vector Laboratories	# SP-2001
BLOXALL Endogenous Blocking Solution, Peroxidase and Alkaline Phosphatase	Vector Laboratories	#SP-6000-100
Hematoxylin Counterstain	Vector Laboratories	#H-3401
Hematoxylin Counterstain	Carl Roth	# T865.3
Eosin	Carl Roth	# X883.2
VectaMount Express Mounting Medium	Vector Laboratories	#H-5700
ProLong Gold Antifade Mountant	Thermo Fisher Scientific	# P36930
DAPI, dilactate	Sigma-Aldrich	# D9564
Dako Target Retrieval Solution, pH 9 (x 10), Concentrate*	Agilent Technologies	#S236784-2
Lambda Protein Phosphatase*	New England Biolabs (NEB)	#P0753S
Chemicals		
Xylol (Isomere) ROTI Histol (Xylene substitutes)	Carl Roth Carl Roth	#9713 #6640
Xylene (mixture of isomers) ≥98.5%, AnalaR NORMAPUR ACS, Reag. Ph. Eur. analytical reagent (for Tissue Processor)	VWR Chemicals	#28975.360
Ethanol ROTIPURAN ≥99.8%, p.a.	Carl Roth	#9065
ETHANOL 96 % DENATURED WITH MEK, IPA AND BITREX® (MIN. 96.0 %)	TH.GEYER	#11832327
Ethanol denatured ≥99.5%, GPR RECTAPUR® (denatured with 1% MEK) (for Tissue Processor)	VWR Chemicals	#85033.360
Surgipath Paraplast	Leica Biosystems	#39602012
Tween-20	Sigma-Aldrich	#P7949-2.5L
Triton X-100	Sigma-Aldrich	#X100
Sodium chloride 99.5-100.5%, AnalaR NORMAPUR® ACS, Reag. Ph. Eur. analytical reagent, NaCl	VWR Chemicals	#27810.364
Trizma base, ary Standard and Buffer, ≥99.9% (titration), crystalline, $NH_2C(CH_2OH)_3$	Sigma-Aldrich	#T1503
EDTA disodium salt dihydrate 99.0-101.0%	VWR Chemicals	# 20302.293

Formalin solution, neutral buffered, 10%	Sigma-Aldrich	#HT501128-4L
Formaldehyde solution, phosphate buffered, 4%	Walter CMP GmbH	# WAL60622
Treatments		
LPS-free mTNFα	BioLegend	#575208
Tamoxifen	Sigma-Aldrich	#T5648
Equipment		
Vacuum tissue processor	Leica Biosystems	Model: ASP200S
Modular Tissue Embedding Center	Leica Biosystems	Model: EG1150
Fully Automated Rotary Microtome	Leica Biosystems	Model: RM2255
Cold Plate for Modular Tissue Embedding System	Leica Biosystems	Model: EG1150C
Water Bath for Paraffin Sections	Leica Biosystems	Model: HI1210
Flattening table for clinical histopathology	Leica Biosystems	Model: HI1220
TintoRetriever Pressure Cooker	BioSB	#BSB7008
Microwaves	Bomann	#MW6014CB
Shaker	Grant Instruments	Model: PMR-30
Confocal Microscope	ZEISS	Model: LSM 980 with Airyscan 2
Light Microscope	Leica Biosystems	Model: DM750
Slidescanner for brightfield images	Hamamatsu	#C13220-21MDEU
General Supplies		
Staining trough acc. to Coplin*	Carl Roth	#YC09.1
Polysine Adhesion Slides	Epredia	#J2800AMNZ
Tissue embedding cassettes	Kabe Labortechnik	#054681
Cover Glasses	DWK Life sciences	#235505508
Hydrophobic Barrier PAP Pen	Vector Laboratories	#H-4000
Stain Tray	Simport Scientific	#M918-2
Set for histology and cytology with 12 dishes	Bio Optica	#10-10
Plastic Staining Dish	BioSB	#BSB 7009
Slide Holder (24 Slides)	BioSB	#BSB 7010
Staining dish with attached lid	Bio Optica	#10-30
Plastic slide basket	Bio Optica	#10-42
Disposable Blades	Leica Biosystems	#14035838382
Software		
QuPath (Open Software for Bioimage Analysis)		https://qupath.github.io/
Prism - GraphPad		https://www.graphpad.com/features

* We suggest that the indicated reagents and materials are not replaced to ensure the highest possible experimental performance. The rest of the reagents, materials and general supplies could be replaced based on the availability and capacity of the respective consumables.

Supplementary Table 2

Reagent Preparation

"Homemade" Tris-EDTA Antigen Retrieval Buffer at pH 9, 1x

Tris-EDTA Retrieval Buffer	**Amount**	**Final Concentration**
Trizma base	1,21g	10mM
EDTA	0,37g	1mM
HCl	Until pH 9	n/a
H_2O	1L	n/a
Tween-20	0,5ml	0,05% (v/v)

To prepare 1L of 1x Tris-EDTA Antigen Retrieval Buffer stock solution, dissolve the indicated amount of Trizma and EDTA in 900ml of double-distilled water (ddH_2O). Adjust the pH at 9 if necessary and fill up to 1L with ddH_2O. Store the Buffer at 4°C for long-term use.

TBS 10x Concentrated

TBS	**Amount**	**Final Concentration**
Trizma base	24,2g	200mM
NaCl	87,75g	1.500mM
HCl	Until pH 7,4	n/a
H_2O	1L	n/a

To prepare 1L of 10X TBS stock solution, dissolve the indicated amount of Trizma and NaCL in 900ml of double-distilled water (ddH_2O). Adjust the pH at 7.4 with 12N HCl and fill up to 1L with ddH_2O. TBS is stable at 4°C for 3 months. To make 1x TBS working solution, dilute 100ml of 10x TBS in 900ml of ddH_2O. Store the TBS solutions at 4°C.

Washing Buffer (WB), 1x

TBS-T 0.1% (v/v)	**Amount**	**Final Concentration**
1x TBS	1L	n/a
Tween-20	1ml	0,1% (v/v)
Total	n/a	1L

The washing buffers should be prepared freshly on the day of use. Store them at 4°C for short-term use.

2. Publication 2
Declaration and Rationale

STING induces ZBP1-mediated necroptosis independently of TNFR1 and FADD

https://doi.org/10.1038/s41586-025-09536-4

Declaration: This study uncovers a novel role for the cGAS-STING signalling axis in driving necroptotic cell death and delineates the molecular mechanisms underlying this process, while also revealing a central role for STING-driven necroptosis in the pathogenesis of STING-associated vasculopathy with onset in infancy (SAVI). While STING is classically recognized as a central mediator of innate immunity, primarily through the TBK1-IRF3-dependent induction of type I interferons, its role in regulating programmed cell death has remained poorly defined. Here, we identify ZBP1 as the key mediator of STING-driven necroptosis, acting independently of TNFR1. Through a combination of pharmacological STING agonists, genetic knockout models, transcriptomic analysis and *in vivo* experimentation, we demonstrate that STING activation licenses necroptosis by inducing a type I IFN-dependent transcriptional program that upregulates both ZBP1 and MLKL. This enables ZBP1-RIPK3-MLKL-mediated necroptosis independently of the canonical TNFR1-FADD-RIPK1-RIPK3 axis. Importantly, we reveal a dual role for STING, not only as a transcriptional inducer of necroptotic effectors, but also as an amplifier of inflammatory signalling that promotes both TNFR1- and ZBP1-dependent necroptosis. Notably, aberrant STING activation in SAVI patients bearing gain-of-function STING mutations orchestrates a necroptotic transcriptional program that almost entirely overlaps with that observed in *Casp8*$^{E\text{-}KO}$ mice. This is further confirmed in the *Sting1*^{N153S} SAVI mouse model, where co-deletion of *Ripk3* rescues both immune-cell-driven pathology and lethality. These findings clarify how STING directly interfaces with regulated necroptotic cell death and underscore its relevance in both homeostatic and inflammatory contexts. This newly defined STING-driven necroptotic axis offers mechanistic insight into interferonopathies such as SAVI and suggests new avenues for therapeutic intervention in STING-driven chronic inflammatory and autoimmune diseases characterized by excessive necroptosis.

Contribution:

- Contributed to the design and coordination of the experimental approach.
- Generated and analysed all mouse models used in the study.
- Optimised, performed, analysed, and quantified all immunohistochemical (IHC) and immunofluorescent (IF) stainings across all examined tissues and experimental conditions, as well as all *in vitro* IF experiments in cultured cells.
- Performed cytokine and blood analysis and prepared mRNA from mouse tissue.
- Performed the viability assays and western blots presented in Figure 1i and Extended Data Figures 2d, 6e.
- Interpreted the experimental results, prepared all figures, and drafted and edited the manuscript.

Article

STING induces ZBP1-mediated necroptosis independently of TNFR1 and FADD

https://doi.org/10.1038/s41586-025-09536-4

Received: 9 December 2024

Accepted: 14 August 2025

[redacted]

Open access

Check for updates

Konstantinos Kelepouras[1,2,3], Julia Saggau[1,2,3,4,5,11], Debora Bonasera[1,2,3,4,5,11], Christine Kiefer[1,2,3], Federica Locci[6], Hassan Rakhsh-Khorshid[1,2,3], Louisa Grauvogel[7], Ana Beatriz Varanda[4,5], Martin Peifer[7], Elena Loricchio[8], Antonella Montinaro[9], Marijana Croon[3,10], Aleksandra Trifunovic[3,10], Giusi Prencipe[8], Antonella Insalaco[8], Fabrizio De Benedetti[8], Henning Walczak[4,5,9] & Gianmaria Liccardi[1,2,3] ✉

Conditional deletion of caspase-8 in mouse epidermal keratinocytes ($Casp8^{E\text{-}KO}$) causes necroptosis-driven lethal dermatitis[1–7]. Here we find that the loss of *Casp8* leads to an accumulation of cytosolic DNA that is responsible for the activation of a CGAS–STING-mediated transcriptional program. Genetic and biochemical evidence indicate that STING upregulates both ZBP1 and MLKL. Combined caspase-8-deficiency- and STING-activation-driven accumulation of Z-nucleic acids activates ZBP1 and triggers the formation of a ZBP1–RIPK1–RIPK3 complex independently of the FADD–RIPK1–RIPK3 complex, enabling execution of necroptosis. Genetically, we reveal a functional overlap between STING and ZBP1 as drivers of lethal dermatitis independently of TNFR1, identifying an aetiology of necroptotic inflammation. As gain-of-function mutations in human *STING* cause STING-associated vasculopathy with onset in infancy (SAVI), we assessed the role of STING-induced necroptosis in SAVI's aetiology. Chronic activation of STING in patients orchestrates a necroptotic transcriptional program that is confirmed in the $Sting1^{N153S}$ SAVI preclinical mouse model in which immune-cell-driven pathology and lethality are rescued by *Ripk3* co-deletion. These findings establish STING-driven ZBP1-mediated necroptosis as a central pathogenic mechanism in both caspase-8-deficient inflammation and SAVI and suggest that targeting the ZBP1–RIPK3–MLKL axis holds therapeutic potential for interferonopathies characterized by excessive necroptosis.

In contrast to deletion of *Ripk3* or *Mlkl*, loss of *Tnfr1* does not prevent, and only delays, the embryonic lethality and the lethal dermatitis of $Casp8^{-/-}$ and $Casp8^{E\text{-}KO}$ mice, respectively[1,8,9]. Thus, RIPK3–MLKL-induced signalling beyond TNFR1-mediated necroptosis is responsible for aberrantly activated necroptosis. Similarly, removal of *Tnfr1* only minimally delays the observed lethal dermatitis induced by loss of *Ripk1* or *Fadd* in epidermal keratinocytes ($Ripk1^{E\text{-}KO}$ or $Fadd^{E\text{-}KO}$)[10–12]. Notably, $Ripk1^{E\text{-}KO}$ mice can survive through adulthood already with single co-deletion of *Zbp1*, and $Fadd^{E\text{-}KO}$ mice are completely rescued by co-deletion of *Zbp1* and *Tnfr1*, suggesting ZBP1-dependent but TNFR1-independent necroptosis involvement[7,13,14]. Although it was shown that activation of ZBP1 depends on its binding to cytosolic Z-DNA or Z-RNA[15–20], the pathway responsible for ZBP1 upregulation and its consequent role in necroptosis remained unclear.

Previous studies have indicated that the loss of caspase-8 induces upregulation of ZBP1 in mouse embryonic fibroblasts (MEFs)[21]. Histological examination of skin obtained from $Casp8^{-/-}$ mice crossed with either RIPK3- or MLKL-deficient mice ($Casp8^{-/-}Ripk3^{-/-}$ and $Casp8^{-/-}Mlkl^{-/-}$) revealed a significant upregulation of ZBP1 and STAT1 phosphorylation (p-STAT1) also in vivo (Fig. 1a). ZBP1 upregulation was indeed detectable despite the absence of any visible necroptosis-induced skin lesions or histologically detectable immune cell infiltration (Fig. 1a). This suggested that caspase-8 prevents the sustained tonic activation of interferon (IFN) signalling, probably responsible for driving ZBP1 expression independently of cell death.

Given that *Zbp1* deletion is required to neutralize aberrantly activated necroptosis[14–16,20,22–24], we hypothesized that the activation of this IFN-mediated transcriptional response would have a pathological role in regulating an arm of inflammatory necroptosis. We therefore aimed to identify the critical pathway component responsible for this IFN-mediated transcriptional ZBP1 upregulation.

[1]Genome Instability, Inflammation and Cell Death Laboratory, Institute of Biochemistry I, Centre for Biochemistry, Faculty of Medicine, University of Cologne, Cologne, Germany. [2]Centre for Molecular Medicine Cologne (CMMC), University of Cologne, Cologne, Germany. [3]Cologne Excellence Cluster on Cellular Stress Responses in Ageing-Associated Diseases (CECAD), Medical Faculty, University of Cologne, Cologne, Germany. [4]Cell Death, Inflammation and Immunity Laboratory, CECAD Cluster of Excellence, University of Cologne, Cologne, Germany. [5]Cell Death, Inflammation and Immunity Laboratory, Institute of Biochemistry I, Centre for Biochemistry, Faculty of Medicine, University of Cologne, Cologne, Germany. [6]Department of Plant–Microbe Interactions, Max Planck Institute for Plant Breeding Research, Cologne, Germany. [7]Department of Translational Genomics, Centre of Integrated Oncology Cologne-Bonn, Medical Faculty, University of Cologne, Cologne, Germany. [8]Division of Rheumatology, Ospedale Pediatrico Bambino Gesù, IRCCS, Rome, Italy. [9]Centre for Cell Death, Cancer and Inflammation, UCL Cancer Institute, University College London, London, UK. [10]Institute for Mitochondrial Diseases and Ageing, Medical Faculty and Centre for Molecular Medicine Cologne (CMMC), University of Cologne, Cologne, Germany. [11]These authors contributed equally: Julia Saggau, Debora Bonasera. ✉e-mail: gianmaria.liccardi@uk-koeln.de

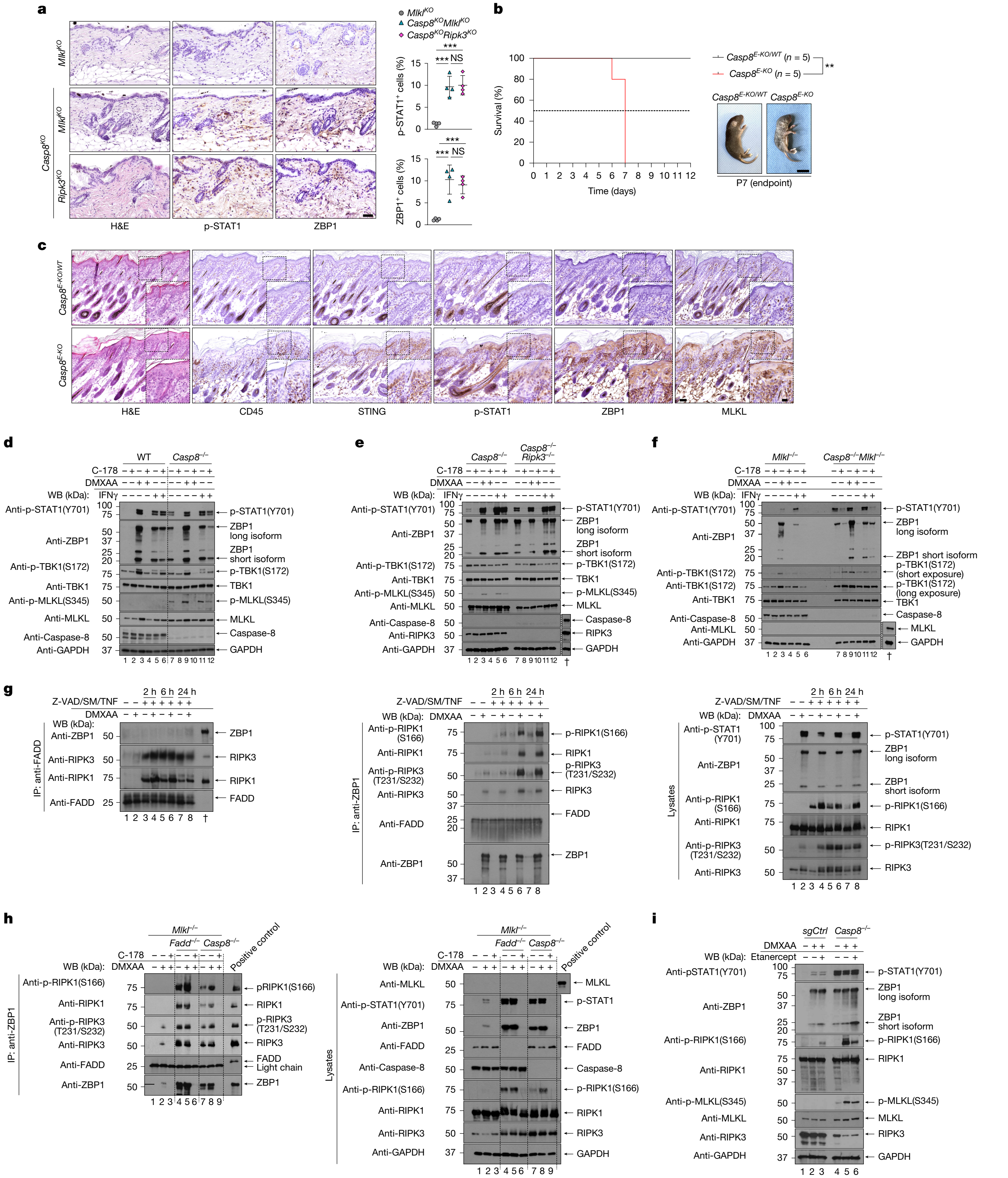

Fig. 1 | See next page for caption.

By doing so, we would establish a mechanistic link between necroptosis activation and the clinical manifestations of interferonopathies specifically driven by untoward activation of this upstream regulator.

STING orchestrates necroptosis through ZBP1

To address this question, we generated *Casp8*$^{E\text{-}KO}$ mice (Fig. 1b). As expected, these mice succumbed to keratinocyte necroptosis-driven

Fig. 1 | STING induces ZBP1–MLKL upregulation and ZBP1–RIPK1–RIPK3 complex formation. a, Representative images of consecutive skin sections from 12-week-old mice of the indicated genotypes stained with haematoxylin and eosin (H&E) and the indicated antibodies. $n = 4$ per group. Scale bar, 50 µm. Immunostaining quantification is shown. Data are mean ± s.e.m. Each dot represents one mouse. *P* values were calculated using one-way analysis of variance (ANOVA) followed by Tukey's multiple-comparison test. **b**, Kaplan–Meier survival graph of mice of the indicated genotypes with representative images. $n = 5$ per group. Scale bars, 1 cm. *P* values were calculated using two-sided Gehan–Breslow–Wilcoxon tests. **c**, Representative images of consecutive skin sections from P5 mice of the indicated genotypes stained with the indicated antibodies. $n = 5$ per group. Scale bars, 50 µm (main images) and 20 µm (insets). **d**–**f**, Immunoblot analysis with the indicated antibodies of lysates from immortalized WT and *Casp8*$^{-/-}$ (**d**), *Casp8*$^{-/-}$ and *Casp8*$^{-/-}$*Ripk3*$^{-/-}$ (**e**), and *Mlkl*$^{-/-}$ and *Casp8*$^{-/-}$*Mlkl*$^{-/-}$ (**f**) MEFs treated with C-178 (10 µM), DMXAA (20 µg ml^{-1}) and IFNγ (1,000 U ml^{-1}) for 48 h. The dagger symbols indicate lysates from WT (**e**) or *Casp8*$^{-/-}$ (**f**) MEFs. **g**, Lysates from immortalized *Mlkl*$^{-/-}$ MEFs pretreated with DMXAA overnight, followed by treatment with recombinant TNF (100 ng ml^{-1}), Z-VAD-FMK (20 µM) and BV6 (2 µM) for 48 h were immunoprecipitated with anti-FADD and anti-ZBP1 antibodies. An immunoblot analysis using the indicated antibodies is shown. SM, Smac mimetics. **h**, Lysates from immortalized *Mlkl*$^{-/-}$, *Fadd*$^{-/-}$*Mlkl*$^{-/-}$ and *Casp8*$^{-/-}$*Mlkl*$^{-/-}$ MEFs treated with DMXAA and/or C-178 for 48 h were immunoprecipitated with anti-ZBP1 antibodies. An immunoblot analysis using the indicated antibodies is shown. **i**, Immunoblot analysis with the indicated antibodies of lysates from *Casp8*$^{-/-}$ and sgCtrl MEFs treated with DMXAA and/or etanercept (50 µg ml^{-1}) for 48 h. Representative immunoblot data are shown from two independent experiments. $^{**}P \leq 0.01$, $^{***}P \leq 0.001$; NS, not significant ($P > 0.05$).

dermatitis (Fig. 1b and Extended Data Fig. 1a,b) and systemic inflammation (Extended Data Fig. 1c–f) by postnatal day 7 (P7)[1]. Transcriptional analysis of P5 *Casp8*$^{E\text{-}KO}$ lesion-containing skin using bulk 3′ mRNA sequencing (RNA-seq) identified the upregulation of 1,808 genes, including *Mlkl*, *Zbp1* and, notably, numerous other IFN-stimulated genes (ISGs) (Extended Data Fig. 1g,h). Functional grouping associated these genes with inflammation, cell death and IFN response pathways (Extended Data Fig. 1i–n). Unexpectedly, we observed that the IFN response signature was associated with innate immune signalling, cytosolic DNA sensing and, specifically, the STING signalling pathway (Extended Data Fig. 1i–n). Histological examination of *Casp8*$^{E\text{-}KO}$ skin at P5 confirmed an expected infiltration of CD45^{+} immune cells in the dermis in response to keratinocyte necroptosis; however, it also revealed elevated STING levels in epidermal cells that were causative of necroptotic cell death (Fig. 1c). Notably, these same cells also exhibited increased p-STAT1, MLKL and, decisively, de novo upregulation of ZBP1 (Fig. 1c). We therefore hypothesized that caspase-8 deficiency drives STING-mediated IFN response in keratinocytes that, in turn, was responsible for ZBP1 and MLKL upregulation, thereby priming these cells to necroptosis.

To test this hypothesis, we used caspase-8-deficient, caspase-8 and RIPK3-deficient and caspase-8 and MLKL-deficient MEFs. As previously reported[21], caspase-8 deficiency resulted in endogenous upregulation of ZBP1 that was accompanied by basal activation of p-STAT1, confirming activation of the IFN response (Fig. 1d–f). Notably, treatment of caspase-8-deficient MEFs with the mouse STING antagonist C-178 (ref. 25) completely abolished the activation of STAT1 and the increased expression of ZBP1 (Fig. 1d–f), thereby providing a functional link between STING activation induced by caspase-8 deficiency and IFN-response signalling. Consistently, treatment with the mouse STING agonist (DMXAA) or IFNγ enhanced the basal level of ZBP1, which was completely abolished or slightly reduced, respectively, by co-treatment with C-178 or co-deletion of *Sting1* (Fig. 1d–f and Extended Data Fig. 2a). Thus, these data suggest that the loss of caspase-8 leads to aberrant STING activation, which drives IFN-dependent transcriptional upregulation of both ZBP1 and MLKL and therefore necroptosis execution.

STING induces ZBP1–RIPK1–RIPK3 complex

As DMXAA treatment could also lead to STING-dependent phosphorylation of MLKL (Fig. 1d,e), we next investigated STING-mediated sensitization to necroptosis in WT, *Casp8*$^{-/-}$, *Ripk3*$^{-/-}$, *Mlkl*$^{-/-}$, *Casp8*$^{-/-}$*Ripk3*$^{-/-}$, *Casp8*$^{-/-}$*Mlkl*$^{-/-}$, *Zbp1*$^{-/-}$, *Casp8*$^{-/-}$ and *Zbp1*$^{-/-}$ MEFs, primary cells, and human HT29 and HaCaT cell lines. STING agonism (ADU-S100 for human cells) enhanced TNF-induced cell death, which was completely prevented in MLKL- or RIPK3-deficient or -inhibited cells, confirming that STING activation predominantly sensitizes cells to necroptosis (Extended Data Fig. 2b–f). However, *Zbp1*$^{-/-}$ cells still underwent TNF-induced necroptosis but were unresponsive to STING-activation-induced necroptosis (STAIN), indicating that ZBP1 is essential for enhanced cell death induction by STING (Extended Data Fig. 2b,e). STING-agonist-induced sensitization was further exacerbated by *Casp8* deletion alone (Extended Data Fig. 2c,e); however, co-treatment with the TNF blocker etanercept only partially inhibited this sensitization (Extended Data Fig. 2g). Complete inhibition was achieved only after *Zbp1* co-deletion, confirming that STING-induced necroptosis is dependent on ZBP1 expression (Extended Data Fig. 2h). Together, these results suggested also a STING-dependent TNFR1 activation alongside a TNFR1-independent pathway of STAIN through ZBP1.

Investigation of complex-II and necrosome formation revealed the formation of a FADD–RIPK1–RIPK3 complex after treatment with SM, Z-VAD and TNF, with only a modest increase in RIPK1 and RIPK3 recruitment after DMXAA co-treatment (Fig. 1g). Notably, despite input lysates showing significantly elevated levels of p-RIPK1 and p-RIPK3 after DMXAA co-treatment, this did not correspond to an increased recruitment of the activated RIP kinases to FADD. Similarly, although ZBP1 was upregulated in a STING-dependent manner, it was not detected in FADD pull-downs (Fig. 1g). Notably, endogenous ZBP1 pull-down demonstrated that STING-induced upregulation of ZBP1 resulted in the formation of a FADD-independent complex, which was also formed even after DMXAA treatment alone (Fig. 1g). Consistently, in *Casp8*$^{-/-}$*Mlkl*$^{-/-}$ and *Fadd*$^{-/-}$*Mlkl*$^{-/-}$ MEFs, we detected constitutive formation of the ZBP1–RIPK1–RIPK3 complex under basal conditions, correlating with sustained endogenous ZBP1 expression (Fig. 1h). After DMXAA treatment, both the recruitment and phosphorylation of RIPK1 and RIPK3 within this complex were markedly enhanced, confirming that STING activation amplifies ZBP1-driven complex formation and kinase activation even in the absence of FADD (Fig. 1h). Importantly, co-treatment with C-178 potently suppressed ZBP1 expression and consequently ZBP1-complex assembly (Fig. 1h). These findings establish that STING signalling is sufficient to drive the formation of a FADD- and TNFR1-independent ZBP1–RIPK1–RIPK3 platform, capable of initiating necroptosis in the absence of additional inflammatory inputs. Consistently, co-treatment with the TNF inhibitor etanercept did not diminish p-MLKL in caspase-8-deficient MEFs, and the levels of p-RIPK1 were only partially affected after co-treatment with DMXAA (Fig. 1i). Collectively, these results identify a pathway of STAIN mediated by a ZBP1–RIPK1–RIPK3-containing complex that forms independently of the TNF-induced FADD–RIPK1–RIPK3 complex-II, while also contributing to autocrine TNF release.

STAIN occurs independently of TNFR1

To investigate STAIN in vivo, we generated *Sting1*$^{E\text{-}KO}$ mice, which were viable and fertile (Supplementary Fig. 2), and *Casp8*$^{E\text{-}KO}$*Sting1*$^{E\text{-}KO}$ mice. Moreover, we generated *Casp8*$^{E\text{-}KO}$*Tnfr1*$^{-/-}$ mice, which, contrary to published reports[1], succumbed to lethal dermatitis at P10 (Fig. 2a). Notably, *Casp8*$^{E\text{-}KO}$*Sting1*$^{E\text{-}KO}$ mice survived until P11, demonstrating a clear similarity and a small, albeit significant, survival advantage to *Tnfr1* full-body co-deletion (Fig. 2a and Supplementary Fig. 2).

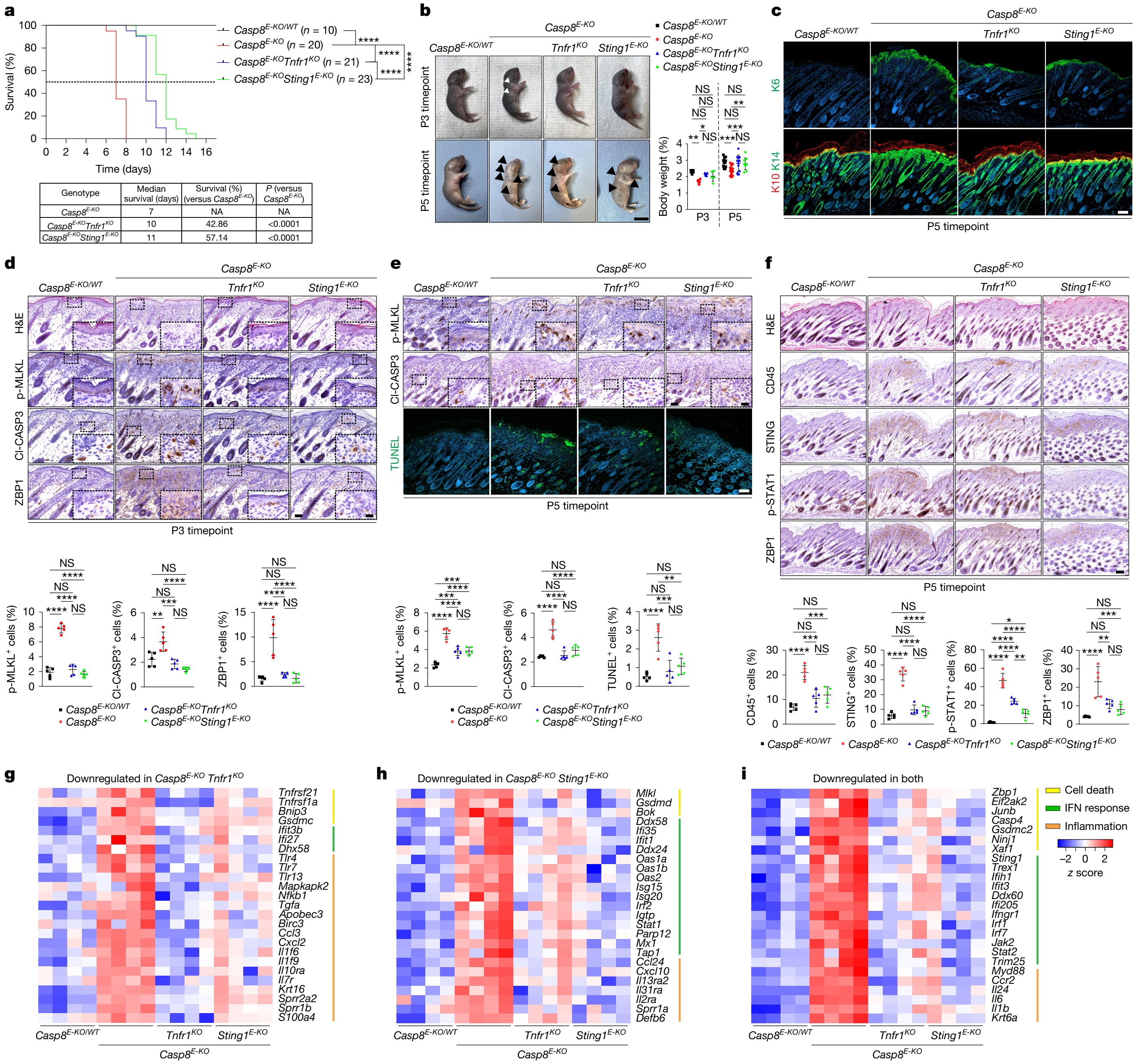

Fig. 2 | STING-induced necroptosis occurs independently of TNF–TNFR1 signalling. a, Kaplan–Meier survival curves of *n* mice of the indicated genotypes. The table shows the median survival and the relative survival advantage (%). *P* values were calculated using two-sided Gehan–Breslow–Wilcoxon tests. **b**, Representative images and quantification of the body weight of mice of the indicated genotypes at P3 ($n = 5$ per group) and P5 ($n = 15, 15, 12$ and 10 for the respective genotypes). The arrows indicate areas with lesions. Scale bar, 1 cm. **c**, Representative images of skin sections from P5 mice of the indicated genotypes ($n = 5$ per group) stained for K6 (Alexa Fluor 488, green), K10 (Alexa Fluor 594, red) and K14 (Alexa Fluor 488, green) and nuclei (DAPI, blue). Scale bar, 100 µm. **d**–**f**, Representative images of consecutive skin sections from mice of the indicated genotypes ($n = 5$ per group) at P3 stained with H&E and the indicated antibodies (**d**), at P5 stained with H&E, the indicated antibodies and TUNEL (fluorescein, green) (**e**) and at P5 stained with H&E and the indicated antibodies (**f**). Scale bars, 50 µm (main bright-field images; **d** and **e** (top and middle)), 20 µm (insets in **d** and **e**), 100 µm (confocal images; **e** (bottom)) and 100 µm (**f**). Immunostaining quantification is shown. **g**–**i**, Significantly downregulated genes in the skin from P5 *Casp8*$^{E\text{-}KO}$*Tnfr1*^{KO} (**g**), *Casp8*$^{E\text{-}KO}$*Sting1*$^{E\text{-}KO}$ (**h**) and both *Casp8*$^{E\text{-}KO}$*Tnfr1*^{KO} and *Casp8*$^{E\text{-}KO}$*Sting1*$^{E\text{-}KO}$ (**i**) mice compared with *Casp8*$^{E\text{-}KO}$ mice. Representative genes involved in cell death (yellow), IFN response (green) and inflammation (orange) categories are highlighted. Expression values were normalized using DESeq2, row-scaled and colour coded by intensity (red, high; blue, low). Differential expression analysis was performed using the Wald test as implemented in DESeq2, with *P* values adjusted for multiple testing using the Benjamini–Hochberg method ($P < 0.05$). In **b** and **d**–**f**, data are mean ± s.e.m.; *P* values were calculated using two-way ANOVA followed by Tukey's multiple-comparison test; $^{*}P \leq 0.05$, $^{****}P \leq 0.0001$.

Macroscopically, both *Casp8*$^{E\text{-}KO}$*Tnfr1*$^{-/-}$ and *Casp8*$^{E\text{-}KO}$*Sting1*$^{E\text{-}KO}$ mice maintained a normal body weight and exhibited no or significantly fewer lesions at P3 and P5, respectively, compared with *Casp8*$^{E\text{-}KO}$ mice (Fig. 2b). This was corroborated by a significant decrease in skin inflammation (keratin-6 (K6), K10, K14) (Fig. 2c) and by the rescue of organ inflammation (Extended Data Fig. 3a–c). Immunohistochemical analysis of P3 skin sections confirmed the observed delay in necroptosis activation, evidenced by diminished numbers of MLKL phosphorylated at Ser345 (p-MLKL(Ser345))[26], and ZBP1-positive epidermal keratinocytes, particularly in the skin of *Casp8*$^{E-KO}$*Sting1*$^{E-KO}$ mice (Fig. 2d). Similarly, skin sections from P5 mice showed clear reductions in p-MLKL(Ser345)[26], cleaved CASP3 (Cl-CASP3) and TUNEL staining in both genotypes (Fig. 2e). Loss of STING in keratinocytes coincided with the absence of p-STAT1 and ZBP1 in the epidermis, whereas, in *Casp8*$^{E-KO}$*Tnfr1*$^{-/-}$ mice, staining for these markers was partially reduced in both stromal and immune cells (Fig. 2f). This indicated a tissue-compartment-specific difference in early necroptosis inhibition between keratinocyte-specific STING and constitutive TNFR1 absence.

We next assessed the following three manifestations of inflammation in *Casp8*$^{E-KO}$*Tnfr1*$^{-/-}$ and *Casp8*$^{E-KO}$*Sting1*$^{E-KO}$ mice: (1) immune cell infiltration; (2) cytokine profiles from whole skin homogenates; and (3) differential gene expression using quantitative PCR with reverse transcription (RT–qPCR) and RNA-seq. No major differences were observed in immune cell recruitment with the exception of an enhanced infiltration of CD3^{+} T cells in both genotypes, albeit more significantly after *Sting1* co-deletion in keratinocytes, and a significant reduction in F4/80^{+} macrophages in *Casp8*$^{E-KO}$*Tnfr1*$^{-/-}$ mice (Extended Data Fig. 3d). The levels of most cytokines were similarly lower in skin lysates from both genotypes with only a few showing significant differences in downregulation (that is, IL-10, CXCL13 and M-CSF) (Extended Data Fig. 3e,f). Importantly, TNF levels were similarly downregulated, indicating analogous inhibition of immune cell infiltration and overall inflammatory response (Extended Data Fig. 3e,f). Notably, RT–qPCR analysis revealed that IFNγ and IFNβ were significantly attenuated by keratinocyte-specific STING deficiency, implying that STING in these cells drives the intrinsic cytokine expression needed for immune cell infiltration through IFN-response activation (Extended Data Fig. 3g). Comparative RNA-seq analysis of skin tissue from *Casp8*$^{E-KO}$, *Casp8*$^{E-KO}$*Tnfr1*$^{-/-}$ and *Casp8*$^{E-KO}$*Sting1*$^{E-KO}$ mice revealed that genes specifically downregulated after constitutive TNFR1 absence were predominantly involved in TNF-, TLR- and NF-κB-driven inflammatory pathways (Fig. 2g). By contrast, keratinocyte-specific deletion of *Sting1* resulted in specific downregulation of many ISGs, as well as *Mlkl* and *Gsdmd* (Fig. 2h). Furthermore, genes such as *Eif2ak2*, *Gsdmc*, *Ninj1*, *Il6* and *Il1b* were significantly downregulated in both models, suggesting their involvement in amplifying inflammatory cell death rather than initiating disease-causing necroptosis (Fig. 2i). Importantly, *Zbp1* was downregulated in both *Casp8*$^{E-KO}$*Tnfr1*$^{-/-}$ and *Casp8*$^{E-KO}$*Sting1*$^{E-KO}$ mice (Fig. 2i and Extended Data Fig. 3g), suggesting that, while *Sting1* deletion in keratinocytes contributes to intrinsic *Zbp1* levels, a substantial portion of *Zbp1* expression is keratinocyte independent, probably mediated by immune cell infiltration. Moreover, the ability of STING to initiate IFN response, transcriptionally upregulate ZBP1 and, notably, also MLKL (Fig. 2h,i and Extended Data Fig. 3g) underpins its central role in sustaining necroptosis initiation and propagation by providing essential components required for necroptosis execution.

To further elucidate the complementary, independent roles of TNFR1 and STING in *Casp8*$^{E-KO}$-mediated necroptosis and their functional interplay with ZBP1, we generated *Casp8*$^{E-KO}$*Tnfr1*$^{-/-}$*Zbp1*$^{-/-}$ and *Casp8*$^{E-KO}$*Tnfr1*$^{-/-}$*Sting1*$^{E-KO}$ mice. Notably, heterozygous deletion of *Zbp1* or *Sting1* prevented equally the postnatal lethality observed in *Casp8*$^{E-KO}$*Tnfr1*$^{-/-}$ mice (Fig. 3a). These mice reached the end-point criteria at around 4 weeks of age owing to severe dermatitis (Fig. 3a–c), accompanied by reduced body weight, multiorgan inflammation and haematological abnormalities (Fig. 3d,e and Extended Data Fig. 4a–d). Notably, homozygous constitutive co-deletion of *Zbp1* or keratinocyte-specific co-deletion of *Sting1* in *Casp8*$^{E-KO}$*Tnfr1*$^{-/-}$ mice rescued all of the pathological phenotypes observed in *Casp8*$^{E-KO}$*Tnfr1*$^{-/-}$ mice. Both *Casp8*$^{E-KO}$*Tnfr1*$^{-/-}$*Zbp1*$^{-/-}$ and *Casp8*$^{E-KO}$*Tnfr1*$^{-/-}$*Sting1*$^{E-KO}$ mice appeared completely normal and were indistinguishable from control mice up until 4 weeks of age (Fig. 3a–e and Extended Data Fig. 4a–d).

This result was further corroborated by the histological analysis of the skin of both *Casp8*$^{E-KO}$*Tnfr1*$^{-/-}$*Zbp1*$^{-/-}$ or *Casp8*$^{E-KO}$*Tnfr1*$^{-/-}$*Sting1*$^{E-KO}$ mice at 4 weeks of age, which did not reveal any signs of dermatitis (Fig. 3f). By contrast, severe epidermal thickening could be readily observed in both *Casp8*$^{E-KO}$*Tnfr1*$^{-/-}$*Zbp1*$^{-/+}$ and *Casp8*$^{E-KO}$*Tnfr1*$^{-/-}$*Sting1*$^{E-KO/+}$ mice. These mice displayed elevated immune cell infiltration, increased levels of p-STAT1 and ZBP1 as well as p-MLKL(Ser345)-positive cells in the epidermis. As expected, Cl-CASP3 was also detected due to immune cell infiltration, leading to secondary apoptosis (Fig. 3f).

Constitutive absence of ZBP1 completely rescued the lethal dermatitis observed in *Casp8*$^{E-KO}$*Tnfr1*$^{-/-}$ mice through adulthood (Extended Data Fig. 4e,f). Yet, keratinocyte-specific absence of STING significantly extended the survival, with approximately 50% of *Casp8*$^{E-KO}$*Tnfr1*$^{-/-}$*Sting1*$^{E-KO}$ mice surviving at least up to 14 weeks (Fig. 3a). *Casp8*$^{E-KO}$*Tnfr1*$^{-/-}$*Sting1*$^{E-KO}$ mice at 12–14 weeks of age showed epidermal thickening, immune cell infiltration and elevated levels of ZBP1, predominantly located in the dermis, accompanied by increased levels of Cl-CASP3 (Extended Data Fig. 4f). These mice also exhibited haematological abnormalities and systemic inflammation (Extended Data Fig. 4g and Supplementary Fig. 3). Notably, a few cells in the epidermis of *Casp8*$^{E-KO}$*Tnfr1*$^{-/-}$*Sting1*$^{E-KO}$ mice remained positive for ZBP1 staining (Extended Data Fig. 4f), probably owing to incomplete STING depletion from epidermal keratinocyte.

Collectively, the results presented so far identify a role of aberrant STING activation as a driver of a transcriptional programme responsible for the upregulation of ZBP1 and MLKL in addition to that of many other ISGs. This is both necessary and sufficient to trigger lethal inflammatory disease caused by ZBP1–MLKL-dependent but TNFR1–FADD-independent necroptosis in a cell-intrinsic manner.

Compartmental STING shapes necroptosis

Next, we sought to determine whether constitutive co-deletion of *Sting1* would mimic the protective benefits observed after ZBP1 co-deletion in *Casp8*$^{E-KO}$*Tnfr1*$^{-/-}$ mice. To this end, we first generated *Casp8*$^{E-KO}$*Sting1*$^{-/-}$ mice which, notably, survived substantially longer than *Casp8*$^{E-KO}$*Tnfr1*$^{-/-}$ mice (Fig. 4a). These mice displayed delayed onset and reduced severity of skin pathology, as evidence by the levels of CD45^{+} cells, p-STAT1, ZBP1 and p-MLKL(S345), which were indistinguishable from those of healthy controls at P5 (Fig. 4b and Supplementary Fig. 4). Systemically, by P5, *Casp8*$^{E-KO}$*Sting1*$^{-/-}$ mice, similarly to *Casp8*$^{E-KO}$*Tnfr1*$^{-/-}$ mice, showed no signs of inflammation (Extended Data Fig. 5a–c). Compared with *Casp8*$^{E-KO}$*Sting1*$^{E-KO}$ mice, *Casp8*$^{E-KO}$*Sting1*$^{-/-}$ mice not only survived longer (Fig. 4c) but, by P11 (the endpoint of *Casp8*$^{E-KO}$*Sting1*$^{E-KO}$ mice), they also showed no significant epidermal thickening, a marked reduction in p-MLKL(Ser345) levels in the epidermis, early infiltration of ZBP1-expressing CD45^{+} cells, probably driven by TNF-mediated immune cell recruitment (Fig. 4d and Supplementary Fig. 4), and reduced systemic inflammation (Extended Data Fig. 5d,e). To determine whether the observed prolonged survival was solely due to suppression of ZBP1-driven necroptosis, we also generated *Casp8*$^{E-KO}$*Zbp1*$^{-/-}$ mice, which we predicted would phenocopy the survival of *Casp8*$^{E-KO}$*Sting1*$^{-/-}$ mice. Unexpectedly, these mice developed severe, lethal dermatitis and systemic inflammation indistinguishable in timing and severity from *Casp8*$^{E-KO}$ mice (Fig. 4a,b and Extended Data Fig. 5a–c), underscoring that ZBP1 loss alone was insufficient to delay disease onset, progressions and severity. As *Casp8*$^{E-KO}$*Tnfr1*$^{-/-}$*Zbp1*$^{-/-}$ mice exhibited full rescue with complete absence of dermatitis and systemic inflammation (Fig. 3 and Extended Data Fig. 4), we concluded that (1) TNF–TNFR1 acts as the initial necroptosis checkpoint that must be bypassed to engage into ZBP1-mediated necroptosis; (2) ZBP1-mediated necroptosis acts as a second, independent, necroptotic checkpoint; (3) given the survival of the *Casp8*$^{E-KO}$*Sting1*$^{-/-}$ mice encompassing and surpassing the survival of the *Casp8*$^{E-KO}$*Tnfr1*$^{-/-}$ mice (Fig. 4e), STING signalling not only licenses the ZBP1 necroptotic checkpoint but also partially contributes to TNF–TNFR1-driven cell death and inflammation, probably through autocrine TNF production and

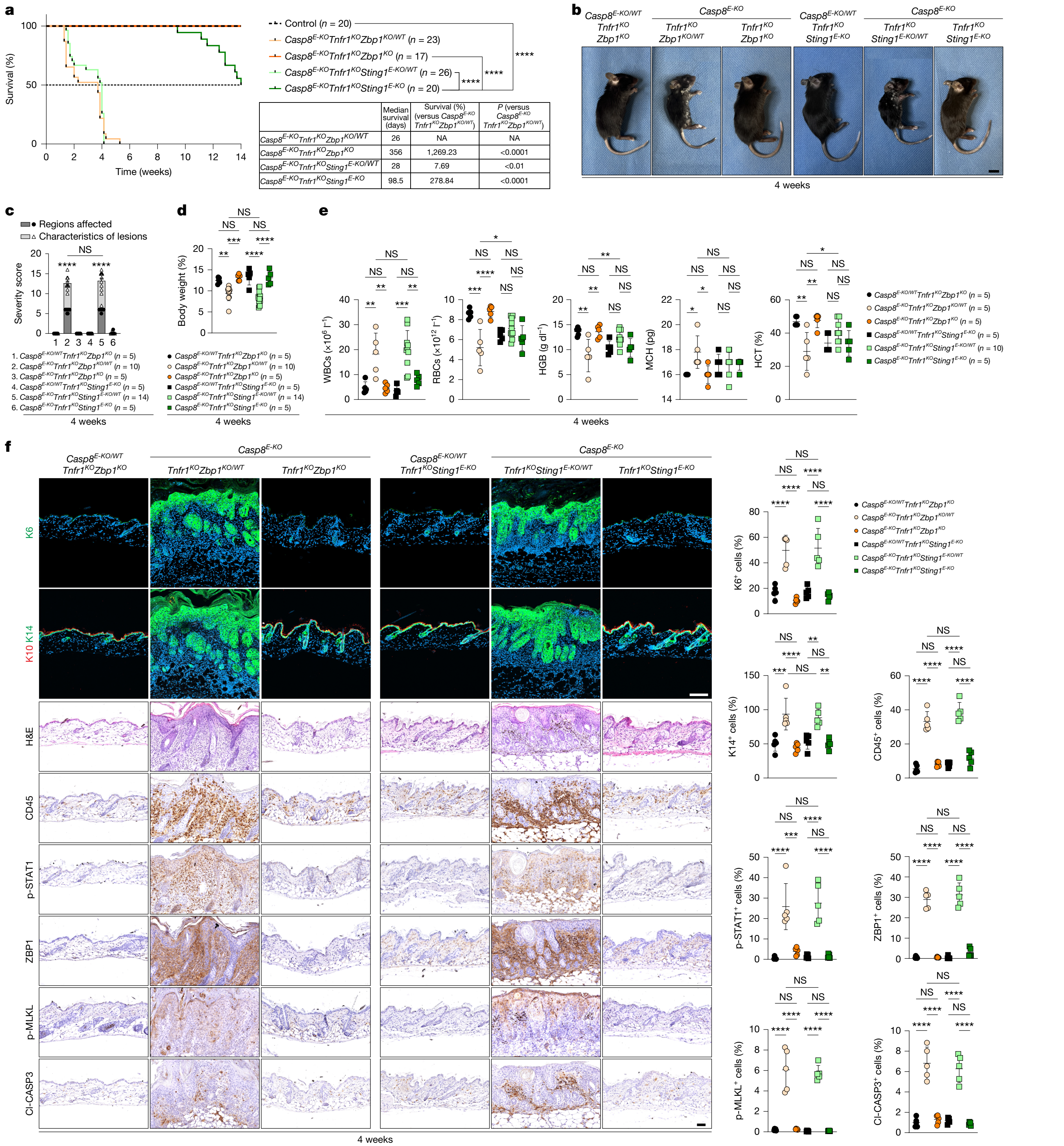

	Median survival (days)	Survival (%) (versus $Casp8^{E\text{-}KO}Tnfr1^{KO}Zbp1^{KO/WT}$)	P (versus $Casp8^{E\text{-}KO}Tnfr1^{KO}Zbp1^{KO/WT}$)
$Casp8^{E\text{-}KO}Tnfr1^{KO}Zbp1^{KO/WT}$	26	NA	NA
$Casp8^{E\text{-}KO}Tnfr1^{KO}Zbp1^{KO}$	356	1,269.23	<0.0001
$Casp8^{E\text{-}KO}Tnfr1^{KO}Sting1^{E\text{-}KO/WT}$	28	7.69	<0.01
$Casp8^{E\text{-}KO}Tnfr1^{KO}Sting1^{E\text{-}KO}$	98.5	278.84	<0.0001

Fig. 3 | Keratinocyte STING licensing of ZBP1 mediates TNF-independent necroptosis. a, Kaplan–Meier survival curves of *n* mice of the indicated genotypes. The table shows the median survival and the relative survival advantage (%). *P* values were calculated using two-sided Gehan–Breslow–Wilcoxon tests. NA, not applicable. **b**–**e**, Representative images (**b**) and quantification of the dermatitis severity score (**c**), body weight (**d**) and white blood cell (WBC), red blood cell (RBC), haemoglobin (HGB), mean corpuscular haemoglobin (MCH) and haematocrit (HCT) values in the peripheral blood (**e**) of 4-week-old mice of the indicated genotypes. *n* values are indicated. Control mice included age-matched $Casp8^{E\text{-}KO/WT}Tnfr1^{KO}Zbp1^{KO}$ and $Casp8^{E\text{-}KO/WT}Tnfr1^{KO}Sting1^{E\text{-}KO}$ littermates. Scale bar, 1 cm (**b**). **f**, Representative images of consecutive skin sections from 4-week-old mice of the indicated genotypes stained for K6 (Alexa Fluor 488, green), K10 (Alexa Fluor 594, red), K14 (Alexa Fluor 488, green), nuclei (DAPI, blue), H&E and the indicated antibodies (*n* = 5 per group). Scale bars, 50 µm (bright-field images, bottom 6 rows) and 100 µm (confocal images, top two rows). Immunostaining quantification is shown. For **c**–**f**, data are mean ± s.e.m.; each dot represents one mouse; *P* values were calculated using two-way ANOVA followed by Tukey's multiple-comparison test; *$P \leq 0.05$, **$P \leq 0.01$, ***$P \leq 0.001$, ****$P \leq 0.0001$; NS, not significant ($P > 0.05$).

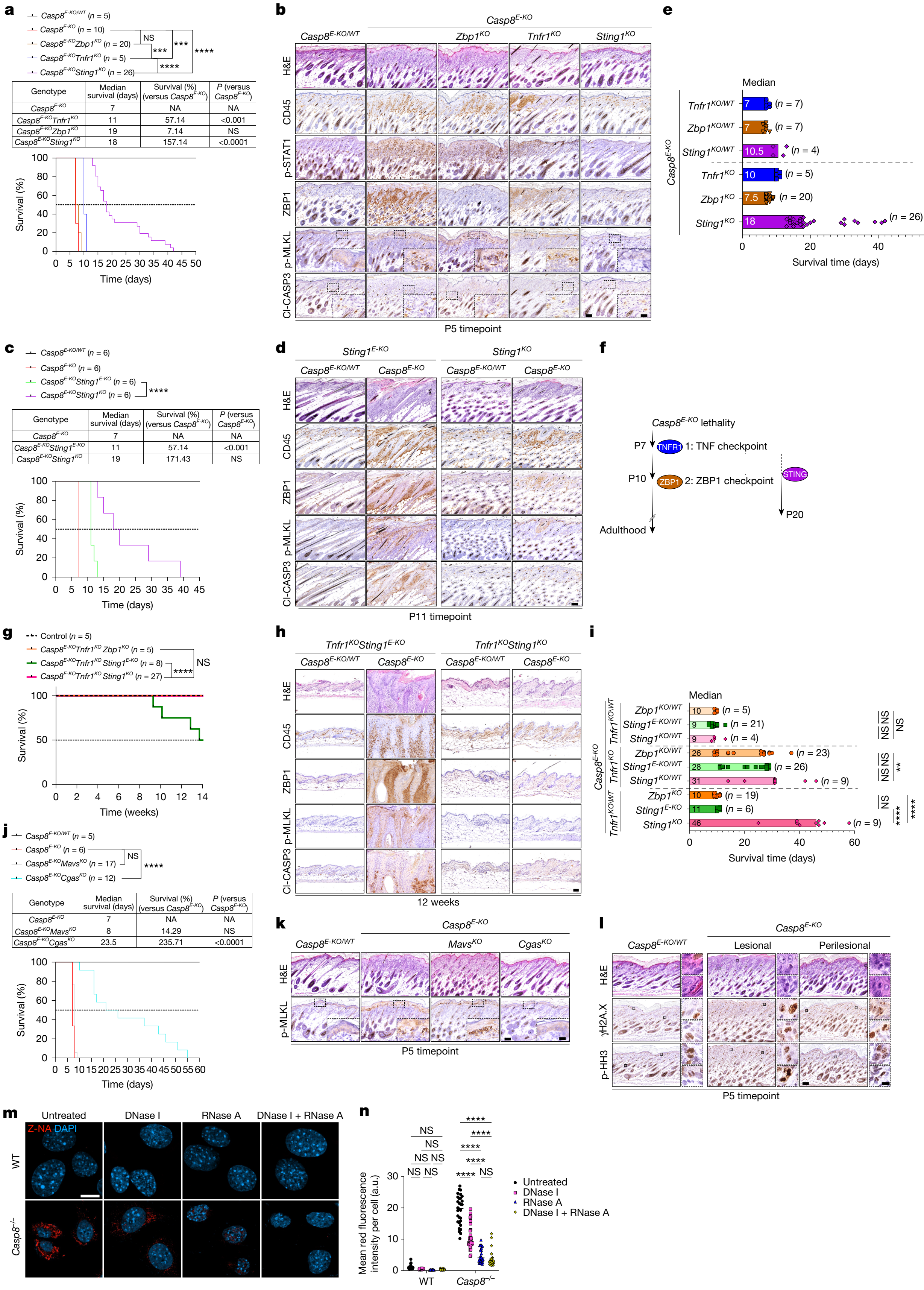

Fig. 4 | See next page for caption.

Fig. 4 | STING regulates necroptosis checkpoints through CGAS–gDNA and ZBP1/Z-NA sensing. a–**d**, Kaplan–Meier survival curves of *n* mice of the indicated genotypes. **a**,**c**, The median survival and the relative survival advantage (%). **b**,**d**, Representative images of consecutive skin sections from P5 (**b**) or P11 (**d**) mice of the indicated genotypes stained with the indicated antibodies. $n = 5$ (**b**) and $n = 3$ (**d**) per group. For **b** and **d**, scale bars, 100 μm (main images) and 20 μm (insets). **e**, The median survival of *n* mice of the indicated genotypes. **f**, Graphical representation of the TNFR1 and ZBP1 distinct necroptotic checkpoints and their dependence on STING. **g**, Kaplan–Meier survival curves of *n* mice of the indicated genotypes. Control mice included age-matched $Casp8^{E\text{-}KO/WT}Tnfr1^{KO}Zbp1^{KO}$, $Casp8^{E\text{-}KO/WT}Tnfr1^{KO}Sting1^{E\text{-}KO}$ and $Casp8^{E\text{-}KO/WT}Tnfr1^{KO}Sting1^{KO}$ littermates. **h**, Representative images of consecutive skin sections from 12-week-old mice of the indicated genotypes stained with the indicated antibodies. $n = 3$ per group. Scale bar, 50 μm. **i**, The median survival of *n* mice of the indicated genotypes. **j**, Kaplan–Meier survival curves of *n* mice of the indicated genotypes. The table shows the median survival and the relative survival advantage (%). **k**,**l**, Representative images of consecutive skin sections from P5 mice of the indicated genotypes stained as indicated. $n = 3$ (**k**) and $n = 5$ (**l**). For **k** and **l**, scale bars, 100 μm (main images) and 20 μm or 10 μm (insets). **m**,**n**, Representative confocal images of the indicated MEFs stained for Z-NA (Alexa Fluor 594, red) and nuclei (DAPI, blue) under basal conditions or after treatment with DNase I (25 U ml^{-1}) and/or RNase A (1 mg ml^{-1}) (**m**) and quantification of mean Z-NA (red) fluorescence intensity (**n**). Data are mean ± s.e.m. *P* values were calculated using two-way ANOVA followed by Tukey's multiple-comparisons test. For **a**, **c**, **e**, **g**, **i** and **j**, *P* values were calculated using two-sided Gehan–Breslow–Wilcoxon tests; each dot in the graphs represents one mouse; $^{**}P \le 0.01$, $^{***}P \le 0.001$, $^{****}P \le 0.0001$; NS, not significant ($P > 0.05$).

NF-κB pathway engagement (Fig. 4f). Consistently, transcriptional upregulation of several inflammatory genes, including *Tnf*, *Zbp1* and *Mlkl*, was completely suppressed in $Casp8^{E\text{-}KO}Sting1^{-/-}$ mice, and RNA-seq analysis revealed a similar downregulation for NF-kB signature genes compared with in $Casp8^{E\text{-}KO}Tnfr1^{-/-}$ mice (Extended Data Fig. 5f,g). This confirmed the requirement for STAIN, as well as a functional overlap between STING and TNFR1 in regulating NF-kB-driven inflammatory programme in the absence of caspase-8. Thus, the extended survival observed in $Casp8^{E\text{-}KO}Sting1^{-/-}$ mice compared with $Casp8^{E\text{-}KO}Tnfr1^{-/-}$ mice is best explained by STING's dual contribution to both necroptotic arms. Collectively, this establishes the STING axis as an independent and genetically separable checkpoint downstream of caspase-8 loss, which also overlaps with the TNFR1-dependent pathway to amplify inflammatory necroptosis (Fig. 4f).

To fully disentangle the functional overlap between STING and ZBP1, we generated $Casp8^{E\text{-}KO}Tnfr1^{-/-}Sting1^{-/-}$ mice. Notably, these mice remained viable, healthy and phenotypically indistinguishable from control littermates and $Casp8^{E\text{-}KO}Tnfr1^{-/-}Zbp1^{-/-}$ mice (Fig. 4g). At 12 weeks of age (shortly before $Casp8^{E\text{-}KO}Tnfr1^{-/-}Sting1^{E\text{-}KO}$ mice reach their survival endpoint), $Casp8^{E\text{-}KO}Tnfr1^{-/-}Sting1^{-/-}$ mice showed no signs of lethal dermatitis (Fig. 4h, Extended Data Fig. 5h and Supplementary Fig. 4). Moreover, whereas $Casp8^{E\text{-}KO}Tnfr1^{-/-}Sting1^{E\text{-}KO}$ mice at 12 weeks of age revealed severe systemic disease, $Casp8^{E\text{-}KO}Tnfr1^{-/-}Sting1^{-/-}$ mice appeared indistinguishable from the littermate controls (Extended Data Fig. 5i–k and Supplementary Fig. 4). Histological examination of skin sections showed suppression of lethal dermatitis as evidenced by normalized epidermal thickness, loss of p-MLKL and ZBP1 expression and CD45^{+}, and Cl-CASP3-positive cells (Fig. 4h). This marked phenotypic divergence confirms that the residual necroptosis observed in $Casp8^{E\text{-}KO}Tnfr1^{-/-}Sting1^{E\text{-}KO}$ mice was possibly due to incomplete *Sting1* deletion. Although STING expression in non-keratinocyte compartments might also have a pivotal role in sustaining and propagating systemic necro-inflammation, STING activation in keratinocytes is essential to initiate ZBP1-mediated necroptosis and early inflammation. Gene dosage analysis revealed that the survival of $Casp8^{E\text{-}KO}Tnfr1^{-/WT}$ mice was significantly prolonged after homozygous constitutive co-deletion of *Sting1*, particularly when compared to homozygous co-deletion of *Zbp1* or keratinocyte-specific *Sting1* deletion (Fig. 4i). This confirms a role of STING also in regulating TNFR1-induced necroptosis and cell-extrinsic necroptotic inflammation. This dual role of STING, as both a trigger and amplifier of necroptosis, highlights its essential and non-redundant function in TNFR1-independent, ZBP1-mediated pathology.

gDNA activates CGAS–STING in $Casp8^{E\text{-}KO}$

To determine the source of STING activation downstream of *Casp8* loss, we generated $Casp8^{E\text{-}KO}Cgas^{-/-}$ mice. *Cgas* co-deletion fully phenocopied the protection observed in $Casp8^{E\text{-}KO}Sting1^{-/-}$ mice, as evidence by the survival analysis and comparable suppression of tissue inflammation through histological analysis at P5 (Fig. 4j,k and Supplementary Fig. 4). To exclude alternative nucleic-acid-sensing pathways, we also generated $Casp8^{E\text{-}KO}Mavs^{-/-}$ mice. *Mavs* deletion did not rescue lethality or reduce tissue pathology (Fig. 4j,k and Supplementary Fig. 4). These results indicate that activation of STING after *Casp8* loss is entirely dependent on CGAS, placing cytosolic DNA sensing upstream of the type I IFN response signature observed in $Casp8^{E\text{-}KO}$ mice.

To identify the origin of the DNA species activating CGAS, we first examined the potential role of mitochondrial DNA (mtDNA), as a CGAS agonist[27]. Immunofluorescence staining in $Casp8^{-/-}$, $Casp8^{-/-}Mlkl^{-/-}$ and $Casp8^{-/-}Ripk3^{-/-}$ MEFs revealed cytosolic accumulation of DNA, but no detectable co-localization with the mitochondrial transcription factor A (TFAM) (Extended Data Fig. 6a). mtDNA accumulation was excluded as treatment with 2′,3′-dideoxycytidine (ddC) or IMT1B showed incomplete reduction in DNA staining (Extended Data Fig. 6b), of which the successful depletion was confirmed by RT–qPCR (Extended Data Fig. 6c). By contrast, there was no reduction in ISG transcription (including *Zbp1*) (Extended Data Fig. 6d). These results were further corroborated at the protein level—ZBP1 expression and p-STAT1 levels remained unchanged and could be completely abrogated only after treatment with the STING antagonist C-178 (Extended Data Fig. 6e).

Previous research showed that caspase-8 deficiency induces chromosomal instability[28] and DNA damage[29], which can result in nuclear DNA leakage into the cytosol, known to be a potent activator of CGAS. In agreement with this, we observed that skin obtained from $Casp8^{E\text{-}KO}$, $Casp8^{-/-}Ripk3^{-/-}$, $Casp8^{-/-}Mlkl^{-/-}$ as well as $Casp8^{E\text{-}KO}Tnfr1^{-/-}Sting1^{-/-}$ and $Casp8^{E\text{-}KO}Tnfr1^{-/-}Zbp1^{-/-}$ mice exhibited mitotic abnormalities, with many p-HH3-positive cells displaying aberrant chromosome segregation and elevated γH2A.X foci (Fig. 4l and Extended Data Fig. 6f). These findings suggest that caspase-8 deficiency compromises genome integrity independently of necroptosis, as previously reported[28–31], supporting a model in which genomic DNA released due to caspase-8-loss-induced genome instability acts as a primary trigger of CGAS–STING activation in this context.

Z-NAs and ZBP1 are amplified by STING

To understand how ZBP1 is activated after its upregulation by STING, we used $Casp8^{-/-}$, $Casp8^{-/-}Mlkl^{-/-}$ and $Casp8^{-/-}Ripk3^{-/-}$ MEFs and performed immunofluorescence staining to specifically detect Z-form nucleic acids (Z-NAs)[22]. Our results revealed specific cytosolic accumulation of both Z-DNA and Z-RNA in these cells, with the Z-NA signal being completely abolished only after treatment with both DNase I and RNase A, confirming the presence of both nucleic acid species in the Z-conformation (Fig. 4m,n and Extended Data Fig. 7a,b).

We next assessed the co-localization between ZBP1 and Z-NAs. Clear spatial overlap was observed, indicating physical proximity and probable interaction (Extended Data Fig. 7c–e). Importantly, treatment with the STING agonist DMXAA further enhanced the Z-NA signal intensity, suggesting that STING activation promotes the accumulation and/or stabilization of Z-NAs, the natural ligands of ZBP1 (Extended Data Fig. 7c–e). Given the consistent co-localization with Z-NA under conditions of STING agonism, we conclude that STING enhances ZBP1 activation through increased generation or exposure to Z-NAs. This correlates well with our biochemical findings indicating that STING activation leads to increased recruitment and phosphorylation of RIPK1 and RIPK3 in ZBP1 immunoprecipitates, further supporting functional activation of ZBP1 in this context.

STAIN is functionally linked to SAVI

In the genetic model we studied so far, aberrant STING activation is caused by caspase-8 deficiency. Yet, constitutive STING signalling can also result from gain-of-function (GOF) mutations in *STING1* (refs. 32,33) independently of caspase-8, as evident in patients with SAVI. SAVI is an autosomal-dominant genetic interferonopathy characterized by early-onset systemic inflammation, chronic anaemia, cutaneous lesions, polyarthritis-like symptoms and interstitial lung disease. Conventional immunosuppressive treatments, anti-malarials, TNF inhibitors and B-cell-depleting biologics have provided limited to no therapeutic effect[34,35]. Recently, new regimens have included JAK1/2 inhibitors (such as ruxolitinib); however, their efficacy has yielded only a temporary reduction in symptoms[32,36].

Considering the identification of aberrant STAIN as a critical driver of lethal inflammatory necroptosis, we hypothesized that STAIN could contribute or even cause the clinical manifestation of SAVI. We therefore examined a set of longitudinal samples obtained from paediatric patients affected by SAVI[37]. For each patient, samples were collected before and after conventional treatment, which included ruxolitinib for an average duration of 18 months (Extended Data Fig. 8a). Assessment of cell-death-involved inflammatory cytokines in the plasma of these patients (Supplementary Table 1) revealed that nearly all of the assessed cytokines were elevated in all samples, independently of the treatment and duration, suggesting a potential contribution of cell-death-induced inflammation to clinical manifestations and persistence of SAVI (Extended Data Fig. 8b and Supplementary Fig. 5). This analysis confirmed known cytokines[38] and identified additional top-ranked candidates (IL-21, CXCL1, IL-1β, IFNα and CD40L) as potential circulating biomarkers (Extended Data Fig. 8b). RNA-seq analysis in whole blood cells obtained from plasma-matching patients samples revealed a significant upregulation of genes involved in both type I and/or type II IFN responses especially in 11 out of 15 samples, which included almost all post-treatment samples (Fig. 5a). Further transcriptional and functional investigation confirmed sustained IFN response activation and, notably, the differential upregulation of *MLKL* and *ZBP1* (Fig. 5b). We further functionally grouped these genes and categorized them into three categories—cell death, IFN response and inflammation (Extended Data Fig. 8c and Supplementary Fig. 6)—and evaluated the levels of executioners, inhibitors and modulators of all functionally upregulated cell death modalities (Extended Data Fig. 8d–f). By doing so, we excluded transcriptional priming of mitochondrial apoptosis due to high expression of inhibitors of apoptosis. Pyroptosis appeared to be predominantly executed in patient 2. Cell death pathways triggered by TNF or other death ligands did not appear to be significantly transcriptionally upregulated or were accompanied by concomitant upregulation of checkpoint genes such as cIAPs and the linear ubiquitin chain assembly complex. Importantly, *RIPK3*, *MLKL* and *ZBP1* were consistently overexpressed, indicative of priming towards necroptosis execution in all patient samples (Extended Data Fig. 8d–f). This was confirmed by RT–qPCR analysis, in which the expression of a small panel of genes used to classify interferonopathies clinically and its fluctuations before and after treatment mirrored the expression levels of *MLKL*, *ZBP1*, and the inflammatory chemokines *CXCL1* and *CXCL8* (ref. 39) (Supplementary Fig. 7). This suggested a functional correlation between STING-mediated IFN response, the transcriptional expression of *ZBP1* and *MLKL*, and the cell-autonomous cytokines known to be released by necroptosis.

Importantly, transcriptomic comparison of upregulated pathways in the *Casp8*$^{E\text{-}KO}$ mice (versus the control) with the pathways upregulated in IFN^{high} SAVI samples revealed a significant functional overlap of 73% of all pathways (Fig. 5c). Within these, we identified a set of key genes overlapping between *Casp8*$^{E\text{-}KO}$ mice and IFN^{high} SAVI samples (Supplementary Table 2), suggesting that these pathways and genes are descriptive of an established necroptotic program within the SAVI transcriptome and vice versa of the newly characterized STING-driven necroptosis.

STAIN leads to lethality in SAVI mice

We next turned to the established preclinical SAVI mouse model bearing the heterozygous *Sting1*^{N153S} GOF mutation (hereafter *Sting1*^{N153S} mice), which closely phenocopies human SAVI, faithfully recapitulating key clinical features of this disease[40] (Extended Data Fig. 9a–f).

Histological analysis of skin, lung, thymus and spleen collected from *Sting1*^{N153S} mice, presenting the complete clinical manifestations of SAVI, revealed robust ZBP1 upregulation (Extended Data Fig. 9g). Importantly, necroptosis, detected through p-MLKL(Ser345) staining, was restricted to the skin, while the lung and thymus displayed both p-MLKL(Ser345)- and Cl-CASP3-positive staining (Extended Data Fig. 9g). Spleen exhibited strong Cl-CASP3 staining only, indicative of dominant apoptosis in that compartment at the endpoint (Extended Data Fig. 9g). To determine the role of necroptosis in disease manifestation and pathogenesis and confirm preclinically the translational relevance of our findings, we generated *Sting1*^{N153S}*Ripk3*$^{-/-}$ mice. These mice showed no signs of disease and exhibited unaffected survival at least up until 35 weeks of age, which was the median survival of the *Sting1*^{N153S} mice (Fig. 5d,e). Histological analysis of 35-week-old *Sting1*^{N153S}*Ripk3*$^{-/-}$ mice showed a complete absence of p-MLKL(Ser345) staining with a clear rescue in skin, lung, thymus and splenic inflammation and architecture, providing conclusive evidence for the role of STAIN in the inflammatory manifestations of SAVI (Fig. 5f).

The complex multiorgan inflammation characteristic of the SAVI mice is known to derive from STING-GOF-induced triggering of pathogenic early-onset immune dysregulation (6–8 weeks)[41,42]. High-resolution immunophenotyping of the lung, spleen and thymus revealed that co-deletion of *Ripk3* significantly ameliorates the immune abnormalities induced by STING GOF (Fig. 5g–i and Extended Data Fig. 10). In the thymus, *Sting1*^{N153S}*Ripk3*$^{-/-}$ mice showed recovery of double-negative thymocytes (Extended Data Fig. 10b). $CD8^+$ and double-positive (DP; $CD4^+CD8^+$) thymocytes, along with their activation status ($CD69^+$), were significantly normalized, pointing to a contributing (but not complete) role for necroptosis in thymic T cell attrition (Fig. 5g and Extended Data Fig. 10b). In the lung, where SAVI pathology often manifests with both inflammation and fibrosis, *Ripk3* co-deletion mitigated the expansion of inflammatory monocytes and macrophages, antigen-presenting dendritic cells and granulocytes (Fig. 5h and Extended Data Fig. 10d). Although T cell restoration was more modest, the overall pattern again indicated a broad rescue of immune homeostasis. In the spleen, RIPK3 co-deficiency led to marked improvements in both the lymphoid and myeloid compartments. *Sting1*^{N153S} mice exhibited severe T cell and natural killer cell lymphopaenia accompanied by expansion of antigen-presenting dendritic cells, granulocytes, inflammatory monocytes and macrophages, all of which are hallmarks of chronic STING activation (Fig. 5i and Extended Data Fig. 10f). These aberrations were consistently and significantly rescued in *Sting1*^{N153S}*Ripk3*$^{-/-}$ mice. A similar normalization was observed in bone-marrow-derived and splenic myeloid subsets of the spleen, confirming that RIPK3-dependent necroptosis is a major driver of haematopoietic dysregulation (Extended Data Fig. 10f). Importantly, the frequency of immature erythroid precursors ($Ter119^+CD71^+$) was also

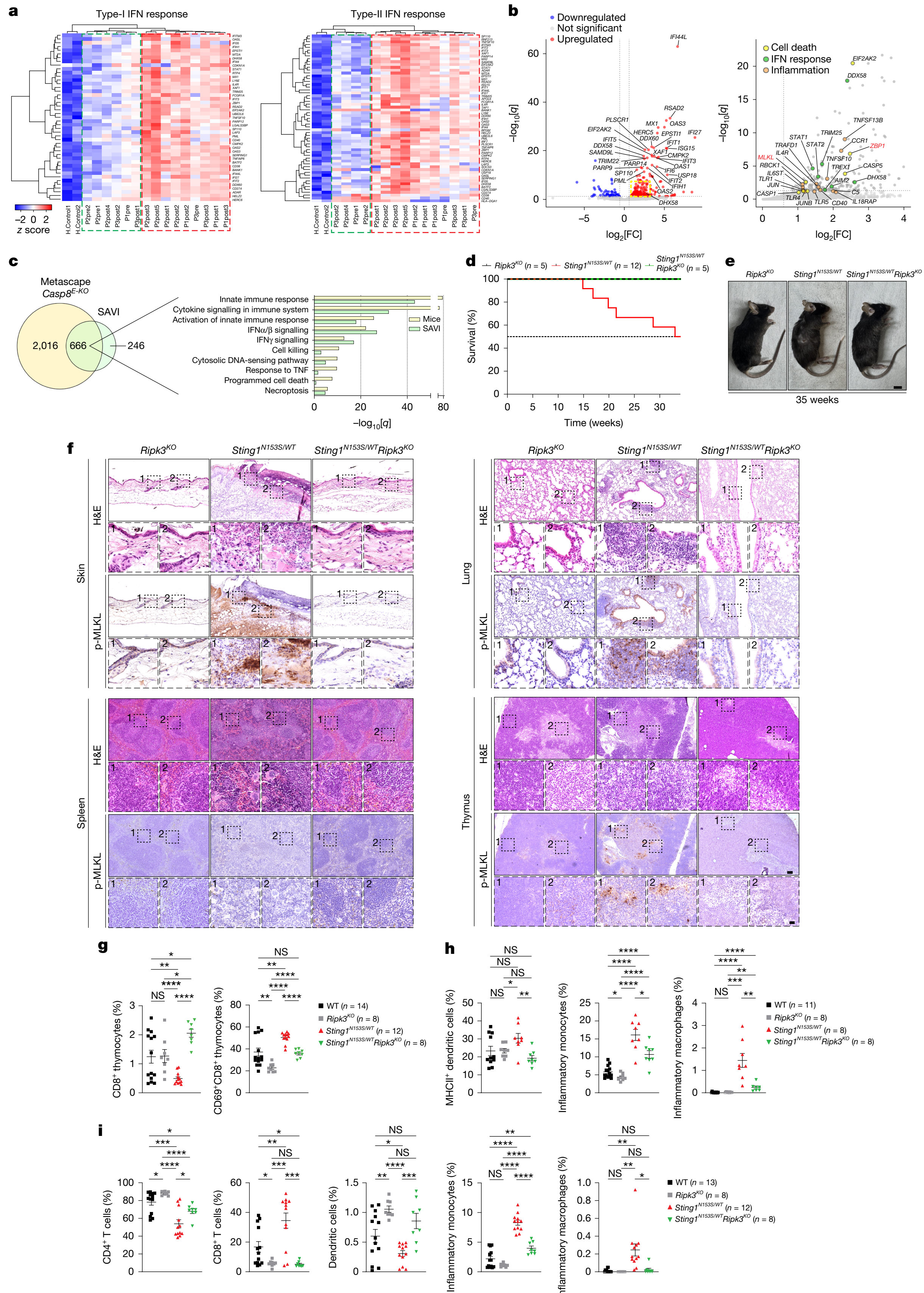

Fig. 5 | See next page for caption.

Fig. 5 | STAIN shapes SAVI transcriptional signatures immune dysregulation and lethality. a, Type I and type II IFN response signatures in SAVI samples (P(x) post(y) or pre(y), where x = patient number, y = sample number, pre = pre-treatment and post = post-treatment; see Extended Data Fig. 8a). Genes upregulated in SAVI versus controls ($P < 0.05$) that overlap with Hallmark IFNα and IFNγ response gene sets (GSEA) are shown. Expression values are row-scaled and colour coded (red, high; blue, low). The green and red boxes indicate IFN^{low} and IFN^{high} signature samples, respectively. **b**, Differentially expressed genes in type II IFN^{high} SAVI samples compared with controls ($P_{adj} < 0.05$ and fold change (FC) > 1.5). IFN-responsive genes (left) and genes belonging to cell death (yellow), IFN response (green) and inflammation (orange) are annotated. **c**, Pathway comparative analysis from Metascape data. The pathway overlap between *Casp8*$^{E\text{-}KO}$ mice and SAVI IFN^{high} samples is shown. The bar plot displays $-\log_{10}[q]$ values for ten representative overlapping pathways. **d**,**e**, Kaplan–Meier survival curves (**d**) and representative images (**e**) of *n* mice of the indicated genotypes. *P* values were calculated using two-sided Gehan–Breslow–Wilcoxon tests. **f**, Representative images of the indicated consecutive tissue sections from 35-week-old mice of the indicated genotypes stained with H&E and p-MLKL (Ser345). *n* = 3 per group. Scale bars, 100 µm (main images) and 20 µm (insets). **g**–**i**, Flow cytometry analysis of thymus (**g**), lung (**h**) and spleen (**i**) from 6–8-week-old mice of the indicated genotypes (*n* values are indicated). $CD8^+$ thymocytes are plotted as the percentage of viable cells, and $CD69^+CD8^+$ thymocytes, $MHCII^+$ dendritic cells, and $CD4^+$ and $CD8^+$ T cells are depicted as the percentage of their respective parental populations; all other populations were plotted as the percentage of $CD45^+$ cells. For **a** and **b**, differential expression analysis was performed using the Wald test as implemented in DESeq2; *P* values were adjusted for multiple testing using the Benjamini–Hochberg method. For **g**–**i**, age-matched WT and *Ripk3*-KO littermates were used as controls; data are mean ± s.e.m.; each dot represents one mouse; *P* values were calculated using two-tailed unpaired *t*-tests; $^*P \leq 0.05$, $^{**}P \leq 0.01$, $^{***}P \leq 0.001$, $^{****}P \leq 0.0001$; NS, not significant ($P > 0.05$).

reduced, indicating a reversal of extramedullary erythropoiesis and systemic inflammation (Extended Data Fig. 10g).

These findings propose that early necroptosis of immune cells, particularly T cells, contributes directly to the loss of immune homeostasis and the unleashing of systemic inflammation. This cascade probably facilitates the organ-specific inflammatory pathologies observed in SAVI, including dermatitis, interstitial lung inflammation and splenomegaly. In this way, necroptosis acts not only as a mechanism of immune cell loss, but also as a driver of systemic disease progression, reinforcing the functional and translational relevance of our findings.

Collectively, our findings reveal that caspase-8 deficiency in keratinocytes aberrantly activates a STING-mediated upregulation of ZBP1 and MLKL that, in turn, leads to ZBP1–MLKL-mediated necroptosis. We find that caspase-8 deficiency leads to the accumulation of genomic instability and activation of CGAS. Importantly, aberrant STING activation enables necroptosis by facilitating the formation of a ZBP1–RIPK1–RIPK3 complex, which forms and drives necroptosis independently of the TNF–TNFR1-induced FADD–RIPK1–RIPK3 complex. Activation of STING also induces further accumulation and stabilization of Z-NAs, which in turn serve as ligands for ZBP1 activation (Supplementary Fig. 8). Co-ablation of STING in keratinocytes or constitutively together with full-body depletion of *Tnfr1* revealed a substantial or complete additional survival advantage to *Casp8*$^{E\text{-}KO}$ mice, respectively. This provides genetic proof that aberrantly activated STING is capable of driving a TNFR1-independent necroptosis pathway in vivo responsible for ZBP1–RIPK3–MLKL-mediated necroptosis. Our analysis provides compelling evidence that STING enables necroptosis not only by inducing the transcriptional upregulation of ZBP1 but also by contributing to autocrine TNF production potentially through NF-κB activation. This dual role positions STING as a central inducer and amplifier of necroptotic signalling. Importantly, the extended survival and broader rescue observed after systemic *Sting1* deletion, compared with the deletion of either *Zbp1* or *Tnfr1* alone, suggest that STING partially governs both the TNFR1 and ZBP1 checkpoints. Thus, STING not only licenses the ZBP1 axis and its activation but also reinforces the TNFR1-dependent pathway, underscoring its unique role as a shared upstream regulator of inflammatory necroptosis.

The necroptosis-driven lethal inflammation observed in *Casp8*$^{E\text{-}KO}$ mice shares transcriptional commonalities with SAVI, providing further functional links between aberrant STAIN and development of SAVI. In the *Sting1*^{N153S} mice, *Ripk3* co-deletion alone robustly improves survival and overall necroptosis-induced cell death in all tissues and ameliorates early immune dysfunction. The genetic and pathological rescue in affected tissues at the endpoint underscores that necroptosis contributes not only to disease initiation but also to its clinical progression and organ-specific pathology. These findings establish necroptosis as an important effector pathway underlying both the onset and manifestation of SAVI and possibly other autoinflammatory diseases arising from pathogenic STING activation. Importantly, the robust rescue observed in *Sting1*^{N153S} mice with RIPK3 co-deficiency alone, without the necessity for caspase-8 inactivation, demonstrates that caspase-8 expression in SAVI is functionally irrelevant for controlling necroptosis. This, together with our biochemical data demonstrating the role of STING in (1) the formation of a ZBP1–RIPK1–RIPK3 complex independent of TNFR1 and FADD and (2) the upregulation of Z-NAs required to activate ZBP1, explains the activation of necroptosis in patients despite maintaining functional expression of caspase-8.

In summary, our study identifies a STING-driven necroptotic signalling axis that underlies severe inflammatory disease in vivo. This positions STING as a central node in a feedforward necroptotic inflammatory circuit that underlies sustained tissue pathology. By establishing STAIN as a pathogenic mechanism in SAVI, our findings offer a conceptual advance in understanding interferonopathies and identify the STING–ZBP1–necroptosis axis as a rational and tractable target for therapeutic intervention in this otherwise treatment-refractory disease.

Online content

Any methods, additional references, Nature Portfolio reporting summaries, source data, extended data, supplementary information, acknowledgements, peer review information; details of author contributions and competing interests; and statements of data and code availability are available at https://doi.org/10.1038/s41586-025-09536-4.

1. Kovalenko, A. et al. Caspase-8 deficiency in epidermal keratinocytes triggers an inflammatory skin disease. *J. Exp. Med.* **206**, 2161–2177 (2009).
2. Lee, P. et al. Dynamic expression of epidermal caspase 8 simulates a wound healing response. *Nature* **458**, 519–523 (2009).
3. Weinlich, R. et al. Protective roles for caspase-8 and cFLIP in adult homeostasis. *Cell Rep.* **5**, 340–348 (2013).
4. Kaiser, W. J. et al. RIP3 mediates the embryonic lethality of caspase-8-deficient mice. *Nature* **471**, 368–372 (2011).
5. Oberst, A. et al. Catalytic activity of the caspase-8-FLIP complex inhibits RIPK3-dependent necrosis. *Nature* **471**, 363–367 (2011).
6. Alvarez-Diaz, S. et al. The pseudokinase MLKL and the kinase RIPK3 have distinct roles in autoimmune disease caused by loss of death-receptor-induced apoptosis. *Immunity* **45**, 513–526 (2016).
7. Koerner, L. et al. ZBP1 causes inflammation by inducing RIPK3-mediated necroptosis and RIPK1 kinase activity-independent apoptosis. *Cell Death Differ.* **31**, 938–953 (2024).
8. Dillon, C. P. et al. RIPK1 blocks early postnatal lethality mediated by caspase-8 and RIPK3. *Cell* **157**, 1189–1202 (2014).
9. Peltzer, N. & Walczak, H. Cell death and inflammation—a vital but dangerous liaison. *Trends Immunol.* **40**, 387–402 (2019).
10. Silke, J., Rickard, J. A. & Gerlic, M. The diverse role of RIP kinases in necroptosis and inflammation. *Nat. Immunol.* **16**, 689–697 (2015).
11. Dannappel, M. et al. RIPK1 maintains epithelial homeostasis by inhibiting apoptosis and necroptosis. *Nature* **513**, 90–94 (2014).
12. Bonnet, M. C. et al. The adaptor protein FADD protects epidermal keratinocytes from necroptosis in vivo and prevents skin inflammation. *Immunity* **35**, 572–582 (2011).

13. Lin, J. et al. RIPK1 counteracts ZBP1-mediated necroptosis to inhibit inflammation. *Nature* **540**, 124–128 (2016).
14. Ingram, J. P. et al. ZBP1/DAI drives RIPK3-mediated cell death induced by IFNs in the absence of RIPK1. *J. Immunol*. **203**, 1348–1355 (2019).
15. Thapa, R. J. et al. DAI senses influenza A virus genomic RNA and activates RIPK3-dependent cell death. *Cell Host Microbe* **20**, 674–681 (2016).
16. Koehler, H. et al. Vaccinia virus E3 prevents sensing of Z-RNA to block ZBP1-dependent necroptosis. *Cell Host Microbe* **29**, 1266–1276 (2021).
17. Jiao, H. P. et al. Z-nucleic-acid sensing triggers ZBP1-dependent necroptosis and inflammation. *Nature* **580**, 391–395 (2020).
18. Devos, M. et al. Sensing of endogenous nucleic acids by ZBP1 induces keratinocyte necroptosis and skin inflammation. *J. Exp. Med.* **217**, e20191913 (2020).
19. Jiao, H. et al. ADAR1 averts fatal type I interferon induction by ZBP1. *Nature* **607**, 776–783 (2022).
20. DeAntoneo, C., Herbert, A. & Balachandran, S. Z-form nucleic acid-binding protein 1 (ZBP1) as a sensor of viral and cellular Z-RNAs: walking the razor's edge. *Curr. Opin. Immunol*. **83**, 102347 (2023).
21. Rodriguez, D. A. et al. Caspase-8 and FADD prevent spontaneous ZBP1 expression and necroptosis. *Proc. Natl Acad. Sci. USA* **119**, e2207240119 (2022).
22. Zhang, T. et al. Influenza virus Z-RNAs induce ZBP1-mediated necroptosis. *Cell* **180**, 1115–1129 (2020).
23. Newton, K. et al. RIPK1 inhibits ZBP1-driven necroptosis during development. *Nature* **540**, 129–133 (2016).
24. Solon, M. et al. ZBP1 and TRIF trigger lethal necroptosis in mice lacking caspase-8 and TNFR1. *Cell Death Differ.* **31**, 672–682 (2024).
25. Haag, S. M. et al. Targeting STING with covalent small-molecule inhibitors. *Nature* **559**, 269–273 (2018).
26. Kelepouras, K. et al. The importance of murine phospho-MLKL-S345 in situ detection for necroptosis assessment in vivo. *Cell Death Differ.* **31**, 897–909 (2024).
27. Kim, J., Kim, H. S. & Chung, J. H. Molecular mechanisms of mitochondrial DNA release and activation of the cGAS-STING pathway. *Exp. Mol. Med.* **55**, 510–519 (2023).
28. Liccardi, G. et al. RIPK1 and caspase-8 ensure chromosome stability independently of their role in cell death and inflammation. *Mol. Cell* **73**, 413–428 (2019).
29. Boege, Y. et al. A dual role of caspase-8 in triggering and sensing proliferation-associated DNA damage, a key determinant of liver cancer development. *Cancer Cell* **32**, 342–359 (2017).
30. Hakem, A. et al. Caspase-8 is essential for maintaining chromosomal stability and suppressing B-cell lymphomagenesis. *Blood* **119**, 3495–3502 (2012).
31. Vucur, M. et al. RIP3 inhibits inflammatory hepatocarcinogenesis but promotes cholestasis by controlling caspase-8- and JNK-dependent compensatory cell proliferation. *Cell Rep.* **4**, 776–790 (2013).
32. Liu, Y. et al. Activated STING in a vascular and pulmonary syndrome. *N. Engl. J. Med.* **371**, 507–518 (2014).
33. Jeremiah, N. et al. Inherited STING-activating mutation underlies a familial inflammatory syndrome with lupus-like manifestations. *J. Clin. Invest.* **124**, 5516–5520 (2014).
34. Munoz, J. et al. Stimulator of interferon genes-associated vasculopathy with onset in infancy: a mimic of childhood granulomatosis with polyangiitis. *JAMA Dermatol*. **151**, 872–877 (2015).
35. Chia, J. et al. Failure to thrive, interstitial lung disease, and progressive digital necrosis with onset in infancy. *J. Am. Acad. Dermatol*. **74**, 186–189 (2016).
36. Volpi, S. et al. Efficacy and adverse events during Janus kinase inhibitor treatment of SAVI syndrome. *J. Clin. Immunol*. **39**, 476–485 (2019).
37. Raffaele, C. G. L. et al. A patient with stimulator of interferon genes-associated vasculopathy with onset in infancy without skin vasculopathy. *Rheumatology* **59**, 905–907 (2020).
38. de Cevins, C. et al. Single-cell RNA-sequencing of PBMCs from SAVI patients reveals disease-associated monocytes with elevated integrated stress response. *Cell Rep. Med.* **4**, 101333 (2023).
39. Zhu, K. Z. et al. Necroptosis promotes cell-autonomous activation of proinflammatory cytokine gene expression. *Cell Death Dis.* **9**, 500 (2018).
40. Warner, J. D. et al. STING-associated vasculopathy develops independently of IRF3 in mice. *J. Exp. Med.* **214**, 3279–3292 (2017).
41. Siedel, H., Roers, A., Rosen-Wolff, A. & Luksch, H. Type I interferon-independent T cell impairment in a Tmem173 N153S/WT mouse model of STING associated vasculopathy with onset in infancy (SAVI). *Clin. Immunol*. **216**, 108466 (2020).
42. Motwani, M. et al. Hierarchy of clinical manifestations in SAVI N153S and V154M mouse models. *Proc. Natl Acad. Sci. USA* **116**, 7941–7950 (2019).

Methods

Mice

$Casp8^{fl/fl}$ mice were provided by S. M. Hedrick[43] and the *K14-Cre*[44] and $Tnfr1^{-/-}$ (ref. 45) mice were obtained as previously described. $Zbp1^{-/-}$ mice were purchased from Cyagen (*C57BL/6NCya-*$Zbp1^{em1}$*/Cya*, S-KO-16146) and $Sting1^{fl/fl}$ (*B6;SJL-*$Sting1^{tm1.1Camb}$*/J*, 031670)[46], $Sting1^{-/-}$ (*B6(Cg)-*$Sting1^{tm1.2Camb}$*/J*, 025805)[46], $Cgas^{-/-}$ (*B6(C)-*$Cgas^{tm1d(EUCOMM)Hmgu}$*/J*, 026554)[47] and $Sting1^{N153S/WT}$ (*B6J.B6N-*$Sting1^{em1Jmin}$*/J*, 033543)[40] mice were purchased from The Jackson Laboratory. $Mlkl^{-/-}$ mice were generated by the Walczak laboratory[48] and $Casp8^{+/-}$ and $Ripk3^{-/-}$ mice were provided by R. Hakem, V. Dixit and K. Newton, respectively[49]. $Mavs^{-/-}$ mice were provided by the SFB1403 consortium[19]. All mice were maintained on a C57BL/6N background; C57BL/6J strains were backcrossed for at least ten generations. Male mice carrying the *K14-cre* transgene were crossed to obtain all $Casp8^{E\text{-}KO}$ models. $Casp8^{-/WT}Ripk3^{-/-}$ or $Casp8^{-/WT}Mlkl^{-/-}$ were bred to obtain $Casp8^{-/-}Ripk3^{-/-}$ and $Casp8^{-/-}Mlkl^{-/-}$ double-knockout mice, respectively. Mice heterozygous for $Sting1^{N153S}$ ($Sting1^{N153S/WT}$) were bred with $Ripk3^{-/-}$ mice to obtain $Sting1^{N153S/WT}Ripk3^{-/-}$ mice. Mice were housed under SPF conditions in individually ventilated cages (12 h–12 h light–dark cycle) at the University of Cologne's Medical Faculty and CECAD animal facilities, with ad libitum access to food and water. Temperature and humidity were controlled. Animals were monitored daily and euthanized after reaching predefined humane-endpoint criteria for disease severity. No additional exclusion criteria were applied. Experimental groups were not randomized because group assignment was determined by genotype; within each genotype, female and male mice were enrolled without preference and allocated to experimental conditions at random. Sample size was estimated to reach necessary statistical power. The age of mice at analysis is reported in the corresponding figure legends. All mouse scoring was performed at least by three independent scientists, experiments and the immunohistochemical evaluation of pathology were performed under blinded conditions. All of the procedures complied with German animal welfare regulations and were approved by local authorities (Landesamt für Natur, Umwelt und Verbraucherschutz Nordrhein-Westfalen).

Cell lines

Casp8-knockout cell lines were generated by CRISPR–Cas9-mediated gene editing. WT and *Zbp1*-knockout MEFs were electroporated with *Casp8*-targeting gRNA (Mm.Cas9.CASP8.1.AA, IDT) using the 4D-Nucleofector System and Nucleofector Kit V (Lonza) according to the manufacturer's instructions. $Casp8^{-/-}$ $Sting1^{-/-}$ double-knockout cell lines were generated by isolating and transfecting $Casp8^{fl/fl}Sting1^{-/-}$ MEFs with cre-GFP plasmid (13776, Addgene), followed by FACS-based single-cell cloning and expansion. Knockout efficiency was confirmed by western blotting and genomic sequencing. HT29 and HaCaT cells were obtained from ATCC. HT29 $ZBP1^{-/-}$ cells were generated via CRISPR–Cas9 (sgRNA: CAGCTGGGCAAGTTTCACCG), and the HT29 $Casp8^{-/-}$ cell line was kindly provided by the Pasparakis laboratory. All primary MEFs were isolated from corresponding mouse strains and immortalized as described previously[48].

Cell death assay

Immortalized MEFs were seeded to 96-well plate (1×10^4 cells per well) and incubated with either DMSO or pretreated with 20 μg ml^{-1} DMXAA (D5817, Sigma-Aldrich). Similarly, HaCaT and HT-29 cell lines were pretreated with 10 μM ADU-S100 (HY-12885B, MedChemExpress)[50]. The next day, medium containing DMSO, DMXAA or ADU-S100 was replenished and cells were additionally treated with 100 ng ml^{-1} recombinant TNF (in house), 20 μM Z-VAD-FMK (APE-A1902-25MG, APExBIO), 2 μM BV6 (S7597, Selleck Chemicals) or combinations of them. In experiments using RIPK3, MLKL, TNF or STING inhibitors, 10 μM GSK'872 (S8465, Selleck Chemicals), 1 μM NSA (S8251, Selleck Chemicals), 50 μg ml^{-1} etanercept (Enbrel, PAA115147, Pfizer) or 1 μM C-178 (S6667, Selleck Chemicals)[25] were added as pretreatments, respectively. Cell viability was measured in the Spark Multimode Microplate Reader (TECAN) using the CellTiter-Glo Luminescent Cell Viability Assay (G7573, Promega).

Protein lysate preparation and western blot analysis

Cell lysates were prepared and analysed by western blotting as previously described[28]. A list of the antibodies used is provided in Supplementary Table 3. Uncropped blot images are provided in Supplementary Fig. 1.

Immunoprecipitation

G-Sepharose beads (20 μl; P3296, Sigma-Aldrich) were incubated with 1.5 μg of FADD antibody (ab124812, Abcam) or 1 μg of ZBP1 antibody (AG-20B-0010-C100, Adipogen) per mg of protein lysate for 4 h at 4 °C with rotation. Cleared protein lysates were subsequently added to the bead–antibody complexes and incubated overnight at 4 °C with rotation. Beads were washed five times with wash buffer (150 mM NaCl, 150 mM Tris-HCl 1 M, pH 7.4, 5% glycerol, 0.5% Triton X-100), and bound proteins were eluted by boiling in 60 μl of 2× SDS loading dye for 5 min.

Dermatitis scoring criteria

Skin lesions in $Casp8^{fl/fl}Tnfr1^{-/-}Zbp1^{-/-}K14\text{-}cre^{tg/WT}$, $Casp8^{fl/fl}Zbp1^{-/-}Tnfr1^{-/WT}$ $K14\text{-}cre^{tg/WT}$, $Casp8^{fl/fl}Tnfr1^{-/-}Sting1^{fl/fl}K14\text{-}cre^{tg/WT}$, $Casp8^{fl/fl}Tnfr1^{-/-}$ $Sting1^{fl/WT}K14\text{-}cre^{tg/WT}$ and $Casp8^{fl/fl}Tnfr1^{-/-}Sting1^{-/-}K14\text{-}cre^{tg/WT}$ mice were scored using an adjusted version of the scoring system previously described[48]. Two main clinical criteria were assessed to determine a total score: (1) the number of body regions presenting lesions and (2) the characteristics of each lesion. For the first criteria skin from six different body regions were assessed and appearance of lesions in each of these body regions generated a score of 1 (head = 1, neck = 1, back = 1, abdomen = 1, flank = 1 and tail = 1). For the second criteria, the characteristic of each lesion was defined by its severity. Punctuated small crusts received a score of 1, coalescent crusts received a score of 2 and ulceration received a score of 3. The sum of all individual scores according to these two was calculated to determine the total severity. Scoring of skin lesions was performed in a blinded manner by three independent researchers.

Histological and immunohistochemical analysis of paraffin-embedded tissues

Tissues were collected, fixed and processed as previously described[26,51]. H&E staining, along with detection of p-MLKL(Ser345) and Cl-CASP3, were performed accordingly[26]. For immunodetection of ZBP1, STING, p-STAT1(Tyr701), CD3, Ly6G, pHH3-S10 and γH2AX-S139, the slides were retrieved in Tris-EDTA-based antigen-retrieval buffer, pH 9 (S236784-2, Agilent Technologies), for 10 min at 114–121 °C using the TintoRetriever Pressure Cooker. For F4/80, CD45, K6A, K10 and K14 staining, the slides were retrieved in sodium citrate buffer, pH 6 (C9999, Sigma-Aldrich), under the same conditions. For delicate tissues prone to detachment (skin from adult mice), antigen retrieval was performed at 60 °C in a water bath overnight. Primary antibodies were incubated at 4 °C overnight or at room temperature for 45 minutes (for ZBP1). The blocking steps, antibody detection procedures, counterstaining and mounting were performed as previously described[26]. For p-STAT1, Ly6G and F4/80, HRP-conjugated secondary antibody incubation was followed by TSA-biotin signal amplification (NEL700A001KT, Akoya Biosciences; 1:100) and then detection was performed using the Avidin-Biotin Complex-HRP amplification system (PK-6100, Vector Laboratories). TUNEL staining was performed using the DeadEnd Fluorometric TUNEL System (Promega, G3250) according to the manufacturer's instructions. A list of the antibodies used is provided in Supplementary Table 4.

Immunocytochemistry and immunofluorescence

For DNA, mitochondrial and TFAM staining, cells were fixed in 4% methanol-free formaldehyde (Cell Signaling Technology, 47746) for 15 min at room temperature, quenched with 50 mM ammonium chloride in PBS and permeabilized with 0.1% Triton X-100 in PBS for 10 min at 37 °C. For ZBP1 and Z-DNA/Z-RNA staining, cells were fixed for 10 min and permeabilized with 0.4% Triton X-100 in PBS for 10 min at 37 °C. After blocking, the following primary antibodies diluted in blocking buffer were incubated at 4 °C overnight: mouse anti-ZBP1 (AG-20B-0010-C100, Adipogen, 1:100), anti-Z-DNA/Z-RNA (Z22) (Ab00783-23.0, Absolute Antibody, 1:200), anti-TFAM (ABE483, EMD Millipore; 1:200) and anti-DNA (CBL186, EMD Millipore, 1:100). After washing, cells were incubated with secondary antibodies (Thermo Fisher Scientific, 1:500), including, goat anti-mouse Alexa Fluor 488 (A11001), goat anti-rabbit Alexa Fluor Plus 594 (A32740), goat anti-rabbit Alexa Fluor Plus 488 (A32731) and goat anti-mouse Alexa Fluor Plus 594 (A32742). Cell plating, blocking, washing steps and mounting were performed as previously described[28]. For mitochondrial staining, cells were incubated with 200 nM MitoTracker Deep Red (M22426, Thermo Fisher Scientific) for 30 min at 37 °C before fixation. For nucleic acid degradation, cells were treated with DNase I or RNase A as previously described[22].

Image analysis

Image acquisition, analysis and quantification of whole-tissue digital images were performed as previously described[26]. For mouse tissue confocal microscopy, three representative images per biological replicate ($n = 5$) were acquired and quantified in Fiji (ImageJ) with BioVoxxel Toolbox for Voronoi segmentation. DAPI-stained nuclei served as seeds to generate Voronoi cells approximating cell boundaries. A custom Fiji script identified positive cells by overlapping cell boundaries and target fluorophore signals. Positive cell counts from three images per replicate were pooled. Immunocytochemical images were manually segmented in Fiji, and the mean fluorescence intensity was quantified by rolling-ball background subtraction using a custom script. Co-localization of Z-NA and ZBP1 was assessed using the BIOP JACoP plugin after background subtraction. At least 10 images and 30 cells per staining condition were analysed. Data are presented as mean ± s.e.m. and plotted in GraphPad Prism. Statistical significance was determined by ordinary one-way or two-way ANOVA with Tukey's multiple-comparison test.

Blood cell analysis

Whole blood cell count analysis was performed in peripheral blood using VETSCAN HM5 analyser (Zoetis) according to the manufacturer's instructions.

RNA isolation from mouse tissue

RNA was extracted from skin tissue using the RNeasy Plus Mini kit (74136, Qiagen). Skin was weighted at 30 mg, snap-frozen in liquid nitrogen and stored at −80 °C before being lysed. Skin tissues were lysed in lysis buffer (Buffer RLT + 40 µl DTT 1 M per ml + 0.5% Reagent DX) according to the kit's manufacturer instructions in TissueLyser II (85300, Qiagen) using 7 mm stainless steel beads (69990, Qiagen). Extracted RNA was stored at −80 °C.

RNA isolation from whole blood in human samples

Whole blood from patients with SAVI and healthy donors was collected either with Tempus Tubes (4342792, Applied Biosystems) or PAXgene Tubes (762165, Qiagen) and total RNA was isolated using the Tempus Spin RNA Isolation kit (4380204) or with PAXgene Blood RNA kit (Qiagen), according to manufacturer's instructions.

RT–qPCR

cDNA was prepared using the Lunascript RT SuperMix kit (M3010, New England Biolabs). RT–qPCR was performed using Luna Universal qPCR Master Mix (M3003, New England Biolabs) in QuantStudio 5 (A34322, Thermo Fisher Scientific). The housekeeper genes *Gapdh* and *HPRT* were used for transcripts normalization in mice and patients with SAVI, respectively. The relative fold change in gene expression (that is, relative quantification) of the samples was calculated as $2^{-\Delta\Delta C_t}$ to the controls (littermates for mice and healthy individuals for patients with SAVI). The primer for *mZbp1* was obtained from Integrated DNA Technologies (Mm.PT.58.21951435). Sequences for all other primers used are listed in Supplementary Table 5.

3′ mRNA-seq libraries and sequencing

A total of 2 µg of RNA was provided to the Cologne Centre for Genomics (CCG) for 3′ mRNA-seq. Library preparation was performed using the Lexogen QuantSeq 3′ mRNA sequencing protocol. The resulting libraries were assessed for quality using a TapeStation system and quantified using qPCR. Sequencing was then carried out on the NovaSeq 6000 platform, using a single-read (SR) 1×100 bp sequencing strategy.

Differential expression analysis

RNA-seq reads were aligned to the reference genome (hg38 or mm10) using STAR aligner, followed by transcript quantification with RSEM. For mouse data, technical batch effects from two sequencing runs were corrected using ComBat_seq (sva package). One sample per genotype was excluded to maintain consistency after a WT control sample showed abnormal upregulation of *Zbp1*. The removed samples were those that clustered the least with *Zbp1* expression in all other genotypes. An additional round of sequencing was performed to analyse the $Casp8^{E\text{-}KO}Sting1^{-/-}$ in comparison to all of the other genotypes. The analysis was performed as independent experiment. For patient data, single-sample gene set enrichment analysis was performed using the gsva method (gsva package) with the hallmark gene sets. The nine samples with highest IFNγ scores were classified as IFN^{high} samples and used for differential expression and pathway analyses (patient samples classified as IFN^{high}: P1post1, P1post2, P1post3, P2post1, P2post2, P2post3, P2post5, P3post1, P3post3). Differential expression analysis was performed using DESeq2 (v.1.44.0). Volcano plots were generated using ggplot2 (v.3.5.1) and heat maps were created using heatmap.2 (gplots, v.3.2.0) with row-wise scaling on the DEseq2-normalized expression data. For RNA-seq data, statistical significance of differential expression was assessed using two-sided Wald tests implemented in the DESeq2 package, with Benjamini–Hochberg correction for multiple testing (adjusted $P < 0.05$).

Pathway analysis

Pathway analysis was performed using Metascape[52] or the GSEA GUI tool (v.4.3.3). For Metascape, significantly upregulated genes ($q < 0.05$) were submitted to the web-tool (Express Analysis). Enrichment was calculated using Metascape's default cumulative hypergeometric test with Benjamini–Hochberg correction, and enrichment q values were plotted as $-\log[q]$. Mouse samples were analysed using *Homo sapiens* as a reference species to enable human–mouse pathway comparison. For GSEA, DESeq2-normalized counts were used as the input and analysed using the default parameters with gene set permutation type. The gene set 'inflammatory cell death' was manually curated and contains the following genes: *TNF*, *TNFRSF1A*, *TNFRSF10*, *TNFRSF10B*, *RIPK1*, *FADD*, *CASP8*, *CFLAR*, *RIPK3*, *MLKL*, *CASP1*, *TNFSF10*, *FASLG*, *FAS*, *ZBP1*, *ADAR*, *TRIM25*, *EIF2AK2*, *IL1B*, *TLR4*, *BIRC2*, *RBCK1*, *TREX1*, *NLRC4*, *TLR5* and *NAIP*. The gene sets REACTOME_RIP_MEDIATED_NFKB_ACTIVATION_VIA_ZBP1 and REACTOME_ZBP1_DAI_MEDIATED_INDUCTION_OF_TYPE_I_IFNS were merged to give the customized ZBP1-mediated process geneset.

Protein extraction from mouse skin tissue and mouse serum and human plasma isolation

Total protein was extracted from mouse skin tissue in cell lysis buffer 2 (895347, R&D Systems) in TissueLyser II (85300, Qiagen) using 7 mm stainless steel beads (69990, Qiagen). Extracted proteins were stored at −80 °C. For human plasma isolation, whole blood was collected in EDTA blood collection tubes. Subsequently, the samples were centrifuged at 1,500*g* for 15 min, and the resultant supernatant (plasma) was carefully aspirated, aliquoted and stored at −80 °C for further analysis.

Luminex assay

Cytokine analysis in skin protein lysates from mice was conducted using the Mouse Premixed Multi-Analyte Kit (R&D Systems) according to the manufacturer's instructions. For cytokine analysis in plasma from patients with SAVI and healthy donors, the corresponding human multi-analyte kit from R&D Systems was used.

Flow cytometry analysis

Spleen, lung and thymus were dissected from 6–8-week-old mice. Lung digestion and single-cell suspensions were prepared as described previously[53]. Red blood cell lysis (1× RBC lysis buffer, BioLegend) was performed for 4 min on ice for lung and spleen samples; spleens for erythrocyte analysis and thymi were not subjected to RBC lysis. The samples were blocked with anti-mouse CD16/32 antibodies (101320, BioLegend, 1:100 dilution), washed with FACS buffer (PBS supplemented with 1% FBS and 5 mM EDTA), then stained with viability dye (65-0865-18, Thermo Fisher Scientific, 1:1,000) followed by surface marker staining in Brilliant Stain Buffer (566349, BD). All of the incubation steps were performed for 30 min at 4 °C. Data were acquired on the BD FACSymphony A3 system and analysed using FlowJo v.10.10 and GraphPad Prism. Statistical significance was determined using unpaired *t*-tests. A list of all of the antibodies used is provided in Supplementary Table 6. The gating strategy is included in Supplementary Fig. 9.

Depletion of mtDNA and measurement of relative mtDNA levels

Immortalized MEFs were treated with 150 µM ddC or 10 µM IMT1B for 96 h, or with medium alone as a control. DNA was isolated using the DNeasy Blood & Tissue Kit (Qiagen) according to the manufacturer's protocol for cells. Relative mtDNA levels were measured using RT–qPCR with the Brilliant III Ultra-Fast SYBR QPCR Master Mix (Agilent Technologies) using different primers. qPCR was performed on the QuantStudio K FlexSystem (Applied Biosystems, Life Technologies). The samples were adjusted for total DNA content by *Actb*. Relative mtDNA levels were determined using the comparative ($2^{-\Delta\Delta C_t}$) quantification method. A list of the sequences for all of the primers used is provided in Supplementary Table 7.

Extraction of the total RNA from MEFs

Total RNA was isolated from MEFs using TRIzol reagent (Life Technologies). MEFs were pelleted and resuspended in 1 ml of TRIZOL. After incubation of 5 min at room temperature, chloroform was added and subsequent phase separation was performed according to the manufacturer's instructions. The RNA pellet was resuspended in RNase/DNase-free H_2O (Gibco).

RT–PCR and RT–qPCR

The total RNA that was previously isolated was treated with DNase (New England Biolabs). Digested RNA (100 ng µl^{-1} per sample) was reverse transcribed using the high-capacity reverse transcription kit (Applied Biosystems, Life Technologies). The generated cDNA was amplified using the Brilliant III Ultra-Fast SYBR QPCR Master Mix (Agilent Technologies) using different primers listed in Supplementary Table 8. qPCR was performed on the QuantStudio K FlexSystem (Applied Biosystems, Life Technologies). The samples were adjusted for total RNA content by *HPRT*. The relative expression of mRNAs was determined using the comparative ($2^{-\Delta\Delta C_t}$) quantification method.

Ethics statement

The study involving the collection of the included patient samples was approved by the local Institutional Ethical Committee of Bambino Gesù Children's Hospital, Rome, Italy (PNRR-MR1-2022-12375873). Written informed consent to participate in this study was provided by the participants' legal guardian/next of kin. Clinical information relative to patient samples is listed in Supplementary Table 9. Patient data are available on request.

Statistical analysis

Survival curves were compared using two-sided Gehan–Breslow–Wilcoxon tests. Data in graphs are shown as the mean ± s.e.m. unless otherwise indicated, with each dot representing one mouse or individual sample. For comparisons involving more than two groups, statistical significance was determined using one-way or two-way ANOVA followed by Tukey's or Šidák's multiple-comparison test as appropriate. In some cases, two-tailed unpaired *t*-tests were performed when comparing two groups, as specified in the figure legends. Flow cytometry data were analysed using two-way ANOVA or unpaired *t*-tests as indicated. *P* values are provided in the figures or figure legends; $P > 0.05$ was considered to be not significant. For cell viability assays, data represent the mean ± s.e.m. of at least two independent experiments, each performed with three technical replicates. The details on sample size, replicates and statistical tests are provided in each figure legend.

Reporting summary

Further information on research design is available in the Nature Portfolio Reporting Summary linked to this article.

Data availability

RNA-seq data for human patients are available on request. RNA-seq data for mouse tissues are available through the Gene Expression Omnibus of the National Institutes of Health under accession number GSE304254 (RNA-seq). Source data are provided with this paper.

43. Beisner, D. R., Ch'en, I. L., Kolla, R. V., Hoffmann, A. & Hedrick, S. M. Cutting edge: innate immunity conferred by B cells is regulated by caspase-8. *J. Immunol.* **175**, 3469–3473 (2005).
44. Hafner, M. et al. Keratin 14 Cre transgenic mice authenticate keratin 14 as an oocyte-expressed protein. *Genesis* **38**, 176–181 (2004).
45. Pfeffer, K. et al. Mice deficient for the 55 kd tumor necrosis factor receptor are resistant to endotoxic shock, yet succumb to *L. monocytogenes* infection. *Cell* **73**, 457–467 (1993).
46. Jin, L. et al. MPYS is required for IFN response factor 3 activation and type I IFN production in the response of cultured phagocytes to bacterial second messengers cyclic-di-AMP and cyclic-di-GMP. *J. Immunol.* **187**, 2595–2601 (2011).
47. Schoggins, J. W. et al. Pan-viral specificity of IFN-induced genes reveals new roles for cGAS in innate immunity. *Nature* **505**, 691–695 (2014).
48. Peltzer, N. et al. LUBAC is essential for embryogenesis by preventing cell death and enabling haematopoiesis. *Nature* **557**, 112–117 (2018).
49. Newton, K., Sun, X. & Dixit, V. M. Kinase RIP3 is dispensable for normal NF-kappa Bs, signaling by the B-cell and T-cell receptors, tumor necrosis factor receptor 1, and Toll-like receptors 2 and 4. *Mol. Cell. Biol.* **24**, 1464–1469 (2004).
50. Diepstraten, S. T. et al. Putting the STING back into BH3-mimetic drugs for TP53-mutant blood cancers. *Cancer Cell* **42**, 850–868.e9 (2024).
51. Bankhead, P. et al. QuPath: open source software for digital pathology image analysis. *Sci. Rep.* **7**, 16878 (2017).
52. Zhou, Y. Y. et al. Metascape provides a biologist-oriented resource for the analysis of systems-level datasets. *Nat. Commun.* **10**, 1523 (2019).
53. Albert, M. C. et al. Identification of FasL as a crucial host factor driving COVID-19 pathology and lethality. *Cell Death Differ.* **31**, 544–557 (2024).

Acknowledgements We thank the members of the Liccardi and Walczak laboratories as well as N. Peltzer and A. Annibaldi for discussions; the members of the CECAD imaging facility, particularly M. Babaki, P. Zentis and C. Jüngst, the staff at the Histology Core Facility of SFB 1403, especially E. Stade, and the staff of the CECAD in vivo Research Facility of the University of Cologne for their support. We thank M. Guschlbauer and the staff of the animal facilities of the medical faculty of the University of Cologne for their constant support and assistance. We thank M. Pasparakis, the CRC1403 and the CECAD animal facility for providing mouse models for initial experiments not included here. G.L. is funded by the Institute of Biochemistry I (IBC1) of the Medical Faculty of the University of Cologne, Köln Fortune, the CANcer TARgeting (CANTAR) network funded by the NRW-funded Research Programme Netzwerke 2021, two

Collaborative Research Centre (CRC) grants (SFB1399 project C06 (413326622); SFB1530 project A03 (455784452)) funded by the Deutsche Forschungsgemeinschaft (DFG) and is associated to the CRC SFB1403 also funded by the DFG; H.W. by the Alexander von Humboldt Foundation, a Wellcome Trust Investigator Award (214342/Z/18/Z), a Medical Research Council Grant (MR/S00811X/1), a Cancer Research UK Programme Grant (A27323), three CRC grants (SFB1399 project C06 (413326622); SFB1530 project A03 (455784452) and SFB1403 project A12 (414786233)) funded by the DFG and the CANcer TARgeting (CANTAR), funded by Netzwerke 2021; and G.P. and F.D.B. by the European Union, Next Generation EU, NRRP M6C2, Investment 2.1 Enhancement and strengthening of biomedical research in the NHS (PNRR-MR1-2022-12375873). Open access funding was provided by Universität zu Köln.

Author contributions G.L. conceived and led the study, developed the overarching research strategy and supervised all aspects of the work. G.L. and K.K. designed experiments. G.L., H.W. and K.K. discussed and interpreted the data. K.K. performed all in vivo experiments, all immunohistochemistry and immunofluorescence in mouse tissue and cultured cells and conducted all image acquisition and analysis. G.L., K.K., J.S., C.K. and D.B. performed in vitro experiments. G.L. optimized and performed all immunoprecipitations. J.S., C.K. and H.R.-K. provided support with mouse scoring and dissections. D.B. and K.K. performed cytokine analysis in mice. A.B.V., L.G. and M.P. analysed all RNA-seq data. F.L. performed and analysed all RT–qPCR data. K.K., J.S., D.B., C.K. and H.R.-K. collected organs and cells from N153 mice. J.S. and D.B. performed the flow cytometry experiment. A.M., J.S. and D.B. planned and analysed the flow cytometry experiment. K.K. and M.C. performed the mitochondrial DNA experiments, and discussed and analysed the data with A.T.; E.L., G.P., A.I. and F.D.B. collected data from patients with SAVI and provided mRNA and plasma samples from these patients. J.S. and D.B. processed and analysed samples from patients with SAVI. K.K., J.S. and D.B. prepared mRNA from mice. G.L. and K.K. prepared the figures. K.K., H.W. and G.L. wrote the manuscript.

Funding Open access funding provided by Universität zu Köln.

Competing interests The authors declare no competing interests.

Additional information

Supplementary information The online version contains supplementary material available at https://doi.org/10.1038/s41586-025-09536-4.

Correspondence and requests for materials should be addressed to Gianmaria Liccardi.

Peer review information *Nature* thanks the anonymous reviewers for their contribution to the peer review of this work. Peer reviewer reports are available.

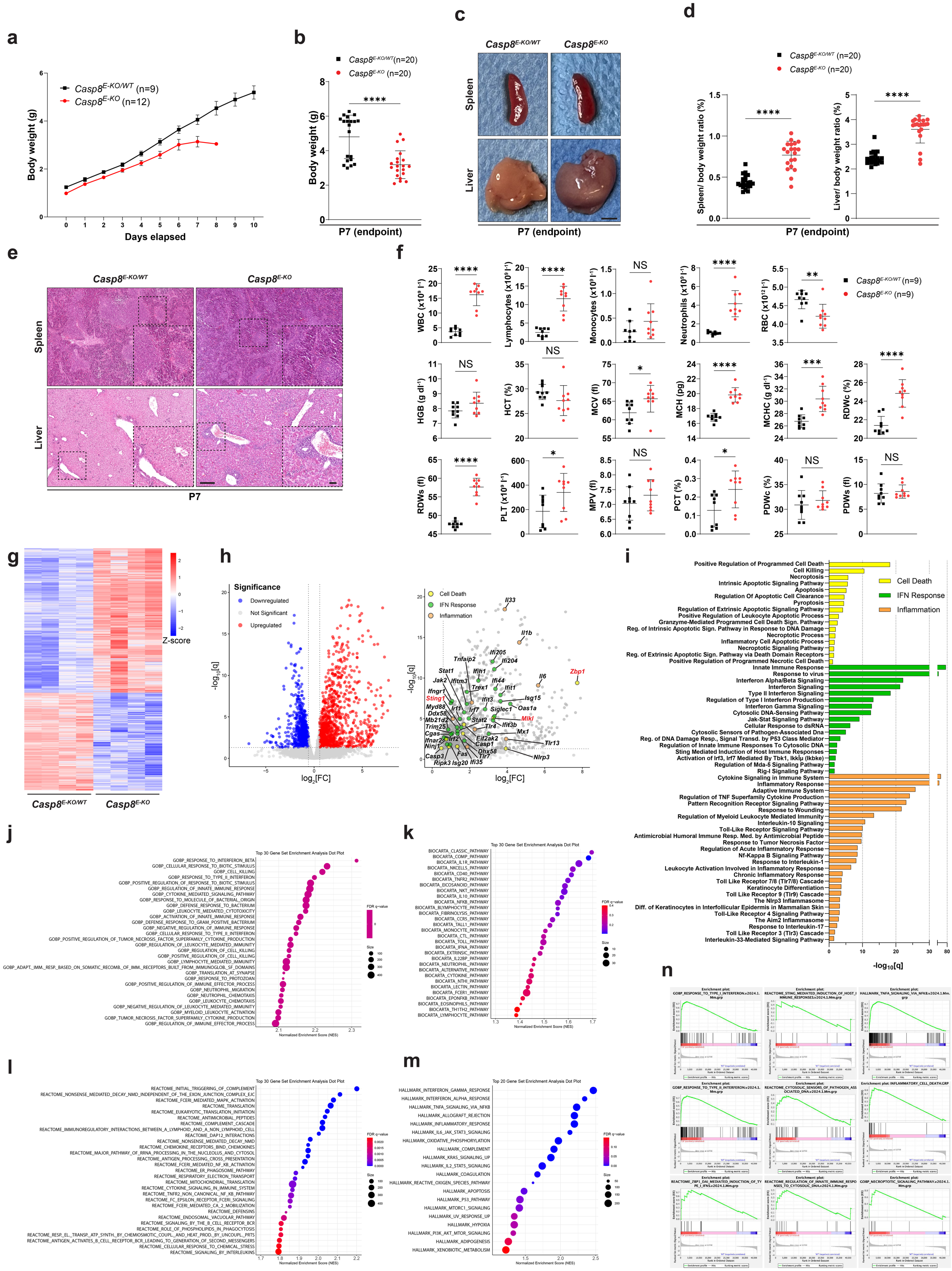

Extended Data Fig. 1 | See next page for caption.

Extended Data Fig. 1 | *Caspase-8* Loss Reprograms Keratinocytes to Induce ISGs, Necroptosis and DNA Sensing. **a**, Graph of the trajectory of body weight changes in *n* mice of indicated genotypes. **b**, Graph of body weight of *n* mice of indicated genotypes at survival endpoint (P7). **c**-**e**, Representative images (**c**), graphs of organ-to-body-weight ratio (**d**) and representative images of tissue sections stained with H&E (**e**) of spleen and liver of *n* mice of indicated genotypes. Scale bars: 2 mm (spleen and liver images), 200 µm (main bright-field images) and 50 µm (insets). **f**, Peripheral blood analysis of indicated values in mice of indicated genotypes at survival endpoint. $n = 9$ per group. **g**, Heatmap of row-scaled expression values of differentially expressed genes in *Casp8*$^{E\text{-}KO}$ versus *Casp8*$^{E\text{-}KO/WT}$ skin ($p\text{-}adj < 0.05$). **h**, Volcano plots depicting differentially expressed genes in *Casp8*$^{E\text{-}KO}$ versus *Casp8*$^{E\text{-}KO/WT}$ skin at P5. Genes with $|FC| > 1.5$ and $p\text{-}adj < 0.05$ are displayed. **i**, Pathway enrichment analysis of upregulated genes in *Casp8*$^{E\text{-}KO}$ versus *Casp8*$^{E\text{-}KO/WT}$ skin ($p\text{-}adj < 0.05$, $FC > 1$), using Metascape. Bar plot shows $-\log_{10}(q)$ values for enriched pathways. **j**-**m**, Dot plots of Gene Set Enrichment Analysis (GSEA) for top 20 or 30 upregulated pathways in *Casp8*$^{E\text{-}KO}$ versus *Casp8*$^{E\text{-}KO}$ control skin. Gene Ontology Biological Process (GOBP) (**j**), BioCarta (**k**), Reactome (**l**) and Hallmark (**m**) databases. Dot size indicates gene set size; colour intensity represents $-\log_{10}(p\text{-}adj)$. **n**, Enrichment plots for representative pathways identified by GSEA. Black vertical lines show positions of pathway genes in the ranked gene list. In **a**, **b**, **d** and **f**, data are presented as mean ± s.e.m.; each dot represents one mouse; *P* values were calculated via two-tailed unpaired t-test; $^{*}P \le 0.05$, $^{**}P \le 0.01$, $^{***}P \le 0.001$, $^{****}P \le 0.0001$; NS, not significant ($P > 0.05$). In **g**, **h**, differential gene expression analysis was performed using the Wald test as implemented in DESeq2, with *P* values adjusted for multiple testing using the Benjamini-Hochberg method (*p-adj*). MCV, mean corpuscular volume; MCHC, mean corpuscular haemoglobin concentration; RDWc, red cell distribution width (coefficient of variation); RDWs, red cell distribution width (standard deviation); PLT, platelets; MPV, mean platelet volume; PCT, plateletcrit; PDWc, platelet distribution width (coefficient of variation); PDWs, platelet distribution width (standard deviation).

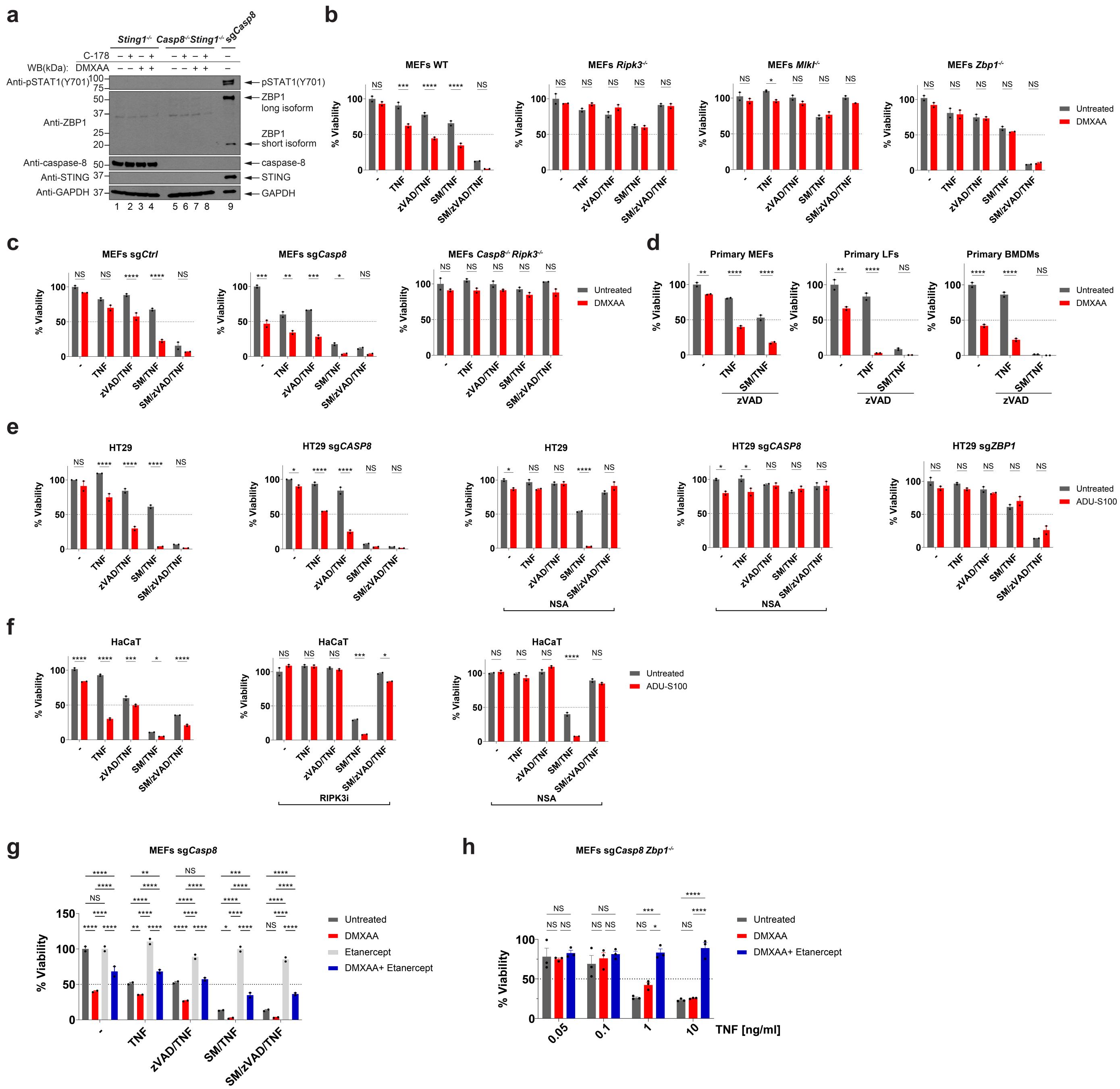

Extended Data Fig. 2 | STING sensitizes to Necroptosis via ZBP1 Independently of TNFR1. a, Immunoblot analysis with the indicated antibodies of lysates from immortalized *Sting1*$^{-/-}$ and *Casp8*$^{-/-}$ *Sting1*$^{-/-}$ MEFs treated with C-178 (10 µM) and DMXAA (20 µg ml^{-1}) for 48 h; sg*Casp8*$^{-/-}$ MEFs were used as control. **b**-**d**, Relative cell viability of immortalized WT, *Ripk3*$^{-/-}$, *Mlkl*$^{-/-}$ and *Zbp1*$^{-/-}$ MEFs (**b**), sg*Ctrl*, sg*Casp8*$^{-/-}$, *Casp8*$^{-/-}$;*Ripk3*$^{-/-}$ MEFs (**c**) and primary WT MEFs, lung fibroblasts (LFs) and bone-marrow-derived macrophages (BMDMs) assessed by CellTiter-Glo assay, pre-treated with DMXAA overnight, followed by treatment with recombinant TNF (100 ng ml^{-1}), Z-VAD-FMK (20 µM) and/or BV6 (2 µM) for 48 h. **e**, **f**, Relative cell viability of HT-29, HT-29 *CASP8*$^{-/-}$, HT-29 *ZBP1*$^{-/-}$ (**e**) and HaCaT (**f**) cells assessed by CellTiter-Glo assay, pre-treated with ADU-S100 (10 µM) alone or in combination with NSA (1 µM) or GSK'872 (RIPK3i, 10 mM) overnight, followed by treatment with recombinant TNF, Z-VAD-FMK and/or BV6 for 48 h. **g**, Relative cell viability of sg*Casp8*$^{-/-}$ MEFs assessed by CellTiter-Glo assay, pre-treated with DMXAA and/or Etanercept (50 µg ml^{-1}) overnight, followed by treatment with recombinant TNF, Z-VAD-FMK and/or BV6 for 48 h. **h**, Relative cell viability of immortalized sg*Casp8*$^{-/-}$;*Zbp1*$^{-/-}$ MEFs assessed by CellTiter-Glo assay, pre-treated with DMXAA and/or Etanercept overnight, followed by titration with recombinant TNF (0.05, 0.1, 1 and 10 ng ml^{-1}) for 48 h. In **b**-**h**, data are presented as mean ± s.e.m.; each dot represents an independent experiment each containing three technical replicates; *P* values were calculated via two-way Anova followed by Šidák multiple comparisons test; *$P \leq 0.05$, **$P \leq 0.01$, ***$P \leq 0.001$, ****$P \leq 0.0001$; NS, not significant ($P > 0.05$).

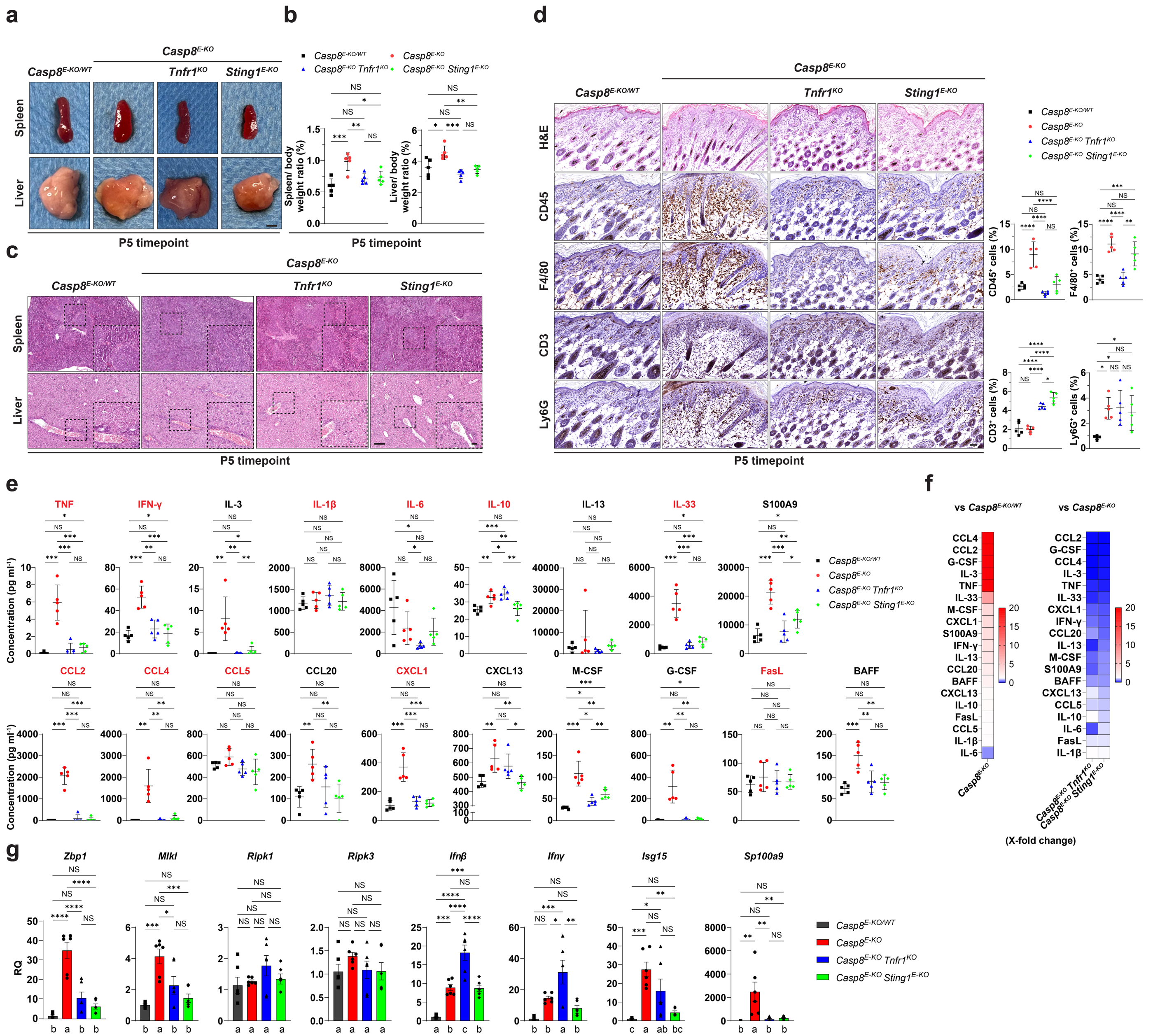

Extended Data Fig. 3 | TNFR1 or STING Loss Reveals Distinct Immune and Transcriptional Responses. **a**-**c**, Representative images (**a**), graphs of organ-to-body-weight ratio (**b**) and representative images of tissue sections stained with H&E (**c**) of spleen and liver of P5 mice of indicated genotypes. *n* = 5 per group. Scale bars: 2 mm (spleen and liver images), 200 µm (main bright-field images) and 50 µm (insets). **d**, Representative images of consecutive skin sections from P5 mice of indicated genotypes stained with H&E and the indicated antibodies. *n* = 5 per group. Scale bar: 50 µm. Graphs show immunostaining quantification. **e**, Graphs of cytokine levels (pg ml^{-1}) of skin homogenates from P5 mice of indicated genotypes, analysed via Luminex-Multiplex assay for the indicated targets. *n* = 5 per group. Cytokines highlighted in red denote those implicated in necroptosis, as detailed in Supplementary Table 1. Data are presented as mean ± s.e.m.; each dot represents one mouse; *P* values were calculated via two-tailed t-test. **f**, Heatmaps showing X-fold changes in cytokine levels relative to *Casp8*$^{E\text{-}KO/WT}$ control and *Casp8*$^{E\text{-}KO}$ respectively at P5. **g**, RT–qPCR analysis of mRNA expression of the indicated genes in skin from P5 mice of indicated genotypes. Graphs represent relative quantification (log_2RQ) normalized to *Gapdh*, with expression levels shown relative to *Casp8*$^{E\text{-}KO/WT}$. Data represent three biological replicates from two independent experiments. Different letters indicate statistically significant differences between groups, determined by one-way ANOVA followed by Tukey's HSD test (FDR = 0.05). In **b** and **d**, data in graphs are presented as mean ± s.e.m.; each dot represents one mouse; *P* values were calculated via two-way Anova followed by Tukey's multiple comparisons test; **P* ≤ 0.05, ***P* ≤ 0.01, ****P* ≤ 0.001, *****P* ≤ 0.0001; NS, not significant (*P* > 0.05).

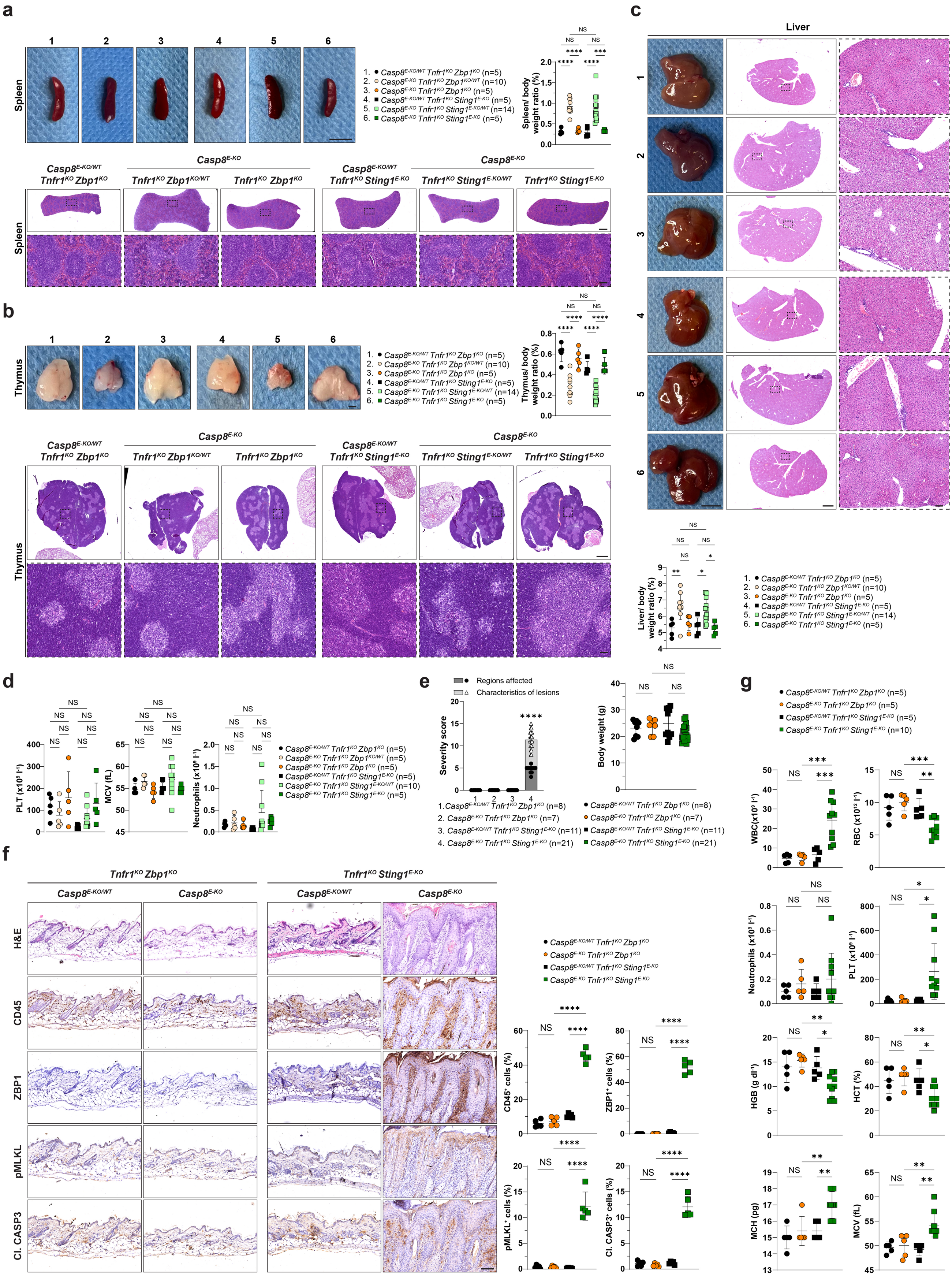

Extended Data Fig. 4 | See next page for caption.

Extended Data Fig. 4 | *Sting1$^{E\text{-}KO}$* Delays Lethal Inflammation in *Casp8$^{E\text{-}KO}$ Tnfr1$^{-/-}$* Mice. **a**-**c**, Representative images, graphs of organ-to-body-weight ratio and representative images of tissue sections stained with H&E of spleen (**a**), thymus (**b**) and liver (**c**) of 4-week-old mice of indicated genotypes. *n* values are indicated. Scale bars: 5 mm (spleen and liver images), 1 mm (thymus images), 1 mm (main bright-field images) and 100 µm (insets). **d**, Neutrophil, PLT and MCV values in peripheral blood from 4-week-old mice of indicated genotypes. *n* values are indicated. **e**, Graphs of dermatitis severity score and body weight of 12-14-week-old mice of indicated genotypes. *n* values are indicated. Control mice included age-matched *Casp8$^{E\text{-}KO/WT}$; Tnfr1^{KO}; Zbp1^{KO} and Casp8$^{E\text{-}KO/WT}$; Tnfr1^{KO}; Sting1$^{E\text{-}KO}$* littermates. **f**, Representative images of consecutive skin sections from 12-14-week-old mice of indicated genotypes stained with H&E and the indicated antibodies $n = 5$ per group. Scale bar: 100 µm. Graphs show immunostaining quantification. **g**, Peripheral blood analysis of indicated values in 12-14-week-old mice of indicated genotypes. *n* values are indicated. In **a**-**g**, data in graphs are presented as mean ± s.e.m.; each dot represents one mouse; *P* values were calculated via two-way Anova followed by Tukey's multiple comparisons test; *$P \le 0.05$, **$P \le 0.01$, ***$P \le 0.001$, ****$P \le 0.0001$; NS, not significant ($P > 0.05$).

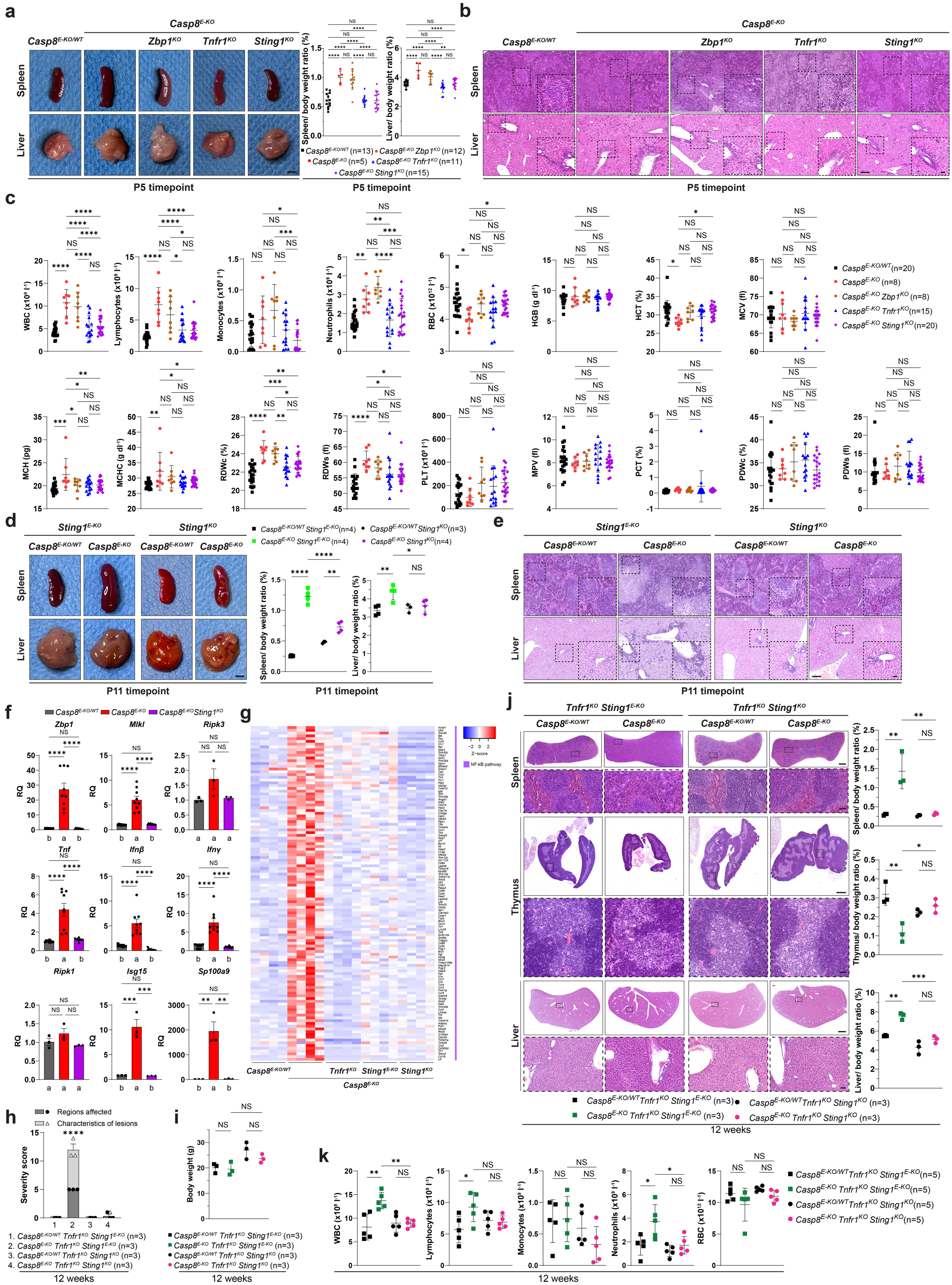

Extended Data Fig. 5 | See next page for caption.

Extended Data Fig. 5 | *Sting1*$^{-/-}$ inhibits early necroptosis and immune dysregulation in Casp8$^{E\text{-}KO}$. **a**, **b**, Representative images, graphs of organ-to-body-weight ratio (**a**) and H&E-stained tissue sections (**b**) of spleen and liver from P5 mice of indicated genotypes. *n* values are indicated. Scale bars: 2 mm (spleen and liver images), 200 µm (main bright-field images) and 50 µm (insets). **c**, Peripheral blood analysis of indicated values in P5 mice of indicated genotypes. *n* values are indicated. **d**, **e**, Representative images, graphs of organ-to-body-weight ratio (**d**) and H&E-stained tissue sections (**e**) of spleen and liver from *n* mice of indicated genotypes at the survival endpoint of *Casp8*$^{E\text{-}KO}$*; Sting1*$^{E\text{-}KO}$ mice (P11). Scale bars: 2 mm (spleen and liver images), 200 µm (main bright-field images) and 50 µm (insets). **f**, RT–qPCR analysis of gene expression in skin from P5 mice of indicated genotypes. Graphs represent relative quantification ($\log_2$ RQ) normalized to *Gapdh*, relative to *Casp8*$^{E\text{-}KO/WT}$. Data represent three biological replicates from one or two independent experiments as indicated. Different letters indicate statistically significant differences between groups, determined by one-way ANOVA followed by Tukey's HSD test (FDR = 0.05). **g**, Heatmap of NF-κB-associated genes downregulated in *Casp8*$^{E\text{-}KO}$*; Tnfr1*^{KO}, *Casp8*$^{E\text{-}KO/WT}$*; Sting1*^{KO}, or both, compared to *Casp8*$^{E\text{-}KO}$ mice. Expression values are DESeq2-normalized, row-scaled, and colour-coded by intensity (red, high; blue, low). Differential expression was determined using the Wald test in DESeq2 with Benjamini–Hochberg adjusted *p*-values (*p-adj* < 0.05). **h**-**k**, Graphs of dermatitis score (**h**) and body weight (**i**), representative images of indicated H&E-stained tissue sections with corresponding graphs of organ-to-body-weight ratio (**j**), and peripheral blood analysis of indicated values (**k**) in 12-week-old mice of indicated genotypes. *n* values are indicated. Scale bars: 1 mm (main images) and 100 µm (insets). In **a**, **c**, **d** and **h**-**k**, data in graphs are presented as mean ± s.e.m.; each dot represents one mouse; *P* values were calculated via two-way Anova followed by Tukey's multiple comparisons test; **P* ≤ 0.05, ***P* ≤ 0.01, ****P* ≤ 0.001, *****P* ≤ 0.0001; NS, not significant (*P* > 0.05).

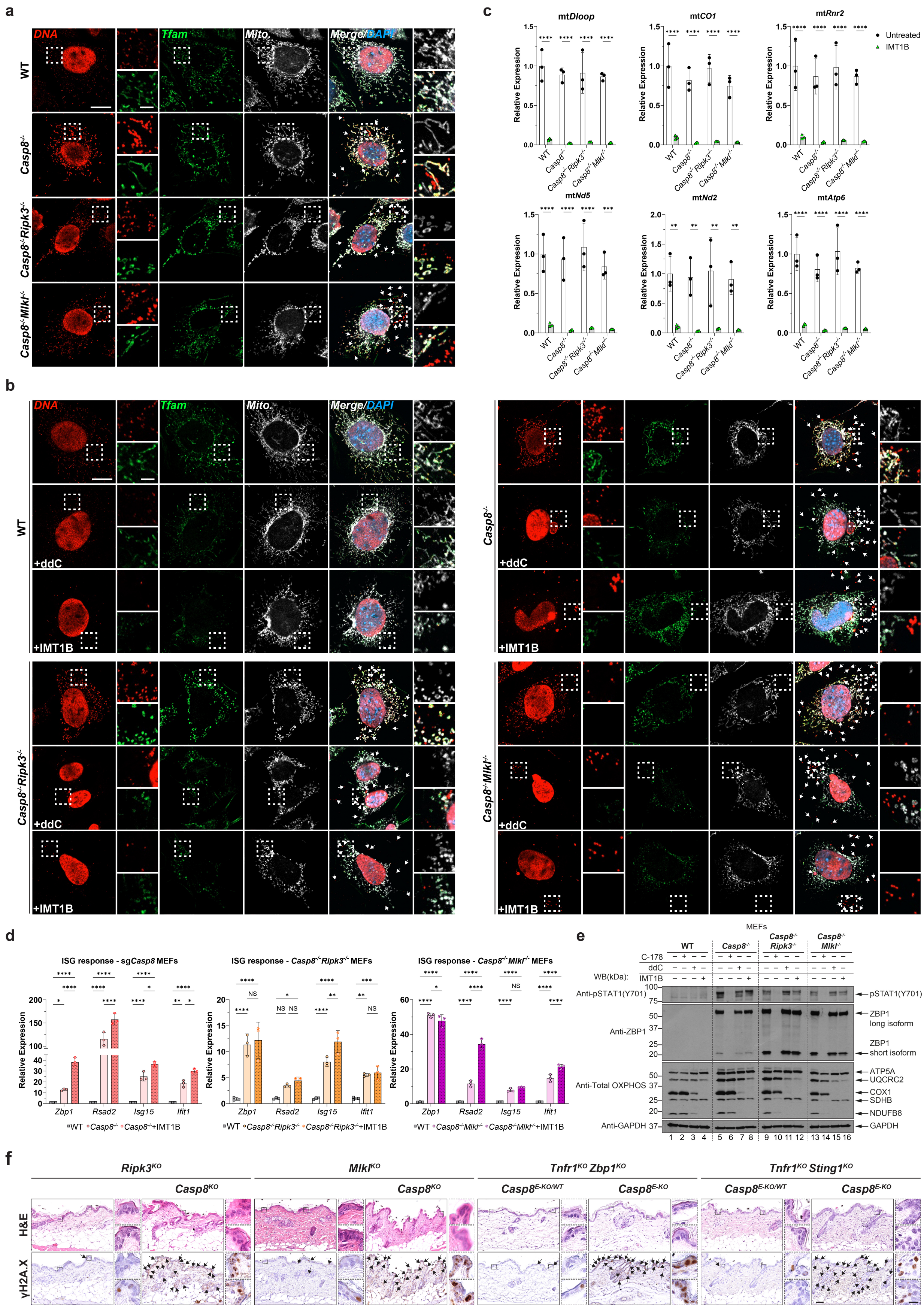

Extended Data Fig. 6 | See next page for caption.

Extended Data Fig. 6 | STING Activation is not mediated by Mitochondrial DNA. a, **b**, Confocal images of indicated MEFs stained for DNA (Alexa Fluor 594, red), TFAM (Alexa Fluor 488, green), mitochondria (MitoTracker Deep Red) and nuclei (DAPI, blue) untreated (**a**, **b**) or following 96 h treatment with ddC (150 μM) or IMT1B (10 μM) (**b**). Insets highlight magnified regions. Arrows mark DNA foci lacking TFAM and MitoTracker signals. Images represent single optical slices (0.4 μm). n≥ 20 cells/condition. Scale bars: 10 μm and 1 μm (insets). **c**, **d** RT–qPCR analysis of indicated mitochondrial genes to assess mtDNA depletion (**c**), and of indicated ISGs to assess IFN response (**d**), in the indicated MEFs. Data are shown as relative expression ($\log_2$) to untreated WT control normalized to *beta-Actin*; graphs represent mean ± s.e.m. $n = 3$ technical replicates; P values were calculated via two-way Anova followed by Tukey's multiple comparisons test; $^{*}P \le 0.05$, $^{**}P \le 0.01$, $^{***}P \le 0.001$, $^{****}P \le 0.0001$; NS, not significant ($P > 0.05$). **e**, Immunoblot analysis of lysates from the indicated MEFs treated with C-178 (10 μM), ddC, or IMT1B as above for 96 h. **f**, Representative images of consecutive skin sections from 12-4-week-old mice of indicated genotypes stained with H&E and the indicated antibodies. $n = 5$ per group. Arrows indicate γH2A.X positive areas/cells. Scale bars: 100 μm (main images) and 10 μm (insets).

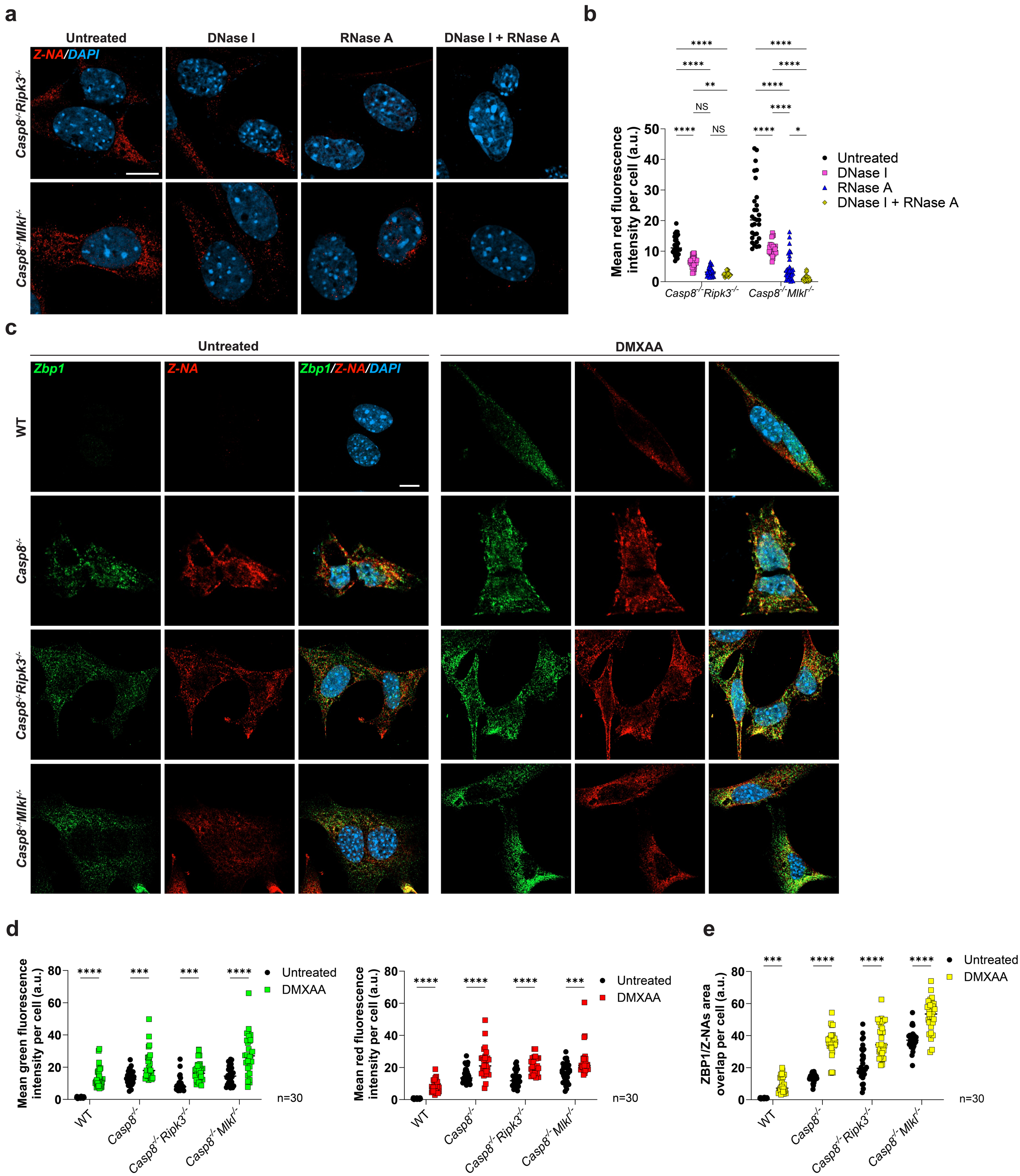

Extended Data Fig. 7 | STING activation enhances ZBP1-Associated Z-NA Accumulation. **a**, **b**, Confocal images of indicated MEFs stained for Z-NA (Alexa Fluor 594, red) and nuclei (DAPI, blue) under basal conditions or following treatment with DNase I (25 U mL^{-1}) and/or RNase A (1 mg mL^{-1}) (**a**) and quantification of mean Z-NA (red) fluorescence intensity (**b**). **c**-**e**, Confocal images of indicated MEFs stained for Z-NA (Alexa Fluor 594, red), ZBP1 (Alexa Fluor 488, green) and nuclei (DAPI, blue) untreated or following 48 h treatment with DMXAA (20 µg ml^{-1}) (**c**), quantification of ZBP1 (green) and Z-NA fluorescent intensity (red) (**d**) and their area of overlap (**e**). Images represent single optical slices (0.4 µm). Scale bar: 10 µm. In **b**, **d** and **e**, data are presented as mean ± s.e.m.; each dot represents one cell and 30 cells/condition were analysed via two-way Anova followed by Tukey's multiple comparisons test; $^{*}P \le 0.05$, $^{**}P \le 0.01$, $^{***}P \le 0.001$, $^{****}P \le 0.0001$; NS, not significant ($P > 0.05$).

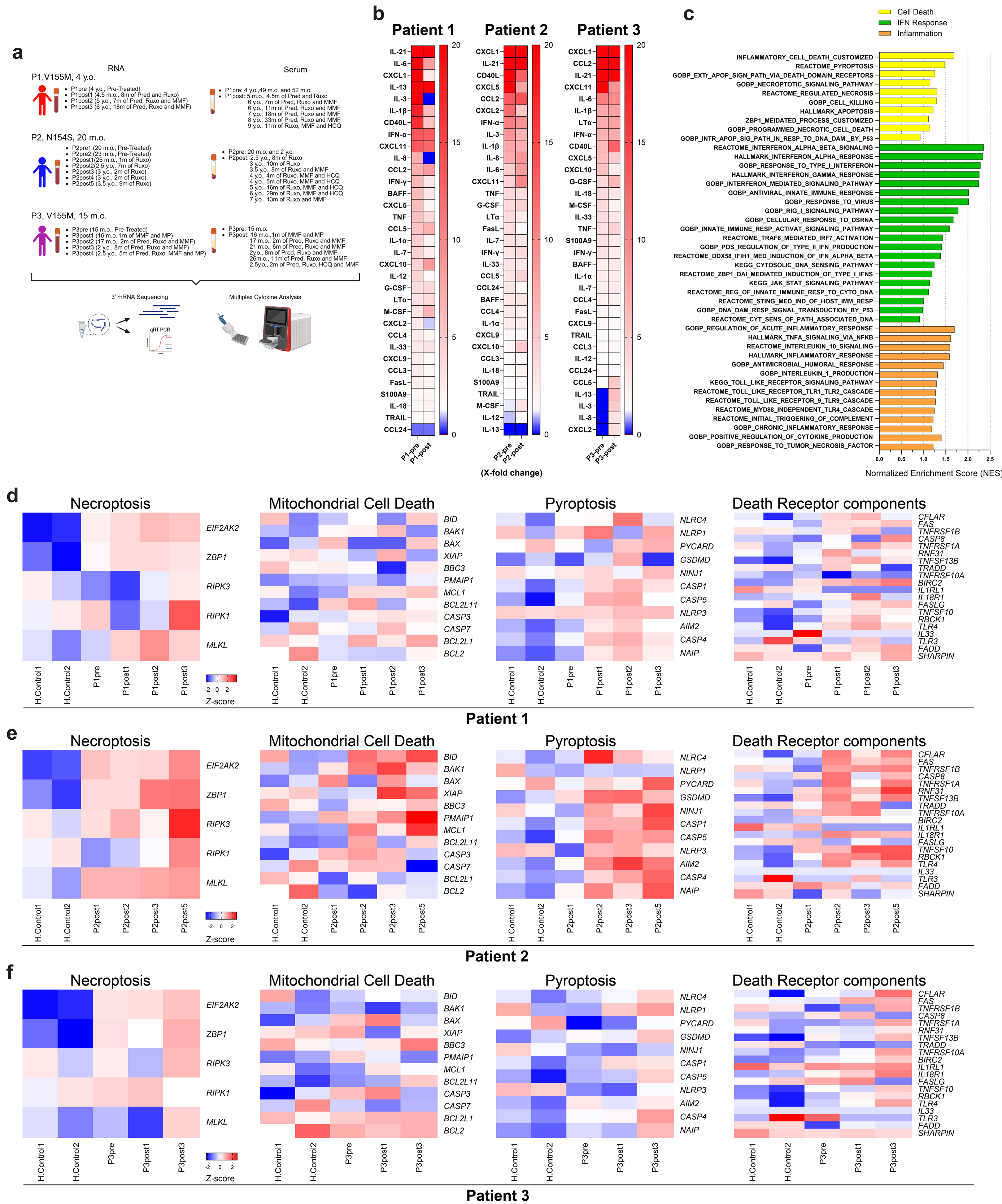

Extended Data Fig. 8 | See next page for caption.

Extended Data Fig. 8 | SAVI longitudinal Samples Show Inflammatory IFN and Necroptosis Signatures. a, Schematic representation of SAVI patient samples, illustrating patient mutations, sample types, and timepoints of sample collection during the treatment course. Notation: P(x)post/pre(y), where x = patient number, y = sample number, pre = pre-treatment, and post = post-treatment, Pred: Prednisone, MTX: Methotrexate, Ruxo: Ruxolitinib, MMF: Mycophenolate, HCQ: Hydroxychloroquine and MP: Metilprednisolone. This image was created in BioRender. Saggau, J. (2025) https://BioRender.com/9yrgm6e. **b**, Heatmaps showing X-fold changes in cytokine levels relative to healthy controls for each patient. **c**, Pathway enrichment analysis bar plot from GSEA analysis for Gene Ontology Biological Process (GOBP), Hallmark, Reactome, and KEGG databases, as well as manually curated gene sets for inflammatory cell death and ZBP1-mediated processes in high-IFN patient samples. **d-f**, Heatmaps depicting DEseq2-normalized expression levels of selected genes involved in necroptosis, mitochondrial cell death, pyroptosis, and death receptor components in IFN-high samples from Patient 1 (**d**), Patient 2 (**e**), and Patient 3 (**f**) and healthy donors. Expression values are DESeq2-normalized, row-scaled, and colour-coded by intensity (red, high; blue, low). Differential expression was determined using the Wald test in DESeq2 with Benjamini–Hochberg adjusted *P*-values (p-adj < 0.05).

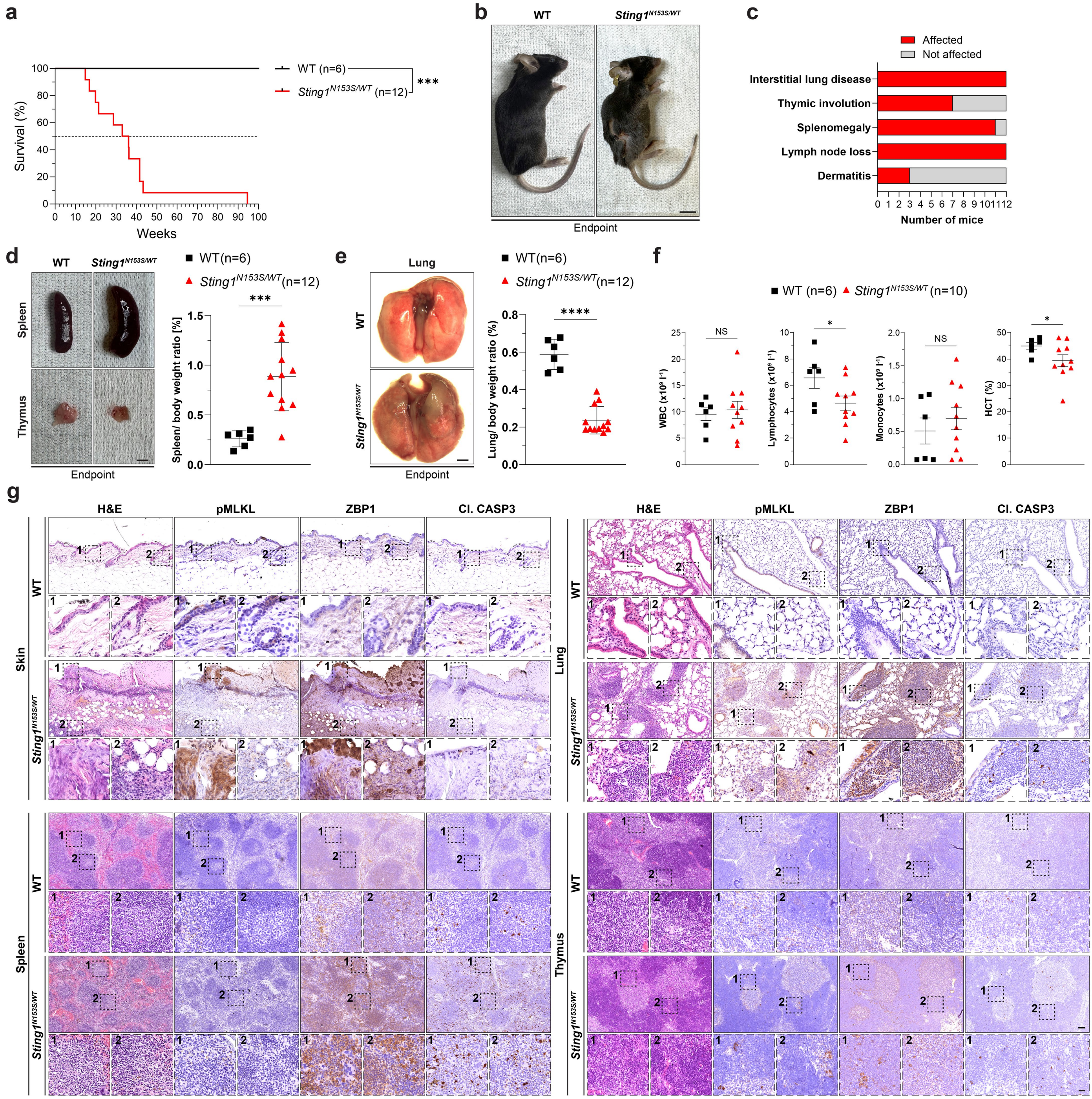

Extended Data Fig. 9 | STAIN promotes Systemic Inflammation in SAVI mice. **a**, Kaplan–Meier survival curves of mice of indicated genotypes. *n* values are indicated. *p* values were calculated by two-sided Gehan–Breslow–Wilcoxon test. **b**-**e**, Representative images (**b**), bar plot showing the distribution of SAVI-associated clinical manifestations (**c**) and representative images and graphs of organ-to-body-weight ratio of spleen, thymus (**d**) and lung (**e**) of *Sting1*$^{N153S/WT}$ mice at survival endpoint (*n* indicated. Examined lymph nodes include axillary, inguinal, and submandibular). Scale bars: 3 mm (spleen and thymus images) and 2 mm (lung images). **f**, Peripheral blood analysis of indicated values in endpoint *Sting1*$^{N153S/WT}$ mice. *n* values are indicated. **g**, Representative images of consecutive skin, lung, spleen and thymus sections from *Sting1*$^{N153S/WT}$ at survival endpoint stained with H&E and the indicated antibodies. *n* = 5 per group. Scale bars: 100 µm (main images) and 20 µm (insets). In **a**-**g**, age-matched WT littermates were used as controls. In **d**-**f**, data are presented as mean ± s.e.m.; each dot represents one mouse; *P* values were calculated via two-tailed unpaired t-test; **P* ≤ 0.05, ****P* ≤ 0.001, *****P* ≤ 0.0001; NS, not significant (*P* > 0.05).

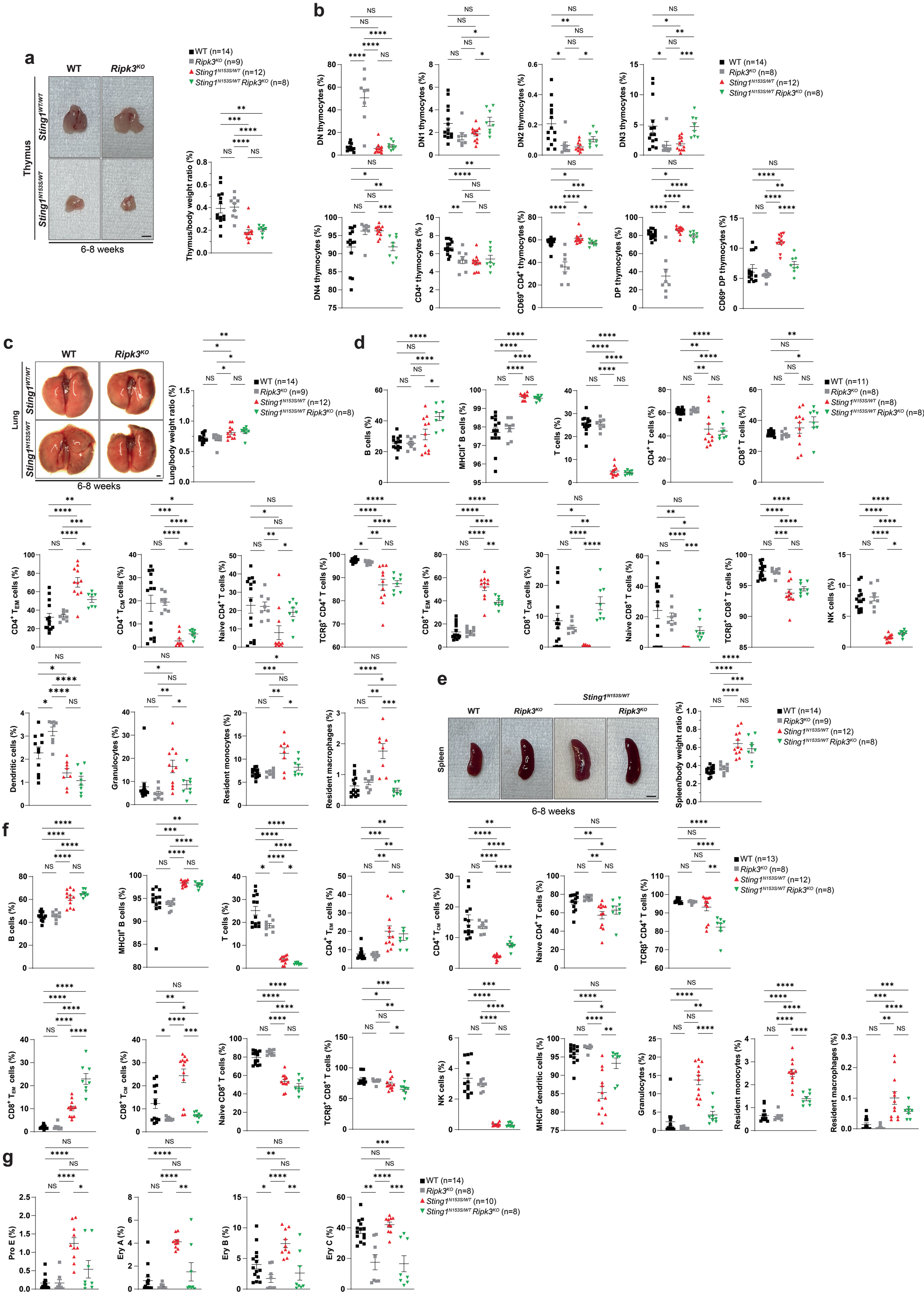

Extended Data Fig. 10 | See next page for caption.

Extended Data Fig. 10 | STAIN promotes Immune Depletion in SAVI mice. **a**, **b**, Representative images, organ-to-body-weight ratio (**a**) and flow cytometric thymocyte phenotyping (**b**) of thymi from 6-8-week-old mice of indicated genotypes. *n* values are indicated. $CD4^{-}CD8^{-}$ (double negative; DN), $CD4^{+}CD8^{+}$ (double positive; DP) and $CD4^{+}$ thymocytes are depicted as percentage of viable cells. All other populations were plotted as percentage of their parental populations. **c**, **d**, Representative images, organ-to-body-weight ratio (**c**) and flow cytometric phenotyping (**d**) of lungs from 6-8-week-old mice of indicated genotypes. *n* values are indicated. Immune cells are depicted as percentage of $CD45^{+}$ cells and their respective sub-populations are shown as percentage of parental populations. **e**-**g**, Representative images, organ-to-body-weight ratio (**e**) and flow cytometric immune cell phenotyping (**f**) and erythrocyte phenotyping (**g**) of spleens of 6-8-week-old mice of the indicated genotypes. *n* values are indicated. Immune cell types are depicted as percentage of $CD45^{+}$ cells, their respective sub-populations are shown as percentage of parental populations and erythrocytes were plotted as percentage of live cells. In **a**-**g**, age-matched WT and *Ripk3*^{KO} littermates were used as controls,;data are presented as mean ± s.e.m.; each dot represents one mouse; *P* values were calculated via two-way Anova followed by Tukey's multiple comparisons test (**a**, **c** and **e**) or via two-tailed unpaired t-test (**b**, **d**, **f** and **g**); $^{*}P \le 0.05$, $^{**}P \le 0.01$, $^{***}P \le 0.001$, $^{****}P \le 0.0001$; NS, not significant ($P > 0.05$). The gating strategy for cell populations shown in **b**,**d**,**f** and **g** is provided in Supplementary Fig. 9.

Supplementary Figure 1

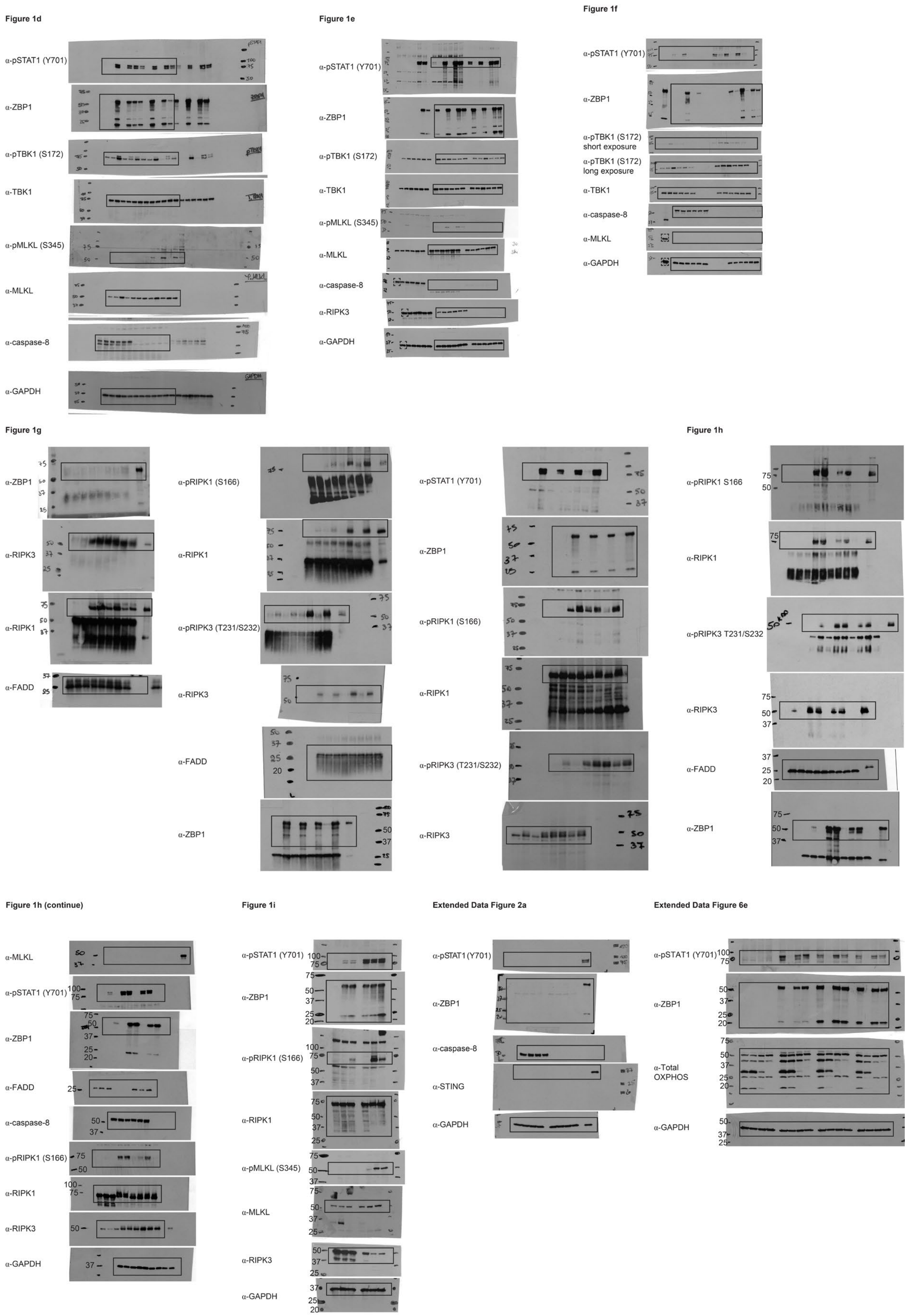

Uncropped western blot images. GAPDH was used as a loading control and was blotted on the same membranes, provided that no proteins of interest ran near ~37 kDa. At least two membranes per western blot/figure were used to ensure proper loading control assessment.

Supplementary Figure 2

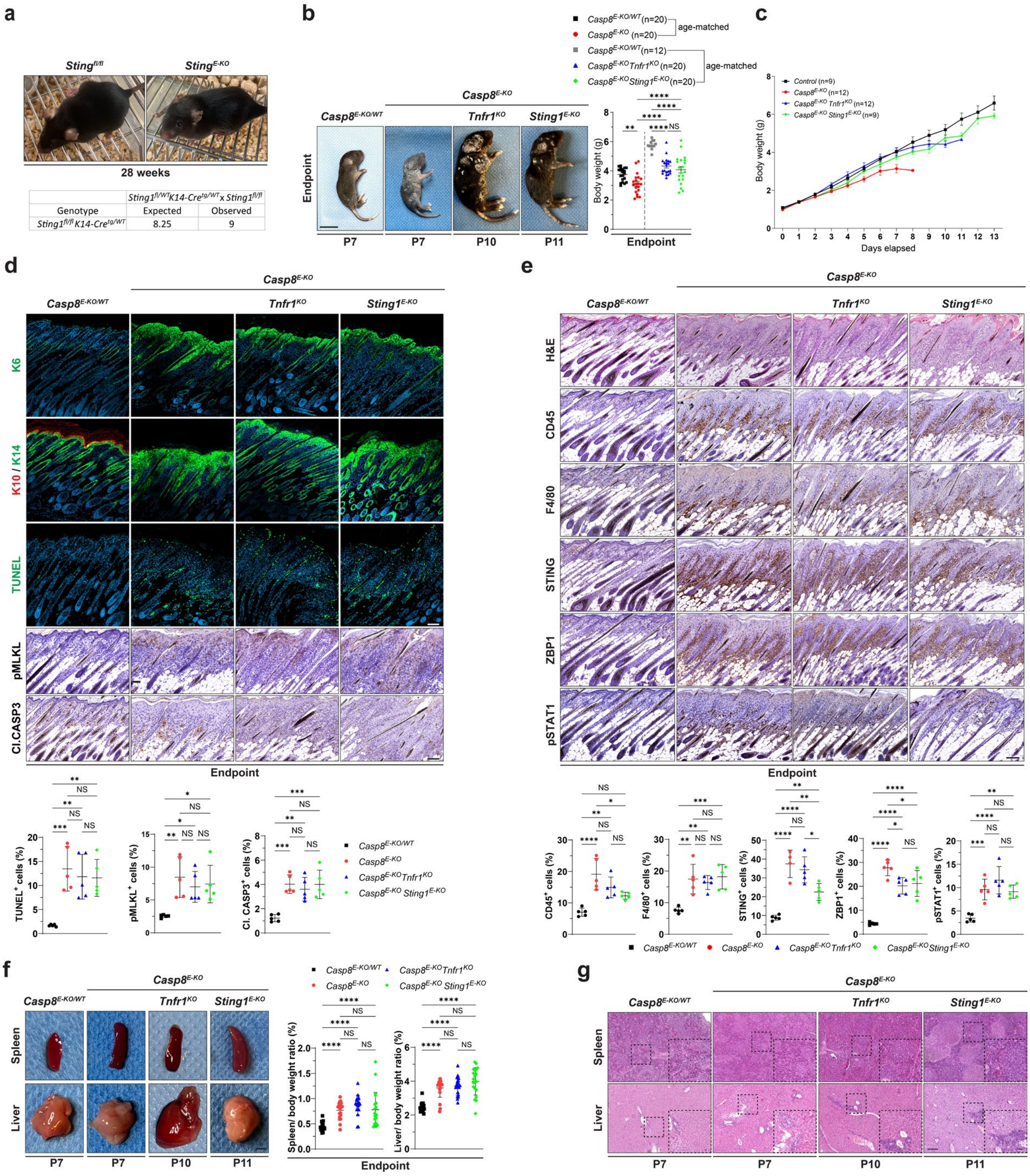

a, Representative images of *Sting1*$^{E\text{-}KO}$ and *Sting1*$^{fl/fl}$ mice and table of expected and observed numbers of weaned offspring with the designated genotypes resulting from intercrosses of parents with the indicated genotypes. **b**, Representative images and graphs of body weight of *n* mice with the indicated genotypes at their survival endpoint as indicated. Scale bar: 1 cm. **c**, Graph of the trajectory of body weight changes in mice with the indicated genotypes. *n* values are indicated. **d**, **e**, Representative images of consecutive skin sections from mice with the indicated genotypes stained for K6 (Alexa Fluor 488, green), K10 (Alexa Fluor 594, red), K14 (Alexa Fluor 488, green), TUNEL (fluorescein, green), nuclei (DAPI, blue), pMLKL-S345, Cl.CASP3 (**d**) and H&E, CD45, F4/80, STING, pSTAT1-Y701 and ZBP1 (**e**) at the indicated survival endpoint. *n*=5 per group. Scale bars: 100 µm. Graphs show immunostaining quantification. **f**, **g**, Representative images, graphs of organ-to-body-weight ratio (**f**) and representative images of tissue sections stained with H&E (**g**) of spleen and liver of mice with the indicated genotypes at survival endpoint as indicated. *n*=20 per group. Control mice included age-matched *Casp8*$^{E\text{-}KO/WT}$ littermates. Scale bars: 2 mm (spleen and liver images), 200 µm (bright-field images) and 50 µm (inserts). In **b**-**f**, data are presented as mean ± s.e.m.; each dot represents one mouse; control mice included age-matched *Casp8*$^{E\text{-}KO/WT}$ littermates; *P* values were calculated via two-way Anova followed by Tukey's multiple comparisons test; *$P \leq 0.05$, **$P \leq 0.01$, ***$P \leq 0.001$, ****$P \leq 0.0\ 01$; NS, not significant (P>0.05).

Supplementary Figure 3

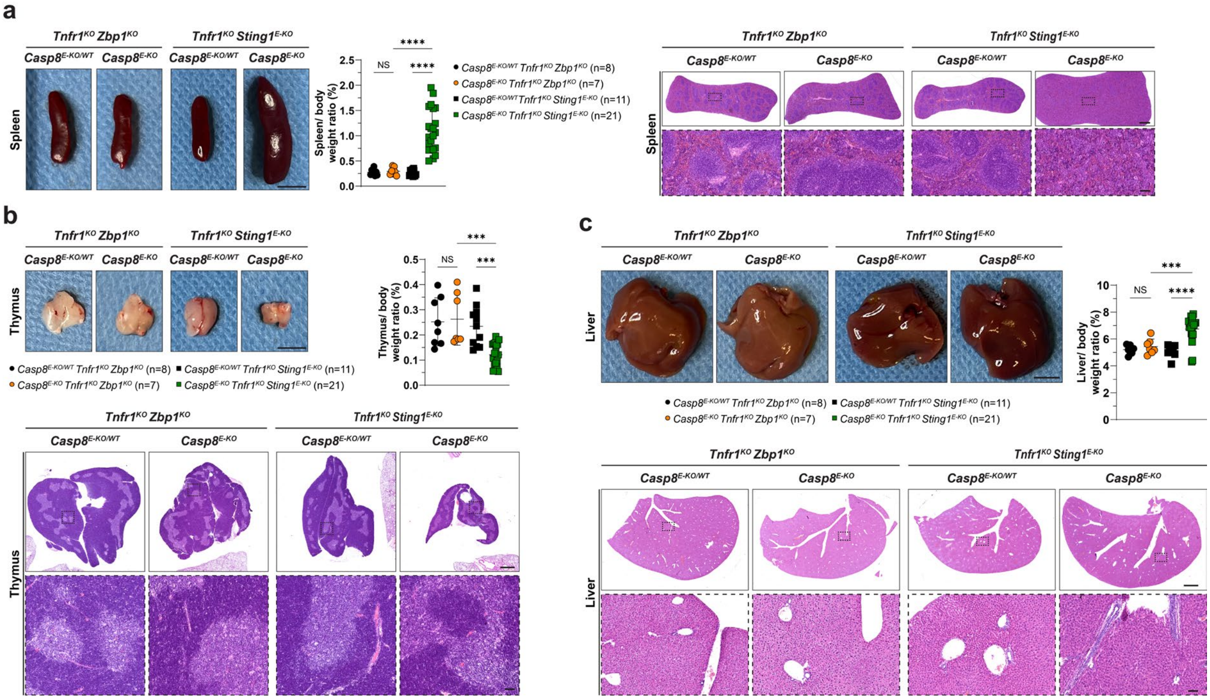

a-**c**, Representative images, graphs of organ-to-body-weight ratio and representative images of tissue sections stained with H&E of spleen (**a**), thymus (**b**) and liver (**c**) of 12-14-week-old mice with the indicated genotypes. *n* values are indicated. Scale bars: 5mm (spleen, liver and thymus images), 1 mm (bright-field images) and 100 µm (insets). Data in graphs are presented as mean ± s.e.m.; each dot represents one mouse; *P* values were calculated via two-way Anova followed by Tukey's multiple comparisons test; ***$P \leq 0.001$, ****$P \leq 0.0001$; NS, not significant (P>0.05).

Supplementary Figure 4

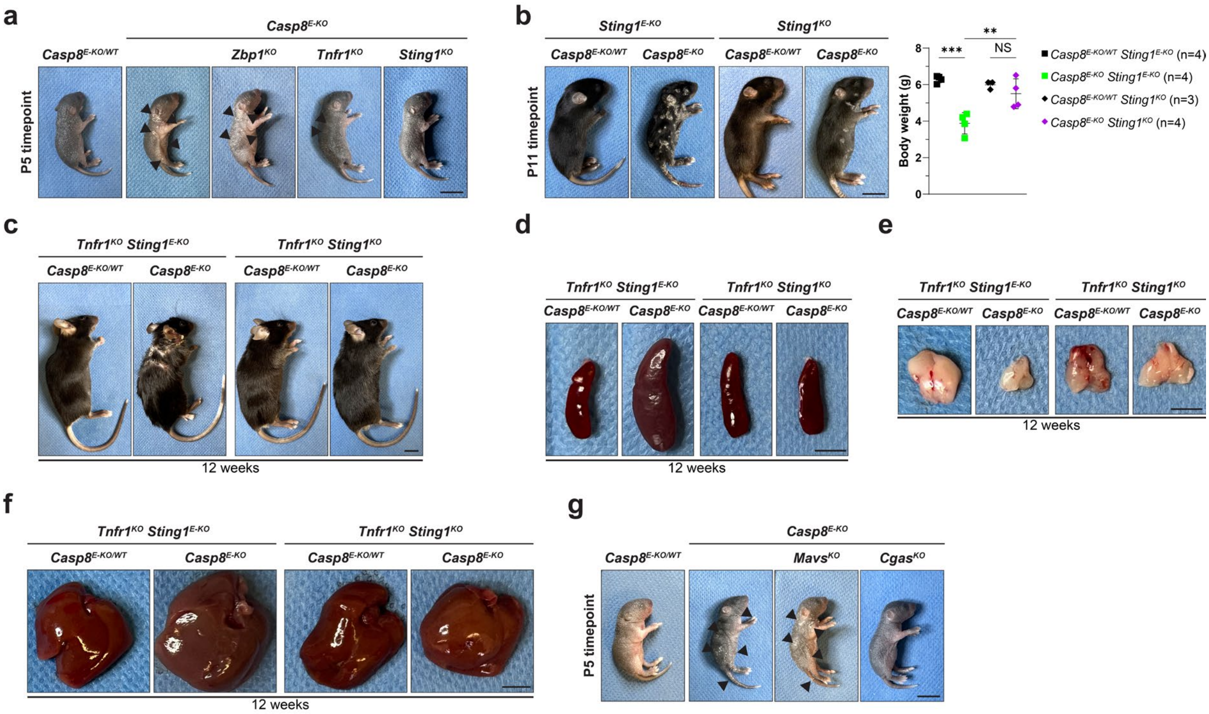

a, Representative images of mice with the indicated genotypes at P5. $n = 5$ per group. Scale bar: 1 cm. **b**, Representative images and graph of body weight of n mice of the indicated genotypes at the survival endpoint of $Casp8^{E\text{-}KO}$ $Sting1^{KO}$ mice (P11). Control mice included age-matched $Casp8^{E\text{-}KO/WT}$ $Sting1^{E\text{-}KO}$ and $Casp8^{E\text{-}KOWT}$ $Sting1^{KO}$ littermates. Scale bar: 1 cm. Data in graph are presented as mean ± s.e.m.; each dot represents one mouse; P values were calculated via two-way Anova followed by Tukey's multiple comparisons test; $^{**}P \leq 0.01$, $^{***}P \leq 0.001$; NS, not significant (P>0.05). **c**-**f**, Representative images of mice (**c**) and spleen (**d**), thymus (**e**) and liver (**f**) of 12-week-old mice of the indicated genotypes. n=3 per group. Control mice included age-matched $Casp8^{E\text{-}KO/WT}$ $Tnfr1^{KO}$ $Sting1^{E\text{-}KO}$ and $Casp8^{E\text{-}KO/WT}$ $Tnfr1^{KO}$ $Sting1^{KO}$ littermates. Scale bars: 1 cm (mouse images), 5mm (spleen, liver and thymus images). **g**, Representative images of mice with the indicated genotypes at P5. n=3 per group. Scale bar: 1 cm. In **a**, **g** arrows indicate areas with lesions.

Supplementary Figure 5

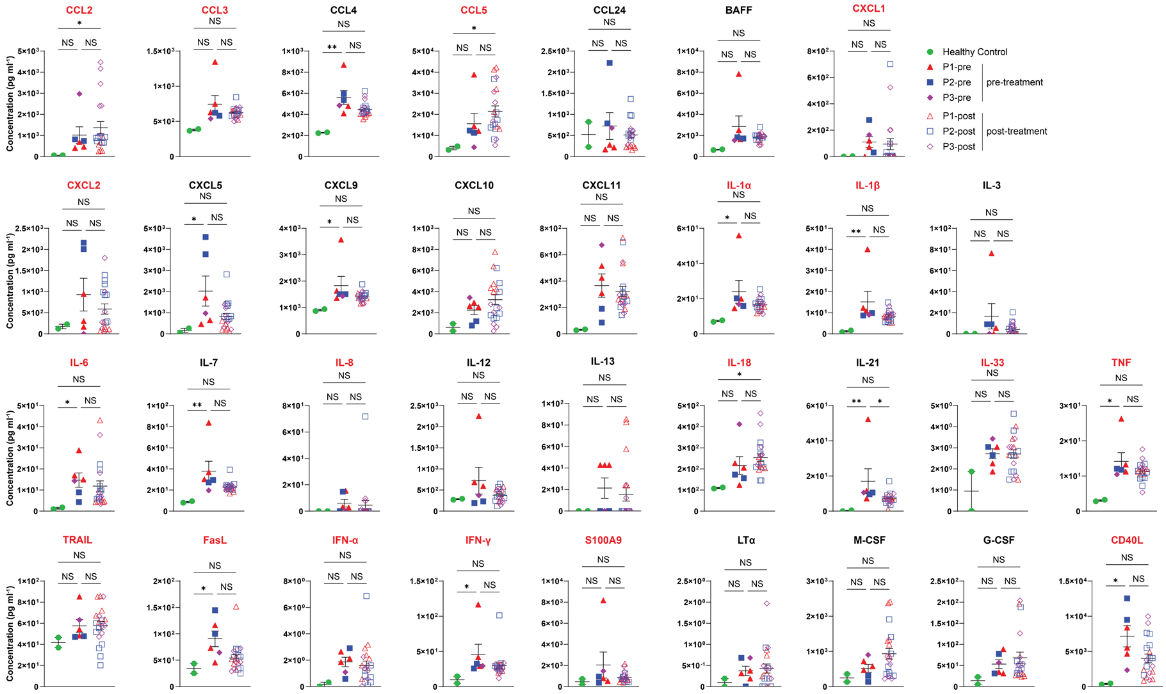

Graphs of cytokine levels (pg ml^{-1}) in plasma samples from SAVI patients, pre- and post-treatment as indicated and healthy controls, analysed via Luminex-Multiplex assay for the indicated targets. Cytokines highlighted in red denote those implicated in necroptosis, as detailed in Supplementary Table 1. Data are presented as mean ± s.e.m.; *P* values were calculated via Kruskal-Wallis test followed by Dunn's multiple comparisons test; *$P \leq 0.05$, **$P \leq 0.01$; NS, not significant (P>0.05).

Supplementary Figure 6

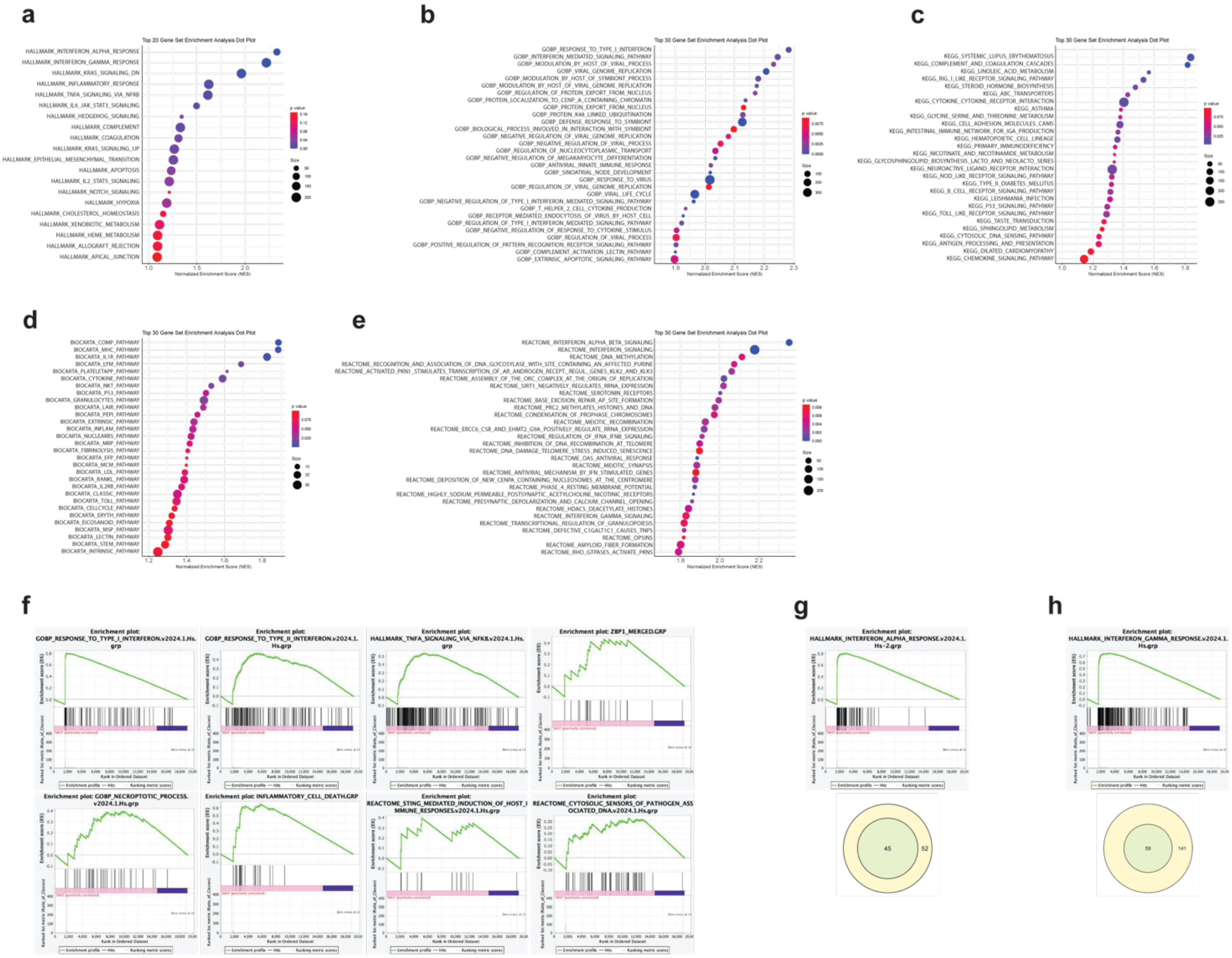

a-e, Dot plots from Gene Set Enrichment Analysis (GSEA) for top 20 or 30 upregulated pathways in SAVI IFN-high patients versus healthy donors. Hallmark (**a**), Gene Ontology Biological Process (GOBP) (**b**), KEGG (**c**), BioCarta (**d**), and Reactome (**e**) databases. Dot size represents gene count; colour intensity indicates $-\log_{10}(p\text{-}adj)$. **f**, Enrichment plots for representative enriched pathways. Normalised Enrichment scores (NES) and positions of gene set members (black vertical lines) in the ranked gene list are shown. **g**, **h**, Enrichment plots for Type I (**g**) and Type II (**h**) interferon responses. Venn diagrams next to each plot show the overlap between upregulated interferon-related genes in IFN-high SAVI sample vs healthy control (green) and the genes in the Hallmark interferon gene sets (yellow).

Supplementary Figure 7

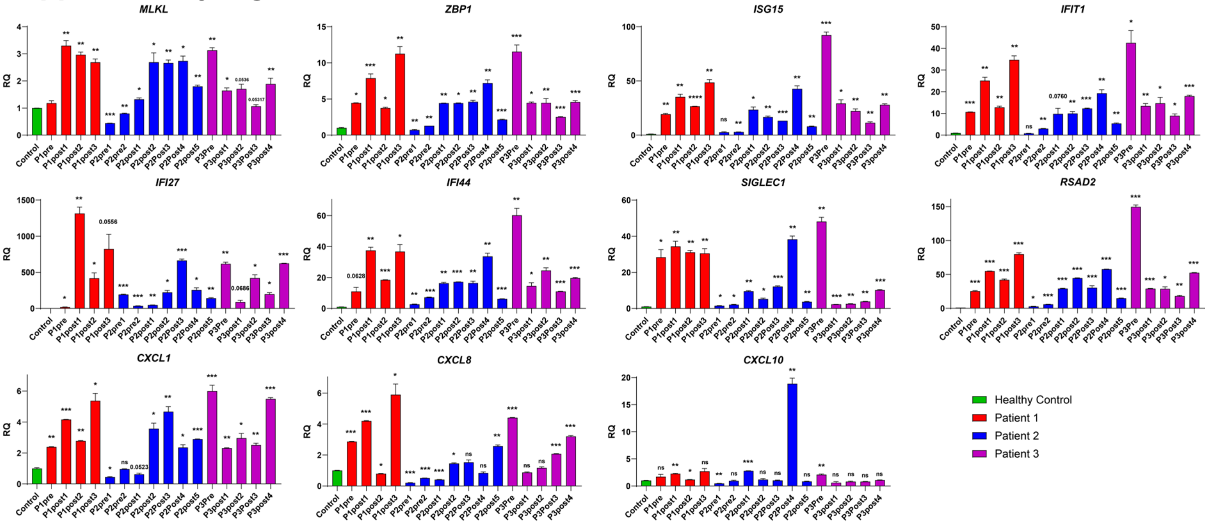

RT-qPCR analysis of mRNA expression of the indicated genes in whole blood of SAVI patients, pre- and post-treatment as indicated and healthy controls. Graphs represent relative quantification (RQ, $\log_2$) to healthy controls. Transcript levels were normalised to the housekeeper gene *HPRT.* Data are presented as mean ± s.d. from three technical replicates; *P* values were calculated via two-tailed t-test; **P* ≤ 0.05, ***P* ≤ 0.01, ****P* ≤ 0.001, *****P* ≤ 0.0001; NS, not significant (*P*>0.05).

Supplementary Figure 8

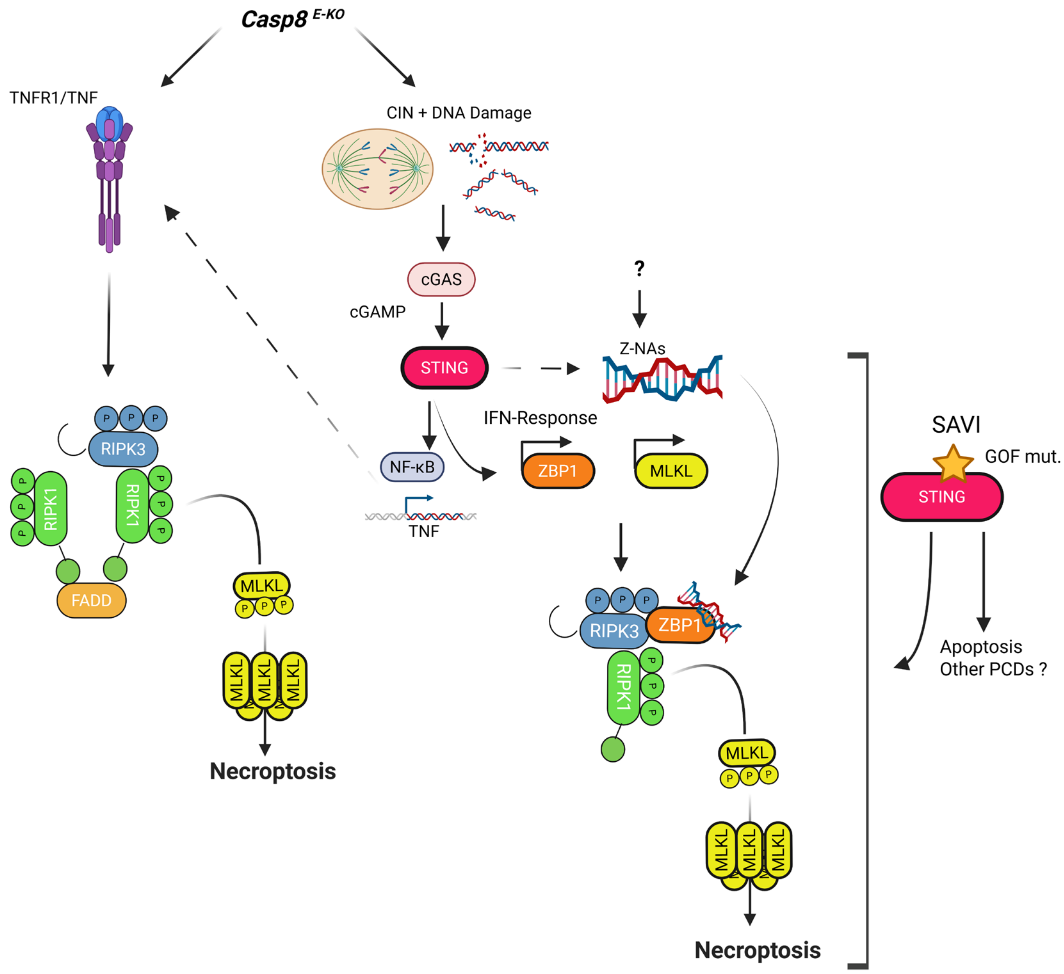

Our model illustrates the existence of two parallel, mechanistically distinct necroptotic pathways that become activated upon caspase-8 deficiency: a canonical TNF–TNFR1–FADD–RIPK1–RIPK3 axis (left), and a STING-driven, ZBP1–RIPK3–MLKL axis (right). Upon loss of Casp8, mitotic errors and DNA damage result in the accumulation of cytosolic DNA, activating the cGAS–STING pathway. STING activation induces a robust type I interferon response and NF-κB signalling, leading to transcriptional upregulation of key necroptotic effectors including ZBP1 and MLKL. Concurrently, STING promotes the accumulation or stabilization of endogenous Z-form nucleic acids (Z-NAs), which serve as ligands for ZBP1 activation. Activated ZBP1 forms a necrosome-like complex with RIPK3 and RIPK1, enabling MLKL phosphorylation and necroptotic cell death in a TNFR1-independent manner. STING also partially amplifies the canonical TNFR1 checkpoint by promoting autocrine TNF expression through NF-κB activation, thereby reinforcing TNF-mediated necroptosis. This positions STING as a central, shared regulator of both necroptotic checkpoints. Genetic evidence demonstrates that ZBP1 and STING are required for the TNFR1-independent arm of necroptosis in caspase-8-deficient keratinocytes, and that STING function extends beyond the epidermis to drive systemic inflammation via cell-extrinsic necroptosis in immune and stromal cells. Together, these data identify aberrant STING activation as a dual-function driver of necroptosis initiation and propagation, offering mechanistic insight into inflammatory disease in settings of caspase-8 loss. In the context of a STING gain-of-function (GOF) mutation, as observed in the SAVI model, necroptosis plays both pathogenic role as well as contributes to the manifestation of the disease. However, the presence of cleaved caspase-

3–positive cells in affected tissues also suggests activation of apoptotic pathways. Thus, while our findings identify necroptosis as a major contributor to SAVI pathogenesis and manifestation, they do not exclude the involvement of other programmed cell death (PCD) modalities. Created in *https://BioRender.com/l84v2zc.*

Supplementary Figure 9

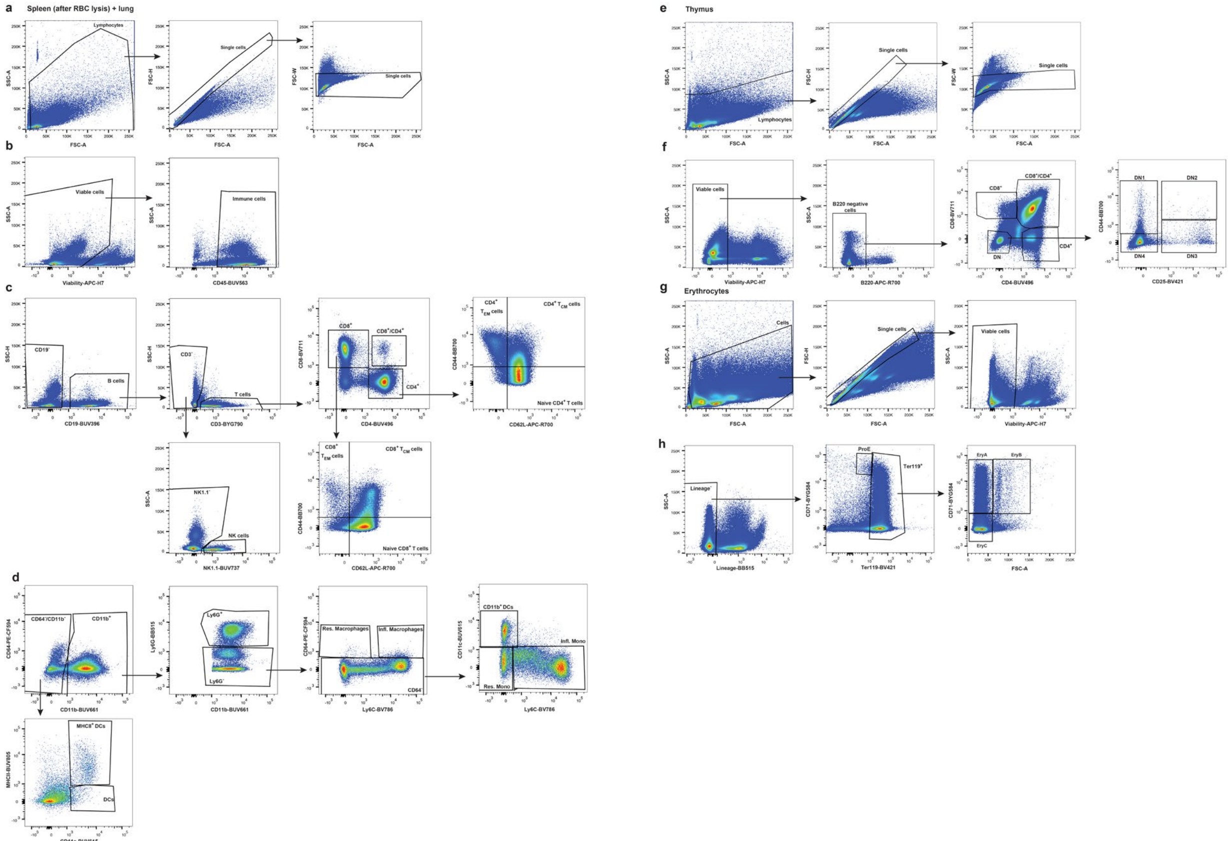

a-d, Gating strategy to determine single cell (**a)**, viable immune cell (**b**), lymphocyte (**c**) and myeloid (**d**) cell populations in the spleen and lung. **e-f**, Thymocyte population gating into single cells (**e**) and T cell developmental stages. **g-h**, Gating of erythrocyte populations from spleen homogenates.

Supplementary Table 1

	Necroptosis		Apoptosis		Pyroptosis				
Cytokine	**Released**	**Activates**	**Released**	**Activates**	**Released**	**Activates**	**Immune Cell Attractant**	**Immune Cell Type Attracted**	**Pathway involvement (activated/produced by)**
IL-7[54]	No	No	No	No	No	No	No	None	NF-κB, STAT5
CXCL10[55,56]	No	No	Yes	No	Yes	No	Yes	T cells, NK cells	IFNγ, NF-κB
IL-12[57]	No	No	No	No	Yes	No	Yes	NK cells, T helper cells	NF-κB, STAT4
G-CSF[58]	No	No	No	No	Yes	No	No	Neutrophils	NF-κB
LTα[56,59]	Yes	No	Yes	No	Yes	No	Yes	T cells, B cells	NF-κB, STAT3
M-CSF[56,60]	Yes	No	Yes	No	Yes	No	No	Macrophages	NF-κB
CXCL2[56,61]	Yes	No	Yes	No	Yes	No	Yes	Neutrophils, Macrophages	NF-κB, AP-1
CCL4[62]	No	No	No	No	Yes	No	Yes	T cells, NK cells	NF-κB, IRF
IL-33[63]	Indirectly	No	No	No	Yes	No	Yes	Th2 cells, ILC2	NF-κB, ST2 receptor
CXCL9[56,64]	Yes	No	No	No	Yes	No	Yes	T cells, NK cells	IFNγ, NF-κB
CCL3[56]	Yes	No	Yes	No	Yes	No	Yes	T cells, Monocytes, NK cells	NF-κB, AP-1
FasL[65]	No	Yes	No	Yes	No	No	No	None	NF-κB, FAS signaling
S100A9[56,66]	Yes	No	Yes	No	Yes	No	Yes	Neutrophils, Macrophages	NF-κB, TLR signaling
IL-18[56,67]	Yes	No	Yes	No	Yes	Yes	Yes	NK cells, T helper cells	NF-κB, Caspase-1
TRAIL[68]	No	Yes	No	Yes	No	No	No	None	NF-κB, TRAIL signaling
CCL24[69]	No	No	No	No	Yes	No	Yes	Eosinophils, Th2 cells	NF-κB, IL-4 signaling
IL-21[70]	No	No	No	No	No	No	Yes	B cells, T follicular helper cells	STAT3, NF-κB
IL-6[56,71]	Yes	No	Yes	Yes	Yes	No	Yes	T cells, B cells, Macrophages	NF-κB, STAT3
CXCL1[56,72]	Yes	No[20]	Yes	No	Yes	No	Yes	Neutrophils, Eosinophils	NF-κB, AP-1
IL-13[73]	No	No	No	No	No	No	Yes	Eosinophils, Macrophages	STAT6, NF-κB
IL-3[74]	No	No	No	No	No	No	Yes	Basophils, Eosinophils	NF-κB, STAT5
IL-1β[56,75]	Yes	No	Yes	Yes	Yes	Yes	Yes	Neutrophils, Macrophages, T cells	NF-κB, Caspase-1
IL-1α[56,76]	Yes	No	(indirectly)	No	Yes (alarmin role)	No	Yes	Neutrophils, Macrophages	NF-κB, Caspase-1
CD40L[56,77]	Indirectly	No	Indirectly	No	Indirectly	No	Yes	B cells, T cells	NF-κB, MAPK
IFN-α[78]	No	indirectly + personal comms	No	indirectly + personal comms	No	No	Yes	NK cells, Dendritic cells	STAT1, IRF
CXCL11[79]	No	No	No	No	No	No	Yes	T cells, NK cells	IFNγ, NF-κB
IL-8[56,80]	Yes	No	Yes	No	Yes	No	Yes	Neutrophils, T cells	NF-κB, AP-1
CCL2[56,81]	Yes	No	Yes	No	Yes	No	Yes	Monocytes, T cells	NF-κB, STAT3
IFN-γ[56,82]	Yes	Yes	Yes	Yes	No	No	Yes	Macrophages, T cells	STAT1, NF-κB
BAFF[83]	No	No	No	No	No	No	Yes	B cells, T cells	NF-κB
CXCL5[56,84]	Yes	No	Yes	No	Yes	No	Yes	Neutrophils, Eosinophils	NF-κB, AP-1
TNF[56,85]	Yes	Yes	No	Yes	Yes	No	Yes	Neutrophils, Macrophages, T cells	NF-κB, MAPK
CCL5[56,86]	Yes	No	Yes	No	Yes	No	Yes	T cells, NK cells, Macrophages	NF-κB, AP-1

List of cytokines and their roles in different cell death modalities.

Supplementary Table 2

IFN response	
Human Gene	**Mouse Orthologue**
IFITM3	*Ifitm3*
ISG15	*Isg15*
IRF7	*Irf7*
STAT1	*Stat1*
STAT2	*Stat2*
IFI35	*Ifi35*
IFI27	*Ifi27*
IFI44	*Ifi44*
GBP3	*Gbp3*
GBP5	*Gbp5*
SIGLEC1	*siglec1*
MX1	*Mx1*
MX2	*Mx2*
USP18	*Usp18*
RSAD2	*Rsad2*
RTP4	*Rtp4*
BST2	*Bst2*
XAF1	*Xaf1*
PARP9	*Parp9*
PARP12	*Parp12*
PARP14	*Parp14*
HERC5	*Herc6*
TAP1	*Tap1*
TRIM5	*Trim5*
EPSTI1	*Epsti1*
SAMD9L	*Samd9l*
TRIM25	*trim25*

Necroptosis	
Human Gene	**Mouse Orthologue**
MLKL	*Mlkl*
ZBP1	*Zbp1*
EIF2AK2	*Eif2ak2*
JUNB	*Junb*

Nucleic acid sensing	
Human Gene	**Mouse Orthologue**
DDX58	*Ddx58*
TREX1	*Trex1*
IFIH1	*Ifih1*
IFIT1	*Ifit1*
IFIT3	*Ifit3*
ZC3HAV1	*Zc3hav1*
DDX60	*Ddx60*
OASL	*Oasl1*
OAS1	*Oas1a*
	Oas1b
	Oas1c
	Oas1g
OAS2	*Oas2*
OAS3	*Oas3*
HELZ2	*Helz2*
DHX58	*Dhx58*

Shared upregulated genes in IFN-high SAVI and *Casp8*$^{E\text{-}KO}$ mice, categorized by IFN response, nucleic acid sensing, and necroptosis. Table presents selected differentially upregulated genes categorised into three groups: IFN response, nucleic acid sensing, and necroptosis. These genes were identified as upregulated in IFN-high SAVI samples relative to controls and show overlap with genes upregulated in *Casp8*$^{E\text{-}KO}$ mice compared to their respective controls.

Supplementary Table 3

Antibody	Identifier	Source	Dilution
FADD	05-486	Millipore	1:1000
RIPK1	3493	Cell Signalling Technology	1:1000
	610459	BD Biosciences	1:500
pRIPK1 (S166)	31122	Cell Signalling Technology	1:500
RIPK3	95702	Cell Signalling Technology	1:1000
pRIPK3 (T231/S232)	91702	Cell Signalling Technology	1:500
MLKL	MABC604	Millipore	1:1000
pMLKL (S345)	37333	Cell Signalling Technology	1:1000
ZBP1	AG-20B-0010-C100	Adipogen	1:1000
pSTAT1 (Y701)	5483	Cell Signalling Technology	1:250
TBK1	3013	Cell Signalling Technology	1:1000
pTBK1 (S172)	72971	Cell Signalling Technology	1:500
caspase-8	ALX-804-447	Enzo Life Sciences	1:1000
STING	13647	Cell Signalling Technology	1:1000
Total OXPHOS	ab110413	Abcam	1:500
GAPDH	G9545	Sigma-Aldrich	1:10000

anti-mouse IgG	JIM-115-035-174	Jackson ImmunoResearch	1:5000
anti-rat IgG	JIM-112-035-175	Jackson ImmunoResearch	1:5000
anti-rabbit IgG	JIM-211-032-171	Jackson ImmunoResearch	1:5000

List of antibodies used for Western Blot analysis.

Supplementary Table 4

Antibody	Identifier	Source	Dilution
pMLKL (S345)	37333	Cell Signalling Technology	1:2000
Cl. CASP3 (skin)	9664	Cell Signalling Technology	1:100
Cl. CASP3 (other tissues)	9661	Cell Signalling Technology	1:200
ZBP1	AG-20B-0010-C100	Adipogen	1:800
STING	13647	Cell Signalling Technology	1:200
pSTAT1 (Y701)	9167	Cell Signalling Technology	1:50
CD3	ab5690	Abcam	1:1400
Ly6G	87048	Cell Signalling Technology	1:100
pHH3 (S10)	06-570	Sigma-Aldrich	1:500
γH2AX (S139)	9718	Cell Signalling Technology	1:50
F4/80	MCA497R	BioRad	1:50
CD45	550539	BD Biosciences	1:200
Keratin-6A	905701	Biolrgend	1:400
Keratin-10	ab9026	Abcam	1:200
Keratin-14	905304	Biolegend	1:400
goat anti-rabbit	MP-7451	Vector Laboratories	kit
goat anti-rat	MP-7444-15	Vector Laboratories	kit
mouse-on-mouse	MP-2400	Vector Laboratories	kit
biotinylated goat anti-rabbit	BA-1000	Vector Laboratories	1:200
biotinylated goat anti-rat	BA-9400	Vector Laboratories	1:200
goat anti-rabbit Alexa Fluor Plus 488	A32731	Thermo Fisher Scientific	1:400
goat anti-mouse Alexa Fluor Plus 594	A32742	Thermo Fisher Scientific	1:400

Antibodies used for *in situ* immunohistochemistry and immunofluorescence.

Supplementary Table 5

Target gene	Forward primer	Reverse primer
m*Isg15*	GTGCTCCAGGACGGTCTTAC	CTCGCTGCAGTTCTGTACCA
m*Tnf*	CAGGCGGTGCCTATGTCTC	CGATCACCCCGAAGTTCAGTAG
m*S100a9*	TGGTGGAAGCACAGTTGGCAAC	CAGCATCATACACTCCTCAAAGC
m*Mlkl*	AATTGTACTCTGGGAAATTGCCA	TCTCCAAGATTCCGTCCACAG
m*Ripk3*	TCTGTCAAGTTATGGCCTACTGG	GGAACACGACTCCGAACCC
m*Ripk1*	GACTGTGTACCCTTACCTCCGA	CACTGCGATCATTCTCGTCCTG
m*Ifnβ*	CAGCTCCAAGAAAGGACGAAC	GGCAGTGTAACTCTTCTGCAT
m*Ifnγ*	CGGCACAGTCATTGAAAGCCTA	GTTGCTGATGGCCTGATTGTC
m*Gapdh*	CTCCCACTCTTCCACCTTCG	GCCTCTCTTGCTCAGTGTCC

h*MLKL*	TAATTCTGAGAAGATCCGCAAG	GGAGAGTTTCTTTAAGATTTCAT
h*ZBP1*	GCAAACTCCGAAGCCATCCAGA	CCAAGTTGAGGAATCACCTGGTG
h*ISG15*	GCGAACTCATCTTTGCCAGTA	CCAGCATCTTCACCGTCAG
h*IFIT1*	CTGGCAGAAGCCCAGACTTACC	AGGCCCATCCTTCCTCACAGTCT
h*IFI27*	CGTCCTCCATAGCAGCCAAGAT	ACCCAATGGAGCCCAGGATGAA
h*IFI44*	TGGTACATGTGGCTTTGCTC	CCACCGAGATGTCAGAAAGAG
h*SIGLEC1*	ACCTGGAGGAAACTGACAGTGG	CTCAGTGTCACTGCCTGTCCTT
h*RSAD2*	CCAGTGCAACTACAAATGCGGC	CGGTCTTGAAGAAATGGCTCTCC
h*CXCL1*	TCCTGCATCCCCCATAGTTA	CTTCAGGAACAGCCACCAGT
h*CXCL8*	TCTGGCAACCCTAGTCTGCT	AAACCAAGGCACAGTGGAAC
h*CXCL10*	GTGGATGTTCTGACCCTGCT	GAGGATGGCAGTGGAAGTCC
h*HPRT*	AGCCAGACTTTGTTGGATTTG	TTTACTGGCGATGTCAATAGG

Primer sequences used for RT-qPCR in tissue samples.

Supplementary Table 6

Antibody	**Fluorochrome**	**Identifier**	**Source**	**Dilution**
B220	FITC	103205	BioLegend	1:200
B220	AF700	103232	BioLegend	1:200
CD11b	BUV661	612977	BD Biosciences	1:250
CD11b	FITC	101205	BioLegend	1:200
CD11c	BV605	117334	BioLegend	1:200
CD19	BUV395	565965	BD Biosciences	1:100
CD25	BV421	562606	BD Biosciences	1:100
CD3	PE-Cy7	100219	BioLegend	1:200
CD3	FITC	100203	BioLegend	1:200
CD4	BUV496	612952	BD Biosciences	1:200
CD44	BB700	566507	BD Biosciences	1:200
CD45	BUV563	612924	BD Biosciences	1:250
CD5	FITC	553020	BD Biosciences	1:100
CD62L	AF700	104441	BioLegend	1:100
CD64	PE-Dazzle	139319	BioLegend	1:100
CD69	APC	560689	BD Biosciences	1:100
CD71	PE	113807	BioLegend	1:100
CD8	BV711	563046	BD Biosciences	1:100
GR-1	FITC	108405	BioLegend	1:200
Ly6C	BV785	128041	BioLegend	1:150
Ly6G	FITC	551460	BD Biosciences	1:100
MHCII	BUV805	748844	BD Biosciences	1:100
NK1.1	BUV737	741715	BD Biosciences	1:100
TCRβ	PE	553172	BD Biosciences	1:100
Ter119	BV421	116233	BioLegend	1:200

Antibodies for flow cytometric analysis.

Supplementary Table 7

Target gene	Forward primer	Reverse primer
mt*Dloop*	AATCTACCATCCTCCGTGAAACC	TCAGTTTAGCTACCCCCAAGTTTAA
mt*Co1*	GCAGGAGCATCAGTAGACCTAAC	GGAGTTTGATACTGTGTTATGGCTGG
mt*Co3*	GACGTAATTCGTGAAGGAACCTACC	GATAGAACGCTCAGAAGAATCCTGC
mt*Nd2*	GCATGAGGAGGACTTAACCAAACAC	GAGGTTGAGTAGAGTGAGGGATGG
mt*Nd5*	GGCCTATTAATCGCAGCTACAGG	GTAGTAGTGCTGAAACTGGTGTAGG
mt*Atp6*	CCTTCCACAAGGAACTCCAATTTCAC	CTAGAGTAGCTCCTCCGATTAGGTG
mt*Rnr2*	GGGATAACAGCGCAATCCTA	GATTGCTCCGGTCTGAACTC
Actb	CATTGCTGACAGGATGCAGAAGG	TGCTGGAAGGTGGACAGTGAGG

Primer sequences targeting mtDNA-encoded genes used for RT–qPCR.

Supplementary Table 8

Target gene	Forward primer	Reverse primer
m*Zbp1*	TGTTGACTTGAGCACAGGAG	TTCAGGCGGTAAAGGACTTG
m*Isg15*	CTAGAGCTAGAGCCTGCAG	AGTTAGTCACGGACACCAG
m*Usp18*	GAGAGGACCATGAAGAGGA	TAAACCAACCAGACCATGAG
m*Rsad2*	CCCGTGAGTGTCAACTACCAC	GCCCAAGTATTCACCCCTGTC
m*Ifit1*	CAAGGCAGGTTTCTGAGGAG	GACCTGGTCACCATCAGCAT
m*Hprt*	TCCTCCTCAGACCGCTTTT	CATAACCTGGTTCATCATCGC

Primer sequences used for RT-qPCR in MEFs.

Supplementary Table 9

Vials code	Patient ID	Mutation Status	Processing date	Sample collected	PRE/POST TREATMENT	Disease Response (CR/PR/SD)	Assessment	Notes
I-3200P	1	c.[463G>A]; p.[Val155Met]	29/11/2017	Plasma	PRE-treatment	Active disease		First visit
I-3239P	1		13/12/2017	Plasma	PRE-treatment	SD		
I-3445P	1		22/02/2018	Plasma	PRE-treatment	SD		
I-3851P	1		06/07/2018	Plasma	POST-treatment	PR		
I-4577P	1		04/02/2019	Plasma	POST-treatment	PR		
I-5022P	1		04/06/2019	Plasma	POST-treatment	PR		
I-5945P	1		10/01/2020	Plasma	POST-treatment	PR		
I-7874P	1		14/04/2021	Plasma	POST-treatment	PR		
I-9675P	1		21/03/2022	Plasma	POST-treatment	PR		
I-3200TT	1		29/11/2017	RNA	PRE-treatment	Active disease		First visit
I-3445TT	1		22/02/2018	RNA	PRE-treatment	SD		
I-3851TT	1		06/07/2018	RNA	POST-treatment	PR		
I-4577TT	1		04/02/2019	RNA	POST-treatment	PR		
I-5945TT	1		10/01/2020	RNA	POST-treatment	PR		
I-2202P	2	c.[461A>G]; p.[Asn154Ser]	27/10/2016	Plasma	PRE-treatment	Active disease		
I-2406P	2		26/01/2017	Plasma	PRE-treatment	SD		
I-3047P	2		04/10/2017	Plasma	POST-treatment	PR		
I-3214P	2		05/12/2017	Plasma	POST-treatment	PR		
I-4001P	2		30/08/2018	Plasma	POST-treatment	PR		
I-4490P	2		15/01/2019	Plasma	POST-treatment	PR		
I-4631P	2		12/02/2019	Plasma	POST-treatment	PR		
I-5934P	2		09/01/2020	Plasma	POST-treatment	PR		
I-7616P	2		15/02/2021	Plasma	POST-treatment	PR		
I-9677P	2		21/03/2022	Plasma	POST-treatment	PR		
I-2193Pax	2		26/10/2016	RNA	PRE-treatment	Active disease		
I-2406Pax	2		26/01/2017	RNA	PRE-treatment	SD		
I-2491Pax	2		01/03/2017	RNA	POST-treatment	PR		
I-3047Pax	2		04/10/2017	RNA	POST-treatment	PR		
I-3214Pax	2		05/12/2017	RNA	POST-treatment	PR		
I-3214TT	2		05/12/2017	RNA	POST-treatment	PR		
I-4001TT	2		30/08/2018	RNA	POST-treatment	PR		
I-7953P	3	c.[463G>A]; p.[Val155Met]	27/04/2021	Plasma	PRE-treatment	Active disease		
I-8045P	3		12/05/2021	Plasma	POST-treatment	SD		
I-8304P	3		06/07/2021	Plasma	POST-treatment	PR		
I-8913P	3		03/11/2021	Plasma	POST-treatment	PR		
I-9288P	3		27/01/2022	Plasma	POST-treatment	PR		
I-9810P	3		12/04/2022	Plasma	POST-treatment	PR		
I-10153P	3		13/06/2022	Plasma	POST-treatment	PR		
I-7953TT	3		27/04/2021	RNA	PRE-treatment	Active disease		
I-8045TT	3		12/05/2021	RNA	POST-treatment	SD		
I-8304TT	3		06/07/2021	RNA	POST-treatment	PR		
I-9288TT	3		27/01/2022	RNA	POST-treatment	PR		
I-10153TT	3		13/06/2022	RNA	POST-treatment	PR		

Clinical characterization of patients and patient sample information.

54 Minton, K. Inflammasomes: ubiquitin lines up for inflammasome activity. *Nat Rev Immunol* **14**, 580-581, doi:10.1038/nri3730 (2014).
55 Chen, L. *et al.* Genetic Drivers of Epigenetic and Transcriptional Variation in Human Immune Cells. *Cell* **167**, 1398-1414 e1324, doi:10.1016/j.cell.2016.10.026 (2016).
56 Tanzer, M. C. *et al.* Quantitative and Dynamic Catalogs of Proteins Released during Apoptotic and Necroptotic Cell Death. *Cell Rep* **30**, 1260-1270 e1265, doi:10.1016/j.celrep.2019.12.079 (2020).
57 Smith, N. L. *et al.* Developmental Origin Governs CD8(+) T Cell Fate Decisions during Infection. *Cell* **174**, 117-130 e114, doi:10.1016/j.cell.2018.05.029 (2018).
58 Corey, S. J. *et al.* Granulocyte colony-stimulating factor receptor signaling involves the formation of a three-component complex with Lyn and Syk protein-tyrosine kinases. *Proc Natl Acad Sci U S A* **91**, 4683-4687, doi:10.1073/pnas.91.11.4683 (1994).
59 Etemadi, N. *et al.* Lymphotoxin alpha induces apoptosis, necroptosis and inflammatory signals with the same potency as tumour necrosis factor. *FEBS J* **280**, 5283-5297, doi:10.1111/febs.12419 (2013).
60 Yi, L. *et al.* Macrophage colony-stimulating factor and its role in the tumor microenvironment: novel therapeutic avenues and mechanistic insights. *Front Oncol* **14**, 1358750, doi:10.3389/fonc.2024.1358750 (2024).
61 Sinha, S. K. *et al.* Local M-CSF (Macrophage Colony-Stimulating Factor) Expression Regulates Macrophage Proliferation and Apoptosis in Atherosclerosis. *Arterioscler Thromb Vasc Biol* **41**, 220-233, doi:10.1161/ATVBAHA.120.315255 (2021).
62 Bystry, R. S., Aluvihare, V., Welch, K. A., Kallikourdis, M. & Betz, A. G. B cells and professional APCs recruit regulatory T cells via CCL4. *Nat Immunol* **2**, 1126-1132, doi:10.1038/ni735 (2001).
63 Shlomovitz, I. *et al.* Necroptosis directly induces the release of full-length biologically active IL-33 in vitro and in an inflammatory disease model. *FEBS J* **286**, 507-522, doi:10.1111/febs.14738 (2019).
64 Veerman, K., Tardiveau, C., Martins, F., Coudert, J. & Girard, J. P. Single-Cell Analysis Reveals Heterogeneity of High Endothelial Venules and Different Regulation of Genes Controlling Lymphocyte Entry to Lymph Nodes. *Cell Rep* **26**, 3116-3131 e3115, doi:10.1016/j.celrep.2019.02.042 (2019).
65 Huang, D. C. *et al.* Activation of Fas by FasL induces apoptosis by a mechanism that cannot be blocked by Bcl-2 or Bcl-x(L). *Proc Natl Acad Sci U S A* **96**, 14871-14876, doi:10.1073/pnas.96.26.14871 (1999).
66 Christmann, C. *et al.* Interleukin 17 Promotes Expression of Alarmins S100A8 and S100A9 During the Inflammatory Response of Keratinocytes. *Front Immunol* **11**, 599947, doi:10.3389/fimmu.2020.599947 (2020).
67 Chan, A. H. & Schroder, K. Inflammasome signaling and regulation of interleukin-1 family cytokines. *J Exp Med* **217**, doi:10.1084/jem.20190314 (2020).
68 Montinaro, A. & Walczak, H. Harnessing TRAIL-induced cell death for cancer therapy: a long walk with thrilling discoveries. *Cell Death Differ* **30**, 237-249, doi:10.1038/s41418-022-01059-z (2023).
69 Diny, N. L. *et al.* Macrophages and cardiac fibroblasts are the main producers of eotaxins and regulate eosinophil trafficking to the heart. *Eur J Immunol* **46**, 2749-2760, doi:10.1002/eji.201646557 (2016).
70 Spolski, R. & Leonard, W. J. Interleukin-21: a double-edged sword with therapeutic potential. *Nat Rev Drug Discov* **13**, 379-395, doi:10.1038/nrd4296 (2014).
71 Shkarina, K. *et al.* Optogenetic activators of apoptosis, necroptosis, and pyroptosis. *J Cell Biol* **221**, doi:10.1083/jcb.202109038 (2022).
72 Han, K. Q. *et al.* Targeted silencing of CXCL1 by siRNA inhibits tumor growth and apoptosis in hepatocellular carcinoma. *Int J Oncol* **47**, 2131-2140, doi:10.3892/ijo.2015.3203 (2015).

73 Terabe, M., Park, J. M. & Berzofsky, J. A. Role of IL-13 in regulation of anti-tumor immunity and tumor growth. *Cancer Immunol Immunother* **53**, 79-85, doi:10.1007/s00262-003-0445-0 (2004).
74 Broughton, S. E. *et al.* The GM-CSF/IL-3/IL-5 cytokine receptor family: from ligand recognition to initiation of signaling. *Immunol Rev* **250**, 277-302, doi:10.1111/j.1600-065X.2012.01164.x (2012).
75 Wertman, R. S. *et al.* Distinct sequential death complexes regulate pyroptosis and IL-1beta release in response to Yersinia blockade of immune signaling. *Sci Adv* **10**, eadl3629, doi:10.1126/sciadv.adl3629 (2024).
76 Cohen, I. *et al.* Differential release of chromatin-bound IL-1alpha discriminates between necrotic and apoptotic cell death by the ability to induce sterile inflammation. *Proc Natl Acad Sci U S A* **107**, 2574-2579, doi:10.1073/pnas.0915018107 (2010).
77 Qiu, X., Klausen, C., Cheng, J. C. & Leung, P. C. CD40 ligand induces RIP1-dependent, necroptosis-like cell death in low-grade serous but not serous borderline ovarian tumor cells. *Cell Death Dis* **6**, e1864, doi:10.1038/cddis.2015.229 (2015).
78 Takaoka, A. *et al.* Integration of interferon-alpha/beta signalling to p53 responses in tumour suppression and antiviral defence. *Nature* **424**, 516-523, doi:10.1038/nature01850 (2003).
79 Petkovic, V., Moghini, C., Paoletti, S., Uguccioni, M. & Gerber, B. I-TAC/CXCL11 is a natural antagonist for CCR5. *J Leukoc Biol* **76**, 701-708, doi:10.1189/jlb.1103570 (2004).
80 Harada, A. *et al.* Essential involvement of interleukin-8 (IL-8) in acute inflammation. *J Leukoc Biol* **56**, 559-564 (1994).
81 Deshmane, S. L., Kremlev, S., Amini, S. & Sawaya, B. E. Monocyte chemoattractant protein-1 (MCP-1): an overview. *J Interferon Cytokine Res* **29**, 313-326, doi:10.1089/jir.2008.0027 (2009).
82 Bertheloot, D., Latz, E. & Franklin, B. S. Necroptosis, pyroptosis and apoptosis: an intricate game of cell death. *Cell Mol Immunol* **18**, 1106-1121, doi:10.1038/s41423-020-00630-3 (2021).
83 Mackay, F., Schneider, P., Rennert, P. & Browning, J. BAFF AND APRIL: a tutorial on B cell survival. *Annu Rev Immunol* **21**, 231-264, doi:10.1146/annurev.immunol.21.120601.141152 (2003).
84 Sokulsky, L. A. *et al.* A Critical Role for the CXCL3/CXCL5/CXCR2 Neutrophilic Chemotactic Axis in the Regulation of Type 2 Responses in a Model of Rhinoviral-Induced Asthma Exacerbation. *J Immunol* **205**, 2468-2478, doi:10.4049/jimmunol.1901350 (2020).
85 Brenner, D., Blaser, H. & Mak, T. W. Regulation of tumour necrosis factor signalling: live or let die. *Nat Rev Immunol* **15**, 362-374, doi:10.1038/nri3834 (2015).
86 Appay, V. & Rowland-Jones, S. L. RANTES: a versatile and controversial chemokine. *Trends Immunol* **22**, 83-87, doi:10.1016/s1471-4906(00)01812-3 (2001).

3. Publication 3

The RIPK1 death domain restrains ZBP1- and TRIF-mediated cell death and inflammation

https://doi.org/10.1016/j.immuni.2024.04.016

Declaration: This study aimed to investigate how RIPK1, through its dual kinase and scaffolding functions, can both promote and prevent apoptosis and necroptosis, mechanisms that have remained incompletely understood. By generating and characterizing a RIPK1 death domain (DD)-disruptive mutant (R588E), the work revealed that DD-dependent RIPK1 signalling is essential for preventing RIPK3-mediated necroptosis, predominantly via ZBP1 and secondarily via TRIF, during development, while postnatal inflammation involved TNFR1-TRADD-FADD-caspase-8-mediated apoptosis that was partially dependent on RIPK3. Mechanistically, DD-dependent oligomerisation of RIPK1 and its interaction with FADD determine how ZBP1 and TRIF activate RIPK3. In wild-type cells, DD-dependent recruitment of ZBP1 and RIPK3 to Complex II occurs in a RIPK1 kinase-dependent manner, whereas in *Ripk1*$^{R588E/R588E}$ cells, RIPK1 associates with ZBP1 and RIPK3 independently of its kinase activity to drive RIPK3-MLKL-mediated necroptosis. Similarly, TRIF-mediated activation of RIPK3 requires RIPK1 kinase activity in wild-type cells but not in *Ripk1*$^{R588E/R588E}$ cells. These findings establish DD-dependent RIPK1 oligomerisation as a critical checkpoint linking the regulation of cell death and inflammation and provide new insight into how RIPK1 integrates pro-survival and pro-death signals to maintain tissue homeostasis.

Contribution:

- As a contributing author, I included this work as the third publication in my cumulative thesis. I contributed specifically to the experiment shown in Figure S6C, applying an endogenous ZBP1 immunoprecipitation method developed by my supervisor, Dr. Gianmaria Liccardi, to assess ZBP1 interactions. My contribution involved providing this methodological approach for complex assessment, assisting with key experimental steps including sample preparation, immunoprecipitation workflow, and troubleshooting, thereby supporting the mechanistic analysis of ZBP1 interactions with RIPK1 and RIPK3 also presented in Figure 7F.

Article

Immunity

The RIPK1 death domain restrains ZBP1- and TRIF-mediated cell death and inflammation

Graphical abstract

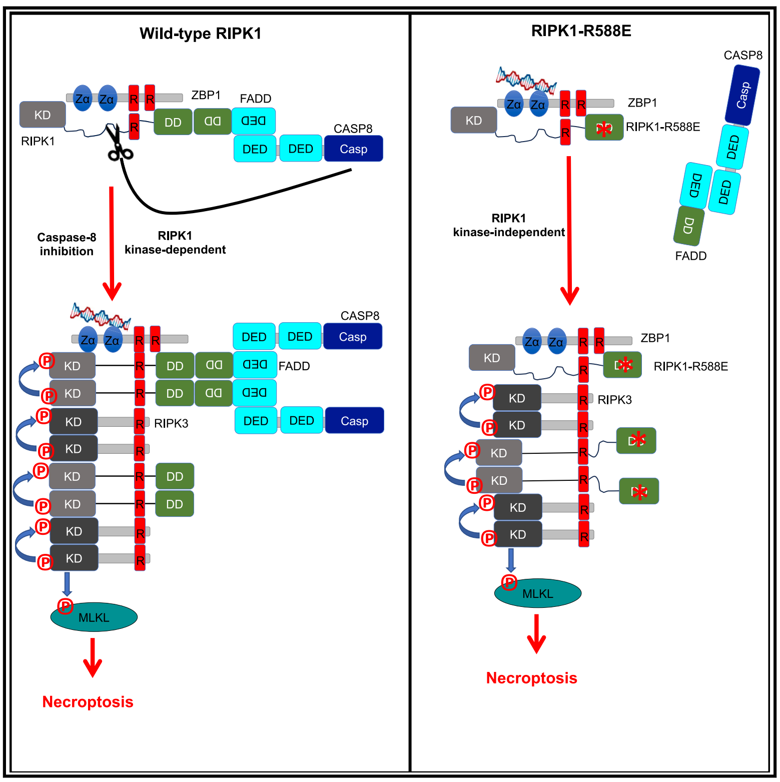

Authors

Takashi Imai, Juan Lin,
Göksu Gökberk Kaya, ...,
Gianmaria Liccardi, Chun Kim,
Manolis Pasparakis

Correspondence

linjuan2020@xmu.edu.cn (J.L.),
pasparakis@uni-koeln.de (M.P.)

In brief

RIPK1 regulates cell death via kinase-dependent and kinase-independent mechanisms. Utilizing mice expressing RIPK1 with a point mutation disrupting its death domain, Imai et al. show that RIPK1 death domain interactions are critical to suppress ZBP1- and TRIF-induced activation of RIPK3 and necroptosis.

Highlights

- ZBP1 and TRIF induce necroptosis-mediated perinatal death in *Ripk1*$^{R588E/R588E}$ mice
- TRADD induces inflammation and early postnatal death in *Ripk1*$^{R588E/R588E}$*Mlkl*$^{-/-}$
- RIPK3 causes MLKL-independent postnatal inflammation in *Ripk1*$^{R588E/R588E}$ mice
- The RIPK1 DD determines how ZBP1 and TRIF engage and activate RIPK3

Imai et al., 2024, Immunity *57*, 1497–1513
July 9, 2024 © 2024 The Author(s). Published by Elsevier Inc.
https://doi.org/10.1016/j.immuni.2024.04.016

CellPress

Immunity

CellPress OPEN ACCESS

Article

The RIPK1 death domain restrains ZBP1- and TRIF-mediated cell death and inflammation

Takashi Imai,[1,2,8] Juan Lin,[1,2,3,8,*] Göksu Gökberk Kaya,[1,2] Eunjin Ju,[1,2] Vangelis Kondylis,[4,5] Konstantinos Kelepouras,[6] Gianmaria Liccardi,[4,6] Chun Kim,[1,2,7] and Manolis Pasparakis[1,2,4,9,*]

[1]Institute for Genetics, University of Cologne, 50674 Cologne, Germany

[2]Cologne Excellence Cluster on Cellular Stress Responses in Aging-Associated Diseases (CECAD), University of Cologne, 50931 Cologne, Germany

[3]Research Unit of Cellular Stress of Chinese Academy of Medical Sciences, Cancer Research Center of Xiamen University, School of Medicine, Xiamen University, Xiamen, China

[4]Center for Molecular Medicine (CMMC), University of Cologne, 50931 Cologne, Germany

[5]Institute of Pathology, Faculty of Medicine and University Hospital Cologne, 50931 Cologne, Germany

[6]Institute of Biochemistry I, Center for Biochemistry, Faculty of Medicine, University of Cologne, Joseph-Stelzmann-Str. 52, 50931 Cologne, Germany

[7]Department of Medicinal and Life Sciences, Hanyang University (ERICA Campus), Ansan 15588, Republic of Korea

[8]These authors contributed equally

[9]Lead contact

*Correspondence: linjuan2020@xmu.edu.cn (J.L.), pasparakis@uni-koeln.de (M.P.)

https://doi.org/10.1016/j.immuni.2024.04.016

SUMMARY

RIPK1 is a multi-functional kinase that regulates cell death and inflammation and has been implicated in the pathogenesis of inflammatory diseases. RIPK1 acts in a kinase-dependent and kinase-independent manner to promote or suppress apoptosis and necroptosis, but the underlying mechanisms remain poorly understood. Here, we show that a mutation (R588E) disrupting the RIPK1 death domain (DD) caused perinatal lethality induced by ZBP1-mediated necroptosis. Additionally, these mice developed postnatal inflammatory pathology, which was mediated by necroptosis-independent TNFR1, TRADD, and TRIF signaling, partially requiring RIPK3. Our biochemical mechanistic studies revealed that ZBP1- and TRIF-mediated activation of RIPK3 required RIPK1 kinase activity in wild-type cells but not in *Ripk1*$^{R588E/R588E}$ cells, suggesting that DD-dependent oligomerization of RIPK1 and its interaction with FADD determine the mechanisms of RIPK3 activation by ZBP1 and TRIF. Collectively, these findings revealed a critical physiological role of DD-dependent RIPK1 signaling that is important for the regulation of tissue homeostasis and inflammation.

INTRODUCTION

Receptor-interacting protein kinase 1 (RIPK1) is a critical regulator of cell death and inflammation and is implicated in the pathogenesis of inflammatory diseases.[1–3] RIPK1 is a serine/threonine kinase that contains an N-terminal kinase domain, an intermediate domain that includes an RIP homotypic interaction motif (RHIM), and a C-terminal death domain (DD).[1] The role of RIPK1 is most studied in tumor necrosis factor receptor 1 (TNFR1) signaling, where it exerts kinase-dependent and -independent functions. Ligand-induced trimerization of TNFR1 induces the DD-dependent recruitment of RIPK1 as well as of the TNFR1-associated DD (TRADD) adapter protein, which interacts with the intracellular DD of the receptor independently of each other.[1–5] RIPK1 and TRADD nucleate the formation of a signaling complex (often termed complex I) that includes the ubiquitin ligases cellular inhibitors of apoptosis (cIAP1/2) and the linear ubiquitin chain assembly complex (LUBAC),[2] which ubiquitinate RIPK1 and other proteins to facilitate the activation of IκB kinase (IKK)/nuclear factor κB (NF-κB)-dependent transcription of inflammatory and pro-survival genes. Within complex I, RIPK1 acts in a kinase-independent manner to promote inflammatory and pro-survival signaling, while its kinase activity is suppressed by multiple mechanisms, including phosphorylation by canonical and non-canonical IKKs.[2] De-stabilization of complex I triggers RIPK1 autophosphorylation resulting in the DD-dependent recruitment of Fas-associated death domain protein (FADD) and the formation of a cytosolic death-inducing complex (often termed complex II) that triggers caspase-8 activation and apoptosis.[1–3] When caspase-8 is inhibited, RIPK1 activates RIPK3, which phosphorylates mixed lineage kinase-like protein (MLKL), inducing its oligomerization and translocation to the plasma membrane, triggering necroptosis.[1–3,6]

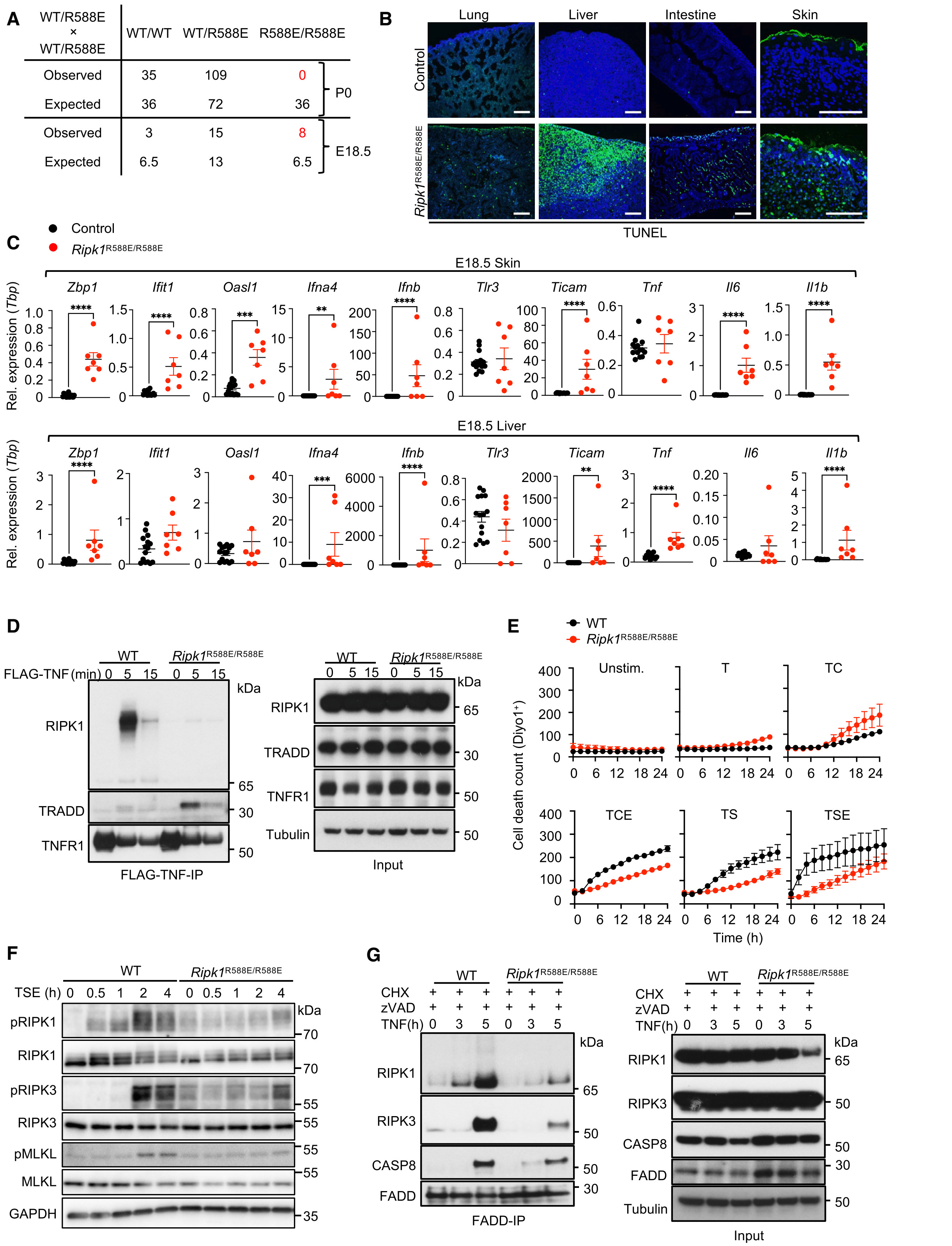

Figure 1. Mutation of the RIPK1 DD causes perinatal lethality

(A) Table showing the numbers of P0 offspring and E18.5 embryos from intercrossing *Ripk1*$^{WT/R588E}$ parents.

(B) Representative images from tissue sections from E18.5 embryos stained with TUNEL. Control n = 16 and *Ripk1*$^{R588E/R588E}$ n = 8.

(legend continued on next page)

Genetic studies provided important insights into the role of RIPK1 in organismal physiology. Ripk1$^{-/-}$ mice die perinatally and are rescued by combined inhibition of TRADD-FADD-caspase-8-mediated apoptosis and RIPK3-MLKL-dependent necroptosis.[7–11] By contrast, mice expressing kinase-inactive RIPK1 are viable, do not develop spontaneous pathology, and are protected from inflammation and tissue injury in different disease models.[12–14] Therefore, RIPK1 acts as a scaffold to inhibit cell death and safeguard mouse survival and tissue homeostasis, while its kinase activity drives apoptosis and necroptosis and causes inflammatory pathologies. Mutation of the RIPK1 RHIM causes perinatal lethality that is rescued by genetic deficiency of RIPK3, MLKL, or Z-DNA-binding protein 1 (ZBP1), revealing a critical role of the RIPK1 RHIM in suppressing ZBP1-mediated necroptosis.[15–17] Furthermore, mutation of the caspase-8 cleavage site (D325) of RIPK1 causes embryonic lethality in mice that is rescued by combined inhibition of caspase-8-mediated apoptosis and RIPK3-MLKL-mediated necroptosis.[18–21] In humans, loss-of-function mutations of RIPK1 or hemizygous mutations of its caspase-8 cleavage site cause autoinflammation and immunodeficiency.[19,20,22–24] Thus, caspase-8-mediated cleavage as well as RHIM-dependent interactions of RIPK1 are critical to prevent necroptosis and apoptosis and the development of inflammatory pathologies.

The functional significance of DD-dependent interactions of RIPK1 with other DD-containing proteins remains incompletely understood. Mice expressing RIPK1 with mutation of lysine at position 612 (K612R, equivalent to K627 in the human protein) within the DD are viable but develop TNFR1-mediated systemic inflammation, which is partially ameliorated by RIPK3 deficiency and fully rescued by combined loss of RIPK3 and caspase-8.[25,26] K612R mutation alters the ubiquitination pattern of RIPK1 and partially prevents its recruitment in TNFR1 signaling complexes I and II.[25,26] Furthermore, mice expressing RIPK1 with mutation of lysine 584 (K584R, equivalent to K599 in the human protein) within the DD are viable and show no pathology while being resistant to TNF-induced lethality.[27] The K584R mutation disrupts RIPK1 dimerization but has no significant effect on its interaction with TNFR1 or FADD.[27] Together, these studies support the notion that the DD of RIPK1 is primarily involved in the regulation of TNFR1 signaling. However, a limitation of these experiments is that the generated mutations only partially affect the DD-dependent interactions of RIPK1, which does not allow drawing definite conclusions on the physiological role of the RIPK1 DD.

To study the role of DD-dependent RIPK1 interactions, we generated mice expressing RIPK1 with a mutation of arginine at position 588 to glutamic acid (R588E), which corresponds to R603 in the human protein that was shown to be essential for DD-dependent interactions based on structural and functional studies.[28] Our genetic and biochemical studies reported here revealed that the RIPK1 DD regulates TNFR1, ZBP1, and TRIF signaling and exhibits important physiological functions for tissue homeostasis and inflammation.

RESULTS

Mutation of the RIPK1 DD causes perinatal death and sensitizes cells to TNF-induced apoptosis

To elucidate the function of the RIPK1 DD, we generated mice expressing RIPK1 with a mutation substituting arginine at position 588 with glutamic acid (RIPK1-R588E) using CRISPR-Cas9-mediated gene editing in mouse zygotes (Figure S1A). Genotyping of newborn pups from heterozygous *Ripk1*$^{\mathrm{WT/R588E}}$ parents failed to identify homozygous *Ripk1*$^{\mathrm{R588E/R588E}}$ progeny (Figure 1A). However, *Ripk1*$^{\mathrm{R588E/R588E}}$ embryos were alive at embryonic day 18.5 (E18.5) (Figure 1A), although they were smaller and looked affected (Figure S1B). E18.5 *Ripk1*$^{\mathrm{R588E/R588E}}$ embryos showed disorganized tissue structure with increased numbers of dying cells in the lung, liver, intestine, and skin compared with littermate controls (Figures 1B and S1C). Moreover, quantitative RT-PCR (RT-qPCR) analysis revealed increased expression of type I interferons (IFNs) as well as IFN-stimulated genes (ISGs) and inflammatory cytokines in skin and liver of *Ripk1*$^{\mathrm{R588E/R588E}}$ embryos at E18.5 (Figure 1C). Therefore, mutation of the RIPK1 DD caused perinatal lethality associated with cell death and increased expression of ISGs and inflammatory genes.

To assess how the R588E mutation affected the recruitment of RIPK1 to the TNFR1 signaling complex, we immunoprecipitated complex I from FLAG-TNF-stimulated primary mouse embryonic fibroblasts (MEFs) with anti-FLAG antibodies followed by immunoblotting. These experiments showed that the R588E mutation nearly completely prevented the recruitment of RIPK1 to TNFR1 (Figure 1D). Increased amounts of TRADD were recruited to TNFR1 in *Ripk1*$^{\mathrm{R588E/R588E}}$ cells, consistent with RIPK1 and TRADD competing for binding to the TNFR1 DD (Figure 1D).[5] Furthermore, TNF-induced activation of NF-κB and mitogen-activated protein kinase (MAPK) signaling was slightly reduced in *Ripk1*$^{\mathrm{R588E/R588E}}$ compared with wild-type (WT) MEFs (Figure S1D), in line with a partial requirement of RIPK1 for TNFR1-mediated inflammatory signaling.[29–31]

Ripk1$^{\mathrm{R588E/R588E}}$ MEFs showed increased susceptibility to cell death upon treatment with TNF alone (T) or in the presence of cycloheximide (CHX) (TC treatment), which induces

(C) RT-qPCR analysis of mRNA expression of the indicated genes in skin and liver from E18.5 embryos.
(D) Immunoblot analysis with the indicated antibodies of FLAG-TNF immunoprecipitates and total lysates from primary wild-type (WT) and *Ripk1*$^{\mathrm{R588E/R588E}}$ MEFs treated with FLAG-TNF (1 μg mL^{-1}) for the indicated periods of time. Representative data shown from two independent experiments.
(E) Cell death measured by DiYO1 uptake in primary MEFs of the indicated genotypes treated with combinations of TNF (T, 20 ng mL^{-1}), CHX (C, 1 μg mL^{-1}), Emricasan (E, 5 μM), and the Smac-mimetic compound birinapant (S, 5 μM) for 24 h. Data are representative of three independent experiments.
(F) Immunoblot analysis with the indicated antibodies of WT or *Ripk1*$^{\mathrm{R588E/R588E}}$ primary MEFs stimulated with T (20 ng mL^{-1}), S (5 μM), and E (5 μM) for the indicated periods of time. Representative data shown from two independent experiments.
(G) Immunoblot analysis with the indicated antibodies of FADD immunoprecipitates and total lysates from primary WT and *Ripk1*$^{\mathrm{R588E/R588E}}$ MEFs stimulated with T (20 ng mL^{-1}), C (1 μg mL^{-1}), and zVAD (20 μM) for the indicated periods of time. Representative data shown from two independent experiments.
Scale bars, 100 μm. Each dot represents one mouse. Graphs show mean ± SEM. *$p \leq 0.05$; **$p \leq 0.01$; ***$p \leq 0.001$; ****$p \leq 0.0001$ for all figures. For gel source data, see supplemental information.
See also Figure S1.

A

*Ripk1*WT/R588E*Ripk3*−/−*Fadd*WT/− × *Ripk1*WT/R588E*Ripk3*−/−*Fadd*−/−	Observed	Expected
*Ripk1*WT/WT*Ripk3*−/−*Fadd*−/−	3	3.625
*Ripk1*WT/R588E*Ripk3*−/−*Fadd*−/−	5	7.25
*Ripk1*R588E/R588E*Ripk3*−/−*Fadd*−/−	3	3.625
*Ripk1*WT/WT*Ripk3*−/−*Fadd*WT/−	3	3.625
*Ripk1*WT/R588E*Ripk3*−/−*Fadd*WT/−	11	7.25
*Ripk1*R588E/R588E*Ripk3*−/−*Fadd*WT/−	4	3.625

B

*Ripk1*WT/R588E*Ripk3*−/− × *Ripk1*WT/R588E*Ripk3*−/−	Observed	Expected
*Ripk1*WT/WT*Ripk3*−/−	49	48.25
*Ripk1*WT/R588E*Ripk3*−/−	103	96.5
*Ripk1*R588E/R588E*Ripk3*−/−	41	48.25

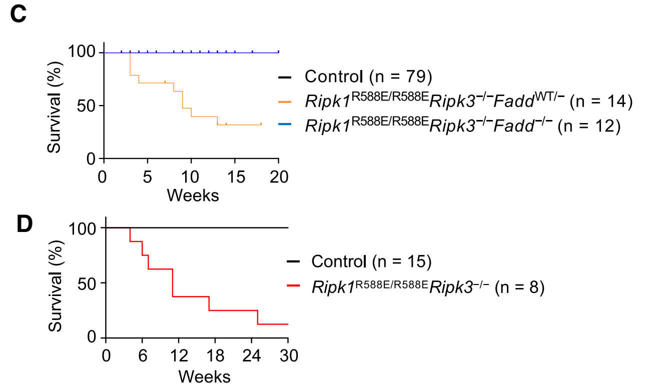

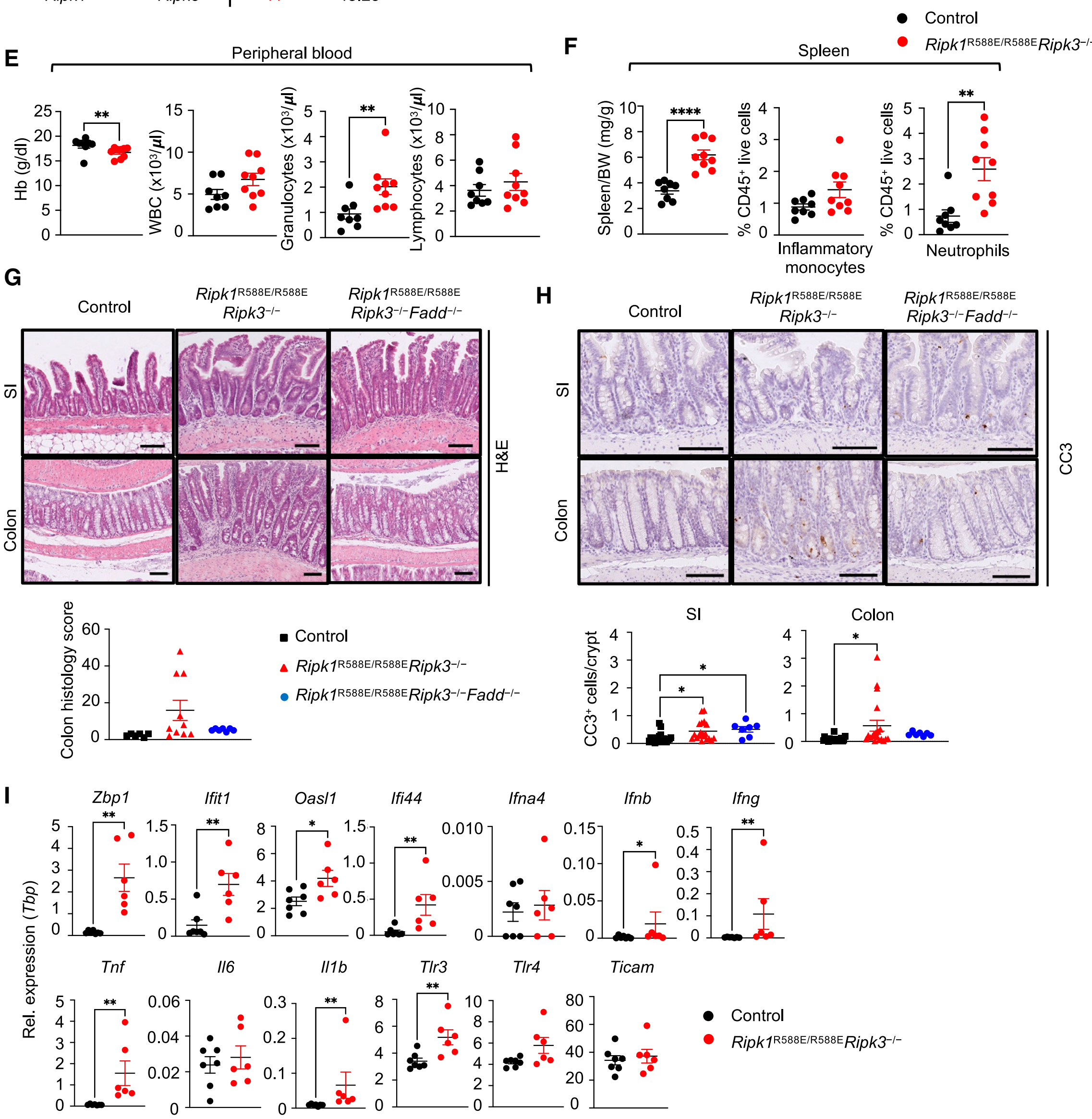

Figure 2. RIPK3 deficiency rescues the perinatal lethality of *Ripk1*$^{R588E/R588E}$ mice

(A and B) Tables showing the numbers of P0 offspring from intercrossing parents with the indicated genotypes.

(C and D) Kaplan-Meier survival graphs of mice with the indicated genotypes.

(E) Hemoglobin (Hb), white blood cells (WBCs), granulocyte, and lymphocyte counts in the blood from mice with the indicated genotypes at 12 weeks of age.

(legend continued on next page)

RIPK1-independent, TRADD-dependent apoptosis[32] (Figure 1E). However, *Ripk1*$^{R588E/R588E}$ MEFs were resistant to treatment with TNF in the presence of the SMAC-mimetic compound birinapant (S) (TS treatment), which induces RIPK1-mediated apoptosis[32] (Figure 1E). Moreover, *Ripk1*$^{R588E/R588E}$ MEFs were also more resistant to necroptosis induced by TC or TS treatment in the presence of the caspase inhibitor emricasan (E) (TCE or TSE treatment, respectively) compared with WT MEFs (Figure 1E). Consistent with the suppression of RIPK1-mediated necroptosis, *Ripk1*$^{R588E/R588E}$ MEFs showed impaired phosphorylation of RIPK1, RIPK3, and MLKL in response to TSE stimulation (Figure 1F). Moreover, immunoprecipitation with anti-FADD antibodies revealed strongly reduced, but not completely abolished, interaction with RIPK1, RIPK3, and caspase-8 in *Ripk1*$^{R588E/R588E}$ MEFs in response to TC stimulation in the presence of the caspase inhibitor zVAD (Figure 1G). Taken together, these results showed that the R588E mutation strongly inhibited the DD-dependent interaction of RIPK1 with TNFR1 and FADD and protected cells from RIPK1-mediated apoptosis and necroptosis, while it sensitized cells to RIPK1-independent apoptosis.

RIPK3-dependent signaling causes perinatal lethality in *Ripk1*$^{R588E/R588E}$ mice

The increased numbers of CC3$^+$ cells in *Ripk1*$^{R588E/R588E}$ embryos together with the finding that the RIPK1-R588E mutation sensitized cells to TNF-induced RIPK1-independent apoptosis, suggested that the perinatal lethality of *Ripk1*$^{R588E/R588E}$ mice could be caused by excessive FADD-caspase-8-dependent apoptosis. Because FADD or caspase-8 deficiency causes RIPK3-MLKL-dependent embryonic lethality,[33–35] we crossed *Ripk1*$^{R588E/R588E}$ with *Fadd*$^{-/-}$*Ripk3*$^{-/-}$ mice. *Ripk1*$^{R588E/R588E}$*Ripk3*$^{-/-}$*Fadd*$^{-/-}$ mice were born at the Mendelian ratio, demonstrating that combined inhibition of RIPK3-mediated necroptosis and FADD-caspase-8-mediated apoptosis rescued the perinatal lethality of *Ripk1*$^{R588E/R588E}$ mice (Figure 2A). *Ripk1*$^{R588E/R588E}$*Ripk3*$^{-/-}$*Fadd*$^{WT/-}$ mice also were viable (Figure 2A), showing that heterozygous knockout of FADD combined with RIPK3 deficiency was sufficient to rescue the perinatal lethality of *Ripk1*$^{R588E/R588E}$ mice. To address whether RIPK3 deficiency alone could also rescue the perinatally lethal phenotype, we intercrossed *Ripk1*$^{WT/R588E}$*Ripk3*$^{-/-}$ mice and found that *Ripk1*$^{R588E/R588E}$ *Ripk3*$^{-/-}$ animals were born at near Mendelian ratio (Figure 2B). Therefore, RIPK3 deficiency alone or together with FADD knockout prevented the perinatal lethality of *Ripk1*$^{R588E/R588E}$ mice.

Ripk1$^{R588E/R588E}$*Ripk3*$^{-/-}$*Fadd*$^{-/-}$ mice survived until the age of 20 weeks when they were sacrificed because of the development of lymphoproliferative disease (Figures 2C and S1E), as shown earlier in *Fadd*$^{-/-}$*Ripk3*$^{-/-}$ mice.[35] By contrast, *Ripk1*$^{R588E/R588E}$ *Ripk3*$^{-/-}$*Fadd*$^{WT/-}$ as well as *Ripk1*$^{R588E/R588E}$ Ripk3$^{-/-}$ mice died prematurely, with most animals not surviving beyond the age of 5 months (Figures 2C and 2D). Early death was often associated with reduced body weight and diarrhea in *Ripk1*$^{R588E/R588E}$*Ripk3*$^{-/-}$ mice (Figure S1F and data not shown). Hematological analysis revealed slightly reduced levels of hemoglobin, indicating mild anemia, as well as increased numbers of granulocytes in peripheral blood from *Ripk1*$^{R588E/R588E}$*Ripk3*$^{-/-}$ mice compared with littermate controls (Figure 2E). Moreover, *Ripk1*$^{R588E/R588E}$*Ripk3*$^{-/-}$ mice had enlarged spleens that contained increased numbers of neutrophils and inflammatory monocytes, reduced numbers of natural killer (NK) cells, but normal numbers of B and T cells (Figures 2F and S1G). Thymocyte T cell populations were not altered in *Ripk1*$^{R588E/R588E}$ *Ripk3*$^{-/-}$ mice (Figure S1H). Histological analyses revealed inflammation with increased numbers of CC3$^+$ epithelial cells in the colon of *Ripk1*$^{R588E/R588E}$*Ripk3*$^{-/-}$ mice that were suppressed by additional knockout of FADD, although there was a large variability between individual animals (Figures 2G and 2H). Moreover, RT-qPCR analysis showed increased mRNA expression of IFNs, ISGs, and inflammatory cytokines in the colon of *Ripk1*$^{R588E/R588E}$*Ripk3*$^{-/-}$ mice compared with littermate controls (Figure 2I). About one-third of the *Ripk1*$^{R588E/R588E}$ *Ripk3*$^{-/-}$ mice also displayed mild immune cell infiltrates in the liver (data not shown). Collectively, RIPK3 deficiency rescued the perinatal lethality, but *Ripk1*$^{R588E/R588E}$*Ripk3*$^{-/-}$ animals died prematurely between 1 and 6 months of age due to FADD-caspase-8-dependent apoptosis.

TNFR1 causes RIPK3-independent pathology in *Ripk1*$^{R588E/R588E}$ mice

The increased expression of TNF in the colon of *Ripk1*$^{R588E/R588E}$ *Ripk3*$^{-/-}$ mice (Figure 2I) suggested that TNF might contribute to the pathology and early lethality of these animals. TNF stimulation induced RIPK1-kinase activity-independent cell death in *Ripk1*$^{R588E/R588E}$ MEFs, which was partially dependent on RIPK3 (Figures 3A and 3B). Treatment with the caspase-inhibitor E prevented the TNF-induced death of *Ripk1*$^{R588E/R588E}$*Ripk3*$^{-/-}$ MEFs, suggesting that they undergo caspase-8-dependent apoptosis (Figure 3A). While TNFR1 deficiency alone did not rescue the perinatal lethality of *Ripk1*$^{R588E/R588E}$ mice, *Ripk1*$^{R588E/R588E}$*Ripk3*$^{-/-}$*Tnfr1*$^{-/-}$ mice were born at the Mendelian ratio and did not show early lethality at least up to 6 months of age, demonstrating that TNFR1 drives the RIPK3-independent pathology (Figures 3C, 3D, and S2A). *Ripk1*$^{R588E/R588E}$*Ripk3*$^{-/-}$ *Tnfr1*$^{WT/-}$ mice showed an intermediate phenotype with about 40% of these animals succumbing by the age of 6 months compared with about 90% of the *Ripk1*$^{R588E/R588E}$*Ripk3*$^{-/-}$ mice (Figure 3D). Analysis of mice at the age of 13–20 or

(F) Graphs depicting spleen weight/body weight (BW) ratio and percentage of inflammatory monocytes and neutrophils in splenic leukocytes from mice with the indicated genotypes at 12 weeks of age.

(G and H) Representative images of small intestine (SI) and colon sections from mice with the indicated genotypes stained with H&E (G) or immunostained with anti-CC3 (H). Graphs show the histology score of the colon (G) and quantification of CC3$^+$ cells (H) in mice with the indicated genotypes. (H&E; control $n = 6$, *Ripk1*$^{R588E/R588E}$*Ripk3*$^{-/-}$ $n = 10$, *Ripk1*$^{R588E/R588E}$*Fadd*$^{-/-}$*Ripk3*$^{-/-}$ $n = 7$, CC3; control $n = 20$, *Ripk1*$^{R588E/R588E}$*Ripk3*$^{-/-}$ $n = 19$, *Ripk1*$^{R588E/R588E}$*Fadd*$^{-/-}$*Ripk3*$^{-/-}$ $n = 7$).

(I) RT-qPCR analysis of mRNA expression of the indicated genes in the colon from 12-week-old mice.

Scale bars, 100 μm. Each dot represents one mouse. Graphs show mean ± SEM. *$p \le 0.05$; **$p \le 0.01$; ***$p \le 0.001$; ****$p \le 0.0001$ for all figures.
See also Figure S1.

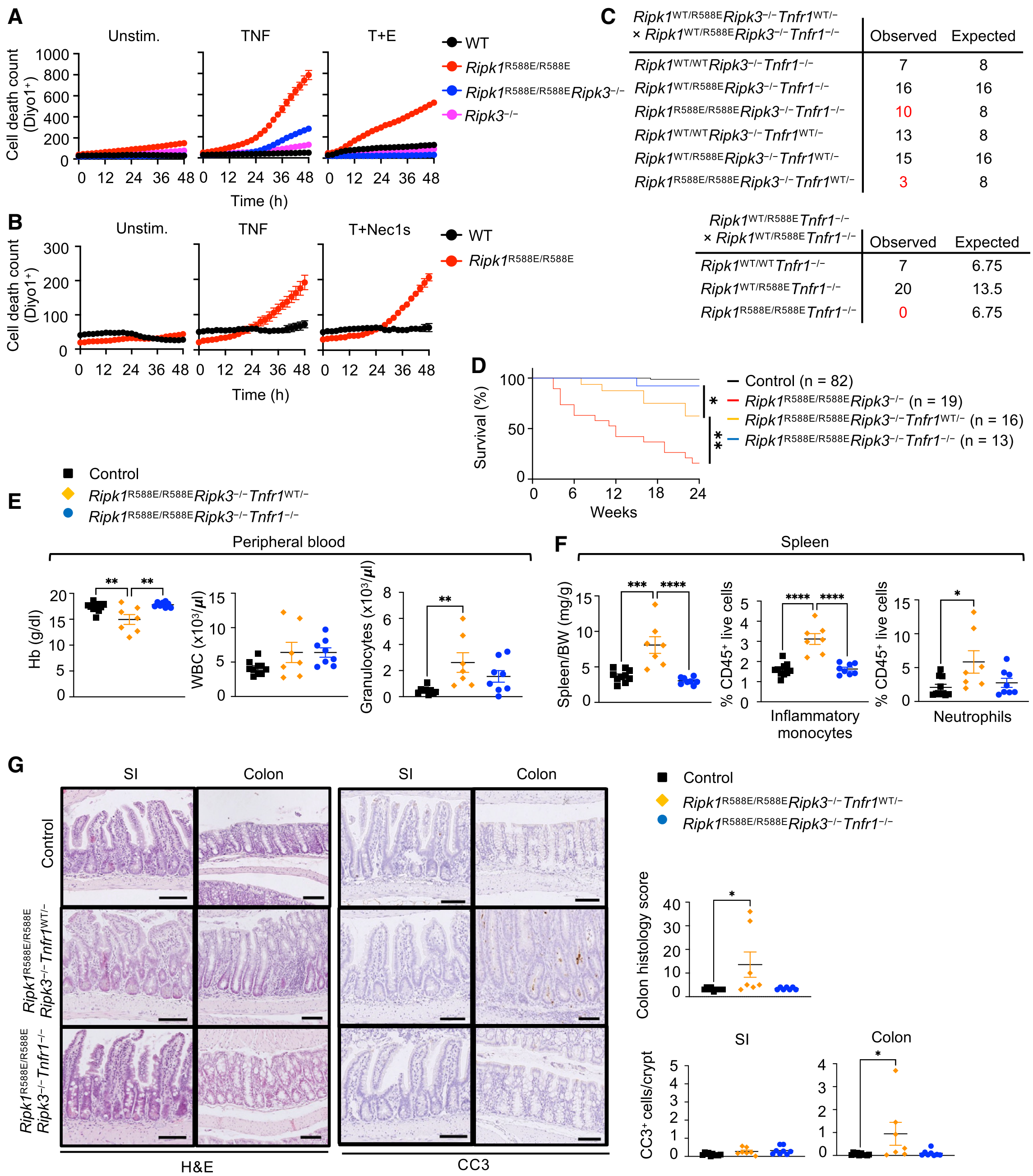

Ripk1WT/R588E Ripk3−/− Tnfr1WT/− × Ripk1WT/R588E Ripk3−/− Tnfr1−/−	Observed	Expected
Ripk1WT/WT Ripk3−/− Tnfr1−/−	7	8
Ripk1WT/R588E Ripk3−/− Tnfr1−/−	16	16
Ripk1R588E/R588E Ripk3−/− Tnfr1−/−	10	8
Ripk1WT/WT Ripk3−/− Tnfr1WT/−	13	8
Ripk1WT/R588E Ripk3−/− Tnfr1WT/−	15	16
Ripk1R588E/R588E Ripk3−/− Tnfr1WT/−	3	8

Ripk1WT/R588E Tnfr1−/− × Ripk1WT/R588E Tnfr1−/−	Observed	Expected
Ripk1WT/WT Tnfr1−/−	7	6.75
Ripk1WT/R588E Tnfr1−/−	20	13.5
Ripk1R588E/R588E Tnfr1−/−	0	6.75

Figure 3. TNFR1 signaling mediates the late pathology of *Ripk1*$^{R588E/R588E}$*Ripk3*$^{-/-}$ mice

(A and B) Cell death measured by DiYO1 uptake in primary MEFs of the indicated genotypes stimulated with T (20 ng mL^{-1}) with or without E (5 μM) or the RIPK1 inhibitor Necrostatin-1s (Nec1s) (20 μM) for 48 h. Data are representative of three independent experiments.

(C) Tables showing the numbers of P0 offspring from intercrossing parents with the indicated genotypes.

(D) Kaplan-Meier survival graph of mice with the indicated genotypes. *p* values were calculated by the Log-rank test.

(E and F) Blood Hb, WBC, and granulocyte counts (E) and spleen weight/BW ratio and flow cytometry analysis of splenic leukocytes (F) in 13- to 20-week-old mice with the indicated genotypes.

(G) Representative images of SI and colon sections from 13- to 20-week-old control (n = 10), *Ripk1*$^{R588E/R588E}$*Ripk3*$^{-/-}$*Tnfr1*$^{WT/-}$ (n = 7), and *Ripk1*$^{R588E/R588E}$*Ripk3*$^{-/-}$*Tnfr1*$^{-/-}$ (n = 8) mice stained with H&E or immunostained for CC3. Graphs show colon histology score and quantification of CC3^{+} cells in mice with the indicated genotypes.

Scale bars, 100 μm. Each dot represents one mouse. Graphs show mean ± SEM. *$p \leq 0.05$; **$p \leq 0.01$; ***$p \leq 0.001$; ****$p \leq 0.0001$ for all figures.

See also Figure S2.

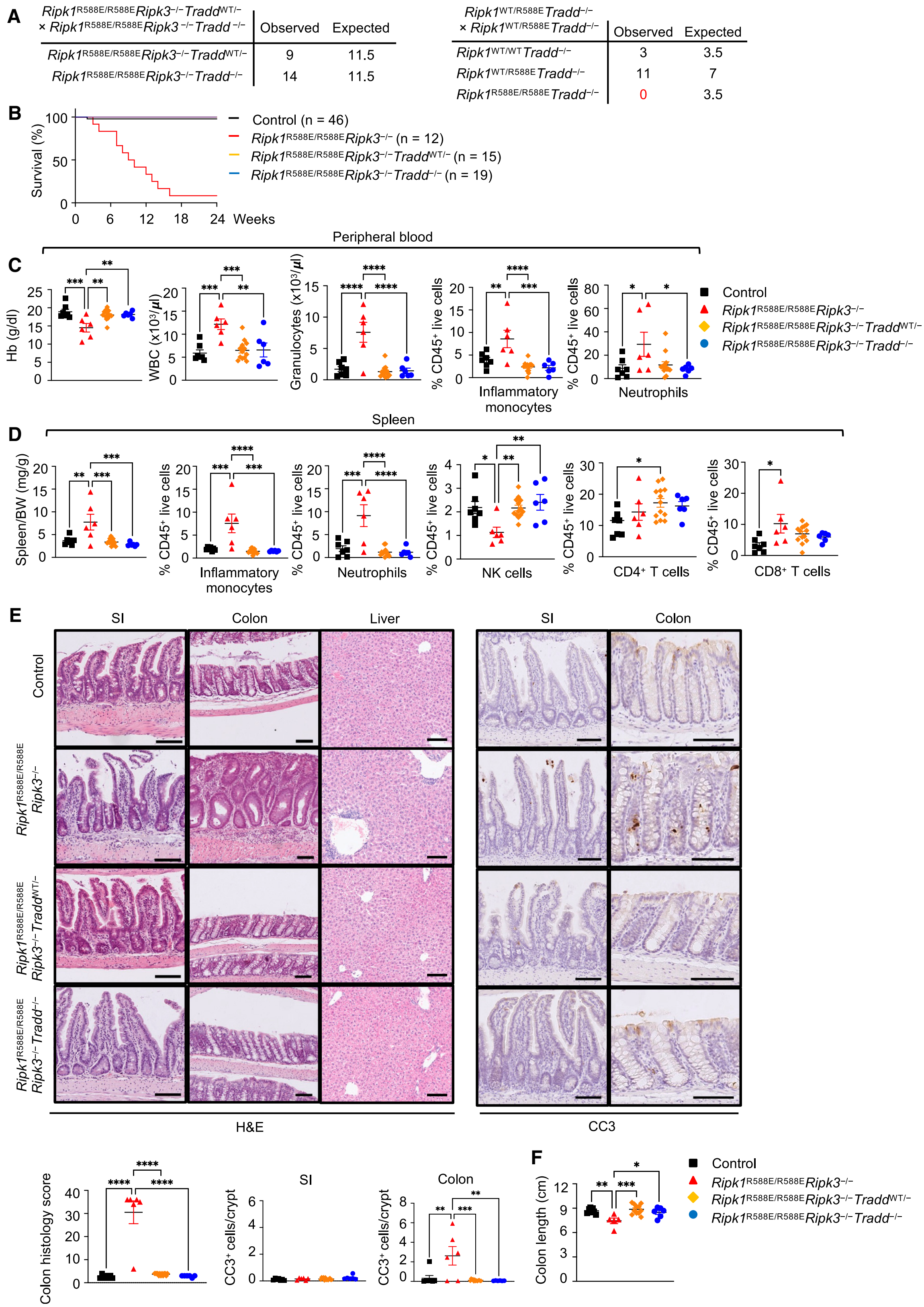

(legend on next page)

23–32 weeks revealed that TNFR1 deficiency prevented the development of anemia, splenomegaly, granulocytosis, and monocytosis and averted cell death and inflammation in the colon of *Ripk1*$^{R588E/R588E}$*Ripk3*$^{-/-}$*Tnfr1*$^{-/-}$ mice, whereas TNFR1 heterozygosity had a partial effect (Figures 3E–3G and S2B–S2D). Thus, TNFR1 drives the RIPK3-independent postnatal pathology of *Ripk1*$^{R588E/R588E}$*Ripk3*$^{-/-}$ mice.

TRADD mediates the TNFR1-mediated pathology in adult *Ripk1*$^{R588E/R588E}$*Ripk3*$^{-/-}$ mice

We hypothesized that TRADD-mediated apoptosis could drive the TNFR1-mediated pathology of *Ripk1*$^{R588E/R588E}$*Ripk3*$^{-/-}$ mice. Indeed, *Ripk1*$^{R588E/R588E}$*Ripk3*$^{-/-}$*Tradd*$^{-/-}$ as well as *Ripk1*$^{R588E/R588E}$*Ripk3*$^{-/-}$*Tradd*$^{WT/-}$ mice were born at the Mendelian ratio and did not show early lethality or signs of pathology at least until the age of 6 months (Figures 4A, 4B, and S3A). However, TRADD deficiency alone could not rescue the perinatal lethality of *Ripk1*$^{R588E/R588E}$ mice (Figure 4A). Analysis of mice at the age of 13–19 or 23–32 weeks showed that heterozygous or homozygous TRADD deficiency normalized the levels of hemoglobin and the numbers of granulocytes and inflammatory monocytes in the peripheral blood and prevented the development of splenomegaly and the expansion of neutrophils and inflammatory monocytes as well as the reduction of NK cells in the spleen (Figures 4C, 4D, S3B, and S3C). Furthermore, loss of one or two alleles of *Tradd* prevented the development of colitis, as shown by histological analysis as well as the normal colon length in these animals compared with the shortened colons of *Ripk1*$^{R588E/R588E}$*Ripk3*$^{-/-}$ mice (Figures 4E, 4F, and S3D). Immunostaining for CC3 revealed that homozygous or heterozygous TRADD deficiency prevented epithelial cell apoptosis in the colon of *Ripk1*$^{R588E/R588E}$*Ripk3*$^{-/-}$ mice (Figures 4E and S3D). Moreover, TRADD deficiency also averted the mild immune cell infiltration in the liver of *Ripk1*$^{R588E/R588E}$*Ripk3*$^{-/-}$ mice (Figure 4E). Taken together, these results showed that TNFR1 mediates the postnatal RIPK3-independent pathology of *Ripk1*$^{R588E/R588E}$*Ripk3*$^{-/-}$ mice by inducing TRADD-dependent signaling.

Ripk1$^{R588E/R588E}$*Mlkl*$^{-/-}$ mice are born normally but exhibit severe inflammation and die before weaning age

RIPK3 induces MLKL-dependent necroptosis but also mediates apoptosis and cell-death-independent inflammatory signaling.[36–38] To assess whether RIPK3 induces the pathology of *Ripk1*$^{R588E/R588E}$ mice by necroptosis-dependent or -independent functions, we crossed them with Mlkl$^{-/-}$ mice. *Ripk1*$^{R588E/R588E}$*Mlkl*$^{-/-}$ mice were born at the Mendelian ratio but showed about 50% reduced body weight compared with their littermate controls and did not survive beyond weaning age (Figures 5A–5C). Hematological and flow cytometric analysis revealed strongly reduced numbers of B, T, and NK cells and elevated numbers of neutrophils in peripheral blood from 2- to 4- day-old *Ripk1*$^{R588E/R588E}$*Mlkl*$^{-/-}$ mice (Figure 5D). Furthermore, *Ripk1*$^{R588E/R588E}$*Mlkl*$^{-/-}$ mice showed reduced cellularity in the spleen, with higher ratio of inflammatory monocytes and neutrophils but reduced numbers of B cells and CD4^{+} T cells compared with littermate controls (Figure 5E). In addition, *Ripk1*$^{R588E/R588E}$*Mlkl*$^{-/-}$ mice showed strongly reduced cellularity in the thymus with a dramatic decrease of CD4^{+}CD8^{+} thymocytes, as well as intestinal pathology with increased numbers of CC3^{+} cells in the small intestine (SI) and colon (Figures 5F–5H). Therefore, MLKL deficiency rescued the perinatal lethality, but *Ripk1*$^{R588E/R588E}$*Mlkl*$^{-/-}$ mice showed a more severe postnatal phenotype compared with *Ripk1*$^{R588E/R588E}$*Ripk3*$^{-/-}$ mice. These results showed that RIPK3 causes perinatal lethality by inducing MLKL-dependent necroptosis but exhibits necroptosis-independent functions that promote the postnatal phenotype of *Ripk1*$^{R588E/R588E}$ mice.

We hypothesized that the MLKL-independent function of RIPK3 might be mediated by TNFR1-TRADD-mediated apoptosis. Indeed, we found that *Ripk1*$^{R588E/R588E}$*Mlkl*$^{-/-}$*Tradd*$^{WT/-}$ mice did not show early lethality, had normal body weight, and appeared healthy at least until the age of 9 months (Figures 5C and S4A). Hematological and flow cytometry analysis of blood, spleen, and thymus did not reveal considerable abnormalities in *Ripk1*$^{R588E/R588E}$*Mlkl*$^{-/-}$*Tradd*$^{WT/-}$ mice compared with their littermate control animals at the age of 9 weeks (Figures S4B–S4E). Furthermore, *Ripk1*$^{R588E/R588E}$*Mlkl*$^{-/-}$*Tradd*$^{WT/-}$ mice had a normal colon length and showed only very mild hyperplasia without signs of epithelial cell apoptosis in the colon (Figures S4F and S4G). Thus, TRADD-mediated signaling caused the early postnatal pathology in *Ripk1*$^{R588E/R588E}$*Mlkl*$^{-/-}$ mice as well as the late postnatal phenotype of *Ripk1*$^{R588E/R588E}$*Ripk3*$^{-/-}$ mice. TNF-induced cell death in *Ripk1*$^{R588E/R588E}$ cells fully depended on TRADD and partially on RIPK3 but not on MLKL (Figure 5I), arguing that RIPK3 acts in an MLKL-independent fashion to promote TRADD-dependent apoptosis when the RIPK1 DD is mutated.

ZBP1 and TRIF induce perinatal lethality and early postnatal pathology in *Ripk1*$^{R588E/R588E}$ mice

Increased expression of ZBP1 and TRIF (also known as TICAM-1) was detected in the tissues of E18.5 *Ripk1*$^{R588E/R588E}$

Figure 4. TRADD mediates the late pathology of *Ripk1*$^{R588E/R588E}$*Ripk3*$^{-/-}$ mice

(A) Tables showing the numbers of P0 offspring from intercrossing parents with the indicated genotypes.

(B) Kaplan-Meier survival graph of mice with the indicated genotypes.

(C) Graphs depicting Hb, WBC, and granulocyte counts as well as flow cytometry analysis of inflammatory monocyte and neutrophil ratios in the blood from mice with the indicated genotypes.

(D) Graphs depicting spleen weight/BW ratio and flow cytometry analysis of splenic leukocytes from mice with the indicated genotypes.

(E) Representative images from sections of SI, colon, and liver of mice with the indicated genotypes stained with H&E or immunostained for CC3. Graphs depict colon histology score and quantification of CC3^{+} cells in mice with the indicated genotypes. Control (n = 7), *Ripk1*$^{R588E/R588E}$*Ripk3*$^{-/-}$ (n = 6), *Ripk1*$^{R588E/R588E}$*Ripk3*$^{-/-}$*Tradd*$^{WT/-}$ (n = 13), and *Ripk1*$^{R588E/R588E}$*Ripk3*$^{-/-}$*Tradd*$^{-/-}$ (n = 6).

(F) Graph depicting colon length in mice with the indicated genotypes.

Scale bars, 100 μm. All analyses were performed in 13- to 19- week-old mice. Each dot represents one mouse. Graphs show mean ± SEM.*$p \leq 0.05$; **$p \leq 0.01$; ***$p \leq 0.001$; ****$p \leq 0.0001$ for all figures.

See also Figure S3.

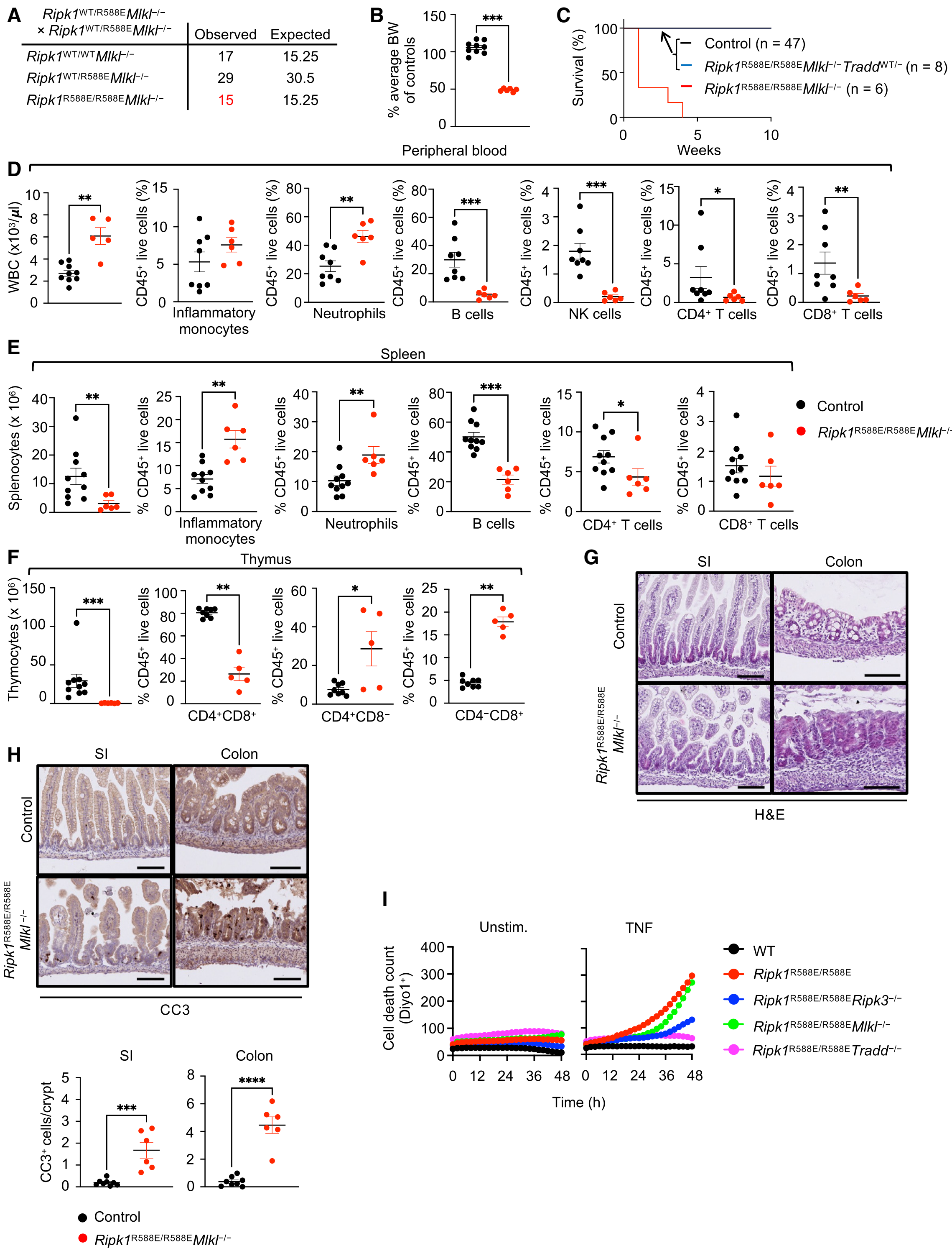

Figure 5. *Ripk1*$^{R588E/R588E}$*Mlkl*$^{-/-}$ mice develop early postnatal pathology

(A) Table showing the numbers of P0 offspring from *Ripk1*$^{WT/R588E}$*Mlkl*$^{-/-}$ parents.

(B) Graphs depicting relative BW at 2–4 days of age.

(C) Kaplan-Meier survival graphs of mice with the indicated genotypes.

(D) WBC and flow cytometry analysis of leucocytes in the blood from mice with the indicated genotypes at 2–4 days of age.

(E and F) Cell numbers and flow cytometry analysis of splenic leukocytes (E) or thymocytes (F) from mice with the indicated genotypes at 2–4 days of age.

(G) Representative H&E-stained sections from SI and colon from control (*n* = 8) and *Ripk1*$^{R588E/R588E}$*Mlkl*$^{-/-}$ (*n* = 6) mice at 4–7 days of age.

(legend continued on next page)

embryos (Figure 1C), suggesting that ZBP1 or TRIF could be implicated in triggering necroptosis and perinatal lethality in *Ripk1*$^{R588E/R588E}$ mice. We did not observe live *Ripk1*$^{R588E/R588E}$*Ticam1*$^{-/-}$ progeny at P0, showing that TRIF deficiency did not rescue the perinatal lethality (Figure 6A). *Ripk1*$^{R588E/R588E}$*Zbp1*$^{-/-}$ progeny were born, but at a lower than expected Mendelian ratio, were smaller than their littermate controls, and most of them died before weaning (Figures 6A–6C). 2-week-old *Ripk1*$^{R588E/R588E}$*Zbp1*$^{-/-}$ mice showed splenomegaly, elevated numbers of neutrophils and inflammatory monocytes, and reduced numbers of B and T cells in the spleen and peripheral blood compared with littermate controls (Figures 6D and 6E). Histological analysis revealed blunted and shortened villi in the SI, but we did not detect increased numbers of CC3^{+} cells or signs of inflammation in the SI or colon of *Ripk1*$^{R588E/R588E}$*Zbp1*$^{-/-}$ mice (Figure 6F). RT-qPCR analysis revealed increased expression of TLR3, TLR4, and TRIF in the liver of *Ripk1*$^{R588E/R588E}$*Zbp1*$^{-/-}$ mice (Figure 6G), indicating that TRIF-mediated signaling might be involved in driving the pathology of *Ripk1*$^{R588E/R588E}$*Zbp1*$^{-/-}$ mice. Indeed, *Ripk1*$^{R588E/R588E}$ *Zbp1*$^{-/-}$*Ticam1*$^{-/-}$ mice were born at the Mendelian ratio, had a normal body weight, and did not show the early postnatal lethality of *Ripk1*$^{R588E/R588E}$*Zbp1*$^{-/-}$ mice (Figures 6A–6C). Analysis of mice at the age of 2 weeks revealed that TRIF deficiency prevented the hematological abnormalities as well as the intestinal pathology and increased ISG and inflammatory gene expression of *Ripk1*$^{R588E/R588E}$*Zbp1*$^{-/-}$ mice (Figures 6D–6G). *Ripk1*$^{R588E/R588E}$*Zbp1*$^{-/-}$*Ticam1*$^{-/-}$ mice reached adulthood and appeared healthy up to about 6 months of age, showing normal body weight without detectable hematological or intestinal abnormalities compared with littermate controls (Figures S5A–S5D). *Ripk1*$^{R588E/R588E}$*Zbp1*$^{-/-}$*Ticam1*$^{WT/-}$ animals also survived to adulthood, showing slightly lower body weight together with a small increase in spleen size and the numbers of granulocytes and inflammatory monocytes in peripheral blood (Figures S5A–S5D). Histological analysis did not reveal inflammation with only marginally increased numbers of CC3^{+} cells in *Ripk1*$^{R588E/R588E}$*Zbp1*$^{-/-}$*Ticam1*$^{WT/-}$ mice (Figure S5E). However, about 50% of the *Ripk1*$^{R588E/R588E}$ *Zbp1*$^{-/-}$*Ticam1*$^{-/-}$ mice died between 25 and 30 weeks of age (Figure 6B), showing that in aged animals, ZBP1- and TRIF-independent mechanisms cause late lethality. We detected increased expression of type I and II IFNs as well as TNF and interleukin 1β (IL-1β) in colon tissues from aged *Ripk1*$^{R588E/R588E}$*Zbp1*$^{-/-}$*Ticam1*$^{-/-}$ mice compared with littermate controls (Figure S5F). Moreover, *Ripk1*$^{R588E/R588E}$*Zbp1*$^{-/-}$ *Ticam1*$^{-/-}$ MEFs were equally sensitive to TNF-induced death as *Ripk1*$^{R588E/R588E}$ cells (Figure S5G). Together, these findings indicate that TNF-TNFR1-TRADD-mediated apoptosis could be implicated in driving the ZBP1- and TRIF-independent pathology in older mice.

The RIPK1 DD regulates ZBP1- and TRIF-mediated cell death

Our genetic studies showed that ZBP1 and TRIF induce RIPK3-mediated pathology in *Ripk1*$^{R588E/R588E}$ mice, suggesting that RIPK1 suppresses ZBP1- and TRIF-mediated activation of RIPK3 in a DD-dependent manner. To assess the role of the RIPK1 DD in ZBP1-mediated cell death, we stimulated MEFs with interferon-γ (IFNγ) in the presence of E and the TNF inhibitor etanercept (Et), which we showed previously induces ZBP1-mediated necroptosis.[15,39] In WT MEFs, stimulation with IFNγ alone did not induce cell death, while IFNγ together with E induced the death of small numbers of cells that were not suppressed by the addition of Et (Figure 7A). By contrast, IFNγ stimulation induced cell death in *Ripk1*$^{R588E/R588E}$ MEFs, which was not prevented by Et and was not further increased by the addition of E (Figure 7A). Cell death induced by IFNγ, IFNγ+E, or IFNγ+E+Et was partially reduced in *Ripk1*$^{R588E/R588E}$*Zbp1*$^{-/-}$ and completely prevented in *Ripk1*$^{R588E/R588E}$*Zbp1*$^{-/-}$*Ticam*$^{-/-}$, *Ripk1*$^{R588E/R588E}$*Ripk3*$^{-/-}$, and *Ripk1*$^{R588E/R588E}$*Mlkl*$^{-/-}$ MEFs (Figure 7A), showing that IFNγ stimulation triggers ZBP1- and TRIF-dependent necroptosis when DD-dependent RIPK1 signaling is suppressed.

Consistent with the cell death assay results, stimulation with IFNγ, IFNγ+E, or IFNγ+E+Et induced robust phosphorylation of RIPK3 and MLKL in *Ripk1*$^{R588E/R588E}$ MEFs, which was strongly reduced by the absence of ZBP1 and prevented by combined loss of ZBP1 and TRIF (Figure 7B). Unstimulated *Ripk1*$^{R588E/R588E}$ MEFs also showed weak RIPK3 and MLKL phosphorylation, which was suppressed by combined deficiency of ZBP1 and TRIF (Figure 7B). WT MEFs showed RIPK3 and MLKL phosphorylation upon stimulation with IFNγ+E or IFNγ+E+Et, but not IFNγ alone (Figure 7B). We also detected strong RIPK1 phosphorylation in unstimulated *Ripk1*$^{R588E/R588E}$ MEFs that was further enhanced by IFNγ, IFNγ+E, or IFNγ+E+Et stimulation (Figure 7B). Weak RIPK1 phosphorylation was detected in WT MEFs stimulated with IFNγ+E or IFNγ+E+Et but not IFNγ alone (Figure 7B). Both the spontaneous and IFNγ-induced RIPK1 phosphorylation in *Ripk1*$^{R588E/R588E}$ MEFs was enhanced in the absence of MLKL but was inhibited in the absence of RIPK3 or of both ZBP1 and TRIF (Figure 7B), suggesting that interaction with RIPK3 triggers the autophosphorylation of RIPK1-R588E downstream of ZBP1 and TRIF signaling. IFNγ+E-induced RIPK1 phosphorylation was also suppressed in Ripk3$^{-/-}$ cells, while TRIF deficiency did not inhibit phosphorylation of RIPK1 or RIPK3 in cells expressing WT or DD mutant RIPK1 (Figure S6A). These results showed that RIPK3 is required for RIPK1 activation in response to IFNγ+E stimulation both in cells expressing WT or R588E mutant RIPK1.

We then asked whether RIPK1 kinase activity contributes to IFNγ-induced cell death. IFNγ-, IFNγ+E-, or IFNγ+E+Et-induced death of *Ripk1*$^{R588E/R588E}$ MEFs was not inhibited by the RIPK1

(H) Representative images and quantification of SI and colon sections immunostained for CC3 in control (n = 8) and *Ripk1*$^{R588E/R588E}$*Mlkl*$^{-/-}$ (n = 6) mice at 2–9 days of age.

(I) Cell death measured by DiYO1 uptake in primary MEFs of the indicated genotypes stimulated with T (20 ng mL^{-1}) for 48 h. Data are representative of three independent experiments.

Scale bars, 100 μm. Each dot represents one mouse. Graphs show mean ± SEM. *$p \leq 0.05$; **$p \leq 0.01$; ***$p \leq 0.001$; ****$p \leq 0.0001$ for all figures.
See also Figure S4.

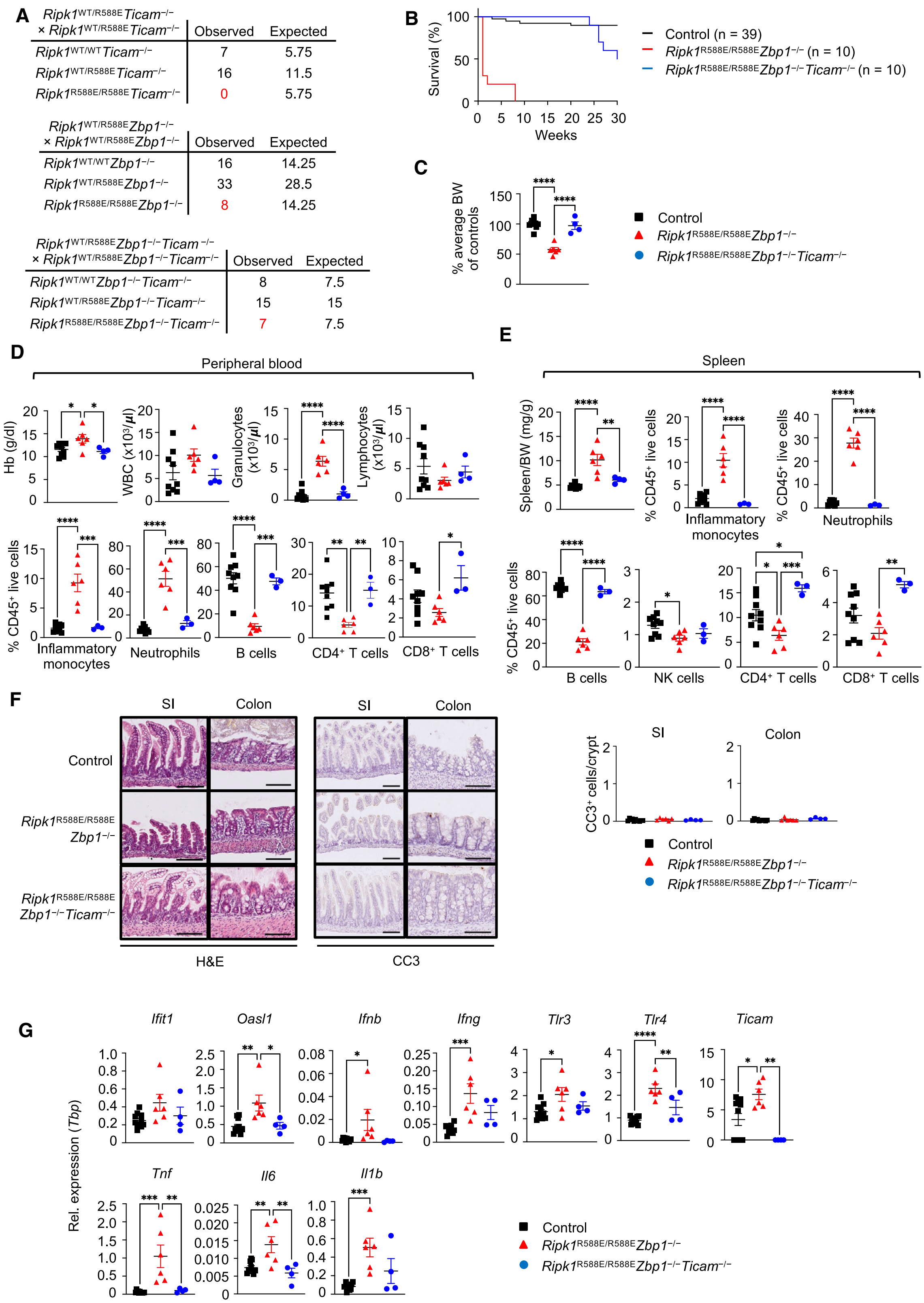

Figure 6. ZBP1 and TRIF cause perinatal lethality and postnatal pathology in *Ripk1*$^{R588E/R588E}$ mice

(A) Tables showing the numbers of P0 offspring from intercrossing parents with the indicated genotypes.

(B and C) Graphs depicting Kaplan-Meier survival curve (B) and relative BW (C) of mice with the indicated genotypes.

(legend continued on next page)

inhibitor Nec1s but was prevented by the RIPK3 inhibitor GSK′872 (Figure 7C). By contrast, Nec1s, as well as GSK′872, prevented the death of WT MEFs treated with IFNγ+E or IFNγ+E+Et (Figure 7C). Consistent with the cell death assay results, Nec1s prevented RIPK3 and MLKL phosphorylation in WT but not in *Ripk1*$^{R588E/R588E}$ MEFs treated with IFNγ+E+Et (Figure 7D). Moreover, Nec1s could not inhibit RIPK3 phosphorylation in *Ripk1*$^{R588E/R588E}$*Mlkl*$^{-/-}$ MEFs stimulated with IFNγ or IFNγ+E, although it fully suppressed IFNγ+E-induced RIPK3 phosphorylation in Mlkl$^{-/-}$ MEFs (Figure S6B). Furthermore, the RIPK3 kinase inhibitor GSK′872 could not prevent IFNγ- or IFNγ+E-induced RIPK1 phosphorylation in *Ripk1*$^{R588E/R588E}$*Mlkl*$^{-/-}$ cells (Figure S6B), showing that RIPK3 functions as a scaffold to activate RIPK1 in *Ripk1*$^{R588E/R588E}$ cells. Collectively, these results showed that RIPK1 kinase activity is required for ZBP1-mediated activation of RIPK3 in WT but not in *Ripk1*$^{R588E/R588E}$ MEFs.

We then assessed how RIPK1 DD mutation affects its interaction with RIPK3 and ZBP1. First, phosphorylated RIPK1 co-immunoprecipitated with phosphorylated RIPK3 in unstimulated *Ripk1*$^{R588E/R588E}$*Mlkl*$^{-/-}$ but not in Mlkl$^{-/-}$ MEFs, further supporting that RIPK3 interacts with and activates RIPK1-R588E under steady-state conditions (Figure 7E). This interaction was less obvious in cells expressing MLKL, most likely because MLKL-mediated necroptosis prevents the accumulation of complexes containing phosphorylated RIPK3. We previously showed that overexpressed ZBP1 co-immunoprecipitated with RIPK3 but not RIPK1, with the latter detected in the ZBP1-induced signaling complex only in the presence of caspase inhibitors, suggesting that RIPK3 is the preferred partner of ZBP1.[15,16] To assess how the R588E mutation affected the interaction of RIPK1 with ZBP1, we immunoprecipitated endogenous ZBP1 from immortalized WT and *Ripk1*$^{R588E/R588E}$ MEFs stimulated with IFNγ or IFNγ+E for 24 h. After stimulation with IFNγ+E, ZBP1 co-immunoprecipitated with RIPK3 and RIPK1 in both WT and *Ripk1*$^{R588E/R588E}$ MEFs (Figure S6C). However, upon stimulation with IFNγ alone, ZBP1 co-immunoprecipitated with RIPK1 but not RIPK3 in *Ripk1*$^{R588E/R588E}$ MEFs, while we did not detect RIPK1 or RIPK3 interacting with ZBP1 in WT MEFs (Figure S6C). This result suggested that ZBP1 preferentially interacted with RIPK1 in *Ripk1*$^{R588E/R588E}$ cells. However, considering that phosphorylated RIPK3 and MLKL are readily detected in IFNγ-treated *Ripk1*$^{R588E/R588E}$ MEFs, we reasoned that MLKL-dependent necroptosis might prevent the accumulation of ZBP1-RIPK1-RIPK3 complexes and repeated the ZBP1 immunoprecipitation in Mlkl$^{-/-}$ and *Ripk1*$^{R588E/R588E}$*Mlkl*$^{-/-}$ MEFs. Indeed, we detected both phosphorylated RIPK1 and RIPK3 in ZBP1 immunoprecipitates from *Ripk1*$^{R588E/R588E}$*Mlkl*$^{-/-}$ MEFs stimulated with IFNγ alone (Figure 7F), arguing that ZBP1 induces the formation of a RIPK1-RIPK3 complex that accumulates in the absence of MLKL. In addition, caspase-8 was detected in the ZBP1 immunoprecipitates in WT MEFs stimulated with IFNγ+E but not in *Ripk1*$^{R588E/R588E}$ MEFs (Figure 7F), consistent with a RIPK1 DD-dependent recruitment of FADD and caspase-8. Moreover, the presence of phosphorylated RIPK3 in ZBP1 immunoprecipitates from IFNγ+E-stimulated cells was inhibited by Nec1s in Mlkl$^{-/-}$ but not in *Ripk1*$^{R588E/R588E}$*Mlkl*$^{-/-}$ MEFs (Figure 7G). To directly assess how the recruitment of FADD-caspase-8 regulates the ZBP1-induced signaling complex, we analyzed Mlkl$^{-/-}$ and *Fadd*$^{-/-}$*Mlkl*$^{-/-}$ MEFs by immunoblotting. Similarly to *Ripk1*$^{R588E/R588E}$*Mlkl*$^{-/-}$ cells, *Fadd*$^{-/-}$*Mlkl*$^{-/-}$ MEFs showed phosphorylation of RIPK1 and RIPK3 in response to IFNγ or IFNγ+E. Importantly, Nec1s did not prevent RIPK3 phosphorylation in *Fadd*$^{-/-}$*Mlkl*$^{-/-}$ MEFs, suggesting that FADD-mediated DD-dependent interactions determine whether RIPK1 kinase activity is required for ZBP1-mediated RIPK3 activation (Figure S6D). Together, these results showed that ZBP1 interacts with both RIPK1 and RIPK3 upon IFNγ stimulation and that this interaction and the signaling outcome are regulated by the RIPK1 DD.

We then assessed the role of the RIPK1 DD in TRIF-mediated signaling. Poly(I:C) stimulation induced TRIF-dependent RIPK3-MLKL-mediated necroptosis in *Ripk1*$^{R588E/R588E}$ but not in WT MEFs (Figure S6E). Stimulation with poly(I:C) in the presence of E also induced necroptosis in WT cells; however, this was weaker compared with *Ripk1*$^{R588E/R588E}$ cells (Figure S6E). We then assessed if RIPK1 kinase activity is required for TLR3-TRIF-induced necroptosis of *Ripk1*$^{R588E/R588E}$ MEFs. Consistent with previous studies, treatment with Nec1s or GSK′872 prevented poly(I:C)-induced necroptosis in WT MEFs (Figure S6F). However, poly(I:C)-induced death of *Ripk1*$^{R588E/R588E}$ MEFs was prevented by GSK′872 but not by Nec1s (Figure S6F). Consistent with the cell death assays, poly(I:C) stimulation induced RIPK3 phosphorylation in *Ripk1*$^{R588E/R588E}$*Mlkl*$^{-/-}$ cells, which was not prevented by Nec1s (Figure S6G). Taken together, these findings revealed a critical role of the RIPK1 DD in controlling ZBP1- and TRIF-mediated necroptosis.

DISCUSSION

RIPK1 is best known for its function in regulating TNFR1 signaling via DD-dependent interactions with the intracellular domain of TNFR1 in complex I and FADD in complex II.[1–3] Hence, we anticipated that abrogation of DD-mediated RIPK1 interactions would primarily affect TNFR1-mediated responses. However, our genetic studies showed that mutation of the RIPK1 DD caused necroptosis-mediated perinatal lethality that was not induced by TNFR1 but rather by ZBP1 and TRIF (Figure S7A). *Ripk1*$^{R588E/R588E}$*Ripk3*$^{-/-}$ mice survived to adulthood but developed inflammatory pathology mediated by TNFR1-TRADD-FADD-dependent signaling and died prematurely. *Ripk1*$^{R588E/R588E}$*Mlkl*$^{-/-}$ animals were runted and died

(D) Graphs depicting Hb, WBC, granulocyte, and lymphocyte counts as well as flow cytometry analysis of leucocyte populations in the blood from mice with the indicated genotypes.
(E) Spleen weight/BW ratio and flow cytometry analysis of splenic leukocytes from mice with the indicated genotypes.
(F) Representative images of sections stained with H&E or immunostained for CC3 and graphs depicting quantification of CC3$^+$ cells in SI and colon from control (n = 11), *Ripk1*$^{R588E/R588E}$*Zbp1*$^{-/-}$ (n = 6), and *Ripk1*$^{R588E/R588E}$*Zbp1*$^{-/-}$*Ticam*$^{-/-}$ (n = 4) mice.
(G) RT-qPCR analysis of mRNA expression of the indicated genes in the liver from mice with the indicated genotypes. Scale bars, 100 μm. All analyses were performed in 2-week-old mice. Each dot represents one mouse. Graphs show mean ± SEM. *$p \leq 0.05$; **$p \leq 0.01$; ***$p \leq 0.001$; ****$p \leq 0.0001$ for all figures.
See also Figure S5.

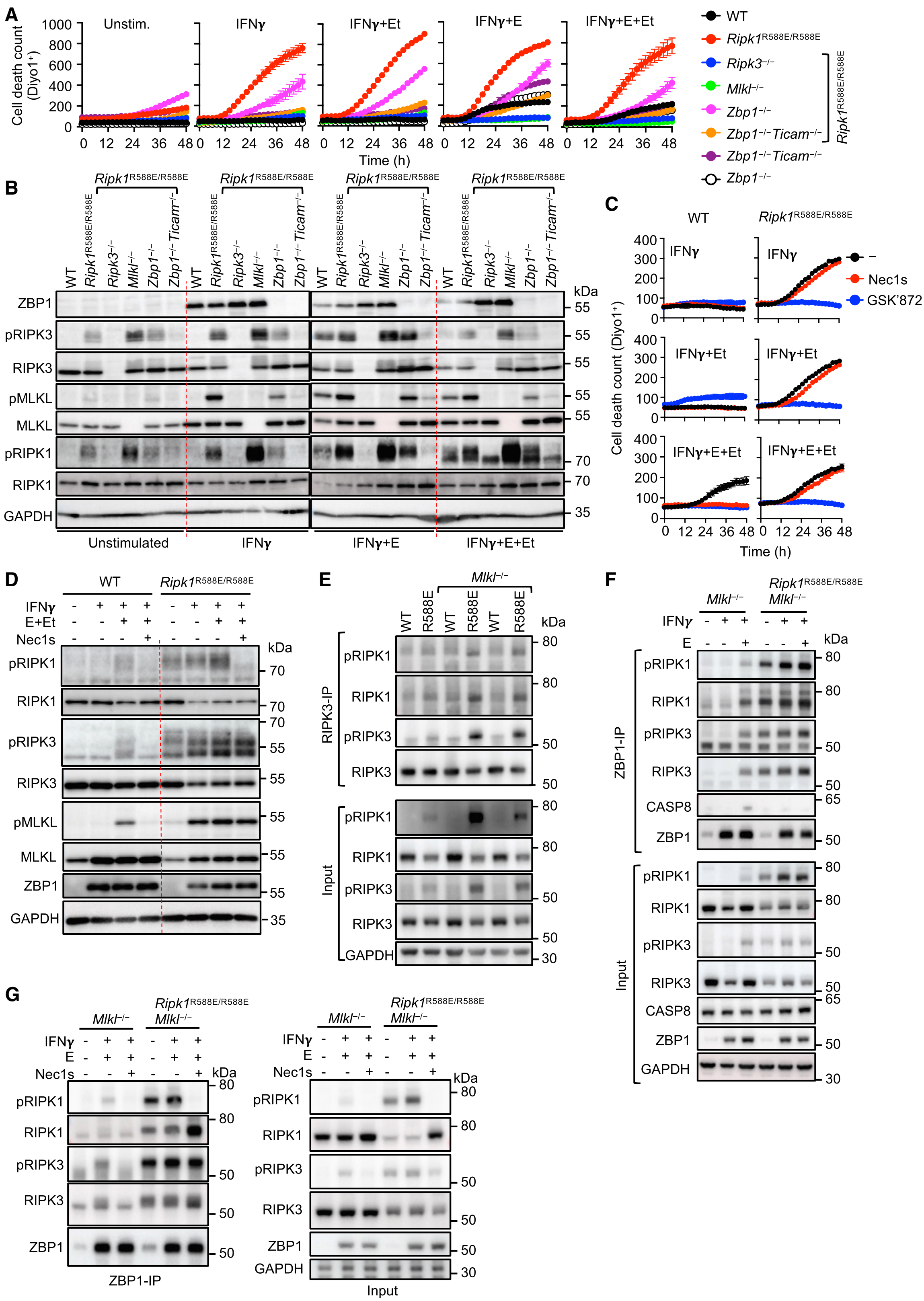

(legend on next page)

before weaning as opposed to *Ripk1*$^{R588E/R588E}$*Ripk3*$^{-/-}$ mice that could survive for several months, revealing a necroptosis-independent role of RIPK3. Homozygous or heterozygous TRADD deficiency fully rescued the postnatally lethal phenotype of *Ripk1*$^{R588E/R588E}$*Mlkl*$^{-/-}$ mice, showing that TRADD-dependent signaling drives the necroptosis-independent pathology in these animals. Moreover, TNF-induced apoptosis in *Ripk1*$^{R588E/R588E}$ cells depended on TRADD and partially on RIPK3, suggesting that RIPK3 promotes the MLKL-independent phenotype by cooperating with TRADD to induce TNFR1-mediated apoptosis. Although the detailed molecular mechanism by which TRADD and RIPK3 cooperate to drive the necroptosis-independent phenotype remains unclear, these two proteins may directly interact in TNFR1 signaling, as suggested previously.[40]

Our genetic experiments showed that ZBP1 and TRIF induce necroptosis-dependent perinatal lethality as well as necroptosis-independent postnatal pathology in *Ripk1*$^{R588E/R588E}$ mice (Figure S7). Although a large fraction of *Ripk1*$^{R588E/R588E}$*Zbp1*$^{-/-}$ mice were born alive, they were runted and succumbed during the first 2–3 weeks of life. *Ripk1*$^{R588E/R588E}$*Zbp1*$^{-/-}$*Ticam*$^{-/-}$ mice were born at the Mendelian ratio and survived for up to 6 months of age without exhibiting signs of severe pathology, showing that TRIF and ZBP1 drive both RIPK3-dependent and -independent signaling to cause the postnatal inflammatory pathology. We found increased expression of TNF and other inflammatory mediators in 2-week-old *Ripk1*$^{R588E/R588E}$*Zbp1*$^{-/-}$ mice that were inhibited by additional TRIF deficiency, suggesting that TRIF likely promotes postnatal inflammatory pathology by inducing TNF expression causing TNFR1-TRADD-mediated cell death. About 50% of *Ripk1*$^{R588E/R588E}$*Zbp1*$^{-/-}$*Ticam*$^{-/-}$ mice died between 25 and 30 weeks of age, suggesting that ZBP1- and TRIF-independent signaling drive late lethality in older mice. The mechanisms causing late lethality in *Ripk1*$^{R588E/R588E}$*Zbp1*$^{-/-}$*Ticam*$^{-/-}$ mice remain unknown at present. However, we detected increased expression of TNF in these animals at the age of 5–6 months, suggesting that TNFR1-TRADD-dependent signaling might be implicated in causing this pathology, likely by inducing apoptosis. Together, these results revealed a critical function of the RIPK1 DD in suppressing aberrant activation of ZBP1- and TRIF-dependent signaling, which is essential for the survival and maintenance of tissue homeostasis in the perinatal period and during adult life.

Consistent with the genetic data, *Ripk1*$^{R588E/R588E}$ MEFs were sensitive to ZBP1- and TRIF-mediated necroptosis. In addition, we detected constitutive phosphorylation of RIPK1 and RIPK3 in unstimulated *Ripk1*$^{R588E/R588E}$ MEFs, which depended on ZBP1 and TRIF expression and was enhanced by stimulation with IFNγ or poly(I:C). RIPK1 inhibition with Nec1s could prevent RIPK3 phosphorylation and necroptosis induced by IFNγ or poly(I:C) treatment in the presence of E in WT cells, demonstrating that RIPK1 kinase activity is required for ZBP1- and TRIF-mediated activation of RIPK3 in cells with intact RIPK1 DD-dependent signaling. By contrast, Nec1s could not inhibit IFNγ- or poly(I:C)-induced RIPK3 phosphorylation and necroptosis in *Ripk1*$^{R588E/R588E}$ cells, suggesting that the presence of a functional DD dictates the mechanism by which ZBP1 and TRIF activate RIPK3. To dissect the underlying molecular interactions, we undertook endogenous immunoprecipitation experiments and found that ZBP1 binds phosphorylated RIPK1 and RIPK3 in unstimulated *Ripk1*$^{R588E/R588E}$*Mlkl*$^{-/-}$ cells and this interaction was enhanced by IFNγ stimulation. Nec1s prevented the association of ZBP1 with RIPK3 in Mlkl$^{-/-}$ but not in *Ripk1*$^{R588E/R588E}$*Mlkl*$^{-/-}$ cells, further supporting that the RIPK1 DD determines how ZBP1 engages and activates RIPK3. Based on our results, we propose that the RIPK1 DD serves a dual function: on the one hand, it recruits caspase-8 via FADD, resulting in RIPK1 cleavage destabilizing the complex. In addition, DD-dependent interactions with FADD promote conformational changes in RIPK1, resulting in its autophosphorylation and the formation of ordered oligomers that recruit and activate RIPK3. We envision that these ordered oligomers likely resemble the helical rod aggregates of RIPK1 and RIPK3 reported by Chen et al. for TNFR1-induced necroptosis.[41] DD mutation prevented FADD-caspase-8 recruitment and RIPK1 cleavage, but also the DD-dependent formation of ordered RIPK1 oligomers, likely resulting in ZBP1-RIPK1 aggregates with a different structure that does not allow RIPK1 autophosphorylation but permits its RHIM-dependent interaction with RIPK3. Our results suggest that RIPK3 is recruited to these ZBP1-RIPK1 aggregates, where it is activated and phosphorylates MLKL to induce necroptosis. RIPK1-R588E is activated in a RIPK3 scaffold-dependent fashion, likely within RIPK1-RIPK3 oligomers; however, its kinase activity is not required for RIPK3 activation and necroptosis induction.

Mutations affecting the RIPK1 DD were found to cause early-onset colitis associated with increased apoptosis, autoinflammation, and immunodeficiency in human patients.[24] Our findings in *Ripk1*$^{R588E/R588E}$ mice are relevant for

Figure 7. The DD of RIPK1 inhibits ZBP1- and TRIF-mediated necroptosis

(A) Cell death measured by DiYO1 uptake in primary MEFs of the indicated genotypes treated with combinations of IFNγ (1,000 U mL^{-1}), etanercept (Et, 50 μg mL^{-1}), and E (5 μM) for 48 h. Data are representative of two independent experiments. Graphs show mean ± SEM.

(B) Immunoblot analysis with the indicated antibodies of lysates from primary MEFs from mice with the indicated genotypes stimulated with combinations of IFNγ, Et, and E for 24 h. Representative data shown from two independent experiments.

(C) Cell death measured by DiYO1 uptake in primary WT and *Ripk1*$^{R588E/R588E}$ MEFs treated with combinations of IFNγ, Et, and E with or without Nec1s (20 μM) or GSK′872 (3 μM) for 48 h. Data are representative of two independent experiments. Graphs show mean ± SEM.

(D) Immunoblot analysis with the indicated antibodies of lysates from primary WT and *Ripk1*$^{R588E/R588E}$ MEFs stimulated with combinations of IFNγ, Et, and E with or without Nec1s for 24 h. Representative data shown from two independent experiments.

(E) Immunoblot analysis with the indicated antibodies of RIPK3 immunoprecipitates and total lysates from primary MEFs of the indicated genotypes.

(F) Immunoblot analysis with the indicated antibodies of ZBP1 immunoprecipitates and total lysates from immortalized Mlkl$^{-/-}$ and *Ripk1*$^{R588E/R588E}$*Mlkl*$^{-/-}$ MEFs treated with combinations of IFNγ and E for 24 h. Representative data shown from two independent experiments.

(G) Immunoblot analysis with the indicated antibodies of ZBP1 immunoprecipitates and total lysates from immortalized Mlkl$^{-/-}$ and *Ripk1*$^{R588E/R588E}$*Mlkl*$^{-/-}$ MEFs treated with combinations of IFNγ, E, and Nec1s for 24 h. Representative data shown from two independent experiments.

See also Figure S6.

understanding the mechanisms causing cell death and inflammation in these patients and suggest that TNF-neutralizing antibodies or RIPK1 kinase inhibitors might be ineffective in treating this condition. Furthermore, R603 in human RIPK1 (which corresponds to R588 in mouse RIPK1) is specifically targeted by the NleB family of enteropathogenic bacterial effector proteins that catalyze arginine GlcNAcylation of host DD proteins also including FADD and TRADD to counteract host defense responses.[42–44] Therefore, our studies on the effects of the R588E mutation in regulating RIPK1 DD-dependent signaling in mice provide valuable insights for better understanding the role of DD-dependent RIPK1 interactions in host defense to enteropathogenic bacteria and in the regulation of tissue homeostasis.

Limitations of the study

Our genetic and biochemical studies provide important mechanistic information on the role of the RIPK1 DD in regulating ZBP1, TRIF, and TNFR1 signaling and controlling mouse perinatal survival and adult tissue homeostasis. However, while our genetic models constitute valuable tools for understanding RIPK1 biology, it remains unclear whether our results might directly relate to human disease. Moreover, while our genetic and biochemical studies support a model whereby the RIPK1 DD determines how ZBP1 and TRIF engage and activate RIPK3, this needs to be validated experimentally by structural studies. Obtaining direct insight into the three-dimensional structure of the ZBP1-RIPK1-RIPK3 complex in WT and *Ripk1*$^{R588E/R588E}$ cells, for example, using super-resolution imaging and/or cryoelectron microscopy (cryo-EM) approaches, will be required to elucidate the detailed molecular interactions controlling ZBP1- and TRIF-mediated signaling.

STAR★METHODS

Detailed methods are provided in the online version of this paper and include the following:

- KEY RESOURCES TABLE
- RESOURCE AVAILABILITY
  - Lead contact
  - Materials availability
  - Data and code availability
- EXPERIMENTAL MODEL AND STUDY PARTICIPANT DETAILS
  - Mice
- METHOD DETAILS
  - Immunoblotting
  - Cell death assays
  - Immunohistochemistry and histology
  - Blood cell analysis
  - Flow Cytometry
  - Generation of immortalized mouse embryonic fibroblasts
  - Immunoprecipitation Assays
  - Gene expression analysis by RT–qPCR
  - Histopathological analysis
  - Histological sub-scores
- QUANTIFICATION AND STATISTICAL ANALYSIS

SUPPLEMENTAL INFORMATION

Supplemental information can be found online at https://doi.org/10.1016/j.immuni.2024.04.016.

ACKNOWLEDGMENTS

We thank J. Kuth, C. Uthoff-Hachenberg, E. Stade, E. Gareus, P. Roggan, L. Elles, M. Hahn, and J. von Rhein for their technical assistance. We also thank B. Zevnik and the CECAD Transgenic Core Facility for CRISPR-Cas9-assisted gene targeting in mice. Research reported in this publication was supported by funding from the European Research Council (ERC) under the European Union's Horizon 2020 research and innovation programme (grant agreement no. 787826), the Deutsche Forschungsgemeinschaft (DFG, German Research Foundation), projects: SFB1403 (project no. 414786233) to M.P., SFB1399 (project no. 413326622) to M.P. and G.L., SFB1530 (project no. 455784452) to G.L., and under Germany's Excellence Strategy–EXC 2030 CECAD (project no. 390661388) to M.P., the state of North Rhein-Westphalia, project CANTAR (NW21-062A) to M.P. and G.L., and from the National Natural Science Foundation of China (32170765) to J.L. J.L. was supported by a postdoctoral fellowship from the Alexander Von Humboldt Foundation. T.I. was supported by the Takeda Scientific Foundation and the Miyata Cardiac Research Promotion Foundation.

AUTHOR CONTRIBUTIONS

T.I., J.L., C.K., and M.P. conceived the study and designed the experiments. T.I. analyzed mice and performed histological and *in vitro* analyses. J.L. analyzed *Ripk1*$^{R588E/R588E}$ and *Ripk1*$^{R588E/R588E}$*Ripk3*$^{-/-}$*Fadd*$^{-/-}$ mice and conducted *in vitro* biochemical analyses in Figures 1D and 1G. K.K. and G.L. performed ZBP1-IP experiments together with T.I., and J.L. and G.G.K. analyzed gut histopathology. E.J. conducted *in vitro* analyses in Figures S6B, S6D, and S6G with T.I. V.K. analyzed liver histopathology. C.K. designed and generated *Ripk1*$^{R588E/R588E}$ mice. M.P. supervised the experiments. T.I., J.L., and M.P. interpreted data. T.I. and M.P. wrote the paper.

DECLARATION OF INTERESTS

The authors declare no competing interests.

Received: July 4, 2023
Revised: February 5, 2024
Accepted: April 17, 2024
Published: May 13, 2024

REFERENCES

1. Newton, K. (2020). Multitasking Kinase RIPK1 Regulates Cell Death and Inflammation. Cold Spring Harb. Perspect. Biol. *12*, a036368. https://doi.org/10.1101/cshperspect.a036368.
2. Varfolomeev, E., and Vucic, D. (2022). RIP1 post-translational modifications. Biochem. J. *479*, 929–951. https://doi.org/10.1042/BCJ20210725.
3. Li, W., and Yuan, J. (2023). Targeting RIPK1 kinase for modulating inflammation in human diseases. Front. Immunol. *14*, 1159743. https://doi.org/10.3389/fimmu.2023.1159743.
4. Ermolaeva, M.A., Michallet, M.C., Papadopoulou, N., Utermöhlen, O., Kranidioti, K., Kollias, G., Tschopp, J., and Pasparakis, M. (2008). Function of TRADD in tumor necrosis factor receptor 1 signaling and in TRIF-dependent inflammatory responses. Nat. Immunol. *9*, 1037–1046. https://doi.org/10.1038/ni.1638.
5. Haas, T.L., Emmerich, C.H., Gerlach, B., Schmukle, A.C., Cordier, S.M., Rieser, E., Feltham, R., Vince, J., Warnken, U., Wenger, T., et al. (2009). Recruitment of the linear ubiquitin chain assembly complex stabilizes the TNF-R1 signaling complex and is required for TNF-mediated gene induction. Mol. Cell *36*, 831–844. https://doi.org/10.1016/j.molcel.2009.10.013.
6. Pasparakis, M., and Vandenabeele, P. (2015). Necroptosis and its role in inflammation. Nature *517*, 311–320. https://doi.org/10.1038/nature14191.
7. Dillon, C.P., Weinlich, R., Rodriguez, D.A., Cripps, J.G., Quarato, G., Gurung, P., Verbist, K.C., Brewer, T.L., Llambi, F., Gong, Y.N., et al. (2014). RIPK1 blocks early postnatal lethality mediated by caspase-8

and RIPK3. Cell *157*, 1189–1202. https://doi.org/10.1016/j.cell.2014.04.018.

8. Rickard, J.A., O'Donnell, J.A., Evans, J.M., Lalaoui, N., Poh, A.R., Rogers, T., Vince, J.E., Lawlor, K.E., Ninnis, R.L., Anderton, H., et al. (2014). RIPK1 regulates RIPK3-MLKL-driven systemic inflammation and emergency hematopoiesis. Cell *157*, 1175–1188. https://doi.org/10.1016/j.cell.2014.04.019.
9. Kaiser, W.J., Daley-Bauer, L.P., Thapa, R.J., Mandal, P., Berger, S.B., Huang, C., Sundararajan, A., Guo, H., Roback, L., Speck, S.H., et al. (2014). RIP1 suppresses innate immune necrotic as well as apoptotic cell death during mammalian parturition. Proc. Natl. Acad. Sci. USA *111*, 7753–7758. https://doi.org/10.1073/pnas.1401857111.
10. Anderton, H., Bandala-Sanchez, E., Simpson, D.S., Rickard, J.A., Ng, A.P., Di Rago, L., Hall, C., Vince, J.E., Silke, J., Liccardi, G., and Feltham, R. (2019). RIPK1 prevents TRADD-driven, but TNFR1 independent, apoptosis during development. Cell Death Differ. *26*, 877–889. https://doi.org/10.1038/s41418-018-0166-8.
11. Dowling, J.P., Alsabbagh, M., Del Casale, C., Liu, Z.G., and Zhang, J. (2019). TRADD regulates perinatal development and adulthood survival in mice lacking RIPK1 and RIPK3. Nat. Commun. *10*, 705. https://doi.org/10.1038/s41467-019-08584-5.
12. Berger, S.B., Kasparcova, V., Hoffman, S., Swift, B., Dare, L., Schaeffer, M., Capriotti, C., Cook, M., Finger, J., Hughes-Earle, A., et al. (2014). Cutting Edge: RIP1 kinase activity is dispensable for normal development but is a key regulator of inflammation in SHARPIN-deficient mice. J. Immunol. *192*, 5476–5480. https://doi.org/10.4049/jimmunol.1400499.
13. Newton, K., Dugger, D.L., Maltzman, A., Greve, J.M., Hedehus, M., Martin-McNulty, B., Carano, R.A., Cao, T.C., van Bruggen, N., Bernstein, L., et al. (2016). RIPK3 deficiency or catalytically inactive RIPK1 provides greater benefit than MLKL deficiency in mouse models of inflammation and tissue injury. Cell Death Differ. *23*, 1565–1576. https://doi.org/10.1038/cdd.2016.46.
14. Polykratis, A., Hermance, N., Zelic, M., Roderick, J., Kim, C., Van, T.M., Lee, T.H., Chan, F.K.M., Pasparakis, M., and Kelliher, M.A. (2014). Cutting edge: RIPK1 Kinase inactive mice are viable and protected from TNF-induced necroptosis in vivo. J. Immunol. *193*, 1539–1543. https://doi.org/10.4049/jimmunol.1400590.
15. Jiao, H., Wachsmuth, L., Kumari, S., Schwarzer, R., Lin, J., Eren, R.O., Fisher, A., Lane, R., Young, G.R., Kassiotis, G., et al. (2020). Z-nucleic-acid sensing triggers ZBP1-dependent necroptosis and inflammation. Nature *580*, 391–395. https://doi.org/10.1038/s41586-020-2129-8.
16. Lin, J., Kumari, S., Kim, C., Van, T.M., Wachsmuth, L., Polykratis, A., and Pasparakis, M. (2016). RIPK1 counteracts ZBP1-mediated necroptosis to inhibit inflammation. Nature *540*, 124–128. https://doi.org/10.1038/nature20558.
17. Newton, K., Wickliffe, K.E., Maltzman, A., Dugger, D.L., Strasser, A., Pham, V.C., Lill, J.R., Roose-Girma, M., Warming, S., Solon, M., et al. (2016). RIPK1 inhibits ZBP1-driven necroptosis during development. Nature *540*, 129–133. https://doi.org/10.1038/nature20559.
18. Zhang, X., Dowling, J.P., and Zhang, J. (2019). RIPK1 can mediate apoptosis in addition to necroptosis during embryonic development. Cell Death Dis. *10*, 245. https://doi.org/10.1038/s41419-019-1490-8.
19. Tao, P., Sun, J., Wu, Z., Wang, S., Wang, J., Li, W., Pan, H., Bai, R., Zhang, J., Wang, Y., et al. (2020). A dominant autoinflammatory disease caused by non-cleavable variants of RIPK1. Nature *577*, 109–114. https://doi.org/10.1038/s41586-019-1830-y.
20. Lalaoui, N., Boyden, S.E., Oda, H., Wood, G.M., Stone, D.L., Chau, D., Liu, L., Stoffels, M., Kratina, T., Lawlor, K.E., et al. (2020). Mutations that prevent caspase cleavage of RIPK1 cause autoinflammatory disease. Nature *577*, 103–108. https://doi.org/10.1038/s41586-019-1828-5.
21. Newton, K., Wickliffe, K.E., Dugger, D.L., Maltzman, A., Roose-Girma, M., Dohse, M., Kőműves, L., Webster, J.D., and Dixit, V.M. (2019). Cleavage of RIPK1 by caspase-8 is crucial for limiting apoptosis and necroptosis. Nature *574*, 428–431. https://doi.org/10.1038/s41586-019-1548-x.
22. Uchiyama, Y., Kim, C.A., Pastorino, A.C., Ceroni, J., Lima, P.P., de Barros Dorna, M., Honjo, R.S., Bertola, D., Hamanaka, K., Fujita, A., et al. (2019). Primary immunodeficiency with chronic enteropathy and developmental delay in a boy arising from a novel homozygous RIPK1 variant. J. Hum. Genet. *64*, 955–960. https://doi.org/10.1038/s10038-019-0631-3.
23. Cuchet-Lourenço, D., Eletto, D., Wu, C., Plagnol, V., Papapietro, O., Curtis, J., Ceron-Gutierrez, L., Bacon, C.M., Hackett, S., Alsaleem, B., et al. (2018). Biallelic RIPK1 mutations in humans cause severe immunodeficiency, arthritis, and intestinal inflammation. Science *361*, 810–813. https://doi.org/10.1126/science.aar2641.
24. Li, Y., Führer, M., Bahrami, E., Socha, P., Klaudel-Dreszler, M., Bouzidi, A., Liu, Y., Lehle, A.S., Magg, T., Hollizeck, S., et al. (2019). Human RIPK1 deficiency causes combined immunodeficiency and inflammatory bowel diseases. Proc. Natl. Acad. Sci. USA *116*, 970–975. https://doi.org/10.1073/pnas.1813582116.
25. Tu, H., Tang, Y., Zhang, J., Cheng, L., Joo, D., Zhao, X., and Lin, X. (2021). Linear Ubiquitination of RIPK1 on Lys612 Regulates Systemic Inflammation via Preventing Cell Death. J. Immunol. *207*, 602–612. https://doi.org/10.4049/jimmunol.2100299.
26. Li, X., Zhang, M., Huang, X., Liang, W., Li, G., Lu, X., Li, Y., Pan, H., Shi, L., Zhu, H., et al. (2020). Ubiquitination of RIPK1 regulates its activation mediated by TNFR1 and TLRs signaling in distinct manners. Nat. Commun. *11*, 6364. https://doi.org/10.1038/s41467-020-19935-y.
27. Meng, H., Liu, Z., Li, X., Wang, H., Jin, T., Wu, G., Shan, B., Christofferson, D.E., Qi, C., Yu, Q., et al. (2018). Death-domain dimerization-mediated activation of RIPK1 controls necroptosis and RIPK1-dependent apoptosis. Proc. Natl. Acad. Sci. USA *115*, E2001–E2009. https://doi.org/10.1073/pnas.1722013115.
28. Jang, T.H., Zheng, C., Li, J., Richards, C., Hsiao, Y.S., Walz, T., Wu, H., and Park, H.H. (2014). Structural study of the RIPoptosome core reveals a helical assembly for kinase recruitment. Biochemistry *53*, 5424–5431. https://doi.org/10.1021/bi500585u.
29. Dannappel, M., Vlantis, K., Kumari, S., Polykratis, A., Kim, C., Wachsmuth, L., Eftychi, C., Lin, J., Corona, T., Hermance, N., et al. (2014). RIPK1 maintains epithelial homeostasis by inhibiting apoptosis and necroptosis. Nature *513*, 90–94. https://doi.org/10.1038/nature13608.
30. Wong, W.W., Gentle, I.E., Nachbur, U., Anderton, H., Vaux, D.L., and Silke, J. (2010). RIPK1 is not essential for TNFR1-induced activation of NF-kappaB. Cell Death Differ. *17*, 482–487. https://doi.org/10.1038/cdd.2009.178.
31. Van, T.M., Polykratis, A., Straub, B.K., Kondylis, V., Papadopoulou, N., and Pasparakis, M. (2017). Kinase-independent functions of RIPK1 regulate hepatocyte survival and liver carcinogenesis. J. Clin. Invest. *127*, 2662–2677. https://doi.org/10.1172/JCI92508.
32. Ting, A.T., and Bertrand, M.J.M. (2016). More to Life than NF-κB in TNFR1 Signaling. Trends Immunol. *37*, 535–545. https://doi.org/10.1016/j.it.2016.06.002.
33. Kaiser, W.J., Upton, J.W., Long, A.B., Livingston-Rosanoff, D., Daley-Bauer, L.P., Hakem, R., Caspary, T., and Mocarski, E.S. (2011). RIP3 mediates the embryonic lethality of caspase-8-deficient mice. Nature *471*, 368–372. https://doi.org/10.1038/nature09857.
34. Oberst, A., Dillon, C.P., Weinlich, R., McCormick, L.L., Fitzgerald, P., Pop, C., Hakem, R., Salvesen, G.S., and Green, D.R. (2011). Catalytic activity of the caspase-8-FLIP(L) complex inhibits RIPK3-dependent necrosis. Nature *471*, 363–367. https://doi.org/10.1038/nature09852.
35. Alvarez-Diaz, S., Dillon, C.P., Lalaoui, N., Tanzer, M.C., Rodriguez, D.A., Lin, A., Lebois, M., Hakem, R., Josefsson, E.C., O'Reilly, L.A., et al. (2016). The Pseudokinase MLKL and the Kinase RIPK3 Have Distinct Roles in Autoimmune Disease Caused by Loss of Death-Receptor-Induced Apoptosis. Immunity *45*, 513–526. https://doi.org/10.1016/j.immuni.2016.07.016.
36. Moriwaki, K., Balaji, S., McQuade, T., Malhotra, N., Kang, J., and Chan, F.K.M. (2014). The necroptosis adaptor RIPK3 promotes injury-induced cytokine expression and tissue repair. Immunity *41*, 567–578. https://doi.org/10.1016/j.immuni.2014.09.016.

37. Mandal, P., Berger, S.B., Pillay, S., Moriwaki, K., Huang, C., Guo, H., Lich, J.D., Finger, J., Kasparcova, V., Votta, B., et al. (2014). RIP3 induces apoptosis independent of pronecrotic kinase activity. Mol. Cell *56*, 481–495. https://doi.org/10.1016/j.molcel.2014.10.021.

38. Newton, K., Dugger, D.L., Wickliffe, K.E., Kapoor, N., de Almagro, M.C., Vucic, D., Komuves, L., Ferrando, R.E., French, D.M., Webster, J., et al. (2014). Activity of protein kinase RIPK3 determines whether cells die by necroptosis or apoptosis. Science *343*, 1357–1360. https://doi.org/10.1126/science.1249361.

39. Schwarzer, R., Jiao, H., Wachsmuth, L., Tresch, A., and Pasparakis, M. (2020). FADD and Caspase-8 Regulate Gut Homeostasis and Inflammation by Controlling MLKL- and GSDMD-Mediated Death of Intestinal Epithelial Cells. Immunity *52*, 978–993.e6. https://doi.org/10.1016/j.immuni.2020.04.002.

40. Wang, L., Chang, X., Feng, J., Yu, J., and Chen, G. (2019). TRADD Mediates RIPK1-Independent Necroptosis Induced by Tumor Necrosis Factor. Front. Cell Dev. Biol. *7*, 393. https://doi.org/10.3389/fcell.2019.00393.

41. Chen, X., Zhu, R., Zhong, J., Ying, Y., Wang, W., Cao, Y., Cai, H., Li, X., Shuai, J., and Han, J. (2022). Mosaic composition of RIP1-RIP3 signalling hub and its role in regulating cell death. Nat. Cell Biol. *24*, 471–482. https://doi.org/10.1038/s41556-022-00854-7.

42. Pearson, J.S., Giogha, C., Ong, S.Y., Kennedy, C.L., Kelly, M., Robinson, K.S., Lung, T.W.F., Mansell, A., Riedmaier, P., Oates, C.V.L., et al. (2013). A type III effector antagonizes death receptor signalling during bacterial gut infection. Nature *501*, 247–251. https://doi.org/10.1038/nature12524.

43. Ding, J., Pan, X., Du, L., Yao, Q., Xue, J., Yao, H., Wang, D.C., Li, S., and Shao, F. (2019). Structural and Functional Insights into Host Death Domains Inactivation by the Bacterial Arginine GlcNAcyltransferase Effector. Mol. Cell *74*, 922–935.e6. https://doi.org/10.1016/j.molcel.2019.03.028.

44. Li, S., Zhang, L., Yao, Q., Li, L., Dong, N., Rong, J., Gao, W., Ding, X., Sun, L., Chen, X., et al. (2013). Pathogen blocks host death receptor signalling by arginine GlcNAcylation of death domains. Nature *501*, 242–246. https://doi.org/10.1038/nature12436.

45. Bonnet, M.C., Preukschat, D., Welz, P.S., van Loo, G., Ermolaeva, M.A., Bloch, W., Haase, I., and Pasparakis, M. (2011). The adaptor protein FADD protects epidermal keratinocytes from necroptosis in vivo and prevents skin inflammation. Immunity *35*, 572–582. https://doi.org/10.1016/j.immuni.2011.08.014.

46. Newton, K., Sun, X., and Dixit, V.M. (2004). Kinase RIP3 is dispensable for normal NF-kappa Bs, signaling by the B-cell and T-cell receptors, tumor necrosis factor receptor 1, and Toll-like receptors 2 and 4. Mol. Cell. Biol. *24*, 1464–1469. https://doi.org/10.1128/MCB.24.4.1464-1469.2004.

47. Pfeffer, K., Matsuyama, T., Kündig, T.M., Wakeham, A., Kishihara, K., Shahinian, A., Wiegmann, K., Ohashi, P.S., Krönke, M., and Mak, T.W. (1993). Mice deficient for the 55 kd tumor necrosis factor receptor are resistant to endotoxic shock, yet succumb to L. monocytogenes infection. Cell *73*, 457–467. https://doi.org/10.1016/0092-8674(93)90134-c.

STAR★METHODS

KEY RESOURCES TABLE

REAGENT or RESOURCE	SOURCE	IDENTIFIER
Antibodies		
Anti-rabbit-IgG, HRP conjugated	GE Healthcare	Cat# NA934; RRID:AB_772206
Anti-mouse-IgG, HRP conjugated	GE Healthcare	Cat# NA931; RRID:AB_772210
Anti-rat-IgG, HRP conjugated	Jackson Laboratories	Cat# 112-035-003; RRID:AB_2338128
Anti-goat-IgG, HRP conjugated	Jackson Laboratories	Cat# 705-035-003; RRID:AB_2340390
TNFR1	Cell Signaling Technology	Cat# 3736, RRID:AB_2241018
TRADD	Bio-Rad	Cat# AHP2533
FADD	Millipore	Cat# 05-486; RRID:AB_2100627
RIPK1	BD Biosciences, Cell Signaling Technology, Santa Cruz Biotechnology	Cat# 610459; RRID:AB_397832, Cat# 3493, RRID:AB_2305314, Cat#sc-7881, RRID:AB_2178118
RIPK3	Enzo LifeSciences	Cat# ADI-905-242-100; RRID:AB_2039527
ZBP1	Adipogen	Cat# AG-20B-0010; RRID:AB_2490191
MLKL	Millipore	Cat#MABC604; RRID:AB_2820284
IκBα	Santa Cruz Biotechnology	Cat# sc-371, RRID:AB_2235952
p65	Santa Cruz Biotechnology	Cat# sc-372, RRID:AB_632037
p38	Cell Signaling Technology	Cat# 9212, RRID:AB_330713
JNK	Cell Signaling Technology	Cat# 9252, RRID:AB_2250373
p44/42 MAPK	Cell Signaling Technology	Cat# 9102, RRID:AB_330744
Caspase-8	Cell Signaling Technology	Cat# 4790, RRID:AB_10545768
GAPDH	Novus Biologicals	Cat# NB300-221; RRID:AB_10077627
α-tubulin	Sigma	Cat# T6074, RRID:AB_477582
Phosphorylated RIPK1 (S166)	Cell Signaling Technology	Cat# 31122; RRID:AB_2799000
Phosphorylated RIPK3 (S232)	Abcam, Cell Signaling Technology	Cat# ab195117, RRID:AB_2768156, Cat# 91702; RRID:AB_2937060
Phosphorylated MLKL (S345)	Cell Signaling Technology	Cat# 37333; RRID:AB_2799112
Phosphorylated IκBα (Ser32)	Cell Signaling Technology	Cat# 2859, RRID:AB_561111
Phosphorylated p65 (Ser536)	Cell Signaling Technology	Cat# 3033, RRID:AB_331284
Phosphorylated p38 (Thr180 / Tyr182)	Cell Signaling Technology	Cat# 9211, RRID:AB_331641
Phosphorylated JNK (Thr183/Tyr185)	Cell Signaling Technology	Cat# 4668, RRID:AB_823588
Phosphorylated p44/42 MAPK (Thr202 / Tyr204)	Cell Signaling Technology	Cat# 4370, RRID:AB_2315112
Ly6C, PerCP/Cyanine5.5	Biolegend	Cat# 128011, RRID:AB_1659242
NK1.1, Alexa Fluor 647	Biolegend	Cat# 108719, RRID:AB_493186
CD4, Alexa Fluor 700	Biolegend	Cat# 100536, RRID:AB_493701
CD45, Super Bright™ 702	Thermo Fisher Scientific	Cat# 67-0451-82, RRID:AB_2662424
CD3, Brilliant Violet 785	Biolegend	Cat# 100232, RRID:AB_2562554
CD11b, Brilliant Violet 421	Biolegend	Cat# 101251, RRID:AB_2562904
CD8, Brilliant Violet 510	Biolegend	Cat# 100752, RRID:AB_2563057
B220, Super Bright™ 600	Thermo Fisher Scientific	Cat# 63-0452-82, RRID:AB_2637457
CD11c, PE-Cyanine7	BD Bioscience	Cat# 561022, RRID:AB_2033997
Ly6G, PE	Biolegend	Cat# 127607, RRID:AB_1186104
Biotinylated anti-rat secondary antibody	ThermoFisher Scientific	Cat# D-20697, RRID:AB_2536518
Biotinylated anti-rabbit secondary antibody	ThermoFisher Scientific	Cat# B-2770, RRID:AB_2536431
Cleaved caspase-3	Cell signaling	Cat# 9661, RRID:AB_2341188
FADD	Santa Cruz Biotechnology	Cat# sc-6036, RRID:AB_2100742

(*Continued on next page*)

Continued

REAGENT or RESOURCE	SOURCE	IDENTIFIER
Chemicals and recombinant proteins		
ECL SuperSignal West PicoPlus chemiluminescent substrate	Thermo Scientific	Cat#34578
Near-IR Live/Dead Kit	Thermo Fisher Scientific	Cat#L10119
Cycloheximide	Sigma	Cat#239763
Z-VAD-FMK	Enzo LifeSciences	Cat# ALX-260-020-M005
Emricasan	Selleckchem	Cat#S7775
Birinapant	BioVision	Cat#2597
Etanercept	Amgen, Sandoz	Enbrel00E2, Erelzi00E2
Nec-1s	Selleckchem	S8641
Ripk3 inhibitor, GSK2399872 (GSK'872)	Sigma Aldrich	Cat# 5303890001
Recombinant mouse TNF	VIB Protein Service Facility	N/A
FLAG-hTNF	VIB Protein Service Facility, Ghent	N/A
Recombinant mouse interferon gamma	ImmunoTools	Cat#12343537
Poly (I:C)	EDM Millipore	Cat#42424-50-0
DiYO-1	AAT Bioquest	Cat# ABD-17580
Anti-FLAG M2 affinity gel	Sigma-Aldrich	Cat# A2220
Dynabeads Protein G	Thermo Fisher Scientific	Cat#10003D
Protein G Sepharose	Sigma Aldrich	Cat# P3296
Critical commercial assays		
DeadEnd Fluorometric TUNEL System	Promega	Cat# G3250
Avidin/Biotin Blocking Kit	Biozol	Cat#VEC-SP-2001
Vectastain Elite ABC-HRP kit	Biozol	Cat# VEC-PK-6100
DAB substrate	Biozol	Cat# VEC-SK-4100
RNAzol RT	Sigma Aldrich	Cat# R4533
Direct-zol-96 RNA kits	Zymo Research	Cat# R2054
Tbp	ThermoScientific	Mm00446973_m1
Zbp1	ThermoScientific	Mm00457979_m1
Ifit1	ThermoScientific	Mm00515153_m1
Oasl1	ThermoScientific	Mm00455081_m1
Ifna4	ThermoScientific	Mm00833969_s1
Ifnb	ThermoScientific	Mm00439546_s1
Ifng	ThermoScientific	Mm01168134_m1
Tlr3	ThermoScientific	Mm01207404_m1
Tlr4	ThermoScientific	Mm00445273_m1
Ticam	ThermoScientific	Mm00844508_s1
Tnf	ThermoScientific	Mm00443258_m1
Il6	ThermoScientific	Mm00446190_m1
Il1b	ThermoScientific	Mm00434228_m1
Experimental models: Organisms/strains		
Mouse: *Fadd*$^{-/-}$, C57BL/6N	Bonnet et al.[45]	N/A
Mouse: *Ripk3*$^{-/-}$, C57BL/6N	Newton et al.[46]	N/A
Mouse: *Mlkl*$^{-/-}$, C57BL/6N	Lin et al.[16]	N/A
Mouse: *Tnfr1*$^{-/-}$, C57BL/6N	Pfeffer et al.[47]	N/A
Mouse: *Tradd*$^{-/-}$, C57BL/6N	Ermolaeva et al.[4]	N/A
Mouse: *Zbp1*$^{-/-}$, C57BL/6N	Jiao et al.[15]	N/A
Mouse: *Ticam1*$^{-/-}$, C57BL/6N	Dannappel et al.[29]	N/A
Mouse: *Ripk1*$^{R588E/R588E}$, C57BL/6N	This paper	N/A

(*Continued on next page*)

Continued

REAGENT or RESOURCE	SOURCE	IDENTIFIER
Software and algorithms		
Prism 9.0	Graphpad Inc	RRID: SCR_002798
IncuCyte S3 live-cell imaging and analysis platform	Essen BioScience	RRID:SCR_019874
OMERO	OMERO	RRID:SCR_002629
QuPath	QuPath	RRID:SCR_018257
Abacus Junior Vet analyser	Diatron	N/A
BD LSRFortessa Cell Analyzer	BD Biosciences	RRID:SCR_018655
FlowJo	FlowJo	RRID:SCR_008520
Other		
Nanozoomer S360	Hamamatsu	RRID:SCR_022537
Spinning disk confocal microscope	PerkinElmer UltraView ERS	RRID:SCR_020405
QuantStudio 5 Real-Time PCR System	Applied Biosystems	Cat# A28574

RESOURCE AVAILABILITY

Lead contact

Further information and reasonable requests for resources and reagents should be directed to and will be fulfilled by the Lead Contact, Manolis Pasparakis (pasparakis@uni-koeln.de).

Materials availability

Fadd$^{fl/fl}$, Mlkl$^{-/-}$, Zbp1$^{-/-}$ and Ticam$^{-/-}$ mice can be obtained from Manolis Pasparakis, Institute for Genetics, Cologne Excellence Cluster on Cellular Stress Responses in Aging-Associated Diseases (CECAD), University of Cologne, 50931 Cologne, Germany. Email address: pasparakis@uni-koeln.de.

Data and code availability

- All data reported in this paper will be shared by the lead author upon request.
- This paper does not report original code
- Any additional information required to reanalyze the data reported in this paper is available from the lead contact upon request.

EXPERIMENTAL MODEL AND STUDY PARTICIPANT DETAILS

Mice

Ripk3$^{-/-}$,[46] *Fadd*$^{fl/fl}$,[45] Mlkl$^{-/-}$,[16] Tnfr1$^{-/-}$,[47] Tradd$^{-/-}$,[4] Zbp1$^{-/-}$[15] and Ticam$^{-/-}$[29] mice have been described previously. To generate Ripk1R588E mice, we injected Cas9 protein, a 126 bp ssDNA repair oligo, tracrRNA, and crRNA into the pronucleus of fertilized oocytes obtained from C57BL/6 mice. The ssDNA oligo that introduces the R588E mutation in murine RIPK1 gene, has the following sequence: 5′-tcagtccatctctttcatagtcatggtcgatttcatcgatctgagactcagtgaagcccagcttctcggcacagtttttccactgccttcccaggttttc cctgatagggttcaggtgttcatcag-3′. The crRNA oligo contains the sequence 5′-ACTCAGTGAAGCCCAGCTTG-3′, targeting the death domain (DD) of the murine Ripk1 gene. The injected embryos were transferred to foster mothers and allowed to develop to term. Mutations in the genome of progeny were determined by analysis of genomic DNA by sequencing. Mice used in this study were maintained in the animal facility of the CECAD Research Center, University of Cologne, in individually ventilated cages (Tecniplast, Greenline GM500) at 22 °C (±2 °C) and a relative humidity of 55% (±5%) under a 12-h light/12-h dark cycle on sterilized bedding (Aspen wood, Abedd) with access to a sterilized commercial pelleted diet (Ssniff Spezialdiäten) and acidified water ad libitum. The microbiological status of the mice was examined as recommended by the Federation of European Laboratory Animal Science Associations (FELASA), and the mice were free of all listed pathogens. All animal procedures were conducted in accordance with European, national and institutional guidelines, and protocols were approved by local government authorities (Landesamt für Natur, Umwelt und Verbraucherschutz Nordrhein-Westfalen).

METHOD DETAILS

Immunoblotting

Cell lysates were prepared by direct cell lysis in NP-40 buffer (1% NP-40, 150 mM NaCl and 50 mM Tris-HCl pH 7.8) or IP buffer (20 mM Tris pH 7.4, 150 mM NaCl, 2 mM EDTA, 1% Triton X-100), supplemented with protease and phosphatase inhibitors, followed by denaturation in Laemmli sample buffer (Bio-Rad, 1610737). Lysates were separated by SDS–PAGE, transferred to Immobilon-P

PVDF membranes (Millipore, 05317) and analysed by immunoblotting with primary antibodies against RIPK1 (BD, 610459 or Cell Signaling Technology, 3493), TRADD (Bio-Rad, AHP2533), TNFR1 (Cell Signaling Technology, 3736), p-IκBα (Cell Signaling Technology, 2859), IκBα (Santa Cruz Biotechnology, sc-371), p-p65 (Cell Signaling Technology, 3033), p65 (Santa Cruz Biotechnology, sc-372), p-p38 (Cell Signaling Technology, 9211), p38 (Cell Signaling Technology, 9212), p-JNK (Cell Signaling Technology, 4668), JNK (Cell Signaling Technology, 9252), p-p44/42 MAPK (ERK1/2) (Cell Signaling Technology, 4370), p44/42 MAPK (ERK1/2) (Cell Signaling Technology, 9102), RIPK3 (Enzo, ADI-905-242-100 or Cell Signaling Technology, 95702), caspase-8 (Cell Signaling Technology, 4790), FADD (Santa Cruz Biotechnology, sc-6036), α-tubulin (Sigma, T6074), ZBP1 (Adipogen, AG-20B-0010), p-RIPK3 (Abcam, ab195117 or Cell Signaling Technology, 91702), p-MLKL (Cell Signaling Technology, 37333), MLKL (Millipore, MABC604), α-tubulin (Sigma, T6074) and GAPDH (Novus Biologicals, NB300-221). Secondary horseradish peroxidase (HRP)-coupled antibodies against rat (Jackson ImmunoResearch, 112-035-003), rabbit (GE Healthcare, NA934) or mouse (GE Healthcare, NA931) were used to detect proteins using chemiluminescence with ECL SuperSignal West PicoPlus chemiluminescent substrate (Thermo Scientific, 34578), and signal was measured with a Fusion Solo X system (Vilber).

Cell death assays

Primary MEFs were maintained at 37 °C and 5% CO2 in DMEM (ThermoFisher, 41965-039) supplemented with 10% FCS (Biosell), 1% penicillin-streptomycin (ThermoFisher Scientific15140130), 1% L-glutamine (ThermoFisher Scientific, 25030-123) and 1 mM sodium pyruvate (ThermoFisher Scientific, 11360). For cell death assays, cells were seeded in 96-well plates at a density of 1×10^4 cells per well. The next day, cells were pre-treated with combinations of 20 μM Z-VAD-FMK (Enzo LifeSciences, ALX-260-020-M005), 5 μM Emricasan (Selleckchem, S7775), 1 μg ml^{-1} CHX (Sigma, 239763), or 5 μM Birinapant (BioVision, 2597) in the presence of the dead cell stain DiYO-1 (AAT Bioquest, ABD-17580) for 30 min, before addition of 20 ng ml^{-1} recombinant mouse TNF (VIB Protein Service Facility, Ghent). Besides, cells were treated with 1000 U ml^{-1} IFNγ (ImmunoTools, 12343537) or 2.5 μg ml^{-1} Poly (I:C) (EDM Millipore, 42424-50-0) in addition to combination of 5 μM Emricasan and 50 μg ml^{-1} Etanercept (Enbrel, Amgen) in the presence of DiYO-1. Cells were imaged for the indicated duration of time in 2 h intervals using the IncuCyte S3 live-cell imaging and analysis platform (Essen BioScience). DiYO1-positive cells were automatically counted as dead cells in two to four images per well, and counts were averaged using the IncuCyte software package version 2019B rev2.

Immunohistochemistry and histology

Tissue samples from mice were fixed in 4% paraformaldehyde and embedded in paraffin. Sections of 5 μm were subjected to histological analysis by hematoxylin and eosin (H&E) staining. For immunohistochemical analysis, slides were rehydrated and incubated with peroxidase blocking buffer (0.04 M sodium citrate, 0.121 M Na_2HPO_2, 0.03 M NaN_3, 3% H_2O_2) for 15 min. Slides were washed and antigen retrieval was performed in citrate Tris buffer (pH 6) in a pressure cooker. Sections were blocked in 4% FCS with Avidin/Biotin Blocking Kit (Biozol, VEC-SP-2001) for 30 min. For CC3 staining, a primary anti-CC3 antibody (Cell signaling, 9661), a biotinylated anti-rabbit secondary antibody (ThermoFisher Scientific, B-2770), Vectastain Elite ABC-HRP kit (Biozol, VEC-PK-6100), and DAB substrate (Biozol, VEC-SK-4100) were used. After counterstaining with hematoxylin sections were mounted with Entellon (MERCK) mounting medium. Histological sections were scanned using a Nanozoomer S360 (Hamamatsu) slide scanner. Images were analysed and processed using the OMERO software package (https://openmicroscopy.org) and QuPath. Quantification of $CC3^+$ cells was performed on histological sections immunostained with antibodies against CC3. The total number of $CC3^+$ cells in SI and colon was divided by the number of crypts to show the average number in one crypt. A hundred crypts for SI and colon were analysed per mouse. Counting was performed in a blinded fashion. TUNEL assay was performed using DeadEnd Fluorometric TUNEL System (Promega, G3250) as per the manufacturer's instructions and imaged using a spinning disk confocal microscope (Perkin Elmer UltraView ERS UltraView ERS).

Blood cell analysis

Whole blood-cell-count analysis was performed in peripheral blood using an Abacus Junior Vet analyser (Diatron) according to the manufacturer's instructions.

Flow Cytometry

Whole blood samples, splenocytes and thymocytes were stained with Near-IR Live/Dead Kit (Thermo Fisher Scientific, L10119) for dead cell exclusion, followed by surface staining with fluorochrome labeled antibodies; anti-Ly6C (Biolegend, 128011), NK1.1 (Biolegend, 108719), CD4 (Biolegend, 100536), CD45 (Thermo Fisher Scientific, 67-0451-82), CD3 (Biolegend, 100232), CD11b (Biolegend, 101251), CD8 (Biolegend, 100752), B220 (Thermo Fisher Scientific, 63-0452-82) CD11c (BD Biosciense, 561022), Ly6G (Biolegend, 127607). Cells were analyzed using BD LSRFortessa Cell Analyzer (BD Biosciences) and FlowJo (FlowJo).

Generation of immortalized mouse embryonic fibroblasts

Immortalized mouse embryonic fibroblasts (iMEFs) were generated using lentiviral gene transfer. 24 h prior to transduction, 100,000 cells/well were seeded in a 12-well plate. Cells were incubated with 1.5 ml fresh medium + 1 ml SV40-containing supernatant + 8 μg ml^{-1} polybrene (Sigma Aldrich, H9268) for 24h. On the next day, virus containing medium was removed and replaced with fresh medium and cell pools were used for experiments.

Immunoprecipitation Assays

For TNFR1 complex I IPs, 4×10^6 MEF were seeded on a 10 cm tissue culture plate. The next day, cells were treated with 1 $\mu g\ ml^{-1}$ FLAG-hTNF (VIB Protein Service Facility, Ghent). The cells were washed two times in ice-cold PBS, followed by lysis in NP-40 lysis buffer supplemented with protease and phosphatase inhibitors. The cell lysates were cleared by centrifugation for 15 min at 4 °C and the supernatants were then incubated overnight with anti-FLAG M2 affinity gel (Sigma-Aldrich, A2220). The next day, the beads were washed three times in NP-40 lysis buffer and the TNFR1 signaling complex was eluted from the beads using 2x NuPAGE LDS sample buffer (Thermo Fisher Scientific, NP0007). For FADD-IPs, the cell lysates were incubated overnight with anti-FADD antibody (Santa Cruz Biotechnology, sc-6036) and Dynabeads Protein G (Thermo Fisher Scientific, 10003D) were added and incubated for 3 h. The beads were washed three times and the bound protein was eluted with 2x NuPAGE LDS sample buffer. For ZBP1- or RIPK3-IPs, cells were lysed in DISC lysis buffer (20 mM Tris-HCL pH 7.5, 150 mM NaCl, 2 mM EDTA, 1% Triton X-100, 10% glycerol) supplemented with protease and phosphatases inhibitors. Cell lysates were left in the −80 °C to aid cell lysis for 20 min, then rotated at 4 °C until thawed. Cell lysates were collected by centrifugation at 4 °C at 14000 rpm for 15 min. 2 mg of protein lysates were incubated with 2ug (1ug/mg) of ZBP1 antibody (Adipogen, AG-20B-0010-C100) or RIPK3 (Enzo LifeSciences, ADI-905- 242-100) and left rotating for 4 hours at 4 °C. Samples containing antibody were then incubated with 25 μl of Protein G Sepharose (Sigma Aldrich,P3296) and left rotating overnight at 4 °C. Beads bound immunocomplexes were then washed five times in wash buffer (1x PBS, 1% Triton X-100, 1 mM EDTA, 5% glycerol) and drained via fine needle aspiration following the final wash. Samples were eluted by boiling for 10 min in 60 μl of 2x Laemmli sample buffer and resolved by western blotting.

Gene expression analysis by RT–qPCR

Total RNA was extracted with RNAzol (Sigma Aldrich, R4533) and Direct-zol-96 RNA kit (Zymo Research, R2054), according to the manufacturer's instructions, followed by cDNA synthesis using the LunaScript RT SuperMix kit (New England Biolabs, E3010L). RT–qPCR was performed using TaqMan probes and Luna Universal Probe qPCR Master Mix (New England Biolabs, M3004X) in a QuantStudio 5 Real-Time PCR System (Applied Biosystems). Reactions were run in technical duplicates with *Tbp* as a reference gene. Relative expression of gene transcripts is shown using the $2^{-\Delta Ct}$ method and is represented in dot plot graphs as mRNA expression values relative to the reference gene.

Histopathological analysis

Histopathological evaluation was performed on 5 mm thick H&E-stained sections of paraffin-embedded swiss-rolls of intestinal tissues, using a modified version of the scoring system described in Schwarzer et al.[39]. In brief, histopathology scores are composed of four parameters: epithelial hyperplasia, quantity and localization of tissue inflammation, epithelial cell death and epithelial injury. An ''area factor'' for the fraction of affected tissue was assigned and multiplied with the respective parameter score (1 = 0-25%; 2 = 25-50%; 3 = 50-75%, 4 = 75-100%). If different severities for the same parameter were observed in the same sample, each area was judged individually and multiplied with the correlating area factor. Area factors for a given sample always added up to 4. The histology score was calculated as the sum of all parameter scores multiplied with their area factors. Maximum score was 64. Scores are based on one swiss-roll section per mouse and were performed in a blinded fashion.

Histological sub-scores

1. crypt hyperplasia
   0 = normal crypt proliferation
   1 = signs of increased proliferating – expansion of TA compartment
   2 = obvious increase in proliferating cells – reduced numbers of differentiated cells; increased nuclear/cytoplasm ratio; differentiated cells mainly in the upper part of the crypt; shortening of villi
   3 = almost complete absence of differentiated cells, severe villus atrophy (small intestine)
2. epithelial injury/erosion
   0 = no alterations in epithelial structure, no mucosal damage
   1 = discrete focal lympho-epithelial erosions
   2 = surface mucosal erosion
   3 = extensive epithelial erosions (ulcers, mucosa denudation and damage extending into deeper layers of the bowel wall
3. extend of inflammation in the tissue
   0 = absent
   1 = increased amounts of immune cells in the lamina propria
   2 = inflammation extending into the submucosa
   3 = transmural inflammation extending into muscularis and serosa
4. death of epithelial cells
   0 = absent (except for physiologically standard cell death)
   1 = increase in the occurrence of individual dying IECs or small clusters of dying cells

2 = clearly visible IEC death with cell shedding, areas with epithelial thinning and early stages of crypt abscess formation
3 = clear presence of erosive lesions (ulcer formation) histology scoring

QUANTIFICATION AND STATISTICAL ANALYSIS

Data shown in graphs are the mean or mean ± SEM. A non-parametric Mann–Whitney test or one-way ANOVA with Tukey's multiple-comparisons test was performed. Survival curves were compared using the Log–rank test. All statistical analyses were performed with GraphPad Prism 9. *p $\leq$ 0.05; **p $\leq$ 0.01; ***p $\leq$ 0.001; ****p $\leq$ 0.0001 for all figures.

Immunity, Volume *57*

Supplemental information

The RIPK1 death domain restrains ZBP1- and TRIF-mediated cell death and inflammation

Takashi Imai, Juan Lin, Göksu Gökberk Kaya, Eunjin Ju, Vangelis Kondylis, Konstantinos Kelepouras, Gianmaria Liccardi, Chun Kim, and Manolis Pasparakis

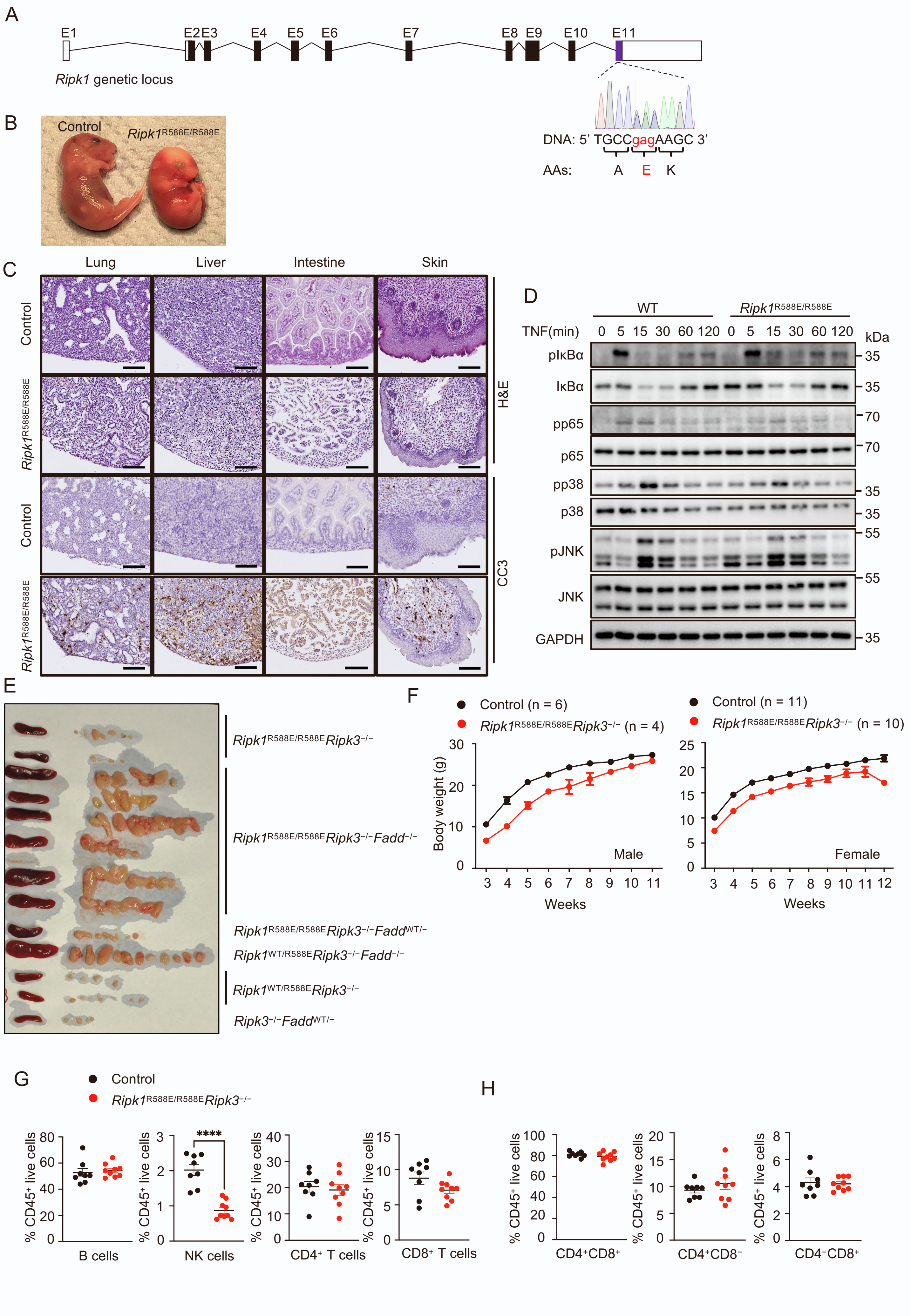
A
E1
E2
E3
E4
E5
E6
E7
E8
E9
E10
E11
Ripk1 genetic locus
DNA: 5' TGCCgagAAGC 3'
AAs: A E K
B
Control
Ripk1R588E/R588E
C
Lung
Liver
Intestine
Skin
Control
Ripk1R588E/R588E
H&E
CC3
D
WT
Ripk1R588E/R588E
TNF(min) 0 5 15 30 60 120 0 5 15 30 60 120
kDa
pIκBα
IκBα
pp65
p65
pp38
p38
pJNK
JNK
GAPDH
35
70
55
E
Ripk1R588E/R588E Ripk3−/−
Ripk1R588E/R588E Ripk3−/− Fadd−/−
Ripk1R588E/R588E Ripk3−/− FaddWT/−
Ripk1WT/R588E Ripk3−/− Fadd−/−
Ripk1WT/R588E Ripk3−/−
Ripk3−/− FaddWT/−
F
Control (n = 6)
Ripk1R588E/R588E Ripk3−/− (n = 4)
Control (n = 11)
Ripk1R588E/R588E Ripk3−/− (n = 10)
Body weight (g)
Male
Female
Weeks
G
Control
Ripk1R588E/R588E Ripk3−/−
% CD45+ live cells
B cells
NK cells
CD4+ T cells
CD8+ T cells
****
H
CD4+CD8+
CD4+CD8−
CD4−CD8+

Figure S1. *Ripk1*$^{R588E/R588E}$ knock-in mutation causes perinatal lethality rescued by RIPK3 deficiency alone or together with FADD. Related to Figures 1 and 2

(A) Schematic depiction of the generation of *Ripk1*$^{R588E/R588E}$ mice. CRISPR/Cas9 gene targeting in mouse zygotes was used to introduce a mutation of three nucleotides (CGC to gag) in exon 11 resulting in substitution of arginine at position 588 with glutamic acid. Sanger sequencing of DNA from the obtained founder confirmed the correct targeting. **(B)** Pictures of E18.5 *Ripk1*$^{R588E/R588E}$ and littermate control embryos. **(C)** Representative images from tissue sections from E18.5 embryos stained with hematoxylin and eosin (H&E), immunostained for cleaved caspase 3 (CC3). Control n = 18 for H&E, n = 16 for anti-CC3; *Ripk1*$^{R588E/R588E}$ n = 8 for H&E and anti-CC3. **(D)** Immunoblot analysis with the indicated antibodies of lysates from primary WT or *Ripk1*$^{R588E/R588E}$ MEFs stimulated with TNF (20 ng ml^{-1}) for the indicated periods of time. Representative data shown from three independent experiments. **(E)** Photographs of spleens and lymph nodes from mice with the indicated genotypes. **(F)** Graphs depicting body weight curves of control and *Ripk1*$^{R588E/R588E}$*Ripk3*$^{-/-}$ mice. **(G, H)** Flow cytometry analysis of splenic leukocytes (**G**) and thymocytes (**H**) from mice with the indicated genotypes at 12 weeks of age. AAs, amino acids. Scale bars, 100 µm. Each dot represents one mouse. Graphs show mean ± SEM. $^{*}p \leq 0.05$; $^{**}p \leq 0.01$; $^{***}p \leq 0.001$; $^{****}p \leq 0.0001$ for all figures.

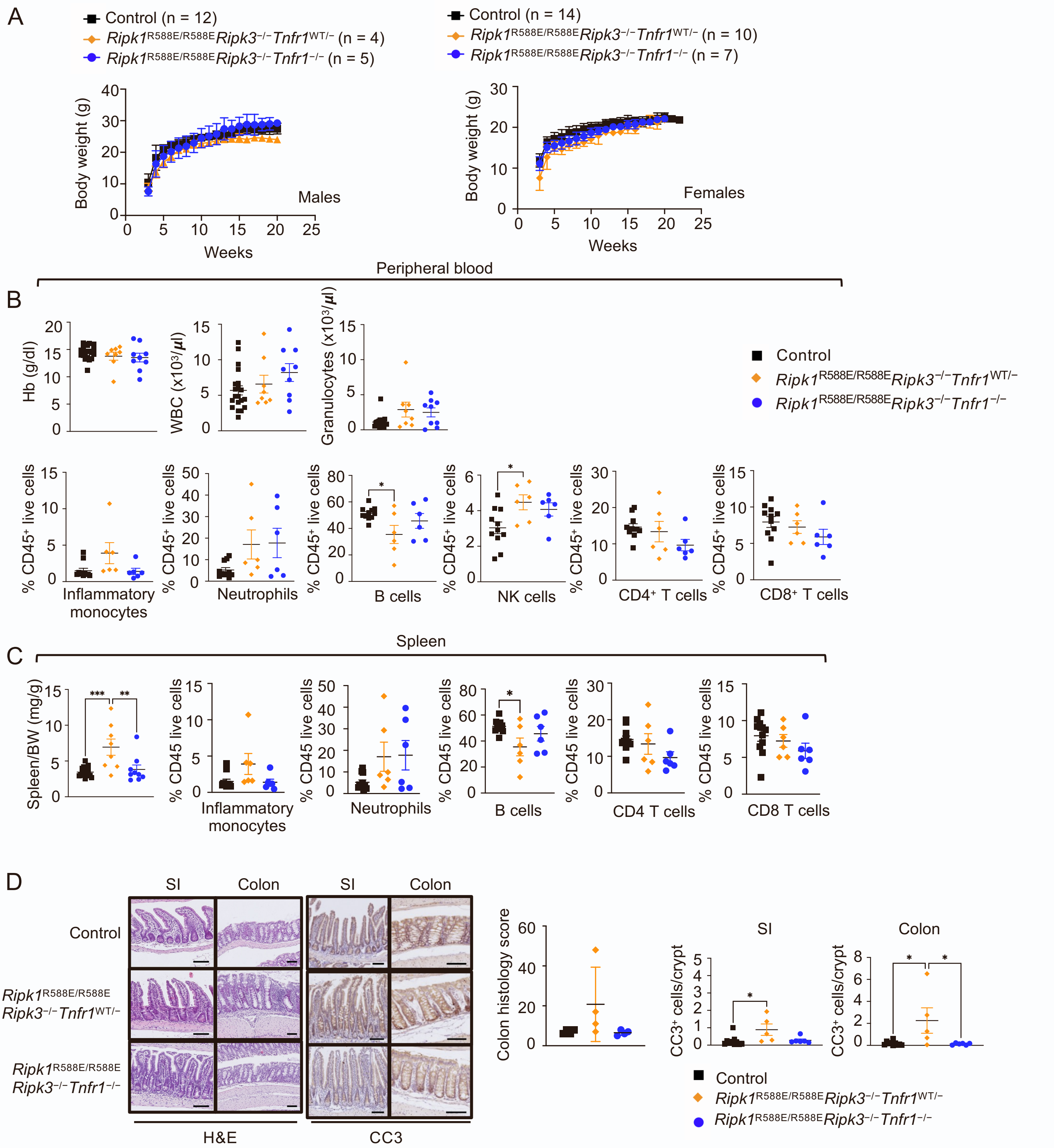

Figure S2. TNFR1 signaling mediates the postnatal pathology of *Ripk1*$^{R588E/R588E}$*Ripk3*$^{-/-}$ mice. Related to Figure 3

(A) Graphs depicting BW curves of mice with the indicated genotypes. **(B, C)** Graphs depicting Hb, WBC and granulocyte counts in the blood and flow cytometry analysis of leukocytes in blood (**B**) and spleen (**C**) from mice with the indicated genotypes at 23 to 32 weeks of age. **(D)** Representative images of SI and colon sections stained with H&E or immunostained for CC3 from control (n = 10), *Ripk1*$^{R588E/R588E}$*Ripk3*$^{-/-}$*Tnfr1*$^{WT/-}$ (n = 5) and *Ripk1*$^{R588E/R588E}$*Ripk3*$^{-/-}$*Tnfr1*$^{-/-}$ (n = 6) mice at 23 to 32 weeks of age (left). Graphs show colon histology score and quantification of CC3$^+$ cells in SI and colon sections of mice with the indicated genotypes (right). Scale bars, 100 μm. Each dot represents one mouse. Graphs show mean ± SEM. *p ≤ 0.05; **p ≤ 0.01; ***p ≤ 0.001; ****p ≤ 0.0001 for all figures.

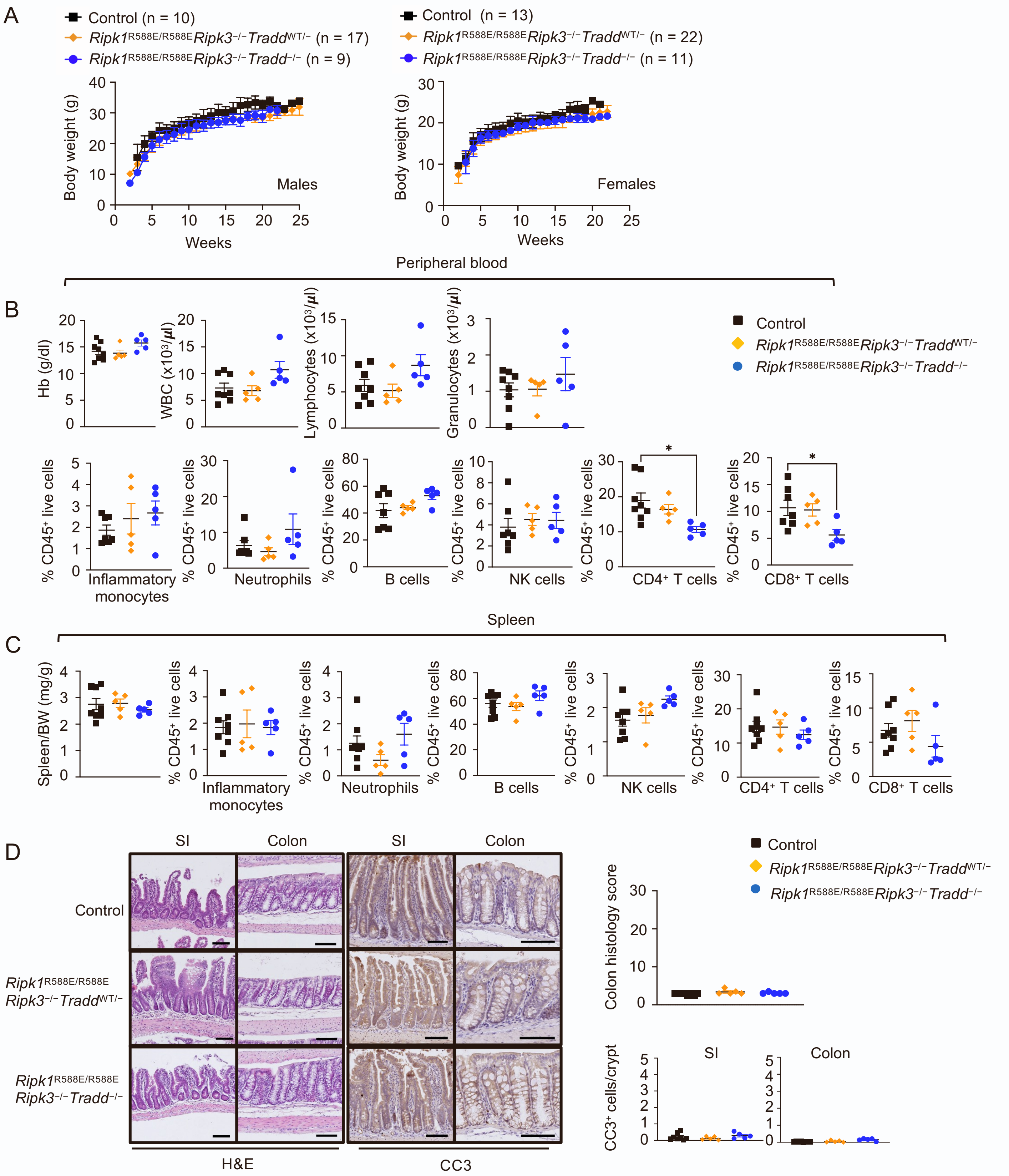

Figure S3. TRADD deficiency fully prevents the postnatal pathology of *Ripk1*$^{R588E/R588E}$*Ripk3*$^{-/-}$ mice. Related to Figure 4

(**A**) Graphs depicting BW curves of mice with the indicated genotypes. **(B, C)** Graphs depicting Hb, WBC, lymphocyte and granulocyte counts in the blood and flow cytometry analysis of blood (**B**), spleen weight/BW ratio and flow cytometry analysis of splenic leukocytes (**C**) from mice with the indicated genotypes at 23 to 32 weeks of age. **(D)** Representative images of SI and colon sections stained with H&E or immunostained for CC3 from control (n = 8), *Ripk1*$^{R588E/R588E}$*Ripk3*$^{-/-}$*Tradd*$^{WT/-}$ (n = 5) and *Ripk1*$^{R588E/R588E}$*Ripk3*$^{-/-}$*Tradd*$^{-/-}$ (n = 5) mice at 23 to 32 weeks of age (left). Graphs show colon histology score and quantification of CC3^{+} cells in SI and colon sections of mice with the indicated genotypes (right). Scale bars, 100 μm. Each dot represents one mouse. Graphs show mean ± SEM. $^{*}p \leq 0.05$; $^{**}p \leq 0.01$; $^{***}p \leq 0.001$; $^{****}p \leq 0.0001$ for all figures.

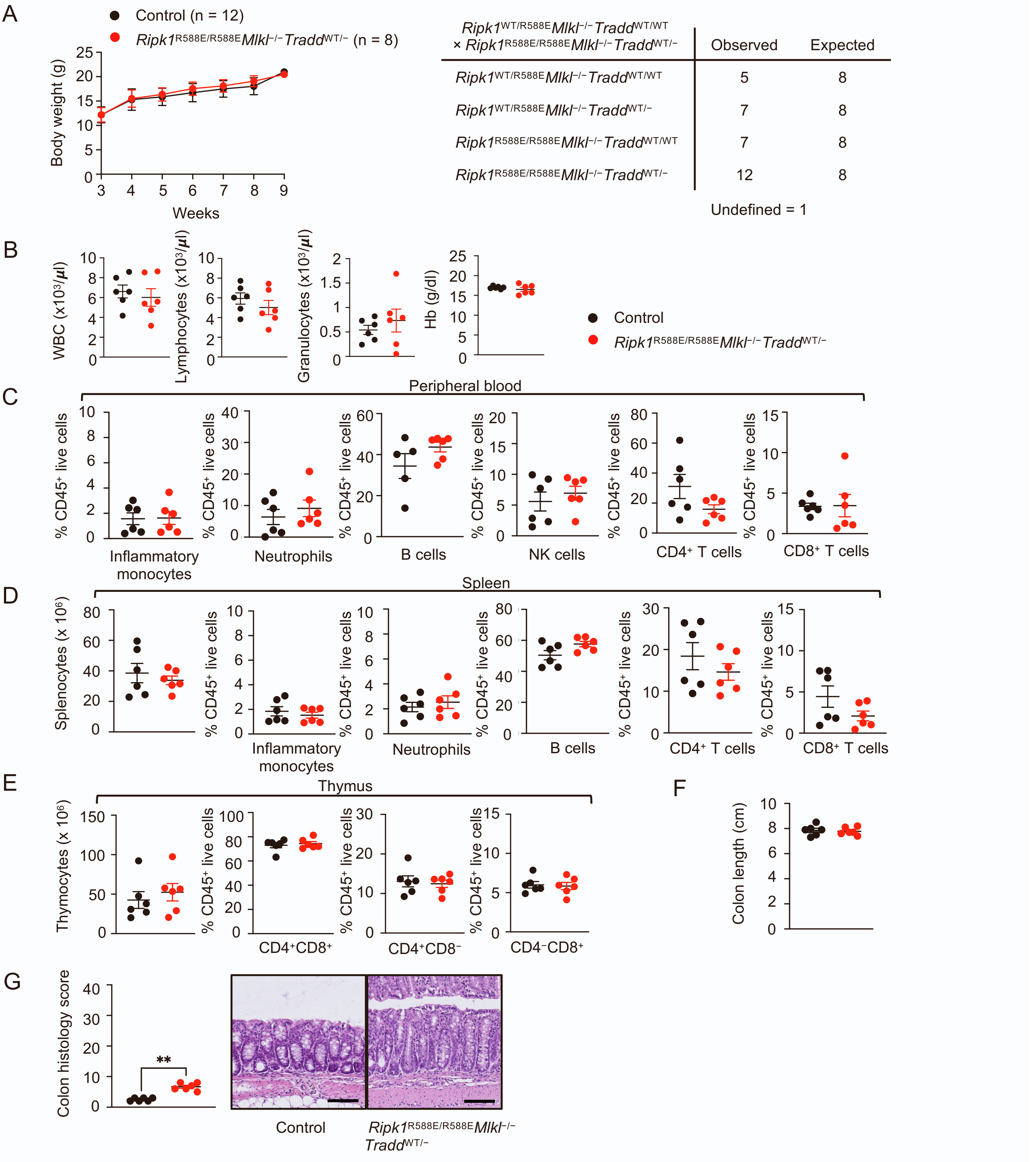

Figure S4. TRADD deficiency prevents the postnatal pathology of *Ripk1*$^{R588E/R588E}$*Mlkl*$^{-/-}$ mice. Related to Figure 5

(**A**) Graphs depicting BW curves of mice with the indicated genotypes. Tables showing the numbers of P0 offspring from intercrossing parents with the indicated genotypes. **(B-E)** Graphs depicting Hb, WBC, lymphocyte and granulocyte counts in the blood (**B**) and flow cytometry analysis of blood (**C**), flow cytometry analysis of splenic leukocytes (**D**) and thymocytes (**E**) from mice with the indicated genotypes. **(F)** Graph depicting colon length in mice with the indicated genotypes. **(G)** Representative images of colon sections stained with H&E from control (n = 6) and *Ripk1*$^{R588E/R588E}$*Mlkl*$^{-/-}$*Tradd*$^{WT/-}$ (n = 6) mice. Graphs show colon histology score of mice with the indicated genotypes. Scale bars, 100 μm. All analyses were performed in 9-week-old mice. Each dot represents one mouse. Graphs show mean ± SEM. *p ≤ 0.05; **p ≤ 0.01; ***p ≤ 0.001; ****p ≤ 0.0001 for all figures.

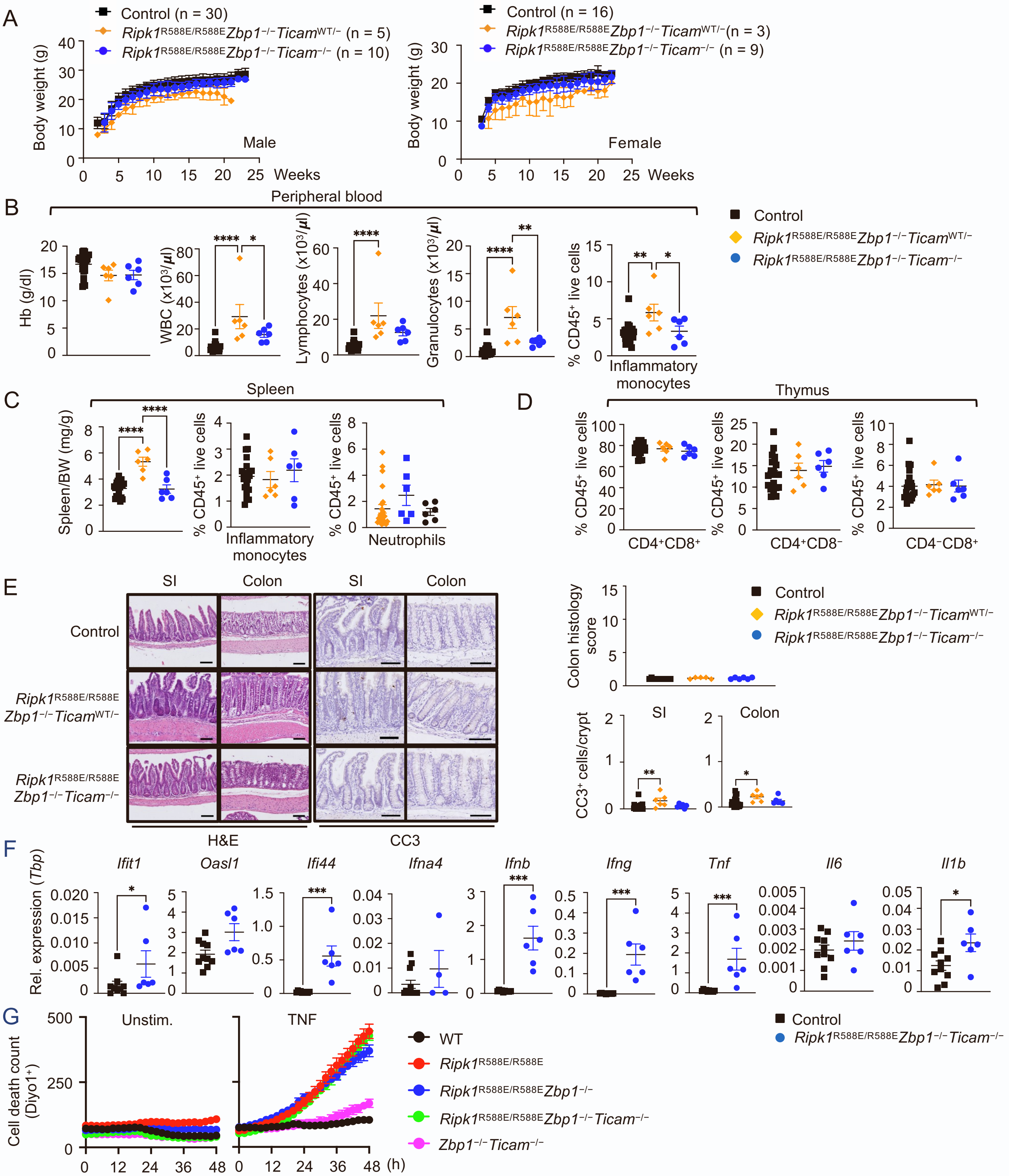

A
Control (n = 30)
Ripk1R588E/R588E Zbp1−/− TicamWT/− (n = 5)
Ripk1R588E/R588E Zbp1−/− Ticam−/− (n = 10)
Body weight (g)
Male
Weeks
Control (n = 16)
Ripk1R588E/R588E Zbp1−/− TicamWT/− (n = 3)
Ripk1R588E/R588E Zbp1−/− Ticam−/− (n = 9)
Female
B
Peripheral blood
Hb (g/dl)
WBC (x10³/µl)
Lymphocytes (x10³/µl)
Granulocytes (x10³/µl)
% CD45⁺ live cells
Inflammatory monocytes
Control
Ripk1R588E/R588E Zbp1−/− TicamWT/−
Ripk1R588E/R588E Zbp1−/− Ticam−/−
C
Spleen
Spleen/BW (mg/g)
Inflammatory monocytes
Neutrophils
D
Thymus
CD4⁺CD8⁺
CD4⁺CD8⁻
CD4⁻CD8⁺
E
SI
Colon
Control
Ripk1R588E/R588E Zbp1−/− TicamWT/−
Ripk1R588E/R588E Zbp1−/− Ticam−/−
H&E
CC3
Colon histology score
CC3⁺ cells/crypt
F
Rel. expression (Tbp)
Ifit1
Oasl1
Ifi44
Ifna4
Ifnb
Ifng
Tnf
Il6
Il1b
G
Cell death count (Diyo1⁺)
Unstim.
TNF
(h)
WT
Ripk1R588E/R588E
Ripk1R588E/R588E Zbp1−/−
Ripk1R588E/R588E Zbp1−/− Ticam−/−
Zbp1−/− Ticam−/−
Control
Ripk1R588E/R588E Zbp1−/− Ticam−/−

Figure S5. ZBP1- and TRIF-dependent signaling mediates the pathology of *Ripk1*$^{R588E/R588E}$ mice. Related to Figure 6

(**A**) Graphs depicting BW curves of mice with the indicated genotypes. **(B)** Graphs depicting blood Hb, WBC, lymphocyte and granulocyte counts and flow cytometry analysis of inflammatory monocytes in blood from mice with the indicated genotypes. (**C, D**) Graphs depicting spleen weight/BW ratio and flow cytometry analysis of spleen (**C**) and thymus (**D**) from mice with the indicated genotypes. **(E)** Representative images from SI and colon sections stained with H&E or immunostained for CC3 from control (n = 21), *Ripk1*$^{R588E/R588E}$*Zbp1*$^{-/-}$*Ticam*$^{WT/-}$ (n = 6) and *Ripk1*$^{R588E/R588E}$*Zbp1*$^{-/-}$*Ticam*$^{-/-}$ (n = 6) mice. Graphs show colon histology score and quantification of CC3^{+} cells in SI and colon from mice with the indicated genotypes. **(F)** RT-qPCR analysis of mRNA expression of the indicated genes in colon from mice with the indicated genotypes. **(G)** Cell death measured by DiYO1 uptake in primary MEFs of the indicated genotypes stimulated with TNF (20 ng ml^{-1}) for 48 h. Data are representative of two independent experiments. Scale bars, 100 µm. Mice were analyzed at 20 to 30 weeks of age. Each dot represents one mouse. Graphs show mean ± SEM. *$p \leq 0.05$; **$p \leq 0.01$; ***$p \leq 0.001$; ****$p \leq 0.0001$ for all figures.

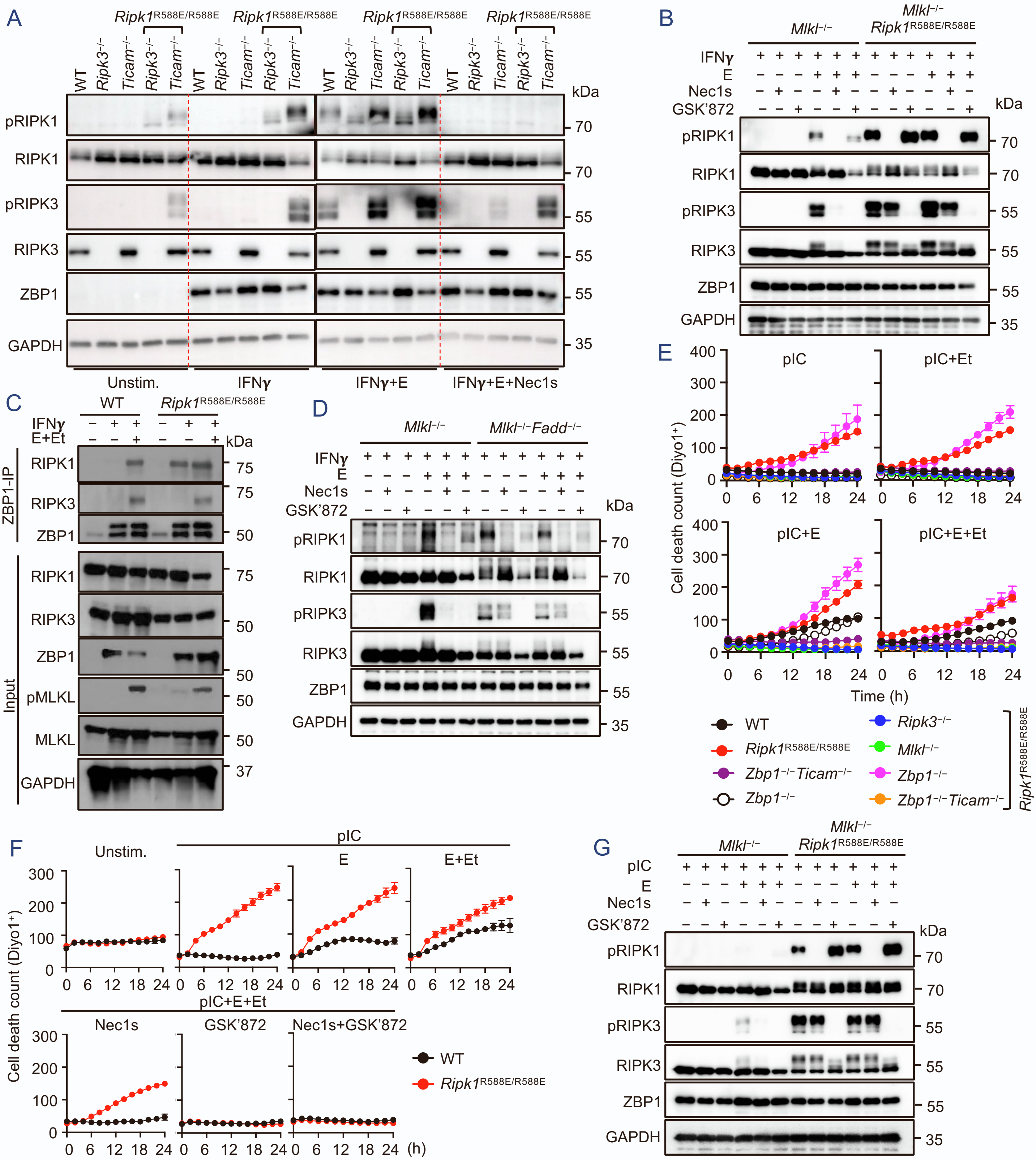

A
B
C
D
E
F
G
pRIPK1
RIPK1
pRIPK3
RIPK3
ZBP1
GAPDH
pMLKL
MLKL
kDa
Unstim.
IFNγ
IFNγ+E
IFNγ+E+Nec1s
ZBP1-IP
Input
Nec1s
GSK'872
Cell death count (Diyo1⁺)
Time (h)
pIC
pIC+Et
pIC+E
pIC+E+Et
E+Et
Nec1s+GSK'872
WT

Figure S6. The DD of RIPK1 inhibits ZBP1- and TRIF-mediated necroptosis. Related to Figure 7

(A) Immunoblot analysis with the indicated antibodies of lysates from primary MEFs from mice with the indicated genotypes stimulated with combinations of IFNγ, E and Nec1s for 24 h. Representative data shown from two independent experiments. **(B)** Immunoblot analysis with the indicated antibodies of lysates from immortalized *Mlkl*$^{-/-}$ and *Ripk1*$^{R588E/R588E}$*Mlkl*$^{-/-}$ MEFs stimulated with combinations of IFNγ, E, Nec1s (20 μM) or GSK'872 (3 μM) for 24 h. Representative data shown from two independent experiments. **(C)** Immunoblot analysis with the indicated antibodies of ZBP1 immunoprecipitates and total lysates from immortalized WT and *Ripk1*$^{R588E/R588E}$ MEFs treated with combinations of IFNγ, E and Et for 24h. Representative data shown from two independent experiments. **(D)** Immunoblot analysis with the indicated antibodies of lysates from immortalized *Mlkl*$^{-/-}$ and *Fadd*$^{-/-}$*Mlkl*$^{-/-}$ MEFs stimulated with combinations of IFNγ, E, Nec1s or GSK'872 for 24 h. Representative data shown from two independent experiments. **(E, F)** Cell death measured by DiYO1 uptake in primary WT and *Ripk1*$^{R588E/R588E}$ MEFs treated with combinations of poly (I:C) (pIC) (2.5 μg ml^{-1}), Et, E, Nec1s or GSK'872 for 24 h. Data are representative of two independent experiments. **(G)** Immunoblot analysis with the indicated antibodies of lysates from immortalized *Mlkl*$^{-/-}$ and *Ripk1*$^{R588E/R588E}$*Mlkl*$^{-/-}$ MEFs stimulated with combinations of pIC, E, Nec1s or GSK'872 for 24 h. Representative data shown from two independent experiments. Graphs show mean ± SEM.

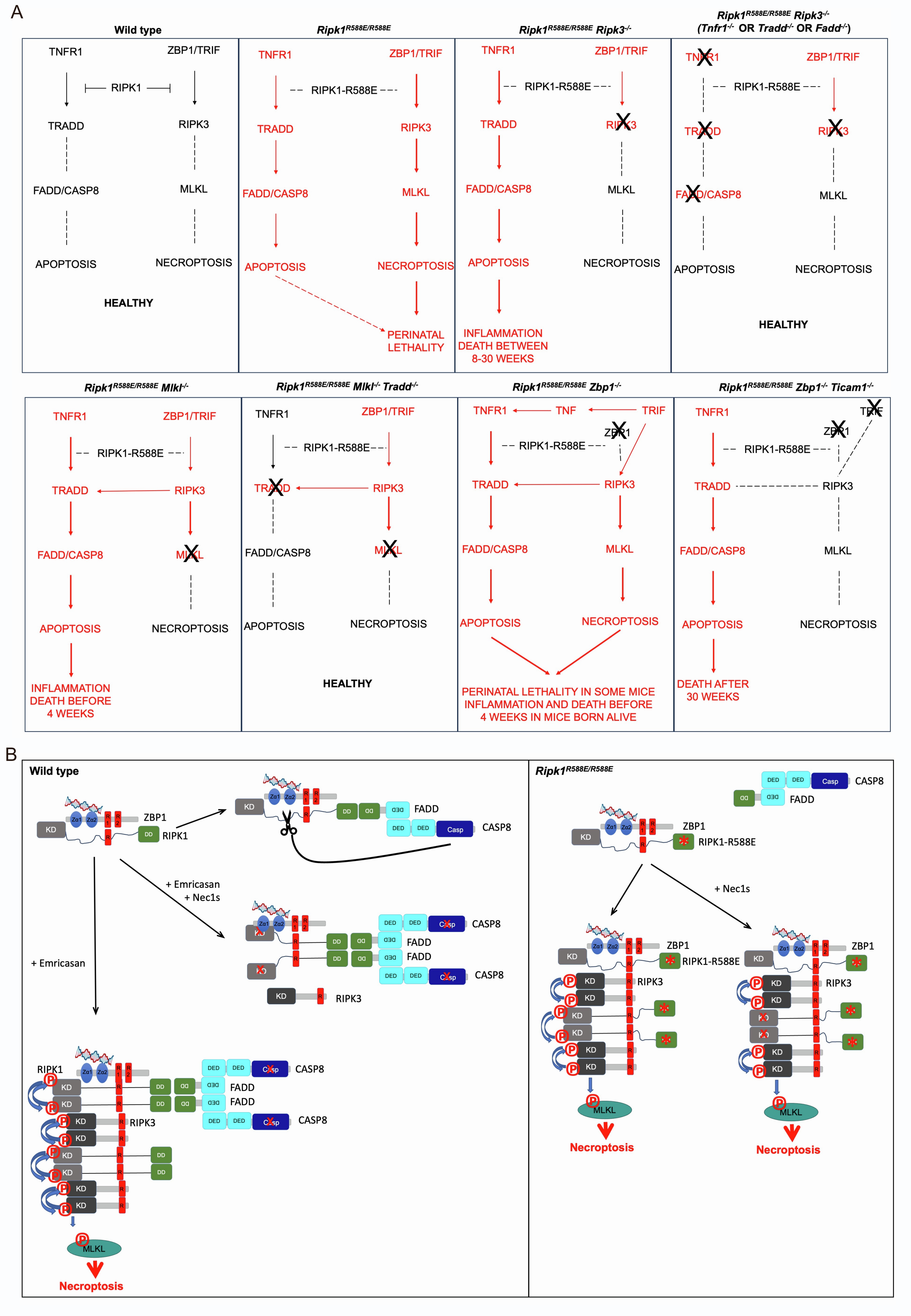
A
Wild type
TNFR1
ZBP1/TRIF
RIPK1
TRADD
RIPK3
FADD/CASP8
MLKL
APOPTOSIS
NECROPTOSIS
HEALTHY
Ripk1R588E/R588E
TNFR1
ZBP1/TRIF
RIPK1-R588E
TRADD
RIPK3
FADD/CASP8
MLKL
APOPTOSIS
NECROPTOSIS
PERINATAL LETHALITY
Ripk1R588E/R588E Ripk3-/-
TNFR1
ZBP1/TRIF
RIPK1-R588E
TRADD
RIPK3
FADD/CASP8
MLKL
APOPTOSIS
NECROPTOSIS
INFLAMMATION DEATH BETWEEN 8-30 WEEKS
Ripk1R588E/R588E Ripk3-/- (Tnfr1-/- OR Tradd-/- OR Fadd-/-)
TNFR1
ZBP1/TRIF
RIPK1-R588E
TRADD
RIPK3
FADD/CASP8
MLKL
APOPTOSIS
NECROPTOSIS
HEALTHY
Ripk1R588E/R588E Mlkl-/-
TNFR1
ZBP1/TRIF
RIPK1-R588E
TRADD
RIPK3
FADD/CASP8
MLKL
APOPTOSIS
NECROPTOSIS
INFLAMMATION DEATH BEFORE 4 WEEKS
Ripk1R588E/R588E Mlkl-/- Tradd-/-
TNFR1
ZBP1/TRIF
RIPK1-R588E
TRADD
RIPK3
FADD/CASP8
MLKL
APOPTOSIS
NECROPTOSIS
HEALTHY
Ripk1R588E/R588E Zbp1-/-
TNFR1
TNF
TRIF
ZBP1
RIPK1-R588E
TRADD
RIPK3
FADD/CASP8
MLKL
APOPTOSIS
NECROPTOSIS
PERINATAL LETHALITY IN SOME MICE INFLAMMATION AND DEATH BEFORE 4 WEEKS IN MICE BORN ALIVE
Ripk1R588E/R588E Zbp1-/- Ticam1-/-
TNFR1
TRIF
ZBP1
RIPK1-R588E
TRADD
RIPK3
FADD/CASP8
MLKL
APOPTOSIS
NECROPTOSIS
DEATH AFTER 30 WEEKS
B
Wild type
ZBP1
RIPK1
FADD
CASP8
+ Emricasan + Nec1s
CASP8
FADD
FADD
CASP8
RIPK3
+ Emricasan
RIPK1
CASP8
FADD
FADD
RIPK3
CASP8
MLKL
Necroptosis
Ripk1R588E/R588E
CASP8
FADD
ZBP1
RIPK1-R588E
+ Nec1s
ZBP1
RIPK1-R588E
RIPK3
MLKL
Necroptosis
ZBP1
RIPK3
MLKL
Necroptosis

Figure S7. Schematic depiction of the role of the RIPK1 DD in regulating ZBP1, TRIF and TNFR1 signaling and its physiological function in regulating survival and inflammation in mice. Related to all figures

(A) Schematics outlining the key findings from our genetic crosses dissecting the pathways causing perinatal or postnatal lethality and inflammation in *Ripk1*$^{R588E/R588E}$ mice. **(B)** (Left panel) In wild type cells, DD-dependent recruitment of FADD-caspase-8 to the ZBP1- and TRIF-induced signaling complexes results in RIPK1 cleavage and complex destabilization. Caspase-8 inhibition prevents RIPK1 cleavage but inhibition of RIPK1 kinase activity prevents the formation of ordered RIPK1 aggregates. Disordered RIPK1 associated with FADD/Casp8 fail to recruit and activate RIPK3. Caspase-8 inhibition prevents RIPK1 cleavage. DD-dependent interactions impose conformational changes on RIPK1 facilitating the recruitment of RIPK3 and the formation of ZBP1/RIPK1/RIPK3 aggregates resulting in activation and autophosphorylation of RIPK1 and RIPK3 causing necroptosis. RIPK1 kinase activity is required for RIPK3 recruitment and activation. RIPK3 scaffold function and in part its kinase activity are required for full RIPK1 activation and autophosphorylation. (Right panel) Mutation of the DD prevents the recruitment of FADD/caspase-8 suppressing RIPK1 cleavage. In addition, DD mutation prevents the DD-dependent conformational changes and oligomerisation of RIPK1. RIPK3 is recruited to the ZBP1/RIPK1 aggregates and is activated by autophosphorylation forming ordered oligomers resulting in necroptosis. RIPK1 is activated within the ordered RIPK3 oligomers, but its kinase activity is not required for RIPK3 activation and necroptosis. RIPK3 scaffold function but not its kinase activity is required for RIPK1 activation and autophosphorylation. Please note that the schematics above are necessarily an over-simplification that cannot fully capture the three-dimensional arrangements of the protein complexes depicted, which very likely consist of oligomers of the indicated proteins interacting with each other.

III. Discussion

This work collectively advances our understanding of necroptotic cell death both as a biological process and as a pathological mechanism in disease. In the first study[515], we addressed a major technical limitation in the necroptosis field by developing and validating a protocol for the specific immunohistochemical and immunofluorescent detection of phosphorylated murine MLKL at serine 345 (pMLKL-S345), a hallmark of necroptosis activation. Despite the widespread use of cleaved-caspase-3 as a general cell death marker, our data show its limitations in the context of necroptosis, as it cannot reliably differentiate between necroptotic and secondary apoptotic events. Given that necroptosis proceeds independently of caspase activation, using cleaved-caspase-3 as a proxy can be misleading, particularly in models lacking caspase-8, FADD or RIPK1[154,155,159,516]. In fact, our comparison in *Casp8$^{E\text{-}KO}$* mice highlighted distinct staining patterns of pMLKL-S345 and cleaved-caspase-3, with the former marking dying keratinocytes in the epidermis and the latter labelling fibroblasts and immune cells in the dermis, likely indicative of secondary apoptotic events triggered by necroptosis-induced inflammation. These results further highlight the spatial and functional distinction between necroptotic and apoptotic processes, without the need for complex genetic knockout models traditionally required to assess the involvement of necroptosis *in vivo*.

Moreover, our protocol enabled the spatially resolved detection of necroptosis in the *Fadd$^{iIEC\text{-}KO}$* mouse model, revealing distinct regional necroptotic activity along the intestinal tract. Previous studies have associated both colitis and ileitis resulting from intestinal FADD deletion with TNFR1- and ZBP1-mediated MLKL-driven necroptosis, while ileitis is further exacerbated by caspase-8-GSDMD-mediated pyroptosis[139,141]. In those studies, intestinal inflammation and epithelial damage were primarily assessed using CD45 as a general marker of immune cell infiltration and cleaved-caspase-3 to evaluate residual caspase-8 activity[138,139,141], however not specific for necroptosis. Here, we show robust pMLKL-S345 staining in the ileum but not the colon, supporting the idea that necroptosis is more prominent in the ileum. The absence of signal in the colon may reflect differences arising from developmental versus adult deletion of FADD or suboptimal timing of tissue collection. These findings underscore the utility of our protocol in providing a direct, cell-type- and tissue-type-specific readout of necroptotic activity, enabling more accurate interpretation of disease mechanisms.

Our data further underscore the utility of pMLKL-S345 detection for studying necroptosis in infectious disease models, where its role has previously been inferred primarily from MLKL- or RIPK3-deficient mice or *in vitro* assays[71,517]. While necroptosis has been implicated in the pathogenesis of respiratory viral infections such as influenza A virus (IAV)[179,180,194,518] and respiratory syncytial virus (RSV)[519,520], its role in SARS-CoV-2 infection remains controversial. Some studies show involvement of RIPK3 and ZBP1 in cytokine production and lung injury[521], while others argue necroptosis is dispensable for disease pathogenesis in studies employing MLKL-deficient mice[522]. We show that SARS-CoV infection in mice induces clear pMLKL-S345 positivity in lung epithelial cells, indicating necroptotic activation, as previously suggested[523], in both infected and potentially bystander cells. Although MLKL-deficient mice did not exhibit improved disease outcomes, suggesting that necroptosis may not be the primary driver of pathogenesis[522], our findings demonstrate that necroptotic signalling is nonetheless occurring *in vivo*. This highlights that the presence of necroptosis does not necessarily equate to overt pathology but may still contribute to disease-relevant processes in humans. Moreover, despite potential differences between SARS-CoV-1 and SARS-CoV-2 infections, these results suggest that necroptosis could play a role in COVID-19-related complications beyond acute pathogenesis, including acute respiratory distress syndrome (ARDS) and post-acute sequelae ("long COVID"), where its contribution still remains unresolved. Collectively, our findings reinforce the relevance of necroptosis in viral infection models, highlight the broader applicability of pMLKL-S345 detection as a robust tool for *in vivo* studies, and open avenues for evaluating necroptosis-targeted interventions in viral infection settings.

Importantly, this method also facilitates the dissection of RIPK3's dual roles in regulating both apoptosis and necroptosis. Given that RIPK3 not only drives necroptosis through MLKL activation but can also support caspase-8-mediated apoptosis[524,525], RIPK3 knockout models alone are insufficient to distinguish between these two functions. Disentangling this dual role typically requires the generation and phenotypic comparison of mice deficient in either RIPK3 or MLKL, which often necessitates complex genetic crossings. Our analysis of *Shpn*$^{m/m}$ and *Shpn*$^{m/m}$ *Ripk3*$^{-/-}$ mice revealed tissue-specific distinctions: in the skin, RIPK3 appeared to facilitate primarily apoptosis, whereas in the spleen, it functioned primarily to drive necroptosis. These findings corroborate earlier observations showing that RIPK3 deficiency, like caspase-8 heterozygous deletion, partly ameliorates the inflammatory skin phenotype in at least 50% of *Shpn*$^{m/m}$ mice analysed, whereas MLKL deficiency does not, highlighting an apoptosis-dependent function for RIPK3 in this tissue[516,526]. Conversely, the splenic inflammation and architectural disruption observed in *Shpn*$^{m/m}$ mice were alleviated by deletion of either RIPK3 or MLKL, indicating that necroptosis is the dominant mechanism of cell death in the spleen. Similarly, in the TNF-induced SIRS model, we confirm that apoptosis is the dominant mode of cell death driving lethality, at least in the examined C57Bl/6N background, with necroptosis contributing secondarily by amplifying inflammatory responses and tissue injury. The observed protection upon deletion of RIPK3 or MLKL in this setting may therefore reflect either the inhibition of secondary necroptosis or the suppression of RIPK3-caspase-8-dependent apoptotic signalling. This interpretation is consistent with prior findings showing that either RIPK3 deletion or inactivation of RIPK1 kinase activity protects mice from TNF-induced SIRS in this genetic background form both low and high doses of TNF[524]. Interestingly, although MLKL-deficient mice exhibit greater protection against high-dose compared to low-dose TNF-induced lethality, at similar levels with *Ripk3*$^{-/-}$ mice, the underlying mechanisms remain unclear[524]. Our staining data indicate that increasing TNF levels do not result in a correspondent increase in pMLKL-S345 positivity, supporting the idea that necroptosis is not the initiating mode of cell death but may become a critical contributor to intestinal damage when apoptosis is excessive or prolonged, as suggested by the intensity and distribution of cleaved-caspase-3 staining. Together, these findings highlight the importance of spatial and molecular resolution in elucidating the dynamic interplay between apoptotic and necroptotic pathways *in vivo*.

Our second study[527], uncovered a necroptotic axis regulated by STING, revealing a previously unrecognized role for this innate immune adaptor in directly driving necroptotic cell death and demonstrating its contribution to the pathogenesis of STING-associated vasculopathy with onset in infancy (SAVI). While STING is established as a central mediator of type I interferon responses via TBK1-IRF3, its involvement in necroptosis was largely speculative, as discussed in section 5.1. We show that aberrant STING activation, either in caspase-8 deficiency or STING gain-of-function, licenses necroptosis by initiating a type I IFN-dependent transcriptional program that upregulates ZBP1 and MLKL. This pathway operates independently of TNFR1, distinguishing it from canonical TNF-driven necroptosis. Specifically, STING activation promotes the formation of a ZBP1-RIPK1-RIPK3 complex that functions independently of the canonical FADD-RIPK1-RIPK3 necrosome, enabling TNF-TNFR1-independent necroptotic execution. This alternative complex is already assembled upon caspase-8 deletion, as observed in *Casp8*$^{-/-}$ *Mlkl*$^{-/-}$ and *Fadd*$^{-/-}$ *Mlkl*$^{-/-}$ MEFs, and is further reinforced by STING agonism even in *Mlkl*$^{-/-}$ MEFs. Critically, its formation is strictly STING-dependent, as co-treatment with the STING antagonist C-178 completely abolishes complex assembly.

Beyond transcriptional licensing, STING also amplifies TNFR1-mediated necroptosis by promoting autocrine TNF production via NF-κB, establishing a dual-checkpoint model in caspase-8-deficient tissues. The first checkpoint is TNFR1/FADD-dependent, while the second is ZBP1-mediated and TNFR1-independent. Genetic evidence supports STING's dual role, as in *Casp8*$^{E\text{-}KO}$ mice, co-deletion of STING provides a stronger survival advantage than deletion of either ZBP1 or TNFR1 alone. This indicates that STING both licenses ZBP1 and sustains TNFR1-driven necroptosis. The role of STING in amplifying TNFR1-mediated necroptosis is further supported by the fact that, in the skin of *Casp8*$^{E\text{-}KO}$ *Sting1*$^{E\text{-}KO}$ mice at P5, TNF release is normalized to wild-type levels, similarly to *Casp8*$^{E\text{-}KO}$ *Tnfr1*$^{-/-}$ mice. At the transcriptional level, STING deletion leads to significant downregulation of NF-κB signature genes in the skin of *Casp8*$^{E\text{-}KO}$ *Sting1*$^{E\text{-}KO}$ and even more strikingly, in *Casp8*$^{E\text{-}KO}$ *Sting1*$^{-/-}$ mice. Similarly, the lethal dermatitis of *Casp8*$^{E\text{-}KO}$ mice bearing one functional *Tnfr1* allele was significantly prolonged only by homozygous deletion of STING, but not ZBP1, highlighting the contribution of STING-dependent TNF/NF-κB signalling to necroptotic amplification. Concordantly, pharmacological inhibition of TNF in DMXAA-treated *Casp8*$^{-/-}$ MEFs using etanercept significantly, though not completely, ameliorates lethality, further underscoring the role of STING-mediated TNF/NF-κB signalling in amplifying necroptosis.

Thus, STING acts as both initiator and amplifier of necroptotic signalling, coordinating these parallel pathways and placing itself at the centre of a dual-checkpoint necroptosis architecture. This model is further supported by genetic data showing that co-deletion of *Sting1* and *Tnfr1* in *Casp8*$^{E\text{-}KO}$ mice rescues lethal dermatitis to the same extent as co-deletion of *Zbp1* and *Tnfr1* by 14 weeks of age, reinforcing the idea that STING is an upstream regulator of both ZBP1 expression and ZBP1-driven necroptotic complex formation. We thus establish a model in which: (i) TNF-TNFR1 acts as the initial necroptosis checkpoint that must be bypassed to trigger ZBP1-mediated necroptosis; (ii) ZBP1-driven necroptosis constitutes a second, independent checkpoint; (iii) STING governs both, since *Casp8*$^{E\text{-}KO}$ *Sting1*$^{-/-}$ mice survive longer and more robustly than *Casp8*$^{E\text{-}KO}$ *Tnfr1*$^{-/-}$ and *Casp8*$^{E\text{-}KO}$ *Zbp1*$^{-/-}$ mice, implying that STING not only licenses ZBP1 but also contributes to TNF-mediated inflammation, via NF-κB activation.

Importantly, STING's contribution extends beyond transcriptional licensing and TNF/TNFR1 regulation. In *Casp8*$^{-/-}$ MEFs treated with the STING agonist DMXAA, cell death occurs with minimal changes in ZBP1 or MLKL protein levels compared to DMXAA-treated wild-type MEFs. Analyses in caspase-8/MLKL and FADD/MLKL double-knockout MEFs reveal that STING promotes RIPK1 and RIPK3 phosphorylation within ZBP1 immunoprecipitates, suggesting it facilitates kinase activation within the ZBP1-RIPK1-RIPK3 necroptosis-inducing complex.

It is also plausible that, because STING additionally regulates TNFR1-induced necroptosis, inefficient RIPK1 processing within Complex II due to caspase-8 loss provides additional RIPK1 substrates for the TNFR1/FADD-independent ZBP1-RIPK1-RIPK3 complex, as seen in the ZBP1 immunoprecipitates from DMXAA-treated MEFs. However, upon loss of caspase-8, the TNFR1-induced RIPK1-RIPK3-MLKL necrosome is sufficient to drive necroptotic death. Indeed, to activate the ZBP1-killing platform, the TNFR1 checkpoint must be bypassed, as sole deletion of ZBP1 in $Casp8^{E\text{-}KO}$ or $Fadd^{E\text{-}KO}$ mice does not provide any survival advantage, in contrast to the complete rescue of simultaneous ZBP1 and TNFR1 co-deletion. Interestingly, the stronger survival advantage STING co-deletion alone provides in $Casp8^{E\text{-}KO}$ mice, consistent with its role in regulating both TNFR1-dependent and ZBP1-dependent checkpoints, suggests that the difference between TNFR1- and ZBP1-mediated necroptosis is largely temporal rather than purely qualitative. This is reinforced by the fact that even partial inhibition of TNF-induced necroptosis, as revealed by STING co-deletion, may allow sufficient time for ZBP1 to engage its killing platform, explaining why delayed or diminished TNF signalling can shift cell death toward ZBP1-mediated necroptosis. Therefore, STING's regulation occurs both by directly mediating ZBP1 necroptosis and via partial modulation of TNFR1-induced necroptosis. The temporal aspect of STING's modulation allows sufficient time for ZBP1-dependent necroptosis to engage, emphasizing the role of STING in coordinating the timing and magnitude of necroptotic signalling.

Nevertheless, STING is not the only source of TNF as combined deletion of *Sting1* and *Tnfr1* is required to prevent lethal dermatitis. Notably, in both $Casp8^{E\text{-}KO}$ $Tnfr1^{KO}$ $Zbp1^{KO}$ and $Casp8^{E\text{-}KO}$ $Tnfr1^{KO}$ $Sting1^{KO}$ mice, despite the presence of intact RIPK1 and RIPK3, necrotposis is prevented, highlighting (i) the central role of ZBP1 in mediating the activation of RIPK3 within the ZBP1-RIPK1-RIPK3 complex when the TNFR1 checkpoint is compromised and (ii) the upstream regulatory contributions of the STING-ZBP1 axis and STING-TNFR1 crosstalk in modulating necroptotic output.

Prior studies indicate that the RIPK1 RHIM domain normally restricts ZBP1 interaction with RIPK3 to prevent MLKL-driven necroptosis, as seen in the perinatal lethality of $Ripk1^{-/-}$ or $Ripk1^{RHIM/RHIM}$ mice[163,164]. Yet this couldn't sufficiently explain why RIPK1 fails to prevent ZBP1-RIPK3-driven lethal dermatitis in $Casp8^{E\text{-}KO}$ $Tnfr1^{-/-}$ or $Fadd^{E\text{-}KO}$ $Tnfr1^{-/-}$[135,136] mice, particularly given our observation that RIPK1 is phosphorylated at S166 and complexes with both ZBP1 and RIPK3 upon loss of caspase-8 or FADD to drive necroptosis. Interestingly, recent work we co-authored demonstrated that when RIPK1 lacks its death domain (DD; R588E disruptive mutation) and can no longer be recruited to Complex II, it instead associates with ZBP1 and RIPK3 in an active, S166-phosphorylated state, driving RIPK3-MLKL-dependent necroptosis[207]. By contrast, in wild-type MEFs, stimulation with IFNγ results in the recruitment of both ZBP1 and RIPK3 to Complex II via RIPK1 in a kinase-dependent manner, leading only to marginal cell death when caspases are inhibited. These observations suggest that: (i) the DD-dependent recruitment of RIPK1 in Complex II may restrict ZBP1-RIPK3 interactions via caspase-8-mediate RIPK1 cleavage and complex destabilisation therefore preventing cell death[207], (ii) the inhibitory function of RIPK1 RHIM domain depends on RIPK1 recruitment in Complex II, and therefore TNFR1 or FADD loss renders the RIPK1 RHIM checkpoint redundant, and (iii) in the absence of TNFR1-dependent Complex II assembly and RIPK1 processing, RIPK1 might instead promote ZBP1-RIPK3-mediated necroptosis via RHIM-RHIM interactions[207]. However, this proposed model highlights a mechanistic paradox. In both cases, RIPK1 DD-dependent caspase-8-mediated RIPK1 cleavage in Complex II[91,92,207] and RHIM disruption of RIPK1 is preventing RIPK1 from binding RIPK3 and ZBP1[163,164], yet the outcomes are opposite. Caspase-8 cleavage of RIPK1 restricts ZBP1-RIPK3 interaction and prevents necroptosis[207], whereas RHIM mutation liberates RIPK3 and ZBP1 to interact and drive robust necroptosis[163,164]. Therefore, further studies are required to delineate how RIPK1 regulates this alternative, TNFR1/FADD-independent but ZBP1-dependent necroptotic pathway, potentially employing a double DD and RHIM RIPK1 mutant. Another alternative explanation would be that RIPK1-dependent recruitment of RIPK3 and caspase-8-mediated cleavage of RIPK3 contributes to these outcomes. However, RIPK3 cleavage at D333 has been shown to be redundant for canonical TNF-induced necroptosis[93,94] or viral infection with M45mutRHIM MCMV[93], which sensitizes cells to ZBP1-RIPK3-driven necroptosis. Nonetheless, this mechanism should be further investigated in the context of sterile inflammation too.

The dual checkpoint of necroptosis activation downstream of caspase-8-deficiency extends beyond keratinocytes to immune and stromal compartments, as evidenced by systemic inflammation in *Casp8$^{E\text{-}KO}$* mice and the extended rescue observed in *Casp8$^{E\text{-}KO}$ Tnfr1$^{-/-}$ Sting1$^{-/-}$* mice in which STING was deleted systemically. These mice were entirely protected from all pathological features and remained viable, healthy, and phenotypically indistinguishable from both control littermates and *Casp8$^{E\text{-}KO}$ Tnfr1$^{-/-}$ Zbp1$^{-/-}$* by the 14th week of age. This rescue stands in sharp contrast to the partial and transient protection seen in *Casp8$^{E\text{-}KO}$ Tnfr1$^{-/-}$ Sting1$^{E\text{-}KO}$* mice, where STING deletion is restricted to keratinocytes, which developed delayed yet ultimately fatal dermatitis driven by systemic inflammation and immune cell infiltration. This pronounced phenotypic divergence underscores a key concept: while STING activation in keratinocytes is required to initiate ZBP1-mediated necroptosis and early inflammatory responses, STING expression in non-keratinocyte compartments, particularly in immune and stromal cells, is also critical for sustaining and amplifying systemic necro-inflammation. These findings reveal that STING not only facilitates cell-intrinsic ZBP1 transcription in keratinocytes but also orchestrates the broader necroptotic environment that fuels immune-mediated inflammation. Thus, STING functions both as an initiator and an amplifier of necroptosis, playing a central, non-redundant role in driving TNFR1-independent, ZBP1-mediated pathology.

While overactive STING in humans has been linked to mutations that stabilizes STING in an active state or promote its cGAMP-independent oligomerisation, in our system, STING overactivation following caspase-8 loss is mediated by cGAS. Interestingly, the cytosolic DNA that triggers type I interferon responses and necroptosis downstream of cGAS-STING originates from the nucleus. This finding aligns with previous studies that revealed necroptosis-independent functions of caspase-8 in preventing chromosomal instability[224] and DNA damage [219], both of which can result in the leakage of nuclear DNA into the cytosol. In contrast, other studies have suggested that executioner caspases restrain interferon signalling by directly cleaving cGAS, IRF3, and MAVS[507]. However, based on our data, caspase-8 appears to regulate cGAS-STING activation not by directly cleaving these effectors, but rather by preventing loss of genome integrity that lead to nuclear DNA leakage and subsequent cGAS activation. Notably, in our MEFs, whether caspase-8-proficient, caspase-8-deficient, or treated with the pan-caspase inhibitor zVAD to inhibit caspase enzymatic activity, we did not observe any STING or IRF3 protein cleavage patterns that would suggest direct caspase-mediated processing. These findings support the view that caspase-8 functions primarily to restrain RIPK1-driven canonical necroptosis and, by activating downstream executioner caspases, participates in apoptotic body formation, rather than directly regulating IFN responses through cleavage of cytosolic DNA/RNA sensors or downstream effectors. In this context, previously reported cleavage of such proteins may reflect nonspecific proteolysis during apoptosis rather than a targeted regulatory mechanism.

In addition to the cGAS-STING axis, the MDA5/RIG-I-MAVS pathway represents another potent mechanism for cytosolic nucleic acid sensing, particularly in mediating type I IFN responses upon recognition of viral or cytosolic RNA[528]. Although this pathway has previously been implicated in the context of caspase-8 deficiency[134,529,530], our data show that full-body deletion of MAVS did not provide any survival advantage to $Casp8^{E\text{-}KO}$ mice. This suggests that the MAVS axis is not relevant for driving the type I IFN response or initiating necroptosis in caspase-8-deficient settings. The previously reported susceptibility of caspase-8-deficient MEFs to cell death following RNA virus infection[529] may be an artifact arising from the compromised viability of primary $Casp8^{-/-}$ cells in culture systems. Similarly, conclusions from studies using synthetic DNA molecules such as poly(dA:dT) in $Casp8^{-/-}$ cells[134] must be interpreted with caution, as poly(dA:dT) can additionally to cGAS, activate the AIM2 inflammasome[531] and the RIG-I/MAVS axis[532], particularly when reverse-transcribed or insufficiently processed in the cytosol.

Moreover, mitochondrial membrane permeabilisation can lead to the release of both mitochondrial DNA (mtDNA) and mitochondrial RNA (mtRNA), with the latter capable of activating the MDA5/RIG-I-MAVS pathway[533]. However, the fact that MAVS deletion conferred no survival advantage to $Casp8^{E\text{-}KO}$ mice indirectly rules out mitochondrial permeabilisation, and thus a mitochondrial origin, for the cytosolic DNA that activates cGAS in this context. This conclusion is further reinforced by experiments in which caspase-8-deficient MEFs were treated with ddC (2′,3′-dideoxycytidine; inhibitor of mitochondrial DNA polymerase γ, POLG) or IMT1B (inhibitor of mitochondrial RNA polymerase, POLRMT). Despite effective depletion of mtDNA (and mtRNA in the case of IMT1B), cytosolic DNA foci and ISG expression persisted independently of cell death. These findings strongly support the notion that the DNA activating STING upon caspase-8 loss is of nuclear, rather than mitochondrial, origin. Consequently, this also argues against a role for STING in solely mediating intrinsic apoptosis, as previously suggested[497,534,535] and instead positions STING as a central driver of necroptosis in this context.

While chromosomal instability and/or DNA damage-induced cytosolic DNA explains the activation of the cGAS-STING pathway upon loss of caspase-8, the mechanism of ZBP1 activation appears more complex. Loss of caspase-8 leads to the upregulation of both Z-DNA and Z-RNA species, with Z-RNA being the predominant form, and both having the potential to activate ZBP1. Early structural and biophysical studies demonstrated that ZBP1 Zα domains are capable of binding Z-DNA *in vitro*, either under conditions of torsional stress or by using synthetic DNA sequences prone to adopting the Z-conformation[170-174]. However, subsequent research has revealed that Z-RNA is the physiologically relevant ligand that activates ZBP1 *in vivo*. This has been shown in multiple contexts, including influenza A virus (IAV) infection[181,204], splicing perturbation[536], and studies of ZBP1-driven liquid-liquid phase separation[537]. The functional specificity for Z-RNA is further supported by sterile inflammation models, where ZBP1 deletion rescues the inflammatory phenotype in ADAR1-deficient mice, a setting in which endogenous Z-RNA accumulates and drives immune activation[215,538]. In contrast, ZBP1 deletion fails to rescue disease in TREX1-deficient mice, where inflammation is driven by endogenous retroelement-induced cytosolic DNA, potentially prone to Z-DNA formation, but solely dependent on cGAS-STING-mediated sensing[215,238,379]. Similarly, mice carrying RHIM-domain mutant RIPK1, or mice with keratinocyte-specific deletion of RIPK1 develop spontaneous ZBP1-dependent necroptosis, in which ZBP1 activation relies on endogenous retroelement-derived Z-RNA[204]. These findings raise the possibility that, in the caspase-8-deficient context, Z-RNA species may represent the more physiologically relevant triggers for ZBP1-mediated necroptosis, particularly given their relative abundance. Nonetheless, Z-NAs in this setting appear to arise from diverse sources. On one hand, STING agonism induces Z-NA formation in wild-type MEFs, suggesting that interferon responses can de-repress endogenous retroelements, as previously reported[539]. However, the Z-NA signal observed in wild-type MEFs treated with DMXAA is consistently weaker than in caspase-8-deficient cells, indicating the presence of additional signals unique to caspase-8 loss. These may include Z-DNA generated as a consequence of caspase-8 -deficiency-driven chromosomal instability and DNA damage, complementing Z-RNA sensing from retroelements and together enhancing ZBP1 activation and necroptosis induction, potentially by further promoting the formation of ZBP1 liquid-liquid phase separation condensates[537].

While caspase-8 deficiency requires cGAS-dependent sensing of cytosolic DNA to activate the STING pathway, gain-of-function mutations in human STING lead to spontaneous, cGAS-cGAMP-independent activation of STING-dependent inflammatory signalling, which underlies the pathology and clinical manifestations of STING-associated vasculopathy with onset in infancy (SAVI)[442-444]. In SAVI patients, a constitutive and chronic STING-mediated inflammatory response, particularly within immune cells and endothelial populations, has been implicated as the primary driver of disease pathology. This inflammation manifests in a wide range of clinical symptoms, including lung inflammation, scarring, and fibrosis, increased vascular permeability, occlusion, and rupture leading to tissue ischemia, as well as necrotic skin ulcers and general immune dysregulation.

Although the inflammatory nature of SAVI is well recognized, the precise modes of cell death responsible for tissue damage remain poorly defined. Evidence from murine models has highlighted a central role for T cells in driving lung pathology. For instance, *Rag1*$^{-/-}$ *Sting1*^{N153S} mice, which lack both T and mature B cells, show no histological signs of lung disease, and Tcrβ$^{-/-}$ *Sting1*^{N153S} mice, lacking mature T cells, develop only mild pulmonary involvement[492,493]. This T-cell dependency is further supported by the observation of T and NK cell cytopenia, alongside expansion of inflammatory macrophages and monocytes in these models[442,498]. Interestingly, bone marrow transplantation from *Sting1*^{V154M} mice into irradiated wild-type hosts was sufficient to transfer the myeloid abnormalities, confirming that hematopoietic immune cells are capable of driving the disease phenotype[492].

Mechanistically, T cell cytopenia has been linked to defective development and activation, which appears to be IFN-γ-dependent, yet independent of type I and III interferons[494,495]. Additional studies have implicated STING-induced ER stress as a driver of T cell exhaustion and death[496]. Consistent with these findings, spontaneous cell death of T cells, monocytes, and endothelial cells has been documented in SAVI patients[323,442]. Additionally, *in vitro*, STING agonists induce apoptosis in isolated T cells, as evidenced by Annexin V staining and flow cytometry, though this effect is not observed in other primary cell types such as MEFs, BMDCs, or BMDMs, raising concerns that the T cell phenotype may reflect context-specific sensitivity rather than a general mechanism[497].

To gain further mechanistic insight, we performed transcriptomic analysis in whole blood from SAVI patients, revealing robust activation of apoptotic, pyroptotic, and necroptotic gene programs. Interestingly, while upstream initiators of apoptosis and pyroptosis were elevated, effector molecules, were frequently downregulated, suggesting a negative feedback loop or suppression of execution phases. We specifically excluded transcriptional priming towards execution of mitochondrial apoptosis, as *CASP3/7* were either downregulated or *BCL2*, *BCLXL*, and *MCL1* were upregulated in conjunction with *XIAP*. Pyroptosis appeared to be predominantly primed to be executed in Patient 2, whereas the other two patients exhibited either downregulation of GSDMD (Patient 1) or NINJ1 (Patient 3). Importantly, when the transcriptional levels of *CASP8* were increased, *cFLIP* was also upregulated or maintained at similar levels suggesting the counter-balancing activity of the caspase-8-FLIP heterodimer in activating extrinsic apoptosis. In contrast, the inhibition of caspase activity by the caspase-8-cFLIP heterodimer correlated with the consistent overexpression of RIPK3, MLKL and ZBP1 in all patients. This persistent engagement of necroptosis, together with sustained caspase-8-cFLIP expression, further points to a state in which necroptosis predominates, fuelling inflammatory responses and potentially secondarily activating intrinsic apoptosis and pyroptosis. In addition to this intrinsic regulation, which is consistent with the role of STING in partly inducing also TNFR1-mediated necroptosis, STING overactivation could further bypass caspase-8-mediated inhibition through the persistent engagement of the novel, alternative, caspase-8-independent ZBP1-RIPK1-RIPK3 killing platform, providing an additional mechanism by which necroptosis is sustained and inflammation amplified.

While previous studies have shown that *in vitro* JAK inhibitor treatment of SAVI PBMCs reduces ISG expression[540], our analysis of patient samples after clinical JAK inhibition (ruxolitinib) revealed no significant downregulation of interferon-stimulated genes, suggesting that STING can maintain inflammatory signalling independently of JAK/STAT-mediated IFN response amplification routes. This aligns with murine studies showing that STING directly drives transcriptional responses even in the absence of IFNAR or IFNGR signalling[493,541]. Accordingly, neither inflammatory cytokine profiling, encompassing persistently elevated levels of IL-21, CXCL1, IL-1β, IFN-α, and CD40L, nor transcriptional upregulation of necroptosis mediators, such as RIPK3, ZBP1 and MLKL were affected by ruxolitinib treatment, further indicating that these inflammatory and cell-death programs persist despite JAK inhibition.

Importantly, crossing *Sting1^{N153S}* mice with *Ripk3$^{-/-}$* mice resulted in a significant rescue of T cell depletion in the lung, spleen, and thymus, as well as a marked reduction in inflammatory monocyte populations. These findings, in conjunction with our human data, provide strong evidence that necroptosis is a major effector mechanism in STING-mediated immunopathology. Both human transcriptional analyses and mouse histology reveal significant upregulation of ZBP1, consistent with a role for STING in driving ZBP1-RIPK3-MLKL-mediated necroptosis, as genetically confirmed in *Casp8$^{E\text{-}KO}$* mice. While the formal validation of ZBP1's contribution in the *Sting1^{N153S}* model would require *Sting1^{N153S} Zbp1$^{-/-}$* mice, which we are currently generating, these data are not available within the timeframe of this thesis. Nevertheless, this limitation does not affect the main conclusion, as both STING-ZBP1- and TNFR1-driven pathways as shown in the *Casp8^{E-KO}* model ultimately converge on RIPK3-MLKL-mediated necroptosis. Supporting this conclusion, tissue sections from *Sting1^{N153S}* mice showed elevated levels of phosphorylated MLKL at serine 345 (pMLKL-S345) in both lung and thymus, directly indicating *in vivo* activation of necroptosis. Collectively, these data highlight STING-driven necroptotic cell death as a central pathogenic mechanism in SAVI.

Previous studies have shown that disease in *Sting1^{N153S}* mice proceeds independently of type I interferons, IRF3, and IRF7[492,493,498]. Although IRF3 deficiency does not provide a survival advantage, it leads to a substantial reduction in interferon-stimulated gene (ISG) expression[492,493,498], indicating that IRF3 remains functionally important for regulating interferon responses, even if it is not essential for disease progression. On the other hand, deletion of TNFR1 and TNFR2 has been shown to partially ameliorate T cell loss in the spleen and thymus, and almost completely prevents lung pathology by 10 weeks of age[499].

The clinical significance of these findings becomes evident only when compared with observations in SAVI patients. While IRF3 loss in mice does not improve survival, JAK/STAT inhibition with ruxolitinib provides transient symptomatic relief in humans. Conversely, although TNFR1/2 deletion improves pathology in mice by the 10th week of age, the TNF blocker etanercept shows no therapeutic benefit in patients[491]. At first glance, these discrepancies might be interpreted as species-specific differences in disease mechanisms, complicating translation of preclinical findings. Alternatively, the apparent discrepancy may reflect the time window of analysis, as longer-term survival analyses in the *Tnfr1*/*Tnfr2* double knockout model would likely reveal only a delayed onset of pathology, ultimately converging on similar mortality outcomes. However, our data suggest an alternative interpretation. Rather than reflecting fundamental species divergence, these results indicate a shared mechanistic basis in both humans and mice: STING drives necroptosis through parallel IFN- and TNF/TNFR1-dependent pathways. Consequently, targeting a single axis, whether IFN or TNF signalling, may yield only partial and transient benefits. By contrast, simultaneous inhibition of both pathways, or targeting a convergent downstream effector such as RIPK3, could achieve more complete and durable disease control in SAVI.

Currently, the standard of care for SAVI patients includes the JAK1/2 inhibitor ruxolitinib, often combined with immunosuppressants (methotrexate, mycophenolate mofetil), immunomodulators (hydroxychloroquine), or corticosteroids (prednisone, methylprednisolone). Since etanercept has already been tested clinically, we initially propose a combination therapy with ruxolitinib and etanercept to simultaneously target both arms downstream of STING signalling. However, type I IFN responses downstream of STING can also arise independently of JAK/STAT signalling via IRF3, indicating that direct STING inhibition could, in principle, offer a more precise therapeutic strategy. Unfortunately, current STING inhibitors exhibit weak potency, poor pharmacokinetics, and have yet to reach clinical trials, while genetic heterogeneity of human STING and variable SAVI mutations further complicate their development[542].

Our study provides a mechanistically grounded strategy to overcome the limitations of current therapeutic approaches. We identify RIPK3-driven necroptosis as a convergent downstream effector of both STING- ZBP1- and TNFR1-mediated necroptotic pathways in SAVI pathogenesis. Targeting this shared node offers a single intervention point capable of simultaneously abrogating the pathogenic consequences of STING hyperactivation, circumventing the incomplete efficacy of JAK/STAT or TNF blockade and the pharmacological and genetic limitations of direct STING inhibition. Notably, small-molecule inhibitors of RIPK1, RIPK3, and MLKL are currently under clinical development for other autoinflammatory disorders (phase I/II), highlighting their potential applicability as novel therapeutic strategies in SAVI (Table 3). Thus, our findings not only elucidate the convergent necroptotic mechanisms downstream of STING but also establish RIPK3-MLKL necroptosis as a rational, therapeutically relevant target for durable disease control.

In addition to small-molecule inhibitors, PROTAC (Proteolysis Targeting Chimera) degraders have recently been developed for RIPK1, MLKL and ZBP1. These bifunctional molecules induce proteasomal degradation of their targets, potentially providing more complete and sustained pathway inhibition than conventional inhibitors. While RIPK1-targeting PROTACs may carry risks due to its scaffolding role in preventing inadvertent necroptosis[543-545], MLKL- or ZBP1-targeting PROTACs would avoid the risk of such side effects[546-549].

Although PROTACs are still in early development and therefore not yet ready for clinical use, combinatorial strategies involving ruxolitinib and etanercept, or particularly RIPK3 inhibitors, could be immediately explored to achieve more effective and durable disease control in SAVI.

Inhibitor	Target	Current Status	Selectivity	Disease Models Tested
Necrostatin-1 (Nec-1)	RIPK1	Preclinical	Mouse-specific	Stroke[550], neurodegeneration[551], SARS-CoV-2 and inflammatory diseases [552]
GSK′963	RIPK1	Preclinical	Human & Mouse	TNF-induced SIRS[553]
GSK2982772	RIPK1	Clinical (Phase II) Discontinued	Human	RA[554], UC[555] (failed), plaque psoriasis[556] (minimal efficacy)
DNL788 (SAR443820)	RIPK1	Clinical (Phase II) Discontinued	Human	ALS, MS[557] (failed)
DNL758/ Eclitasertib (SAR443122)	RIPK1	Clinical (Phase II)	Human	CLE (phase II, completed, unpublished), UC (phase II, recruiting), COVID-19 (phase Ib, trend)[558].
GDC-8264	RIPK1	Clinical (Phase II)	Human	aGVHD (Phase Ib, completed, unpublished), AKI, MAKE (phase II, recruiting)[559]
R552 (LY3871801)	RIPK1	Clinical (Phase IIa/IIb)	Human	RA (recruiting)
SIR2446	RIPK1	Clinical (Phase I)	Human	Phase I completed[560]
SIR1-365	RIPK1	Clinical (Phase Ib)	Human	Severe COVID-19[561]
GNE684	RIPK1	Preclinical	Human & Mouse	Cpdm[562]
GSK’074	RIPK1/ RIPK3	Preclinical	Human & Mouse	AAA[563]
GSK‘872	RIPK3	Preclinical	Human & Mouse	TBI[564], PD[565], CSE[566]
GSK‘840	RIPK3	Preclinical	Human & Mouse	RNI[567]
UH15-38	RIPK3	Preclinical	Mouse-specific	IAV[518]
Zharp-99	RIPK3	Preclinical	Human & Mouse	TNF-induced SIRS[568]
NBCs	RIPK3	Preclinical	Mouse-specific	TNF-induced SIRS, TBI[569]
LK01003	RIPK3	Preclinical	Human & Mouse	*in vitro*[570]
Necrosulfonamide (NSA)	MLKL	Preclinical	Human & Mouse	Parkinson’s disease[571], SCI[572], DSS-induced colitis[573], ICH[574], TBI[569], I/R injury[575,576]
MBA-m1	MLKL	Preclinical	Mouse	AAA, Cpdm[577]
MBA-h1	MLKL	Preclinical	Human	*in vitro*[577]
Saracatinib	MLKL	Preclinical	Human & Mouse	Imiquimod (IMQ)-induced psoriasis[578]

Table 3: Small-Molecule Inhibitors of RIPK1, RIPK3, and MLKL. *This table summarizes reported small-molecule inhibitors of RIPK1, RIPK3, and MLKL, including preclinical tool compounds and clinical candidates. For each inhibitor, the target protein, development*

status, species selectivity, and tested disease models or assays are indicated. The table highlights compounds used to block necroptosis, and subsequent inflammation, providing a comprehensive reference for mechanistic and translational studies. SIRS: Systemic Inflammatory Response Syndrome, RA: rheumatoid arthritis, UC: ulcerative colitis, ALS: Amyotrophic lateral sclerosis, MS: multiple sclerosis, CLE: cutaneous lupus erythematosus, aGVHD: acute graft-versus-host disease, AKI: Acute Kidney Injury, MAKE: Major Adverse Kidney Events, Cpdm: chronic proliferative dermatitis, AAA: abdominal aortic aneurysm, TBI: traumatic brain injury, PD: Parkinson's disease, CSE: cigarette smoking-induced emphysema, RNI: retinal neuronal injury, IAV: influenza A virus, SCI: spinal cord injury, ICH: intracerebral hemorrhage, I/R: ischemia/reperfusion.

Together, these findings establish STING as a central regulator of necroptosis, integrating signals from cytosolic DNA sensing, type I IFN responses, and inflammatory cytokines to coordinate both the initiation and amplification of necroptotic cell death. In the context of gain-of-function STING mutations, cGAS-dependent DNA sensing can be bypassed, resulting in constitutive necroptotic signalling and chronic inflammation. Importantly, we demonstrate that necroptosis not only functions as an executioner mechanism but also actively drives systemic inflammation through secondary cell death and cytokine release, thereby amplifying tissue damage in chronic inflammatory settings. By combining a novel tool for *in situ* detection of necroptosis with detailed mechanistic analyses of the STING-ZBP1-RIPK3-MLKL signalling axis, our study provides a comprehensive framework to dissect necroptosis *in vivo*, define its functional consequences, and explore targeted therapeutic modulation. Collectively, these advances illuminate the pathogenic role of RIPK3–MLKL–mediated necroptosis in STING-driven diseases and highlight the necroptotic machinery as a promising therapeutic target in such autoimmune and autoinflammatory disorders, which are characterized by excessive, necroptotic cell death.

IV. References

1 Blanpain, C. & Fuchs, E. Stem cell plasticity. Plasticity of epithelial stem cells in tissue regeneration. *Science* **344**, 1242281, doi:10.1126/science.1242281 (2014).

2 Kotas, M. E. & Medzhitov, R. Homeostasis, inflammation, and disease susceptibility. *Cell* **160**, 816-827, doi:10.1016/j.cell.2015.02.010 (2015).

3 Hanahan, D. & Weinberg, R. A. Hallmarks of cancer: the next generation. *Cell* **144**, 646-674, doi:10.1016/j.cell.2011.02.013 (2011).

4 Medzhitov, R. Origin and physiological roles of inflammation. *Nature* **454**, 428-435, doi:10.1038/nature07201 (2008).

5 Takeuchi, O. & Akira, S. Pattern recognition receptors and inflammation. *Cell* **140**, 805-820, doi:10.1016/j.cell.2010.01.022 (2010).

6 Kumar, H., Kawai, T. & Akira, S. Pathogen recognition by the innate immune system. *Int Rev Immunol* **30**, 16-34, doi:10.3109/08830185.2010.529976 (2011).

7 Turner, M. D., Nedjai, B., Hurst, T. & Pennington, D. J. Cytokines and chemokines: At the crossroads of cell signalling and inflammatory disease. *Biochim Biophys Acta* **1843**, 2563-2582, doi:10.1016/j.bbamcr.2014.05.014 (2014).

8 Chen, G. Y. & Nunez, G. Sterile inflammation: sensing and reacting to damage. *Nat Rev Immunol* **10**, 826-837, doi:10.1038/nri2873 (2010).

9 Gilroy, D. & De Maeyer, R. New insights into the resolution of inflammation. *Semin Immunol* **27**, 161-168, doi:10.1016/j.smim.2015.05.003 (2015).

10 Roh, J. S. & Sohn, D. H. Damage-Associated Molecular Patterns in Inflammatory Diseases. *Immune Netw* **18**, e27, doi:10.4110/in.2018.18.e27 (2018).

11 Clarke, P. G. Developmental cell death: morphological diversity and multiple mechanisms. *Anat Embryol (Berl)* **181**, 195-213, doi:10.1007/BF00174615 (1990).

12 Galluzzi, L. *et al.* Molecular mechanisms of cell death: recommendations of the Nomenclature Committee on Cell Death 2018. *Cell Death Differ* **25**, 486-541, doi:10.1038/s41418-017-0012-4 (2018).

13 Peltzer, N. & Walczak, H. Cell Death and Inflammation - A Vital but Dangerous Liaison. *Trends Immunol* **40**, 387-402, doi:10.1016/j.it.2019.03.006 (2019).

14 Newton, K., Strasser, A., Kayagaki, N. & Dixit, V. M. Cell death. *Cell* **187**, 235-256, doi:10.1016/j.cell.2023.11.044 (2024).

15 Wallach, D., Kang, T. B. & Kovalenko, A. Concepts of tissue injury and cell death in inflammation: a historical perspective. *Nat Rev Immunol* **14**, 51-59, doi:10.1038/nri3561 (2014).

16 Rock, K. L. & Kono, H. The inflammatory response to cell death. *Annu Rev Pathol* **3**, 99-126, doi:10.1146/annurev.pathmechdis.3.121806.151456 (2008).

17 Rock, K. L., Latz, E., Ontiveros, F. & Kono, H. The sterile inflammatory response. *Annu Rev Immunol* **28**, 321-342, doi:10.1146/annurev-immunol-030409-101311 (2010).

18 Anderton, H., Wicks, I. P. & Silke, J. Cell death in chronic inflammation: breaking the cycle to treat rheumatic disease. *Nat Rev Rheumatol* **16**, 496-513, doi:10.1038/s41584-020-0455-8 (2020).

19 Lee, E., Song, C. H., Bae, S. J., Ha, K. T. & Karki, R. Regulated cell death pathways and their roles in homeostasis, infection, inflammation, and tumorigenesis. *Exp Mol Med* **55**, 1632-1643, doi:10.1038/s12276-023-01069-y (2023).

20 Kono, H. & Rock, K. L. How dying cells alert the immune system to danger. *Nature Reviews Immunology* **8**, 279-289, doi:10.1038/nri2215 (2008).

21 Nagata, S., Hanayama, R. & Kawane, K. Autoimmunity and the clearance of dead cells. *Cell* **140**, 619-630, doi:10.1016/j.cell.2010.02.014 (2010).

22 Ashkenazi, A. & Dixit, V. M. Death receptors: Signaling and modulation. *Science* **281**, 1305-1308, doi:DOI 10.1126/science.281.5381.1305 (1998).

23 Newton, K. & Dixit, V. M. Signaling in Innate Immunity and Inflammation. *Csh Perspect Biol* **4**, doi:ARTN a00604910.1101/cshperspect.a006049 (2012).

24 Brenner, D., Blaser, H. & Mak, T. W. Regulation of tumour necrosis factor signalling: live or let die. *Nat Rev Immunol* **15**, 362-374, doi:10.1038/nri3834 (2015).
25 Wajant, H., Pfizenmaier, K. & Scheurich, P. Tumor necrosis factor signaling. *Cell Death and Differentiation* **10**, 45-65, doi:10.1038/sj.cdd.4401189 (2003).
26 Fritsch, J., Zingler, P., Sarchen, V., Heck, A. L. & Schutze, S. Role of ubiquitination and proteolysis in the regulation of pro- and anti-apoptotic TNF-R1 signaling. *Biochim Biophys Acta Mol Cell Res* **1864**, 2138-2146, doi:10.1016/j.bbamcr.2017.07.017 (2017).
27 Haas, T. L. *et al.* Recruitment of the Linear Ubiquitin Chain Assembly Complex Stabilizes the TNF-R1 Signaling Complex and Is Required for TNF-Mediated Gene Induction. *Mol Cell* **36**, 831-844, doi:10.1016/j.molcel.2009.10.013 (2009).
28 Gough, P. & Myles, I. A. Tumor Necrosis Factor Receptors: Pleiotropic Signaling Complexes and Their Differential Effects. *Front Immunol* **11**, doi:ARTN 58588010.3389/fimmu.2020.585880 (2020).

29 Shu, H. B., Takeuchi, M. & Goeddel, D. V. The tumor necrosis factor receptor 2 signal transducers TRAF2 and c-IAP1 are components of the tumor necrosis factor receptor 1 signaling complex. *P Natl Acad Sci USA* **93**, 13973-13978, doi:DOI 10.1073/pnas.93.24.13973 (1996).
30 Vince, J. E. *et al.* TRAF2 Must Bind to Cellular Inhibitors of Apoptosis for Tumor Necrosis Factor (TNF) to Efficiently Activate NF-κB and to Prevent TNF-induced Apoptosis. *J Biol Chem* **284**, 35906-35915, doi:10.1074/jbc.M109.072256 (2009).
31 Dondelinger, Y., Darding, M., Bertrand, M. J. M. & Walczak, H. Poly-ubiquitination in TNFR1-mediated necroptosis. *Cell Mol Life Sci* **73**, 2165-2176, doi:10.1007/s00018-016-2191-4 (2016).
32 Bertrand, M. J. M. *et al.* cIAP1 and cIAP2 facilitate cancer cell survival by functioning as E3 ligases that promote RIP1 ubiquitination. *Mol Cell* **30**, 689-700, doi:10.1016/j.molcel.2008.05.014 (2008).
33 Peltzer, N., Darding, M. & Walczak, H. Holding RIPK1 on the Ubiquitin Leash in TNFR1 Signaling. *Trends Cell Biol* **26**, 445-461, doi:10.1016/j.tcb.2016.01.006 (2016).
34 Kanayama, A. *et al.* TAB2 and TAB3 activate the NF-κB pathway through binding to polyubiquitin chains. *Mol Cell* **15**, 535-548, doi:DOI 10.1016/j.molcel.2004.08.008 (2004).
35 Emmerich, C. H. *et al.* Activation of the canonical IKK complex by K63/M1-linked hybrid ubiquitin chains. *P Natl Acad Sci USA* **110**, 15247-15252, doi:10.1073/pnas.1314715110 (2013).
36 Wan, F. Y. & Lenardo, M. J. The nuclear signaling of NF-κB: current knowledge, new insights, and future perspectives. *Cell Res* **20**, 24-33, doi:10.1038/cr.2009.137 (2010).
37 Lafont, E. *et al.* TBK1 and IKKepsilon prevent TNF-induced cell death by RIPK1 phosphorylation. *Nat Cell Biol* **20**, 1389-1399, doi:10.1038/s41556-018-0229-6 (2018).
38 Ujevic, A. *et al.* TBK1-associated adapters TANK and AZI2 protect mice against TNF-induced cell death and severe autoinflammatory diseases. *Nat Commun* **15**, doi:ARTN 1001310.1038/s41467-024-54399-4 (2024).

39 Kupka, S. *et al.* SPATA2-Mediated Binding of CYLD to HOIP Enables CYLD Recruitment to Signaling Complexes. *Cell Rep* **16**, 2271-2280, doi:10.1016/j.celrep.2016.07.086 (2016).
40 Dziedzic, S. A. *et al.* ABIN-1 regulates RIPK1 activation by linking Met1 ubiquitylation with Lys63 deubiquitylation in TNF-RSC. *Nat Cell Biol* **20**, 58-68, doi:10.1038/s41556-017-0003-1 (2018).
41 Draber, P. *et al.* LUBAC-Recruited CYLD and A20 Regulate Gene Activation and Cell Death by Exerting Opposing Effects on Linear Ubiquitin in Signaling Complexes. *Cell Rep* **13**, 2258-2272, doi:10.1016/j.celrep.2015.11.009 (2015).
42 Kovalenko, A. *et al.* The tumour suppressor CYLD negatively regulates NF-kappaB signalling by deubiquitination. *Nature* **424**, 801-805, doi:10.1038/nature01802 (2003).
43 Priem, D. *et al.* A20 protects cells from TNF-induced apoptosis through linear ubiquitin-dependent and -independent mechanisms. *Cell Death Dis* **10**, doi:ARTN 69210.1038/s41419-019-1937-y (2019).

44 Heger, K. *et al.* OTULIN limits cell death and inflammation by deubiquitinating LUBAC. *Nature* **559**, 120-+, doi:10.1038/s41586-018-0256-2 (2018).
45 Damgaard, R. B. *et al.* The Deubiquitinase OTULIN Is an Essential Negative Regulator of Inflammation and Autoimmunity. *Cell* **166**, 1215-+, doi:10.1016/j.cell.2016.07.019 (2016).
46 Delanghe, T., Dondelinger, Y. & Bertrand, M. J. M. RIPK1 Kinase-Dependent Death: A Symphony of Phosphorylation Events. *Trends Cell Biol* **30**, 189-200, doi:10.1016/j.tcb.2019.12.009 (2020).
47 Dondelinger, Y. *et al.* NF-kappaB-Independent Role of IKKalpha/IKKbeta in Preventing RIPK1 Kinase-Dependent Apoptotic and Necroptotic Cell Death during TNF Signaling. *Mol Cell* **60**, 63-76, doi:10.1016/j.molcel.2015.07.032 (2015).
48 Lafont, E. *et al.* TBK1 and IKKε prevent TNF-induced cell death by RIPK1 phosphorylation. *Nature Cell Biology* **20**, 1389-+, doi:10.1038/s41556-018-0229-6 (2018).
49 Dondelinger, Y. *et al.* Serine 25 phosphorylation inhibits RIPK1 kinase-dependent cell death in models of infection and inflammation. *Nat Commun* **10**, doi:ARTN 172910.1038/s41467-019-09690-0 (2019).

50 Dondelinger, Y. *et al.* NF-κB-Independent Role of IKKα/IKKβ in Preventing RIPK1 Kinase-Dependent Apoptotic and Necroptotic Cell Death during TNF Signaling. *Mol Cell* **60**, 63-76, doi:10.1016/j.molcel.2015.07.032 (2015).
51 Eren, R. O., Kaya, G. G., Schwarzer, R. & Pasparakis, M. IKKε and TBK1 prevent RIPK1 dependent and independent inflammation. *Nat Commun* **15**, doi:10.1038/s41467-023-44372-y (2024).
52 Li, H. X., Kobayashi, M., Blonska, M., You, Y. & Lin, X. Ubiquitination of RIP is required for tumor necrosis factor α-induced NF-κB activation. *J Biol Chem* **281**, 13636-13643, doi:10.1074/jbc.M600620200 (2006).
53 Ea, C. K., Deng, L., Xia, Z. P., Pineda, G. & Chen, Z. J. Activation of IKK by TNFalpha requires site-specific ubiquitination of RIP1 and polyubiquitin binding by NEMO. *Mol Cell* **22**, 245-257, doi:10.1016/j.molcel.2006.03.026 (2006).
54 Zhang, X. *et al.* Ubiquitination of RIPK1 suppresses programmed cell death by regulating RIPK1 kinase activation during embryogenesis. *Nat Commun* **10**, 4158, doi:10.1038/s41467-019-11839-w (2019).
55 Tang, Y. *et al.* K63-linked ubiquitination regulates RIPK1 kinase activity to prevent cell death during embryogenesis and inflammation. *Nat Commun* **10**, 4157, doi:10.1038/s41467-019-12033-8 (2019).
56 O'Donnell, M. A., Legarda-Addison, D., Skountzos, P., Yeh, W. C. & Ting, A. T. Ubiquitination of RIP1 regulates an NF-kappaB-independent cell-death switch in TNF signaling. *Curr Biol* **17**, 418-424, doi:10.1016/j.cub.2007.01.027 (2007).
57 Legarda-Addison, D., Hase, H., O'Donnell, M. A. & Ting, A. T. NEMO/IKKγ regulates an early NF-κB-independent cell-death checkpoint during TNF signaling. *Cell Death and Differentiation* **16**, 1279-1288, doi:10.1038/cdd.2009.41 (2009).
58 Dondelinger, Y. *et al.* RIPK3 contributes to TNFR1-mediated RIPK1 kinase-dependent apoptosis in conditions of cIAP1/2 depletion or TAK1 kinase inhibition. *Cell Death Differ* **20**, 1381-1392, doi:10.1038/cdd.2013.94 (2013).
59 Feltham, R. *et al.* Mind Bomb Regulates Cell Death during TNF Signaling by Suppressing RIPK1's Cytotoxic Potential. *Cell Rep* **23**, 470-484, doi:10.1016/j.celrep.2018.03.054 (2018).
60 Jaco, I. *et al.* MK2 Phosphorylates RIPK1 to Prevent TNF-Induced Cell Death. *Mol Cell* **66**, 698-710 e695, doi:10.1016/j.molcel.2017.05.003 (2017).
61 Menon, M. B. *et al.* p38(MAPK)/MK2-dependent phosphorylation controls cytotoxic RIPK1 signalling in inflammation and infection. *Nat Cell Biol* **19**, 1248-1259, doi:10.1038/ncb3614 (2017).
62 Dondelinger, Y. *et al.* MK2 phosphorylation of RIPK1 regulates TNF-mediated cell death. *Nature Cell Biology* **19**, 1237-1247, doi:10.1038/ncb3608 (2017).
63 Dondelinger, Y., Delanghe, T. & Bertrand, M. M. J. MK2 puts an additional brake on RIPK1 cytotoxic potential. *Cell Death and Differentiation* **25**, 457-459, doi:10.1038/s41418-017-0009-z (2018).

64 Van Herreweghe, F., Festjens, N., Declercq, W. & Vandenabeele, P. Tumor necrosis factor-mediated cell death: to break or to burst, that's the question. *Cell Mol Life Sci* **67**, 1567-1579, doi:10.1007/s00018-010-0283-0 (2010).
65 Moquin, D. M., McQuade, T. & Chan, F. K. M. CYLD Deubiquitinates RIP1 in the TNFα-Induced Necrosome to Facilitate Kinase Activation and Programmed Necrosis. *Plos One* **8**, doi:ARTN e7684110.1371/journal.pone.0076841 (2013).
66 Laurien, L. *et al.* Autophosphorylation at serine 166 regulates RIP kinase 1-mediated cell death and inflammation. *Nat Commun* **11**, doi:ARTN 174710.1038/s41467-020-15466-8 (2020).
67 Meng, H. *et al.* Death-domain dimerization-mediated activation of RIPK1 controls necroptosis and RIPK1-dependent apoptosis. *Proc Natl Acad Sci U S A* **115**, E2001-E2009, doi:10.1073/pnas.1722013115 (2018).
68 Wang, L., Du, F. H. & Wang, X. D. TNF-α induces two distinct caspase-8 activation pathways. *Cell* **133**, 693-703, doi:10.1016/j.cell.2008.03.036 (2008).
69 Micheau, O. & Tschopp, J. Induction of TNF receptor I-mediated apoptosis via two sequential signaling complexes. *Cell* **114**, 181-190, doi:Doi 10.1016/S0092-8674(03)00521-X (2003).
70 Tsuchiya, Y., Nakabayashi, O. & Nakano, H. FLIP the Switch: Regulation of Apoptosis and Necroptosis by cFLIP. *Int J Mol Sci* **16**, 30321-30341, doi:10.3390/ijms161226232 (2015).
71 Ye, K., Chen, Z. M. & Xu, Y. F. The double-edged functions of necroptosis. *Cell Death Dis* **14**, doi:ARTN 16310.1038/s41419-023-05691-6 (2023).
72 Fox, J. L. *et al.* Cryo-EM structural analysis of FADD:Caspase-8 complexes defines the catalytic dimer architecture for co-ordinated control of cell fate. *Nat Commun* **12**, doi:ARTN 81910.1038/s41467-020-20806-9 (2021).
73 Fu, T. M. *et al.* Cryo-EM Structure of Caspase-8 Tandem DED Filament Reveals Assembly and Regulation Mechanisms of the Death-Inducing Signaling Complex. *Mol Cell* **64**, 236-250, doi:10.1016/j.molcel.2016.09.009 (2016).
74 Pop, C. *et al.* FLIP(L) induces caspase 8 activity in the absence of interdomain caspase 8 cleavage and alters substrate specificity. *Biochem J* **433**, 447-457, doi:10.1042/BJ20101738 (2011).
75 Keller, N., Mares, J., Zerbe, O. & Grutter, M. G. Structural and biochemical studies on procaspase-8: new insights on initiator caspase activation. *Structure* **17**, 438-448, doi:10.1016/j.str.2008.12.019 (2009).
76 Yu, J. W., Jeffrey, P. D. & Shi, Y. Mechanism of procaspase-8 activation by c-FLIPL. *Proc Natl Acad Sci U S A* **106**, 8169-8174, doi:10.1073/pnas.0812453106 (2009).
77 Green, D. R. Caspases and Their Substrates. *Csh Perspect Biol* **14**, doi:ARTN a04101210.1101/cshperspect.a041012 (2022).
78 Hillert-Richter, L. K., König, C., Ivanisenko, N. V., Reinhold, D. & Lavrik, I. N. Targeting caspase-8/c-FLIP heterodimer in complex II promotes DL-mediated cell death. *Front Cell Dev Biol* **12**, doi:ARTN 147121610.3389/fcell.2024.1471216 (2024).
79 Fu, T. M. *et al.* Cryo-EM Structure of Caspase-8 Tandem DED Filament Reveals Assembly and Regulation Mechanisms of the Death-Inducing Signaling Complex. *Mol Cell* **64**, 236-250, doi:10.1016/j.molcel.2016.09.009 (2016).
80 Hughes, M. A. *et al.* Co-operative and Hierarchical Binding of c-FLIP and Caspase-8: A Unified Model Defines How c-FLIP Isoforms Differentially Control Cell Fate. *Mol Cell* **61**, 834-849, doi:10.1016/j.molcel.2016.02.023 (2016).
81 Dillon, C. P. *et al.* Survival Function of the FADD-CASPASE-8-cFLIP Complex. *Cell Reports* **1**, 401-407, doi:10.1016/j.celrep.2012.03.010 (2012).

82 Luo, X., Budihardjo, I., Zou, H., Slaughter, C. & Wang, X. D. Bid, a Bcl2 interacting protein, mediates cytochrome c release from mitochondria in response to activation of cell surface death receptors. *Cell* **94**, 481-490, doi:Doi 10.1016/S0092-8674(00)81589-5 (1998).
83 Chaudhary, A. K. *et al.* A potential role of X-linked inhibitor of apoptosis protein in mitochondrial membrane permeabilization and its implication in cancer therapy. *Drug Discov Today* **21**, 38-47, doi:10.1016/j.drudis.2015.07.014 (2016).
84 Jost, P. J. *et al.* XIAP discriminates between type I and type II FAS-induced apoptosis. *Nature* **460**, 1035-U1128, doi:10.1038/nature08229 (2009).
85 Cummins, J. M. *et al.* X-linked inhibitor of apoptosis protein (XIAP) is a nonredundant modulator of tumor necrosis factor-related apoptosis-inducing ligand (TRAIL)-mediated apoptosis in human cancer cells. *Cancer Res* **64**, 3006-3008, doi:Doi 10.1158/0008-5472.Can-04-0046 (2004).
86 Li, M. & Beg, A. A. Induction of necrotic-like cell death by tumor necrosis factor alpha and caspase inhibitors: Novel mechanism for killing virus-infected cells. *J Virol* **74**, 7470-7477, doi:Doi 10.1128/Jvi.74.16.7470-7477.2000 (2000).
87 Oberst, A. *et al.* Catalytic activity of the caspase-8-FLIP complex inhibits RIPK3-dependent necrosis. *Nature* **471**, 363-+, doi:10.1038/nature09852 (2011).
88 Kaiser, W. J. *et al.* RIP3 mediates the embryonic lethality of caspase-8-deficient mice. *Nature* **471**, 368-372, doi:10.1038/nature09857 (2011).
89 Alvarez-Diaz, S. *et al.* The Pseudokinase MLKL and the Kinase RIPK3 Have Distinct Roles in Autoimmune Disease Caused by Loss of Death-Receptor-Induced Apoptosis. *Immunity* **45**, 513-526, doi:10.1016/j.immuni.2016.07.016 (2016).
90 Zhang, H. B. *et al.* Functional complementation between FADD and RIP1 in embryos and lymphocytes. *Nature* **471**, 373-+, doi:10.1038/nature09878 (2011).
91 Newton, K. *et al.* Cleavage of RIPK1 by caspase-8 is crucial for limiting apoptosis and necroptosis. *Nature* **574**, 428-+, doi:10.1038/s41586-019-1548-x (2019).
92 Lalaoui, N. *et al.* Mutations that prevent caspase cleavage of RIPK1 cause autoinflammatory disease. *Nature* **577**, 103-+, doi:10.1038/s41586-019-1828-5 (2020).
93 Newton, K. *et al.* Caspase cleavage of RIPK3 after Asp333 is dispensable for mouse embryogenesis. *Cell Death and Differentiation* **31**, 254-262, doi:10.1038/s41418-023-01255-5 (2024).
94 Tran, H. T. *et al.* RIPK3 cleavage is dispensable for necroptosis inhibition but restricts NLRP3 inflammasome activation. *Cell Death and Differentiation* **31**, 662-671, doi:10.1038/s41418-024-01281-x (2024).
95 Chen, W. *et al.* Diverse sequence determinants control human and mouse receptor interacting protein 3 (RIP3) and mixed lineage kinase domain-like (MLKL) interaction in necroptotic signaling. *J Biol Chem* **288**, 16247-16261, doi:10.1074/jbc.M112.435545 (2013).
96 Sun, L. *et al.* Mixed lineage kinase domain-like protein mediates necrosis signaling downstream of RIP3 kinase. *Cell* **148**, 213-227, doi:10.1016/j.cell.2011.11.031 (2012).
97 Rodriguez, D. A. *et al.* Characterization of RIPK3-mediated phosphorylation of the activation loop of MLKL during necroptosis. *Cell Death Differ* **23**, 76-88, doi:10.1038/cdd.2015.70 (2016).
98 Murphy, J. M. The Killer Pseudokinase Mixed Lineage Kinase Domain-Like Protein (MLKL). *Cold Spring Harb Perspect Biol* **12**, doi:10.1101/cshperspect.a036376 (2020).
99 Gong, Y. N., Guy, C., Crawford, J. C. & Green, D. R. Biological events and molecular signaling following MLKL activation during necroptosis. *Cell Cycle* **16**, 1748-1760, doi:10.1080/15384101.2017.1371889 (2017).
100 Gong, Y. N. *et al.* ESCRT-III Acts Downstream of MLKL to Regulate Necroptotic Cell Death and Its Consequences. *Cell* **169**, 286-300, doi:10.1016/j.cell.2017.03.020 (2017).
101 Yoon, S., Bogdanov, K., Kovalenko, A. & Wallach, D. Necroptosis is preceded by nuclear translocation of the signaling proteins that induce it. *Cell Death and Differentiation* **23**, 253-260, doi:10.1038/cdd.2015.92 (2016).

102 Kaczmarek, A., Vandenabeele, P. & Krysko, D. V. Necroptosis: the release of damage-associated molecular patterns and its physiological relevance. *Immunity* **38**, 209-223, doi:10.1016/j.immuni.2013.02.003 (2013).
103 Murphy, J. M. *et al.* The Pseudokinase MLKL Mediates Necroptosis via a Molecular Switch Mechanism. *Immunity* **39**, 443-453, doi:10.1016/j.immuni.2013.06.018 (2013).
104 Hildebrand, J. M. *et al.* Activation of the pseudokinase MLKL unleashes the four-helix bundle domain to induce membrane localization and necroptotic cell death. *Proc Natl Acad Sci U S A* **111**, 15072-15077, doi:10.1073/pnas.1408987111 (2014).
105 Tanzer, M. C. *et al.* Evolutionary divergence of the necroptosis effector MLKL. *Cell Death Differ* **23**, 1185-1197, doi:10.1038/cdd.2015.169 (2016).
106 Chen, X. *et al.* Translocation of mixed lineage kinase domain-like protein to plasma membrane leads to necrotic cell death. *Cell Res* **24**, 105-121, doi:10.1038/cr.2013.171 (2014).
107 Petrie, E. J., Czabotar, P. E. & Murphy, J. M. The Structural Basis of Necroptotic Cell Death Signaling. *Trends Biochem Sci* **44**, 53-63, doi:10.1016/j.tibs.2018.11.002 (2019).
108 Dondelinger, Y. *et al.* MLKL compromises plasma membrane integrity by binding to phosphatidylinositol phosphates. *Cell Rep* **7**, 971-981, doi:10.1016/j.celrep.2014.04.026 (2014).
109 Su, L. *et al.* A plug release mechanism for membrane permeation by MLKL. *Structure* **22**, 1489-1500, doi:10.1016/j.str.2014.07.014 (2014).
110 Garnish, S. E. *et al.* Conformational interconversion of MLKL and disengagement from RIPK3 precede cell death by necroptosis. *Nat Commun* **12**, 2211, doi:10.1038/s41467-021-22400-z (2021).
111 Liccardi, G. & Annibaldi, A. MLKL post-translational modifications: road signs to infection, inflammation and unknown destinations. *Cell Death Differ* **30**, 269-278, doi:10.1038/s41418-022-01061-5 (2023).
112 Quarato, G. *et al.* Sequential Engagement of Distinct MLKL Phosphatidylinositol-Binding Sites Executes Necroptosis. *Mol Cell* **61**, 589-601, doi:10.1016/j.molcel.2016.01.011 (2016).
113 Petrie, E. J. *et al.* Conformational switching of the pseudokinase domain promotes human MLKL tetramerization and cell death by necroptosis. *Nat Commun* **9**, 2422, doi:10.1038/s41467-018-04714-7 (2018).
114 Davies, K. A. *et al.* The brace helices of MLKL mediate interdomain communication and oligomerisation to regulate cell death by necroptosis. *Cell Death Differ* **25**, 1567-1580, doi:10.1038/s41418-018-0061-3 (2018).
115 Zhu, X. X. *et al.* Spontaneous necroptosis and autoinflammation are blocked by an inhibitory phosphorylation on MLKL during neonatal development. *Cell Res* **32**, 407-410, doi:10.1038/s41422-021-00583-w (2022).
116 Najafov, A. *et al.* TAM Kinases Promote Necroptosis by Regulating Oligomerization of MLKL. *Mol Cell* **75**, 457-+, doi:10.1016/j.molcel.2019.05.022 (2019).
117 Dephoure, N. *et al.* A quantitative atlas of mitotic phosphorylation. *P Natl Acad Sci USA* **105**, 10762-10767, doi:10.1073/pnas.0805139105 (2008).
118 Upton, J. W., Shubina, M. & Balachandran, S. RIPK3-driven cell death during virus infections. *Immunol Rev* **277**, 90-101, doi:10.1111/imr.12539 (2017).
119 Hitomi, J. I. *et al.* Identification of a Molecular Signaling Network that Regulates a Cellular Necrotic Cell Death Pathway. *Cell* **135**, 1311-1323, doi:10.1016/j.cell.2008.10.044 (2008).
120 Xia, X., Lei, L., Wang, S., Hu, J. & Zhang, G. Necroptosis and its role in infectious diseases. *Apoptosis* **25**, 169-178, doi:10.1007/s10495-019-01589-x (2020).
121 Petrie, E. J. *et al.* Viral MLKL Homologs Subvert Necroptotic Cell Death by Sequestering Cellular RIPK3. *Cell Rep* **28**, 3309-3319 e3305, doi:10.1016/j.celrep.2019.08.055 (2019).
122 Muscolino, E., Castiglioni, C., Brixel, R., Frascaroli, G. & Brune, W. Species-Specific Inhibition of Necroptosis by HCMV UL36. *Viruses* **13**, doi:10.3390/v13112134 (2021).
123 McComb, S. *et al.* Type-I interferon signaling through ISGF3 complex is required for sustained Rip3 activation and necroptosis in macrophages. *P Natl Acad Sci USA* **111**, E3206-E3213, doi:10.1073/pnas.1407068111 (2014).

124 Sarhan, J. *et al.* Constitutive interferon signaling maintains critical threshold of MLKL expression to license necroptosis. *Cell Death and Differentiation* **26**, 332-347, doi:10.1038/s41418-018-0122-7 (2019).
125 Martens, S., Bridelance, J., Roelandt, R., Vandenabeele, P. & Takahashi, N. MLKL in cancer: more than a necroptosis regulator. *Cell Death and Differentiation* **28**, 1757-1772, doi:10.1038/s41418-021-00785-0 (2021).
126 Koo, G. B. *et al.* Methylation-dependent loss of RIP3 expression in cancer represses programmed necrosis in response to chemotherapeutics. *Cell Res* **25**, 707-725, doi:10.1038/cr.2015.56 (2015).
127 Polykratis, A. *et al.* Cutting edge: RIPK1 Kinase inactive mice are viable and protected from TNF-induced necroptosis in vivo. *J Immunol* **193**, 1539-1543, doi:10.4049/jimmunol.1400590 (2014).
128 Omoto, S. *et al.* Suppression of RIP3-dependent necroptosis by human cytomegalovirus. *J Biol Chem* **290**, 11635-11648, doi:10.1074/jbc.M115.646042 (2015).
129 Varfolomeev, E. E. *et al.* Targeted disruption of the mouse Caspase 8 gene ablates cell death induction by the TNF receptors, Fas/Apo1, and DR3 and is lethal prenatally. *Immunity* **9**, 267-276, doi:10.1016/s1074-7613(00)80609-3 (1998).
130 Yeh, W. C. *et al.* FADD: Essential for embryo development and signaling from some, but not all, inducers of apoptosis. *Science* **279**, 1954-1958, doi:DOI 10.1126/science.279.5358.1954 (1998).
131 Yeh, W. C. *et al.* Requirement for Casper (c-FLIP) in regulation of death receptor-induced apoptosis and embryonic development. *Immunity* **12**, 633-642, doi:10.1016/s1074-7613(00)80214-9 (2000).
132 Kang, T. B. *et al.* Caspase-8 serves both apoptotic and nonapoptotic roles. *Journal of Immunology* **173**, 2976-2984, doi:DOI 10.4049/jimmunol.173.5.2976 (2004).
133 Fan, C. *et al.* Lack of FADD in Tie-2 expressing cells causes RIPK3-mediated embryonic lethality. *Cell Death Dis* **7**, e2351, doi:10.1038/cddis.2016.251 (2016).
134 Kovalenko, A. *et al.* Caspase-8 deficiency in epidermal keratinocytes triggers an inflammatory skin disease. *J Exp Med* **206**, 2161-2177, doi:10.1084/jem.20090616 (2009).
135 Bonnet, M. C. *et al.* The adaptor protein FADD protects epidermal keratinocytes from necroptosis in vivo and prevents skin inflammation. *Immunity* **35**, 572-582, doi:10.1016/j.immuni.2011.08.014 (2011).
136 Koerner, L. *et al.* ZBP1 causes inflammation by inducing RIPK3-mediated necroptosis and RIPK1 kinase activity-independent apoptosis. *Cell Death Differ* **31**, 938-953, doi:10.1038/s41418-024-01321-6 (2024).
137 Weinlich, R. *et al.* Protective roles for caspase-8 and cFLIP in adult homeostasis. *Cell Rep* **5**, 340-348, doi:10.1016/j.celrep.2013.08.045 (2013).
138 Wittkopf, N. *et al.* Cellular FLICE-like inhibitory protein secures intestinal epithelial cell survival and immune homeostasis by regulating caspase-8. *Gastroenterology* **145**, 1369-1379, doi:10.1053/j.gastro.2013.08.059 (2013).
139 Welz, P. S. *et al.* FADD prevents RIP3-mediated epithelial cell necrosis and chronic intestinal inflammation. *Nature* **477**, 330-334, doi:10.1038/nature10273 (2011).
140 Gunther, C. *et al.* Caspase-8 regulates TNF-alpha-induced epithelial necroptosis and terminal ileitis. *Nature* **477**, 335-339, doi:10.1038/nature10400 (2011).
141 Schwarzer, R., Jiao, H., Wachsmuth, L., Tresch, A. & Pasparakis, M. FADD and Caspase-8 Regulate Gut Homeostasis and Inflammation by Controlling MLKL- and GSDMD-Mediated Death of Intestinal Epithelial Cells. *Immunity* **52**, 978-993 e976, doi:10.1016/j.immuni.2020.04.002 (2020).
142 Tovey Crutchfield, E. C. *et al.* MLKL deficiency protects against low-grade, sterile inflammation in aged mice. *Cell Death Differ* **30**, 1059-1071, doi:10.1038/s41418-023-01121-4 (2023).
143 Newton, K. *et al.* Activity of protein kinase RIPK3 determines whether cells die by necroptosis or apoptosis. *Science* **343**, 1357-1360, doi:10.1126/science.1249361 (2014).
144 Mandal, P. *et al.* RIP3 induces apoptosis independent of pronecrotic kinase activity. *Mol Cell* **56**, 481-495, doi:10.1016/j.molcel.2014.10.021 (2014).

145 Chiou, S. *et al.* The kinase domain of RIPK3 tunes its scaffolding functions. *bioRxiv*, 2025.2004.2029.651198, doi:10.1101/2025.04.29.651198 (2025).
146 Reilly, L. A. O. *et al.* Membrane-bound Fas ligand only is essential for Fas-induced apoptosis. *Nature* **461**, 659-U106, doi:10.1038/nature08402 (2009).
147 Rieuxlaucat, F. *et al.* Mutations in Fas Associated with Human Lymphoproliferative Syndrome and Autoimmunity. *Science* **268**, 1347-1349, doi:DOI 10.1126/science.7539157 (1995).
148 Watanabefukunaga, R., Brannan, C. I., Copeland, N. G., Jenkins, N. A. & Nagata, S. Lymphoproliferation Disorder in Mice Explained by Defects in Fas Antigen That Mediates Apoptosis. *Nature* **356**, 314-317, doi:DOI 10.1038/356314a0 (1992).
149 Kang, T. B. *et al.* Mutation of a self-processing site in caspase-8 compromises its apoptotic but not its nonapoptotic functions in bacterial artificial chromosome-transgenic mice. *J Immunol* **181**, 2522-2532, doi:10.4049/jimmunol.181.4.2522 (2008).
150 Tummers, B. *et al.* Caspase-8-Dependent Inflammatory Responses Are Controlled by Its Adaptor, FADD, and Necroptosis. *Immunity* **52**, 994-1006 e1008, doi:10.1016/j.immuni.2020.04.010 (2020).
151 Fritsch, M. *et al.* Caspase-8 is the molecular switch for apoptosis, necroptosis and pyroptosis. *Nature* **575**, 683-+, doi:10.1038/s41586-019-1770-6 (2019).
152 Dillon, C. P. *et al.* RIPK1 blocks early postnatal lethality mediated by caspase-8 and RIPK3. *Cell* **157**, 1189-1202, doi:10.1016/j.cell.2014.04.018 (2014).
153 Kaiser, W. J. *et al.* RIP1 suppresses innate immune necrotic as well as apoptotic cell death during mammalian parturition. *P Natl Acad Sci USA* **111**, 7753-7758, doi:10.1073/pnas.1401857111 (2014).
154 Rickard, J. A. *et al.* RIPK1 Regulates RIPK3-MLKL-Driven Systemic Inflammation and Emergency Hematopoiesis. *Cell* **157**, 1175-1188, doi:10.1016/j.cell.2014.04.019 (2014).
155 Dannappel, M. *et al.* RIPK1 maintains epithelial homeostasis by inhibiting apoptosis and necroptosis. *Nature* **513**, 90-+, doi:10.1038/nature13608 (2014).
156 Takahashi, N. *et al.* RIPK1 ensures intestinal homeostasis by protecting the epithelium against apoptosis. *Nature* **513**, 95-99, doi:10.1038/nature13706 (2014).
157 Berger, S. B. *et al.* Cutting Edge: RIP1 kinase activity is dispensable for normal development but is a key regulator of inflammation in SHARPIN-deficient mice. *J Immunol* **192**, 5476-5480, doi:10.4049/jimmunol.1400499 (2014).
158 Cusson, N., Oikemus, S., Kilpatrick, E. D., Cunningham, L. & Kelliher, M. The death domain kinase RIP protects thymocytes from tumor necrosis factor receptor type 2-induced cell death. *J Exp Med* **196**, 15-26, doi:10.1084/jem.20011470 (2002).
159 Anderton, H. *et al.* RIPK1 prevents TRADD-driven, but TNFR1 independent, apoptosis during development. *Cell Death Differ* **26**, 877-889, doi:10.1038/s41418-018-0166-8 (2019).
160 Kang, T. B., Jeong, J. S., Yang, S. H., Kovalenko, A. & Wallach, D. Caspase-8 deficiency in mouse embryos triggers chronic RIPK1-dependent activation of inflammatory genes, independently of RIPK3. *Cell Death Differ* **25**, 1107-1117, doi:10.1038/s41418-018-0104-9 (2018).
161 Wang, Y. *et al.* Molecular mechanism of RIPK1 and caspase-8 in homeostatic type I interferon production and regulation. *Cell Rep* **41**, 111434, doi:10.1016/j.celrep.2022.111434 (2022).
162 Thapa, R. J. *et al.* Interferon-induced RIP1/RIP3-mediated necrosis requires PKR and is licensed by FADD and caspases. *P Natl Acad Sci USA* **110**, E3109-E3118, doi:10.1073/pnas.1301218110 (2013).
163 Newton, K. *et al.* RIPK1 inhibits ZBP1-driven necroptosis during development. *Nature* **540**, 129-133, doi:10.1038/nature20559 (2016).
164 Lin, J. *et al.* RIPK1 counteracts ZBP1-mediated necroptosis to inhibit inflammation. *Nature* **540**, 124-128, doi:10.1038/nature20558 (2016).
165 Maelfait, J. & Rehwinkel, J. The Z-nucleic acid sensor ZBP1 in health and disease. *J Exp Med* **220**, doi:ARTN e2022115610.1084/jem.20221156 (2023).

166 Brown, B. A., Lowenhaupt, K., Wilbert, C. M., Hanlon, E. B. & Rich, A. The Zα domain of the editing enzyme dsRNA adenosine deaminase binds left-handed Z-RNA as well as Z-DNA. *P Natl Acad Sci USA* **97**, 13532-13536, doi:DOI 10.1073/pnas.240464097 (2000).

167 Athanasiadis, A. Zalpha-domains: At the intersection between RNA editing and innate immunity. *Semin Cell Dev Biol* **23**, 275-280, doi:10.1016/j.semcdb.2011.11.001 (2012).

168 Schwartz, T., Behlke, J., Lowenhaupt, K., Heinemann, U. & Rich, A. Structure of the DLM-1-Z-DNA complex reveals a conserved family of Z-DNA-binding proteins. *Nat Struct Biol* **8**, 761-765, doi:DOI 10.1038/nsb0901-761 (2001).

169 Herbert, A. *et al.* A Z-DNA binding domain present in the human editing enzyme, double-stranded RNA adenosine deaminase. *P Natl Acad Sci USA* **94**, 8421-8426, doi:DOI 10.1073/pnas.94.16.8421 (1997).

170 Tang, Q. Z-nucleic acids: Uncovering the functions from past to present. *Eur J Immunol* **52**, 1700-1711, doi:10.1002/eji.202249968 (2022).

171 Herbert, A. & Rich, A. Left-handed Z-DNA: structure and function. *Genetica* **106**, 37-47, doi:Doi 10.1023/A:1003768526018 (1999).

172 Kim, D., Lee, Y. H., Hwang, H. Y., Kim, K. K. & Park, H. J. Z-DNA Binding Proteins as Targets for Structure-Based Virtual Screening. *Curr Drug Targets* **11**, 335-344, doi:Doi 10.2174/138945010790711905 (2010).

173 Rahmouni, A. R. & Wells, R. D. Stabilization of Z DNA in vivo by localized supercoiling. *Science* **246**, 358-363, doi:10.1126/science.2678475 (1989).

174 Zheng, G. X., Kochel, T., Hoepfner, R. W., Timmons, S. E. & Sinden, R. R. Torsionally Tuned Cruciform and Z-DNA Probes for Measuring Unrestrained Supercoiling at Specific Sites in DNA of Living Cells. *J Mol Biol* **221**, 107-129, doi:Doi 10.1016/0022-2836(91)90808-J (1991).

175 Rebsamen, M. *et al.* DAI/ZBP1 recruits RIP1 and RIP3 through RIP homotypic interaction motifs to activate NF-κB. *Embo Rep* **10**, 916-922, doi:10.1038/embor.2009.109 (2009).

176 Peng, R. *et al.* Human ZBP1 induces cell death-independent inflammatory signaling via RIPK3 and RIPK1. *Embo Rep* **23**, e55839, doi:10.15252/embr.202255839 (2022).

177 Kaiser, W. J., Upton, J. W. & Mocarski, E. S. Receptor-interacting protein homotypic interaction motif-dependent control of NF-kappa B activation via the DNA-dependent activator of IFN regulatory factors. *J Immunol* **181**, 6427-6434, doi:10.4049/jimmunol.181.9.6427 (2008).

178 Hayashi, T. *et al.* DNA-dependent activator of IFN-regulatory factors enhances the transcription of HIV-1 through NF-κB. *Microbes Infect* **12**, 937-947, doi:10.1016/j.micinf.2010.06.003 (2010).

179 Thapa, R. J. *et al.* DAI Senses Influenza A Virus Genomic RNA and Activates RIPK3-Dependent Cell Death. *Cell Host Microbe* **20**, 674-681, doi:10.1016/j.chom.2016.09.014 (2016).

180 Kuriakose, T. *et al.* ZBP1/DAI is an innate sensor of influenza virus triggering the NLRP3 inflammasome and programmed cell death pathways. *Sci Immunol* **1**, doi:ARTN aag204510.1126/sciimmunol.aag2045 (2016).

181 Zhang, T. *et al.* Influenza Virus Z-RNAs Induce ZBP1-Mediated Necroptosis. *Cell* **180**, 1115-+, doi:10.1016/j.cell.2020.02.050 (2020).

182 Upton, J. W., Kaiser, W. J. & Mocarski, E. S. DAI/ZBP1/DLM-1 Complexes with RIP3 to Mediate Virus-Induced Programmed Necrosis that Is Targeted by Murine Cytomegalovirus vIRA. *Cell Host Microbe* **11**, 290-297, doi:10.1016/j.chom.2012.01.016 (2012).

183 Muendlein, H. I. *et al.* ZBP1 promotes inflammatory responses downstream of TLR3/TLR4 via timely delivery of RIPK1 to TRIF. *Proc Natl Acad Sci U S A* **119**, e2113872119, doi:10.1073/pnas.2113872119 (2022).

184 Muendlein, H. I. *et al.* ZBP1 promotes LPS-induced cell death and IL-1beta release via RHIM-mediated interactions with RIPK1. *Nat Commun* **12**, 86, doi:10.1038/s41467-020-20357-z (2021).

185 Takaoka, A. *et al.* DAI (DLM-1/ZBP1) is a cytosolic DNA sensor and an activator of innate immune response. *Nature* **448**, 501-U514, doi:10.1038/nature06013 (2007).

186 Upton, J. W., Kaiser, W. J. & Mocarski, E. S. Virus inhibition of RIP3-dependent necrosis. *Cell Host Microbe* **7**, 302-313, doi:10.1016/j.chom.2010.03.006 (2010).
187 Brune, W., Menard, C., Heesemann, J. & Koszinowski, U. H. A ribonucleotide reductase homolog of cytomegalovirus and endothelial cell tropism. *Science* **291**, 303-305, doi:10.1126/science.291.5502.303 (2001).
188 Koehler, H. *et al.* Vaccinia virus E3 prevents sensing of Z-RNA to block ZBP1-dependent necroptosis. *Cell Host Microbe* **29**, 1266-1276 e1265, doi:10.1016/j.chom.2021.05.009 (2021).
189 Steain, M. *et al.* Varicella zoster virus encodes a viral decoy RHIM to inhibit cell death. *PLoS Pathog* **16**, e1008473, doi:10.1371/journal.ppat.1008473 (2020).
190 Guo, H. *et al.* Species-independent contribution of ZBP1/DAI/DLM-1-triggered necroptosis in host defense against HSV1. *Cell Death Dis* **9**, 816, doi:10.1038/s41419-018-0868-3 (2018).
191 Koehler, H. *et al.* Inhibition of DAI-dependent necroptosis by the Z-DNA binding domain of the vaccinia virus innate immune evasion protein, E3. *Proc Natl Acad Sci U S A* **114**, 11506-11511, doi:10.1073/pnas.1700999114 (2017).
192 Huang, Z. *et al.* RIP1/RIP3 binding to HSV-1 ICP6 initiates necroptosis to restrict virus propagation in mice. *Cell Host Microbe* **17**, 229-242, doi:10.1016/j.chom.2015.01.002 (2015).
193 Guo, H. *et al.* Herpes simplex virus suppresses necroptosis in human cells. *Cell Host Microbe* **17**, 243-251, doi:10.1016/j.chom.2015.01.003 (2015).
194 Ingram, J. P. *et al.* ZBP1/DAI Drives RIPK3-Mediated Cell Death Induced by IFNs in the Absence of RIPK1. *J Immunol* **203**, 1348-1355, doi:10.4049/jimmunol.1900216 (2019).
195 Yuan, F. *et al.* Z-DNA binding protein 1 promotes heatstroke-induced cell death. *Science* **376**, 609-615, doi:10.1126/science.abg5251 (2022).
196 Li, S. F. *et al.* SARS-CoV-2 Z-RNA activates the ZBP1-RIPK3 pathway to promote virus-induced inflammatory responses. *Cell Res* **33**, 201-214, doi:10.1038/s41422-022-00775-y (2023).
197 Maelfait, J. *et al.* Sensing of viral and endogenous RNA by ZBP1/DAI induces necroptosis. *EMBO J* **36**, 2529-2543, doi:10.15252/embj.201796476 (2017).
198 Sridharan, H. *et al.* Murine cytomegalovirus IE3-dependent transcription is required for DAI/ZBP1-mediated necroptosis. *Embo Rep* **18**, 1429-1441, doi:10.15252/embr.201743947 (2017).
199 Daniels, B. P. *et al.* The Nucleotide Sensor ZBP1 and Kinase RIPK3 Induce the Enzyme IRG1 to Promote an Antiviral Metabolic State in Neurons. *Immunity* **50**, 64-+, doi:10.1016/j.immuni.2018.11.017 (2019).
200 Triantafilou, K., Eryilmazlar, D. & Triantafilou, M. Herpes simplex virus 2-induced activation in vaginal cells involves Toll-like receptors 2 and 9 and DNA sensors DAI and IFI16. *Am J Obstet Gynecol* **210**, doi:ARTN 122.e110.1016/j.ajog.2013.09.034 (2014).
201 Pham, T. H., Kwon, K. M., Kim, Y. E., Kim, K. K. & Ahn, J. H. DNA sensing-independent inhibition of herpes simplex virus 1 replication by DAI/ZBP1. *J Virol* **87**, 3076-3086, doi:10.1128/JVI.02860-12 (2013).
202 Furr, S. R., Chauhan, V. S., Moerdyk-Schauwecker, M. J. & Marriott, I. A role for DNA-dependent activator of interferon regulatory factor in the recognition of herpes simplex virus type 1 by glial cells. *J Neuroinflammation* **8**, 99, doi:10.1186/1742-2094-8-99 (2011).
203 DeFilippis, V. R., Alvarado, D., Sali, T., Rothenburg, S. & Früh, K. Human Cytomegalovirus Induces the Interferon Response via the DNA Sensor ZBP1. *J Virol* **84**, 585-598, doi:10.1128/Jvi.01748-09 (2010).
204 Jiao, H. *et al.* Z-nucleic-acid sensing triggers ZBP1-dependent necroptosis and inflammation. *Nature* **580**, 391-395, doi:10.1038/s41586-020-2129-8 (2020).
205 Devos, M. *et al.* Sensing of endogenous nucleic acids by ZBP1 induces keratinocyte necroptosis and skin inflammation. *J Exp Med* **217**, doi:10.1084/jem.20191913 (2020).
206 Solon, M. *et al.* ZBP1 and TRIF trigger lethal necroptosis in mice lacking caspase-8 and TNFR1. *Cell Death Differ* **31**, 672-682, doi:10.1038/s41418-024-01286-6 (2024).

207 Imai, T. *et al.* The RIPK1 death domain restrains ZBP1-and TRIF-mediated cell death and inflammation. *Immunity* **57**, doi:10.1016/j.immuni.2024.04.016 (2024).
208 Rodriguez, D. A. *et al.* Caspase-8 and FADD prevent spontaneous ZBP1 expression and necroptosis. *Proc Natl Acad Sci U S A* **119**, e2207240119, doi:10.1073/pnas.2207240119 (2022).
209 Matsui, T. *et al.* Proviral silencing in embryonic stem cells requires the histone methyltransferase ESET. *Nature* **464**, 927-931, doi:10.1038/nature08858 (2010).
210 Wang, R. *et al.* Gut stem cell necroptosis by genome instability triggers bowel inflammation. *Nature* **580**, 386-390, doi:10.1038/s41586-020-2127-x (2020).
211 Pestal, K. *et al.* Isoforms of RNA-Editing Enzyme ADAR1 Independently Control Nucleic Acid Sensor MDA5-Driven Autoimmunity and Multi-organ Development. *Immunity* **43**, 933-944, doi:10.1016/j.immuni.2015.11.001 (2015).
212 Mannion, N. M. *et al.* The RNA-editing enzyme ADAR1 controls innate immune responses to RNA. *Cell Rep* **9**, 1482-1494, doi:10.1016/j.celrep.2014.10.041 (2014).
213 de Reuver, R. *et al.* ADAR1 interaction with Z-RNA promotes editing of endogenous double-stranded RNA and prevents MDA5-dependent immune activation. *Cell Reports* **36**, doi:ARTN 10950010.1016/j.celrep.2021.109500 (2021).
214 de Reuver, R. *et al.* ADAR1 prevents autoinflammation by suppressing spontaneous ZBP1 activation. *Nature* **607**, 784-789, doi:10.1038/s41586-022-04974-w (2022).
215 Jiao, H. *et al.* ADAR1 averts fatal type I interferon induction by ZBP1. *Nature* **607**, 776-783, doi:10.1038/s41586-022-04878-9 (2022).
216 Hubbard, N. W. *et al.* ADAR1 mutation causes ZBP1-dependent immunopathology. *Nature* **607**, 769-775, doi:10.1038/s41586-022-04896-7 (2022).
217 Rodero, M. P. & Crow, Y. J. Type I interferon-mediated monogenic autoinflammation: The type I interferonopathies, a conceptual overview. *J Exp Med* **213**, 2527-2538, doi:10.1084/jem.20161596 (2016).
218 Nagata, M., Carvalho Schafer, Y., Wachsmuth, L. & Pasparakis, M. A shorter splicing isoform antagonizes ZBP1 to modulate cell death and inflammatory responses. *EMBO J* **43**, 5037-5056, doi:10.1038/s44318-024-00238-7 (2024).
219 Boege, Y. *et al.* A Dual Role of Caspase-8 in Triggering and Sensing Proliferation-Associated DNA Damage, a Key Determinant of Liver Cancer Development. *Cancer Cell* **32**, 342-359 e310, doi:10.1016/j.ccell.2017.08.010 (2017).
220 Krelin, Y. *et al.* Caspase-8 deficiency facilitates cellular transformation in vitro. *Cell Death Differ* **15**, 1350-1355, doi:10.1038/cdd.2008.88 (2008).
221 Liedtke, C. *et al.* Silencing of caspase-8 in murine hepatocellular carcinomas is mediated via methylation of an essential promoter element. *Gastroenterology* **129**, 1602-1615, doi:10.1053/j.gastro.2005.08.007 (2005).
222 Soung, Y. H. *et al.* CASPASE-8 gene is inactivated by somatic mutations in gastric carcinomas. *Cancer Res* **65**, 815-821 (2005).
223 Soung, Y. H. *et al.* Caspase-8 gene is frequently inactivated by the frameshift somatic mutation 1225_1226delTG in hepatocellular carcinomas. *Oncogene* **24**, 141-147, doi:10.1038/sj.onc.1208244 (2005).
224 Liccardi, G. *et al.* RIPK1 and Caspase-8 Ensure Chromosome Stability Independently of Their Role in Cell Death and Inflammation. *Mol Cell* **73**, 413-+, doi:10.1016/j.molcel.2018.11.010 (2019).
225 Vucur, M. *et al.* RIP3 inhibits inflammatory hepatocarcinogenesis but promotes cholestasis by controlling caspase-8- and JNK-dependent compensatory cell proliferation. *Cell Rep* **4**, 776-790, doi:10.1016/j.celrep.2013.07.035 (2013).
226 Hakem, A. *et al.* Caspase-8 is essential for maintaining chromosomal stability and suppressing B-cell lymphomagenesis. *Blood* **119**, 3495-3502, doi:10.1182/blood-2011-07-367532 (2012).
227 Baker, D. J. *et al.* BubR1 insufficiency causes early onset of aging-associated phenotypes and infertility in mice. *Nat Genet* **36**, 744-749, doi:10.1038/ng1382 (2004).

228 Mackenzie, K. J. *et al.* Ribonuclease H2 mutations induce a cGAS/STING-dependent innate immune response. *EMBO J* **35**, 831-844, doi:10.15252/embj.201593339 (2016).
229 Schumann, T. *et al.* Deficiency for SAMHD1 activates MDA5 in a cGAS/STING-dependent manner. *J Exp Med* **220**, doi:10.1084/jem.20220829 (2022).
230 Lacy, P. Editorial: secretion of cytokines and chemokines by innate immune cells. *Front Immunol* **6**, 190, doi:10.3389/fimmu.2015.00190 (2015).
231 Hemmi, H. *et al.* A Toll-like receptor recognizes bacterial DNA. *Nature* **408**, 740-745, doi:10.1038/35047123 (2000).
232 Bürckstümmer, T. *et al.* An orthogonal proteomic-genomic screen identifies AIM2 as a cytoplasmic DNA sensor for the inflammasome. *Nat Immunol* **10**, 266-272, doi:10.1038/ni.1702 (2009).
233 Unterholzner, L. *et al.* IFI16 is an innate immune sensor for intracellular DNA. *Nat Immunol* **11**, 997-U942, doi:10.1038/ni.1932 (2010).
234 Wu, J. X. *et al.* Cyclic GMP-AMP Is an Endogenous Second Messenger in Innate Immune Signaling by Cytosolic DNA. *Science* **339**, 826-830, doi:10.1126/science.1229963 (2013).
235 Sun, L. J., Wu, J. X., Du, F. H., Chen, X. & Chen, Z. J. J. Cyclic GMP-AMP Synthase Is a Cytosolic DNA Sensor That Activates the Type I Interferon Pathway. *Science* **339**, 786-791, doi:10.1126/science.1232458 (2013).
236 Ahn, J., Gutman, D., Saijo, S. & Barber, G. N. STING manifests self DNA-dependent inflammatory disease. *Proc Natl Acad Sci U S A* **109**, 19386-19391, doi:10.1073/pnas.1215006109 (2012).
237 Gao, D. *et al.* Activation of cyclic GMP-AMP synthase by self-DNA causes autoimmune diseases. *Proc Natl Acad Sci U S A* **112**, E5699-5705, doi:10.1073/pnas.1516465112 (2015).
238 Xiao, N. *et al.* cGAS activation causes lupus-like autoimmune disorders in a TREX1 mutant mouse model. *J Autoimmun* **100**, 84-94, doi:10.1016/j.jaut.2019.03.001 (2019).
239 Yu, Y. *et al.* Post-Translational Modifications of cGAS-STING: A Critical Switch for Immune Regulation. *Cells* **11**, doi:10.3390/cells11193043 (2022).
240 Cheng, Z. L. *et al.* The interactions between cGAS-STING pathway and pathogens. *Signal Transduct Tar* **5**, doi:10.1038/s41392-020-0198-7 (2020).
241 Liu, Y. & Pu, F. Updated roles of cGAS-STING signaling in autoimmune diseases. *Front Immunol* **14**, 1254915, doi:10.3389/fimmu.2023.1254915 (2023).
242 Decout, A., Katz, J. D., Venkatraman, S. & Ablasser, A. The cGAS-STING pathway as a therapeutic target in inflammatory diseases. *Nature Reviews Immunology* **21**, 548-569, doi:10.1038/s41577-021-00524-z (2021).
243 Samson, N. & Ablasser, A. The cGAS-STING pathway and cancer. *Nat Cancer*, doi:10.1038/s43018-022-00468-w (2022).
244 Zhang, X. *et al.* The Cytosolic DNA Sensor cGAS Forms an Oligomeric Complex with DNA and Undergoes Switch-like Conformational Changes in the Activation Loop. *Cell Reports* **6**, 421-430, doi:10.1016/j.celrep.2014.01.003 (2014).
245 Li, X. *et al.* Cyclic GMP-AMP Synthase Is Activated by Double-Stranded DNA-Induced Oligomerization. *Immunity* **39**, 1019-1031, doi:10.1016/j.immuni.2013.10.019 (2013).
246 Kranzusch, P. J., Lee, A. S. Y., Berger, J. M. & Doudna, J. A. Structure of Human cGAS Reveals a Conserved Family of Second-Messenger Enzymes in Innate Immunity. *Cell Reports* **3**, 1362-1368, doi:10.1016/j.celrep.2013.05.008 (2013).
247 Gao, P. *et al.* Structure-Function Analysis of STING Activation by c[G(2′,5′) pA(3′,5′)p] and Targeting by Antiviral DMXAA. *Cell* **154**, 748-762, doi:10.1016/j.cell.2013.07.023 (2013).
248 Civril, F. *et al.* Structural mechanism of cytosolic DNA sensing by cGAS. *Nature* **498**, 332-+, doi:10.1038/nature12305 (2013).
249 Kato, K. *et al.* Structural and Functional Analyses of DNA-Sensing and Immune Activation by Human cGAS. *Plos One* **8**, doi:ARTN e7698310.1371/journal.pone.0076983 (2013).
250 Li, Q. J. & Gao, P. Phase separation in cGAS-STING signaling. *Front Med-Prc* **17**, 855-866, doi:10.1007/s11684-023-1026-6 (2023).

251 Du, M. J. & Chen, Z. J. J. DNA-induced liquid phase condensation of cGAS activates innate immune signaling. *Science* **361**, 704-+, doi:10.1126/science.aat1022 (2018).
252 Andreeva, L. *et al.* cGAS senses long and HMGB/TFAM-bound U-turn DNA by forming protein-DNA ladders. *Nature* **549**, 394-398, doi:10.1038/nature23890 (2017).
253 Xie, W. *et al.* Human cGAS catalytic domain has an additional DNA-binding interface that enhances enzymatic activity and liquid-phase condensation. *P Natl Acad Sci USA* **116**, 11946-11955, doi:10.1073/pnas.1905013116 (2019).
254 Du, M. & Chen, Z. J. DNA-induced liquid phase condensation of cGAS activates innate immune signaling. *Science* **361**, 704-709, doi:10.1126/science.aat1022 (2018).
255 Zhou, W., Mohr, L., Maciejowski, J. & Kranzusch, P. J. cGAS phase separation inhibits TREX1-mediated DNA degradation and enhances cytosolic DNA sensing. *Mol Cell* **81**, 739-755 e737, doi:10.1016/j.molcel.2021.01.024 (2021).
256 Luecke, S. *et al.* cGAS is activated by DNA in a length-dependent manner. *Embo Rep* **18**, 1707-1715, doi:10.15252/embr.201744017 (2017).
257 Zhou, W. *et al.* Structure of the Human cGAS-DNA Complex Reveals Enhanced Control of Immune Surveillance. *Cell* **174**, 300-311 e311, doi:10.1016/j.cell.2018.06.026 (2018).
258 Wu, S., Gabelli, S. B. & Sohn, J. The structural basis for 2′-5′/3′-5′-cGAMP synthesis by cGAS. *Nat Commun* **15**, doi:ARTN 401210.1038/s41467-024-48365-3 (2024).
259 Hall, J. *et al.* The catalytic mechanism of cyclic GMP-AMP synthase (cGAS) and implications for innate immunity and inhibition. *Protein Sci* **26**, 2367-2380, doi:10.1002/pro.3304 (2017).
260 Diner, E. J. *et al.* The Innate Immune DNA Sensor cGAS Produces a Noncanonical Cyclic Dinucleotide that Activates Human STING. *Cell Reports* **3**, 1355-1361, doi:10.1016/j.celrep.2013.05.009 (2013).
261 Zhang, M., Wu, C., Lu, D., Wang, X. & Shang, G. cGAS-STING: mechanisms and therapeutic opportunities. *Sci China Life Sci* **68**, 1309-1323, doi:10.1007/s11427-024-2808-3 (2025).
262 Zhong, L. *et al.* Phosphorylation of cGAS by CDK1 impairs self-DNA sensing in mitosis. *Cell Discov* **6**, 26, doi:10.1038/s41421-020-0162-2 (2020).
263 Gentili, M. *et al.* The N-Terminal Domain of cGAS Determines Preferential Association with Centromeric DNA and Innate Immune Activation in the Nucleus. *Cell Rep* **26**, 3798, doi:10.1016/j.celrep.2019.03.049 (2019).
264 Jiang, H. *et al.* Chromatin-bound cGAS is an inhibitor of DNA repair and hence accelerates genome destabilization and cell death. *Embo Journal* **38**, doi:ARTN e10271810.15252/embj.2019102718 (2019).
265 Liu, H. *et al.* Nuclear cGAS suppresses DNA repair and promotes tumorigenesis. *Nature* **563**, 131-136, doi:10.1038/s41586-018-0629-6 (2018).
266 Mackenzie, K. J. *et al.* cGAS surveillance of micronuclei links genome instability to innate immunity. *Nature* **548**, 461-465, doi:10.1038/nature23449 (2017).
267 Pathare, G. R. *et al.* Structural mechanism of cGAS inhibition by the nucleosome. *Nature* **587**, 668-672, doi:10.1038/s41586-020-2750-6 (2020).
268 Michalski, S. *et al.* Structural basis for sequestration and autoinhibition of cGAS by chromatin. *Nature* **587**, 678-682, doi:10.1038/s41586-020-2748-0 (2020).
269 Kujirai, T. *et al.* Structural basis for the inhibition of cGAS by nucleosomes. *Science* **370**, 455-458, doi:10.1126/science.abd0237 (2020).
270 Cao, D., Han, X., Fan, X., Xu, R. M. & Zhang, X. Structural basis for nucleosome-mediated inhibition of cGAS activity. *Cell Res* **30**, 1088-1097, doi:10.1038/s41422-020-00422-4 (2020).
271 Boyer, J. A. *et al.* Structural basis of nucleosome-dependent cGAS inhibition. *Science* **370**, 450-454, doi:10.1126/science.abd0609 (2020).
272 Zhao, B. *et al.* The molecular basis of tight nuclear tethering and inactivation of cGAS. *Nature* **587**, 673-677, doi:10.1038/s41586-020-2749-z (2020).
273 Volkman, H. E., Cambier, S., Gray, E. E. & Stetson, D. B. Tight nuclear tethering of cGAS is essential for preventing autoreactivity. *Elife* **8**, doi:ARTN e4749110.7554/eLife.47491 (2019).

274 Guey, B. *et al.* BAF restricts cGAS on nuclear DNA to prevent innate immune activation. *Science* **369**, 823-828, doi:10.1126/science.aaw6421 (2020).
275 Barnett, K. C. *et al.* Phosphoinositide Interactions Position cGAS at the Plasma Membrane to Ensure Efficient Distinction between Self- and Viral DNA. *Cell* **176**, 1432-+, doi:10.1016/j.cell.2019.01.049 (2019).
276 Zhou, W., Richmond-Buccola, D., Wang, Q. & Kranzusch, P. J. Structural basis of human TREX1 DNA degradation and autoimmune disease. *Nat Commun* **13**, 4277, doi:10.1038/s41467-022-32055-z (2022).
277 Simpson, S. R., Hemphill, W. O., Hudson, T. & Perrino, F. W. TREX1-Apex predator of cytosolic DNA metabolism. *DNA Repair* **94**, doi:ARTN 10289410.1016/j.dnarep.2020.102894 (2020).
278 Maelfait, J., Bridgeman, A., Benlahrech, A., Cursi, C. & Rehwinkel, J. Restriction by SAMHD1 Limits cGAS/STING-Dependent Innate and Adaptive Immune Responses to HIV-1. *Cell Rep* **16**, 1492-1501, doi:10.1016/j.celrep.2016.07.002 (2016).
279 Gao, D. X. *et al.* Activation of cyclic GMP-AMP synthase by self-DNA causes autoimmune diseases. *P Natl Acad Sci USA* **112**, E5699-E5705, doi:10.1073/pnas.1516465112 (2015).
280 Anindya, R. Cytoplasmic DNA in cancer cells: Several pathways that potentially limit DNase2 and TREX1 activities. *Bba-Mol Cell Res* **1869**, doi:ARTN 11927810.1016/j.bbamcr.2022.119278 (2022).
281 Koyama, R. *et al.* DNase gamma, DNase I and caspase-activated DNase cooperate to degrade dead cells. *Genes Cells* **21**, 1150-1163, doi:10.1111/gtc.12433 (2016).
282 Shang, G. J., Zhang, C. G., Chen, Z. J. J., Bai, X. C. & Zhang, X. W. Cryo-EM structures of STING reveal its mechanism of activation by cyclic GMP-AMP. *Nature* **567**, 389-+, doi:DOI 10.1038/s41586-019-0998-5 (2019).
283 Ouyang, S. Y. *et al.* Structural Analysis of the STING Adaptor Protein Reveals a Hydrophobic Dimer Interface and Mode of Cyclic di-GMP Binding. *Immunity* **36**, 1073-1086, doi:10.1016/j.immuni.2012.03.019 (2012).
284 Burdette, D. L. *et al.* STING is a direct innate immune sensor of cyclic di-GMP. *Nature* **478**, 515-U111, doi:10.1038/nature10429 (2011).
285 Ergun, S. L. & Li, L. Y. Structural Insights into STING Signaling. *Trends Cell Biol* **30**, 399-407, doi:10.1016/j.tcb.2020.01.010 (2020).
286 Hussain, B. *et al.* Activation of STING Based on Its Structural Features. *Front Immunol* **13**, doi:ARTN 80860710.3389/fimmu.2022.808607 (2022).
287 Ritchie, C., Carozza, J. A. & Li, L. Y. Biochemistry, Cell Biology, and Pathophysiology of the Innate Immune cGAS-cGAMP-STING Pathway. *Annu Rev Biochem* **91**, 599-628, doi:10.1146/annurev-biochem-040320-101629 (2022).
288 Pan, J. *et al.* Current understanding of the cGAS-STING signaling pathway: Structure, regulatory mechanisms, and related diseases. *Zool Res* **44**, 183-218, doi:10.24272/j.issn.2095-8137.2022.464 (2023).
289 Ergun, S. L., Fernandez, D., Weiss, T. M. & Li, L. Y. STING Polymer Structure Reveals Mechanisms for Activation, Hyperactivation, and Inhibition. *Cell* **178**, 290-+, doi:10.1016/j.cell.2019.05.036 (2019).
290 Mukai, K. *et al.* Activation of STING requires palmitoylation at the Golgi. *Nat Commun* **7**, doi:ARTN 1193210.1038/ncomms11932 (2016).
291 Haag, S. M. *et al.* Targeting STING with covalent small-molecule inhibitors. *Nature* **559**, 269-273, doi:10.1038/s41586-018-0287-8 (2018).
292 Liu, S. *et al.* The mechanism of STING autoinhibition and activation. *Mol Cell* **83**, 1502-1518 e1510, doi:10.1016/j.molcel.2023.03.029 (2023).
293 Dobbs, N. *et al.* STING Activation by Translocation from the ER Is Associated with Infection and Autoinflammatory Disease. *Cell Host Microbe* **18**, 157-168, doi:10.1016/j.chom.2015.07.001 (2015).

294 Srikanth, S. *et al.* The Ca sensor STIM1 regulates the type I interferon response by retaining the signaling adaptor STING at the endoplasmic reticulum. *Nat Immunol* **20**, 152-+, doi:10.1038/s41590-018-0287-8 (2019).

295 Gui, X. *et al.* Autophagy induction via STING trafficking is a primordial function of the cGAS pathway. *Nature* **567**, 262-+, doi:10.1038/s41586-019-1006-9 (2019).

296 Zhang, B. C. *et al.* STEEP mediates STING ER exit and activation of signaling (vol 21, pg 868, 2020). *Nat Immunol* **21**, 1468-1469, doi:10.1038/s41590-020-0803-5 (2020).

297 Sun, M. S. *et al.* TMED2 Potentiates Cellular IFN Responses to DNA Viruses by Reinforcing MITA Dimerization and Facilitating Its Trafficking. *Cell Rep* **25**, 3086-3098 e3083, doi:10.1016/j.celrep.2018.11.048 (2018).

298 Ran, Y. *et al.* YIPF5 Is Essential for Innate Immunity to DNA Virus and Facilitates COPII-Dependent STING Trafficking (vol 203, pg 1560, 2019). *Journal of Immunology* **208**, 1310-+, doi:10.4049/jimmunol.2101093 (2022).

299 Jeltema, D., Abbott, K. & Yan, N. STING trafficking as a new dimension of immune signaling. *J Exp Med* **220**, doi:ARTN e2022099010.1084/jem.20220990 (2023).

300 Ogawa, E., Mukai, K., Saito, K., Arai, H. & Taguchi, T. The binding of TBK1 to STING requires exocytic membrane traffic from the ER. *Biochem Biophys Res Commun* **503**, 138-145, doi:10.1016/j.bbrc.2018.05.199 (2018).

301 Watkin, L. B. *et al.* COPA mutations impair ER-Golgi transport and cause hereditary autoimmune-mediated lung disease and arthritis. *Nat Genet* **47**, 654-660, doi:10.1038/ng.3279 (2015).

302 Lepelley, A. *et al.* Mutations in lead to abnormal trafficking of STING to the Golgi and interferon signaling. *J Exp Med* **217**, doi:ARTN e2020060010.1084/jem.20200600 (2020).

303 Mukai, K., Shum, A. & Taguchi, T. Homeostatic regulation of STING by retrograde membrane traffic to the ER. *Faseb J* **35**, doi:10.1096/fasebj.2021.35.S1.01855 (2021).

304 Deng, Z. M. *et al.* A defect in COPI-mediated transport of STING causes immune dysregulation in COPA syndrome. *J Exp Med* **217**, doi:ARTN e2020104510.1084/jem.20201045 (2020).

305 Steiner, A. *et al.* Deficiency in coatomer complex I causes aberrant activation of STING signalling. *Nat Commun* **13**, doi:ARTN 232110.1038/s41467-022-29946-6 (2022).

306 Chu, T. T. *et al.* Tonic prime-boost of STING signalling mediates Niemann-Pick disease type C. *Nature* **596**, 570-+, doi:10.1038/s41586-021-03762-2 (2021).

307 Liu, Y. *et al.* Clathrin-associated AP-1 controls termination of STING signalling. *Nature* **610**, 761-767, doi:10.1038/s41586-022-05354-0 (2022).

308 Liu, D. *et al.* STING directly activates autophagy to tune the innate immune response. *Cell Death and Differentiation* **26**, 1735-1749, doi:10.1038/s41418-018-0251-z (2019).

309 Prabakaran, T. *et al.* Attenuation of cGAS-STING signaling is mediated by a p62/SQSTM1-dependent autophagy pathway activated by TBK1. *Embo Journal* **37**, doi:ARTN e9785810.15252/embj.201797858 (2018).

310 Balka, K. R. *et al.* Termination of STING responses is mediated via ESCRT-dependent degradation. *Embo Journal* **42**, doi:10.15252/embj.2022112712 (2023).

311 Gentili, M. *et al.* ESCRT-dependent STING degradation inhibits steady-state and cGAMP-induced signalling. *Nat Commun* **14**, doi:ARTN 61110.1038/s41467-023-36132-9 (2023).

312 Kuchitsu, Y. *et al.* STING signalling is terminated through ESCRT-dependent microautophagy of vesicles originating from recycling endosomes. *Nature Cell Biology* **25**, 453-+, doi:10.1038/s41556-023-01098-9 (2023).

313 Zhang, C. G. *et al.* Structural basis of STING binding with and phosphorylation by TBK1. *Nature* **567**, 394-+, doi:10.1038/s41586-019-1000-2 (2019).

314 Zhao, B. *et al.* A conserved PLPLRT/SD motif of STING mediates the recruitment and activation of TBK1. *Nature* **569**, 718-722, doi:10.1038/s41586-019-1228-x (2019).

315 Liu, S. Q. *et al.* Phosphorylation of innate immune adaptor proteins MAVS, STING, and TRIF induces IRF3 activation. *Science* **347**, 1217-U1217, doi:ARTN aaa263010.1126/science.aaa2630 (2015).

316 Balka, K. R. *et al.* TBK1 and IKKepsilon Act Redundantly to Mediate STING-Induced NF-kappaB Responses in Myeloid Cells. *Cell Rep* **31**, 107492, doi:10.1016/j.celrep.2020.03.056 (2020).

317 Wegner, J., Hunkler, C., Ciupka, K., Hartmann, G. & Schlee, M. Increased IKKε protein stability ensures efficient type I interferon responses in conditions of TBK1 deficiency. *Front Immunol* **14**, 1073608, doi:10.3389/fimmu.2023.1073608 (2023).

318 Venkatraman, R. *et al.* IKKvarepsilon induces STING non-IFN immune responses via a mechanism analogous to TBK1. *iScience* **27**, 110693, doi:10.1016/j.isci.2024.110693 (2024).

319 Heinz, L. X. *et al.* TASL is the SLC15A4-associated adaptor for IRF5 activation by TLR7-9. *Nature* **581**, 316-+, doi:10.1038/s41586-020-2282-0 (2020).

320 Konno, H., Konno, K. & Barber, G. N. Cyclic dinucleotides trigger ULK1 (ATG1) phosphorylation of STING to prevent sustained innate immune signaling. *Cell* **155**, 688-698, doi:10.1016/j.cell.2013.09.049 (2013).

321 de Oliveira Mann, C. C. *et al.* Modular Architecture of the STING C-Terminal Tail Allows Interferon and NF-kappaB Signaling Adaptation. *Cell Rep* **27**, 1165-1175 e1165, doi:10.1016/j.celrep.2019.03.098 (2019).

322 Martin, M., Hiroyasu, A., Guzman, R. M., Roberts, S. A. & Goodman, A. G. Analysis of Drosophila STING Reveals an Evolutionarily Conserved Antimicrobial Function. *Cell Rep* **23**, 3537-3550 e3536, doi:10.1016/j.celrep.2018.05.029 (2018).

323 Cerboni, S. *et al.* Intrinsic antiproliferative activity of the innate sensor STING in T lymphocytes. *J Exp Med* **214**, 1769-1785, doi:10.1084/jem.20161674 (2017).

324 Su, J. *et al.* HIV-2/SIV Vpx targets a novel functional domain of STING to selectively inhibit cGAS-STING-mediated NF-kappaB signalling. *Nat Microbiol* **4**, 2552-2564, doi:10.1038/s41564-019-0585-4 (2019).

325 Yum, S., Li, M. H., Fang, Y. & Chen, Z. J. TBK1 recruitment to STING activates both IRF3 and NF-κB that mediate immune defense against tumors and viral infections. *P Natl Acad Sci USA* **118**, doi:ARTN e210022511810.1073/pnas.2100225118 (2021).

326 Fang, R. *et al.* NEMO-IKKβ Are Essential for IRF3 and NF-κB Activation in the cGAS-STING Pathway. *Journal of Immunology* **199**, 3222-3233, doi:10.4049/jimmunol.1700699 (2017).

327 Abe, T. & Barber, G. N. Cytosolic-DNA-Mediated, STING-Dependent Proinflammatory Gene Induction Necessitates Canonical NF-κB Activation through TBK1. *J Virol* **88**, 5328-5341, doi:10.1128/Jvi.00037-14 (2014).

328 Kagan, J. C., Magupalli, V. G. & Wu, H. SMOCs: supramolecular organizing centres that control innate immunity. *Nature Reviews Immunology* **14**, 821-826, doi:10.1038/nri3757 (2014).

329 Dunphy, G. *et al.* Non-canonical Activation of the DNA Sensing Adaptor STING by ATM and IFI16 Mediates NF-κB Signaling after Nuclear DNA Damage. *Mol Cell* **71**, 745-+, doi:10.1016/j.molcel.2018.07.034 (2018).

330 Fischer, T. D. *et al.* STING induces HOIP-mediated synthesis of M1 ubiquitin chains to stimulate NF-kappaB signaling. *EMBO J* **44**, 141-165, doi:10.1038/s44318-024-00291-2 (2025).

331 Hou, Y. Z. *et al.* Non-canonical NF-κB Antagonizes STING Sensor-Mediated DNA Sensing in Radiotherapy. *Immunity* **49**, 490-+, doi:10.1016/j.immuni.2018.07.008 (2018).

332 Bakhoum, S. *et al.* Chromosomal Instability Drives Metastasis Through a Cytosolic DNA Response. *Int J Radiat Oncol* **102**, S118-S118, doi:DOI 10.1016/j.ijrobp.2018.06.295 (2018).

333 Lin, W. *et al.* STING trafficking activates MAPK-CREB signaling to trigger regulatory T cell differentiation. *P Natl Acad Sci USA* **121**, doi:ARTN e232070912110.1073/pnas.2320709121 (2024).

334 Lau, R. K. *et al.* Structure and Mechanism of a Cyclic Trinucleotide-Activated Bacterial Endonuclease Mediating Bacteriophage Immunity. *Mol Cell* **77**, 723-733 e726, doi:10.1016/j.molcel.2019.12.010 (2020).
335 Whiteley, A. T. *et al.* Bacterial cGAS-like enzymes synthesize diverse nucleotide signals. *Nature* **567**, 194-199, doi:10.1038/s41586-019-0953-5 (2019).
336 Gehrke, N. *et al.* Oxidative damage of DNA confers resistance to cytosolic nuclease TREX1 degradation and potentiates STING-dependent immune sensing. *Immunity* **39**, 482-495, doi:10.1016/j.immuni.2013.08.004 (2013).
337 Wu, J. & Chen, Z. J. Innate immune sensing and signaling of cytosolic nucleic acids. *Annu Rev Immunol* **32**, 461-488, doi:10.1146/annurev-immunol-032713-120156 (2014).
338 Li, X. D. *et al.* Pivotal roles of cGAS-cGAMP signaling in antiviral defense and immune adjuvant effects. *Science* **341**, 1390-1394, doi:10.1126/science.1244040 (2013).
339 Lio, C. W. *et al.* cGAS-STING Signaling Regulates Initial Innate Control of Cytomegalovirus Infection. *J Virol* **90**, 7789-7797, doi:10.1128/JVI.01040-16 (2016).
340 Paijo, J. *et al.* cGAS Senses Human Cytomegalovirus and Induces Type I Interferon Responses in Human Monocyte-Derived Cells. *PLoS Pathog* **12**, e1005546, doi:10.1371/journal.ppat.1005546 (2016).
341 Lam, E., Stein, S. & Falck-Pedersen, E. Adenovirus detection by the cGAS/STING/TBK1 DNA sensing cascade. *J Virol* **88**, 974-981, doi:10.1128/JVI.02702-13 (2014).
342 Ishikawa, H., Ma, Z. & Barber, G. N. STING regulates intracellular DNA-mediated, type I interferon-dependent innate immunity. *Nature* **461**, 788-792, doi:10.1038/nature08476 (2009).
343 Thomsen, M. K. *et al.* Lack of immunological DNA sensing in hepatocytes facilitates hepatitis B virus infection. *Hepatology* **64**, 746-759, doi:10.1002/hep.28685 (2016).
344 Gao, D. X. *et al.* Cyclic GMP-AMP Synthase Is an Innate Immune Sensor of HIV and Other Retroviruses. *Science* **341**, 903-906, doi:10.1126/science.1240933 (2013).
345 Lahaye, X. *et al.* NONO Detects the Nuclear HIV Capsid to Promote cGAS-Mediated Innate Immune Activation. *Cell* **175**, 488-501 e422, doi:10.1016/j.cell.2018.08.062 (2018).
346 Yoh, S. M. *et al.* PQBP1 Is a Proximal Sensor of the cGAS-Dependent Innate Response to HIV-1. *Cell* **161**, 1293-1305, doi:10.1016/j.cell.2015.04.050 (2015).
347 Lian, H. *et al.* ZCCHC3 is a co-sensor of cGAS for dsDNA recognition in innate immune response. *Nat Commun* **9**, doi:ARTN 334910.1038/s41467-018-05559-w (2018).
348 Liu, Z. S. *et al.* G3BP1 promotes DNA binding and activation of cGAS. *Nat Immunol* **20**, 18-28, doi:10.1038/s41590-018-0262-4 (2019).
349 Domizio, J. D. *et al.* The cGAS-STING pathway drives type I IFN immunopathology in COVID-19. *Nature* **603**, 145-151, doi:10.1038/s41586-022-04421-w (2022).
350 Aguirre, S. *et al.* Dengue virus NS2B protein targets cGAS for degradation and prevents mitochondrial DNA sensing during infection. *Nat Microbiol* **2**, 17037, doi:10.1038/nmicrobiol.2017.37 (2017).
351 You, F. P. *et al.* ELF4 is critical for induction of type I interferon and the host antiviral response. *Nat Immunol* **14**, 1237-+, doi:10.1038/ni.2756 (2013).
352 Liu, H. S. *et al.* Innate sensing of picornavirus infection involves cGAS-STING-mediated antiviral responses triggered by mitochondrial DNA release. *Plos Pathogens* **19**, doi:ARTN e101113210.1371/journal.ppat.1011132 (2023).
353 Watson, R. O. *et al.* The Cytosolic Sensor cGAS Detects Mycobacterium tuberculosis DNA to Induce Type I Interferons and Activate Autophagy. *Cell Host Microbe* **17**, 811-819, doi:10.1016/j.chom.2015.05.004 (2015).
354 Liu, N. X., Pang, X. X., Zhang, H. & Ji, P. The cGAS-STING Pathway in Bacterial Infection and Bacterial Immunity. *Front Immunol* **12**, doi:ARTN 81470910.3389/fimmu.2021.814709 (2022).
355 Place, D. E. *et al.* Interferon inducible GBPs restrict motility induced cell-cell fusion. *Plos Pathogens* **16**, doi:ARTN e100836410.1371/journal.ppat.1008364 (2020).

356 Ku, J. W. K. *et al.* Bacterial-induced cell fusion is a danger signal triggering cGAS-STING pathway via micronuclei formation. *P Natl Acad Sci USA* **117**, 15923-15934, doi:10.1073/pnas.2006908117 (2020).
357 Whiteley, L. *et al.* Entry, Intracellular Survival, and Multinucleated-Giant-Cell-Forming Activity of Burkholderia pseudomallei in Human Primary Phagocytic and Nonphagocytic Cells. *Infect Immun* **85**, doi:10.1128/IAI.00468-17 (2017).
358 Barker, J. R. *et al.* STING-Dependent Recognition of Cyclic di-AMP Mediates Type I Interferon Responses during Infection. *Mbio* **4**, doi:ARTN e00018-1310.1128/mBio.00018-13 (2013).
359 Collins, A. C. *et al.* Cyclic GMP-AMP Synthase Is an Innate Immune DNA Sensor for. *Cell Host Microbe* **17**, 820-828, doi:10.1016/j.chom.2015.05.005 (2015).
360 Xu, L. *et al.* Salmonella Induces the cGAS-STING-Dependent Type I Interferon Response in Murine Macrophages by Triggering mtDNA Release. *Mbio* **13**, doi:10.1128/mbio.03632-21 (2022).
361 Dooyema, S. *et al.* Actively Suppress Innate Immune Nucleic Acid Receptor Signaling. *Gastroenterology* **158**, S568-S568 (2020).
362 Deng, L. *et al.* STING-Dependent Cytosolic DNA Sensing Promotes Radiation-Induced Type I Interferon-Dependent Antitumor Immunity in Immunogenic Tumors. *Immunity* **41**, 843-852, doi:10.1016/j.immuni.2014.10.019 (2014).
363 Diamond, J. M. *et al.* Exosomes Shuttle TREX1-Sensitive IFN-Stimulatory dsDNA from Irradiated Cancer Cells to DCs. *Cancer Immunol Res* **6**, 910-920, doi:10.1158/2326-6066.CIR-17-0581 (2018).
364 Xu, M. M. *et al.* Dendritic Cells but Not Macrophages Sense Tumor Mitochondrial DNA for Cross-priming through Signal Regulatory Protein alpha Signaling. *Immunity* **47**, 363-373 e365, doi:10.1016/j.immuni.2017.07.016 (2017).
365 Li, F. *et al.* Simultaneous Activation of Immunogenic Cell Death and cGAS-STING Pathway by Liver- and Mitochondria-Targeted Gold(I) Complexes for Chemoimmunotherapy of Hepatocellular Carcinoma. *J Med Chem* **67**, 1982-2003, doi:10.1021/acs.jmedchem.3c01785 (2024).
366 King, K. R. *et al.* IRF3 and type I interferons fuel a fatal response to myocardial infarction. *Nat Med* **23**, 1481-1487, doi:10.1038/nm.4428 (2017).
367 Marichal, T. *et al.* DNA released from dying host cells mediates aluminum adjuvant activity. *Nat Med* **17**, 996-1002, doi:10.1038/nm.2403 (2011).
368 Lood, C. *et al.* Neutrophil extracellular traps enriched in oxidized mitochondrial DNA are interferogenic and contribute to lupus-like disease. *Nat Med* **22**, 146-153, doi:10.1038/nm.4027 (2016).
369 Kawane, K. *et al.* Chronic polyarthritis caused by mammalian DNA that escapes from degradation in macrophages. *Nature* **443**, 998-1002, doi:10.1038/nature05245 (2006).
370 Krieser, R. J. *et al.* Deoxyribonuclease IIα is required during the phagocytic phase of apoptosis and its loss causes perinatal lethality. *Cell Death and Differentiation* **9**, 956-962, doi:10.1038/sj.cdd.4401056 (2002).
371 Kawane, K. *et al.* Requirement of DNase II for definitive erythropoiesis in the mouse fetal liver. *Science* **292**, 1546-1549, doi:10.1126/science.292.5521.1546 (2001).
372 Chang, H. C. & Liao, T. H. Reassociation of deoxyribonuclease II with the lysosomal membrane isolated from porcine spleen. *Arch Biochem Biophys* **280**, 320-324, doi:10.1016/0003-9861(90)90336-w (1990).
373 Kawane, K. *et al.* Impaired thymic development in mouse embryos deficient in apoptotic DNA degradation. *Nat Immunol* **4**, 138-144, doi:10.1038/ni881 (2003).
374 Yoshida, H., Okabe, Y., Kawane, K., Fukuyama, H. & Nagata, S. Lethal anemia caused by interferon-beta produced in mouse embryos carrying undigested DNA. *Nat Immunol* **6**, 49-56, doi:10.1038/ni1146 (2005).
375 Baum, R. *et al.* Synergy between Hematopoietic and Radioresistant Stromal Cells Is Required for Autoimmune Manifestations of DNase II IFNaR Mice. *Journal of Immunology* **196**, 1348-1354, doi:10.4049/jimmunol.1502130 (2016).

376 Rodero, M. P. *et al.* Type I interferon-mediated autoinflammation due to DNase II deficiency. *Nat Commun* **8**, doi:ARTN 217610.1038/s41467-017-01932-3 (2017).

377 Mazur, D. J. & Perrino, F. W. Identification and expression of the TREX1 and TREX2 cDNA sequences encoding mammalian 3'-->5' exonucleases. *J Biol Chem* **274**, 19655-19660, doi:10.1074/jbc.274.28.19655 (1999).

378 Morita, M. *et al.* Gene-targeted mice lacking the Trex1 (DNase III) 3'-->5' DNA exonuclease develop inflammatory myocarditis. *Mol Cell Biol* **24**, 6719-6727, doi:10.1128/MCB.24.15.6719-6727.2004 (2004).

379 Yang, Y. G., Lindahl, T. & Barnes, D. E. Trex1 exonuclease degrades ssDNA to prevent chronic checkpoint activation and autoimmune disease. *Cell* **131**, 873-886, doi:10.1016/j.cell.2007.10.017 (2007).

380 Gall, A. *et al.* Autoimmunity initiates in nonhematopoietic cells and progresses via lymphocytes in an interferon-dependent autoimmune disease. *Immunity* **36**, 120-131, doi:10.1016/j.immuni.2011.11.018 (2012).

381 Gray, E. E., Treuting, P. M., Woodward, J. J. & Stetson, D. B. Cutting Edge: cGAS Is Required for Lethal Autoimmune Disease in the Trex1-Deficient Mouse Model of Aicardi-Goutieres Syndrome. *Journal of Immunology* **195**, 1939-1943, doi:10.4049/jimmunol.1500969 (2015).

382 Stetson, D. B., Ko, J. S., Heidmann, T. & Medzhitov, R. Trex1 prevents cell-intrinsic initiation of autoimmunity. *Cell* **134**, 587-598, doi:10.1016/j.cell.2008.06.032 (2008).

383 Rice, G. I., Rodero, M. P. & Crow, Y. J. Human Disease Phenotypes Associated With Mutations in. *J Clin Immunol* **35**, 235-243, doi:10.1007/s10875-015-0147-3 (2015).

384 Crow, Y. J. *et al.* Mutations in the gene encoding the 3′-5′ DNA exonuclease TREX1 cause Aicardi-Goutieres syndrome at the locus. *Nature Genetics* **38**, 917-920, doi:10.1038/ng1845 (2006).

385 Napirei, M. *et al.* Features of systemic lupus erythematosus in Dnase1-deficient mice. *Nature Genetics* **25**, 177-181, doi:Doi 10.1038/76032 (2000).

386 Yasutomo, K. *et al.* Mutation of DNASE1 in people with systemic lupus erythematosus. *Nat Genet* **28**, 313-314, doi:10.1038/91070 (2001).

387 Sisirak, V. *et al.* Digestion of Chromatin in Apoptotic Cell Microparticles Prevents Autoimmunity. *Cell* **166**, 88-101, doi:10.1016/j.cell.2016.05.034 (2016).

388 Al-Mayouf, S. M. *et al.* Loss-of-function variant in DNASE1L3 causes a familial form of systemic lupus erythematosus. *Nat Genet* **43**, 1186-1188, doi:10.1038/ng.975 (2011).

389 White, M. J. *et al.* Apoptotic caspases suppress mtDNA-induced STING-mediated type I IFN production. *Cell* **159**, 1549-1562, doi:10.1016/j.cell.2014.11.036 (2014).

390 Rongvaux, A. *et al.* Apoptotic caspases prevent the induction of type I interferons by mitochondrial DNA. *Cell* **159**, 1563-1577, doi:10.1016/j.cell.2014.11.037 (2014).

391 Victorelli, S. *et al.* Apoptotic stress causes mtDNA release during senescence and drives the SASP. *Nature* **622**, 627-636, doi:10.1038/s41586-023-06621-4 (2023).

392 Yu, C. H. *et al.* TDP-43 Triggers Mitochondrial DNA Release via mPTP to Activate cGAS/STING in ALS. *Cell* **183**, 636-649 e618, doi:10.1016/j.cell.2020.09.020 (2020).

393 Kim, J. *et al.* VDAC oligomers form mitochondrial pores to release mtDNA fragments and promote lupus-like disease. *Science* **366**, 1531-1536, doi:10.1126/science.aav4011 (2019).

394 García, N. & Chávez, E. Mitochondrial DNA fragments released through the permeability transition pore correspond to specific gene size. *Life Sci* **81**, 1160-1166, doi:10.1016/j.lfs.2007.08.019 (2007).

395 West, A. P. *et al.* Mitochondrial DNA stress primes the antiviral innate immune response. *Nature* **520**, 553-557, doi:10.1038/nature14156 (2015).

396 Torres-Odio, S. *et al.* Loss of Mitochondrial Protease CLPP Activates Type I IFN Responses through the Mitochondrial DNA-cGAS-STING Signaling Axis. *Journal of Immunology* **206**, 1890-1900, doi:10.4049/jimmunol.2001016 (2021).

397 Wu, Z. *et al.* Mitochondrial DNA Stress Signalling Protects the Nuclear Genome. *Nat Metab* **1**, 1209-1218, doi:10.1038/s42255-019-0150-8 (2019).

398 Zecchini, V. *et al.* Fumarate induces vesicular release of mtDNA to drive innate immunity. *Nature* **615**, 499-506, doi:10.1038/s41586-023-05770-w (2023).
399 Aarreberg, L. D. *et al.* Interleukin-1β Induces mtDNA Release to Activate Innate Immune Signaling via cGAS-STING. *Mol Cell* **74**, 801-+, doi:10.1016/j.molcel.2019.02.038 (2019).
400 Ho, S. S. W. *et al.* The DNA Structure-Specific Endonuclease MUS81 Mediates DNA Sensor STING-Dependent Host Rejection of Prostate Cancer Cells. *Immunity* **44**, 1177-1189, doi:10.1016/j.immuni.2016.04.010 (2016).
401 Donne, R. *et al.* Replication stress triggered by nucleotide pool imbalance drives DNA damage and cGAS-STING pathway activation in NAFLD. *Dev Cell* **57**, 1728-1741 e1726, doi:10.1016/j.devcel.2022.06.003 (2022).
402 Li, S. *et al.* Cytosolic DNA sensing by cGAS/STING promotes TRPV2-mediated Ca(2+) release to protect stressed replication forks. *Mol Cell* **83**, 556-573 e557, doi:10.1016/j.molcel.2022.12.034 (2023).
403 Shen, Y. J. *et al.* Genome-derived cytosolic DNA mediates type I interferon-dependent rejection of B cell lymphoma cells. *Cell Rep* **11**, 460-473, doi:10.1016/j.celrep.2015.03.041 (2015).
404 Erdal, E., Haider, S., Rehwinkel, J., Harris, A. L. & McHugh, P. J. A prosurvival DNA damage-induced cytoplasmic interferon response is mediated by end resection factors and is limited by Trex1. *Gene Dev* **31**, 353-369, doi:10.1101/gad.289769.116 (2017).
405 Hartlova, A. *et al.* DNA damage primes the type I interferon system via the cytosolic DNA sensor STING to promote anti-microbial innate immunity. *Immunity* **42**, 332-343, doi:10.1016/j.immuni.2015.01.012 (2015).
406 Coquel, F., Neumayer, C., Lin, Y. L. & Pasero, P. SAMHD1 and the innate immune response to cytosolic DNA during DNA replication. *Curr Opin Immunol* **56**, 24-30, doi:10.1016/j.coi.2018.09.017 (2019).
407 Bhattacharya, S. *et al.* RAD51 interconnects between DNA replication, DNA repair and immunity. *Nucleic Acids Res* **45**, 4590-4605, doi:10.1093/nar/gkx126 (2017).
408 Glück, S. *et al.* Innate immune sensing of cytosolic chromatin fragments through cGAS promotes senescence. *Nature Cell Biology* **19**, 1061-+, doi:10.1038/ncb3586 (2017).
409 Dou, Z. *et al.* Cytoplasmic chromatin triggers inflammation in senescence and cancer. *Nature* **550**, 402-406, doi:10.1038/nature24050 (2017).
410 Wiseman, H. & Halliwell, B. Damage to DNA by reactive oxygen and nitrogen species: role in inflammatory disease and progression to cancer. *Biochem J* **313 (Pt 1)**, 17-29, doi:10.1042/bj3130017 (1996).
411 Ahn, J. *et al.* Inflammation-driven carcinogenesis is mediated through STING. *Nat Commun* **5**, doi:ARTN 516610.1038/ncomms6166 (2014).
412 Harding, S. M. *et al.* Mitotic progression following DNA damage enables pattern recognition within micronuclei. *Nature* **548**, 466-+, doi:10.1038/nature23470 (2017).
413 Gratia, M. *et al.* Bloom syndrome protein restrains innate immune sensing of micronuclei by cGAS. *J Exp Med* **216**, 1199-1213, doi:10.1084/jem.20181329 (2019).
414 Heijink, A. M. *et al.* BRCA2 deficiency instigates cGAS-mediated inflammatory signaling and confers sensitivity to tumor necrosis factor-alpha-mediated cytotoxicity. *Nat Commun* **10**, 100, doi:10.1038/s41467-018-07927-y (2019).
415 Wang, Z. *et al.* cGAS/STING axis mediates a topoisomerase II inhibitor-induced tumor immunogenicity. *J Clin Invest* **129**, 4850-4862, doi:10.1172/JCI127471 (2019).
416 Shen, J. *et al.* PARPi Triggers the STING-Dependent Immune Response and Enhances the Therapeutic Efficacy of Immune Checkpoint Blockade Independent of BRCAness. *Cancer Res* **79**, 311-319, doi:10.1158/0008-5472.CAN-18-1003 (2019).
417 Sato, Y. & Hayash, M. Micronucleus is not a potent inducer of the cGAS/STING pathway. *Life Sci Alliance* **7**, doi:ARTN e20230242410.26508/lsa.202302424 (2024).
418 Takaki, T., Millar, R., Hiley, C. T. & Boulton, S. J. Micronuclei induced by radiation, replication stress, or chromosome segregation errors do not activate cGAS-STING. *Mol Cell* **84**, doi:10.1016/j.molcel.2024.04.017 (2024).

419 Reijns, M. A. M. *et al.* Enzymatic Removal of Ribonucleotides from DNA Is Essential for Mammalian Genome Integrity and Development. *Cell* **149**, doi:10.1016/j.cell.2012.04.011 (2012).
420 Hiller, B. *et al.* Mammalian RNase H2 removes ribonucleotides from DNA to maintain genome integrity. *J Exp Med* **209**, 1419-1426, doi:10.1084/jem.20120876 (2012).
421 Pokatayev, V. *et al.* RNase H2 catalytic core Aicardi-Goutieres syndrome-related mutant invokes cGAS-STING innate immune-sensing pathway in mice. *J Exp Med* **213**, 329-336, doi:10.1084/jem.20151464 (2016).
422 Crow, Y. J. & Manel, N. Aicardi-Goutieres syndrome and the type I interferonopathies. *Nat Rev Immunol* **15**, 429-440, doi:10.1038/nri3850 (2015).
423 Bartsch, K. *et al.* Absence of RNase H2 triggers generation of immunogenic micronuclei removed by autophagy. *Hum Mol Genet* **26**, 3960-3972, doi:10.1093/hmg/ddx283 (2017).
424 Kretschmer, S. *et al.* SAMHD1 prevents autoimmunity by maintaining genome stability. *Ann Rheum Dis* **74**, doi:ARTN e1710.1136/annrheumdis-2013-204845 (2015).
425 Franzolin, E. *et al.* The deoxynucleotide triphosphohydrolase SAMHD1 is a major regulator of DNA precursor pools in mammalian cells. *P Natl Acad Sci USA* **110**, 14272-14277, doi:10.1073/pnas.1312033110 (2013).
426 Thomas, C. A. *et al.* Modeling of TREX1-Dependent Autoimmune Disease using Human Stem Cells Highlights L1 Accumulation as a Source of Neuroinflammation. *Cell Stem Cell* **21**, 319-+, doi:10.1016/j.stem.2017.07.009 (2017).
427 De Cecco, M. *et al.* L1 drives IFN in senescent cells and promotes age-associated inflammation. *Nature* **566**, 73-78, doi:10.1038/s41586-018-0784-9 (2019).
428 Niu, Y. *et al.* Disrupting endogenous retroelements with a reverse transcriptase inhibitor alleviates DSS-induced colitis in mice. *Mucosal Immunol*, doi:10.1016/j.mucimm.2023.10.004 (2023).
429 Lima-Junior, D. S. *et al.* Endogenous retroviruses promote homeostatic and inflammatory responses to the microbiota. *Cell* **184**, 3794-3811 e3719, doi:10.1016/j.cell.2021.05.020 (2021).
430 Crow, Y. J. Type I interferonopathies: a novel set of inborn errors of immunity. *Ann Ny Acad Sci* **1238**, 91-98, doi:10.1111/j.1749-6632.2011.06220.x (2011).
431 Okude, H., Ori, D. & Kawai, T. Signaling Through Nucleic Acid Sensors and Their Roles in Inflammatory Diseases. *Front Immunol* **11**, doi:ARTN 62583310.3389/fimmu.2020.625833 (2021).
432 Crow, Y. J. & Stetson, D. B. The type I interferonopathies: 10 years on. *Nature Reviews Immunology* **22**, 471-483, doi:10.1038/s41577-021-00633-9 (2022).
433 Crowl, J. T., Gray, E. E., Pestal, K., Volkman, H. E. & Stetson, D. B. Intracellular Nucleic Acid Detection in Autoimmunity. *Annu Rev Immunol* **35**, 313-336, doi:10.1146/annurev-immunol-051116-052331 (2017).
434 Lee-Kirsch, M. A. The Type I Interferonopathies. *Annu Rev Med* **68**, 297-315, doi:10.1146/annurev-med-050715-104506 (2017).
435 Kong, L. Z. *et al.* Understanding nucleic acid sensing and its therapeutic applications. *Exp Mol Med* **55**, 2320-2331, doi:10.1038/s12276-023-01118-6 (2023).
436 Ablasser, A. & Hur, S. Regulation of cGAS- and RLR-mediated immunity to nucleic acids. *Nat Immunol* **21**, 17-29, doi:10.1038/s41590-019-0556-1 (2020).
437 Hopfner, K. P. & Hornung, V. Molecular mechanisms and cellular functions of cGAS-STING signalling. *Nat Rev Mol Cell Bio* **21**, 501-521, doi:10.1038/s41580-020-0244-x (2020).
438 Rice, G. I. *et al.* Mutations involved in Aicardi-Goutieres syndrome implicate SAMHD1 as regulator of the innate immune response. *Nature Genetics* **41**, 829-U889, doi:10.1038/ng.373 (2009).
439 Rice, G. I. *et al.* Assessment of interferon-related biomarkers in Aicardi-Goutières syndrome associated with mutations in TREX1, RNASEH2A, RNASEH2B, RNASEH2C, SAMHD1, and ADAR: a case-control study. *Lancet Neurol* **12**, 1159-1169, doi:10.1016/S1474-4422(13)70258-8 (2013).

440 Giordano, A. M. S. *et al.* DNA damage contributes to neurotoxic inflammation in Aicardi-Goutieres syndrome astrocytes. *J Exp Med* **219**, doi:ARTN e2021112110.1084/jem.20211121 (2022).

441 Zhao, K. *et al.* Modulation of LINE-1 and Alu/SVA Retrotransposition by Aicardi-Goutieres Syndrome-Related SAMHD1. *Cell Reports* **4**, 1108-1115, doi:10.1016/j.celrep.2013.08.019 (2013).

442 Liu, Y. *et al.* Activated STING in a vascular and pulmonary syndrome. *N Engl J Med* **371**, 507-518, doi:10.1056/NEJMoa1312625 (2014).

443 Crow, Y. J. & Casanova, J. L. STING-Associated Vasculopathy with Onset in Infancy - A New Interferonopathy. *New Engl J Med* **371**, 568-571, doi:10.1056/NEJMe1407246 (2014).

444 Ladoux, C., Pasquet, M., Crow, Y. J., Frémond, M. L. & Roditis, L. STING-Associated Vasculopathy with Onset in infancy (SAVI) Presenting as Massive Intra Alveolar Hemorrhage. *J Clin Immunol* **43**, 699-702, doi:10.1007/s10875-023-01431-9 (2023).

445 Rice, G. *et al.* Heterozygous mutations in TREX1 cause familial chilblain lupus and dominant Aicardi-Goutieres syndrome. *Am J Hum Genet* **80**, 811-815, doi:10.1086/513443 (2007).

446 Ravenscroft, J. C., Suri, M., Rice, G. I., Szynkiewicz, M. & Crow, Y. J. Autosomal Dominant Inheritance of a Heterozygous Mutation in Causing Familial Chilblain Lupus. *Am J Med Genet A* **155a**, 235-237, doi:10.1002/ajmg.a.33778 (2011).

447 Günther, C., Meurer, M., Stein, A., Viehweg, A. & Lee-Kirsch, M. Familial chilblain lupus - a monogenic form of cutaneous lupus erythematosus due to a heterozygous mutation in TREX1. *J Invest Dermatol* **129**, S50-S50 (2009).

448 König, N. *et al.* Familial chilblain lupus due to a gain-of-function mutation in STING. *Ann Rheum Dis* **76**, 468-472, doi:10.1136/annrheumdis-2016-209841 (2017).

449 Lee-Kirsch, M. A. *et al.* Familial chilblain lupus, a monogenic form of cutaneous lupus erythematosus, maps to chromosome 3p. *Am J Hum Genet* **79**, 731-737, doi:10.1086/507848 (2006).

450 Vece, T. J. *et al.* Copa Syndrome: a Novel Autosomal Dominant Immune Dysregulatory Disease. *J Clin Immunol* **36**, 377-387, doi:10.1007/s10875-016-0271-8 (2016).

451 Alsohime, F. *et al.* JAK Inhibitor Therapy in a Child with Inherited USP18 Deficiency. *N Engl J Med* **382**, 256-265, doi:10.1056/NEJMoa1905633 (2020).

452 Meuwissen, M. E. *et al.* Human USP18 deficiency underlies type 1 interferonopathy leading to severe pseudo-TORCH syndrome. *J Exp Med* **213**, 1163-1174, doi:10.1084/jem.20151529 (2016).

453 Kaul, A. *et al.* Systemic lupus erythematosus. *Nat Rev Dis Primers* **2**, 16039, doi:10.1038/nrdp.2016.39 (2016).

454 Inoue, K., Ishizawa, M. & Kubota, T. Monoclonal anti-dsDNA antibody 2C10 escorts DNA to intracellular DNA sensors in normal mononuclear cells and stimulates secretion of multiple cytokines implicated in lupus pathogenesis. *Clin Exp Immunol* **199**, 150-162, doi:10.1111/cei.13382 (2020).

455 Gerovska, D. & Arauzo-Bravo, M. J. Systemic Lupus Erythematosus Patients with DNASE1L3 Deficiency Have a Distinctive and Specific Genic Circular DNA Profile in Plasma. *Cells* **12**, doi:ARTN 106110.3390/cells12071061 (2023).

456 Yasutomo, K. *et al.* Mutation of DNASE1 in people with systemic lupus erythematosus. *Nature Genetics* **28**, 313-314, doi:Doi 10.1038/91070 (2001).

457 Namjou, B. *et al.* Evaluation of the TREX1 gene in a large multi-ancestral lupus cohort. *Genes Immun* **12**, 270-279, doi:10.1038/gene.2010.73 (2011).

458 Banchereau, J. & Pascual, V. Type I interferon in systemic lupus erythematosus and other autoimmune diseases. *Immunity* **25**, 383-392, doi:10.1016/j.immuni.2006.08.010 (2006).

459 Bennett, L. *et al.* Interferon and granulopoiesis signatures in systemic lupus erythematosus blood. *J Exp Med* **197**, 711-723, doi:10.1084/jem.20021553 (2003).

460 Swaak, A. J., Groenwold, J., Aarden, L. A., Statius van Eps, L. W. & Feltkamp, E. W. Prognostic value of anti-dsDNA in SLE. *Ann Rheum Dis* **41**, 388-395, doi:10.1136/ard.41.4.388 (1982).
461 Hooks, J. J. *et al.* Immune interferon in the circulation of patients with autoimmune disease. *N Engl J Med* **301**, 5-8, doi:10.1056/NEJM197907053010102 (1979).
462 Lande, R. *et al.* Neutrophils Activate Plasmacytoid Dendritic Cells by Releasing Self-DNA-Peptide Complexes in Systemic Lupus Erythematosus. *Sci Transl Med* **3**, doi:ARTN 73ra1910.1126/scitranslmed.3001180 (2011).

463 Gkirtzimanaki, K. *et al.* IFNα Impairs Autophagic Degradation of mtDNA Promoting Autoreactivity of SLE Monocytes in a STING-Dependent Fashion. *Cell Reports* **25**, 921-+, doi:10.1016/j.celrep.2018.09.001 (2018).
464 Kato, Y. *et al.* Apoptosis-derived membrane vesicles drive the cGAS-STING pathway and enhance type I IFN production in systemic lupus erythematosus. *Ann Rheum Dis* **77**, 1507-1515, doi:10.1136/annrheumdis-2018-212988 (2018).
465 Sharma, S. *et al.* Suppression of systemic autoimmunity by the innate immune adaptor STING. *P Natl Acad Sci USA* **112**, E710-E717, doi:10.1073/pnas.1420217112 (2015).
466 Motwani, M. *et al.* cGAS-STING Pathway Does Not Promote Autoimmunity in Murine Models of SLE. *Front Immunol* **12**, doi:ARTN 60593010.3389/fimmu.2021.605930 (2021).

467 Sun, X. *et al.* Targeting STING in dendritic cells alleviates psoriatic inflammation by suppressing IL-17A production. *Cell Mol Immunol* **21**, 738-751, doi:10.1038/s41423-024-01160-y (2024).
468 Yu, Y. *et al.* Cytosolic DNA–Mediated STING-Dependent Inflammation Contributes to the Progression of Psoriasis. *J Invest Dermatol* **142**, 898-906 e894, doi:10.1016/j.jid.2021.08.430 (2022).
469 Willemsen, J. *et al.* TNF leads to mtDNA release and cGAS/STING-dependent interferon responses that support inflammatory arthritis. *Cell Reports* **37**, doi:ARTN 10997710.1016/j.celrep.2021.109977 (2021).

470 Li, R. R. *et al.* signaling in the regulation of rheumatoid synovial aggression. *Ann Transl Med* **10**, doi:ARTN 43110.21037/atm-21-4533 (2022).

471 Wang, Y., Su, G. H., Zhang, F., Chu, J. X. & Wang, Y. S. Cyclic GMP-AMP Synthase Is Required for Cell Proliferation and Inflammatory Responses in Rheumatoid Arthritis Synoviocytes. *Mediat Inflamm* **2015**, doi:Artn 19232910.1155/2015/192329 (2015).

472 Li, X. H. *et al.* Activation of the STING-IRF3 pathway involved in psoriasis with diabetes mellitus. *J Cell Mol Med* **26**, 2139-2151, doi:10.1111/jcmm.17236 (2022).
473 Li, Y. B. *et al.* Plasma-derived DNA containing-extracellular vesicles induce STING-mediated proinflammatory responses in dermatomyositis. *Theranostics* **11**, 7144-7158, doi:10.7150/thno.59152 (2021).
474 Paul, S. *et al.* Centromere defects, chromosome instability, and cGAS-STING activation in systemic sclerosis. *Nat Commun* **13**, 7074, doi:10.1038/s41467-022-34775-8 (2022).
475 Patel, S. *et al.* The common R71H-G230A-R293Q human is a null allele (vol 198, pg 776, 2017). *Journal of Immunology* **198**, 4547-4547, doi:10.4049/jimmunol.1700477 (2017).

476 Jin, L. *et al.* Identification and characterization of a loss-of-function human MPYS variant. *Genes Immun* **12**, 263-269, doi:10.1038/gene.2010.75 (2011).
477 Wang, Y., Wang, F. & Zhang, X. L. STING-associated vasculopathy with onset in infancy: a familial case series report and literature review. *Ann Transl Med* **9**, doi:ARTN 17610.21037/atm-20-6198 (2021).

478 Li, J., An, S. & Du, Z. Familial Interstitial Lung Disease Caused by Mutation of the STING1 Gene. *Front Pediatr* **8**, 543, doi:10.3389/fped.2020.00543 (2020).

479 Konno, H. *et al.* Pro-inflammation Associated with a Gain-of-Function Mutation (R284S) in the Innate Immune Sensor STING. *Cell Rep* **23**, 1112-1123, doi:10.1016/j.celrep.2018.03.115 (2018).
480 Wang, Y., Wang, F. & Zhang, X. STING-associated vasculopathy with onset in infancy: a familial case series report and literature review. *Ann Transl Med* **9**, 176, doi:10.21037/atm-20-6198 (2021).
481 Patel, S. & Jin, L. TMEM173 variants and potential importance to human biology and disease. *Genes Immun* **20**, 82-89, doi:10.1038/s41435-018-0029-9 (2019).
482 Lin, B. *et al.* Case Report: Novel SAVI-Causing Variants in STING1 Expand the Clinical Disease Spectrum and Suggest a Refined Model of STING Activation. *Front Immunol* **12**, 636225, doi:10.3389/fimmu.2021.636225 (2021).
483 Fremond, M. L. & Crow, Y. J. STING-Mediated Lung Inflammation and Beyond. *J Clin Immunol* **41**, 501-514, doi:10.1007/s10875-021-00974-z (2021).
484 Jeremiah, N. *et al.* Inherited STING-activating mutation underlies a familial inflammatory syndrome with lupus-like manifestations. *Journal of Clinical Investigation* **124**, 5516-5520, doi:10.1172/Jci79100 (2014).
485 Picard, C. *et al.* Severe Pulmonary Fibrosis as the First Manifestation of Interferonopathy (Mutation). *Chest* **150**, E65-E71, doi:10.1016/j.chest.2016.02.682 (2016).
486 Munoz, J. *et al.* Stimulator of Interferon Genes-Associated Vasculopathy With Onset in Infancy A Mimic of Childhood Granulomatosis With Polyangiitis. *Jama Dermatol* **151**, 872-877, doi:10.1001/jamadermatol.2015.0251 (2015).
487 Chia, J. *et al.* Failure to thrive, interstitial lung disease, and progressive digital necrosis with onset in infancy. *J Am Acad Dermatol* **74**, 186-189, doi:10.1016/j.jaad.2015.10.007 (2016).
488 Fremond, M. L. *et al.* Efficacy of the Janus kinase 1/2 inhibitor ruxolitinib in the treatment of vasculopathy associated with TMEM173-activating mutations in 3 children. *J Allergy Clin Immunol* **138**, 1752-1755, doi:10.1016/j.jaci.2016.07.015 (2016).
489 Rodero, M. P., Fremond, M. L., Rice, G. I., Neven, B. & Crow, Y. J. JAK inhibition in STING-associated interferonopathy. *Ann Rheum Dis* **75**, e75, doi:10.1136/annrheumdis-2016-210504 (2016).
490 Sanchez, G. A. M. *et al.* JAK1/2 inhibition with baricitinib in the treatment of autoinflammatory interferonopathies. *Journal of Clinical Investigation* **128**, 3041-3052, doi:10.1172/Jci98814 (2018).
491 Volpi, S. *et al.* Efficacy and Adverse Events During Janus Kinase Inhibitor Treatment of SAVI Syndrome. *J Clin Immunol* **39**, 476-485, doi:10.1007/s10875-019-00645-0 (2019).
492 Motwani, M. *et al.* Hierarchy of clinical manifestations in SAVI N153S and V154M mouse models. *Proc Natl Acad Sci U S A* **116**, 7941-7950, doi:10.1073/pnas.1818281116 (2019).
493 Luksch, H. *et al.* STING-associated lung disease in mice relies on T cells but not type I interferon. *J Allergy Clin Immunol* **144**, 254-266 e258, doi:10.1016/j.jaci.2019.01.044 (2019).
494 Siedel, H., Roers, A., Rösen-Wolff, A. & Luksch, H. Type I interferon-independent T cell impairment in a Tmem173 N153S/WT mouse model of STING associated vasculopathy with onset in infancy (SAVI). *Clin Immunol* **216**, doi:ARTN 10846610.1016/j.clim.2020.108466 (2020).
495 Bennion, B. G. *et al.* STING Gain-of-Function Disrupts Lymph Node Organogenesis and Innate Lymphoid Cell Development in Mice. *Cell Reports* **31**, doi:ARTN 10777110.1016/j.celrep.2020.107771 (2020).
496 Wu, J. *et al.* STING-mediated disruption of calcium homeostasis chronically activates ER stress and primes T cell death. *J Exp Med* **216**, 867-883, doi:10.1084/jem.20182192 (2019).
497 Gulen, M. F. *et al.* Signalling strength determines proapoptotic functions of STING. *Nat Commun* **8**, 427, doi:10.1038/s41467-017-00573-w (2017).
498 Warner, J. D. *et al.* STING-associated vasculopathy develops independently of IRF3 in mice. *J Exp Med* **214**, 3279-3292, doi:10.1084/jem.20171351 (2017).
499 Luksch, H. *et al.* Tissue inflammation induced by constitutively active STING is mediated by enhanced TNF signaling. *Elife* **14**, doi:ARTN e10135010.7554/eLife.101350 (2025).

500 Tang, C. H. *et al.* Agonist-Mediated Activation of STING Induces Apoptosis in Malignant B Cells. *Cancer Res* **76**, 2137-2152, doi:10.1158/0008-5472.CAN-15-1885 (2016).
501 Chattopadhyay, S. *et al.* Viral apoptosis is induced by IRF-3-mediated activation of Bax. *Embo Journal* **29**, 1762-1773, doi:10.1038/emboj.2010.50 (2010).
502 Riley, J. S. *et al.* Mitochondrial inner membrane permeabilisation enables mtDNA release during apoptosis. *Embo Journal* **37**, doi:ARTN e9923810.15252/embj.201899238 (2018).
503 McArthur, K. *et al.* BAK/BAX macropores facilitate mitochondrial herniation and mtDNA efflux during apoptosis. *Science* **359**, 883-+, doi:ARTN eaao604710.1126/science.aao6047 (2018).
504 Cui, Y. *et al.* Mycobacterium bovis Induces Endoplasmic Reticulum Stress Mediated-Apoptosis by Activating IRF3 in a Murine Macrophage Cell Line. *Front Cell Infect Microbiol* **6**, 182, doi:10.3389/fcimb.2016.00182 (2016).
505 Petrasek, J. *et al.* STING-IRF3 pathway links endoplasmic reticulum stress with hepatocyte apoptosis in early alcoholic liver disease. *Proc Natl Acad Sci U S A* **110**, 16544-16549, doi:10.1073/pnas.1308331110 (2013).
506 Diepstraten, S. T. *et al.* Putting the STING back into BH3-mimetic drugs for TP53-mutant blood cancers. *Cancer Cell* **42**, doi:10.1016/j.ccell.2024.04.004 (2024).
507 Ning, X. H. *et al.* Apoptotic Caspases Suppress Type I Interferon Production via the Cleavage of cGAS, MAVS, and IRF3. *Mol Cell* **74**, 19-+, doi:10.1016/j.molcel.2019.02.013 (2019).
508 Robinson, N. *et al.* Type I interferon induces necroptosis in macrophages during infection with Salmonella enterica serovar Typhimurium. *Nat Immunol* **13**, 954-962, doi:10.1038/ni.2397 (2012).
509 Legarda, D. *et al.* CYLD Proteolysis Protects Macrophages from TNF-Mediated Auto-necroptosis Induced by LPS and Licensed by Type I IFN. *Cell Rep* **15**, 2449-2461, doi:10.1016/j.celrep.2016.05.032 (2016).
510 Brault, M., Olsen, T. M., Martinez, J., Stetson, D. B. & Oberst, A. Intracellular Nucleic Acid Sensing Triggers Necroptosis through Synergistic Type I IFN and TNF Signaling. *Journal of Immunology* **200**, 2748-2756, doi:10.4049/jimmunol.1701492 (2018).
511 Chen, D. *et al.* PUMA amplifies necroptosis signaling by activating cytosolic DNA sensors. *Proc Natl Acad Sci U S A* **115**, 3930-3935, doi:10.1073/pnas.1717190115 (2018).
512 Gaidt, M. M. *et al.* The DNA Inflammasome in Human Myeloid Cells Is Initiated by a STING-Cell Death Program Upstream of NLRP3. *Cell* **171**, 1110-+, doi:10.1016/j.cell.2017.09.039 (2017).
513 Swanson, K. V. *et al.* A noncanonical function of cGAMP in inflammasome priming and activation. *J Exp Med* **214**, 3611-3626, doi:10.1084/jem.20171749 (2017).
514 Webster, S. J. *et al.* Detection of a microbial metabolite by STING regulates inflammasome activation in response to Chlamydia trachomatis infection. *PLoS Pathog* **13**, e1006383, doi:10.1371/journal.ppat.1006383 (2017).
515 Kelepouras, K. *et al.* The importance of murine phospho-MLKL-S345 in situ detection for necroptosis assessment in vivo. *Cell Death Differ* **31**, 897-909, doi:10.1038/s41418-024-01313-6 (2024).
516 Rickard, J. A. *et al.* TNFR1-dependent cell death drives inflammation in Sharpin-deficient mice. *Elife* **3**, doi:ARTN e0346410.7554/eLife.03464 (2014).
517 Weinlich, R., Oberst, A., Beere, H. M. & Green, D. R. Necroptosis in development, inflammation and disease. *Nat Rev Mol Cell Bio* **18**, 127-136, doi:10.1038/nrm.2016.149 (2017).
518 Gautam, A. *et al.* Necroptosis blockade prevents lung injury in severe influenza. *Nature* **628**, 835-843, doi:10.1038/s41586-024-07265-8 (2024).
519 Santos, L. D. *et al.* TNF-mediated alveolar macrophage necroptosis drives disease pathogenesis during respiratory syncytial virus infection. *Eur Respir J* **57**, doi:Artn 200376410.1183/13993003.03764-2020 (2021).

520 Simpson, J., Spann, K. M. & Phipps, S. MLKL Regulates Rapid Cell Death-independent HMGB1 Release in RSV Infected Airway Epithelial Cells. *Front Cell Dev Biol* **10**, doi:ARTN 89038910.3389/fcell.2022.890389 (2022).

521 Li, S. *et al.* SARS-CoV-2 Z-RNA activates the ZBP1-RIPK3 pathway to promote virus-induced inflammatory responses. *Cell Res* **33**, 201-214, doi:10.1038/s41422-022-00775-y (2023).

522 Bader, S. M. *et al.* Necroptosis does not drive disease pathogenesis in a mouse infective model of SARS-CoV-2 in vivo. *Cell Death Dis* **15**, doi:ARTN 10010.1038/s41419-024-06471-6 (2024).

523 Martinez Lagunas, K. *et al.* Cleavage of cFLIP restrains cell death during viral infection and tissue injury and favors tissue repair. *Sci Adv* **9**, eadg2829, doi:10.1126/sciadv.adg2829 (2023).

524 Newton, K. *et al.* RIPK3 deficiency or catalytically inactive RIPK1 provides greater benefit than MLKL deficiency in mouse models of inflammation and tissue injury. *Cell Death Differ* **23**, 1565-1576, doi:10.1038/cdd.2016.46 (2016).

525 Mandal, P. *et al.* RIP3 Induces Apoptosis Independent of Pronecrotic Kinase Activity. *Mol Cell* **56**, 481-495, doi:10.1016/j.molcel.2014.10.021 (2014).

526 Kumari, S. *et al.* Sharpin prevents skin inflammation by inhibiting TNFR1-induced keratinocyte apoptosis. *Elife* **3**, doi:10.7554/eLife.03422 (2014).

527 Kelepouras, K. *et al.* STING induces ZBP1-mediated necroptosis independently of TNFR1 and FADD. *Nature*, doi:10.1038/s41586-025-09536-4 (2025).

528 Rehwinkel, J. & Gack, M. U. RIG-I-like receptors: their regulation and roles in RNA sensing. *Nature Reviews Immunology* **20**, 537-551, doi:10.1038/s41577-020-0288-3 (2020).

529 Rajput, A. *et al.* RIG-I RNA Helicase Activation of IRF3 Transcription Factor Is Negatively Regulated by Caspase-8-Mediated Cleavage of the RIP1 Protein. *Immunity* **34**, 340-351, doi:10.1016/j.immuni.2010.12.018 (2011).

530 Wallach, D. *et al.* Anti-inflammatory functions of the "apoptotic" caspases. *Ann N Y Acad Sci* **1209**, 17-22, doi:10.1111/j.1749-6632.2010.05742.x (2010).

531 Hornung, V. *et al.* AIM2 recognizes cytosolic dsDNA and forms a caspase-1-activating inflammasome with ASC. *Nature* **458**, 514-U516, doi:10.1038/nature07725 (2009).

532 Ablasser, A. *et al.* RIG-I-dependent sensing of poly(dA:dT) through the induction of an RNA polymerase III-transcribed RNA intermediate. *Nat Immunol* **10**, 1065-U1040, doi:10.1038/ni.1779 (2009).

533 Yoon, J., Kim, S., Lee, M. H. Y. & Kim, Y. Mitochondrial nucleic acids in innate immunity and beyond. *Exp Mol Med* **55**, 2553-2563, doi:10.1038/s12276-023-01121-x (2023).

534 van der Horst, D. *et al.* SAM68 directs STING signaling to apoptosis in macrophages. *Commun Biol* **7**, doi:ARTN 28310.1038/s42003-024-05969-1 (2024).

535 Pang, E. S. *et al.* Discordance in STING-Induced Activation and Cell Death Between Mouse and Human Dendritic Cell Populations. *Front Immunol* **13**, doi:ARTN 79477610.3389/fimmu.2022.794776 (2022).

536 Yang, Z. H. *et al.* ZBP1 senses splicing aberration through Z-RNA to promote cell death. *Mol Cell* **85**, doi:10.1016/j.molcel.2025.03.023 (2025).

537 Xie, F. Y. *et al.* ZBP1 condensate formation synergizes Z-NAs recognition and signal transduction. *Cell Death Dis* **15**, doi:ARTN 48710.1038/s41419-024-06889-y (2024).

538 Zhang, T. *et al.* ADAR1 masks the cancer immunotherapeutic promise of ZBP1-driven necroptosis. *Nature* **606**, 594-+, doi:10.1038/s41586-022-04753-7 (2022).

539 Wang, Y. L. *et al.* Endogenous Retrovirus Elements Are Co-Expressed with IFN Stimulation Genes in the JAK-STAT Pathway. *Viruses-Basel* **15**, doi:ARTN 6010.3390/v15010060 (2023).

540 de Cevins, C. *et al.* Single-cell RNA-sequencing of PBMCs from SAVI patients reveals disease-associated monocytes with elevated integrated stress response. *Cell Rep Med* **4**, doi:ARTN 10133310.1016/j.xcrm.2023.101333 (2023).

541 Stinson, W. A. *et al.* The IFN-gamma receptor promotes immune dysregulation and disease in STING gain-of-function mice. *JCI Insight* **7**, doi:10.1172/jci.insight.155250 (2022).

542 Zhang, S., Zheng, R., Pan, Y. & Sun, H. Potential Therapeutic Value of the STING Inhibitors. *Molecules* **28**, doi:10.3390/molecules28073127 (2023).

543 Zhang, Z. *et al.* Development of Potent and Selective RIPK1 Degraders Targeting Its Nonenzymatic Function for Cancer Treatment. *J Med Chem* **68**, 15120-15136, doi:10.1021/acs.jmedchem.5c01340 (2025).

544 Yu, X. *et al.* Development of a RIPK1 degrader to enhance antitumor immunity. *Nat Commun* **15**, 10683, doi:10.1038/s41467-024-55006-2 (2024).

545 Mannion, J. *et al.* A RIPK1-specific PROTAC degrader achieves potent antitumor activity by enhancing immunogenic cell death. *Immunity* **57**, 1514-1532 e1515, doi:10.1016/j.immuni.2024.04.025 (2024).

546 Li, S. *et al.* Discovery of Covalent MLKL PROTAC Degraders via Optimization of a Theophylline Derivative Ligand for Treating Necroptosis. *J Med Chem* **67**, 15353-15372, doi:10.1021/acs.jmedchem.4c00949 (2024).

547 Rathje, O. H., Perryman, L., Payne, R. J. & Hamprecht, D. W. PROTACs Targeting MLKL Protect Cells from Necroptosis. *J Med Chem* **66**, 11216-11236, doi:10.1021/acs.jmedchem.3c00665 (2023).

548 Wang, Z. *et al.* Structurally Specific Z-DNA Proteolysis Targeting Chimera Enables Targeted Degradation of Adenosine Deaminase Acting on RNA 1. *J Am Chem Soc* **146**, 7584-7593, doi:10.1021/jacs.3c13646 (2024).

549 Huang, R. *et al.* Targeted Degradation of ZBP1 with Covalent PROTACs for Anti-Inflammatory Treatment of Infections. *Angew Chem Int Ed Engl* **64**, e202423524, doi:10.1002/anie.202423524 (2025).

550 Deng, X. X., Li, S. S. & Sun, F. Y. Necrostatin-1 Prevents Necroptosis in Brains after Ischemic Stroke via Inhibition of RIPK1-Mediated RIPK3/MLKL Signaling. *Aging Dis* **10**, 807-817, doi:10.14336/AD.2018.0728 (2019).

551 Chen, K. Q., Wang, S. Z., Lei, H. B. & Liu, X. Necrostatin-1: a promising compound for neurological disorders. *Front Cell Neurosci* **18**, 1408364, doi:10.3389/fncel.2024.1408364 (2024).

552 Cao, L. & Mu, W. Necrostatin-1 and necroptosis inhibition: Pathophysiology and therapeutic implications. *Pharmacol Res* **163**, 105297, doi:10.1016/j.phrs.2020.105297 (2021).

553 Berger, S. B. *et al.* Characterization of GSK'963: a structurally distinct, potent and selective inhibitor of RIP1 kinase. *Cell Death Discov* **1**, 15009, doi:10.1038/cddiscovery.2015.9 (2015).

554 Weisel, K. *et al.* A randomized, placebo-controlled experimental medicine study of RIPK1 inhibitor GSK2982772 in patients with moderate to severe rheumatoid arthritis. *Arthritis Res Ther* **23**, 85, doi:10.1186/s13075-021-02468-0 (2021).

555 Weisel, K. *et al.* A randomised, placebo-controlled study of RIPK1 inhibitor GSK2982772 in patients with active ulcerative colitis. *BMJ Open Gastroenterol* **8**, doi:10.1136/bmjgast-2021-000680 (2021).

556 Weisel, K. *et al.* Response to Inhibition of Receptor-Interacting Protein Kinase 1 (RIPK1) in Active Plaque Psoriasis: A Randomized Placebo-Controlled Study. *Clin Pharmacol Ther* **108**, 808-816, doi:10.1002/cpt.1852 (2020).

557 Hincelin-Mery, A. *et al.* Safety, pharmacokinetics, and target engagement of a brain penetrant RIPK1 inhibitor, SAR443820 (DNL788), in healthy adult participants. *Clin Transl Sci* **17**, e13690, doi:10.1111/cts.13690 (2024).

558 Clot, P. F. *et al.* Immunomodulatory and clinical effects of receptor-interacting protein kinase 1 (RIPK1) inhibitor eclitasertib (SAR443122) in patients with severe COVID-19: a phase 1b, randomized, double-blinded, placebo-controlled study. *Respir Res* **25**, 107, doi:10.1186/s12931-024-02670-z (2024).

559 Jones, N. S. *et al.* A phase I, randomized, ascending-dose study to assess safety, pharmacokinetics, and activity of GDC-8264, a RIP1 inhibitor, in healthy volunteers. *Clin Transl Sci* **16**, 1997-2009, doi:10.1111/cts.13607 (2023).
560 Sun, A. L. A. *et al.* A phase I randomized study to evaluate safety, pharmacokinetics, and pharmacodynamics of SIR2446M, a selective RIPK1 inhibitor, in healthy participants. *Clin Transl Sci* **17**, e13857, doi:10.1111/cts.13857 (2024).
561 Chavez-Tapia, N. *et al.* Safety and efficacy of selective RIPK1 inhibitor SIR1-365 in hospitalized patients with severe COVID-19: A multicenter, randomized, double-blind, phase 1b trial. *J Intensive Med* **5**, 70-78, doi:10.1016/j.jointm.2024.07.003 (2025).
562 Webster, J. D. *et al.* RIP1 kinase activity is critical for skin inflammation but not for viral propagation. *J Leukoc Biol* **107**, 941-952, doi:10.1002/JLB.3MA1219-398R (2020).
563 Zhou, T. *et al.* Identification of a novel class of RIP1/RIP3 dual inhibitors that impede cell death and inflammation in mouse abdominal aortic aneurysm models. *Cell Death Dis* **10**, 226, doi:10.1038/s41419-019-1468-6 (2019).
564 Min, Y. & Yu, Z. Q. GSK'872 Improves Prognosis of Traumatic Brain Injury by Switching Receptor-Interacting Serine/Threonine-Protein Kinase 3-dependent Necroptosis to Cysteinyl Aspartate Specific Proteinase-8-Dependent Apoptosis. *World Neurosurg* **187**, e136-e147, doi:10.1016/j.wneu.2024.04.051 (2024).
565 Park, J. S. *et al.* Neuroprotective and anti-inflammatory effects of the RIPK3 inhibitor GSK872 in an MPTP-induced mouse model of Parkinson's disease. *Neurochem Int* **181**, 105896, doi:10.1016/j.neuint.2024.105896 (2024).
566 Chen, D. *et al.* RIP3-dependent necroptosis contributes to the pathogenesis of chronic obstructive pulmonary disease. *JCI Insight* **6**, doi:10.1172/jci.insight.144689 (2021).
567 Feng, Y. *et al.* GSK840 Alleviates Retinal Neuronal Injury by Inhibiting RIPK3/MLKL-Mediated RGC Necroptosis After Ischemia/Reperfusion. *Invest Ophthalmol Vis Sci* **64**, 42, doi:10.1167/iovs.64.14.42 (2023).
568 Xia, K. *et al.* Discovery of a Potent RIPK3 Inhibitor for the Amelioration of Necroptosis-Associated Inflammatory Injury. *Front Cell Dev Biol* **8**, 606119, doi:10.3389/fcell.2020.606119 (2020).
569 Sun, X., Wu, Y., Xu, F. & Liu, C. Screening of potent RIPK3 inhibitors to attenuate necroptosis and inflammation in mouse traumatic brain injury models. *Exp Neurol* **372**, 114633, doi:10.1016/j.expneurol.2023.114633 (2024).
570 Su, H. *et al.* Structure-based design of potent and selective inhibitors targeting RIPK3 for eliminating on-target toxicity in vitro. *Nat Commun* **16**, 4288, doi:10.1038/s41467-025-59432-8 (2025).
571 Leem, Y. H., Kim, D. Y., Park, J. E. & Kim, H. S. Necrosulfonamide exerts neuroprotective effect by inhibiting necroptosis, neuroinflammation, and alpha-synuclein oligomerization in a subacute MPTP mouse model of Parkinson's disease. *Sci Rep* **13**, 8783, doi:10.1038/s41598-023-35975-y (2023).
572 Jiao, J., Wang, Y., Ren, P., Sun, S. & Wu, M. Necrosulfonamide Ameliorates Neurological Impairment in Spinal Cord Injury by Improving Antioxidative Capacity. *Front Pharmacol* **10**, 1538, doi:10.3389/fphar.2019.01538 (2019).
573 Yang, W. *et al.* Necrosulfonamide ameliorates intestinal inflammation via inhibiting GSDMD-medicated pyroptosis and MLKL-mediated necroptosis. *Biochem Pharmacol* **206**, 115338, doi:10.1016/j.bcp.2022.115338 (2022).
574 Zhang, X. *et al.* Necrosulfonamide Alleviates Acute Brain Injury of Intracerebral Hemorrhage via Inhibiting Inflammation and Necroptosis. *Front Mol Neurosci* **15**, 916249, doi:10.3389/fnmol.2022.916249 (2022).
575 He, F. *et al.* Necrosulfonamide improves post-resuscitation myocardial dysfunction via inhibiting pyroptosis and necroptosis in a rat model of cardiac arrest. *Eur J Pharmacol* **926**, 175037, doi:10.1016/j.ejphar.2022.175037 (2022).
576 Ueda, S. *et al.* Protective effect of necrosulfonamide on rat pulmonary ischemia-reperfusion injury via inhibition of necroptosis. *J Thorac Cardiovasc Surg* **163**, e113-e122, doi:10.1016/j.jtcvs.2021.01.037 (2022).

577 Ros, U. *et al.* MLKL activity requires a splicing-regulated, druggable intramolecular interaction. *Mol Cell* **85**, 1589-1605 e1512, doi:10.1016/j.molcel.2025.03.015 (2025).
578 Li, J. *et al.* Saracatinib inhibits necroptosis and ameliorates psoriatic inflammation by targeting MLKL. *Cell Death Dis* **15**, 122, doi:10.1038/s41419-024-06514-y (2024).